

APPLICATIONS OF PARTICLE ACCELERATORS

M. Uesaka[†], Japan Atomic Energy Commission, Tokyo, Japan

Abstract

Applications of particle accelerators amid global policies of carbon neutrality and economic security, are reviewed. Downsizing of high energy large scaled accelerators by advanced technologies enables a variety of medical and industrial uses. One of the highlights is upgrade of sustainable supply chain of medical radioisotopes by the best mix of research reactors and accelerators. ⁹⁹Mo/^{99m}Tc for diagnosis are going to be produced by low enriched U reactor and proton-cyclotron, electron rhodotron and electron linac. Moreover, the theranostics by ¹⁷⁷Lu (beta) and ²¹¹At/²²⁵Ac (alpha) are going to be realized. Proton-cyclotron and electron linac are expected to produce them soon. This new affordable radiation therapy should play an important role in the IAEA project of Rays of Hopes. Next, proof-of-principle trials of on-site bridge inspection of the portable X-band (9.3 GHz) electron linac X-ray/neutron sources are under way. The technical guideline for the practical inspection is to be formed in a couple of years. They are also expected to apply on-site material analysis at the decommissioning of TEPCO Fukushima Daiichi Nuclear Power Station.

DOWNSIZING OF ACCELERATORS

Particle, energy and choice of accelerator are schematically described in Fig. 1. What kind of reaction is needed gives the choice of particle, energy and finally type of accelerator. If you induce chemical, atomic and nuclear reactions, the ranges of the energy become eV, keV and more than MeV, respectively. In order for the beam to penetrate into a macroscopic specimen, at least hundreds keV is necessary for the beam energy. Depending on the beam energy from hundreds keV to GeV, the choice of accelerator varies as electrostatic, linac, cyclotron and synchrotron, basically. Other new accelerators are now available, too. As for the linear collider, the linac is again chosen to reduce SR loss.

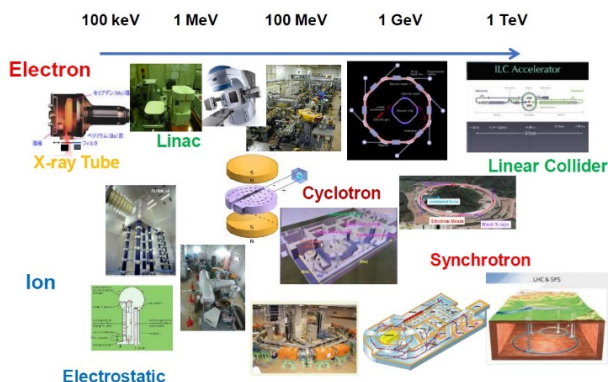


Figure 1: Particle, energy and choice of accelerator.

Downsizing of high energy big accelerator is crucial for saving the space, budget and so on. Higher RFs like S/C/X-bands are adopted for smaller electron linac. Even laser plasma acceleration (THz) and optical dielectric laser acceleration are under development. Concerning ion accelerators, superconducting magnet and optimization of alignment are the key techniques for downsizing. Laser plasma ion injector is expected to be used for the quantum knife, which is the carbon superconducting synchrotron, of QST (National Institutes for Quantum Science and Technology) in Japan.

This downsizing of accelerators offers a variety of applications in a limited space with a reasonable budget and further portability for on-site one-table-top operation [1, 2].

MEDICAL RI PRODUCTION BY BEST MIX OF RESEARCH REACTORS AND ACCELERATORS

Most of medical radioisotopes are produced by highly enriched uranium (U) research reactors and supplied via air transportation in the world. Actually, those research reactors are facing the aging problem. Due to the security on nuclear and supply chain, the current supply chain of ⁹⁹Mo is expected to shift to regional supply chain based on low enriched U research reactors and accelerators such as electron rhodotron, linac and proton cyclotron (see Fig. 2).

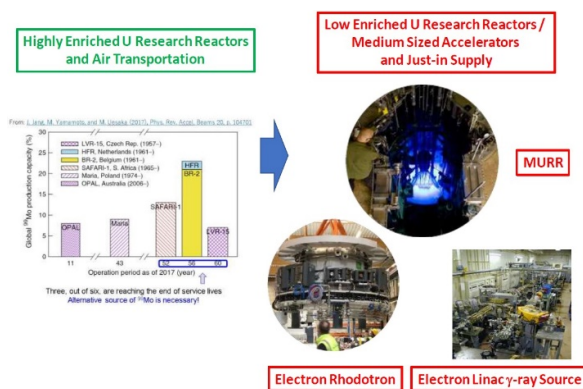


Figure 2: Supply chain shift of ⁹⁹Mo.

Figure 3 explains theranostics (“therapeutic and diagnosis”) by using ²²⁵Ac. These are the very famous and outstanding achievement of treatment of prostate cancer with multiple metastasis by Dr. Kratochwil’s group of University Hospital Heidelberg [3]. Theranostics is a combination of therapy and diagnosis using the different RIs and the same carrier. Here, the ²²⁵Ac-PSMA (Prostate Specific Membrane Antigen) is used as therapy while the ⁶⁸Ga-PSMA PET (Positron Emission Tomography) is used as diagnosis. Not only the prostate cancer but also multiple metastasis disappears remarkably.

[†] uesaka.mits@gmail.com

EIC TRANSVERSE EMITTANCE GROWTH DUE TO CRAB CAVITY RF NOISE: ESTIMATES AND MITIGATION*

T. Mastoridis[†], P. Fuller, P. Mahvi, Y. Matsumura
 California Polytechnic State University, San Luis Obispo, CA, USA

Abstract

The Electron-Ion Collider (EIC) requires crab cavities to compensate for a 25 mrad crossing angle and achieve maximum luminosity. The crab cavity Radio Frequency (RF) system will inject low levels of noise to the crabbing field, generating transverse emittance growth and potentially limiting luminosity lifetime. In this work, we estimate the transverse emittance growth rate as a function of the Crab Cavity RF noise and quantify RF noise specifications for reasonable performance. Finally, we evaluate the possible mitigation of the RF noise induced emittance growth via a dedicated feedback system.

INTRODUCTION AND SIMULATIONS

A theoretical formalism evaluating the transverse emittance growth rate due to RF phase ($\sigma_{\Delta\phi}$) and amplitude ($\sigma_{\Delta A}$, $\Delta A = \Delta V/V$) noise was derived in [1]. The emittance growth rate depends on:

- Operational and accelerator parameters. There is little or no control of these values. This term is effectively inversely proportional to $1/\beta^*$ for a given full crabbing angle θ_{cc} .
- The bunch length. This term is almost constant over the EIC operational range.
- The RF noise power spectral density sampled by the beam. This term depends on the RF and LLRF technology.

Simulations were performed [2] to confirm the above relationships for the EIC, using PyHEADTAIL, a macro-particle tracking code that simulates collective beam dynamics [3]. There was very good agreement between simulations and the theoretical expressions.

BUNCH LENGTH EFFECTS

The EIC Electron Storage Ring (ESR) and Hadron Storage Ring (HSR) bunch lengths vary depending on the collision energy and hadron species. The verified theoretical expressions were used to estimate the effect of the planned EIC bunch lengths on the EIC transverse emittance growth rates due to RF noise, shown in Table 1. The results were also compared to the High-Luminosity Large Hadron Collider (HL-LHC). The terms $C_{\Delta\phi}(\sigma_\phi)$ and $C_{\Delta A}(\sigma_\phi)$ show the scaling of the phase and amplitude noise effects respectively due

Table 1: HL-LHC and EIC ESR/HSR Bunch Length and $C_{\Delta\phi}(\sigma_\phi)$, $C_{\Delta A}(\sigma_\phi)$ Terms

	σ_z (cm)	σ_ϕ (rad)	$C_{\Delta\phi}$	$C_{\Delta A}$
HL-LHC	7.5	0.630	0.726	0.137
ESR 5 GeV	0.7	0.058	0.996	0.002
ESR 10 GeV	0.7	0.058	0.996	0.002
ESR 18 GeV	0.9	0.074	0.995	0.003
HSR 41 GeV	7.5	0.309	0.913	0.043
HSR 100 GeV	7	0.289	0.922	0.038
HSR 275 GeV	6	0.248	0.942	0.029
Au 41 GeV	11.6	0.479	0.816	0.092
Au 110 GeV	7	0.289	0.922	0.038

to the bunch length. σ_ϕ is the bunch length in radians with respect to the crab cavity frequency.

Clearly, there is lower sensitivity to amplitude noise in the EIC than in the HL-LHC due to the shorter bunch length, especially for the ESR. This is significant if a bunch-by-bunch transverse feedback system is employed in the EIC. Such a system acts on the bunch centroid and can thus only counteract the effects of phase noise in the crabbing system. Since phase noise is dominant in the EIC, a bunch-by-bunch transverse feedback can considerably reduce transverse emittance growth due to crab cavity RF noise.

RF NOISE REQUIREMENTS

Using the verified theoretical expressions, we can then set an RF noise requirement to achieve a target transverse emittance growth rate. The target emittance growth rate for the HL-LHC is 1%/hr to minimize the impact on luminosity. For the EIC ESR, the emittance growth rate must be lower than the emittance damping time due to synchrotron radiation. For the HSR, the emittance growth rate target is set equal to the Intra-Beam Scattering (IBS) growth rate. This is possibly an optimistic threshold since the EIC Strong Hadron Cooling is designed to just counteract the IBS to maintain luminosity. There are also additional sources of growth (beam-beam effects for example). So, the HSR thresholds might have to be lowered further in the future.

The target transverse emittance growth rate for all EIC energy cases are presented in [2]. In summary, the ESR target growth rate is many orders of magnitude higher than the rate for the HSR due to the strong synchrotron radiation damping. The HSR also has much higher target rates than the HL-LHC. This is due to the very tight HL-LHC specification to achieve minimal impact on luminosity and the much lower transverse emittance. Using these targets and the theoretical

* This work is partially supported by the U.S. Department of Energy, Office of Science, Office of High Energy Physics, under Award Number DE-SC-0019287.

[†] tmastori@calpoly.edu

MODEL PARAMETERS DETERMINATION IN EIC STRONG-STRONG SIMULATION*

D. Xu[†], Y. Luo, C. Montag, Brookhaven National Laboratory, Upton, NY, USA
Y. Hao, Michigan State University, East Lansing, MI, USA
J. Qiang, Lawrence Berkeley National Laboratory, Berkeley, CA, USA

Abstract

The emittance growth of ion beam is subject to numerical noises in the strong-strong beam-beam simulation for the Electron-Ion Collider (EIC). This paper discusses the impacts of model parameters: number of macroparticles, longitudinal slices, and transverse grids, on the beam size evolution in Particle-In-Cell (PIC) based strong-strong simulations. This study helps us better understand the causes of emittance growth in strong-strong beam-beam simulation.

INTRODUCTION

The beam-beam interaction is one of the most important phenomena to limit the luminosity in colliders. Beam-beam simulation is an essential tool to study beam-beam effects. Two models are often used in simulations: weak-strong and strong-strong. The weak-strong model is used to study the single particle dynamics, while the strong-strong model is used to study the coherent motion.

The particle-in-cell (PIC) approach is widely used in strong-strong simulation. It uses a computational grid to obtain the charge density distribution. The beam-beam force can be calculated from an arbitrary beam distribution by solving the 2D Poisson equation. Both beam distribution are updated during collision.

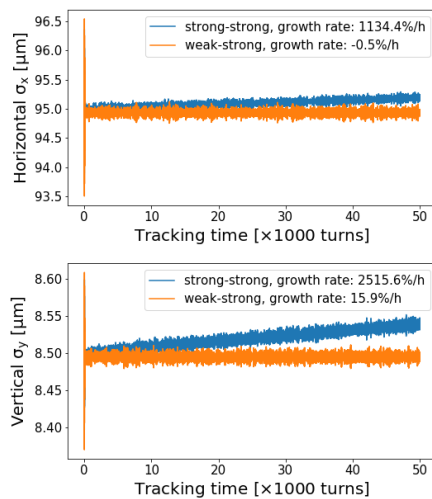


Figure 1: Strong-strong versus weak-strong simulation for EIC. The beam parameters can be found in [1], and the growth rate is linearly fitted from the last 60% tracking data.

* Work supported by Brookhaven Science Associates, LLC under Contract No. DE-SC0012704 with the U.S. Department of Energy.

[†] dxu@bnl.gov

Therefore, this kind of method is self-consistent. However, the PIC based strong-strong simulation is subject to numerical noise. The discrepancy between the weak-strong and strong-strong simulation for Electron-Ion Collider (EIC) has been found, as shown in Fig. 1. It is important to understand the difference in case there is some coherent mechanism shadowed by the large numerical noise.

In the following section, the strong-strong simulation is performed by the code BeamBeam3D [2].

SCALING LAW OF MACROPARTICLES

In PIC simulation, both bunches are represented by a number of macroparticles. In real beam, there are about 10^{11} charged particles per bunch. Due to the limitation of computation resources, only several million macroparticles are used in simulation. Therefore we are sampling the particle distribution at a rate about one in 10^5 particles. The sub-sampling causes artificial Monte Carlo noise.

The numerical errors are unavoidable in PIC simulation. In each time step, each macroparticle is interpolated on a finite grid. The Poisson equation is solved on that grid. The field is then interpolated according to the position of the macroparticle. The interpolations generate numerical errors.

The numerical noise will cause the particle diffusion in phase space. More macroparticles can reduce the impact of numerical errors. If the beam size or emittance growth is purely determined by numerical noise, it should obey the scaling law [3]

$$\frac{1}{\sigma} \frac{d\sigma}{dt} \propto \frac{1}{M} \quad (1)$$

where M is the number of macroparticles, and σ is beam size.

To understand the proton size growth in EIC strong-strong simulation, we scanned the number of electron macroparticles from 0.5 million to 4 million with a step of 0.5 million. All other parameters remain same. The scanned result is shown in Fig. 2. The horizontal and vertical growth rate are fitted with two different models:

$$g_{x,y} = \frac{A_{x,y}}{M B_{x,y}} \quad \text{or} \quad g_{x,y} = \frac{A_{x,y}}{M} + B_{x,y} \quad (2)$$

where $g_{x,y}$ are horizontal or vertical growth rate which is calculated from the tracking data, $A_{x,y}$ and $B_{x,y}$ are fitting parameters. Two more examples of $M_e = 6$ million and $M_e = 8$ million are used to validate the fitting model. From Fig. 2, model 2 is a better guess.

The proton macroparticles are also scanned, and the corresponding results are shown in Fig. 3. We can see that the

TOLERANCES OF CRAB DISPERSION AT THE INTERACTION POINT IN THE HADRON STORAGE RING OF THE ELECTRON-ION COLLIDER*

Y. Luo[†], J. S. Berg, M. Blaskiewicz, C. Montag, V. Ptitsyn, F. Willeke, D. Xu
Brookhaven National Laboratory, Upton, NY, USA

Y. Hao, Facility for Rare Isotope Beams, Michigan State University, East Lansing, MI, USA

J. Qiang, Lawrence Berkeley National Laboratory, Berkeley, CA, USA

V. Morozov, Oak Ridge National Laboratory, Oak Ridge, TN, USA

T. Satogata, Thomas Jefferson National Accelerator Facility, Newport News, VI, USA

Abstract

The Electron Ion Collider (EIC) presently under construction at Brookhaven National Laboratory will collide polarized high energy electron beams with hadron beams with luminosities up to $1 \times 10^{34} \text{cm}^{-2} \text{s}^{-1}$ in the center mass energy range of 20-140 GeV. Due to the detector solenoid in the interaction region, the design horizontal crabbing angle will be coupled to the vertical plane if uncompensated. In this article, we study the tolerances of crab dispersion at the interaction point in the EIC Hadron Storage Ring (HSR). Both strong-strong and weak-strong simulations are used. We found that there is a tight tolerance of vertical crabbing angle at the interaction point in the HSR.

INTRODUCTION

The Electron Ion Collider (EIC) presently under construction at Brookhaven National Laboratory will collide polarized high energy electron beams with hadron beams with luminosities up to $1 \times 10^{34} \text{cm}^{-2} \text{s}^{-1}$ in center mass energy range of 20-140 GeV [1]. To reach such a high luminosity, we adopt high bunch intensities for both beams, small transverse beam sizes at the interaction point (IP), a large crossing angle 25 mrad, and a novel strong hadron cooling in the Hadron Storage Ring (HSR) at store energies. To compensate the geometric luminosity loss due to the large crossing angle, crab cavities are installed on both sides of IP to restore head-on collision.

Based on the operational experiences of previous and existing lepton and hadron colliders, we must have a very good control of optics parameters at IP to achieve the design luminosity and to maintain a stable physics store. Those parameters include orbit, Twiss parameters, momentum dispersion, local coupling, and so on. In the EIC, the horizontal crab cavities will create a z -dependent horizontal offset along the bunch length at IP. Here z is the longitudinal offset w.r.t. the bunch center. Conventionally, we define dx/dz as the horizontal crab dispersion. There are other three terms of first order crab dispersion: dx'/dz , dy/dz , dy'/dz . dy/dz is the vertical crab dispersion. In this article, we also call dx/dz and dy/dz at IP as horizontal and vertical crabbing angles.

We adopt a local crabbing compensation scheme for the EIC. We need to have $dx/dz = 12.5 \times 10^{-3}$ at IP and to keep other 3 first order crab dispersion to be zero or close to zero as possible. However, due to the detector solenoid in the interaction region (IR), horizontal crab dispersion may be coupled to the vertical plane and generate non-zero vertical crab dispersion at IP. To avoid vertical orbit excursions at the non-collisional symmetric points in IRs, we intentionally tilt the Electron Storage Ring (ESR) by 200 μrad with the axis connecting IP6 and IP8. Therefore, the ESR and HSR will not be in a same horizontal plane anymore. This generates an equivalent vertical crabbing angle 50 μrad at IP for both rings. Other coupling sources, such as residual magnet roll errors, vertical orbit in sextupoles, and crab cavity roll error, also can couple horizontal crab dispersion to vertical plane.

Vertical crab dispersion or vertical crabbing angle at IP will generate a z -dependent vertical offset along the bunch length. Offset beam-beam interaction may cause the proton beam emittance blow up and leads to a bad proton beam life. In this article, we will study the tolerances of crab dispersion at IP, in particular, we will focus on the vertical crab dispersion dy/dz . The design beam and machine parameters for the collision between polarized 10 GeV electrons and 275 GeV protons are used. At this mode, the design transverse beam sizes at IP are (95 μm , 8.5 μm). Both beams reach their maximum beam-beam parameters in the EIC, that is, 0.1 for the electron beam and 0.015 for the proton beam [2]. The design peak luminosity is $1.0 \times 10^{34} \text{cm}^{-2} \text{s}^{-1}$.

STRONG-STRONG SIMULATION

Two kinds of beam-beam simulation models have been used for the EIC: strong-strong and weak-strong [3–5]. In the strong-strong model, both beams are represented by a half to 2 millions of macro-particles. At IP, each bunch is longitudinally sliced. Each slice of one bunch will interact with all slices from the opposite bunch in a timed order. The space charge or beam-beam force is calculated with Particle-in-cell (PIC) Poisson solver. The ring lattice is simply represented by a linear uncoupled 6×6 matrix. Synchrotron motion is included.

In our simulation, the horizontal crab cavities are virtually placed on both sides IP with an exact $\pi/2$ horizontal betatron phase advances to IP. This arrangement constructs a closed local horizontal crab dispersion bump. To introduce a vertical crab dispersion dy/dz at IP, similarly we place a vertical

* Work supported by Brookhaven Science Associates, LLC under Contract No. DE-SC0012704 with the U.S. Department of Energy.

[†] yluo@bnl.gov

EXPERIMENTS ON A CONDUCTION COOLED SUPERCONDUCTING RADIO FREQUENCY CAVITY WITH FIELD EMISSION CATHODE

Y. Ji, R.C. Dhuley, C. Edward, J.C.T. Thangaraj
Fermi National Accelerator Laboratory, Batavia, IL, USA

D. Mihalcea, P. Piot O. Mohsen

Department of Physics and Northern Illinois Center for Accelerator & Detector Development,
Northern Illinois University, DeKalb, IL, USA

I. Salehinia, V. Korampally

Department of Engineering, Northern Illinois University, DeKalb, IL, USA

Abstract

To achieve Ampere-class electron beam accelerators the pulse delivery rate need to be much higher than the typical photo injector repetition rate of the order of a few kilohertz. We propose here an injector which can, in principle, generate electron bunches at the same rate as the operating RF frequency. A conduction-cooled superconducting radio frequency (SRF) cavity operating in the CW mode and housing a field emission element at its region of high axial electric field can be a viable method of generating high-repetition-rate electron bunches. In this paper, we report the development and experiments on a conduction-cooled Nb₃Sn cavity with a niobium rod intended as a field emitter support. The initial experiments demonstrate ~0.4 MV/m average accelerating gradient, which is equivalent of peak gradient of 3.2 MV/m. The measured RF cavity quality factor is 1.4×10^8 slightly above our goal. The achieved field gradient is limited by the relatively low input RF power and by the poor coupling between the external power supply and the RF cavity. With ideal coupling the field gradient can be as high as 0.6 MV/m still below our goal of about 1 MV/m.

INTRODUCTION

High current (>100 mA) electron beam accelerators have applications ranging from building new radiation sources to medical applications and water treatment in large metropolitan areas.[1] The high charge beam requires continuous wave (CW) operation of the accelerator and electron bunch emission rate close to the operating RF frequency.

Unlike normal conducting copper cavities, superconducting RF (SRF) cavities made of niobium or Nb₃Sn can be operated in the CW mode, which makes them an ideal building block of a high-repetition rate field emission electron source. Normally, SRF cavities are operated in liquid helium that provides the cryogenic environment. However, they can also be conduction-cooled with compact, closed-cycle 4 K cryocoolers as demonstrated by Dhuley et al. [2, 3]. In this work, Dhuley et al. produced the first-ever practical CW gradients using an SRF cavity without liquid helium [4, 5], making the SRF cavity highly accessible for other applications such as high-repetition-rate field emitters.

Mohsen et al. has developed a multiphysics simulation model for a SRF cavity based field [6]. Using Dhuley et

al.'s conduction-cooled 650 MHz Nb₃Sn cavity and pulse tube cryocooler parameters, Mohsen calculated that a niobium rod inside the cavity with its tip near the center of the cavity can produce peak field of 8 MV/m at its tip. Using Dhuley's conduction-cooled SRF cavity test setup, Mohsen et al.'s initial experiments using a niobium rod placed inside a bulk niobium cavity produced a tip CW gradient of ~0.9 MV/m. The performance in the experiment was limited by contamination on the stem and the flange. To overcome this limitation, the next set of experiments were conducted using a high-Q₀ Nb₃Sn cavity and a surface-cleaned niobium rod. This paper presents the preliminary results from the new configuration and future experiment plans.

EXPERIMENTAL SETUP

The cavity used in this experiment is a single-cell, 650 MHz, SRF grade niobium (RRR>300) niobium cavity coated with Nb₃Sn on the RF surface. The RF power system provides up to 10 W of CW power at f=650 MHz and Δf=5 MHz. The cavity is cooled by high purity 5N aluminum thermal link, connected to a cryocooler with 2 W of cooling capacity at 4.2 K.

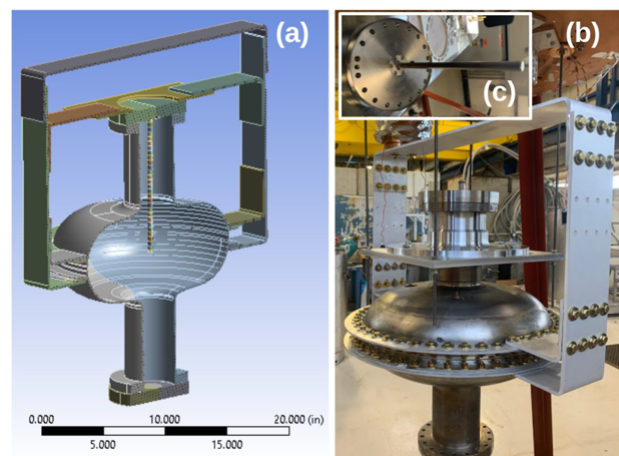


Figure 1: (a) CAD model of the support rod inside the RF cavity. (b) Picture of the RF cavity and (c) the support rod with flange.

Figure 1 displays the rod used to extend the field-emitter into the center of the SRF cavity, where the electric

DIAGNOSES AND REPAIR OF A CRACK IN THE DRIFT TUBE LINAC ACCELERATING STRUCTURE AT LANSCE*

W. C. Barkley[†], D. A. Bingham, M. J. Borden, J. A. Burkhart, D. J. Evans,
 J. T. M. Lyles, J. P. Montross, J. F. O'Hara, B. J. Roller, M. Sanchez Barrueta
 Los Alamos National Laboratory, Los Alamos, NM, USA

Abstract

Many were perplexed at the inability of Module 3 at LANSCE to maintain full power and duty factor while running production beam. First occurring during the 2018 production run, the Drift Tube LINAC module began to intermittently trip off, leading to a series of root cause investigations. These analyses included eliminating the usual suspects: vacuum leak, debris in tank, drive line window, amplifier tube degradation, etc...The throttling back of repetition rate from 120 to 60 Hz allowed continued production with a diminished beam, one that reduced neutron flux to three experimental areas. During the annual long shutdown in 2019, a more thorough investigation involving the use of x-ray detection, high resolution camera and borescope was performed. Although x-ray detection was able to broadly indicate areas of arcing, the best diagnostics turned out to be the high resolution camera and borescope. After a tenacious search, a 30 cm long crack in a weld was discovered at one of the ion port grates. Because this area was inaccessible from the outside for welding and in a confined space, non-intrusive repairs were unsuccessfully tried first. Ultimately, an expert welder had to enter the tank under high-level institutional management scrutiny to perform a weld on copper with very unfamiliar welding conditions. This paper describes the diagnoses, discovery, unsuccessful solutions and ultimate repair of the crack in the accelerating structure.

INTRODUCTION

The Drift Tube LINAC (DTL) at LANSCE accelerates two species of proton beam from 750 keV to 100 MeV energy through a set of four accelerating structures (Fig. 1). The four modules accomplish this acceleration when driven with 201.25 MHz RF power that generates electrical fields in the regions between the noses of each drift tube. The beams experience nearly zero fields while inside the drift tubes.

Arcing may occur when initiated by a vacuum leak, debris, compromised vacuum window or other initiating mechanism. When excessive arcing in Module 3 occurred during the middle of the 2018 run cycle, the usual causes were investigated and eliminated. As the staff pursued the problem further, a work around was construed whereby the machine could be operated at reduced repetition rate (60 vs. 120 Hz, Table 1) to preserve run cycle availability rather than taking the downtime hit and its unpredictable duration. Although neutron experiments are accomplished

more efficiently with greater flux, the experimental areas at LANSCE are not all dependent on repetition rate.



Figure 1: LANSCE DTL modules.

Table 1: History of Stable RF, Module 3

Date	PRF Hz	RF Gate Length usec	Beam Pulse usec	Average RF Power kW
7/16/2017	120	1010	625	153.75
11/16/2017	120	810	475	116.85
11/17/2017	120	830	525	129.15
11/27/2017	120	830	565	138.99
6/28/2018	120	880	625	153.75
9/18/2018	120	760	520	127.92
9/20/2018	120	700	400	98.4
9/24/2018	60	1010	625	76.875
9/24/2018	60	1060	625	76.875
9/26/2018	60	1060	725	89.175
10/9/2018	60	1040	725	89.175

A more disciplined and thorough diagnosis for the arc down phenomenon could be accomplished during the long outage, scheduled for a few months away. Resources were dedicated to this vital task and it was performed systematically such that the likely causes could be entertained and accepted or eliminated.

Diagnosis

Any tests to diagnose the Module 3 arcing issue with RF on would need to be performed at the end of the run cycle

* Work supported by the United States Department of Energy, National Nuclear Security Agency, under contract DE-AC52-06NA25396.

[†] barkley@lanl.gov

IN SITU PLASMA PROCESSING OF SUPERCONDUCTING CAVITIES AT JLAB*

T. Powers[†], N. Brock, T. Ganey

Thomas Jefferson National Accelerator Facility, Newport News, VA, USA

Abstract

Jefferson Lab has an ongoing R&D program in plasma processing which is close to going into production processing in the CEBAF accelerator. Plasma processing is a common technique for removing hydrocarbons from surfaces, which increases the work function and reduces the secondary emission coefficient. The initial focus of the effort is processing C100 cavities by injecting RF power into the HOM coupler ports. The goal will be to improve the operational gradients and the energy margin of the CEBAF linacs by processing cryomodules in situ. Results from processing a cryomodule in the cryomodule test bunker as well as cavity vertical test results will be presented. This work describes the systems and methods used at JLAB for processing cavities using an argon/oxygen gas mixture.

METHODS

Plasma processing [1] is being explored by a number of facilities that work with superconducting cavities [2]. Between 2015 and 2018 it was used to process 32 cavities in the SNS accelerator at ORNL where they achieved an average improvement in operational gradients of 2.5 MV/m [3, 4]. Unlike helium processing which relies on ion bombardment of the field emitters, plasma processing uses atomic oxygen produced in an RF plasma to break down the hydrocarbons on the surface of the cavity. Processing of SRF cavities is done using a mixture noble gas such as argon, neon or helium and oxygen. The discharge is operated at pressures between 50 and 250 mTorr.

Gas Supply and Vacuum Systems.

Process gas was supplied by a mobile cart that had a cylinder of argon, 80% argon / 20% oxygen, and 95% argon / 5% methane. Using a series of valves and flow controllers we were able vary the percentage of oxygen in the process gas as well as to regulate the flow and pressure in the cavities. The pumping system consisted of two turbo molecular pumps, a 300 L/s primary pump and a 70 L/s secondary pump. The 70 L/s pump was used as part of a differentially pumped RGA system. In addition to monitoring the argon to oxygen ratio, the RGA is used to monitor H₂, CO, CO₂ and H₂O, which are hydrocarbon fragments that are produced when the free oxygen interacts with the hydrocarbons. Two gas supply and pumping systems have been fabricated which will allow us to process two cryomodules simultaneously in the CEBAF accelerator.

RF System

Two 2-channel and one 1-channel RF systems which is described in [5], have been fabricated. Each RF system is capable of processing one cavity at a time by applying up to 100 W of RF power through a higher order mode (HOM) coupler antenna. The output of two RF sources and network analyzer are combined and after amplification are applied to one of the HOM antennae on a C100 cavity. The system monitors the incident and reflected power and the power that is emitted from the fundamental power coupler. The latter is effectively acting as a field probe for the electric field in the cell furthest away from the HOM couplers.

Figure 1 is a plot of the relative electric field amplitudes for some of the modes of a C100 cavity. The data was taken using standard bead pull methods and scaled by the real part of S₁₁ [5, 6]. Control over which cell or combination of cells is processed is accomplished by selecting which of the field patterns is applied to the cavity. Using the modes in Fig. 1 as an example if one were to apply RF to the HOM coupler at 1913.24 MHz and increase the RF power a plasma would ignite in the cell with the highest RF fields, which is cell 4. Moving from cell to cell is accomplished by turning on an additional RF source at the frequency that supports a plasma in the new cell then turning off the original cell. It is described in detail in Ref. [5].

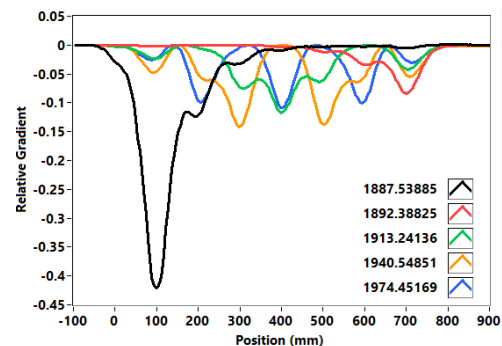


Figure 1: Relative gradient for the 5 modes that are used for plasma processing a C100 cavity. Note: the center of the cells are on even 100 mm intervals between 100 and 700 mm.

Using our off-line system we were able to confirm that by applying two frequencies, we could establish plasma in two adjacent cells. The standard processing combination that was chosen was to process in cell 7, then 5/6, then 3/4, then 1/2. Using this protocol reduced the processing time by 40%.

Cryomodule Issues

One of the issues with processing a C100 cryomodule is that both of the HOM coupler antennas are located on the

* Funding provided by SC Nuclear Physics Program through DOE SC Lab funding announcement Lab-20-2310.

[†] powers@jlab.org

SPIN POLARIZED ELECTRON PHOTOEMISSION AND DETECTION STUDIES

A. C. Rodriguez Alicea, University of Puerto Rico - Mayaguez, Mayaguez, PR, USA
O. Chubenko, S. Karkare, Arizona State University, Tempe, AZ, USA
R. Palai, University of Puerto Rico - Rio Piedras, San Juan, PR, USA
L. Cultrera, Brookhaven National Laboratory, Upton, NY, USA

Abstract

The experimental investigation of new photocathode materials is time-consuming, expensive, and difficult to accomplish. Computational modelling offers fast and inexpensive ways to explore new materials, and operating conditions, that could potentially enhance the efficiency of polarized electron beam photocathodes. We report on Monte-Carlo simulation of electron spin polarization (ESP) and quantum efficiency (QE) of bulk GaAs at 2, 77, and 300 K using the data obtained from Density Functional Theory (DFT) calculations at the corresponding temperatures. The simulated results of ESP and QE were compared with reported experimental measurements, and showed good agreement at 77 and 300 K.

INTRODUCTION

Photocathodes are very important in accelerator physics, they generate high brightness spin polarized electron beams that will allow scientist to unravel mysteries about the fundamental particle interactions and cosmology history [1]. Spin polarized electron beams can be characterized by quantum efficiency (QE), electron spin polarization (ESP), and lifetime. GaAs photocathodes as a source for spin polarized electrons was first proposed in 1974, and shortly after experiments obtained 40% ESP and 10% QE from bulk crystals of the material using circularly polarized light [2]. Due to the degenerate light-hole and heavy-hole band states in the $P_{3/2}$ valence band, the theoretical limit of ESP for these bulk GaAs sources was about 50%. To overcome this problem, strained layers (SL) of GaAs alloys have been studied, since the pseudomorphic strain alleviates the electron level's degeneracy limitation. Although the SL enabled measured ESP over 90%, its QE drastically dropped to below 1% [3]. Deploying a distributed Bragg reflectors (DBR) allows the material to retain more light, and increases the QE to around 10% [4]. Several other approaches have been explored, but desirable beam properties, high ESP with high QE and long lifetime, have not been achieved [5], which warrants further investigation beyond III-V semiconductors as photocathodes.

The experimental investigation of new photocathode materials is time-consuming, expensive, and difficult to accomplish. Computational modeling offers an inexpensive way to explore new materials and operating conditions that could potentially enhance the efficiency of GaAs based photocathodes, with relatively more ease and at much lower cost. The main objective of the present work is to develop a framework where the *ab-initio* numerical calculation data of electronic

band structures can be used to provide inputs to a Monte Carlo (MC) simulations, that have successfully reproduced experimental observations of QE and ESP in bulk GaAs [6], in order to predicts the photoemission from novel materials. The QE and ESP strongly depend on the experimental conditions such as, photon energy and temperature. The present work investigate how these parameters can change with temperature for bulk GaAs and compare the results with experimental observations from Liu *et al.* [7]. Once the framework has been completed for this material, we can explore new ones and screen possible candidates for experimental studies, making the overall process of research and development more feasible.

CALCULATION DETAILS

Density functional theory (DFT) calculations can predict various macroscopic properties of materials, taking as input only the basic crystal structure. For mott insulators, in which the correlation and spin attributes of the material makes their electrical properties deviate from classical predictions, DFT calculations tend to over-delocalize valence electrons and to over-stabilize conduction bands, resulting in smaller intrinsic energy gaps compared to what is observed experimentally. The Hubbard correction takes into account the energy contributions of spin correlations and enables for more precise predictions for such materials [8]. This approach has been implemented in this work using *Quantum Espresso* program package to obtain accurate prediction of GaAs electronic band structure, dielectric permittivity, and phonon dispersion of GaAs [9].

All the energy approximations used for DFT calculation are dependent on the lattice structure, which is affected by temperature variations. To compensate for the temperature variation, we changed the lattice constant of the crystal following the empirical formula $a = a_o + 7.3321 \times 10^{-5}(T)$, where a_o is the optimal lattice for 0 K, found to be 10.4549 a. u. with the relaxation calculation [10]. We selected 2, 77 and 300 K for the representative temperatures of liquid Helium, liquid Nitrogen and room temperature respectively.

The formulas used for the calculation of different parameters are as follow; from the energy in k -space diagrams (band structure) we can estimate the effective masses using the relation $1/m^* = d^2E/dk^2 m_0/\hbar^2$ [11]. The selected path goes through the three symmetry points in the Brillouin zone, L , X , and Γ , in three different directions to give the effective masses as harmonic average, $m^* = 3 \cdot (\frac{1}{m_x^*} + \frac{1}{m_y^*} + \frac{1}{m_z^*})^{-1}$ [12].

PRELIMINARY STUDY OF A HIGH GAIN THz FEL IN A RECIRCULATING CAVITY*

A. Fisher[†], P. Musumeci

Department of Physics and Astronomy, University of California Los Angeles, CA, USA

Abstract

Recent experimental results have shown a large improvement in the single pass efficiency of an FEL at 160 GHz by introducing a waveguide to match the average electron longitudinal velocity to the subluminal radiation group velocity. We now consider the possibility of using a cavity to recirculate a portion of the THz radiation to seed successive electron bunch passes through the undulator. The effects of waveguide dispersion are discussed along with a method to correct the group velocity delay of the radiation pulse. Finally, we simulate power outcoupling for four electron beam passes and evaluate the benefit of dispersion correction.

INTRODUCTION

Among the electromagnetic radiation sources in the 0.1-10 THz frequency range, FELs have the unique ability to provide high peak and average power at tunable frequencies with repetition rates limited only by the availability of electron beams. While FEL lasing conditions are relaxed at longer wavelengths, radiation diffraction and FEL slippage reduce the interaction length and gain for a single pass. For this reason, most operating and planned THz FEL facilities employ cavity designs where the gain can be increased over hundreds of micropulses [1–6].

A promising option to increase the single pass gain is a THz waveguide FEL where the radiation group velocity is tuned to match the average longitudinal velocity of the electron beam, eliminating slippage effects. The electron beam can then be compressed without limit, increasing the peak current and making it possible to seed the interaction with a large bunching factor. Recent experimental results have demonstrated 10% average energy extraction from a 5.5 MeV electron beam in a 1-meter undulator [7]. In this high gain regime, the interaction quickly saturates and significant tapering of the undulator parameters is necessary to maintain the resonant conditions [8].

The efficiency can be increased further by recirculating a fraction of the produced THz radiation to seed the interaction of successive electron bunches [9, 10]. This could increase the frequency range of the waveguide FEL as the gain is limited at higher frequencies by wakefield effects, smaller bunching factors, and reduced charge transmission. Additionally, it could compensate for cases where the electron beam brightness is insufficient to achieve large energy extraction in a single pass.

The article is organized as follows. First we discuss a preliminary cavity design for the Pegasus beamline including

comments on undulator tapering. Next we present ideal simulations with no outcoupling to emphasize the benefit of seeding with radiation. Finally, we discuss a method for dispersion correction and its effect on the interaction at different power outcoupling fractions.

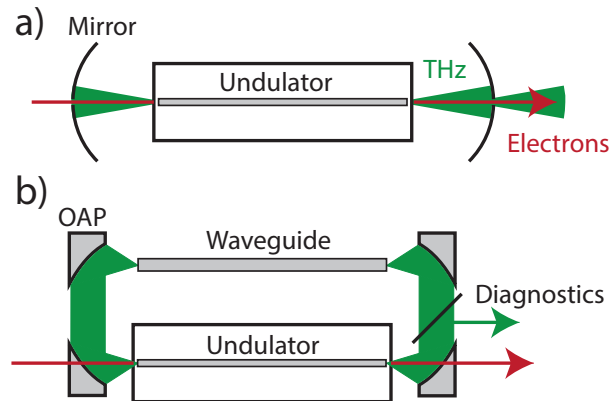


Figure 1: Two cavity designs for the Pegasus beamline with differing complexity.

CAVITY DESIGN

Figure 1 shows two possible cavity designs for the Pegasus beamline at UCLA where space constraints in the bunker restrict the electron beam path to a straight line. Electron bunches are generated by illuminating a Cu photocathode in a RF gun with a 40 fs laser pulse. Multiple beams with tunable delay (necessary to inject electron bunches at the decelerating radiation phase) can be produced by separating the pulse with polarizing beamsplitters and using tunable delay lines.

The first cavity design consists of two concave mirrors on either side of the undulator. A small hole in the upstream mirror is needed to accommodate the focused, incoming electron beam and the radiation is outcoupled with a larger hole in the downstream mirror. The simple design is appealing, but the radiation will experience significant waveguide dispersion on the return trip reducing the peak electric field that can seed the next pass. A more complicated but versatile design uses an off-axis parabolic (OAP) mirror to reflect the THz radiation outside the beamline. An outcoupling THz beamsplitter reflects some radiation to a diagnostics section for spectral and temporal measurements. A second waveguide (with larger radius to reduce dispersion) confines the radiation and limits diffraction losses of the large bandwidth pulse. We can easily switch between multiple pass measurements and single pass measurements by replacing

* This work was supported by DOE grant No. DE-SC0009914.

[†] afisher000@g.ucla.edu

UNCERTAINTY QUANTIFICATION OF BEAM PARAMETERS IN A LINEAR INDUCTION ACCELERATOR INFERRED FROM BAYESIAN ANALYSIS OF SOLENOID SCANS*

M. A. Jaworski, D. C. Moir, S. Szustkowski
 Los Alamos National Laboratory, Los Alamos, NM, USA

Abstract

Linear induction accelerators (LIAs) such as the DARHT at Los Alamos National Laboratory make use of the beam envelope equation to simulate the beam and design experiments. Accepted practice is to infer beam parameters using the solenoid scan technique with optical transition radiation (OTR) beam profiles. These scans are then analyzed with an envelope equation solver to find a solution consistent with the data and machine parameters (beam energy, current, magnetic field, and geometry). The most common code for this purpose with flash-radiography LIAs is *xtr*. The code assumes the machine parameters are perfectly known and that beam profiles will follow a normal distribution about the best fit and solves by minimizing a χ^2 -like metric. We construct a Bayesian model for the beam parameters allowing matching parameters, such as solenoid position, to vary within reasonable uncertainty bounds. Posterior distribution functions are constructed using Markov-Chain Monte Carlo (MCMC) methods to evaluate the accuracy of the *xtr* solution uncertainties and the impact of finite precision in measurements.

INTRODUCTION

Without some quantification of uncertainties in the measurement and analysis of experiments, model differentiation becomes difficult or impossible. In fields with ever increasing accuracy of models and theories, the demands on experimental measurement precision and analysis are even greater if new advances are to be made. Such is the case in the mature technology of linear induction accelerators (LIAs) such as the DARHT [1].

More practical considerations also demand uncertainty quantification (UQ) efforts. Multiple measurements techniques may be applied to the same physical quantity at which point a comparison of measurement precision may be decisive. Efforts in this direction include an analysis of the solenoid scan method (e.g. Ref. [2]), emittance mask methods [3], or PIC-based analysis of the same experiments [4].

THEORY AND BACKGROUND

Analysis of solenoid scans in LIAs have continuously developed with code capabilities and experimental methods [2, 4]. The most common analysis determines a set of beam initial conditions, upstream of the solenoid magnet being varied, which can then be used to simulate the beam

through the remainder of a machine. The beam envelope equation is most relevant to this type of analysis as it includes space-charge effects on the beam; various derivations can be found in the literature [5, 6]. The general form of the envelope equation is given as follows:

$$r_m'' + \frac{\gamma' r_m'}{\beta^2 \gamma} + \frac{\gamma'' r_m}{2\beta^2 \gamma} + \left(\frac{qB}{2mc\beta\gamma} \right)^2 r_m \cdots - \frac{\epsilon_N^2}{(\beta\gamma)^2 r_m^3} - \frac{K}{r_m} = 0 \quad (1)$$

Leading order effects on the propagation of the beam arise from modifications to the space charge of the beam as might arise from neutralizing of the space charge, current, or ground planes impinged by the beam (e.g. foil focusing [3, 7]).

In beam envelope solutions, the beam edge, a , is associated with the 2 RMS radius of the marginal distribution of the beam. When evaluating the quantities in Eq. (1) at this position, significant corrections are found by inclusion of beam potential depression (BPD). Taking into account this reduction in γ with respect to the beam radius and wall radius creates BPD modifications to Eq. (1) when calculating γ'_a and γ''_a .

Two codes are compared: *xtr* and *simpleEnvelope*. The *xtr* code has been developed over a number of years by personnel at LANL and most physics effects have been validated against experimental measurements. In addition to BPD effects, *xtr* also takes into account beam diamagnetism effects, which can reduce the effective field of a solenoid magnet by $\approx 1\%$ [8]. A new, python-based code, *simpleEnvelope*, has been developed to further simulate LIAs with the beam envelope code and enable new modes of analysis. Effects listed above related to space charge and BPD are included in both codes, though *simpleEnvelope* has not implemented beam diamagnetism.

Analysis of Solenoid Scans

xtr implements an internal profile optimization routine to obtain beam initial radius, divergence, and emittance (R_0, R'_0 , and ϵ_N) whereas *simpleEnvelope* is called within a Bayesian framework script: *BayesBeam*. The *xtr* solution is obtained by minimizing a χ^2 -like figure of merit given as:

$$\text{FOM}_{\text{xtr}} = \left[\sum_{i=1}^N \frac{(r_{\text{meas},i}/r_{t,i} - 1)^2}{N} \right]^{1/2} \quad (2)$$

* This work was supported by the U.S. Department of Energy (Contract No. 89233218CNA000001).

ERL-BASED COMPACT X-RAY FEL*

F. Lin†, V.S. Morozov, Oak Ridge National Laboratory, Oak Ridge, TN, USA
 J. Guo, Y. Zhang, Thomas Jefferson National Accelerator Facility, Newport News, VA, USA

Abstract

We propose to develop an energy-recovery-linac (ERL)-based X-ray free-electron laser (XFEL). Taking advantage of the demonstrated high-efficiency energy recovery of the beam power in the ERL, the proposed concept offers the following benefits: i) recirculating the electron beam through high-gradient superconducting RF (SRF) cavities shortens the linac, ii) energy recovery in the SRF linac saves the klystron power and reduces the beam dump power, iii) the high average beam power produces a high average photon brightness. In addition, such a concept has the capability of delivering optimized high-brightness CW X-ray FEL performance at different energies with simultaneous multipole sources. In this paper, we will present the preliminary results on the study of feasibility, optics design and parameter optimization of such a device.

INTRODUCTION

A Free-Electron Laser (FEL) that has been invented and experimentally demonstrated in the 1970s [1, 2] holds a great potential to serve as a high-power and coherent photon source. FEL performance extends beyond the limitations of fully coherent laser light sources by covering a broad range of wavelength from infrared down to X-ray with a stable and well-characterized temporal structure in the femtosecond time domain. Particularly, XFEL allows scientists to probe the structure of various molecules in detail, and simultaneously explore the dynamics of atomic and molecular processes on their own time scales.

Techniques have been developed and improved to amplify the spontaneous radiation to provide intense quasi-coherent radiation [3-6]. The FEL process strongly depends on the local electron beam properties: current, energy, emittance and energy spread. Therefore, all existing XFELs [7-15] are driven by linear accelerators to ensure preservation of the electron beam quality from the source for achieving a high peak brightness. Normal conducting RF cavities, with very high accelerating gradients of up to 60 MV/m, are used to keep the linac length as short as possible. This limits the bunch repetition rate up to about 100 Hz in a pulsed beam operation mode, resulting in average photon brightness of as much as 10 orders of magnitude lower than the peak one. Therefore, several XFEL facilities [9, 13] have started considering a CW beam operation mode that is made possible by the high-gradient SRF technology. There were two ERL-based concepts [16, 17]

explored to produce FELs in the UV and/or soft X-ray regions.

CONCEPT

We propose an ERL-based compact XFEL facility, schematically illustrated in Fig. 1. Note that the energy gain of 2 GeV from the SRF is chosen for this study only, considering relatively realistic SRF gradient, magnet fields, and geometric footprint of such a facility. Optimization of these parameters can be carried out in each individual case. We leverage the ongoing world-wide efforts on the further improvement of injector and XFEL techniques and focus on the feasibility study of the accelerator system.

Electron beams are generated from the source and accelerated to 250 MeV before the first bunch compression (BC). Then the beams are accelerated in the ERL by SRF cavities with the desired energy gain of 2 GeV. Since space charge effects are significantly suppressed at the GeV electron beam energy, one can utilize the first arc to compress the beam for the second time if needed. The electron beams are either directed into different undulators that can be designed and optimized for particular XFEL radiations parameters or bypass the undulator sections. Electron beams that have been used to produce XFEL can be energy recovered in the ERL after the second arc and dumped downstream. The bypassed electron beams will double energy up to ~ 4 GeV after the ERL and propagate through the third arc. Same as in the first ~ 2 GeV energy loop, the ~ 4 GeV electron beams will either be directed into different undulator sections or bypass the undulators. Again, the electron beams that have produced XFEL will be energy recovered and dumped, and the bypassed electron beams will be further accelerated to ~ 6 GeV for XFEL production and energy-recovered in the ERL before the final dump.

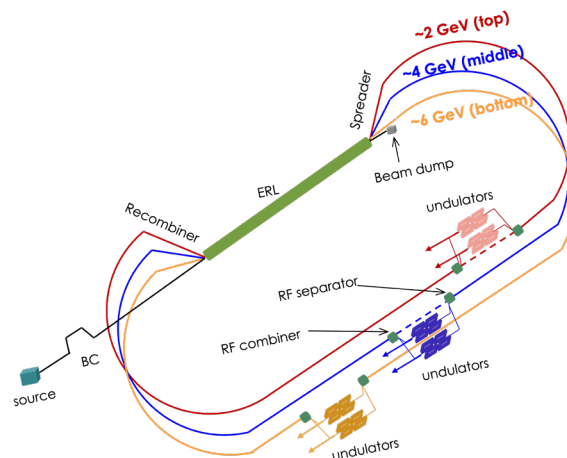


Figure 1: Schematic drawing of the proposed ERL-based XFEL facility.

* Work supported by UT-Battelle, LLC, under contract DE-AC05-00OR22725, and by Jefferson Science Associates, LLC, under contract DE-AC05-06OR23177.

† linf@ornl.gov

ACCELERATOR PHYSICS LESSONS FROM CBETA, THE FIRST MULTI-TURN SRF ERL*

K. E. Deitrick[†], Thomas Jefferson National Accelerator Facility, Newport News, VA, USA
 G. H. Hoffstaetter¹, CLASSE, Cornell University, Ithaca, NY, USA
¹also at Brookhaven National Laboratory, Upton, NY, USA

Abstract

The Cornell-BNL ERL Test Accelerator (CBETA) has been designed, constructed, and commissioned in a collaboration between Cornell and Brookhaven National Laboratory (BNL). It focuses on energy-saving measures in accelerators, including permanent magnets, energy recovery, and superconductors; it has thus been referred to as a green accelerator. CBETA has become the world's first Energy Recovery Linac (ERL) that accelerates through multiple turns and then recovers the energy in superconducting radiofrequency (SRF) cavities through multiple decelerating turns. The energy is then available to accelerate more beam. It has also become the first accelerator that operates 7 beams in the same large-energy aperture Fixed Field Alternating-gradient (FFA) lattice. The FFA is constructed of permanent combined function magnets and transports energies of 42, 78, 114, and 150 MeV simultaneously. Accelerator physics lessons from the commissioning period will be described and applications of such an accelerator from hadron cooling to EUV lithography and from nuclear physics to a compact Compton source will be discussed.

CBETA

CBETA is the first successful demonstration of an SRF multi-turn ERL [1–3]. Shown in Fig. 1, it features a non-scaling fixed-field alternating-gradient (FFA) return loop constructed using permanent magnets [4], which transport the four beam energies (42, 78, 114, and 150 MeV) simultaneously in a common beam pipe [1, 2]. The accelerator has a 6 MeV injector, the main linac cryomodule (MLC), SX and RX splitter sections, FFA return loop (FA, TA, ZX, TB, FB), and the beam stop line.

CBETA can be configured for one to four turns, with the top energies of each configuration corresponding to 42, 78, 114, and 150 MeV, respectively. For a configuration of Y turns, the beam completes $2Y$ passes through the MLC and $2Y - 1$ passes through the FFA return loop. In the SX and RX sections, each beam energy has a corresponding splitter line; this allows for independent control for $\alpha_{x,y}$, $\beta_{x,y}$, horizontal dispersion and its derivative, R_{56} , and orbit; the path length is controlled by moving stages installed in the center of the splitter lines. In the SX section, the splitter lines are labeled S1, S2, S3, and S4, with the lowest line energy being

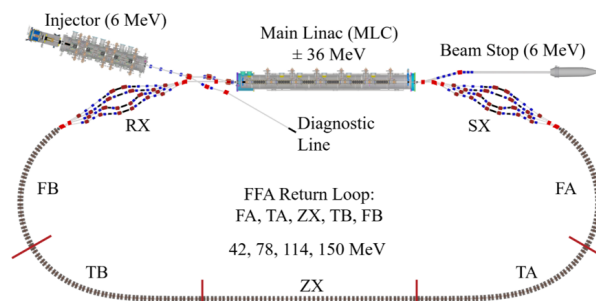


Figure 1: The four-turn configuration of CBETA.

transported in S1 which is located closest to the interior of the loop. Consequently, S4, the highest energy line, is located furthest from the interior. A similar numbering scheme and orientation is applied for the RX section [1, 2].

Select successes of the commissioning period include single-turn high-transmission energy recovery [3], four-turn energy recovery, orbit correction of multiple beams at different energies using a common set of corrector magnets, and measuring seven different beams simultaneously through the FFA arc [1]. CBETA could be used to study a number of critical beam dynamics effects, including beam-breakup instability, halo development and collimation, microbunching, and energy spread growth due to coherent synchrotron radiation (CSR). All of these, among others, are critical areas of study as ERLs are pushed to higher currents for various applications [1].

GREEN ACCELERATORS

As specifications of new facilities are being developed, the trend is for beams of increasingly high energy and current. In many cases, the quality desired may preclude storage rings from being an acceptable design; however, these high-power beams, if produced in linear accelerators, would have infeasible power requirements, especially as sustainability becomes an increasingly important aspect of accelerator design [5, 6].

ERLs operate by recovering the kinetic energy of previously accelerated bunches during deceleration and using that recovered energy to accelerate subsequent bunches. Not only does this minimize the amount of energy required by the SRF cavities, the amount of beam power delivered can actually exceed the installed power supplies. ERL operation does impose some restriction on the application - for example, delivering the beam into a target at an end station would preclude energy recovery; however, ERLs have previously

* Authored by Jefferson Science Associates, LLC under U.S. DOE Contract No. DE-AC05-06OR23177 and Brookhaven Science Associates, LLC under Contract No. DE-SC0012704 with the US Department of Energy (DOE).

[†] kirstend@jlab.org

EMITTANCE MEASUREMENTS AND SIMULATIONS FROM AN X-BAND SHORT-PULSE ULTRA-HIGH GRADIENT PHOTOINJECTOR*

G. Chen[†], D. Doran, S. Kim, W. Liu, J. Power, C. Whiteford, E. Wisniewski
 Argonne National Laboratory, Lemont, IL 60439, USA
 C. Jing¹, E. Knight, S. Kuzikov, Euclid Techlabs LLC, Bollingbrook, IL 60440, USA
 X. Lu¹, P. Piot¹, W. H. Tan, Northern Illinois University, DeKalb, IL 60115, USA
¹ also at Argonne National Laboratory, Lemont, IL 60439, USA

Abstract

A program is under way at the Argonne Wakefield Accelerator facility, in collaboration with the Euclid Techlabs and Northern Illinois University (NIU), to develop a GeV/m-scale photocathode gun, with the ultimate goal of demonstrating a high-brightness photoinjector beamline. The novel X-band photoemission gun (Xgun) is powered by high-power, short RF pulses, 9-ns (FWHM), which, in turn, are generated by the AWA drive beam. In a previous proof-of-principle experiment, an unprecedented 400 MV/m gradient on the photocathode surface was demonstrated. In the current version of the experiment, we added a linac to the beamline to increase the total energy and gain experience tuning the beamline. In this paper, we report on the very first result of emittance measurement as well as several other beam parameters. This preliminary investigation has identified several factors to be improved on in order to achieve one of the ultimate goals: low emittance.

INTRODUCTION

High brightness photoinjectors are enabling technologies for a host of scientific instruments including future linear colliders, next generation free electron lasers (FELs) [1], compact X-ray sources [2], and ultrafast electron diffraction or microscopy [3, 4]. There are two primary approaches for decreasing the transverse emittance for increasing brightness: lowering the thermal emittance of the photocathode or increasing the gradient of the accelerating field on the cathode surface, E_z . The program underway at the Argonne Wakefield Accelerator (AWA) facility, in collaboration with the Euclid Techlabs and Northern Illinois University (NIU), takes the latter approach by attempting to increase E_z in an RF gun to unprecedented levels. The collaboration is developing an ultra-high gradient X-band gun (Xgun) based on the short RF pulse approach at room temperature, motivated by the fact that the probability of RF breakdown is reduced as the RF pulse length decreases [5].

EXPERIMENTAL SETUP

The experimental layout (Fig. 1) consists of two main sections: the AWA drive beamline and the Xgun beamline.

* This work is supported by the U.S. DOE, under award No. DE-SC0018656 to NIU, DOE SBIR grant No. DE-SC0018709 at Euclid Techlabs LLC, and contract No. DE-AC02-06CH11357 with ANL.

[†] b288079@anl.gov

Table 1: List of Operating Parameters

Parameter	Value	Unit
Drive charge	~270	nC
Laser σ_x	0.189	mm
Laser σ_y	0.234	mm
Laser bunch length (FWHM)	300	fs
Xgun peak E-field	280.0±3	MV/m
Xgun phase ¹	31.8	degree
Bunch charge	45±10	pC
Solenoid B-field	0.202	T
Linac peak field	86.9±2	MV/m

¹ Xgun phase is with respect to the zero phase (see Fig. 2).

The drive linac produces a high-charge drive bunch train (up to 400 nC) which is passed into a power extraction and transfer structure (PETS) [6] to generate a high peak-power short rf pulse (3-ns flat top) at 11.7 GHz. The rf power from the PETS is then transferred through a directional coupler [6] and to the Xgun beamline.

In the section of the Xgun beamline, it consists of a 1.5-cell Xgun (more details on its rf properties can be found in Ref. [7, 8]), a brazeless linac (a structure that was designed for wakefield power extractor [8, 9] but here we reversed its use) for further beam acceleration, a spectrometer dipole for energy measurements, some diagnostics and focusing elements are shown in Fig. 1. Given the extracted rf power from the PETS, a variable power splitter was installed to properly adjust the power ratio between the Xgun and the linac. Additionally, in order to achieve in-phase acceleration in the linac, a phase shifter has been introduced for the linac phase adjustment. In the experiment, the power split ratio between the Xgun and the linac is of 50:50. More details on the power splitter and phase shifter can be found in Ref. [8, 10]. The basic operating parameters are summarized in Table 1.

Xgun Phase Scan

The laser injection phase is controlled by a movable delay stage by adding/subtracting additional laser travel distance, thus change the relative laser arrival time on the cathode. Fig. 2 shows a complete phase scan. The charge was measured by an integrated charge transformer (XICT1 in Fig. 1)

CERAMIC ENHANCED ACCELERATOR STRUCTURE LOW POWER TEST AND DESIGNS OF HIGH POWER AND BEAM TESTS*

H. Xu[†], M. R. Bradley, M. A. Holloway, J. Upadhyay, L. D. Duffy
 Los Alamos National Laboratory, Los Alamos, NM, USA

Abstract

A ceramic enhanced accelerator structure (CEAS) uses a concentric ceramic ring placed inside a metallic pillbox cavity to significantly increase the shunt impedance of the cavity. Single cell standing wave CEAS cavities are designed, built, and tested at low power at 5.1 GHz. The results indicate 40% increase in shunt impedance compared to that of a purely metallic pillbox cavity. A beam test setup has been designed to use a single cell CEAS cavity to modulate a 30 keV direct-current (DC) electron beam at an accelerating gradient of 1–2 MV/m to verify the beam acceleration capability of the CEAS concept and to study the potential charging effect on the ceramic component during the operation. Another single cell standing wave CEAS cavity has been designed for high power test at 5.7 GHz for the high accelerating gradient capability.

INTRODUCTION

In the designs of radiofrequency (RF) charged particle accelerators, low-loss ceramic components have been introduced as insertion in a variety of geometries with the purpose of reducing the power dissipation inside the structures, so as to enhance the shunt impedance of the accelerator cavities. Power saving achieved through the accelerator cavity shunt impedance enhancement is particularly desired in applications where the power availability is limited, e. g. space-borne experiments. However, due to the nature of ceramic material as dielectric and insulator, the main challenges of the applications of ceramic insertion in accelerator structures include the charging effects, multipactor, and the triple-point problem.

A ceramic enhanced accelerator structure (CEAS) was proposed to improve the shunt impedance of an accelerator cavity [1], as shown in Fig. 1. Inside an oxygen-free high thermal conductivity (OFHC) copper pillbox enclosure, a high-permittivity low-loss ceramic ring is positioned concentric with the metallic cell sidewall. A semi-loop coupler feeds microwave power into the region inside the ceramic ring. We investigated two types of the ceramic material, the BT37 ceramic (relative permittivity $\epsilon_r = 37.6$, loss tangent $\tan \delta = 2.75 \times 10^{-4}$) produced by Euclid Techlabs, LLC and the Skyworks 3500 series ceramic (relative permittivity $\epsilon_r = 34.5$, loss tangent $\tan \delta = 1.06 \times 10^{-4}$).

The cavity operates in a TM_{020} mode at 5.100 GHz. The radial distribution of the normalized longitudinal electric

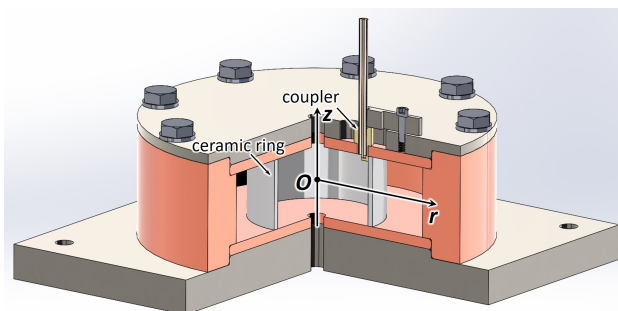


Figure 1: Section view of the low power test structure model of a ceramic enhanced accelerator structure (CEAS).

field and of the normalized azimuthal magnetic field is given in Fig. 2, calculated using the CST eigenmode solver for the CEAS geometry with the Euclid BT37 ceramic. The radial position of the ceramic ring overlaps with the node of the radial distribution of the longitudinal electric field. As a result, the dielectric loss inside the material of the ceramic ring is minimized, and the risk of direct dielectric breakdown is reduced as well. Because the ceramic ring possesses a high dielectric constant and thus is highly reflective, the magnitude of the fields in the region inside the ceramic ring is in general much greater than that beyond the ceramic ring. Therefore, the magnitude of the magnetic field at the metallic cell sidewall is very small, leading to reduced ohmic loss.

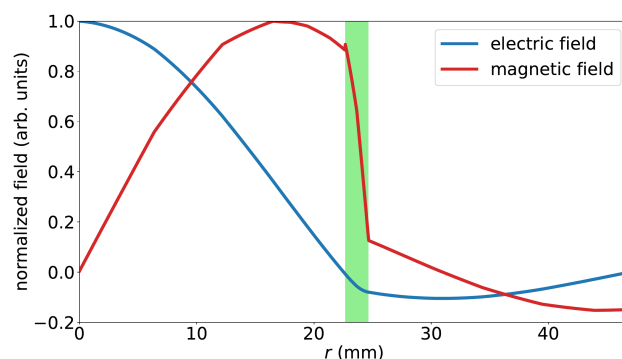


Figure 2: Radial distribution of the normalized longitudinal electric field and of the normalized azimuthal magnetic field at $z = 0$. The light green section represents the radial range of the ceramic ring made of the Euclid BT37 ceramic.

LOW POWER TEST

The goal of the low power test was to conduct the proof-of-principle verification of the CEAS concept, and to confirm the shunt impedance enhancement in a CEAS accelerator

* Work supported by the Laboratory Directed Research and Development program of Los Alamos National Laboratory, under project number 20210083ER.

[†] haoranxu@lanl.gov

SIMULATION AND EXPERIMENTAL RESULTS OF DIELECTRIC DISK ACCELERATING STRUCTURES

S. K. Weatherly^{1,*}, B. Freemire², C. Jing^{2,3}, E. E. Wisniewski^{1,3}, S. Doran³, J. Power³

¹Illinois Institute of Technology, Chicago, IL, USA

²Euclid Beamlabs, Bolingbrook, IL, USA

³Argonne National Laboratory, Lemont, IL, USA

Abstract

A method of decreasing the required footprint of linear accelerators and improving their energy efficiency is to employ Dielectric Disk Accelerators (DDAs) with short RF pulses (~ 9 ns). A DDA is an accelerating structure that utilizes dielectric disks to improve the shunt impedance. Two DDA structures have been designed and tested at the Argonne Wakefield Accelerator. A single cell clamped DDA structure recently achieved an accelerating gradient of 102 MV/m. A multi-cell clamped DDA structure has been designed and is being fabricated. Simulation results for this new structure show a 108 MV/m accelerating gradient with 400 MW of input power with a high shunt impedance and group velocity. The engineering design has been improved from the single cell structure to ensure consistent clamping over the entire structure.

INTRODUCTION

To create high power, small footprint linear accelerators, high gradient structures need to be utilized. Dielectric disk loaded accelerating structures can provide large acceleration to beams while being more compact than traditional accelerating structures. Dielectric accelerating cavities were first proposed because of their theorized high shunt impedances and high accelerating gradients [1]. In recent years Dielectric Loaded Accelerators (DLA) have proven more attractive than Dielectric Disk Accelerators (DDA). DLA structures are copper structures that are lined with dielectric tubes. DDA structures are loaded with dielectric disks equally spaced along the copper structure. DDA structures may be better suited for use in a high power, small footprint linear accelerator than a DLA because a DDA structure has a higher shunt impedance and RF to beam efficiency and a smaller input power requirement to achieve the same accelerating gradient [2]. In this paper, the experimental results from a single cell DDA structure will be presented and designs for a multi-cell structure will be shown.

SINGLE CELL DDA STRUCTURE RESULTS

Two single cell DDAs have been tested at high power at the Argonne Wakefield Accelerator (AWA). The first structure experienced problems due to the braze joint design [3]. To avoid these issues, a single cell clamped DDA structure was designed and high power tested.

* sweatherly@hawk.iit.edu

Design of a Single Cell Structure

A single dielectric cell is made up of two ceramic disks. The ceramic-copper interface was designed with elliptic rounding to minimize the field enhancement in the triple junction region. The head of the ceramic was designed so that it bit into the copper during assembly and was held securely in place, as seen in Fig. 1.

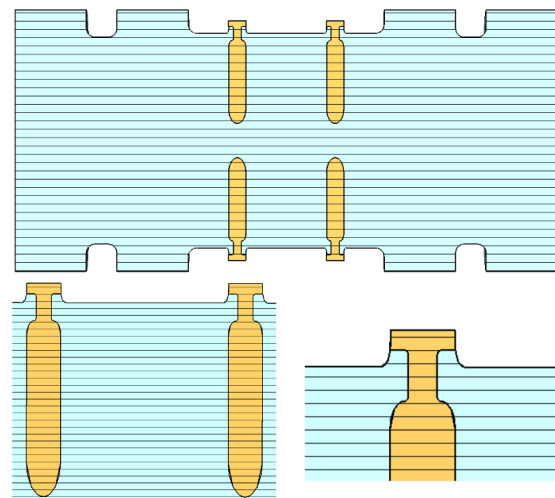


Figure 1: The RF design of the single cell clamped DDA structure. The upper figure shows a cross section of the entire structure. On the bottom left is one dielectric cell and the bottom right shows the detail of the head of the ceramic.

High Power Results

High power testing was conducted at the Argonne Wakefield Accelerator. The goal of high power testing was to determine the maximum accelerating gradient and peak ceramic surface electric field achievable. High power, short RF pulses were produced at the AWA by decelerating high charge bunches and transferring the extracted RF power to the DDA [4].

During testing, the DDA structure withstood up to 320.9 MW of input power and achieved an accelerating gradient of 102 MV/m. The maximum input power was limited by the available drive beam charge at the AWA. During testing and in review of the recorded RF pulses, there was no evidence of breakdown observed. Figure 2 shows the transmitted vs. input power to the DDA structure. The experimental data matches the predicted results well. The

REALISTIC CAD-BASED GEOMETRIES FOR ARBITRARY MAGNETS WITH BEAM DELIVERY SIMULATION (BDSIM)

E. Ramoisiaux, C. Hernalsteens¹, R. Dantinne, E. Gnacadja, S. Musibau,
B. Ndiokubwayo, N. Pauly, R. Tesse, M. Vanwelde

Service de Métrologie Nucléaire, Université libre de Bruxelles, Brussels, Belgium

L. J. Nevay, W. Shields, S. T. Boogert, Royal Holloway, University of London, Egham, UK

¹also at CERN, Geneva, Switzerland

Abstract

Monte Carlo simulations are required to accurately evaluate beam losses and secondary radiation in particle accelerators and beamlines. Detailed Computer-Aided-Design (CAD) geometries are critical to provide the most realistic distribution of material masses but increase the model complexity and often lead to code duplication. Beam Delivery Simulation (BDSIM) and the Python package PYG4OMETRY enable handling such accelerator models within a single, simplified workflow to run complete simulations of primary and secondary particle tracking and interactions with matter using Geant4. Replacing geometries of straight magnets is trivial in BDSIM. However, for curved magnets, the procedure is significantly more complicated and time-consuming for the user. Additional capabilities have therefore been developed to facilitate the design of arbitrary bent magnets by associating externally modelled geometries to the magnet poles, yoke, and beampipe. Individual field descriptions can be associated with the yoke and vacuum pipe separately to provide fine-grained control of the magnet model. The implementation of these new features is described in detail and applied to the modelling of the CERN Proton Synchrotron (PS) combined function magnets.

INTRODUCTION

Accelerator systems are becoming increasingly complex in recent years. Medical hadron therapy installations are evolving towards more compact systems and the high-energy colliders are reaching new records of luminosity. Such systems require prior Monte Carlo simulations to predict the energy deposition and activation of specific elements and to design the concrete shielding.

Multiple Monte Carlo codes have been developed over the years for these kinds of studies such as Geant4 [1, 2], Fluka [3] or MCNPX [4]. However, these codes use numerical integration to simulate the tracking of the primary and the secondary particles inside the magnetic fields in the beamlines leading to less accurate tracking in many fields systems, such as accelerators. Therefore, a complete loss or activation study typically requires the results of previous simulations realised by tracking codes such as MAD-X [5] or Zgoubi [6], depending on the application. On the other hand, only the propagation of the primary beam is computed using these tracking codes. This leads to approximation in the loss patterns distribution given as input to the Monte Carlo codes, impacting the studies results.

As solution, we propose to use Beam Delivery Simulation (BDSIM) [7], a Geant4-based C++ library that provides

a full 3D model of any accelerator-based system. BDSIM includes the particle-matter interactions of Geant4 and the tracking of all particles through the beamline and its magnetic fields. It provides tunable default geometries for any accelerator-based elements allowing effortless beamline design. Figure 1 shows the default geometry for a sector dipole magnet (Sbend). Once the components of a system are defined, BDSIM builds the model based on a sequence of elements provided by the user. Identical components can be called multiple times in the sequence avoiding code duplication.

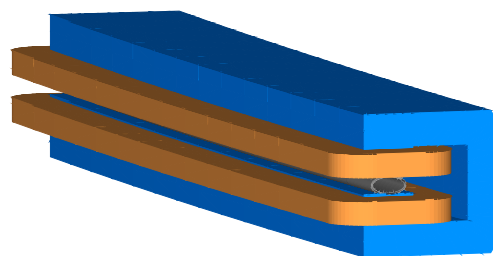


Figure 1: BDSIM model of an Sbend using the default geometry. The coils are represented in brown while, the yoke is represented in blue. An elliptical generic beampipe is represented in grey.

To improve the magnet realism, a user can import Computer-Aided-Design (CAD) files for the external geometry of the magnets. Unfortunately, in the current version of BDSIM, CAD-based external geometry cannot be directly applied to an Sbend. Furthermore, the magnets vacuum pipe design can only be chosen among some predefined default apertures. Therefore, a new feature has been developed to provide extra degrees of freedom to the user. With this feature, an Sbend can be implemented with one external geometry for the whole magnet using a CAD-based external geometry and a subpart of the provided external geometry can be defined as vacuum pipe.

This contribution details the new developments that have been realised in BDSIM for improving the customisation of the outer geometry of magnets and their vacuum pipe. This new feature is illustrated on the combined function magnets of the CERN Proton Synchrotron (PS).

EXTERNAL GEOMETRY CUSTOMISATION

User-defined external geometries are imported into a BDSIM model using Geometry Description Markup Language (GDML) files [8]. Users can create these GDML

ACTIVATION OF THE IBA PROTEUS ONE PROTON THERAPY BEAMLINE USING BDSIM AND FISPACT-II

E. Ramoisiaux, C. Hernalsteens¹, R. Tesse, E. Gnacadja, N. Pauly, M. Vanwelde
 Service de Métrologie Nucléaire, Université libre de Bruxelles, Brussels, Belgium
¹also at CERN, Geneva, Switzerland

Abstract

Cyclotron-based proton therapy systems generate large fluxes of secondary particles due to the beam interactions with the beamline elements, with the energy degrader being the dominant source. Compact systems exacerbate these challenges for concrete shielding and beamline element activation. Our implementation of the Rigorous Two-Step method uses Beam Delivery Simulation (BDSIM), a Geant4-based particle tracking code, for primary and secondary particles transport and fluence scoring, and FISPACT-II for time-dependent nuclear inventory and solving the rate equations. This approach is applied to the Ion Beam Applications (IBA) Proteus@ONE (P1) system, for which a complete model has been built, validated, and used for shielding activation simulations. We detail the first simulations of the activation on quadrupole magnets in high-fluence locations downstream of the degrader. Results show the evolution of the long-lived nuclide concentrations for short and long timescales throughout the facility lifetime for a typical operation scenario.

INTRODUCTION

Cyclotron-based proton therapy systems require an energy degradation system to deliver proton beams from 230 MeV to any desired energy down to 70 MeV covering treatments energy requirements. The interaction of the primary beam with the degrader scatters the primary protons and produces a large number of secondary particles, mainly neutrons [1]. The lost protons and secondary neutrons interact with the beamline elements or the concrete shielding via nuclear reactions, mainly capture and spallation, producing radioactive nuclides; some are long-lived and are responsible for the long-term activation of the proton therapy system and its concrete shielding.

While next-generation proton therapy systems evolve towards more compact designs, research activities requiring higher currents and extended irradiation periods are often conducted in parallel with patient treatments. Consequently, close activation monitoring of the beamline and shielding is a requirement when designing new compact treatment centres.

To tackle this challenge, we established the BDSIM/FISPACT-II methodology, inspired by the Rigorous Two-Step (R2S) method [2], coupling Beam Delivery Simulation (BDSIM) [3], a Geant4-based particle tracking code, with the code and library database FISPACT-II [4]. This methodology, thoroughly detailed in Ref. [5, 6], was applied to the shielding design of the future proton therapy centre of Charleroi, Belgium. The BDSIM model of the IBA Proteus@ONE proton therapy system was already developed and validated against experimental data [7].

We use the BDSIM/FISPACT-II methodology to characterise the activation of critical beamline elements in high

fluence regions during a typical centre lifespan of 20 years and help prepare the future centre decommissioning. This method will be applied on the first quadrupole of the rotating gantry, called Q1G, which was modelled using a cylindrical default geometry made of iron provided by BDSIM. Q1G is placed downstream from the degrader in the shielding wall connecting the vault to the treatment room. Q1G was chosen for this study as its location in the beamline implies that it is exposed to the secondary particles fluence generated from the beam interaction with all the extraction line elements. Figure 1 shows the BDSIM model of the vault with the superconducting synchro-cyclotron (S2C2), the extraction line with the quadrupoles, slits and degrader, and the start of the rotating gantry with the collimator and Q1G. The complex geometries of the S2C2, the degrader, the collimator and the concrete shielding have been implemented in the BDSIM model using Geometry Description Markup Language (GDML) files created for Geant4 by the Python library PYG4OMETRY [8, 9].

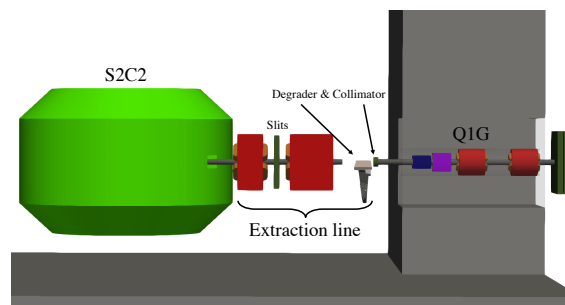


Figure 1: BDSIM model of the vault extraction line and its shielding. The S2C2 and the energy degradation system are shown. The concrete shielding wall separating the cyclotron vault from the treatment area is visible, with the beamline elements fit through a cylindrical cut.

The activity of a compound is determined by its clearance index. The clearance index is defined as the sum A_i/CL_i over all the material radionuclides with A the specific activity and CL the clearance level allowed by the Belgian legislation. If the clearance index exceeds the value of 1, the compound is considered radioactive waste. The main isotopes produced in concrete are listed in Table 1 with their corresponding clearance level.

Table 1: Clearance levels for the main isotopes produced in iron. Data taken from FISPACT-II database.

Nuclide	CL (Bq/g)	Nuclide	CL (Bq/g)
⁵⁴ Mn	0.1	⁴⁹ V	770
⁵⁵ Fe	1000	⁴⁴ Ti	7.2
³ H	100	⁵⁷ Co	1

BEAMLINE OPTIMIZATION METHODS FOR HIGH INTENSITY MUON BEAMS AT PSI

Eremey Valetov*, Paul Scherrer Institut, Villigen PSI, Switzerland
(for the HIMB project)

Abstract

We perform beamline design optimization for the High Intensity Muon Beams (HIMB) project at the Paul Scherrer Institute (PSI), which will deliver muon beams at the unprecedented rate of 10^{10} muons/s to next-generation intensity frontier particle physics and material science experiments. For optimization of the design and operational parameters to maximize the beamline transmission, we use the asynchronous Bayesian optimization package *DeepHyper* and a custom build of *G4beamline* with variance reduction incorporating measured cross sections. We minimize the beam spot size at the final foci using a *COSY INFINITY* model with differential-algebraic system knobs, where we minimize the norms of the respective transfer map components using the Levenberg–Marquardt and simulated annealing optimizers. We obtained a transmission of 1.34×10^{10} muons/s in a *G4beamline* model of the HIMB’s particle physics beamline MUH2 into the experimental area.

INTRODUCTION

The muon beamlines at Paul Scherrer Institute (PSI) presently provide muon rates of the order of $\sim 10^8$ muons/s to world-leading intensity frontier muon particle physics experiments and condensed matter research programs. The next generation of these experiments and programs requires a further increase of the muon rates by two orders of magnitude, to the unprecedented level of $\sim 10^{10}$ muons/s [1].

As an example, Mu3e experiment [2] attempts to detect the neutrinoless decay $\mu^+ \rightarrow e^+e^+e^-$ of a positive muon into two positrons and one electron. In the Standard Model, this is practically forbidden as this charged lepton flavour violation (cLFV) [3] has a vanishingly small branching ratio of $\sim 10^{-54}$. A positive measurement of $\mu^+ \rightarrow e^+e^+e^-$ would provide a clear indication of Beyond-Standard-Model physics. To achieve the sensitivity goal of 10^{-16} with the present rate of $\sim 10^8$ muons/s, Mu3e Phase II would have to run for more than 13 years.

The High Intensity Muon Beams (HIMB) project [4] seeks to deliver muons at $\sim 10^{10}$ muons/s at a proton current of 2.4 mA, making such sensitivities feasible [1].

The MEG II experiment [5], which had its first physics run in 2021, searches for the $\mu^+ \rightarrow e^+\gamma$ decay of a positive muon into a positron and a photon. This highly suppressed cLFV process has a branching ratio of also about 10^{-54} in the Standard Model. An increase in the available muon rates will enable a subsequent, next-generation MEG experiment [1] with an improved sensitivity of $\mathcal{O}(10^{-15})$.

* eremey.valetov@psi.ch

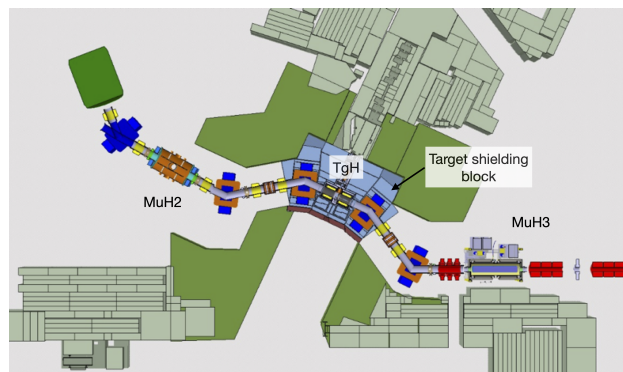


Figure 1: Layout of the HIMB target station and beamlines. The MUH3 beamline is not fully shown; it extends about 38 m from target TgH to the final focus of its branch MUH3.3 and also has a branch MUH3.2.

The muEDM experiment [6], which aims to detect an electric dipole moment of the muon, would also benefit from a novel low-energy, high-brightness muon source coupled to the HIMB [1], compared to using PSI’s $\mu E1$ beamline. The HIMB could provide a muon beam for muonium spectroscopy measurements that is four orders of magnitude more intensive than the current Low Energy Muons (LEM) beamline at PSI. Other particle physics applications of the HIMB are also envisaged [1].

In addition to particle physics applications, the HIMB will provide faster, higher statistics for measurements using the muon spin rotation method (μSR), enabling novel concepts for sample characterization, including the use of pixel-based detectors or microbeams which require an increase in available muon rate [1].

The HIMB project will achieve the increase of the muon beam intensity by two orders of magnitude to 10^{10} muons/s by replacing the existing target TgM with a new graphite target TgH with a slanted target design which increases the surface muon rate, high-acceptance capture solenoids close to the target, and transmission using large-aperture solenoids and dipoles. A partial layout of the HIMB is shown in Fig. 1. The particle physics beamline MUH2 has only solenoid focusing, while the materials science beamline MUH3 has solenoid focusing in the first two straight sections and conventional quadrupole focusing further downstream.

This paper expands on our paper [7] on beamline optimization for the HIMB project by detailing the optimization methods aspect of the same work. For broader information about the HIMB project, please refer to the IMPACT conceptual design report (CDR) [4]. The IMPACT project comprises the HIMB and the TATTOOS projects.

DESIGN OF A 4D EMITTANCE DIAGNOSTIC FOR LOW-ENERGY ION BEAMS

Thomas Roger Curtin, Mark Curtin, Ion Linac Systems, Inc., Albuquerque, NM, USA

Abstract

Characterization of ion beams from an ion injector consisting of an electron-cyclotron-resonance (ECR) source in combination with a low-energy-beam-transport (LEBT) typically exhibits a complex four-dimensional transverse phase-space distribution. The importance of measuring the ion beam correlations following extraction and transport of the low-energy beam is critical to enabling optimization of beam transmission through downstream accelerating structures. A design for a transverse, four-dimensional emittance meter for low-energy protons from the Ion Linac Systems (ILS) ECR-LEBT ion injector is provided.

INTRODUCTION

Detailed knowledge of the transverse beam parameters is essential to enable proper optimization of beam transmission in downstream accelerating structures. Procedures to measure the two-dimensional (2D) transverse beam parameters, where horizontal and vertical motions are separate, have been well established. However, various beamline elements such as skew quadrupole magnets, solenoids, and beamline element field asymmetries generate a correlation between the horizontal and vertical components. The purpose of this diagnostic is to characterize the four-dimensional (4D) beam phase space distribution by capturing multiple downstream transverse (xy) images allowing potential correction of transverse coupling from the source. There are two strategies to properly characterize the 4D emitted beam: the *single-optics/multiple-locations* strategy proposed by Woodley and Emma [1] and the *multiple-optics/single-location* strategy given by Prat and Aiba [2]. The first strategy proposes a long beam line of roughly 150 m consisting of six profile monitors and ~15 quadrupole magnets. The second involves having the 2D beam parameters measured at a single location and having quadrupole strengths change to generate the required optics for the 4D reconstruction. Due to the lack of 150 m of space required to perform the first method, the second method is used for this diagnostic.

4D TRANSVERSE BEAM CHARACTERIZATION

The 4D beam matrix describes the transverse properties of the beam:

$$\sigma^{4D} = \begin{pmatrix} \langle x^2 \rangle & \langle xx' \rangle & \langle xy \rangle & \langle xy' \rangle \\ \langle xx' \rangle & \langle x'^2 \rangle & \langle x'y \rangle & \langle x'y' \rangle \\ \langle xy \rangle & \langle x'y \rangle & \langle y^2 \rangle & \langle yy' \rangle \\ \langle xy' \rangle & \langle x'y' \rangle & \langle yy' \rangle & \langle y'^2 \rangle \end{pmatrix} = \begin{pmatrix} \sigma_{xx} & \sigma_{xy} \\ \sigma_{xy}^T & \sigma_{yy} \end{pmatrix} \quad (1)$$

The matrices σ_{xx} and σ_{yy} describe the 2D horizontal and vertical motions, and σ_{xy} describes the cross-plane coupling. The transport of the 4D beam matrix from s_0 to s can be calculated as follows:

$$\sigma_s^{4D} = R \cdot \sigma_{s_0}^{4D} \cdot R^T \quad (2)$$

Where R between s_0 and s is:

$$\sigma^{4D} = \begin{pmatrix} R_{11} & R_{12} & R_{13} & R_{14} \\ R_{21} & R_{22} & R_{23} & R_{24} \\ R_{31} & R_{32} & R_{33} & R_{34} \\ R_{41} & R_{42} & R_{43} & R_{44} \end{pmatrix} = \begin{pmatrix} R_{xx} & R_{xy} \\ R_{yx} & R_{yy} \end{pmatrix} \quad (3)$$

According to Eqs. (1), (2), and (3), when the lattice between s_0 and s , the elements R_{yx} and R_{xy} are zero allowing the beam sizes and x-y correlation to be expressed in terms of the matrix elements of σ^{4D} as follows:

Assuming the transport matrix elements are known, the 10 independent elements of σ^{4D} at s_0 can be computed by measuring beam sizes and x-y correlations at the point s . The initial simulation considered 8 captured beam images. Future simulations will map out the emittance sensitivity as a function of the number and quality of capture images.

SIMULATION OF DIAGNOSTIC

Presently we plan to validate the 4D emittance diagnostic using the Ion Linac Systems (ILS) Electron Cyclotron Resonance (ECR) 30 keV ion source. The initial layout of the 4D emittance diagnostic is depicted in Fig. 1 below including a pepper-pot 4D emittance diagnostic for cross-checking.

4D Emittance Diagnostic Configurations

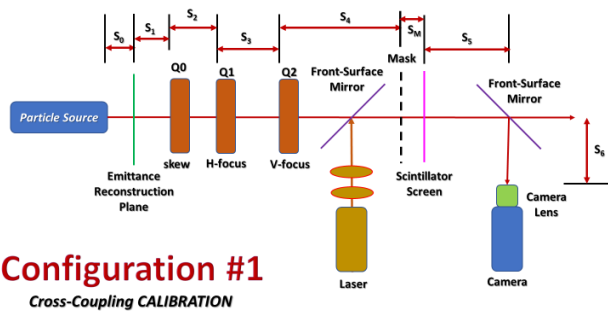


Figure 1: Diagnostic design for manufacture.

The system length is 1 m long in total and follows the ProLAB build below (Fig. 2). The quadrupoles themselves are 0.1 m in length separated by 0.1 m with an aperture radius

COMMISSIONING OF HOM DETECTORS IN THE FIRST CRYMODULE OF THE LCLS-II LINAC

J. Diaz Cruz^{1*}, J.P. Sikora, N. R. Neveu, B. Jacobson, SLAC, Menlo Park, CA, USA
¹also at University of New Mexico, Albuquerque, NM, USA

Abstract

Long-range wakefields (LRWs) may cause emittance dilution effects. LRWs are especially unwanted at facilities with low emittance beams like the LCLS-II at SLAC. Dipolar higher-order modes (HOMs) are a set of LRWs that are excited by off-axis beams. Two 4-channel HOM detectors were built to measure the beam-induced HOM signals for TESLA-type superconducting RF (SRF) cavities; they were tested at the Fermilab Accelerator Science and Technology (FAST) facility and are now installed at SLAC. The HOM detectors were designed to investigate LRW effects on the beam and to help with beam alignment. This paper presents preliminary results of HOM measurements at the first cryomodule (CM01) of the LCLS-II linac and describes the relevant hardware and setup of the experiment.

INTRODUCTION

Off-axis beam transport may result in emittance dilution due to transverse long-range (LRW) and short-range wakefields (SRW) in TESLA-type cavities, as previously showed at the Fermilab Accelerator Science and Technology (FAST) facility [1, 2]. A similar study was performed with an entire cold cryomodule (CM) with 8 SRF cavities and the correlation between beam offset and sub-macropulse centroid slews and centroid oscillations was shown in BPMs downstream the CM [3]. HOMs, which excite LRWs, are proportional to the transverse beam offset and bunch charge; therefore, reducing HOMs may help to mitigate emittance dilution effects, which is critical at the first cryomodule (CM01) of the LCLS-II linac.

Dipolar HOMs are of special interest since they drive beam instabilities which can cause transverse beam dynamic problems. As shown in [4], the dipole modes with the highest R/Q are modes 6 and 7 from the first passband; modes 13 and 14 from the second passband and mode 30 from the third passband. For this project, special interest is taken in the first and second dipole passbands. Each TESLA-type cavity has an Upstream (US) and a Downstream (DS) HOM coupler to damp those modes to avoid beam instabilities, and can also be used to measure HOM signals. A set of HOM measurement chassis were built at SLAC to instrument the US couplers of CM01 with the goal of support injector commissioning activities and to act as beam position diagnostics. Furthermore, the chassis can enable studies in LRW effects on the beam.

* dejorge@slac.stanford.edu

EXPERIMENTAL SETUP

Two 4-channel chassis were built to measure the magnitude of the HOMs at the US and DS couplers of each SRF cavity. Each channel has a 1.3 GHz notch filter to reduce the fundamental resonant frequency; a band-pass filter centered at 1.75 GHz with 300 MHz bandwidth to emphasize the main TE111 HOM dipole modes, in particular modes 7 ($f_7 = 1.739$ GHz) and 14 ($f_{14} = 1.873$ GHz), since these modes have the highest R/Q in their passband; a 31 dB digital step attenuator with 2 dB per step; two cascaded 23 dB amplifiers with enable/disable control and a Schottky diode for HOM detection. An schematic of a single channel is shown in Figure 1. More details about the design and testing of the chassis at [5].

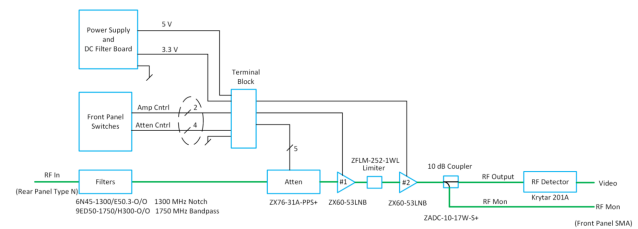


Figure 1: Schematic of a single channel in the 4-channel HOM measurement filter chassis.

All US and DS coupler cables are terminated in loads. The US couplers of CM01 have a -10 dB coupler with the through port followed by a 10 dB attenuator and a termination. This setup is done due to concerns related to the power level of the 1.3 GHz fundamental resonant mode being reflected back to the probe and heating the cable. The -10 dB port of the coupler is connected to the chassis. The two chassis are connected to the US couplers of the cavities inside CM01. The outputs of the chassis are connected to two oscilloscopes, which measure the minimum voltage for each channel, since the output of the Schottky diode is a negative voltage. The scope waveforms are available via EPICS and the minimum voltages can be monitored using PVs. The complete setup is shown in Figure 2. The team is in the process of building another set of chassis to also instrument the DS couplers.

The LCLS-II injector has 5 corrector magnets and 2 BPMs between the RF gun and CM01. There is also a cold BPM inside CM01 in the downstream end, and multiple BPMs downstream CM01, along with other diagnostics and systems, that complete the injector setup.

PRELIMINARY HOM MEASUREMENTS

As part of the injector commissioning activities, the two HOM measurement chassis were tested and are now being

DESIGN OF A SURROGATE MODEL FOR MUED AT BNL USING VSim, elegant AND HPC

S.I. Sosa*, T. Bolin¹, S.G. Biedron^{1,2}

Department of Electrical and Computing Engineering,
 University of New Mexico, Albuquerque, NM, USA

¹ also at Element Aero, Chicago, IL, USA

² also at Department of Mechanical Engineering,
 University of New Mexico, Albuquerque, NM, USA

Abstract

The MeV Ultrafast Electron Diffraction (MUED) instrument at Brookhaven National Laboratory is a unique capability for material science. As part of a plan to make MUED a high-throughput user facility, we are exploring instrumentation developments based on Machine Learning (ML). We are developing a surrogate model of MUED that can be used to support control tasks. The surrogate model will be based on beam simulations that are benchmarked to experimental observations. We use VSim to model the beam dynamics of the radio-frequency gun and Elegant to transport the beam through the rest of the beam-line. We also use High Performance Computing resources from Argonne Leadership Computing Facility to generate the data for the surrogate model based on the original simulation as well as training the ML model.

INTRODUCTION

The MeV Ultra-fast Electron Diffraction (MUED) system at Brookhaven National Laboratory (BNL) is a unique research tool that enables the study of the crystalline structure of materials using electron diffraction [1]. At the center of the MUED operation is the radio-frequency gun, which provides an energy gain of 3 MeV to the electron beam [2]. The high accelerating gradient helps reduce the space charge effect in the beam, which is significantly reduced with increasing energy. The electron gun is a normal conducting radio-frequency cavity, composed of 1.6 cells and designed to operate at 2856 MHz in the TM_{010} , π -mode [2]. The electron beam is produced via photo-electric effect on a Cu cathode using a frequency-tripled Ti:Sapphire laser. The Cu cathode doubles as the wall of the half-cell of the rf gun. A solenoid magnet sits immediately after the rf gun, and it helps focusing the beam. A pair of horizontal and vertical corrector magnets are also used to control the beam towards the collimator, the sample holder and the detector, which sits 4 m downstream. Figure 1 shows a photograph of the beam optics elements of MUED. After the material sample, the beam drifts for a long stretch, which improves the resolution on the diffraction pattern. The MUED detector is a Phosphor screen and is imaged with a cryogen-cooled Andor CCD camera.

* salvadorsg@unm.edu

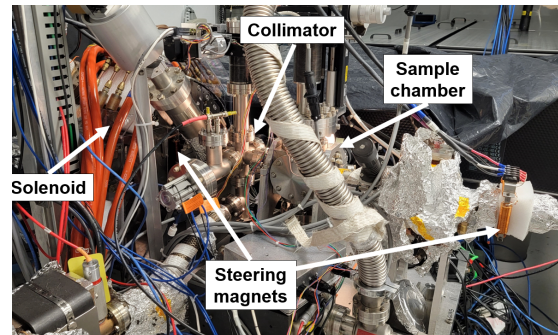


Figure 1: The MUED focusing magnets and sample holder.

MUED also has the capability of laser-pumping the material sample. The Ti:Sapphire laser can be used to photo-excite the material sample, this can drive phase transitions in the material, and can be analyzed by looking at the evolution of the diffraction patterns before and after a time-zero T_0 when the laser pulse arrives at the sample.

With these capabilities on-hand, there is interest in developing the instrumentation of MUED to maximize the throughput of science and users, and to minimize the facility experimental down-time. As MUED users, we are exploring the use of ML and optimization tools to support MUED operations. After our first dedicated beam-time at BNL, we learned that an important concern for experimental data-runs is the energy jitter of the electron beam. Energy variations arise from variations in the rf phase of the gun. Variations in beam energy directly translate into the aperture angle of the diffraction patterns, making the laser-pump measurements particularly noisy. We believe ML and optimization tools can be deployed at MUED to help with the beam stability. In particular, we envision a surrogate model capable of taking the detector images as inputs and producing the required instrument control settings that optimize the beam [3–5].

SURROGATE MODEL FOR MUED

Computer simulations are generally used as a way to understand the dynamics of a system, whether on the developing phase or when trying new system configurations. Simulations can provide accurate results, but more often than not, the computing time required to produce a solution is not suitable for real-time operations.

A WIDE DYNAMIC-RANGE HALO MONITOR FOR 8 GeV PROTON BEAMS AT FNAL*

Y. Hashimoto[†], C. Omori, Y. Sato, T. Toyama, M. Tejima, T. Sasaki, M. Uota
 KEK/J-PARC, Japan

R. Ainsworth, Fermi National Laboratory, Batavia, IL, USA

H. Sakai, Mitsubishi Electric System & Service Co., Ltd., Japan

Abstract

Eliminating harmful beam halos is the most important technique for high-intensity proton accelerators. Therefore, beam halo diagnosis is indispensable and becomes more and more important. At J-PARC, a wide dynamic range monitor was installed in the beam transport line in 2012. The device is a two-dimensional beam profile monitor, and it has a dynamic range of approximately six digits of magnitude by using of Optical Transition Radiation and fluorescence screens. The FNAL accelerator complex has been upgrading in increasing beam intensity and beam quality. A new beam halo diagnostic device is required in the beam transport line between booster and Recycler. It will be manufactured in a collaboration between J-PARC and FNAL as a part of U.S.-Japan Science and Technology Cooperation Program in High Energy Physics. We are redesigning the monitor to satisfy FNAL specifications: the beam energy, intensity, and size. The equipment will be manufactured at J-PARC and will be shipped to FNAL in 2024. In this report, the design of the device will be described.

INTRODUCTION

A two-dimensional beam profile monitor with a six-digit dynamic range was developed in 2012 at J-PARC. It has proved effective for precise beam halo diagnosis for injecting beams in 3 GeV beam transport to the main ring [1, 2]. At J-PARC, we have been developing Unit-2 for diagnosing the halo of the injected beam on the main ring and diagnosing the beam cut effect by MR collimators [3]. In the configuration, it is also a new theme to perform beam halo measurements in phase space by performing simultaneous measurements with Units -2 and -1. In high-intensity proton accelerators, beam diagnostics using equipment for accurately diagnosing such beam halos has been progressed.

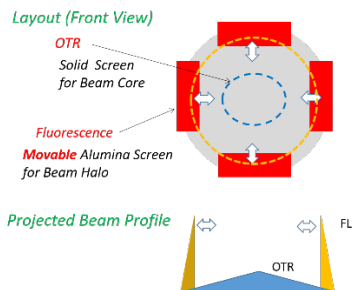


Figure 1: Screen configuration.

* Work supported by U.S.-Japan Science and Technology Cooperation Program in High Energy Physics.

[†] yoshinori.hashimoto@kek.jp

These instruments at J-PARC consist of two parts: the beam core is measured by OTR from a metal thin film target such as titanium, and the beam halo is captured by fluorescence from alumina target. High-sensitivity image measurement is performed by adjusting the gain of the image intensifier (Fig. 1). It makes sense to introduce a precise two-dimensional beam profile monitor with such a high dynamic range to the 8 GeV beam transport line (Fig. 2) of the Recycler from Booster, in upgrading the accelerator at FNAL. In the Japan-US cooperation project: Accelerator and Beamline Research and Technology Development for High-Power Neutrino Beam, we concluded an agreement between KEK and FNAL in FY 2021, and within that framework, we decided to develop this device in a three-year plan. In formulating the specifications of the equipment, we basically take the policy of applying it to FNAL based on the results of J-PARC Unit-1.



Figure 2: FNAL accelerator complex.

OPTICAL SYSTEM DESIGN FOR FNAL 8 GeV BEAM

8 GeV Proton Beam

Table 1 shows the beam intensity and beam size per bunch of the J-PARC 3 GeV beam and the FNAL 8 GeV beam. The value of J-PARC beam intensity was used the lowest intensity for measuring a 6-digit beam halo. Assuming a Gaussian beam, each beam profile is shown in Fig. 3. For the FNAL peak, 0.08, which is obtained by multiplying the intensity ratio with J-PARC by the square of the beam size ratio as a packing factor, was used. This curve can be said to be the light intensity ratio of OTR and fluorescence generated at the target. In other words, when measured with the same set as J-PARC, the light at FNAL is one order of magnitude smaller than at J-PARC. In the following, we discuss how to measure the beam halo with a high dynamic range of 6 orders of magnitude or more even with FNAL.

SYNCHRONOUS HIGH-FREQUENCY DISTRIBUTED READOUT FOR EDGE PROCESSING AT THE FERMILAB MAIN INJECTOR AND RECYCLER

J. R. Berlioz*, M. R. Austin, J. M. Arnold, K. J. Hazelwood*, P. Hanlet,
M. A. Ibrahim*, A. Narayanan¹, D. J. Nicklaus, G. Pradhan,
A. L. Saewert, B. A. Schupbach, K. Seiya, R. M. Thurman-Keup, N. V. Tran
Fermi National Accelerator Laboratory[†], Batavia, IL, USA
J. Jang, H. Liu, S. Memik, R. Shi, M. Thieme, D. Ulusel
Northwestern University[‡], Evanston, IL, USA
¹also at Northern Illinois University, DeKalb, IL, USA

Abstract

The Main Injector was commissioned using data acquisition systems developed for the Fermilab Main Ring in the 1980s. New VME-based instrumentation was commissioned in 2006 for beam loss monitors (BLM), which provided a more systematic study of the machine and improved displays of routine operation. However, current projects are demanding more data and at a faster rate from this aging hardware. One such project, Real-time Edge AI for Distributed Systems (READS), requires the high-frequency, low-latency collection of synchronized BLM readings from around the approximately two-mile accelerator complex. Significant work has been done to develop new hardware to monitor the VME backplane and broadcast BLM measurements over Ethernet, while not disrupting the existing operations-critical functions of the BLM system. This paper will detail the design, implementation, and testing of this parallel data pathway.

INTRODUCTION

The Real-time Edge AI for Distributed Systems (READS) project is a collaboration between the Fermilab Accelerator Division and Northwestern University. The project has two objectives: 1) to create a real-time beam loss de-blending system for the Main Injector (MI) and Recycler (RR) utilizing machine learning (ML) [2], and 2) to implement ML into the future Delivery Ring slow spill regulation system for the Mu2e experiment [3, 4]. This paper focuses on the creation of the data acquisition architecture, capable of data streams into both training sets and firmware implementation of ML models across a distributed network. The details of the ML model and the progress of disentangling the loss sources are not the topic of this paper but are described in detail within our conference sister paper [5].

* Equal paper contribution

[†] Operated by Fermi Research Alliance, LLC under Contract No. De-AC02-07CH11359 with the United States Department of Energy. Additional funding provided by Grant Award No. LAB 20-2261 [1].

[‡] Performed at Northwestern with support from the Departments of Computer Science and Electrical and Computer Engineering.

BLM Data Collection

Beam loss monitors (BLMs) consist of a distributed network of VME front ends (or “nodes”), which captures spatially-identifiable and time-correlated ionizing radiation measurements from 259 argon-gas ionizing chambers, or BLM detectors, installed around the MI and RR [6]. BLM systems report, on a logarithmic scale, losses for all BLM detectors at various times throughout a cycle.

To achieve this, charges measured from the BLMs detectors are integrated in 21 μ s periods. These periods are used to construct three different sliding sums with user-defined time scales: 3 ms, 50 ms, and 1 s [7]. The sliding sums are transmitted via a VME crate controller card to ACNET, Fermilab’s accelerator control system [8], for display and analysis. Simultaneously, these sums also drive primary inputs to a beam abort system, which compares the reported charge readouts and sliding sum values with beam loss abort threshold values for the MI [6].

Currently, the abort system struggles to distinguish and disentangle the source of the beam losses. This is because 1) MI and RR share an enclosure, 2) both machines can and do often have high-intensity beam in them simultaneously, and 3) both machines can generate significant beam loss. Accelerator operators use their expertise to determine the origin of a loss from a beam loss pattern. The process is not automatic, and the manual analysis creates unnecessary downtime. The READS project aims to deploy a ML model that will infer in real-time the machine loss origin.

Having training sets with the appropriate temporal and spatial resolution is paramount for the development of an accurate, realistic ML model. Unfortunately, the current BLM readout system presents a bottleneck for data collection and limits the reaction time for the ML model. Although BLM measurements update at 333 Hz (i.e., 3 ms integration period), the BLM readout system can only provide a maximum data rate of 30 Hz. Furthermore, the interface between the BLM and the abort system imposes operations-critical restrictions on any modifications to the existing BLM system. These reasons were the key motivations for developing an alternative solution through the VME Reader cards.

SYMPLECTIC PARTICLE TRACKING IN A THICK NONLINEAR McMILLAN LENS FOR THE FERMILAB INTEGRABLE OPTICS TEST ACCELERATOR (IOTA)

B. Cathey*, G. Stancari, T. Zolkin, Fermi National Accelerator Laboratory, Batavia, IL, USA

Abstract

The McMillan system is a novel method to increase the tune spread of a beam without decreasing its dynamic aperture due to the system's integrability. While the ideal system is based on an infinitely thin kick, the physical design requires a thick electron lens, including a solenoid. Particle transport through the lens is difficult to simulate due to the nature of the force on the circulating beam. This paper demonstrates accurate simulation of a thick McMillan lens in a solenoid using symplectic integrators derived from Yoshida's method.

INTRODUCTION

As circular accelerators achieve higher beam intensities, beam instabilities increasingly limit design capabilities. Beam instabilities can come from interactions of the beam with the surrounding environment through wakefields and impedance, or from space charge due to the beam itself. Landau damping is one way to mitigate instabilities. Landau damping is the use of a spread of betatron tunes to lower a beam's sensitivity to instabilities. To generate a tune spread nonlinear forces are required, such as octupole magnets creating tune spread dependent on the particle's amplitude. However, octupoles and other nonlinear elements can have a significant drawback in that they reduce the beam's dynamic aperture. There are nonlinear dynamical systems that are integrable, and that can be implemented in accelerators, without loss of dynamic aperture [1–6].

The Integrable Optics Test Accelerator (IOTA) at Fermilab is partly dedicated to the experimental study of novel, integrable, nonlinear focusing lattices [7]. In particular, one straight section is designed to include an electron lens, which will be used for research on nonlinear dynamics, electron cooling, and space-charge compensation [7–10]. Because of their flexibility, electron lenses can be designed to have different effects on the circulating beam [11–15]. In this paper, we focus on the simulation of a realistic McMillan electron lens, the nonlinear element necessary for creating the McMillan integrable system in IOTA [16–18].

BACKGROUND

The McMillan system has two sections: a linear transport and a nonlinear kick [2, 3]. The linear transport requires a $\pi/2$ phase advance in both vertical and horizontal phase spaces, and a round beam at the kick. The two dimensional

McMillan kick is defined as

$$f(r) = \frac{kr}{\frac{r^2}{a^2} + 1}, \quad (1)$$

with k as the kick strength and a as an effective width. This system has two integrals of motion guaranteeing integrability. These are best defined in polar coordinates where:

$$\begin{aligned} r &= \sqrt{x^2 + y^2}, & r' &= \frac{xx' + yy'}{\sqrt{x^2 + y^2}}, \\ \theta &= \arctan 2(y, x), & \theta' &= \frac{xy' - yx'}{\sqrt{x^2 + y^2}}. \end{aligned} \quad (2)$$

One is the angular momentum $L_z = r\theta'$. The other is given by

$$I = \frac{r^2 r'^2}{a^2} + \frac{r^2}{\beta^2} + r'^2 + \theta'^2 - krr'. \quad (3)$$

This system generates a wide tune spread while maintaining integrability [17, 19]. There are two regimes of strength for the McMillan lens based on the lattice beta function. The weak regime occurs when $\beta k < 2$ and has a maximum tune spread of

$$(\Delta\nu_\theta)_{\max} = \frac{1}{4} - \frac{1}{2\pi} \arccos\left(\frac{\beta k}{2}\right). \quad (4)$$

The strong regime is when $\beta k > 2$ and can create a tune spread that reaches the integer resonance.

However, this system cannot be physically achieved with a thin kick. The electron lens must have some length and be contained within a solenoid to magnetically confine the electron beam and keep the lens current consistent throughout beam traversal. These complications are shown in Fig. 1. To predict how they affect particle motion compared to the ideal system, the motion through the lens needs to be simulated.

SYMPLECTIC INTEGRATION OF THE McMILLAN LENS

The most straightforward way to simulate the lens is to solve the equations of motion for a particle in the lens. To do so, the lens is analyzed in isolation from the rest of the lattice, treating the lens beam as a current density with infinite length. The kick in Eq. (1) is created with a current density of the form

$$J(r) = \frac{j_0}{\left(\frac{r^2}{a^2} + 1\right)^2}, \quad (5)$$

* bcathey@fnal.gov

RESIDUAL DOSE AND ENVIRONMENTAL MONITORING FOR THE FERMILAB MAIN INJECTOR TUNNEL USING THE DATA ACQUISITION LOGGING ENGINE (DALE)

N. Chelidze*, R. Ainsworth, B. C. Brown, D. P. Capista,
K. J. Hazelwood*, D. K. Morris, M. J. Murphy
Fermi National Accelerator Laboratory[†], Batavia, IL, USA

Abstract

The Recycler and the Main Injector are part of the Fermilab Accelerator complex used to deliver proton beam to the different experiments. It is very important to control and minimize losses in both machines during operation, to reduce personnel dose from residual activation and to preserve component lifetime. To minimize losses, we need to identify the loss points and adjust the components accordingly. The Data Acquisition Loss Engine (DALE) platform has been developed within the Main Injector department and upgraded throughout the years. DALE is used to survey the entire enclosure for residual dose rates and environmental readings when unrestricted access to the enclosure is possible. Currently DALE has two radiation meters, which are aligned along each machine, so loss points can be identified for both at the same time. DALE attaches to the enclosure carts and is continuously in motion monitoring dose rates and other environmental readings. In this paper we will describe how DALE is used to provide radiation maps of the residual dose rates in the enclosure. We will also compare the loss points with the Beam Loss monitor data.

INTRODUCTION

The Main Injector and the Recycler are circular accelerators that are used to deliver beam to multiple different experiments. They share the same tunnel and are used in combination to accelerate a proton beam from 8 GeV to 120 GeV [1]. The Recycler (RR) is mounted about 6 ft above the Main Injector (MI), stretching along about 2.1-mile circumference.

The Data Acquisition Loss Engine (DALE) platform has been developed within the Main Injector department to measure the residual radiation dose along the Main Injector and Recycler accelerators. Originally it consisted of one handheld detector and was used to survey one machine (MI or RR) at a time. Currently DALE has two detectors which allows both machines to be surveyed simultaneously. Besides measuring the residual activation of the accelerators, DALE is also capable of measuring other environmental parameters in the tunnel.

The goal of DALE surveys historically have been to identify the loss points in the accelerators after beam operation. DALE surveys complemented so-called “Expert Surveys”

which were detailed local radiation surveys performed by experts. The data gained from both allowed experts to adjust the accelerator components accordingly by alignment which would lower or eliminate the loss points.

DALE HARDWARE AND SOFTWARE COMPONENTS

DALE connects to two radiation detectors, one mounted high on a vertical rod and is aligned to the Recycler machine, and the lower one is mounted lower on the same rod to be aligned with Main Injector machine. This way simultaneous measurement of activation around the entire ring is possible. It houses a number of additional environmental sensors so it can collect those data while in the tunnel. It also includes two distance sensors, aisle side (wall) and machine side, that measure inner and outer distance to the tunnel walls from the detector, light, temperature, humidity, heat index and air quality sensors. It also uses a wheel counter to keep track of its position in the Main Injector tunnel. DALE has a Wi-Fi capability to connect to its live display and is based off an Arduino Mega 2560. It writes and saves its data to an onboard SD card. A picture of DALE is shown on Figure 1.



Figure 1: DALE on a cart.

* Equal paper contribution.

[†] Operated by Fermi Research Alliance, LLC under Contract No.De-AC02-07CH11359.

THE EFFECT OF THE MAIN INJECTOR RAMP ON THE RECYCLER

N. Chelidze*, R. Ainsworth, K.J. Hazelwood
 Fermi National Accelerator Laboratory[†], Batavia, IL, USA

Abstract

The Recycler and Main Injector are part of the Fermilab Accelerator complex used to deliver a high power proton beam. Both machines share the same enclosure with the Recycler mounted 6 ft above the Main Injector. The Main Injector accelerates beam from 8 GeV to 120 GeV. While the majority of the Recycler has high permeability metal shielding, the effect of the Main Injector ramp is still significant and can affect both the tunes and the orbit. In this paper, we describe the size of these effects.

OPERATIONS

The Main Injector (MI) and Recycler (RR) are part of the Fermilab accelerator complex which are used to deliver beam to various experiments [1]. For the high intensity Neutrino experiments, the Recycler performs slip-stacking at 8 GeV and sends beam to the Main Injector, which accelerates this beam to 120 GeV. The Recycler is also used to rebunch beam from 53 MHz to 2.5 MHz for the Muon campus experiments. The Main Injector can ramp every 1.2 s however, when Muon campus is requesting beam, the time between pulses increases to 1.4 s. Figure 1 shows this in more detail. Depending on the operational mode i.e. if the MI is ramping at 1.2 s vs 1.4 s, the Recycler beam will be injected in the machine at different points with respect to the MI ramp. Due to the Recycler's limited aperture, the machine at high intensity is very sensitive to small orbit or tune changes. As both machines share the same tunnel, stray magnetic fields originate from both the quadrupole and the dipole bus (supply and return) excitations during the MI ramp (8 to 120 GeV). An example schematic of the tunnel is shown in Fig. 2.

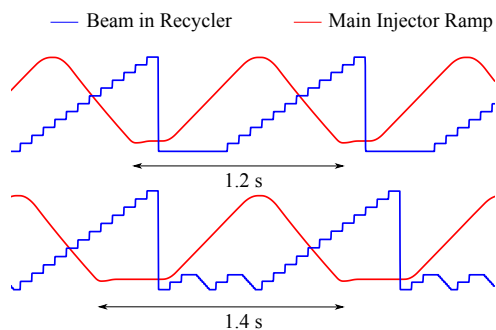


Figure 1: The position of the Recycler beam with respect to the MI ramp. When Muon campus is requesting beam, the MI ramp sits at 8 GeV for extra 0.2 s.

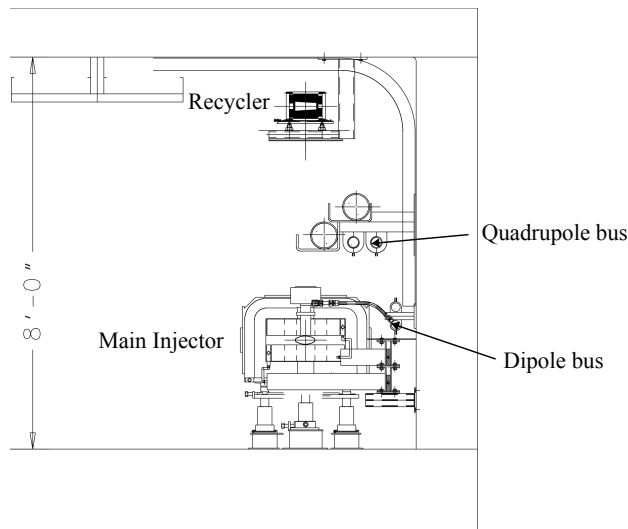


Figure 2: A schematic of the Main Injector enclosure which holds both the Main Injector and Recycler accelerators.

At the top of the ramp the current in the quad and dipole buses are close to 3 kA and 7 kA respectively. Both buses contribute about equally to the transverse magnetic field at the Recycler beam location [2]. In order to compensate for these effects, high-permeability shielding was added to the Recycler however, there is still a measurable effect on both the Recycler's orbit and tunes.

Figure 3 shows the horizontal beam position in the Recycler at different times with respect to the Main Injector ramp. The initial oscillation is caused by a kicker magnet used for tune measurements however, the orbit distortion visible at 9 GeV is caused by the Main Injector ramp.

ORBIT CORRECTION

In order to measure the effect of the MI ramp on the Recycler orbit, beam is injected into the Recycler and held for one full MI ramp. The Recycler closed orbit is measured and averaged at various MI ramp currents that correspond to commonly used MI momentum breakpoints. The orbit measured at the MI ramp current equivalent to 8.9 GeV is used for the ideal reference orbit. The orbit at 8.9 GeV is set each startup by scanning the Recycler beam apertures and finding the BPM position that causes the least loss and the least feed-down effects from higher order elements.

Compensating for the MI ramp in Recycler is a routine enough task that a specific sub-page has been created in the operational Recycler orbit correction and smoothing client application known as R50. The R50 client takes the difference of each averaged orbit and the reference orbit and calculates the required dipole trim corrector currents needed

* chelidze@fnal.gov

[†] Operated by Fermi Research Alliance, LLC under Contract No.De-AC02-07CH11359

EFFECT OF ELECTROPOLISHING ON NITROGEN DOPED AND UNDOPED NIOBIUM SURFACES*

V. Chouhan[†], F. Furuta, M. Martinello, T. Ring, G. Wu
 Fermi National Accelerator Laboratory, Batavia, IL, USA

Abstract

Cold electropolishing (EP) of a nitrogen-doped (N-doped) niobium (Nb) superconducting RF (SRF) cavity was found to improve its quality factor. In order to understand the effect of EP temperature on N-doped and undoped surfaces, a systematic EP study was conducted with 2/0 N-doped and heat-treated Nb samples in a beaker. The Nb samples were electropolished at different surface temperatures ranging from 0 to 42 °C. The results showed that the doped surface was susceptible to the sample temperature during EP. EP resulted in the surface pitting on the doped samples where the number density of pits increased at a higher temperature. The surface results were compared with the surface of cutouts from a 9-cell cavity which was 2/0 N-doped and electropolished. This paper shows detailed surface features of the N-doped and undoped Nb surfaces electropolished at different temperatures.

INTRODUCTION

The superconducting RF performance of niobium (Nb) cavities was greatly improved in the last 20 years. N-doping of cavities was a great invention that showed enhancement in the quality factor of the cavities [1]. Cavities for LCLS II and LCLS II HE confirmed advantage of the doping process. The interstitial nitrogen atoms with no niobium nitride phase are necessary to reduce BCS resistance that enhances the quality factor [2]. After the doping is applied, niobium nitride phase formed on the surface is removed by electropolishing (EP) process. The cavities tested in a vertical cryostat revealed that the post-doping EP temperature affects their SRF performance. Cold-EP is applied to improve the cavity performance. Cold-EP temperature was set based on the experience with the cavity performance. Although the effect of cold-EP on the cavity performance is known, a clear understanding on relation between surface feature on N-doped Nb material and a temperature in EP is still lacking. This study was conducted to gain more understanding on this subject so that further improvement on the cavity surface and performance can be achieved.

EXPERIMENTS

EP experiments were conducted with Nb samples which were processed with the 2/0 nitrogen doping (N-doping)

*This work was supported by the United States Department of Energy, Offices of High Energy Physics and Basic Energy Sciences under contract No. DE-AC02-07CH11359 with Fermi Research Alliance.

[†] vchouhan@fnal.gov

recipe [3] or heat-treatment at 800 °C for 3 h in a furnace. The samples during doping and heat-treatment were not covered by a Nb box/foil. The samples were experiencing furnace atmosphere during the process. The samples used in this study were prepared in a size of 1x1 cm² and from the same Nb sheet. The samples after furnace treatment were electropolished in an acid bath having a heat-sink element that maintained the acid at a desired temperature. The standard electrolyte (a mixture of sulfuric and hydrofluoric acids) was used for EP of the samples. With the setup used in this study, the acid temperature can be maintained in a wide range from ultra-cold temperature (-8 °C or below) to room temperature. A thermocouple was attached to the Nb sample to measure its temperature during EP. This makes easy to compare sample temperature with the cavity temperature measured at the outer surface of the cavity during EP. In the sample EP, no acid stirring was applied to avoid any effect of acid flow on the surface. Sample EP was performed at different temperatures and the standard EP voltage of 18 V. A list of samples with their furnace treatment conditions and temperature in EP is given in Table 1. A removal thickness in EP for both doped and undoped samples was ~5 μm. All the samples in the EP process were set vertically with a known orientation. The sample surface was inspected with a confocal laser microscope to compare their surface features after EP.

To compare the sample surface with a cavity surface, cutouts from a 9-cell cavity (CAV0018), which was one of the early cavities treated at FNAL with 2/0 N-doping followed by EP for 7 μm average removal, were inspected with the microscope. The post-doping EP was performed at 14 V and a cavity temperature of ~24 °C. This cavity was processed before the cold-EP temperature was decided.

Table 1: N-doped and undoped samples with furnace treatment conditions and surface temperatures during EP.

Sample	Furnace Treatment	Temperature in EP (°C)
2/0-ND-1	2/0 N-doping	0–3
2/0-ND-2	2/0 N-doping	13–16
2/0-ND-3	2/0 N-doping	22–24
2/0-ND-4	2/0 N-doping	38–42
800C-UD-1	800 °C/3hrs	32–36

STUDY ON ELECTROPOLISHING CONDITIONS FOR 650 MHz NIOBIUM SRF CAVITY*

V. Chouhan†, D. Bice, F. Furuta, M. Martinello, M. K. Ng, H. Park, T. Ring, G. Wu
Fermi National Accelerator Laboratory, Batavia, IL, USA
B. Guilfoyle, M. P. Kelly, T. Reid, Argonne National Laboratory, Lemont, IL, USA

Abstract

The PIP II linear accelerator includes different types of niobium SRF cavities including 650 MHz elliptical low (0.61) and high (0.92) β cavities. The elliptical cavity surface is processed with the electropolishing method. The elliptical cavities especially the low- β 650 MHz cavities showed a rough equator surface after the EP was performed with the standard EP conditions. This work was focused to study the effect of different EP parameters, including cathode surface area, temperature and voltage, and optimize them to improve the cavity surface.

INTRODUCTION

Electropolishing (EP) or buffered chemical polishing (BCP) method is used for processing the inner wall surface of superconducting RF (SRF) cavities used in particle accelerators. The PIP II 800 MeV linear accelerator (linac) includes normal and superconducting accelerating sections to accelerate H^- ions. The superconducting section of the linac uses different types of SRF cavities including half-wave resonator, spoke resonator, and low- and high- β 650 MHz elliptical cavities. The latter two types of cavities are being processed with the EP methods. The EP process is used to make the cavity surface smooth and damage-free. Though extensive studies have been performed on EP of 1.3 GHz cavities and small Nb samples to understand the mechanism of EP [1, 2], limited studies were reported on the large-sized elliptical cavities. This work is aimed to optimize EP parameters for low- β (0.61) 650 MHz (LB650) cavity.

EP SETUP

EP of 650 MHz cavities were performed with a horizontal EP tool available at Argonne National Lab (ANL). Figure 1 shows a photo of the EP tool with a horizontally assembled 650 MHz 5-cell cavity for EP. EP was performed with a standard cathode and a modified cathode. The standard cathode (cathode A) was designed initially with an extended aluminum pieces, called donut, attached to the cathode pipe. In the modified cathode (cathode-B), the donut length was enlarged to make it almost twice of that in the cathode-A. The schematic of the cathode is shown in Fig. 2. A power supply of 20 V x 750 A was used for the standard EP process. A temporary power supply with the rated power of 30 V x 210 A was used for studying the

effect of voltage higher than 18 V, which is the standard voltage applied for EP of Nb SRF cavities. During the EP, the cavity temperature was controlled by spraying water on the exterior of the cavity wall. The cooling system was improved for better control of the cavity temperature.

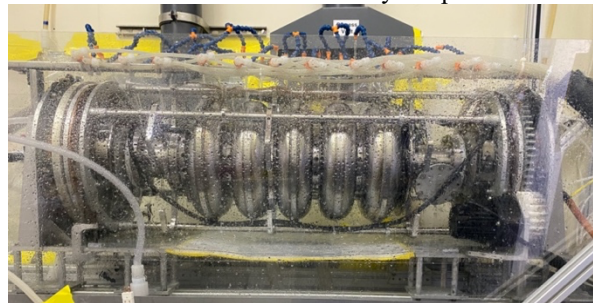


Figure 1: EP tool with a 650 MHz 5-cell cavity.

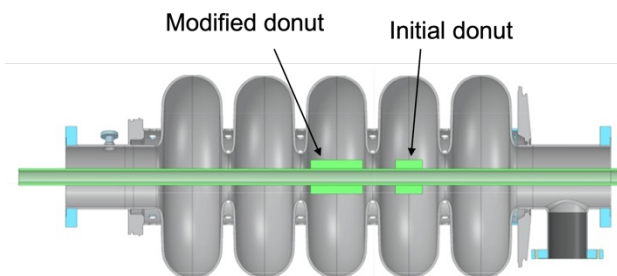


Figure 2: Schematic of the initial (cathode-A) and modified (cathode-B) cathode donuts, which were extended aluminum structure on the cathode pipe.

RESULTS AND DISCUSSION

Polarization Curves

A polarization curve (I - V curve) explains the chemical process occurring on the EP surface as a function of applied voltage [2]. In order to understand the effect of cathode size in the EP process of the LB650 5-cell cavity, I - V curves were measured with both types of cathodes. I - V curves were obtained at a cavity temperature of $\sim 16^\circ\text{C}$. The comparison of I - V curves with both cathodes is shown in Fig. 3. The I - V curve obtained with cathode-A showed a linear relation between EP current and voltage even up to maximum applied voltage of ~ 25 V. The plateau region, in which the current remains constant regardless of a change in applied voltage, was not seen. In contrast to this, the cathode-B resulted in the linear region followed by a current plateau region from 17 V onwards. The voltage, at which the plateau region started, is termed as onset voltage.

* This work was supported by the United States Department of Energy, Offices of High Energy Physics and Basic Energy Sciences under contract No. DE-AC02-07CH11359 with Fermi Research Alliance.

† vchouhan@fnal.gov

TESTS OF THE EXTENDED RANGE SRF CAVITY TUNERS FOR THE LCLS-II-HE PROJECT*

C. Contreras-Martinez[†], T. Arkan, A. Cravatta, B. Hartsell, J. Kaluzny, T. Khabiboulline,
 Y. Pischalnikov, S. Posen, G. Romanov, J. C. Yun, Fermilab, Batavia, IL, USA

Abstract

The LCLS-II HE superconducting linac can produce multi-energy beams by supporting multiple undulator lines simultaneously. This could be achieved by using the cavity SRF tuner in the off-frequency detune mode. This off-frequency operation method was tested in the verification cryomodule (vCM) and CM 1 at Fermilab at 2 K. In both cases, the tuners achieved a frequency shift of -565 ± 80 kHz. This study will discuss cavity frequency during each step as it is being assembled in the cryomodule string and finally when it is being tested at 2 K. Tracking the cavity frequency helped enable the tuners to reach this large frequency shift. The specific procedures of tuner setting during assembly will be presented.

INTRODUCTION

The LCLS-II-HE project will add 19 cryomodules of the type already used for the LCLS-II project. For multi-energy operation in the LCLS-II-HE linac the tuners were modified to meet the off-frequency operation (OFO) specification. This new mode of operation requires the tuner to be able to compress the cavity by -465 kHz from the nominal operation of 1.3 GHz. The OFO is then 1299.535 MHz.

The SRF tuner for the LCLS-II-HE must be capable of bringing 100 % of all cavities to the operational frequency of 1.3 GHz. In the case of OFO at least 62 % of the cavities must be tuned to 1299.535 MHz [1]. Tuning from 1.3 GHz to OFO must be done approximately twice a month. This level of operation pushes the tuner and cavity to new thresholds, which test the longevity of both. Recent results demonstrate that the cavity and tuner can achieve these requirements [2]. The tuner needed to be modified to achieve these results. This paper discusses the successful tuning to OFO (1.3 GHz $-$ 465 kHz) for the vCM and CM1 LCLS-II-HE cryomodules.

CAVITY FREQUENCY TUNER

The tuner for LCLS-II-HE cavities consists of two components, one is the slow-coarse component and the other is the fine-fast component. The slow-coarse component consists of a Phytron stepper [3]. This component is used to tune the cavity to the nominal frequency after cooldown. The second frequency tuning component consists of two piezo actuator encapsulations made by Physik Instrumente (PI) used for fast-fine frequency [3].

This manuscript has been authored by Fermi Research Alliance, LLC under Contract No. DE-AC02-07CH11359 and DE-AC02-76SF00515 with the U.S. Department of Energy, Office of Science, Office of High Energy Physics.

[†] ccontrer@fnal.gov

In addition to the -465 kHz compression from 1.3 GHz the tuner must also compress the cavity from the 2 K landing frequency ($f_{2k \text{ Landing}}$). The $f_{2k \text{ Landing}}$ is the initial frequency after the cavities reach 2 K and no tuning has been performed. The next section will discuss how cavities arrive at this frequency. The results from [4] showed that 95 % of the cavities $f_{2k \text{ Landing}}$ are below 250 kHz. Therefore, the tuner must compress the cavity by -715 kHz, roughly three times larger than the LCLS-II tuners. The LCLS-II-HE tuners were modified from the LCLS-II by decreasing the tuner lever arm ratio from 1:20 to 1:16. The length of the motor arm was also increased by 7 mm. Not all the changes were implemented for cavity one. A full description and discussion of these changes is presented in Ref. [4]. These modifications changed the motor sensitivity from 1.4 Hz/step to 1.84 Hz/step.

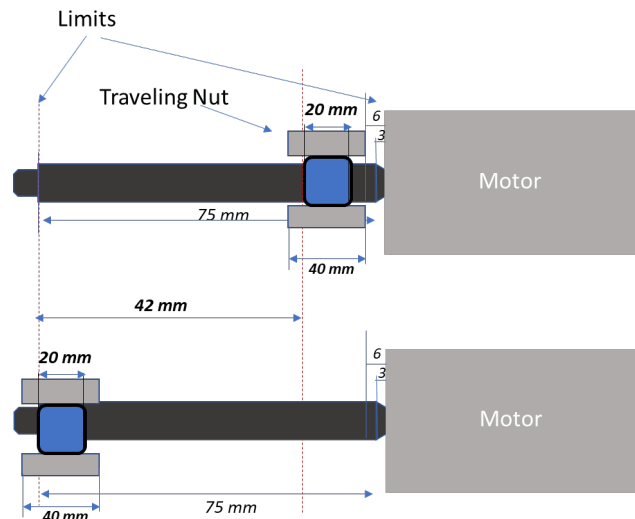


Figure 1: Motor shaft schematic showing the traveling range in mm. the traveling nut is connected to the tuner arm which is responsible for compressing the cavity.

The stepper motor system consists of two limit switches. They stop the motor when they are triggered. Three different parts can set the motor's hard limits. One of the limits is the length of the shaft screw thread, which is 75 mm (see Fig. 1). This limit is critical, if the traveling nut comes out of the threaded screw no movement will be possible. The second limit is the magnetic shielding on the cavity to the right of the end of the shaft screw. Making contact with the magnetic shielding will cause large forces on the stepper motor if it is operated. Large forces can lead to stepper motor failure. The last limit is when the traveling nut frame is too close to the motor body. The limit towards the body of the motor has two different gaps set to prevent

LCLS-II AND HE CRYOMODULE MICROPHONICS AT CMTF IN FERMILAB*

C. Contreras-Martinez, E. Harms, C. Cravatta, J. Holzbauer, S. Posen, L. Doolittle¹, B. Chase,
J. Einstein-Curtis², J. Makara, R. Wang, Fermilab, Batavia, IL, USA

¹ Lawrence National Laboratory, Berkeley, CA, USA

² Previously at Fermilab, now at RadiaSoft, Boulder, CO, USA

Abstract

Microphonics causes the cavity to detune. This study discusses the microphonics of sixteen 1.3 GHz cryomodules, 14 for LCLS-II and 2 for LCLS-II HE tested at CMTF. The peak detuning, as well as the RMS detuning for each cryomodule, will be discussed. For each cryomodule, the data was taken with enough soaking time to prevent any thermalization effects which can show up in the detuning. Each data capture taken was 30 minutes or longer and sampled at 1 kHz.

INTRODUCTION

The LCLS-II is an X-ray FEL linac that uses 9-cell 1.3 GHz SRF cavities. The collaboration between SLAC, Fermilab, Lawrence Berkeley National Lab (LBNL), and Thomas Jefferson Lab (JLab) produced cryomodules tested at Fermilab and JLab. One of the tests done at Fermilab in the cryomodule testing facility (CMTF) facility is to record the level of microphonics. The cryomodules (CM) are shipped to SLAC in California once testing is complete at Fermilab or JLAB.

The cryomodule is roughly 13 m long and contains eight 1.3 GHz SRF cavities. Liquid helium cools the cavities to 2 K. The bandwidth of the cavities is 20 Hz, and during operation, the cavities need to experience a peak detuning of 10 Hz or less. Microphonics on the cryomodules were mitigated by using passive damping techniques. The JT cryogenic valves were modified by adding wiper rings along the valve stem to dampen thermoacoustic oscillations. The valves were also reconfigured to change the helium supply line by altering where the input connects. These techniques are described in detail by Hansen et al. [1]. Changes to the cavity 1 connection and other changes are discussed at length in Refs. [2-4]. These changes result in a substantial decrease in frequency detuning of all eight cavities. The peak detuning before these changes was as high as 200 Hz, and now it can go up to 30 Hz with these changes implemented.

Since all the changes were implemented a peak detuning below 10 Hz was observed in 63 % of all cavities as shown in Fig. 1. For 63 % of all cavities the RMS detuning was below 2 Hz (see Fig. 2). Note that these results could be unique to the CMTF environment. The supply pressure at

SLAC is lower, and so is the inlet temperature. Additionally, the cryogenic plant is further apart from the linac, decreasing the vibration level. Thermalization effects can affect the cavity detuning. Therefore, the data analyzed was captured one week after the cool down to allow these effects to dissipate. The data presented in Figs. 1 and 2 only have two cryomodules operated at 16 MV/m while the rest are at 5 MV/m. The cavities with a peak detuning greater than 10 Hz have similar vibrations,

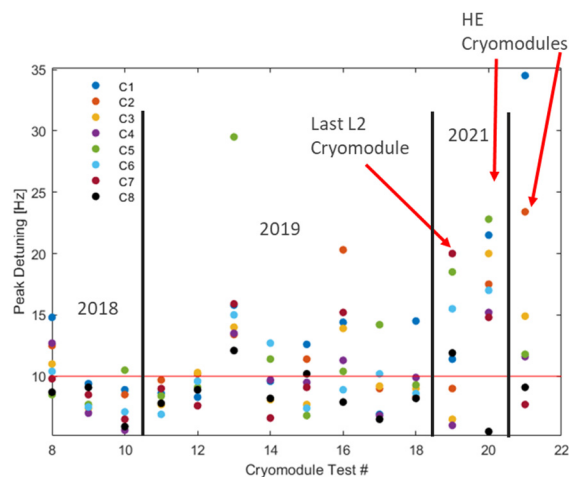


Figure 1: Cavity peak detuning of all 8 cavities from cavities tested from 2018 until 2022. These include cavities from LCLS-II and HE. The cavity peak detuning specification is 10 Hz.

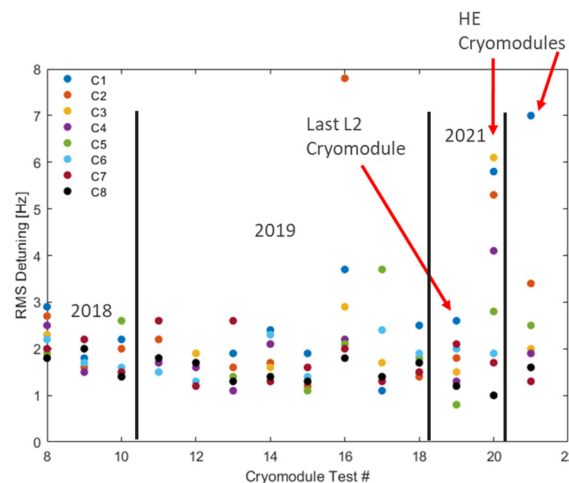


Figure 2: RMS cavity detuning from 2018 to 2022. These include cavities from LCLS-II and HE.

*This manuscript has been authored by Fermi Research Alliance, LLC under Contract No. DE-AC02-07CH11359 with the U.S. Department of Energy, Office of Science, Office of High Energy Physics.
† ccontrer@fnal.gov

SIMULATED LORENTZ FORCE DETUNING COMPENSATION WITH A DOUBLE LEVER TUNER ON A DRESSED ILC/1.3 GHz CAVITY AT ROOM TEMPERATURE*

C. Contreras-Martinez[†], Y. Pischalnikov, J. C. Yun, Fermilab, Batavia, IL, USA

Abstract

Pulsed SRF linacs with high accelerating gradients experience large frequency shifts caused by Lorentz force detuning (LFD). A piezoelectric actuator with a resonance control algorithm can maintain the cavity frequency at the nominal level, thus reducing the RF power. This study uses a double lever tuner with a piezoelectric actuator for compensation and another piezoelectric actuator to simulate the effects of the Lorentz force pulse. A double lever tuner has an advantage by increasing the stiffness of the cavity-tuner system, thus reducing the impact of LFD. The tests are conducted at room temperature and with a dressed 1.3 GHz 9-cell cavity.

INTRODUCTION

The primary source of cavity detuning for linacs operated in high gradient and high beam loading is Lorentz force detuning (LFD). The interaction of the RF magnetic field in the cavity and the wall currents on the cavity gives rise to the Lorentz force. The interaction with the magnetic field caused the equator of the cavity to bend inwards while the magnetic field interaction causes the cavity to bend outwards. Sending more RF power to the cavity can maintain the nominal accelerating gradient, but this has limitations. Piezoelectric (piezos) actuators in conjunction with a resonance control algorithm are widely used to keep the accelerating gradient of the cavity constant. The piezos can expand or contract depending on the polarity of the applied voltage.

The test's purpose is to measure the dynamic parameters of the dressed cavity LCLS-II tuner system [1] and demonstrate that there is no significant difference from the previous test at S1Global, which showed successful compensation of LFD on all the types of cavity-tuner systems [2]. This tuner has high stiffness, and the design allows to replace the piezo and stepper motors through a designated port on the cryomodule. The piezo actuator is excited by a single cycle sine wave before the arrival of the RF pulse. The duration, time advance, and amplitude of the sine wave are optimized manually by trial and error. This method is standard and used by many groups [3].

EXPERIMENTAL SETUP

A schematic of the hardware and signal topology for measurement of the cavity frequency detuning and reso-

nance control is shown in Fig. 1. An RF analog signal generator produces the input signal to excite the cavity in the π mode at 1298.838 MHz at room temperature. The forward power is coupled through a directional coupler and fed to input A of the AD8032 Analog Phase Detector (APD). The transmitted power of the cavity is sent to input B of APD. The output signal of the APD is proportional to the phase shift between the forward and transmitted power of the cavity. The forward and transmitted power phase can then be related to the cavity detuning.

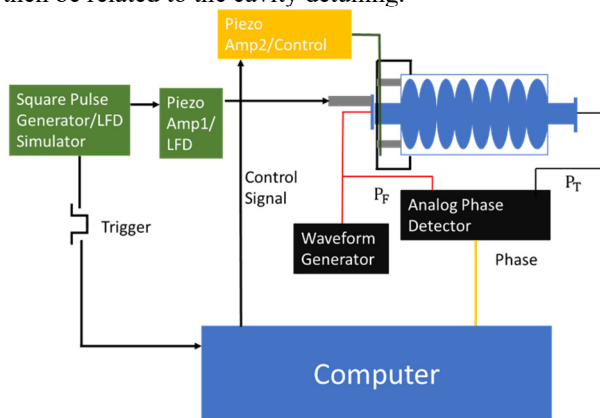


Figure 1: Schematic of signals used to measure the cavity frequency and for resonance control. A square wave pulse generator was used to simulate the LFD pulse and to trigger the control.

The formula to relate the phase of the two signals to the cavity detuning is given by

$$\Delta f = \frac{f_0}{2Q_L} \tan \phi \quad (1)$$

where Δf is the cavity detuning, $f_0/2Q_L$ is the half-bandwidth of the cavity, and ϕ is the phase between the forward and transmitted power. The cavity frequency detuning was digitized with NI-PXI-4472 14-bit ADC. The cavity detuning calculation, recording, and resonance control of the cavity detuning data are done through LabVIEW.

A square pulse with a small duty factor simulates the LFD pulse. The pulse is also used as a trigger for data acquisition and to excite the control signal. The piezos used to control and simulate the LFD pulse are on the same side, which contains a bellow (see Fig. 2) piezos will be called control piezos. The shaker piezos sit directly on the cavity flange while the control piezos connect with the cavity bellow via a split ring interface.

*This manuscript has been authored by Fermi Research Alliance, LLC under Contract No. DE-AC02-07CH11359 with the U.S. Department of Energy, Office of Science, Office of High Energy Physics.

[†] ccontrer@fnal.gov

VALIDATION OF THE 650 MHz SRF TUNER ON THE LOW AND HIGH BETA CAVITIES FOR PIP-II AT 2 K*

C. Contreras-Martinez[†], S. Chandrasekaran, S. Cheban, G. Ereemeev, I. Gonin, T. Khabiboulline, Y. Pischalnikov, O. Prokofiev, A. Sukhanov, J.-C. Yun, Fermilab, Batavia, IL, USA

Abstract

The PIP-II linac will include thirty-six $\beta_G=0.61$ and twenty-four $\beta_G=0.92$ 650 MHz 5 cell elliptical SRF cavities. Each cavity will be equipped with a tuning system consisting of a double lever slow tuner for coarse frequency tuning and a piezoelectric actuator for fine frequency tuning. The same tuner will be used for both the $\beta_G=0.61$ and $\beta_G=0.92$ cavities. Results of testing the cavity-tuner system for the $\beta_G=0.61$ will be presented for the first time.

INTRODUCTION

The proton improvement plan (PIP)-II linac section under construction at Fermilab will consist of five classes of superconducting RF (SRF) cavities made of niobium. The linac will accelerate a proton beam to support experiments for the g-2, mu2e, and DUNE collaborations at Fermilab. Two types of elliptical cavities, the low beta (LB) cavity at $\beta_G=0.61$ and the high beta (HB) cavity at $\beta_G=0.92$, are used to accelerate the proton beam from 185 MeV to 800 MeV [1].

The SRF cavity tuner has three roles. It is needed for active microphonics compensation. It is also used for moving the cavities to the nominal frequency after cooling to 2 K. Lastly, it is used for protecting the cavity during pressure tests. This paper presents the double lever arm tuner testing on the cavity at 2 K. The cavity was placed in the recently upgraded cryostat [2] at the Meson Detector Building (MDB) at Fermilab, pictured in Fig. 1. This double lever tuner will be used for both the HB and LB 650 MHz elliptical cavities. The tuner specifications for the HB and LB 650 MHz cavities are shown in Table 1. There are two components to the tuner, one is the slow and coarse frequency tuning component consisting of a stepper motor. The other is the fast and fine frequency tuning component composed of piezoelectric actuators.

The double lever arm tuner's slow and coarse electromechanical component consists of a stepper motor manufactured by Phytron. Accelerated lifetime tests at Fermilab demonstrate that this stepper motor will survive prolonged operation far exceeding the typical linac lifetime of 25 years [3, 4]. Additionally, after an irradiation hardness test (gamma rays), no performance degradation was observed, demonstrating that the stepper motor can survive under these operating conditions [4].

The fast and fine tuner component consists of two piezoelectric actuator capsules. The piezoelectric actuators are used for fast and fine frequency tuning control of microphonics. The piezoelectric actuators are designed and fabricated by Physik Instrumente (PI) per Fermilab specifications. The accelerated lifetime test demonstrates that the piezo can sustain 2×10^{10} pulses with a peak-to-peak amplitude of 2 V. These are the number of cycles expected for the PIP-II linac, equivalent to 25 years. The irradiation test, with the same parameters as the stepper motor test, also showed minimal degradation for this actuator [4].

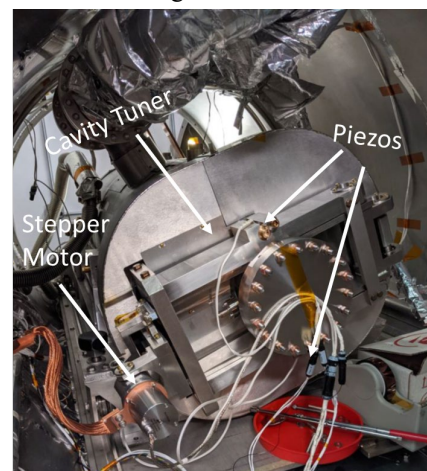


Figure 1: 650 MHz $\beta_G=0.92$ with tuner and other ancillaries inside the STC cryostat at the MDB facility in Fermilab.

SLOW AND COARSE TUNING COMPONENT

The tuner was tested on both the 650 MHz $\beta_G=0.92$ and $\beta_G=0.61$ dressed cavities. Once the cavity is cooled to 2 K the frequency will not be precisely at 650 MHz. Since the tuner can only compress the cavity, which lowers the cavity frequency, the cavity frequency setpoint is set during the production to avoid being below 650 MHz at 2 K. The cavity's frequency at 2 K before tuning is shown in Table 2. This frequency is called the 2 K landing frequency ($f_{2K\text{Landing}}$), note that it is higher than 650 MHz. The slow coarse tuner has three regions of operation. The first region is when the tuner can stretch the cavity via the safety rods; in this region, the piezos are not engaged. The first region is not used during operation. The second region is the unrestrained position where the cavity frequency changes slightly or not at all. This region is due to the safety gap setup at room temperature. The piezos are not engaged in this region, hence the small frequency change. The last region is for normal operation where the piezos are engaged. These regions are shown in Fig. 2.

* This manuscript has been authored by Fermi Research Alliance, LLC under Contract No. DE-AC02-07CH11359 with the U.S. Department of Energy, Office of Science, Office of High Energy Physics.

[†] ccontrer@fnal.gov

SEMANTIC REGRESSION FOR DISENTANGLING BEAM LOSSES IN THE FERMILAB MAIN INJECTOR AND RECYCLER

M. Thieme*[†], J. Arnold, M. R. Austin, M. A. Ibrahim, K. J. Hazelwood*
V. P. Nagaslaev, A. Narayanan[‡], D. J. Nicklaus, G. Pradhan, A. L. Saewert
B. A. Schupbach, K. Seiya, R. M. Thurman-Keup, N. V. Tran, D. Ulusel
Fermi National Accelerator Laboratory[§], Batavia, IL USA
H. Liu, S. Memik, R. Shi
Northwestern University, Evanston, IL USA

Abstract

Fermilab's Main Injector enclosure houses two accelerators: the Main Injector (MI) and the Recycler (RR). In periods of joint operation, when both machines contain high intensity beam, radiative beam losses from MI and RR overlap on the enclosure's beam loss monitoring (BLM) system, making it difficult to attribute those losses to a single machine. Incorrect diagnoses result in unnecessary downtime that incurs both financial and experimental cost. In this work, we introduce a novel neural approach for automatically disentangling each machine's contributions to those measured losses. Using a continuous adaptation of the popular UNet architecture in conjunction with a novel data augmentation scheme, our model accurately infers the machine of origin on a per-BLM basis in periods of joint and independent operation. Crucially, by extracting beam loss information at varying receptive fields, the method is capable of learning both local and global machine signatures and producing high quality inferences using only raw BLM loss measurements.

READS OVERVIEW

The Real-time Edge AI for Distributed Systems (READS) project is a collaboration between the Fermilab Accelerator Division and Northwestern University. The project has two main goals: 1) to create a Machine Learning (ML) system for real-time beam loss de-blending in the Main Injector (MI) accelerator enclosure [2], and 2) to create a separate ML system for slow spill regulation in the Delivery Ring [3] used in the Mu2e experiment [4, 5]. In this paper, we extend our previous work [6] and introduce a novel approach to beam loss de-blending inspired by semantic segmentation models originally developed for biomedical imaging [7].

Beam Loss De-blending

The MI and RR accelerators share a tunnel and one beam loss monitoring (BLM) system. When originally constructed, the 8 GeV permanent magnet Recycler was used as an anti-proton storage ring for the Tevatron collider [8].

* Equal contribution.

[†] Performed at Northwestern University with support from the Departments of Computer Science and Electrical and Computer Engineering.

[‡] Also at Northern Illinois University, DeKalb, IL USA.

[§] Operated by Fermi Research Alliance, LLC under Contract No. De-AC02-07CH11359 with the United States Department of Energy. Additional funding provided by Grant Award No. LAB 20-2261 [1].

As the the 8 GeV anti-proton losses from RR were relatively insignificant compared with the 120 GeV proton losses from MI, there was little need to monitor ionization beam losses from RR. However, when the Tevatron was decommissioned, RR was re-purposed as a proton stacker for MI 120 GeV NuMI beam operation [9] as well as for 8 GeV Muon g-2 experiment beam delivery [10]. As a consequence, normal operation of the accelerator complex sees high intensity beams in both Main Injector and RR simultaneously, and beam losses from both machines are now a significant concern. However, while the origin of radiative losses measured on any of the 259 operational BLMs can be difficult to attribute to a single machine, experts can often attribute losses to either MI or RR based on timing, machine state, and physical location within the ring.

Using streamed, distributed BLM readings and real-time ML inference hardware, this project aims to replicate and then improve upon the machine expert's ability to de-blend, or disentangle, each machines' contribution to the measured losses.

PRELIMINARIES

BLMs are spaced (approximately) evenly within the tunnel and report the incident flux in mR/s. Because this flux is generated when beam is lost from the accelerators, i.e. when beam scrapes the edges of the beampipe and generates a spray of particles that then exit the accelerator, we often refer to it as 'loss'. When we discuss the 'BLM loss profile' we are referring to the pattern of flux measurements over the BLMs at a given time. This is not to be confused with 'loss' in machine learning, which refers to the penalty incurred for prediction errors. In this paper, when we refer to 'loss' or 'BLM loss', it is these flux measurements that we refer to.

TRAINING ON BLM LOSS PROFILES

Following recent progress in Pirate Card development [11], which now allows for the collection of high frequency (333 Hz) data in real-time directly from the BLMs, we have constructed a training dataset using actual accelerator operations data.

A single training example is composed of a single BLM loss profile, also called a 'tick', collected at some time i , and is represented as a 1D vector $x_i \in \mathbb{R}^{259}$ in which each of the 259 element represents the flux over each of the 259

SECOND GENERATION FERMILAB MAIN INJECTOR 8 GeV BEAMLINE COLLIMATION PRELIMINARY DESIGN

K.J. Hazelwood*, P. Adamson, B.C. Brown, D. Capista, R.M. Donahue,
 B.L. Klein, N.V. Mokhov, V.S. Pronskikh, V.I. Sidorov, M.C. Vincent
 Fermi National Accelerator Laboratory, Batavia IL, USA[†]

Abstract

The current Fermilab Main Injector 8 GeV beamline transverse collimation system was installed in 2006. Since then proton beam intensities and rates have increased significantly. With the promise of even greater beam intensity and a faster repetition rate when the PIP-II upgrade completes later this decade, the current collimation system will be insufficient. Over the past 18 months, multiple collimation designs have been investigated, some more traditional and others novel. A preliminary design review was conducted and a design chosen. Work is underway to finalize the chosen design, prototype some of its novel components and procure parts for installation Summer 2023.

NEW COLLIMATION SYSTEM NEED

The Fermilab Main Injector 8 GeV (MI8) beamline is the transfer line for proton beam from the Booster to the Recycler Ring and Main Injector (MI) accelerator as well as the Booster Neutrino experiments (BooNE). The existing transverse collimation system is used to remove beam tails that would otherwise be lost in an uncontrolled fashion at multiple points along the aforementioned machines. The collimators, installed in 2006 [1], were designed to handle beam intensities and repetition rates that were beyond the ability of the Booster to provide then. However, with the end of the Tevatron collider program in 2011, Fermilab has focused on increasing beam power for its neutrino program [2]. Per pulse beam intensity and repetition rates now approach and can exceed the original design expectations of the MI8 collimation system [3]. Later this decade, the PIP-II linear accelerator will provide beam intensities far exceeding the existing collimators abilities [4].

DESIGN SPECIFICATIONS

As seen in Table 1, multiple constraints were specified for the new MI8 collimator system. In addition to these specifications it was also desirable to find a location in the MI8 beamline where the lattice function is at minimal dispersion. The existing MI8 collimators were installed at locations where dispersion was less than ideal, resulting in collimation of higher momentum beam, an undesired effect. The current collimators also happen to be installed adjacent to a tunnel alcove where cables are fed through penetrations to the upstairs service building. Having such high dose rates where

personnel often have to work is not ideal. Locations 825 and 827 were chosen to be the ideal installation locations because of their low dispersion and distance from any radiation sensitive areas in the tunnel.

Table 1: Collimation Design Specifications [5]

Name	Value	Unit
Maximum Beam Intensity [4]	6.5 E12	Protons
Maximum Beam Rate [4]	20	Hz
Maximum Total Collimation	2	%
Maximum Temperature	200	C
Minimum Aisleway Width	4.5	ft
Maximum Power	2	kW
Maximum Total Power	2	kW
Jaw Position Resolution	0.25	mm
Maximum Shielding Dose Rate [6]	0.05	mrem/Hr
Maximum Average Vacuum	1.0 E-7	Torr
Maximum Vacuum	1.0 E-5	Torr

TRADITIONAL DESIGN CANDIDATE

Three existing 8 GeV transverse collimation systems have been designed and installed over the last couple decades, a two stage system in the Recycler Ring [7], another two stage system in Main Injector [8, 9] and the single stage system in the MI8 beamline [3]. All three systems are similar in design; fixed jaws inside a vacuum chamber, encapsulated in tons of steel to absorb lost protons and secondary particles, wrapped in marble to protect personnel from the activated steel. All designs adjust the collimation by moving the entire collimator body. It's because of the success of these operational systems that the first design candidate for the new MI8 collimation system followed this traditional design concept (Fig. 1).

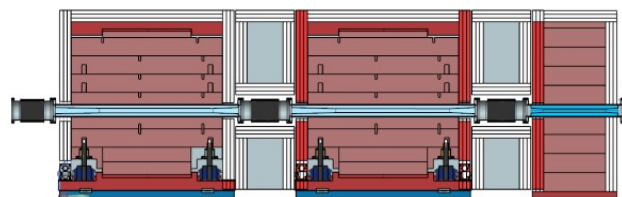


Figure 1: Traditional collimator design candidate elevation cross section. Beam travel is left to right.

Collimator Size

The first improvement implemented in the the Traditional design concept is its size. The current MI8 collimators

* kjh@fnal.gov

[†] Operated by Fermi Research Alliance, LLC under Contract No.De-AC02-07CH11359 with the United States Department of Energy, Batavia, IL USA.

LCLS-II BEAM CONTAINMENT SYSTEM AVERAGE CURRENT MONITOR*

N. Ludlow[†], T. Allison, J. Sikora, J. Welch
SLAC National Accelerator Laboratory, Menlo Park, CA 94025, USA

Abstract

LCLS-II is a 4th generation light source at the SLAC National Accelerator Laboratory. A new Superconducting Continuous Wave (CW) RF accelerator will be used to accelerate a 30 uA electron beam with a 1 MHz bunch rate. The Average Current Monitor (ACM) is part of the Beam Containment System (BCS) for the LCLS-II accelerator. The Beam Containment System is a safety system that provides paths to safely shut the accelerator beam off under a variety of conditions. The Average Current Monitor is a beam diagnostic within the BCS that is used to verify that the accelerator is producing the appropriate current level and to limit beam power to allowed values to protect the machine and beam dumps. The average beam current is obtained by measuring the power level induced by the beam in a low Q cavity. By knowing the Q, the beta, and the coupling of the cavity, the instantaneous charge can be calculated, then integrated over one millisecond to yield the average current. This paper will discuss progress in the checkout process of the ACM LLRF hardware and firmware leading to LCLS-II commissioning.

INTRODUCTION

The LCLS-II Average Current Monitor (ACM) system uses two redundant normal conducting low Q RF cavities that are installed directly into the beam line downstream of the 100 MeV injector. When the beam may pass through them, it induces an RF field inside the cavities which is measured and used to estimate beam current. The cavities have three RF couplers and feedthroughs, two of which are connected to the measurement electronics to measure the cavity field. The third feedthrough is used to inject an independent, diagnostic signal to continuously evaluate ACM cavity functionality [1].

An independent signal, referred to as the Pilot Tone, is injected into the cavity by the ACM LLRF controller at a frequency that is about 1.3 MHz away from the cavity's 1300 MHz resonant frequency. The purpose of the Pilot Tone is to verify the system is still working by maintaining a stable continuous wave signal. Should the measurement electronics fail to detect this signal, then a fault sequence will be initiated which will result in shutting down the accelerator beam operation. The Pilot Tone is also used to verify the cavity has the correct resonant frequency. The mechanism to evaluate proper cavity functionality is discussed in more detail later.

The main purpose of the ACM system is to fault the Beam Containment System (BCS) if the detected beam current surpasses the appropriate limits. These limits can

be adjusted to correspond to the level desired by the accelerator operators. As a safety system, the BCS and thus the ACM must be robustly tested and validated for proper functionality. Hardware and firmware processes must work as designed independently without software intervention. Extensive testing of the system has been performed in preparation for LCLS-II commissioning.

SYSTEM OVERVIEW

ACM Sensors

The ACM system sensors are pillbox cavities installed directly into the beam line that allow for the beam to pass through and induce an RF field inside the cavities. To respond correctly to dark current in the accelerator, with bunch frequencies much greater than 1 MHz, the resonant frequency of the cavities must closely match the 1300 MHz accelerator reference. The cavities are made of stainless steel and have a relatively low loaded Q of about 1200. With an expected maximum bunch frequency of 1 MHz, most of the beam-induced RF from a bunch has decayed by the time of arrival of the next bunch. The loaded Q must also be within a specified range that is determined by the measurement electronics [2].

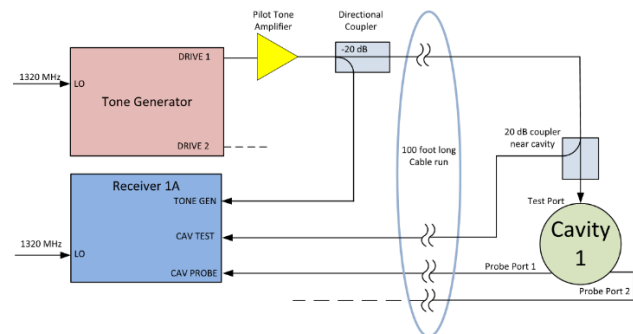


Figure 1: Block diagram showing the connections on one of the cavities. One other receiver connects to Probe Port 2/ Drive 2 on the Tone Generator heads to the second cavity which involves the remaining two receivers.

ACM Receivers

The main function of the ACM receivers is to measure the beam-induced field within the cavity. The receivers measure the field of the cavity through the Probe Port (see Fig. 1) which have a coupling of about 0.5 [2]. Through this port, the receiver picks up two distinct signals: the beam-induced RF field and the Pilot Tone. The charge passing through the cavity can be calculated from the measured induced RF field, then integrated over 1 millisecond to obtain an average current. The average current is continuously calculated with a 1 ms moving average [3].

* This work supported under DOE contract DE-AC02-76SF00515.

[†] nludlow@slac.stanford.edu

WAKER EXPERIMENTS AT FERMILAB RECYCLER RING

O. Mohsen*, R. Ainsworth, N. Eddy

Fermi National Accelerator Laboratory, Batavia, IL 60510, USA

Abstract

Attaining high-intensity hadron beams is often limited due to the transverse collective instabilities, whose understanding is thus required to see and possibly extend the intensity limitations. To explore such instabilities, a novel artificial wake system, the waker, has been built and tested at the Fermilab Recycler Ring (RR). In this report, we show recent upgrades of the waker. Also, we present experimental studies of instabilities at various space charge and wake parameters.

INTRODUCTION

As physics experiments demand more beam power, limitations in the intensity and beam quality are often encountered. It is important to understand the existing beam limitation and to try to overcome them to achieve the required beam parameters for future experiments.

Transverse Mode Coupling Instability (TMCI) is one of the main limitations of high-intensity beams in circular machines [1]. The dependence of the TMCI threshold on Space Charge (SC) has been considered previously. For instance, it was shown in several analytical models that at large SC tune shifts compared to the synchrotron tune, the threshold of TMCI increases [2–4]. It was also suggested that, although the threshold of TMCI increases, a new form of instabilities takes place [5]. Such instabilities, namely *convective instabilities*, may require different treatment than the traditional feedback system which damps the bunch center of charge. Thus, experimental verification of these new instabilities and the development of novel methods to mitigate them are essential at higher beam intensities.

To explore transverse instabilities further, a new program at the Fermilab Recycler Ring has been established. The program uses a dedicated feedback system, hereafter referred to as *the waker*, to induce instabilities in circulating beams. It does so by mimicking the equivalence of a wakefield kick to the beam. Such a system can explore the SC-wake parameter space and study their effect on beam instabilities simultaneously. In this work, we present the waker design, its recent upgrades, and commissioning. Moreover, we present the initial experimental results of the program and we give a brief description of possible upgrades to the current design.

DESIGN

The waker system, depicted in Fig. 1, is designed similar to a damper system [6]. However, by applying multiple kicks along the bunch, the waker induces instabilities rather than damping them. The system consists of a stripline kicker, split-plates Beam Position Monitor (BPM) pickups, two

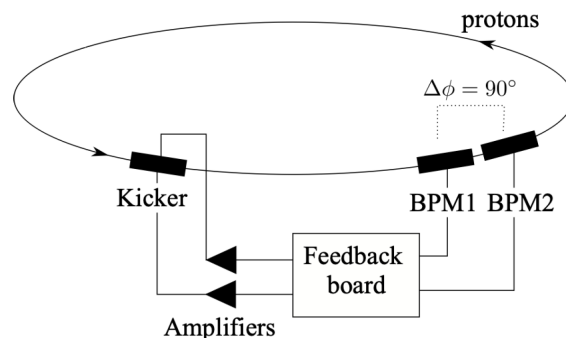


Figure 1: Schematic of the waker system.

amplifiers, and a digital feedback board system. The kickers provide the kick to the beam that mimics the applied wake. The BPMs, separated in phase advance by 90° , are used to measure the beam position and intensity which acts as turn-by-turn feedback to the kicker through the digital board. The two amplifiers (R&K-A010K221-6464R) are used to drive each plate of the kicker providing up to 2.5 kW of power each. Typically, the BPMs measure the position x_i and intensity q_i along different slices of the bunch. This information is used to apply multiple kicks along the bunch in the following turns. The signal from the BPMs as well as the applied kick through the kicker are both analyzed and applied through the feedback board system. The bandwidth requirement of such a system is given by :

$$\Delta\omega \gg \frac{1}{\sigma_t} \quad (1)$$

where σ_t is the bunch duration. Assuming a Gaussian bunch of length $4\sigma_t$, a 100 MHz system with a $\sigma_t = 30$ ns allows for 12 time slices across the bunch. At the Fermilab Recycler, we typically use 2.5 MHz bunches ($\sigma_t \approx 30$ ns) for the Muon program, making a system with 100 MHz bandwidth ideal for such bunches. For diagnostics, we use stripline pickups to observe intra-bunch motion as well as readily available diagnostics in the Recycler to observe beam losses and beam size; e.g. Wall Current Monitors and Ion Profile Monitors (IPM).

EXPERIMENTAL RESULTS

Tune shift in the Recycler can be found by measuring the tune while varying the intensity. To perform the measurement, the beam is kicked and its subsequent motion is recorded for several turns n . The motion is then analyzed using the Fourier transform to look at the frequency spectrum of the beam. Consecutively, the peak in the spectrum with the highest amplitude corresponds to the tune. Each tune

* omohsen@fnal.gov

NOISE IN INTENSE ELECTRON BUNCHES*

S. Nagaitsev^{†,1}, Y.-K. Kim, University of Chicago, Chicago, IL, USA

Z. Huang, G. Stupakov, SLAC, Menlo Park, CA, USA

D. Broemmelsiek, J. Jarvis, A. H. Lumpkin, J. Ruan, G. Saewert, R. Thurman-Keup
 Fermilab, Batavia, IL, USA

Abstract

We report on our investigations into density fluctuations in electron bunches. Noise and density fluctuations in relativistic electron bunches, accelerated in a linac, are of critical importance to various Coherent Electron Cooling (CEC) concepts as well as to free-electron lasers (FELs). For CEC, the beam noise results in additional diffusion that counteracts cooling. In SASE FELs, a microwave instability starts from the initial noise in the beam and eventually leads to the beam microbunching yielding coherent radiation, and the initial noise in the FEL bandwidth plays a useful role. In seeded FELs, in contrast, such noise interferes with the seed signal, so that reducing noise at the initial seed wavelength would lower the seed laser power requirement. Status of the project will be presented.

INTRODUCTION

Noise and density fluctuations in relativistic electron bunches, accelerated in a linac, are of critical importance to various Coherent Electron Cooling (CEC) concepts [1–5] as well as to free-electron lasers (FELs). For CEC, the beam noise results in additional diffusion in a cooled beam that counteracts cooling; and if this noise is not controlled at sufficiently low level, the noise heating effects can overcome cooling. There have been several proposals in the past to suppress the noise in the beam in the frequency range of interest in order to optimize the cooling effects. In SASE FELs a microwave instability starts from the initial noise in the beam and eventually leads to the beam microbunching yielding coherent radiation, and the initial noise in the FEL bandwidth plays a useful role. In seeded FELs, however, such noise interferes with the seed signal, so that reducing noise at the initial seed wavelength would lower the seed laser power requirement [6–8].

Advanced cooling and FEL concepts not only require the knowledge of beam noise level but also call for its control. We are proposing to carry out a systematic theoretical and experimental study of electron beam noise at micrometer wavelengths at the Fermilab FAST facility [9, 10]. Figure 1 shows the energy kick, experienced by a proton in the EIC CEC kicker section [11]. The longitudinal scale of the wake is $\sim 3 \mu\text{m}$, corresponding to the frequency bandwidth of interest of $\sim 40 \text{ THz}$. This wavelength-scale is of general interest in accelerator and beam physics as indicated by the community-driven research opportunities survey. Our research goals are (1) to measure the electron beam density noise level in a $0.5 - 10\text{-}\mu\text{m}$ wavelength range,

(2) to predict the beam noise level in order to compare with the measurements, and (3) to find mechanisms that affect the beam noise to control its level in a predictable manner. In this paper we will describe our progress to date as well as our future experimental plans at Fermilab's FAST electron linac.

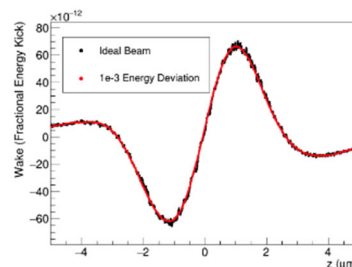


Figure 1: The energy kick, generated by one proton in the CEC kicker section. The longitudinal scale of this kick is $\sim 3 \mu\text{m}$, corresponding to the frequency bandwidth of interest of $\sim 40 \text{ THz}$.

FAST FACILITY AND APPARATUS

The Fermilab Accelerator Science and Technology (FAST) Facility, shown in Fig. 2, is well-suited for this research as it can provide electron bunches with charges $0 - 3 \text{ nC}$, $1 - 30 \text{ ps}$ long rms and energies $50 - 300 \text{ MeV}$. This makes it relevant to future needs of electron-ion colliders as well as injectors for future FELs. Electron bunches are generated by a Cs_2Te photocathode and a UV laser. An L-band rf gun accelerates the beam to 4.5 MeV (typical).

Table 1: FAST and Proposed CEC Beam Parameters

Parameter	FAST	EIC	EIC
Proton beam energy, GeV		100	275
Elect. beam energy, MeV	50 - 300	50	137
Bunch charge, nC	0 - 3	1	1
Emittance, rms norm, μm	~ 3 (at 1 nC)	2.8	2.8
Bunch length, mm	0.3-10	12	8
Drift section (amplifier), m	80	100	100

*Work supported by the DOE ARDAP office.

[†]nsergei@fnal.gov

¹ also at Fermilab

OPTIMIZATION OF SUPERCONDUCTING LINAC FOR PROTON IMPROVEMENT PLAN-II (PIP-II)*

A. Pathak[†], E. Pozdeyev, Fermi National Accelerator Laboratory, Batavia, IL, USA

Abstract

PIP-II is an essential upgrade of the Fermilab complex that will enable the world's most intense high-energy beam of neutrinos for the international Deep Underground Neutrino Experiment at LBNF and support a broad physics program at Fermilab. Ultimately, the PIP-II superconducting linac will be capable of accelerating the H^- CW beam to 800 MeV with an average power of 1.6 MW. To operate the linac with such high power, beam losses and beam emittance growth must be tightly controlled. In this paper, we present the results of global optimization of the Linac options towards a robust and efficient physics design for the superconducting section of the PIP-II linac. We also investigate the impact of the nonlinear field of the dipole correctors on the beam quality and derive the requirement on the field quality using statistical analysis. Finally, we assess the need to correct the quadrupole focusing produced by Half Wave, and Single Spoke accelerating cavities. We assess the feasibility of controlling the beam coupling in the machine by changing the polarity of the field of linac focusing solenoids

INTRODUCTION

The superconducting section of the PIP-II linac [1] aims to deliver a 2 mA (average current), 800 MeV, H^- beam using five distinct families of superconducting (SC) accelerating cavities accompanied by SC solenoids and normal conducting quadrupoles for transverse confinement. At such a high beam power, a meticulous, global optimization of the lattice parameters is essential to avoid transmission loss and beam quality deterioration through emittance growth, particularly at lower energies where the particle dynamics is primarily driven by nonlinear space-charge forces. Here we present the results of a comprehensive lattice optimization study undertaken to ensure a reliable, efficient, and robust physics design through a stable region of operation in the stability chart [2] with an adiabatic variation in the phase advances while keeping the structure phase advances below 90° .

Apart from the beam degradation caused by the nonlinear space-charge forces at high intensities, the dipole corrector's nonlinearities [3,4] and asymmetric transverse RF defocusing produced by the spoke cavities [5–9] can affect the evolution of beam quality along the linac. Therefore, a thorough statistical analysis was performed to investigate the effect of the dipole corrector's nonlinearity on transverse emittance growth, and an upper limit on the uniformity of the

field integral was established for an acceptable beam quality throughout the linac. The SC section of the PIP-II linac uses SC solenoids, guiding a symmetric focusing; therefore, any deviation from a symmetric nature in the transverse (x - y) plane is disfavored. However, the central conductor used in single spoke cavities introduces an asymmetric RF field, and therefore the beam suffers from asymmetric RF defocusing in x and y directions. The asymmetry produced by these cavities was investigated, and compensatory mechanisms using the solenoid current polarity and quadrupolar field generated by the pair of dipole corrector coils with appropriate configurations were compared for efficient asymmetry compensation while keeping minimal coupling between the two transverse planes and also reducing the cryomodule (CM) complexities through minimization of compensating remedies and related power supplies.

LATTICE OPTIMIZATION

We considered the existing physics design of the PIP-II linac with revised CM lengths and performed detailed optimization studies to minimize emittance growth and mitigate the collective resonances causing noticeable emittance exchange between longitudinal and transverse planes, as shown in Figs. 1(c) and 1(d). We performed a comprehensive analysis to quantify the impact of every accelerating and focusing element on beam behavior along the linac and adopted a tuning algorithm to minimize the emittance growth and halo development in all three planes. We determined to operate near a $k_z/k_{x,y} = 1.3$, and therefore, the solenoid fields were adjusted to satisfy the chosen operating point in the Hoffman chart while keeping a smooth phase advance transition and the structure tune per period below 90° . Comparing

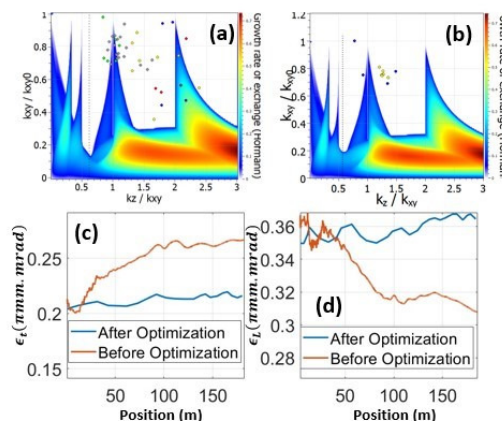


Figure 1: (a) Stability chart before optimization, (b) Stability chart after optimization, (c) Transverse normalized rms emittance, (d) Longitudinal normalized rms emittance.

* This manuscript has been authored by Fermi Research Alliance, LLC under Contract No. DE-AC02-07CH11359 with the US Department of Energy, Office of Science, Office of High Energy Physics.

[†] abhishek@fnal.gov

ACCELERATED LIFETIME TEST OF THE SRF DRESSED CAVITY/TUNER SYSTEM FOR LCLS II HE PROJECT*

Y. Pischnalnikov[†], T. Arkan, C. Contreras-Martinez, B. Hartsell,
 J. Kaluzny, R. Pilipenko, J.C. Yun, Fermilab, Batavia, IL, USA
 W. Lahmadi, Phytron, Waltham, MA, USA

Abstract

The off-frequency detune method is being considered for application in the LCLS-II-HE superconducting linac to produce multi-energy electron beams for supporting multiple undulator lines simultaneously [1]. Design of the tuner has been changed to deliver roughly 3 times larger frequency tuning range. Working requirements for off-frequency operation (OFO) state that cavities be tuned at least twice a month. This specification requires the increase of the tuner longevity by 20 times compared with LCLS-II demands. Accelerated longevity tests of the LCLS-II-HE dressed cavity with tuner were conducted at FNAL's HTS. Detail analysis of wearing and impacts on performances of the tuner's piezo and stepper motor actuators will be presented. Additionally, results of longevity testing of the dressed cavity bellow, when cooled down to 2 K and compressed by 2.6 mm for roughly 2000 cycles, will be presented.

INTRODUCTION

LCLS-II dressed cavity equipped with modified (LCLS-II-HE) tuner [2] installed in the FNAL HTS (Horizontal Test Stand). Cavity was cool down to 2K (and during initial part of test to 4K) and operated for almost 2 months.

Objective of this test was to demonstrate that stepper actuator and piezo actuators could withstand longevity specifications required for LCLS-II-HE OFO. Longevity of the Phytron stepper motor actuator [3], that deployed in the all the SRF cavity tuners of LCLS-II Linac, reported in previous studies [4,5]. Specific of these studies to conduct test for significantly longer range and as close as possible to real LCLS-II-HE conditions. Additionally, this test was validated that more than 400 cycles of compression of bellow on 2.6mm will not damage bellow.

In the Table 1 specifications for tuner components (stepper motor actuator and piezo actuator) and dressed cavity for LCLS-II-HE OFO and LCLS-II presented.

LONGEVITY TEST AT HTS

Test has been run at HTS test 24 hours in day. LabView based program continuously run test and twice a day operator checked on progress. Test executed with following iterations: 1) read/record cavity frequency through NWA, 2) run stepper motor on 30kSteps, 3) read /record stepper motor temperature. Range of stepper motor (set by opera-

tor) was from 0 to +330kSteps that deliver cavity compression on 600kHz. One full cycle is 660kStep. Summary of the parameters for one tuner cycle presented on Table 2. LabView program has many interlocks: a) stepper motor overheating, b) frequency of cavity do not change after driver delivered on stepper motor pulses to move on 30kStep, c) failure of NWA to find the cavity frequency. As soon as any interlock will be triggered, LabView program will halt operation to prevent any damage to tuner/dressed cavity system.

Table 1: Specification for Longevity of the Stepper and Piezo Actuators for LCLS-II & LCLS-II-HE

	LCSI II	LCLS II HE
Frequency tuning required for 95% of the cavities to bring to 1.3GHz after cooldown to T=2K, [kHz]	200	200
Stroke/compression required to tune cavities to 1.3GHz after cooling down to T=2K, [mm]	0.67	0.67
Forces on the shaft/nut system to tune 95% of cavities to f=1.3GHz, [N]	260	325
Forces on the piezo actuator to tune 95% of cavities to f=1.3GHz, [kN]	2.6	2.6
Forces on the shaft/nut system to tune 95% of cavities to OFO f=1.3GHz-465kHz, [N]	N/A	710
Forces on the piezo actuator to tune 95% of cavities to OFO f=1.3GHz-465kHz, [kN]	N/A	6
Longevity of the actuator/Number of the motor steps to tune cavity from 1.3GHz to "safe" position before warm-up (twice a year) during 20 years, [MSteps]	12	10
Longevity of the actuator/Number of the motor steps to tune cavity from 1.3GHz to "1,3GHz-465kHz" and back 20 times a year during 20 years, [MSteps]	N/A	210
Longevity for 20 years operation, [Msteps]	12	220
Overall stroke of traveling nut on the shaft for 20 years of operation, [m]	1.2	22
Overall stroke/cavity compression for 20 years of operation, [m]	0.03	0.69

Stepper motor located inside insulated vacuum environment and will overheat if run continuously. Working range for stepper motor was between T=40K to T=80K. This setting led to stepper work time ~ 110min and idle (cool-down time) ~62min. For one day (24hours) stepper tuner was able to run on ~ 10.3 MSteps that delivered 15.6 tuner's cycles. Summary of the HTS data accumulated for 2-month continuous test of tuner system presented on the Table 3.

All the data collected during 2-month HTS test (cavity frequency vs time) presented on the Figure 1. There are 2 distinct portions: operation at T=4K (at the beginning of test) and T=2K. Figure 1 demonstrated fact that stepper motor actuators (and whole tuner) do not experience any loss of performances after operating in cold/insulated vacuum environment for 414 MSteps that equivalent to 2 lifetimes of LCLS-II-HE OFO. Three plots/cycles (at start, middle and end of test) of cavity frequency retuning vs tuner stroke/stepper motor stroke coincided with very good accuracy.

* This manuscript has been authored by Fermi Research Alliance, LLC under Contract No. DE-AC02-76SF00515 with the U.S. Department of Energy, Office of Science, Office of High Energy Physics.

[†] pischnal@fnal.gov

DIAGNOSTICS FOR LINAC OPTIMIZATION WITH MACHINE LEARNING

R. Sharankova*, M. Mwaniki, K. Seiya, M. Wesley
Fermi National Accelerator Laboratory, Batavia, IL 60510, USA

Abstract

The Fermilab Linac delivers 400 MeV H⁻ beam to the rest of the accelerator chain. Providing stable intensity, energy, and emittance is key since it directly affects downstream machines. To counter fluctuations of Linac output due to various effects to be described below we are working on implementing dynamic longitudinal parameter optimization based on Machine Learning (ML). As inputs for the ML model, signals from beam diagnostics have to be well understood and reliable. In this paper we discuss the status and plans for ML-based optimization as well as preliminary results of diagnostics studies.

THE FERMILAB LINAC

The Fermi National Accelerator Laboratory (Fermilab) Linac accelerates H⁻ beam from 750 keV to 400 MeV. The Linac is preceded by the Pre-Accelerator comprising the Ion Source, the Low Energy Beam Transport (LEBT) line, a radio-frequency quadrupole (RFQ), and the Medium Energy Transport (MEBT) line. The magnetron ion source ionizes hydrogen gas into plasma, then extracts and accelerates a beam of negative H ions. The continuous H⁻ beam is chopped, bunched and accelerated through the rest of the Pre-Accelerator from 35 keV to 750 keV of kinetic energy before entering the Linac. The Linac comprises three parts: a Drift Tube Linac (DTL), a transition section and a Side Coupled Linac (SCL). The DTL is composed of 207 drift tubes spread across 5 tanks. It operates at RF frequency of 201.25 MHz and accelerates beam to 116.5 MeV. The SCL has 7 modules, operating at resonant frequency of 805 MHz and accelerates beam to 401.5 MeV. A buncher and a vernier cavity located in the transition section allow for longitudinal matching between the DTL and the SCL. During regular operations, the Fermilab Linac has an output of roughly 25 mA and pulse length of 35 μ s, with transition efficiency $\geq 92\%$.

LINAC RF & LLRF

DTL RF field amplitude is controlled by the Marx modulator logic controller which in turn controls the 5 MW power tube modulator voltage [1]. The RF phase is controlled by the low level RF (LLRF) module in a VME eXtension for Instrumentation (VXI) crate. Each SCL module is powered by a 12 MW klystron with VXI based LLRF phase and amplitude control. The amplitude and phase are set via the Fermilab control network (ACNET) [2] which sends desired settings to the front-end card in the LLRF VXI crate. In total there are 34 RF parameters (17 phase set points and

17 field gradients) that can be manipulated to affect the overall longitudinal accelerating field in the Linac.

LINAC DAILY TUNING

Stable Linac output is crucial for downstream machines. Ambient temperature and humidity variations are known to affect resonance frequency of the accelerating cavities which induces emittance growth and increased particle loss. In addition, the energy and phase space distribution of particles emerging from the ion source are subject to fluctuations. To counter such effects, operators perform daily tuning. This tuning consists of hand-scanning a handful of RF parameters and trying to maximize beam currents while minimizing losses along the Linac. Figure 1 shows an example of a scan of the RFQ RF phase set point and its effect on total Linac losses and beam currents.

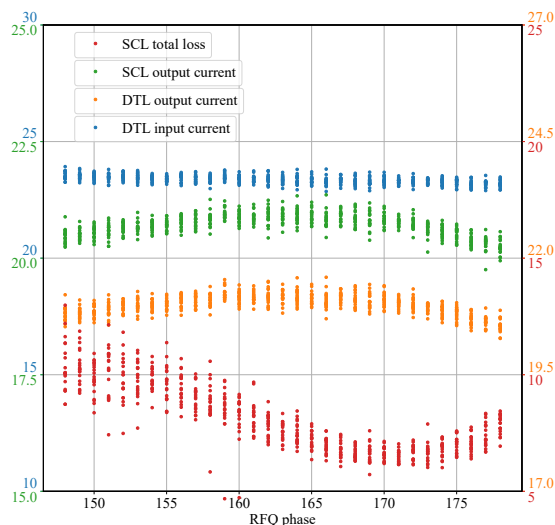


Figure 1: Effect of RFQ phase set point on total Linac beam loss (red) and output beam current (green). Also showing Linac input (blue) and DTL output currents (orange).

RF OPTIMIZATION WITH ML

The hand-tuning procedure outlined above faces several challenges. Human operators cannot optimize in multi-parameter space simultaneously, so there is always the possibility of being off-optimal for the first N-1 devices after tuning device N. Additionally hand-tuning is done when personnel is available, and not necessarily whenever the Linac conditions change.

* rshara01@fnal.gov

CONSIDERATIONS CONCERNING THE USE OF HTS CONDUCTOR FOR ACCELERATOR DIPOLES WITH INDUCTIONS ABOVE 15 T*

M. A. Green, Lawrence Berkeley Laboratory, Berkeley, CA, USA

Abstract

The use of high temperature superconductors for accelerator dipole has been discussed for about twenty years and maybe a little more. Conductors that can potentially be used for accelerator magnets have been available for about fifteen years. These conductors are REBCO tape conductors that can be wound into coils with no reaction after winding and BISSCO cable conductors that require reaction after winding and insulation after reaction in a process similar to Nb3Sn cables. Both conductors are expensive and the process after reacting is expensive. Some unknown factors that remain: Will either conductor degrade in current carrying capacity with repeated cycling like Nb3Sn cables do? The other two issues are problems for both types of HTS conductors and they are; 1) quench protection in the event of a normal region run-away and 2) dealing with the superconducting magnetization inherent with HTS cables and tapes. This paper will discuss the last two issues and maybe will provide a partial solution to these problems.

INTRODUCTION

In the last several years there has been serious discussion about whether HTS conductors in high field accelerator magnets. One approach uses a pure HTS dipole [1], and a second approach is a hybrid magnet with either a low temperature superconductor outer coil with an HTS insert [2]. The outer coil could be niobium titanium at 1.8 K. The first accelerator dipole magnet to reach a central induction above 13 T was hybrid niobium tin and niobium titanium magnet. The LBL magnet reached 13.2 T at 1.8 K and 12.5 T at 4.4 K in 1997 [3]. During the testing magnetic field measurements were done [4]. This magnet had field quality close to what is needed for an accelerator dipole. LBL built a series of block dipole using only Nb3Sn. Some of these magnets reached bore inductions of 16 T with poor field quality. The final magnet could go to 15 T, but the acceptable field quality was between 6 T and 13 T [5, 6]. At low fields, magnetization is an issue, but it is controllable.

LBL produced and tested the first Rutherford cable made from Bi2212 multifilament strands [7]. This conductor must be wound and then reacted in an oxygen atmosphere. As a result, the conductor contains no copper. LBL has fabricated and test a block dipole coil that could carry 8 kA [8]. In the authors opinion, the advantage of block coils is that the stress in the coils can be controlled using strong high modulus metal structures that can take up the stress and hold the coils.

High current tapes made from RECBO tapes, that can carry current at high overall currents densities [9]. HTS tape conductors can have insulation applied to the conductors before winding. Since the conductors can only be bent in the across the thin dimension of the tape (~20 mm radius bends), some have argued that the ends must avoid some kinds of bends, which may make magnet ends more complex [10]. A big issue with REBCO tape conductors is magnetization currents due to the changing field perpendicular to the tape. These currents affect field quality and they can induce large stresses in the coil conductor that damage the coil [11].

This paper proposes a design based on a window frame dipole. Panofsky used a similar design for quadrupoles and combined function magnets [12]. For dipoles wound with flat cables and tapes, one must control conductor magnetization due to fields perpendicular to the conductor flat face.

The negative effects of conductor magnetization in dipoles and quadrupoles have been known since the 1970s [13]. These effects can be troublesome in dipoles and quadrupoles fabricated with flat cables and tapes. In Nb-Ti dipoles these effects can be corrected for [14]. In Nb3Sn and HTS dipoles these effects are much harder to control especially at low fields in cosine dipoles. In symmetrical quadrupoles, magnetization is less of a problem. In a symmetrical dipole, sextupole ($N = 3$) and decapole ($N = 5$) are the multi-poles that cause magnetization problems [15, 16].

A VOPLY DIPOLE BASED DIPOLE

From 1990 to 1999, I worked on compact 1.5 GeV electron synchrotron for UCLA. In June 1992, I travelled to Russia, to visit what is now the Budker Institute of Nuclear Physics (BINP) in Novosibirsk Siberia [17]. This laboratory had been working on compact light sources since the 1970s [18]. I met with Pavel Vobly who was a major force there in magnet design for many years. Our discussions [19] were about a short 7.2 T superconducting dipole for making bends of 30 to 45 degrees. These magnets must have a uniform field across a broad pole width to accommodate the beam bend. These magnets were also designed to have a rapid field drop-off at the magnet ends similar to conventional iron-dominated dipoles.

LBL developed a magnet design that could be used for a variety of machines.

We did a detailed 2D and 3D analysis on 380 mm long 7.2 T dipole that was suitable for the UCLA machine [20, 21]. The pole vertical aperture is 40 mm and the open horizontal aperture is up to 180 mm. The horizontal aperture allowed for the Sagitta of a 45-deg. bend of 1.5 GeV electrons. Figure 1 shows the magnet cross-section.

* This work was supported by the office of Science, under US Department of Energy contract number DE-AC-02-05CH11231.

† magreen@lbl.gov

DEE VOLTAGE REGULATOR FOR THE 88-INCH CYCLOTRON*

M. Kireeff[†], P. Bloemhard, T. Hassan, L. Phair
Lawrence Berkeley National Laboratory, Berkeley, CA, USA

Abstract

A new broadband Dee voltage regulator was designed and built for the 88-Inch Cyclotron at Lawrence Berkeley National Laboratory. The previous regulator was obsolete, consequently, it was difficult to troubleshoot and repair. Additionally, during operation, it displayed problems of distortion and stability at certain frequencies. The new regulator uses off-the-shelf components that can detect and disable the RF during sparking events, protecting the RF driver system. Furthermore, it improves the tuning of the cyclotron and allows consistency in operation.

INTRODUCTION

The 88-inch Cyclotron at Lawrence Berkeley National Laboratory is a sector-focused Cyclotron that has three ion sources with escalating intensities and charge states [1, 2]. These sources can produce mixtures of ions that contain nearly identical charge-to-mass ratios, known as “cocktails” [3].

The cyclotron accelerates protons through uranium to maximum energies of 55 MeV/u. In addition, it supports the ongoing research programs in nuclear structure, astrophysics, heavy element studies, and technology R&D by Lawrence Berkeley National Laboratory (Berkeley Lab) and UC Berkeley. Moreover, it is also home to the Berkeley Accelerator Space Effects Facility that uses these beams to understand the effect of radiation on microelectronics, optics, materials, and cells [4].

The cyclotron has a broadband RF system that operates between the frequency range of 5.5 to 16.5 MHz, Fig. 1. As shown, the 1 V_{pp} RF signal, generated by the frequency synthesizer, goes through the redundant chain, RF drive, and RF clamp circuits. If malfunctions were to occur, compromising the safety of personnel or damaging equipment, these circuits turn off RF signals, stopping the beam and radiation production. Then the RF signal passes into the RF modulator that samples and regulates the Dee voltage amplitude. The modulator also protects the RF system during a sparking event by shutting off the RF, avoiding momentarily overdrive of the RF system, similar to other cyclotron regulators [5, 6].

The signal from the RF modulator is increased by a 10 Watt wideband amplifier. This amplifier is followed by an attenuator switch, which is used to normalize different system attenuations at different frequencies, mainly due to losses on the coaxial cables. Finally, the signal is increased via the 1200A225 amplifier that drives the 150 KW Final

Power Amplifier before being applied to the RF tank that has adjustable RF panels to drive the Dee electrode.

DEE VOLTAGE FEEDBACK

The capacitive Dee probe is displayed on the top right side of Fig. 1. The probe consists of an isolated flush plate that faces the Dee electrode and has a 1 pF capacitance to the Dee electrode. A 1000 pF capacitor is connected to the plate to sample the RF, working as a 1000 divider. The RF feedback voltage is sent to the Dee voltage regulator.

DEE VOLTAGE REGULATOR

Figure 1 displays the new Dee voltage regulator interfaced with the RF system. The feedback voltage is attenuated 3 dB before it is processed by two broadband voltage-controlled attenuators GC2001C are connected in series with the RF system and controlled by the regulator board. These attenuators provide up to 50 dB of attenuation to control and stabilize the Dee voltage. The control board is divided into sections to understand its functionality.

The LM7171 was chosen for the design of the circuit board because it is a high-speed voltage feedback amplifier that has the slewing characteristic of a current feedback amplifier [7]. It can do all of this while being used in all traditional voltage feedback amplifier configurations. The LM7171 is intrinsically stable for gains as low as +2 or -1. This is further shown by its high slew rate of 4100V/μs and a wide unity-gain bandwidth of 200 MHz while only consuming 6.5mA of the supply current.

Usage of ±15 V power supplies allows large signal swings and provides greater dynamic range and signal-to-noise ratio. One necessary aspect to maintain low power supply impedance across frequency is to bypass the power supply [7]. Both positive and negative power supplies should be bypassed individually by placing 0.1 μF ceramic capacitors in parallel with a 10 μF tantalum capacitor directly to the power supply pins of the LM7171. The 51 Ω isolation resistor located at the output of the amplifier increases the stability by reducing the reflections.

Peak-to-Peak Detector

The dashed green section of the Fig. 1 shows a passive peak-to-peak detector. The 50 Ω termination resistor matches the source impedance of the Dee electrode voltage feedback. The detector is a combination of two cascaded parts: the first is the clamp circuit formed by a capacitor and diode at the left, and the second is the peak rectifier circuit formed by a diode and capacitor at the right. It converts the RF signal of peak amplitude V_{peak} into a DC signal. The capacitor of 1nF at the end of the circuit is charged

* Work supported by the U.S. Department of Energy, Office of Science, Office of Nuclear Physics under Contract No. DE-AC02-05CH11231.

[†] mkireeff@lbl.gov

UTILIZING PYTHON TO PREPARE THE VENUS ION SOURCE FOR MACHINE LEARNING*

A. Kireeff[†], D. S. Todd, M. J. Regis, M. Salathe, L. Phair
Lawrence Berkeley National Laboratory, Berkeley, CA, USA

Abstract

The fully-superconducting electron cyclotron resonance (ECR) ion source VENUS is one of the world's two highest-performing ECR ion sources, and a copy of this source will soon be used to produce ion beams at FRIB. The tuning and optimization of ECR ion sources is time consuming and there are few detailed theoretical models to guide this work. To aid in this process, we are working toward utilizing machine learning to both efficiently optimize VENUS and reliably maintain its stability for long campaigns. We have created a Python library to interface with a programmable logic controller (PLC) in order to operate VENUS and collect and store source and beam data. We will discuss the design and safety considerations that went into creating this library, the implementation of the library, and its some of the capabilities it enables.

VENUS OVERVIEW

VENUS (Versatile ECR for NUClear Science) is a third-generation superconducting electron cyclotron resonance (ECR) ion source at Lawrence Berkeley National Laboratory, and it is used as one of the three injector ion sources for the 88-Inch Cyclotron [1], see Fig. 1. In VENUS, like in all ECR ion sources [2], an ion beam is extracted from a confined plasma, as shown in Fig. 2. Axial confinement of the plasma in VENUS is provided by a combination of three NbTi superconducting solenoids: two larger end solenoids and a smaller center coil with reversed polarity that affects the resultant axial field well depth. A sextupole made up of six NbTi superconducting racetrack coils is used for radial confinement. The superposed field of these coils produces a “ B_{\min} ” structure where the magnetic field is a minimum at the center and increases in all directions. Closed surfaces of constant magnetic field magnitude surround this minimum, and electrons are resonantly heated by the injection of microwaves of frequency that correspond to these closed surfaces and satisfy the cyclotron frequency equation $w_c = \frac{eB}{\gamma m}$, where B is the magnetic field, γ is the Lorentz factor, and e and m are the electron charge and mass, respectively. The two frequencies injected into VENUS, 18 GHz and 28 GHz, resonantly heat non-relativistic electrons at magnetic fields of 0.64 and 1.0 tesla, respectively. Beam and support material are introduced to the plasma through a combination of gas injection, ovens, and sputtering, depending on what ion beam is being extracted.

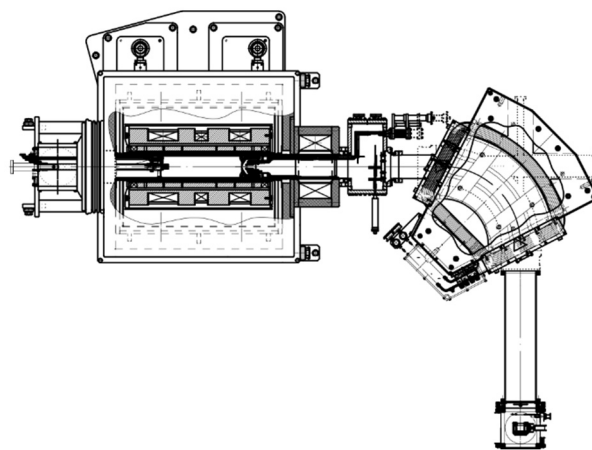


Figure 1: Aerial view of the VENUS Ion Source (left) and its low energy beam line showing the analyzing dipole magnet (upper right) and beam analysis box which includes a faraday cup and vertical and horizontal emittance scanners (bottom right). A second dipole (not shown) follows that directs the selected beam down toward the 88 Inch Cyclotron center.

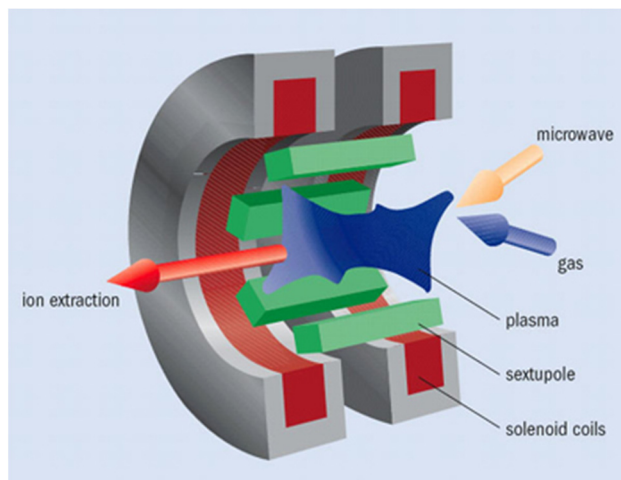


Figure 2: A simplified view of ECR ion source operation. Solenoid coils (middle coil not shown) and sextupole magnets axially and radially confine the plasma, respectively. Gas is injected into the source, it is ionized by microwave-heated electrons, and ions are extracted by establishing a potential difference between the source and beam line.

* Work supported by the U.S. Department of Energy, Office of Science, Office of Nuclear Physics under Contract No. DE-AC02-05CH11231.
[†] akireeff@lbl.gov

VACUUM ELECTRON DEVICES IN THE 88-INCH CYCLOTRON*

M. K. Covo[†], R. Bloemhard, B. F. Ninemire, J. Y. Benitez, D. S. Todd, D. Z. Xie, J. Garcia, L. Phair
 Lawrence Berkeley National Laboratory, Berkeley, CA, USA

Abstract

The 88-Inch Cyclotron at Lawrence Berkeley National Laboratory is a sector-focused cyclotron that has light- and heavy-ion capabilities and supports a local research program in Nuclear Science and is the home of the Berkeley Accelerator Space Effects Facility, which studies effects of radiation on microelectronics, optics, materials, and cells.

The cyclotron utilizes several vacuum electron devices (VEDs) in different systems, mainly to convey plasma heating, high power RF generation, and high-voltage and current DC power generation.

VEDs have been proven reliable, robust, and radiation resistant. They also have wide range, good response against transients, and stable operation with load mismatch during system tuning, instabilities, or breakdowns.

The paper will describe applications of these devices in the 88-Inch Cyclotron.

INTRODUCTION

The Livingston chart shows the evolution of particle accelerators with the astonishing increase of particle energy by an order of magnitude every 7 years [1], demonstrating a power requirement trend of high-power radiofrequency (RF) sources with frequency from tens of MHz to tens of GHz to match the particle accelerators needs.

At all frequencies, the VEDs surpass the solid-state devices (SSDs) technology in producing higher power [2]. For instance, vacuum tubes can generate RF power outputs up to 1 MW continuous wave (CW) and 150 MW pulsed while a single transistor can generate RF power output in the order of hundreds of Watts CW and up to 1 kW pulsed. Consequently, VEDs are largely used in accelerator systems, otherwise, accelerators would require large numbers of transistors operating in parallel in order to reach the lowest power levels [3].

The comparative evolution of the most important VEDs and the SSDs technologies can be observed by the figure-of-merit $P_{avg}f^2$, Fig. 1. The black solid line shows the figure-of-merit technological trend predicted by the Livingston chart. The physical significance of the figure-of-merit derives from the fact that the maximum beam power that can be transported through the RF structure is directly proportional to the cross-sectional area, which is inversely proportional to the operating frequency [4]. Figure 1 shows that the SSDs technology is currently reaching a figure-of-merit 0.1 MW GHz² due to advances in devices based on wide bandgap semiconductor material (GaN).

The reason for the power discrepancy between VED and SSD technologies is that the electron beam flow in a SSD is collision dominated [5]. Thus, it is limited by the capacity to dissipate heat with higher probability of a dielectric breakdown at increased microwave field strengths. Nevertheless, SSD has higher stability and absence of warm-up time.

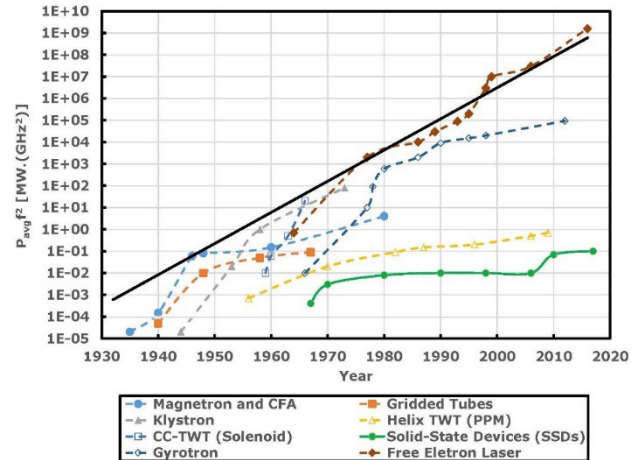


Figure 1: Comparative evolution of major VEDs using the figure-of-merit $P_{avg}f^2$.

Albeit the VED's electron beam flow in vacuum is collisionless, the output power of the VED is limited by the maximum cathode current density available, the maximum anode power density which can be dissipated, the breakdown field strength, the window failure, and the multipactor discharges [3].

VEDs originated in the early 20th century, but they still have a wide variety of commercial and military applications that require high power and efficiency at high frequency, such as commercial satellite communication systems, plasma heating for thermonuclear fusion, radar and electronic warfare systems, medical systems, and accelerators.

The 88-Inch Cyclotron utilizes several VEDs to carry out light- and heavy-ion research that supports a local program in nuclear science. The cyclotron is also the home of the Berkeley Accelerator Space Effects (BASE) Facility. The BASE Facility delivers well-characterized medium energy ion beams to imitate the space environment.

VED amplifiers utilized in the cyclotron convert electromagnetic radiation into coherent radiation through a beam-wave interaction. The coherent radiation requires a bunched electron beam that maintains synchronism with the electromagnetic field. The basic mechanisms for the electromagnetic radiation are [6]:

* Work supported by the U.S. Department of Energy, Office of Science, Office of Nuclear Physics under Contract No. DE-AC02-05CH11231.

[†] mkireffcov@lbl.gov

CRYOGENIC DIELECTRIC STRUCTURE WITH $G\Omega/m$ LEVEL SHUNT IMPEDANCE

C. Jing[†], R. Kostin, Euclid Beamlabs LLC, Solon, OH, USA

Abstract

Shunt impedance is one of the most important parameters characterizing particle acceleration efficiency. It is known that RF losses are reduced at cryogenic temperatures. For example, a record high shunt impedance of $350 M\Omega/m$ was demonstrated recently for all metal X-band accelerating structure, which is more than 2 times higher than that at room temperature. In this article we present a novel hybrid dielectric structure which can achieve even higher shunt impedance due to the fact that losses in dielectric materials reduced much more than in pure copper.

MOTIVATION

Very recently, researchers at SLAC reported a new world record for accelerating gradient in an X-band copper accelerating structure, $150 MV/m$ of stable beam acceleration [1]. The structure was tested in a cryostat at $77 K$, which doubles the Q-factor compared to room temperature, and achieved the highest recorded shunt impedance of $350 M\Omega/m$ in a metallic accelerating structure, one important figure of merit for accelerators. The effort was initiated a few years earlier with a destructive breakdown test of a shorter structure at $45 K$, where a gradient of $250 MV/m$ was reached [2]. This improved performance compared to room temperature structures supports the hypothesis that the breakdown rate can be reduced by immobilizing the crystal defects and decreasing the thermally induced stresses. An investigation in a pulsed DC system demonstrated a similar improvement at cryogenic temperatures [3]. Concurrently, a new ceramic material that has extremely low rf loss at room temperatures ($\tan\delta \sim 6 \times 10^{-6}$ at X-band, more than one order of magnitude improvement compared to $\tan\delta \sim 1 \times 10^{-4}$ for conventional alumina) was used in a Dielectric-Assisted Accelerator (DAA) [4], which achieved a shunt impedance of $617 M\Omega/m$ in C-band. It is well known that the microwave loss of many dielectric materials (e.g., Mg-TiOx-based materials and ultrapure Al_2O_3) can be reduced by a factor of ~ 10 compared to room temperature at liquid Nitrogen temperature or slightly below [5–7]. If we consider the development of an accelerating structure using this new ceramic material at cryogenic temperatures, a $G\Omega/m$ level of shunt impedance may be achievable, which is almost comparable with SRF accelerators, but at a much lower cost. In fact, in 2019 the same group that developed the DAA structure published a simulation result [8], in which they showed a Q factor of 765,000 and a shunt impedance of $3.8 G\Omega/m$ could be achieved at a temperature of $27 K$. However, that structure uses the TM_{02} mode, and can suffer from lower order mode excitation, and thus mode conversion can reduce the overall efficiency. Also, the DAA structure is quite complicated

in terms of dielectric fabrication and must be built in sections; as a result, the unavoidable gaps between adjacent dielectric structures are vulnerable to RF breakdown.

In the last two decades, the theoretical and experimental investigations of dielectric accelerating structures have predominantly used a dielectric-lined waveguide (i.e., dielectric-loaded accelerator, DLA), due to its simple geometry and low fabrication cost [9]. However, in comparison with the prevailing metallic disk-loaded accelerators, the dielectric-lined waveguide suffers from a lower Q-factor and lower shunt impedance. The reason for the low shunt impedance of a conventional DLA structure is the high magnetic field of the TM_{01} mode near the copper surface, which leads to high wall currents and ohmic losses. Recently we have proposed and studied two different variations of dielectric accelerators for cryogenic temperatures ($70K$ or $45K$) operation: 1) the Cryogenic Dielectric Corrugated Accelerator (CDCA, Fig. 1a); 2) the Cryogenic Dielectric Disc Accelerator (CDDA, Fig. 1b). Both of them can achieve $\sim 550 M\Omega/m$ of shunt impedance at X-band.

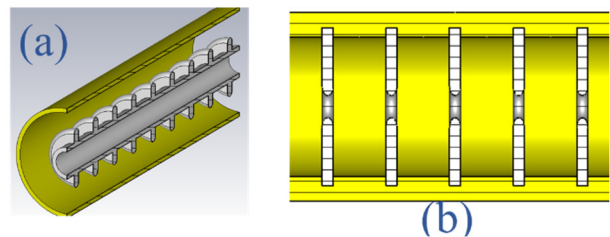


Figure 1: Conceptual view of two variations of dielectric accelerators: a) dielectric corrugated accelerating structure and b) dielectric disk accelerating structure. The grey area represents the dielectric material, and the yellow represents the copper housing for terminating the electric fields and sealing the vacuum.

ACCELERATOR DESIGN

Design of an X-band CDCA

The strategy of CDCA structure for high shunt impedance contains i) introduction of a vacuum gap to reduce the magnetic field near the copper surface (in order to do this, a corrugation has to be introduced, since otherwise the phase velocity of the TM_{01} mode cannot be slowed down to the speed of light), and ii) cooling of the structure to cryogenic temperatures to obtain an extremely low loss tangent in the dielectric material, in order to further reduce the RF loss in the dielectric by a large factor. The trade-off cost of the CDCA structure, in comparison to a conventional DLA structure, is the larger transverse size and a higher ratio of the electric field on the dielectric surface divided by the acceleration gradient. In order to implement a CDCA structure in a practical way, as shown Fig. 2a, we can use the end wall to 1) hold the position of the corrugated

[†] c.jing@euclidtechlabs.com

INTEGRATED PHOTONICS STRUCTURE CATHODES FOR LONGITUDINALLY SHAPED BUNCH TRAINS

S. J. Coleman*, D. Abell, C. Hall, RadiaSoft LLC, Boulder, CO, USA
S.-Y. Kim, P. Piot, J. Power, Argonne National Laboratory, Lemont, IL, USA
R. Kapadia, University of Southern California, Los Angeles, CA, USA
S. Karkare, Arizona State University, Tempe, AZ, USA

Abstract

Compact, high-gradient structure wakefield accelerators can operate at improved efficiency using shaped electron beams, such as a high transformer ratio beam shape, to drive the wakes. These shapes have generally come from a photocathode gun followed by a transverse mask to imprint a desired shape on the transverse distribution, and then an emittance exchanger (EEX) to convert that transverse shape into a longitudinal distribution. This process discards some large fraction of the beam, limiting wall-plug efficiency as well as leaving a solid object in the path of the beam. In this paper, we present a proposed method of using integrated photonics structures to control the emission pattern on the cathode surface. This transverse pattern is then converted into a longitudinal pattern at the end of an EEX. This removes the need for the mask, preserving the total charge produced at the cathode surface. We present simulations of an experimental set-up to demonstrate this concept at the Argonne Wakefield Accelerator.

INTRODUCTION

Beam-driven structure wakefield accelerators – either dielectric wakefield accelerators or structures made using metamaterials – are a promising path for ~ 1 GV m^{-1} accelerating gradients for high energy lepton colliders or X-ray free-electron lasers [1–3]. Achieving an efficient transfer of energy from the drive beam to the witness beam requires specially shaped bunches to achieve a high transformer ratio. These shapes have been achieved [4, 5] using a transverse intercepting mask followed immediately by an emittance exchange beamline (EEX) [6]. While this technique produces the desired longitudinal current distribution to achieve high transformer ratios, the masks discard up to 80% of the bunch charge [7]. This limits the wall-plug efficiency available for these accelerators. A technique which would eliminate the need for the mask would restore the efficiency and introduce new flexibility in structure shaping. In one approach nano-engineered field emission arrays coupled with EEX have been shown to generate bunchlets with spacing as small as 13 nm [8].

We describe a configuration which uses integrated photonics structures (IPS) to shape the transverse profile on the photocathode surface, and transport that engineered shape through the EEX with no substantial loss of initial bunch charge. We propose to generate a horizontal bunchlet comb

whose centroids become, after emittance exchange, a longitudinal bunchlet comb suitable for driving a terahertz dielectric wakefield accelerator.

This technique would reduce requirements on laser and rf power at fixed final bunch charge, or enable substantially higher final bunch charge at fixed power requirements. The technique is also extremely flexible – although we will focus on resonant wakefield excitation [9, 10].

THEORY

Emittance Exchange (EEX) is a tool to manipulate the phase space of a beam, shaping the downstream longitudinal properties by controlling the upstream transverse properties.

The EEX beamline at the Argonne Wakefield Accelerator (AWA) considered throughout this paper consists of a double-dogleg where a transverse deflecting cavity (TDC) is positioned between two identical doglegs, a configuration that provides an exact emittance exchange [11]. A TDC is an rf cavity operating in dipole mode, and has a longitudinal electric field with a spatially-varying gradient, such that the field strength varies linearly with transverse distance from the axis. We specifically consider the AWA EEX beamline parameters for which the TDC is a 1.3-GHz RF cavity operating on the $TM_{110,\pi}$ mode [12]. Placement of the TDC in a dispersive region at the center of the double-dogleg, and careful selection of the TDC voltage and rf wavelength relative to the dogleg dispersion, enables complete exchange of the horizontal and longitudinal phase space coordinates [6]. The bunch evolves as

$$(x, x', z, \delta)_{\text{final}}^T = \mathbb{M}(x, x', z, \delta)_{\text{initial}}^T \quad (1)$$

where the transfer matrix is

$$\mathbb{M} = \begin{pmatrix} 0 & L_c/3 & \kappa L_s & \eta + \kappa \xi L_s \\ 0 & 0 & \kappa & \kappa \xi \\ \kappa \xi & \eta + \kappa \xi L_s & L_c \kappa^2 \xi / 6 & L_c^2 \kappa^2 \xi^2 / 6 \\ \kappa & \kappa \xi L_s & L_c \kappa^2 / 6 & L_c \kappa^2 \xi / 6 \end{pmatrix} \quad (2)$$

and

$$L_s = L + L_{bc} + \frac{L_c}{3}$$

$$L = \frac{2L_b \cos \alpha + L_{bb}}{\cos^2 \alpha}$$

$$\eta = \frac{(2L_b \cos^2 \alpha - 2L_b \cos \alpha - L_{bb} \sin^2 \alpha)}{(\sin \alpha \cos^2 \alpha)}$$

$$\xi = \frac{L_{bb} \sin^3 \alpha + 2LB \sin \alpha - 2\alpha L_b \cos^2 \alpha}{\sin \alpha \cos^2 \alpha}$$

* coleman@radiasoft.net

FACILITATING MACHINE LEARNING COLLABORATIONS BETWEEN LABS, UNIVERSITIES, AND INDUSTRY

J. P. Edelen, D. T. Abell, D. L. Bruhwiler, S. J. Coleman, N. M. Cook, A. Diaw, J. Einstein-Curtis,
 C. C. Hall, M. Kilpatrick, B. Nash, I. V. Pogorelov, RadiaSoft LLC, Boulder, CO, USA
 K. A. Brown, Brookhaven National Laboratory, Upton, NY, USA
 C. Tennant, Thomas Jefferson National Laboratory, Newport News, VA, USA
 P. Piot, Northern Illinois University, DeKalb, IL, USA
 S. Calder, C. Hoffmann, Oak Ridge National Laboratory, Oak Ridge, TN, USA
 A. L. Edelen, B. O’Shea, R. Roussel, SLAC, Menlo Park CA, USA
 E.-C. Huang, Los Alamos National Laboratory, Los Alamos, NM, USA

Abstract

It is clear from numerous recent community reports, papers, and proposals that machine learning is of tremendous interest for particle accelerator applications. The quickly evolving landscape continues to grow in both the breadth and depth of applications including physics modeling, anomaly detection, controls, diagnostics, and analysis. Consequently, laboratories, universities, and companies across the globe have established dedicated machine learning (ML) and data-science efforts aiming to make use of these new state-of-the-art tools. The current funding environment in the U.S. is structured in a way that supports specific application spaces rather than larger collaboration on community software. Here, we discuss the existing collaboration bottlenecks and how a shift in the funding environment, and how we develop collaborative tools, can help fuel the next wave of ML advancements for particle accelerators.

INTRODUCTION

In recent years machine learning (ML) has been identified as having the potential for significant impact on the modeling, operation, and control of particle accelerators (for example, see Refs. [1, 2]). While there has been an impressive amount of progress for ML in accelerators, most solutions are not yet fully incorporated into regular operation. This in turn limits the degree to which open questions in robustness, algorithm transfer, uncertainty quantification, and generalization to unseen conditions can be addressed.

At present, researchers are incentivized to prioritize proof-of-concept demonstrations, publish, and move on to the next proof-of-concept. This results in many ML algorithms never being fully tested under a variety of conditions and never integrated into operations. Funding is primarily awarded and structured around new ML methods and advances for specific applications of accelerators (e.g. photon science, high-energy physics, medical accelerators), leaving research and development for community code infrastructure, standards, and cross-application algorithm transfer under-funded. There is a tremendous need for (1) open-source, portable, extensible software, (2) along with common benchmarks and worked examples, and (3) investment in personnel to support for MLOps and DevOps. Accelerator applications

and control systems share numerous commonalities across different end use-cases. In the following sections we expand on this further.

ML APPLICATIONS TO ACCELERATORS

To orient the reader, we highlight a few use cases for machine learning.

Neural networks (NNs) have been used to create virtual diagnostics [3–5] that supply operators with diagnostic predictions from other measured data. This can be useful when the diagnostic instrument is destructive and cannot be used continuously during downstream operation, or would update too slowly. Similarly, NNs can be used to create comprehensive fast-executing models of accelerator systems [6–10], using combinations of measurement and simulation data. Uncertainty quantification has been investigated [11, 12]. Adaptive feedback methods have also been combined with static ML models to track changes and enable fine-tuning [10, 13, 14].

Anomaly detection has been specifically highlighted as an area where machine learning can significantly impact operational accelerators [15, 16]. ML tools have been applied to detect anomalies in superconducting magnets at CERN [17], RF cavities at DESY [18–20] and RF cavities at JLab [21]. Additionally, machine learning has been used to identify and remove malfunctioning beam position monitors in the Large Hadron Collider (LHC), prior to application of standard optics correction algorithms [22]. Other efforts have sought to use ML for detection of errors in hardware installation [23]. Analysis of the latent space information using autoencoders has also been demonstrated to improve the ability to identify anomalous behavior in LINACs [24].

In terms of optimization and control, machine learning has been employed in a variety of ways. With limited previous data, Bayesian Optimization (BO) adapts a model during tuning. This has been shown in numerous contexts to provide sample-efficient tuning for accelerators [25–28]. Recent advances in BO for accelerators have enabled tuning that respects learned constraints [27, 28], enforces smooth setting changes, and can handle comprehensive multi-objective optimization (e.g. producing the actual Pareto front on an operational accelerator) [28, 29]. Providing an initial solution from a learned global model and fine-tuning with feedback

ONLINE MODELS FOR X-RAY BEAMLINES*

Boaz Nash, Dan T. Abell, Michael Keilman,
Paul Moeller, Ilya V. Pogorelov, RadiaSoft LLC, Boulder, CO, USA
Yonghua Du, Abigail Giles, Joshua Lynch, Thomas Morris,
Maksim Rakitin, Andrew L. Walter, BNL, Upton, NY, USA
Nicholas Goldring, STATE33 INC, Portland, OR, USA

Abstract

X-ray beamlines transport synchrotron radiation from the magnetic source to the sample at a synchrotron light source. Alignment of elements such as mirrors and gratings are often done manually and can be quite time consuming. The use of photon beam models during operations is not common in the same way that they are used to great benefit for particle beams in accelerators. Linear and non-linear optics including the effects of coherence may be computed from source properties and augmented with measurements. In collaboration with NSLS-II, we are developing software tools and methods to include the model of the x-ray beam as it passes on its way to the sample. We are integrating the Blue-Sky beamline control toolkit with the Sirepo interface to several x-ray optics codes. Further, we are developing a simplified linear optics approach based on a Gauss-Schell model and linear canonical transforms as well as developing Machine Learning models for use directly from diagnostics data. We present progress on applying these ideas on NSLS-II beamlines and give a future outlook on this rather large and open domain for technological development.

INTRODUCTION

Here we present further progress in the development of reduced models for use during real-time operation of X-ray beamlines. In Ref. [1], we introduced the concept of a matrix-aperture beamline composed of linear transport sections and physical apertures as shown in Fig. 1. This approach is an approximation with the hope of capturing important transport properties in a computationally efficient manner. Within this approach there exists a hierarchy of methods¹ as shown in Fig. 2. The first row of the table involves second moment propagation representing Gaussian Wigner functions [3]. The second row of the table involves propagating coherent electric fields via linear canonical transform (LCT). Progress in creation of an LCT transport library is reported in Ref. [4]. The final row of the table represents generic partially coherent X-ray propagation via Wigner function passing through the matrix-aperture beamline. Some work towards developing this method was presented in Ref. [5]. The focus of this paper will be the top level method of sigma matrix transport through the matrix-aperture beamline. We refer to this

reduced model as the Gaussian Wigner function moment (GWFM) model. This model provides a computationally efficient calculation of the linear optics through the beamline while also including effects of partial coherence. We apply the sigma matrix transport method to a KB mirror beamline with two apertures and compare results with SRW and Shadow. Finally, the realistic case of an NSLS-II beamline is treated with this method and preliminary results are presented.

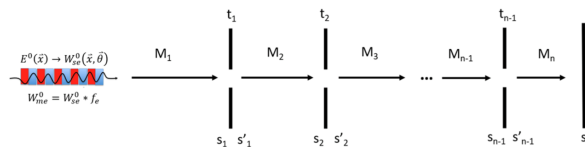


Figure 1: Matrix-aperture beamline schematic with n linear transport sections and $n - 1$ apertures. M_j represents the transport matrix across the j^{th} section of the beamline (from position s_{j-1} to s_j) and t_j represents the transfer function of the j^{th} aperture. An undulator source is depicted in this figure creating partially coherent synchrotron radiation.

\vec{z}_i	M_1	t_1	M_2	t_2	M_3	\vec{z}_f
Σ_i	S_{M_1}	$\Sigma_1 \Sigma'_1$	S_{M_2}	$\Sigma_2 \Sigma'_2$	S_{M_3}	Σ_f
\vec{E}_i	\mathcal{L}_{M_1}	$\vec{E}_1 \vec{E}'_1$	\mathcal{L}_{M_2}	$\vec{E}_2 \vec{E}'_2$	\mathcal{L}_{M_3}	\vec{E}_f
W_i	\mathcal{T}_{M_1}	$W_1 W'_1$	\mathcal{T}_{M_2}	$W_2 W'_2$	\mathcal{T}_{M_3}	W_f

Figure 2: Hierarchy of reduced models for radiation transport through a matrix-aperture beamline.

We remind the reader that the goal of such fast reduced models is to enable the creation of online models incorporating up-to-the-moment diagnostics data such that the model accurately reflects the true state of the beamline settings and X-ray transport from source to sample. Such an online model may be used to automate precise tuning and alignment of the beamline. In addition to physics-based models, we are also developing machine learning-based models for the same purpose. See Ref. [6] for further information on the progress of this effort.

KB MIRROR BEAMLINE

We consider the case of a KB mirror beamline with successive horizontally and vertically focusing mirrors as shown in Fig. 3. We have setup this beamline within the Shadow code to illustrate the method of moment propagation through a matrix-aperture beamline. The transfer matrices along the

* Work supported by the US Department of Energy, Office of Basic Energy Sciences under Award No. DE-SC0020593.

¹ We do not intend to be comprehensive in our scope of all work pertaining to reduced models here. The hybrid method [2] may fit closely within our schema as an alternative to the LCT method, combining wavefront propagation with ray tracing.

PREDICTION OF GASEOUS BREAKDOWN FOR PLASMA CLEANING OF RF CAVITIES*

S. Ahmed[†], Electronics Business Unit, Ansys Inc., San Jose, CA, USA

Abstract

This paper describes the workflow of RF discharge physics implemented in HFSS and illustrates its application to an accelerating cavity. The workflow can be directly applied to multi-cell structures in a complex setting. The entire simulation can be executed in a single run. Full-wave electromagnetic simulations can be performed in HFSS using the modal or terminal solution; the time-domain simulation then takes over to predict the onset of gaseous breakdown. The accuracy and robustness of the simulation can be guaranteed through the full-wave FEM solution in an unstructured mesh and the temporal evolution of plasma density.

INTRODUCTION

With the current state of the art, radiofrequency (RF) cavities are most employed for accelerating electrons (or ions) to achieve high-energy particles for exploring the fundamental nature of the universe [1]. These cavities undergo various steps to qualify the high performance in terms of accelerating gradient, quality factor, etc [2]. However, the performance gradually degrades over the period of use, and hence cleaning such cavities is necessary [2]. The normal procedure adopted in the qualifying stage of the cavity cannot be applied for in-situ cleaning inside the accelerator facility [2]. For in-situ cleaning, the gas processing method known as “helium processing” is commonly used at a cold temperature where the partial pressure of helium gas is much below the breakdown threshold. This technique is a random local ionization process, which may adversely affect cavity performance [2]. Plasma cleaning has been adopted in various accelerator facilities for the removal of surface impurities and contaminants [2, 3].

In plasma cleaning, an ionization discharge of gases inside the cavity volume is induced by the RF or microwave electromagnetic (EM) fields. The development of a procedure for plasma cleaning requires a detailed investigation toward establishing a plasma discharge inside the cavity. Generating an efficient plasma inside a complex cavity structure for a desired frequency and gas type for a given temperature and pressure is challenging. Setting up an experiment is expensive and time-consuming, which may lead to a significant delay in the project. A high-fidelity computer simulation, modeling an arbitrary three-dimensional geometry for tracking the plasma discharge in a complex electromagnetic environment is therefore necessary. Ansys HFSS through its Finite Element Mesh (FEM) for the full-wave EM simulations combined with the elec-

tron impact ionization of gases enables the successful prediction of plasma breakdown for an arbitrary configuration for a wide frequency band and gases. The RF discharge analysis feature has been integrated into the Ansys electronics desktop (AEDT); full-wave electromagnetic and RF discharge simulations can be set up in the same design. The breakdown threshold predicted by the solver helps users determine the RF power and gas pressure at a given temperature for any complex configuration. Therefore, the RF discharge package can be reliably used for the onset prediction of plasma discharge for plasma cleaning as well as the safe operation of helium processing.

MODEL DESCRIPTION

For purposes of illustration, we have selected an RF cavity, however, the workflow can be directly applied to any other structure. The RF discharge simulation in HFSS can be combined with the RF design performed either in the “modal” or “terminal” solution type.

RF Simulation

The model illustrated in Fig. 1 has been set up for the “modal” solution type. The RF power has been fed into the cavity using a co-axial feed through the beam pipe and the dual orthogonal modes are excited simultaneously. The RF modeling has been performed for 1 W of input power, which can be simply scaled for any desired power after the execution of the simulation.

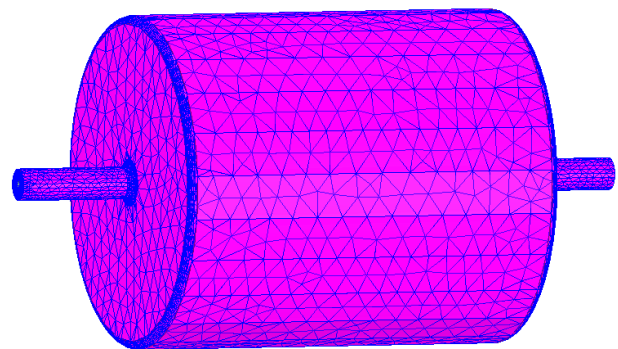


Figure 1: A schematic of the cavity used in the model for operation at 550 MHz.

Figure 2(a-d) shows four eigenmodes excited inside the cavity. The fundamental mode is depicted in Fig. 2a, which represents the accelerating mode. The remaining modes illustrated in Fig. 2(b-d), correspond to the higher-order modes (HOM); the degenerate modes are indeed indicated in Fig. 2(c-d). These eigenmodes due to different EM configurations can create ionization breakdown at different locations and hence play a critical role in the overall cleaning procedure development.

* Work supported by the Electronics Business Unit of Ansys, Inc.

[†] shahid.ahmed@ansys.com

HFSS ENABLES MULTIPACTION ANALYSIS OF HIGH POWER RF/MICROWAVE COMPONENTS*

S. Ahmed[†], Electronics Business Unit, Ansys Inc., San Jose, CA, USA

Abstract

This paper describes system-level simulations for high-power RF/microwave components from full-wave electromagnetics (EM) to RF breakdown under vacuum for arbitrary 3D structures. Full-wave electromagnetic simulations can be performed in HFSS using the modal or terminal solution; the time-domain simulation then takes over to predict the onset of multipaction breakdown. The entire simulation can be executed in a single run for EM analysis and the prediction of RF breakdown. The accuracy and robustness of the simulation can be guaranteed through the FEM unstructured mesh. Particle-in-cell simulation for tracking multipaction electrons in an unstructured FEM mesh is a key success. A comprehensive visualization user interface helps to explain the detailed physics.

INTRODUCTION

The quest for high energy in exploring the fundamental nature of the universe is of utmost interest for particle accelerators [1]. The radiofrequency (RF) components in particle accelerators operated under a vacuum condition and driven by high-power RF electromagnetic (EM) waves may be prone to electron multipaction [2-4]. The RF-triggered electron resonance ignited by the RF multipaction may cause malfunction, which results in detuning, beam loading, arcing, etc, which, in turn, reduces the target energy for accelerating the beam. Therefore, exploring the design challenges of vacuum RF windows, cavities, and other devices to avoid electron multipaction becomes necessary. Setting up an experiment to mitigate the failure of RF devices is expensive and time-consuming, which may lead to a significant delay in the project. Therefore, a high-fidelity computer simulation modeling the arbitrary geometry and tracking the particles (electrons) in a complex electromagnetic environment is desirable. Ansys HFSS through Finite Element Mesh (FEM) for the full-wave RF simulation combined with the particle-in-cell (PIC) technique for tracking particles in EM fields; enables the engineers/physicist successful prediction of system failure against the electron multipaction. The multipaction analysis feature has been integrated into the Ansys electronics desktop (AEDT); full-wave electromagnetic and multipaction simulations can be set up in the same design. The breakdown threshold predicted by the solver helps users determine the multipaction susceptibility of devices under design. Moreover, the animation of multipaction charge particles helps visual inspection.

MODEL DESCRIPTION

For purposes of illustration, we have selected an RF cavity, however, the workflow can be directly applied to any other structure. The multipaction simulation in HFSS can be combined with the RF design performed either in the “modal” or “terminal” solution type.

RF Simulation

The cavity geometry illustrated in Fig. 1 has been set up for the “modal” solution type. The RF power has been fed into the cavity using a co-axial feed through the beam pipe and the dual orthogonal modes are excited simultaneously. The RF modeling has been performed for 1 W of input power, which can be simply scaled for any desired power after the execution of the simulation.

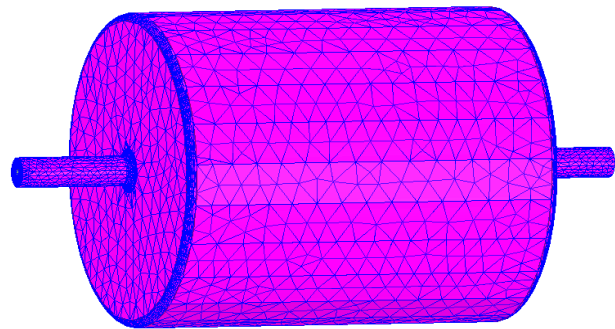


Figure 1: A schematic of the cavity used in the model for operation at 550 MHz.

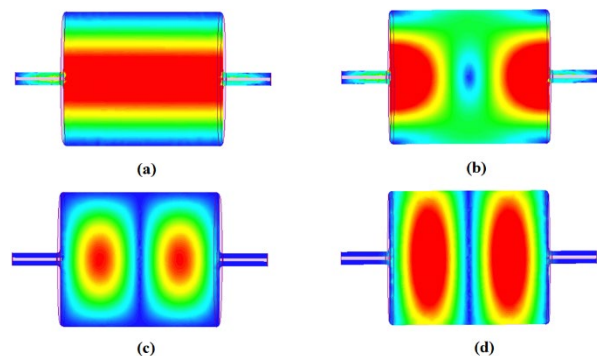


Figure 2: Sub figures (a-d) shows electric field distributions of four modes excited inside the cavity at about 549.82 MHz, 626.7 MHz, 732.44MHz, and 732.47 MHz, respectively.

Figure 2(a-d) shows four eigenmodes excited inside the cavity. The fundamental mode is depicted in Fig. 2a, which represents the accelerating mode. The remaining modes illustrated in Fig. 2(b-d), correspond to the higher-order modes (HOM); the degenerate modes are indeed indicated in Fig. 2(c-d).

* Work supported by Electronics Business Unit of Ansys, Inc.

[†] shahid.ahmed@ansys.com

MODULAR SOLID-STATE SWITCHING AND ARC SUPPRESSION FOR VACUUM TUBE BIAS CIRCUITS

E. L. Atkinson *, T. J. Houlahan, B. E. Jurczyk, R. A. Stubbers
Starfire Industries, LLC, Champaign, IL, USA

Abstract

In this work, we present operational and performance data for a solid-state switching circuit that delivers pulsed power at up to 12 kV and 100 A. This circuit, which is comprised of a series configuration of IGBT-based subcircuits, is suitable for driving the high-power vacuum-tube amplifiers that are typically used in RF accelerator systems. Each subcircuit can switch up to 3 kV, and the subcircuits can be stacked in series to extend the overall voltage capabilities of the switch. The circuit is designed to prevent overvoltage of any single transistor during switching transients or faults, regardless of the number of series subcircuits. Further, the circuit also includes the capability for rapid arc detection and suppression.

Testing has shown effective switching at up to 100 A at 12 kV and for pulse repetition frequencies and durations in the range of 1–200 Hz and 10–50 μ s, respectively. Additionally, the arc suppression circuitry has been shown to reliably limit arcs at 10–12 kV with a quench time of ≤ 1 μ s and with a total energy of < 0.2 J, minimizing the grid erosion in the vacuum-tube during an arc.

INTRODUCTION

In recent years, there has been continued interest in using series-stacked high-power transistors for high-voltage switching applications [1, 2]. These high-voltage switches have been used in a number of applications including high-voltage inverters and fusion systems [3]. This work presents a high-voltage switching circuit that can be used to bias high-power vacuum tube amplifiers such as those used in accelerator systems.

Conventional vacuum tube drive circuitry generally uses a constant high-voltage plate bias, with arc suppression handled by a dedicated crowbar circuit that short-circuits the main capacitor bank in the event of an arc. The method presented instead uses a solid-state switching circuit to both pulse the plate bias and suppress arcs.

This circuit has several advantages compared to conventional drive circuitry. Pulsing the plate voltage allows operation at higher bias voltages, increasing peak RF power output capabilities. For example, the YU-141 maximum DC plate voltage increases to 12 kV when pulsed, compared to 10 kV at a constant plate voltage [4].

Additionally, replacing the crowbar circuit with a solid-state switch allows for faster and more robust arc suppression. Conventional crowbar circuits operate by quickly providing a low-impedance path to drain the capacitor bank in the event of an arc; this drops the HV rail, however, it requires

a crowbar circuit that can repeatedly dissipate very high instantaneous power without damage [5]. In contrast, the solid-state switch can simply be gated off to stop the arc. Since power transistors with very fast switching speeds can be used, the arc suppression response is very fast, decreasing the damage caused by an arc in a vacuum tube.

DESIGN

V_{CE} Balancing Circuit

High-voltage power transistors are widely available with collector-emitter breakdown voltages in the range of 1–4.5 kV, however, high-power RF vacuum tube amplifiers frequently require much higher (≥ 8 kV) biases. Stacking power transistors in series is inherently risky since individual device differences can cause the voltage across each device to be unbalanced, increasing the likelihood of an overvoltage failure on one of the transistors during switching.

To protect against this type of overvoltage failure, a series V_{CE} balancing circuit has been developed. Figure 1 shows a conceptual schematic of how the balancing circuit fits into the overall switching modules. The circuit uses series Zener diodes to set the overvoltage threshold for each transistor; when the voltage exceeds the threshold, the balancing circuit drives the transistor gate to drop V_{CE} to a safe level. The current buffering circuit is designed to source enough current to quickly charge the IGBT gate when the gate driver circuit would otherwise gate off the IGBT.

Arc Suppression

A critical aspect of the design is ensuring that the V_{CE} balancing circuit behavior does not interfere with the fast switching times necessary for effective arc suppression. LT-Spice simulations were used to sweep the gate resistance and current buffering circuit feedback. The final design allows for relatively stable V_{CE} balancing behavior while also preserving a sub-microsecond response time when gating off the transistor due to an arc.

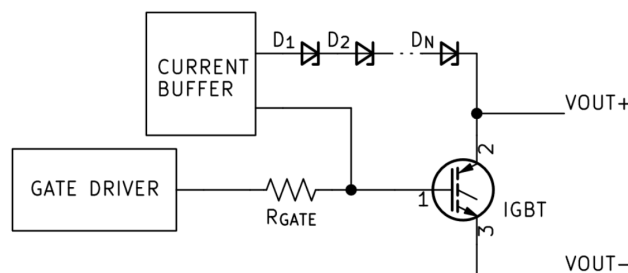


Figure 1: Conceptual schematic of Zener clamping circuit.

* eatkinson@starfireindustries.com

HIGH QUALITY CONFORMAL COATINGS ON ACCELERATOR COMPONENTS VIA NOVEL RADIAL MAGNETRON WITH HIGH-POWER IMPULSE MAGNETRON SPUTTERING

W. M. Huber, A. S. Morrice, I. Haehnlein, B. E. Jurczyk, R. A. Stubbers, T. J. Houlahan
 Starfire Industries LLC, Champaign, IL, USA

Abstract

In this work, we present two configurations of a novel radial magnetron design which are suitable for coating the complex inner surfaces of a variety of modern particle accelerator components. These devices have been used in conjunction with high-power impulse magnetron sputtering (HiPIMS) to deposit copper and niobium films onto the inner surfaces of bellows assemblies, waveguides, and SRF cavities. These films, with thicknesses of up to 3 μm and 40 μm for niobium and copper respectively, have been shown to be conformal, adherent, and conductive. In the case of copper, the post-bake residual resistivity ratio (RRR) values of the resulting films are well within the range specified for electroplating of the LCLS-II bellows and CEBAF waveguide assemblies. In addition to requiring no chemical processing beyond a detergent rinse and solvent degrease, this magnetron design exhibits over 80% target material utilization. Further, in the case of niobium, an enhancement in RRR over that of the bulk (target) material has been observed.

INTRODUCTION

This work continues the investigation of the use of ionized physical vapor deposition (iPVD) as an alternative process to wet chemical electroplating for depositing conformal coatings of various materials for use in accelerator components. Previous investigation utilized a novel radial magnetron design used for coating the inner diameter of LCLS-II bellows components which resulted in conformal, well adhered films with thicknesses of 5 – 10 μm . Resulting films were capable of withstanding extreme temperature fluctuations (77 K to 400 °C vacuum bake-out) and remained well adhered after plastic deformation [1]. Utilizing the results from this previous work, efforts were focused on optimizing RRR values for LCLS-II coatings, and translating similar process conditions for use in coating CEBAF waveguides – with the added challenge of determining process conditions that work well with the high aspect ratio of the waveguides.

As is the case for Cu coatings on other accelerator components, different methods for coating SRF cavities with Nb thin-films have been attempted in the past with varying results [2]. One of the key parameters that determines the effectiveness of Nb thin-films for superconductivity applications, is the grain structure of the resulting film [2]. Part of this work focused on determining process conditions which result in well adhered, high-RRR Nb films on Cu test coupons.

EXPERIMENT

HiPIMS Operation

Each magnetron was driven by a Starfire Industries IMPULSE® 20-20 HiPIMS pulser module. Argon was used as the carrier gas at varying pressures during parameter exploration and optimization. Using HiPIMS with a Positive Kick™ allows ions to be accelerated to energies in the range of 0 – 400 eV. This allows the target material to be implanted into a substrate, resulting in a transition layer that produces better film adhesion. In addition, the Positive Kick enables the formation of fully dense thin-films by implanting metal ions into the bulk film [3]. This is in contrast to other deposition processes where metal ions implant to the surface of the film only, often leading to pinholes and large voids.

Magnetron Design

Two magnetron designs were built and tested: a 0.5" (1.27 cm) diameter magnetron with an azimuthal racetrack and a 1" (2.54 cm) diameter magnetron with an axial race-track. Both designs were tested with various materials. Niobium and copper were tested on the 1" design, while silicon carbide and copper were tested on the 0.5" design. Both magnetrons are comprised of a copper body that facilitates heat transfer between coolant and the magnet pack(s). For copper magnetrons, the copper shell itself acts as the target material. Details regarding the design and construction of the 1" magnetron design are given elsewhere, in Ref. [1]. Figure 1 shows a schematic of the 0.5" magnetron used for coating CEBAF waveguides.

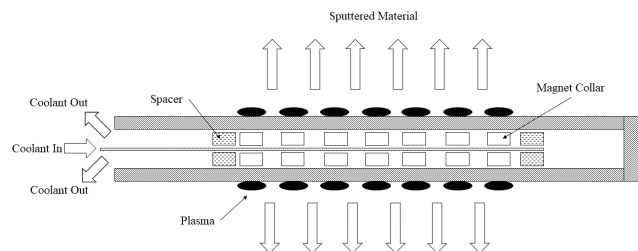


Figure 1: Diagram of 0.5" outer diameter magnetron for coating CEBAF waveguides. Magnet pack creates distinct erosion patterns around each stack of magnets.

LCLS-II Bellows

Optimization was carried over a large parameter space of operating pressures and pulse settings. Efforts focused

MULTIPHYSICS SIMULATION OF THE THERMAL RESPONSE OF A NANOFIBROUS TARGET IN A HIGH-INTENSITY BEAM

W. J. Asztalos*, Y. Torun, Illinois Institute of Technology, Chicago, IL, USA
S. Bidhar, F. Pellemoine, Fermi National Accelerator Laboratory, Batavia, IL, USA
P. Rath, Indian Institute of Technology, Bhubaneswar, India

Abstract

Nanofibrous structures are of high interest to the fields of engineering and materials science, and investigation of their properties as well as discovery of novel applications for them both constitute lively areas of research. A very promising application of nanofiber mats lies in the field of accelerator technology: beam targets made from nanofiber mats offer a solution to the problem of advancing the “intensity frontier”—the limit on the beam intensities that can be realized in fixed target experiments and neutrino production facilities. However, testing has shown that the survivability of these nanofiber targets depends strongly on their manufacturing parameters, such as the packing density of fibers. In this work, we will use multiphysics simulations to perform a thermal study on how nanofiber targets react to high intensity beams, so that the dependency of the targets’ lifetime on their construction parameters can be better understood.

INTRODUCTION

Most neutrino beams are produced by exposing a fixed target to a high-energy proton beam. The intensity of this “primary” beam in turn determines the intensity of the neutrino beam, and so far they have operated at max intensities on the order of one megawatt—the NuMI beamline at Fermilab recently set a record beam power of 893 kW. However, future installations are expected to reach higher intensities: the Long Baseline Neutrino Facility, for example, calls for a primary beam power of 1.2 MW [1], with an accelerator upgrade planned in the horizon of 2030 to raise the power to 2.4 MW, bringing us to the multi-megawatt regime.

Attaining these intensities is not just a matter of accelerator technology—the fixed target must *survive* many beam cycles for these facilities to be practical. The upper bound on the intensities reachable with current technology is known as the *intensity barrier*, and its advancement is therefore necessary to meet the demands of future neutrino experiments.

In facilities such as NuMI, the convention is to use solid graphite targets with water cooling. Although such targets have operated successfully to date, there is question as to whether they will retain suitable lifetimes at the multi-megawatt scale. The primary weakness of these solid targets is that their uniform lattice allows thermal stress waves induced by the pulsed beam to easily propagate, leading to fatigue failure. This issue will only be exacerbated by *larger* amplitude stress waves from higher beam power in the future.

The High Power Targetry Research and Development (HPT R&D) Group at Fermilab has been studying [2,3] a potential solution—a nanofibrous target material, consisting of an electrospun array of Ytria-Stabilized Zirconia nanofibers. These nanofiber “mats” are porous, and so the open space between fibers dissipates any thermal stress waves caused by the beam, avoiding the central weakness of existing targets. Their porosity *also* allows us to cool the targets internally by forcing helium gas through them. They also demonstrate resistance to radiation damage without additional treatment [2]. These advantages suggest that these nanofiber targets pose a novel solution to breaking the intensity barrier.

Such nanofiber targets are an emergent topic, and thus are under rigorous testing. One such test at HiRADMat [2]—a facility at CERN which provides a single pulse beam for thermal shock tests of target materials—revealed that the construction parameters of the nanofiber mats, namely their Solid Volume Fraction (SVF), strongly affect their survival. The SVF, notated f , is defined as the percentage volume of the mat occupied by *solid* material. The target with a higher SVF developed a hole at its center, whereas the one with a lower SVF remained undamaged. The exact mode of failure of the denser target is as of yet unknown; there was no evidence of melting, but one suggested explanation is that pockets of gas in the denser mat may cause such damages by limiting diffusion. While this test demonstrates that lowering the SVF increases target lifetime, it comes at the price of a lower neutrino yield, and so the choice of SVF is delicate.

MODELS AND THEORY

In order to optimize the performance of these targets, it is essential to characterize their thermal properties, which thus allows us to *predict* how they will respond to beam heating for a set of prescribed construction parameters. The nanoscale structure of these targets, however, makes theoretical descriptions and simulations of their behavior difficult. It is impossible to model all of the constituent fibers of a nanofiber target explicitly—however, the fact remains that the behavior at the individual-fiber level cannot be ignored. There are significant nanoscale effects present which add up to change the qualities of the whole.

This task becomes tractable, however, by using Porous Media Models (PMMs), which translate the behavior at the nanoscale to the macroscale by computing *effective material parameters* of a new, *homogenous* material. In this way, the explicit nanoscale geometry is “forgotten”, but the effects are retained by adjusting the properties of a replacement

* wasztalos@hawk.iit.edu

CIRCULAR MODES FOR MITIGATING SPACE-CHARGE EFFECTS AND ENABLING FLAT BEAMS*

O. Gilanliogullari^{†1,2}, B. Mustapha¹, P. Snopok²
¹Argonne National Laboratory, Lemont, IL, USA
²Illinois Institute of Technology, Chicago, IL, USA

Abstract

Flat beams are preferred in high-intensity accelerators and high-energy colliders due to one of the transverse plane emittances being much smaller than the other, which enhances luminosity and beam brightness. However, flat beams are not desirable at low energies due to space charge forces which are significantly enhanced in one plane. The same is true, although to a lesser degree, for non-symmetric elliptical beams. To mitigate this effect and enable flat beams at higher energies, circular mode beam optics can be used. In this paper, we show that circular mode beams offer better control of space charge effects at lower energies and can be transformed into flat beams at higher energies.

INTRODUCTION

High-energy colliders and storage rings require high collision luminosity and beam brightness for future scientific discoveries and applications. Flat beams could enable this need because one of the transverse beam sizes is much smaller, which enhances luminosity and beam brightness. However, at low energy, flat beams can't sustain high beam currents due to space charge effects which cause tune shifts and unstable motion. To mitigate these effects, flat beams can be propagated as circular mode beams through the lattice while maintaining intrinsic flatness through coupling, then converted to flat beams at high energy. The original idea of circular modes was introduced by Derbenev [1] for an electron cooling experiment at Fermilab. Their theory was further developed by Burov *et al.* [2]. Burov also proposed circular modes for high-energy colliders to produce flat beams for luminosity enhancement [3]. Recently, there has been significant interest in beams with non-zero angular momentum, they are proposed to mitigate space charge, either in self-consistent distributions [4] or in hollow rotating beams [5].

In this work, we have developed different lattice designs for low-energy high-intensity beams that are capable of propagating and maintaining circular mode beams. We will look at circular modes formed by skew triplet transformation (adapter) of Gaussian distributions in periodic lattices and evaluate space charge tune shift performance at high current using two simulation codes WARP [6] and TRACK [7].

THEORY

The theory of circular modes is well-understood and discussed in Ref. [2]. There are multiple ways to create circular

* This work was supported by the U.S. Department of Energy, under Contract No. DE-AC02-06CH11357.

[†] ogilanli@hawk.iit.edu

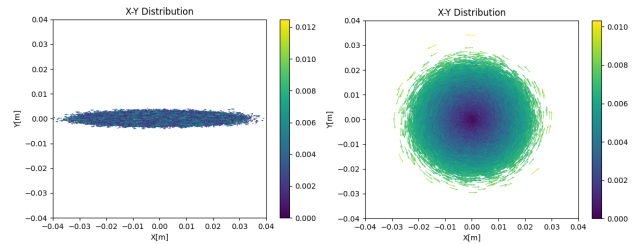


Figure 1: (a) Flat beam, (b) after adapter, circular mode.

modes. One of them, as presented in Refs. [1, 2, 8], is to use a skew quadrupole triplet. The skew triplet transforms a flat beam into a round circular-mode beam, as shown in Fig. 1. Here, the color depicts transverse momentum strength, and the arrows show the direction of the particle motion in the transverse plane. We clearly see that transforming a flat beam into a circular mode decreases the beam size in x and increase it in y , leading to a round beam with non-zero canonical angular momentum.

The canonical angular momentum of the beam is given by $L_z = \epsilon_I - \epsilon_{II}$ [2], where $\epsilon_{I,II}$ are the eigenmode emittances, with the skew triplet transforming the initial emittances $\epsilon_x \rightarrow \epsilon_I$ and $\epsilon_y \rightarrow \epsilon_{II}$. In Ref. [2], these eigen-emittances are called ϵ_+ and ϵ_- corresponding to the opposite directions of rotation. Because of the coupling, the eigenmode emittances are conserved rather than the 2D phase space emittances $\epsilon_{x,y}$. The skew triplet transformation and mapping can be found in Refs. [2, 8] where the vertical degrees of freedom are coupled to the horizontal degrees of freedom using a vortex condition.

Since a circular mode beam is strongly coupled, the state of the system should be considered in terms of coupled beam optics using Mais-Ripken parametrization [9] or its further development by Lebedev *et al.* [10]. The optics can be characterized using the eigenvectors of the system:

$$\vec{v}_I = \begin{pmatrix} \sqrt{\beta_{xI}} \\ -\frac{i(1-u)+\alpha_{xI}}{\sqrt{\beta_{xI}}} \\ \sqrt{\beta_{yI}} e^{i\nu_I} \\ -\frac{i u + \alpha_{yI}}{\sqrt{\beta_{yI}}} e^{i\nu_I} \end{pmatrix}, \quad \vec{v}_{II} = \begin{pmatrix} \sqrt{\beta_{xII}} e^{i\nu_{II}} \\ -\frac{i u + \alpha_{xII}}{\sqrt{\beta_{xII}}} e^{i\nu_{II}} \\ \sqrt{\beta_{yII}} \\ -\frac{i(1-u)+\alpha_{yII}}{\sqrt{\beta_{yII}}} \end{pmatrix}. \quad (1)$$

Here, $\beta_{jI}, \alpha_{jI}, u, \nu_I$ are the beta functions, alpha functions, coupling parameter, and coupling phases, respectively, with $j \in (x,y)$ and $l \in (I,II)$. Circular modes produced using an adapter have a special one-to-one transformation because upon calculation of coupled optics functions, one finds that $\beta_{xI} = \beta_{xII} = \beta_{yI} = \beta_{yII} = \beta_0$ and $\alpha_{xI} = \alpha_{xII} = \alpha_{yI} = \alpha_{yII} = 0$. Additionally, there is a circular beta function for

HADRON MONITOR CALIBRATION SYSTEM FOR NuMI*

N. L. Muldrow[†], P. Snopok, Illinois Institute of Technology, Chicago, IL 60616, USA
 K. Yonehara, Fermi National Accelerator Laboratory, Batavia, IL 60510, USA

Abstract

NuMI (Neutrinos at Main Injector) beamline at Fermi National Accelerator Laboratory provides neutrinos to various neutrino experiments. The hadron monitor consisting of a 5×5 array of ionization chambers is part of the diagnostics for the beamline. A gamma source is needed to calibrate the hadron monitor. We present the status and progress of the development of the calibration system for the hadron monitor. The system based on a Raspberry-Pi-controlled computer numerical control (CNC) system and position sensors would allow us to place the gamma source precisely to calibrate the signal gain of individual pixels. The ultimate outcome of the study is a prototype of the calibration system.

INTRODUCTION

We discuss an experimental setup to update the hadron monitor calibration system for the NuMI beamline at Fermi National Accelerator Laboratory (Fermilab). NuMI is a neutrino beam facility that began operation in 2005. NuMI is a conventional horn-focused neutrino beam designed to accept a 120-GeV proton beam from the Fermilab Main Injector accelerator. A simplified design schematic is shown in Fig. 1. The hadron monitor measures the spatial distribution of the uninteracted and undecayed pions produced by the main injector beam interacting with the carbon target. The hadron monitor is comprised of a grid of 1-mm ionization chambers orientated perpendicular to the beam direction and contained in an aluminum box. The calibration of the hadron monitor involves a radioactive source moved in front of the monitor by a motor-driven motion table to find the highest sensitivity position and observe the spatial sensitivity of the individual pixels [1]. The focus of this project is to create a system to control and display to the user the position of a radioactive source.

CALIBRATION SYSTEM SETUP

The prototype is based on a four-sided frame composed of 40×40 -mm aluminum T-slotted beams 610-mm long. The beams are attached at the four corners using L-brackets. As shown in Fig. 2, the cross beam is attached to three set of rollers moving along the T-slotted framing beam. The two sets of rollers on the left side are held together by a custom square bracket providing extra rigidity. This configuration allows the cross beam to move back and forth along the frame with minimal friction and minimized unwanted lateral motion. This way, the motion of the cross beam can be controlled by a single motor.

* Work supported by the U.S. Department of Energy under award number DE-SC-0020379.

[†] nmuldrow@hawk.iit.edu

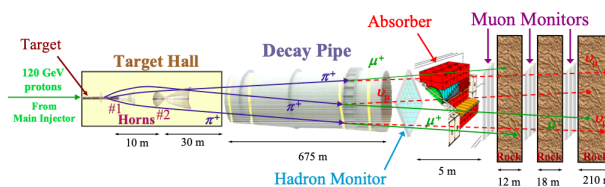


Figure 1: The major components of NuMI. The Fermilab Main Injector delivers protons to a carbon target producing pions which are then focused by pulsed horn magnets into the decay pipe. The hadron monitor measures the spatial distribution of any protons and pions left after decay. These are then absorbed by the hadron absorber [1].

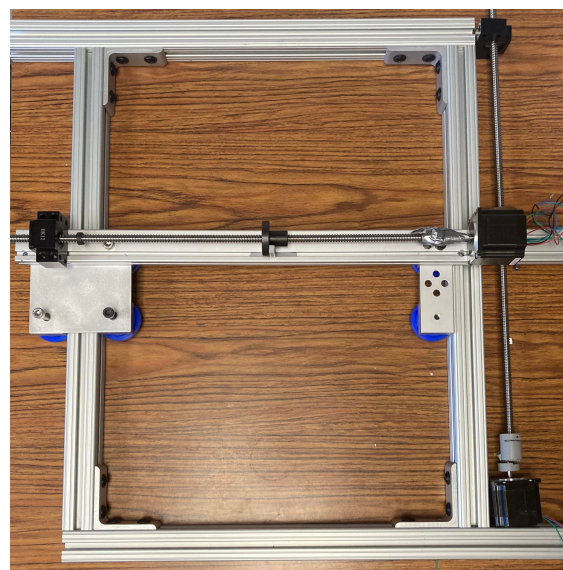


Figure 2: The experimental setup showing the frame, cross-beam, location of the two motors, and the set of the track wheels.

The setup uses two NEMA 23 stepper motors. The first motor is used to push and pull the cross beam along the frame. This motor is connected to a ball screw via a shaft coupler shown in Fig. 3.

As this specific coupler was not readily available, a CAD drawing was created to the project's specifications, and the part was printed using a 3D printer. 3D printing was chosen as the method of construction rather than a custom metal fabrication to reduce cost and time between prototypes. This coupler attaches the motor shaft to the end of the ball screw. A circular flange is screwed into place on the ball screw, and a custom-fitted bracket is screwed into place, as shown in Fig. 4. This piece slots into the bottom of the cross beam. Finally, a mount is placed at the other end of the ball screw, allowing it to rotate in place. When the motor is activated,

EXAMINING THE EFFECTS OF OXYGEN DOPING ON SRF CAVITY PERFORMANCE*

H. Hu[†], Y.-K. Kim, University of Chicago, Chicago, IL, USA
D. Bafia, Fermi National Accelerator Laboratory, Batavia, IL, USA

Abstract

Superconducting radiofrequency (SRF) cavities are resonators with extremely low surface resistance that enable accelerating cavities to have extremely high quality factors (Q_0). High (Q_0) decreases the capital required to keep accelerators cold by reducing power loss. The performance of SRF cavities is largely governed by the surface composition of the first 100 nm of the cavity surface. Impurities such as oxygen and nitrogen have been observed to yield high Q_0 , but their precise roles are still being studied. Here, we compare the performance of cavities doped with nitrogen and oxygen in terms of fundamental material properties to understand how these impurities affect performance. This enables us to have further insight into the underlying mechanisms that enable these surface treatments to yield high Q_0 performance.

INTRODUCTION

The role of impurities in the RF layer, the first 100 nm of the cavity surface, is critical in superconducting radiofrequency (SRF) cavity performance. Nitrogen doping is a surface treatment which introduces a dilute concentration of nitrogen impurities uniformly into the RF layer [1]. Nitrogen doped cavities have displayed quality factors (Q_0) of $> 4 \times 10^{10}$ and maximum accelerating gradients (E_{acc}) of > 38 MV/m [1]. Low temperature baking (LTB) is a surface treatment which relies on the diffusion of oxygen from the native oxide to mitigate high field Q-slope (HFQS) and improve Q_0 at high E_{acc} [2]. Motivated by these studies on LTB, we conduct initial studies on a new surface treatment called oxygen doping. Oxygen doping introduces oxygen impurities uniformly into the RF layer to achieve doping-like performance without any extrinsic impurities [3]. Oxygen doping has been shown to display high Q_0 of 4.2×10^{10} at 20 MV/m with a maximum E_{acc} of 34 MV/m [4]. In addition, oxygen doped cavities display phenomena in performance that are characteristic of a nitrogen doped cavity: the anti-Q slope in which BCS resistance decreases with field, and a dip in resonant frequency near the transition temperature (T_c). This work is an extension of the initial comparisons of oxygen doping and nitrogen doping presented in Ref. [4] by comparing the fundamental material properties of transition temperature, superconducting gap and mean free path.

* Work supported by the Fermi National Accelerator Laboratory, managed and operated by Fermi Research Alliance, LLC under Contract No. DE-AC02-07CH11359 with the U.S. Department of Energy; the University of Chicago.

[†] hannahhu@uchicago.edu

EXPERIMENTAL METHOD

RF tests were conducted on a single-cell TESLA shaped Nb cavity of resonant frequency 1.3 GHz. The cavity was baselined with an 800°C degassing treatment and 40 μm electropolishing (EP) removal [3]. The cavity was then treated according to the following steps: (1) *in-situ* bake at 200°C in an UHV furnace while maintaining 10^{-6} Torr, (2) HF rinse, (3) second round of HF rinse.

After each step of treatment, the cavity was evacuated and assembled at the vertical test stand (VTS) with two flux gates at the equator, resistance temperature detectors (RTDs), and a Helmholtz coil. The cavity was cooled down to 4.2 K with the fast cool down protocol to minimize the trapping of magnetic flux before it was further pumped down to be tested at first 2 K and then < 1.5 K (lowT) [3]. At each temperature, the Q_0 vs. E_{acc} performance is recorded in continuous wave (CW) operation. Next, the liquid helium is boiled off using heaters to gradually warm the cavity up past transition temperature (T_c) at a rate of < 0.1 K/min [5]. The change in resonant frequency (f_0) in temperature is recorded with a vector network analyzer.

Additionally, cavity cutouts of 1 cm in diameter were treated with a similar oxygen doping treatment of a 205°C bake for 19 hours. The sample was analyzed with time of flight secondary ion mass spectrometry (TOF-SIMS) to determine the concentration of each impurity present in the sample at each depth.

RESULTS AND DISCUSSION

The performance and material properties for each of three treatment steps is compared to that of a nitrogen doped single-cell cavity with a treatment recipe of 2/0 + 5 μm EP. The data for the nitrogen doped cavity is reproduced from Ref. [6].

There are two key features in N doped cavity performance that are also displayed in O doped cavities. Shown in Fig. 1 is the behavior of Q_0 vs E_{acc} at 2 K. During the test labeled O doped, the cavity experienced an initial quench at around 19 MV/m from field emissions. This trapped magnetic flux and decreased Q_0 . The test after HF rinse 2 experienced a quench due to multipacting at 20 MV/m, which prevented data from being taken until 25 MV/m and also trapped flux. All three tests display the anti-Q slope phenomenon where Q_0 increases with E_{acc} . Anti-Q slope in N doped cavities arises from a decrease in the BCS surface resistance with field, and this was shown to also be the case for O doped cavities [4, 7].

ADJOINT OPTIMIZATION APPLIED TO FLAT TO ROUND TRANSFORMERS*

T. Antonsen[†], B. L. Beaudoin, S. Bernal, L. Dovlatyan, I. Haber, P. L. O'Shea, D. Sutter
University of Maryland, College Park, MD, USA

Abstract

We present the numerical optimization, using adjoint techniques, of Flat-to-Round (FTR) transformers operating in the strong self-field limit. FTRs transform an unmagnetized beam that has a high aspect ratio, elliptical spatial cross section, to a round beam in a solenoidal magnetic field. In its simplest form the flat to round conversion is accomplished with a triplet of quadrupoles, and a solenoid. FTR transformers have multiple applications in beam physics research, including manipulating electron beams to cool co-propagating hadron beams. Parameters that can be varied to optimize the FTR conversion are the positions and strengths of the four magnet elements, including the orientations and axial profiles of the quadrupoles and the axial profile and strength of the solenoidal magnetic field. The adjoint method we employ allows for optimization of the lattice with a minimum computational effort including self-fields. The present model is based on a moment description of the beam. However, the generalization to a particle description is possible. The optimized designs presented here will be tested in experiments under construction at the University of Maryland.

INTRODUCTION

In this paper we will illustrate the application of the adjoint optimization approach [1] to the design of Flat-to-Round (FTR) or Round-To-Flat (RTF) transformers as have been proposed for use in many applications [2–5].

The adjoint approach is described as follows. A set of moment equations are used to simulate the propagation of a beam through a system of magnets, which converts a beam with an elliptical cross section to one with a round cross section. A general figure of merit will be introduced that quantifies how successfully the shape conversion has been made. Subsequently, we will formally perturb this system by making small changes in the parameters defining the focusing forces. Then we will introduce an adjoint system of equations that will allow one to calculate compactly the changes in the figure of merit due to changes in the focusing parameters. Such an evaluation is then used in a gradient-based optimization scheme.

MOMENT EQUATIONS

In this section we present a system of equations that describes the evolution with distance of the second moments of a charged particle beam distribution in the presence of a combination of transverse forces. These forces include the

Lorentz force of a spatially varying solenoidal (axial) magnetic field, the Lorentz force of a superposition of arbitrarily oriented quadrupole magnetic fields, and the electric and magnetic self-force due to the beam's charge and current densities.

The moments we consider are averages of products of all possible pairs of variables describing the transverse displacement of beam particles and the rate of change of the transverse displacement with distance. Due to the symmetry of this matrix only 10 elements are independent. Thus, our governing system consists of 10 moment evolution equations. We also choose to deal with differential equations for the continuous moments, as this allows us to introduce adjoint equations that include self-field effects and spatial profiles of focusing fields. Detailed derivations of these equations can be found [1]. Here we just present the equations as is:

$$\frac{d}{dz}\mathbf{Q} = \mathbf{P}, \quad (1)$$

$$\frac{d}{dz}\mathbf{P} = \mathbf{E} + \mathbf{O} \cdot \mathbf{Q}, \quad (2)$$

$$\frac{d}{dz}\mathbf{E} = \mathbf{O} \cdot \mathbf{P} + \mathbf{NL}, \quad (3)$$

$$\frac{d}{dz}\mathbf{L} = -\mathbf{N}^\dagger \cdot \mathbf{Q} \quad (4)$$

Where the following variables are defined in terms of the beam moments:

$$\mathbf{Q} = \begin{pmatrix} Q_+ \\ Q_- \\ Q_x \end{pmatrix} = \begin{pmatrix} \langle x^2 + y^2 \rangle / 2 \\ \langle x^2 - y^2 \rangle / 2 \\ \langle xy \rangle \end{pmatrix}, \quad (5)$$

$$\mathbf{P} = \frac{d}{dz}\mathbf{Q} = \begin{pmatrix} P_+ \\ P_- \\ P_x \end{pmatrix} = \begin{pmatrix} \langle xx' + yy' \rangle \\ \langle xx' - yy' \rangle \\ \langle yx' + xy' \rangle \end{pmatrix}, \quad (6)$$

$$\mathbf{E} = \begin{pmatrix} E_+ \\ E_- \\ E_x \end{pmatrix} = \begin{pmatrix} \langle x'^2 + y'^2 \rangle \\ \langle x'^2 - y'^2 \rangle \\ 2 \langle y'x' \rangle \end{pmatrix}, \quad (7)$$

$$\mathbf{L} = \langle xy' - yx' \rangle. \quad (8)$$

The \mathbf{O} and \mathbf{N} matrices represent the magnetic field in the lattice elements as well as the effects of space charge forces

* Work supported by DOE-HEP Awards No. DESC0010301 and DESC0022009

[†] antonsen@umd.edu

FILM DOSIMETRY CHARACTERIZATION OF THE RESEARCH LINAC AT THE UNIVERSITY OF MARYLAND

A.S. Johnson,[†] L.T. Gilde, M.K. Hottinger, T.W. Koeth
 University of Maryland, College Park, MD, USA

Abstract

A heavily modified Varian linac was installed as part of the University of Maryland Radiation Facilities in the early 1980s. The electron linac was initially used for materials testing and pulse radiolysis. Overtime, diagnostics such as spectrometer magnets and scintillator screens have been removed, limiting the ability to describe the electron beam. The beamline is currently configured with a thin titanium window to allow the electrons to escape the vacuum region and interact with samples in air. A calibrated film dosimetry system was used to characterize the transverse beam dimensions and uniformity in air. The results of these experimental measurements will be described in this paper.

INTRODUCTION

The University of Maryland Radiation Facilities consists of a 250 kW TRIGA research reactor, a panoramic Co-60 irradiator, and an electron linac. The electron linac is a modified Varian V7715 installed at the facility in the 1980s [1]. The linac is separated into 2 shielded vaults. The accelerating vault contains the thermionic electron source, RF system, and the accelerating structure within one vault as shown in Fig. 1. After being accelerated, the beam travels through an evacuated beamline equipped with focusing and steering magnets into the other vault. There, it passes through a thin titanium window into the air; samples may be placed in this beam for irradiation experiments. The linac produces a polyenergetic beam with a fixed pulse width of 3 μs, and a pulse rate variable between 10 and 200 pulses per second. The peak beam current during each pulse is approximately 100 mA. Currently, the UMD linac is configured with minimal diagnostic capabilities, therefore, a campaign of external beam measurements was undertaken to better understand the beam characteristics.

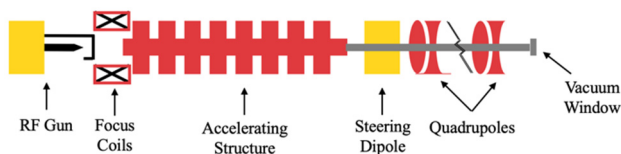


Figure 1: UMD Linac system diagram.

EXPERIMENTAL SETUP

A radiochromic film system from Far West Technology, Inc was obtained as a balance between cost and ease of use [2]. FWT-60 Radiochromic Film Dosimeters with a dose range of 0.5-200 kGy were used for all of the measurements [3]. Film dosimeters were either 1 x 1 cm sheets

for routine dosimetry or 15 x 15 cm sheets for larger beam images. All 1 x 1 cm samples were read out with a FWT-92D Radiochromic Film Reader in a temperature and humidity controlled room, while larger sheets were processed on an Epson Perfection V600 flatbed scanner [4]. UV filters are used on the light fixtures in the film processing room in order to prevent discoloration of the films from UV exposure. While being handled or irradiated outside of the film processing room UV proof bags were used to protect the film.

Film Calibration

Prior to use in the electron beam, the film was calibrated using the University of Maryland Co-60 Irradiator and a calibrated ion chamber. The Co-60 source is a large, panoramic source of gamma radiation with a highly uniform dose region that is ideal for calibrating films. For the initial low dose runs, a calibrated Exradin A19 ion chamber from Standard Imaging was placed in the same location as 5 films, and the dose rate was read with a Standard Imaging SuperMAX Electrometer. By increasing the irradiation time, and extrapolating based on dose rate measured by the ion chamber, it was possible to expose the films to doses ranging from 0-200 kGy. Figure 2 shows the color change resulting from these exposures.

0 kGy	1 kGy	5 kGy
10 kGy	25 kGy	50 kGy
100 kGy	150 kGy	200 kGy

Figure 2: Representative color change of FWT-60 radiochromic films following irradiation to various doses.

Following the irradiations, the films were left to cure for 24 hours before the change in optical density (OD) was measured using either the FWT-92D Radiochromic Film Reader or the Epson Perfection V600. A calibration curve was developed by measuring the OD vs. recorded dose [5].

[†] ajohns37@umd.edu

PRELIMINARY TESTS AND BEAM DYNAMICS SIMULATIONS OF A STRAIGHT-MERGER BEAMLINE*

A. Al Marzouk[†], T. Xu, P. Piot¹, Northern Illinois University, DeKalb, IL, USA
 S. Doran, G. Ha, J. Power, E. Wisniewski, C. Whiteford
 Argonne National Laboratory, Lemont, IL, USA

S. Benson, A. Hutton, G. T. Park, K. Dietrick, J. Guo, S. Wang

Thomas Jefferson National Accelerator Facility, Newport News, VA, USA

R. Ryne, C. Mitchell, J. Qiang, Lawrence Berkeley National Laboratory, Berkeley, CA, USA

¹ also at Argonne National Laboratory, Lemont, IL, USA

Abstract

Beamlines capable of merging beams with different energies are critical to many applications related to advanced accelerator concepts and energy-recovery linacs (ERLs). In an ERL, a low-energy “fresh” bright bunch is generally injected into a superconducting linac for acceleration using the fields established by a decelerated “spent” beam traveling on the same axis. A straight-merger system composed of a selecting cavity with a superimposed dipole magnet was proposed and recently tested at AWA. This paper reports on the experimental results obtained so far along with detailed beam dynamics investigations of the merger concept and its ability to conserve the beam brightness associated with the fresh bunch.

INTRODUCTION

The straight-merger (SM) concept was originally investigated in the context of multi-species beam separation [1] and most recently proposed for electron-beam merging and separation [2] in energy-recovery linacs (ERLs). An SM, diagrammed in Fig. 1(a), consists in superimposing a time-dependent deflecting force $F_c(\varphi) = F_0 \sin(\varphi)$ produced by a transverse-deflecting cavity (TDC) with a magnetostatic transverse force from a dipole magnet F_d . Choosing the TDC deflecting-force amplitude to be $F_0 = F_d$, the total force experienced by a bunch becomes $F_t(\varphi) = F_d[1 + \sin(\varphi)]$; see Fig. 1(b). In the case when the merger is used in an energy-recovery linac, the recirculated bunch (once it has participated in, e.g., the electron-cooling process) passes through the SM with a phase $\varphi = \pi/2$ (maximum deflection) and experiences the transverse force $2F_d$ while a fresh low-energy bunch from the injector passes through the SM at $\varphi = 3\pi/2$ so that the deflecting force vanishes. The latter mode of operation is called the transparent mode as ideally the fresh bunch phase-space quality is not

affected by the SM. One of the advantages of the present SM concept compared to using only a TDC ($F_d = 0$) operated to deflect the spent bunch ($\varphi = \pi/2$) and injecting the fresh bunch at zero crossing (e.g. $\varphi = \pi$) is that the SM does not introduce any correlation to first order. However, the transparency of the SM to the fresh bunch needs to be investigated thoroughly: the field produced by the TDC is time-dependent so that the head and tail of the bunch will experience a weaker deflection force compared to the bunch center. The TDC force arises from both magnetic and electric fields while the superimposed dipole field provides a magnetostatic force. These effects could play a role in the beam dynamics that could ultimately degrade the beam eigen emittances in the case of magnetized beams such as employed in some electron-cooling schemes [3] in hadron collider [4].

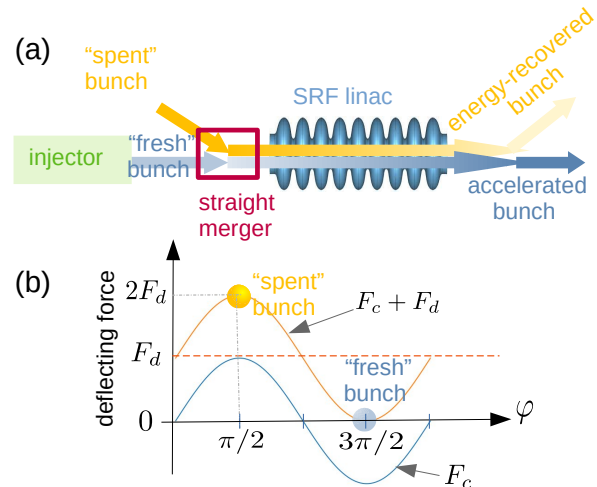


Figure 1: Overview of the SM concept for ERL application (a) and the deflecting force experience by the “fresh” and “spent” bunch (b). The dashed horizontal line represented the magnetostatic force F_d from the dc dipole magnet.

This paper presents preliminary investigation of an SM using first-principle simulation and preliminary experimental results qualitatively supporting the concept. However, it should be stressed that our beam energy is much higher than the one produced out of a typical ERL high-current photoinjector (< 10 MeV) [5].

* This work was support by the U.S. National Science Foundation under award PHY-1549132 to Cornell University and NIU, and by the U.S. Department of Energy, Office of Nuclear Physics, under contract DE-AC02-06CH11357 with ANL and DE-AC05-06OR23177 with JLAB. This research used resources of the National Energy Research Scientific Computing Center, a DOE Office of Science User Facility supported by the Office of Science of the U.S. Department of Energy under Contract No. DE-AC02-05CH11231 using NERSC award BES-ERCAP0020725.
[†] afnan.almarzouk1@gmail.com

DESIGN OF A W-BAND CORRUGATED WAVEGUIDE FOR STRUCTURE WAKEFIELD ACCELERATION

B. Leung^{*1}, X. Lu^{†1,2}, P. Piot^{1,2}, C. Phillips¹, S. Doran², J. Power²

¹Department of Physics, Northern Illinois University, DeKalb, IL 60115, USA

²Argonne National Laboratory, Lemont, IL 60439, USA

Abstract

Current research on structure wakefield acceleration aims to develop radiofrequency (RF) structures that can produce high gradients, with work in the sub-terahertz (sub-THz) regime being particularly interesting because of the potential to create more compact and cost-effective accelerators. Metallic corrugated waveguides at sub-THz frequencies are one such structure. We have designed a W-band corrugated waveguide for a collinear wakefield acceleration experiment at the Argonne Wakefield Accelerator (AWA). Using the CST Studio Suite, we have optimized the structure for the maximum achievable gradient in the wakefield from a nominal AWA electron bunch at 65 MeV for high-frequency structures. Considering a 10 nC symmetric Gaussian bunch with an rms length of 0.5 mm, we achieved an accelerating gradient of 84.6 MV/m. The gradient can be further improved with longitudinally shaped bunches, as will be studied in the future. Simulation results from various codes were benchmarked with each other, and with analytical models, with good agreement. We are investigating the mechanical design, suitable fabrication technologies, and the application of advanced bunch shaping techniques to achieve high-gradient high-efficiency acceleration in this structure by raising the transformer ratio.

INTRODUCTION

Structure Wakefield Acceleration (SWFA) in the terahertz (THz) and sub-THz regime are attractive as compact and cost-effective accelerators due to their small transverse sizes. THz wakefield structures could achieve a high gradient from the strong beam-structure interaction, enabled by a high shunt impedance from the frequency scaling. The wakefield is highly confined in a short RF pulse, which could lead to high-efficiency acceleration. Furthermore, both the high frequency and the short RF pulse length could reduce the probability of RF breakdowns at a certain gradient from previous studies [1].

In one scheme of SWFA, collinear wakefield acceleration (CWA), the drive bunch travels in a structure to generate a wakefield and the witness bunch is accelerated in the same structure. A key figure of merit in the CWA scheme is the transformer ratio, defined as the ratio of the accelerating gradient at the witness bunch to the decelerating gradient at the drive bunch. The transformer ratio for longitudinally symmetric bunches could not pass 2 theoretically, which

* bleung@niu.edu

† xylu@niu.edu

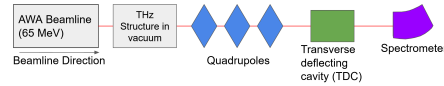


Figure 1: Schematic diagram of a collinear wakefield experiment at the AWA 65 MeV electron beamline, with the THz structure chamber and an LPS system.

limits the achievable efficiency of wakefield accelerators. Longitudinal bunch shaping techniques [2] could break this limit, and when applied to THz structures [3] [4], this could lead to high-gradient high-efficiency wakefield acceleration.

In this paper, we present the design of a W-band corrugated waveguide at 110 GHz for a beam test at the Argonne Wakefield Accelerator (AWA). The AWA beamline makes use of the L-band electron gun and linacs to produce 65 MeV electron bunches. We plan to have a CWA experiment on the corrugated waveguide, where the gradient in the structure would be measured with a single-shot longitudinal phase space (LPS) measurement system, consisting of a set of quadrupoles, a transverse deflecting cavity, and a spectrometer. A schematic diagram of this experiment is shown in Fig. 1.

ANALYTICAL THEORY

Corrugated waveguides have been studied analytically using various approaches. One theory [5] considered the waveguide as a series of resonant cavities connected by apertures, where the apertures are treated as perturbations. The method breaks down when the aperture radius is not far less than the wavelength of the TM_{010} cavity mode. Another theory [6] studied corrugated waveguides excited by relativistic electron bunches. It assumed that the corrugation depth and the cell period were far smaller than the aperture radius, and that the corrugation depth was not much less than the cell period. The accelerating gradient E_z in the fundamental mode predicted by this theory when the corrugated waveguide is excited by a Gaussian bunch (with charge q and rms length σ) can be found as [6]

$$E_z = \frac{1}{4\pi\epsilon_0} \frac{2q}{a^2} e^{-\omega^2\sigma^2/2c^2} \quad (1)$$

with a being the aperture radius, ω being the fundamental angular frequency, ϵ_0 being the vacuum permittivity, and c being the speed of light. This theory is a good description in the high frequency range when $k = \omega/c \gg 1/a$.

For comparison, we utilized a numerical code, the CST Studio Suite, to simulate more general cases, as will be pre-

MACHINE LEARNING FOR SLOW SPILL REGULATION IN THE FERMILAB DELIVERY RING FOR Mu2e

A. Narayanan^{*†1}, J. Arnold, M. Austin, J. R. Berlioz, P. Hanlet, K. J. Hazelwood, M. A. Ibrahim, V. P. Nagaslaev, D. J. Nicklaus, G. Pradhan, P. S. Prieto, B. A. Schupbach, K. Seiya, A. Saewert, R. M. Thurman-Keup, N. V. Tran, D. Ulusel
Fermi National Accelerator Laboratory, Batavia, IL, USA[‡]
J. Jiang^{*}, H. Liu, S. Memik, R. Shi, M. Thieme^{*}
Northwestern University, Evanston, IL, USA
¹also at Northern Illinois University, DeKalb, IL, USA

Abstract

A third-integer resonant slow extraction system is being developed for the Fermilab's Delivery Ring to deliver protons to the Mu2e experiment. During a slow extraction process, the beam on target is liable to experience small intensity variations due to many factors. Owing to the experiment's strict requirements in the quality of the spill, a Spill Regulation System (SRS) is currently under design. The SRS primarily consists of three components - slow regulation, fast regulation, and harmonic content tracker. In this presentation, we shall present the investigations of using Machine Learning (ML) in the fast regulation system, including further optimizations of PID controller gains for the fast regulation, prospects of an ML agent completely replacing the PID controller using supervised learning schemes such as Long Short-Term Memory (LSTM) and Gated Recurrent Unit (GRU) ML models, the simulated impact and limitation of machine response characteristics on the effectiveness of both PID and ML regulation of the spill. We also present here nascent results of Reinforcement Learning efforts, including continuous-action actor-critic methods and soft actor-critic methods, to regulate the spill rate.

RESONANT EXTRACTION FOR Mu2e

Resonant extraction is a beam physics technique employed to extract a slice of beam turn by turn in a circular accelerator by exciting third integer resonance using dedicated sextupole magnets.

Slow extraction at Fermilab is to be done at the Delivery Ring (DR) using a circuit of 6 harmonic sextupoles and 3 fast quadrupoles, driving the horizontal tune from 9.650 to 9.666 to extract 10^{12} protons over the course of 43 ms (≈ 25000 turns) to be sent to the muon production target. Any protons left in the DR after 43 ms would be aborted. The ideal spill quality would be to extract 3×10^7 protons every turn, but we expect the spill quality to be heavily affected with irregularities due to noises that could arise from various accelerator components and other factors.

* Equal contribution

† anarayanan1@niu.edu

‡ This work was supported by the United States Department of Energy under contract DE-AC02-07CH11359 and the READs project [1, 2], also performed in part at Northwestern University with support from the CS and ECE Departments.

The Mu2e experiment imposes strict requirements on the spill quality since the detectors are sensitive to the intensity variations of particles coming off of the muon production target. We thus need a robust regulation system in place to ensure high and steady spill quality.

REGULATION SYSTEM

The spill regulation system (SRS) comprises of slow regulation, fast regulation, and harmonic content canceller. The present design bandwidth of the regulation system is 10 KHz, i.e., 430 data points within one spill. A brief functional overview of the SRS can be found at [3].

Fast Regulation System

The fast regulation in the SRS concerns the control of spill quality *within* one spill to curtail any semi-random noise that might arise and also suppress any high frequency 60 Hz harmonic content that the harmonic content suppressor system is not able to suppress. The fast regulation would be supplemented on top of the slow regulation through a fast feedback loop. This loop will send a control signal update at every time step within one spill, and this signal will superpose to the (already preloaded) quad current ramp of the tune ramping quadrupoles to reduce the instantaneous noises in the spill rate.

One way to implement the fast regulation is through PID feedback control, which is a fairly robust and proven technique. But given the non-linearity of resonance process, low spill time, and the strict requirements from the Mu2e experiment on the spill quality, we also investigate possible use of machine learning to enhance the fast regulation.

If the ideal spill rate is normalized to 1, the quality of the spill is defined by the spill duty factor (SDF),

$$\text{SDF} = \frac{1}{1 + \sigma_{\text{spill}}^2} \quad (1)$$

where σ_{spill} is the standard deviation of the spill rate. An ideal spill would bear a constant spill rate value of 1, giving us an SDF of 1. The goal of the SRS for Mu2e is to obtain an SDF of 0.6 or higher.

WAKEFIELD MODELING IN SUB-THz DIELECTRIC-LINED WAVEGUIDES*

C. Phillips[†], B. Leung, X. Lu¹, P. Piot¹, Northern Illinois University, DeKalb, IL, USA
¹ also at Argonne National Laboratory, Lemont, IL, USA

Abstract

Dielectric-lined waveguides have been extensively studied to potentially support high-gradient acceleration in beam-driven dielectric wakefield acceleration (DWFA) and for beam manipulations. In this paper, we investigate the wakefield generated by a relativistic bunch passing through a dielectric waveguide with different transverse sections. We specifically consider the case of a structure consisting of two dielectric slabs, along with rectangular and square structures. Numerical simulations performed with the fine-difference time-domain of the WARPX program reveal some interesting features of the transverse wake and a possible experiment at the Argonne Wakefield Accelerator (AWA) is proposed.

INTRODUCTION

Wakefields in conventional electron accelerators are generally detrimental as they degrade the beam brightness and are possible sources of instabilities. However, wakefield can also be applied to accelerate particles with unprecedented accelerating gradients. Beam-driven wakefield accelerators could serve as building blocks for the next generation of accelerators required to support research in elementary particle physics or develop compact light sources. A relatively-simple technique to implement beam-driven wakefield acceleration is structure-based wakefield (SWFA): a high-charge “drive” electron bunch passes through a vacuum channel in a structure and produces an electromagnetic field employed to accelerate a properly delayed low-charge “main” electron bunch. A simple implementation of SWFAs consists of a dielectric-lined waveguide (often referred to as DWFA). Such an implementation has been the subject of intense research over the last three decade using cylindrical-symmetric [1, 2] and “slab” structures [3, 4].

The present research focuses on characterizing the electromagnetic-field distribution excited by a drive bunch in structures with different transverse cross sections. It is well known that the transverse section of the structure can lead to dipole-mode suppression in “slab” structures [5] but a general investigation is lacking albeit for the theoretical work reported in [6]. The numerical simulations presented in this paper will guide an experiment planned at the Argonne Wakefield Accelerator (AWA). Here, we specifically investigate the case of three structures with cross-sections

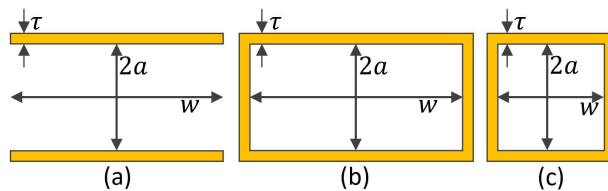


Figure 1: Cross-sectional views [in (x, y) plane] of the slab (a), rectangular (b), and square (c) structures. The structures have the same length along the z direction.

of a “slab”, rectangular and square; see Fig. 1. All the considered structures are made of fused silica with the surfaces external to the beam’s vacuum channel coated with a metal.

STRUCTURE MODELLING

Throughout this paper, we take the beam to propagate along the \hat{z} direction with (x, y) being the transverse positions. The structures are parameterized by their vertical half gap a , full width w , and the dielectric thickness τ ; see Fig. 1. The structures are translational-invariant along the \hat{z} axis with axial length L . The dielectric material is assumed to be isotropic with scalar relative permittivity ϵ . The parameters considered for the present study are summarized in Table 1 and were selected based on their commercial availability. The numerical modeling was performed with WARPX – an advanced electromagnetic framework with particle-in-cell (PIC) capabilities [7]. Although WARPX is principally employed to simulate plasma wakefield accelerators, it has recently been successfully used to model the long-term dynamics in dielectric-lined waveguide [8]. Specifically, we use a fine-difference time-domain “macroscopic” electromagnetic solver. The computation domain extended from $x \in [-w/2, w/2]$, $y \in [-a, a]$, and $z \in [0, L]$. The boundary conditions at the transverse planes $z = 0$ and $z = L$ were set to perfectly-matched layers (PMLs) while all the other boundaries were configured as perfect electrical conductors (PECs) since the outer dielectric surfaces are coated with a metal. To increase simulation speed and given that only the field within and behind the bunch is of interest, a moving

Table 1: Dimensions (all in units of mm) and Relative Electric Permittivity ϵ for the Structures Displayed in Fig. 1

structure type	2				
slab	2	4	0.4	150	3.75
rectangular	2	4	0.4	150	3.75
square	2	2	0.4	150	3.75

* This work was performed under the Chicagoland Accelerator Science Traineeship (CAST) program sponsored by the U.S. DOE award DE-SC0020379 to the Illinois Institute of Technology and Northern Illinois University (NIU). BL, XL, and PP are supported by DOE award DE-SC0022010 to NIU. The AWA facility is sponsored under DOE contract No. DE-AC02-06CH11357 with Argonne National Laboratory.

[†] z1907262@students.niu.edu

TEMPORALLY-SHAPED ULTRAVIOLET PULSES FOR TAILORED BUNCH GENERATION AT ARGONNE WAKEFIELD ACCELERATOR

T. Xu^{1*}, R. Lemons², S. Carbajo^{2,3}, P. Piot^{1,4}

¹Northern Illinois University, DeKalb, IL 60115, USA

²SLAC National Accelerator Laboratory, Menlo Park, CA 94025, USA

³University of California, Los Angeles, CA 90095, USA

⁴Argonne National Laboratory, Lemont, IL 60439, USA

Abstract

Photocathode laser shaping is an appealing technique to generate tailored electron bunches due to its versatility and simplicity. Most photocathodes require photon energies exceeding the nominal photon energy produced by the lasing medium. A common setup consists of an infrared (IR) laser system with nonlinear frequency conversion to the ultraviolet (UV). In this work, we present the numerical modeling of a temporal shaping technique capable of producing electron bunches with linearly-ramped current profiles for application to collinear wakefield accelerators. Specifically, we show that controlling higher-order dispersion terms associated with the IR pulse provides some control over the UV temporal shape. Beam dynamics simulation of an electron-bunch shaping experiment at the Argonne Wakefield Accelerator is presented.

INTRODUCTION

Beam-driven collinear wakefield acceleration requires electron bunches with tailored current profiles to achieve higher transformer-ratios [1]. An important class of current profiles consists of linearly-ramped (“triangular”) distributions. Such electron bunch can be obtained by longitudinal beam shaping techniques which often involves multi-stage phase-space manipulation [2–5]. Laser shaping is a simple yet powerful technique that supports photoinjector generation of longitudinally-shaped electron bunches [6, 7]. It directly controls the distribution of electron bunch at photocathode and does not require any modification of the accelerator beamline.

A laser shaping experiment is under preparation at the Argonne Wakefield Accelerator (AWA). Additional diffraction gratings are being installed in the laser system to achieve a recently demonstrated nonlinear shaping technique named dispersion controlled nonlinear shaping (DCNS) pioneered at the Linac Coherent Light Source [8]. Compared with existing laser-shaping method [6, 7], DCNS does not induce significant energy loss of laser pulses and can be scaled to higher repetition rates. In addition, the pulses generated from DCNS are narrowband and have little to no residual spectral phase across the bandwidth so the pulse shapes are not affected by further nonlinear conversion or general dispersion. In this work, we will describe the principle of DCNS and show that temporally shaped UV pulses can be

obtained by modifying the spectral phase of the IR laser pulse. Finally, we discuss the distortion of electron bunch shapes after photoemission and derive a condition for preserving the sharp tails of the triangular profile.

DISPERSION CONTROLLED NONLINEAR SHAPING

The spectral phase of a laser pulse can be expanded in Taylor series [9],

$$\begin{aligned} \varphi(\omega) = & \varphi_0 + \frac{d\varphi}{d\omega}(\omega - \omega_0) + \frac{1}{2} \frac{d^2\varphi}{d\omega^2}(\omega - \omega_0)^2 \\ & + \frac{1}{6} \frac{d^3\varphi}{d\omega^3}(\omega - \omega_0)^3 + \dots + \frac{1}{n!} \frac{d^n\varphi}{d\omega^n}(\omega - \omega_0)^n \end{aligned} \quad (1)$$

here φ_0 and $d\varphi/d\omega$ are carrier-envelope phase and group delay and neither has any effect on the pulse shape. The second order dispersion (SOD) term, $d^2\varphi/d\omega^2$, also known as *chirp*, results in a group delay linearly dependent on the frequency for each frequency component and stretch the pulse length. The third order dispersion (TOD) term, $d^3\varphi/d\omega^3$ results in a group delay quadratically dependent on frequency,

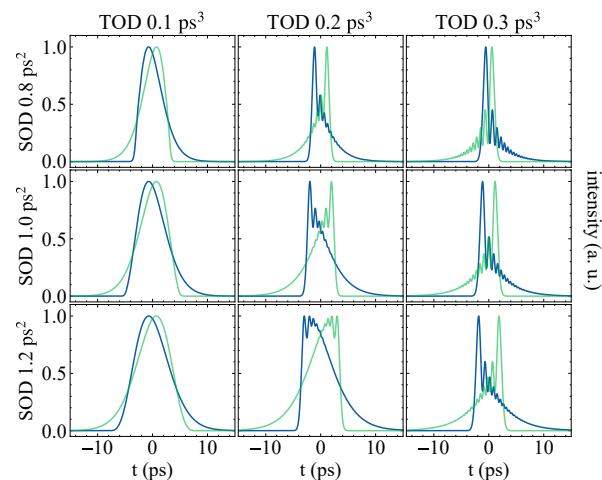


Figure 1: Intensity profile for a pulse with different values of SOD and TOD. Each row has the same magnitude of SOD and each column has the same magnitude of TOD. The blue traces show the intensity profile for a negative SOD and positive TOD while the green traces are for pulses with positive SOD and negative TOD. The intensities are in arbitrary units.

* xu@niu.edu

STUDYING THE EMISSION CHARACTERISTICS OF FIELD EMISSION CATHODES WITH VARIOUS GEOMETRIES*

M.R. Howard^{†1,2}, J.E. Coleman¹, S. Lidia²

¹Los Alamos National Laboratory, Los Alamos, NM, USA

²Facility for Rare Isotope Beams, East Lansing, MI, USA

Abstract

The cathode test stand (CTS) at LANL is designed to hold off voltages of up to 500 kV and can supply pulse durations up to 2.6 μ s. We are able to test both field emission and photocathodes with different geometries and materials at various pulse lengths and pulse-forming network (PFN) voltages. Currently, the test stand is used to evaluate field emission using a velvet cathode over various pulse lengths. The CTS employs various diagnostic tools, including E-dots, B-dots, and a scintillator coupled with a pepperpot mask in order to measure the extracted voltage, current, beam distribution, and transverse emittance. Trak has been used to create and simulate diode geometries, providing potential to study and optimize various beam parameters. These geometries include changing the size and recess of the cathode as well as implementing a Pierce geometry. Here, we will discuss comparisons for various simulated cathodes and how changes in geometry impact given beam parameters. We also show preliminary results taken with the CTS and discuss the relationship between the results and the simulated data.

INTRODUCTION

A thermionic cathode is used to create a long electron beam pulse on the Dual Axis Radiographic Hydrodynamic Testing facility (DARHT) Axis II, which is programmatically kicked into four smaller pulses [1]. The thermionic cathode has drawbacks, one of which being it must be heated to a suitable temperature for the electrons to overcome the work function of a material. A field emission cathode is favoured, as it does not require a heating source. Instead, applying an external electric field onto the cathode with a low work function extracts the electron beam. These cathodes, also known as cold cathodes, are already used in several other facilities, including DARHT Axis I [2], for radiographic purposes. However, these pulses are relatively short in comparison to the 1.7 μ s pulse produced by Axis II [1]. The purpose behind the Cathode Test Stand (CTS) at LANL is to evaluate field emission cathodes across long pulse durations as an eventual replacement for a thermionic cathode.

This write-up will describe the design and set-up of the CTS, including a description of all employed diagnostic devices. We then discuss simulations created using Trak [3]. These simulations revolve around changing the cathode recess and examining the extracted current and

4rms emittance at a given diode voltage. We also show experimental measurements at a variety of charges on the PFN. These measurements will be compared and evaluated against the data collected from the Trak simulations. Finally, simulations for a cathode plug utilizing a Pierce geometry will be shown and the extracted parameters described.

EXPERIMENTAL SETUP

The CTS, designed to hold off voltages up to 500 kV, utilizes a PFN capable of providing a 2.6- μ s-long pulse up to 400 kV and a crowbar which can reduce the pulse length to 0.3 μ s. The cathode is a 15-mm-diameter velvet cloth stretched on an aluminium holder. The cathode is recessed 3 mm into the shroud, and the AK gap is held at 22 mm. Both the cathode and anode shrouds are composed of polished stainless steel.

Voltage measurements in the diode are made using capacitive E-dots probes, one of which is numerically integrated, and one hardware integrated. An additional voltage measurement is made with an E-dot near a ballast resistor. Current measurements are made using several B-dot probes: a differential B-dot in the diode and a Beam Position Monitor array consisting of four differential B-dots. Figure 1 shows the design of the CTS and the locations of the diagnostics.

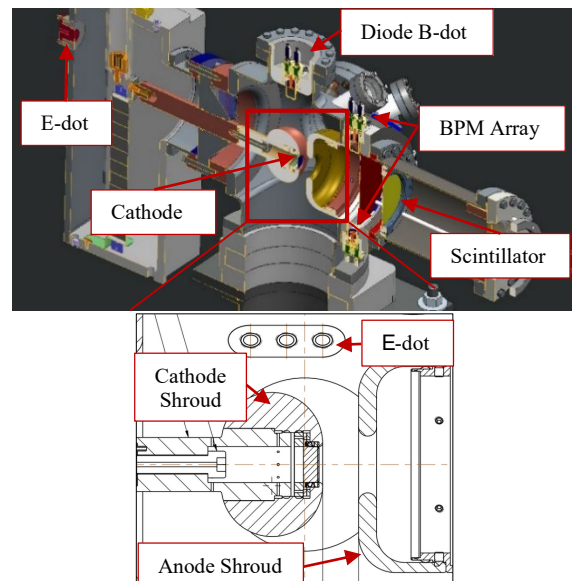


Figure 1: Design of the CTS.

An 87.6 mm alumina scintillator is used to measure the beam current density and spatial profile. This is designed such that it moves between 71.3-131.3 mm from the cathode shroud. Image intensified gated CCD cameras are utilized for cathode and scintillator imaging [4]. Each camera

* LA-UR-22-27965, Work supported by the National Nuclear Security Administration of U.S. Department of Energy under contract 89233218CNA000001. Work partially supported by the US Department of Energy, Office of Science, High Energy Physics under Cooperative Agreement award number DE-SC0018362 and Michigan State University.

[†] mrhoward@lanl.gov

DESIGN STUDY FOR NON-INTERCEPTING GAS-SHEET PROFILE MONITOR AT FRIB*

A. Lokey[†], S. Lidia, Facility for Rare Isotope Beams, Michigan State University, East Lansing, MI, USA

Abstract

Non-invasive profile monitors offer a significant advantage for continuous, online monitoring of transverse beam profile and tuning of beam parameters during operation. This is due to both the non-destructive nature of the measurement and the unique feature that some monitors have of being able to determine both transverse profiles in one measurement. One method of interest for making this measurement is the use of a thin gas curtain, which intercepts the beam and generates both ions and photons, which can be collected at a detector situated perpendicular to the gas sheet. This study will investigate the requirements for developing such a measurement device for use at the Facility for Rare Isotope Beams (FRIB), which produces high-intensity, multi charge state, heavy ion beams. Included will be initial design specifications and an analysis of alternatives between ionization and beam-induced fluorescence measurement techniques for acquiring signal from the gas sheet.

INTRODUCTION

The Facility for Rare Isotope Beams will produce high intensity heavy ion beams of many species and charge states. To characterize the transverse profile of the beam, measurements [1] can be made by either intercepting the beam directly, using techniques such as a wire scanner, SEM grid, or impinging the beam directly on a detector [2]. This has the disadvantage of being susceptible to damage from thermal cycling and sputtering, especially at high intensities.

Therefore, there is an interest in developing a non-invasive method for measuring the transverse profile which can provide information of the state of the beam in both transverse profile directions. For example, it may be advantageous to monitor the spread of the charge states in multi-charge state beams at locations such as bends in the folding LINAC sections of FRIB, as demonstrated in Fig. 1.

One way to accomplish this is by creating a thin gas sheet that the beam interacts with in a minimally invasive way and measuring the distribution of ions, electrons or photons formed [3].

Preliminary work is being done to develop a gas-sheet style monitor based on this success with residual and introduced gas monitors that can be used with high-intensity heavy ions. Similar devices have been successfully developed for lighter ion and proton machines at facilities such as Fermilab and J-PARC [1, 4-6].

* This material is based upon work supported by the U.S Department of Energy, Office of Science, Office of Nuclear Physics and used resources of the Facility for Rare Isotope Beams (FRIB), which is a DOE Office of Science User Facility, under Award Number DE-SC0000661.

[†] lokey@frib.msu.edu

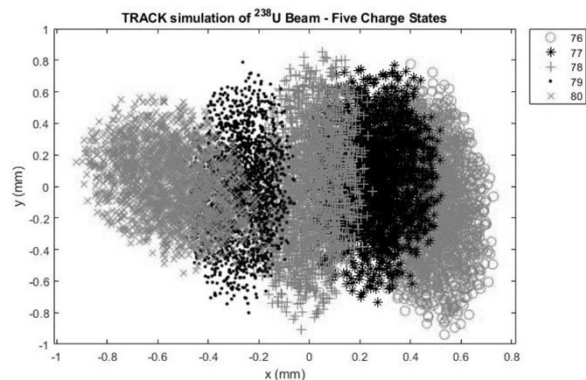


Figure 1: Example of charge state spread generated from TRACK simulation data at a 60 degree bend.

BEAM INDUCED FLUORESCENCE

Beam-induced fluorescence, or BIF monitors measure photons emitted from a working gas when excited by the beam. Imaging is accomplished using photomultiplier tubes or very sensitive intensified camera arrays. The wavelength of the photon is dependent on the energy loss in the beam-gas interaction [7].

The advantage of this technique is that the system is simpler compared to gas ionization monitors, which require electrodes to sweep the ions or electrons to the detector, as well as possibly a parallel dipole to guide them along a spiral path to the desired location and prevent image broadening. There is also better time resolution from photons than ions, due to the difference in time it takes them to travel to the detector. However, the main drawback of this technique is low signal intensity compared to measurement of ionization, since the fluorescence cross section of a gas is generally much lower than its ionization cross section and the light collected will only a small fraction of the total light emitted. Optical systems can gather photons at a small solid angle, therefore amplification and noise reduction for the signal is required [7].

Fluorescence Cross Section

Fluorescence cross section has a q^2 dependence, where q is the charge of the ion and the differential particle energy loss of the beam-gas interaction. Total photon yield is proportional to the gas pressure, the number of particles in a bunch, and the square of the ion charge. For ions at a high charge state, the fluorescence cross section should be high enough to yield enough light for measurement to be made [8].

STUDY OF NONLINEAR DYNAMICS IN THE 4-D HÉNON MAP USING THE SQUARE MATRIX METHOD AND ITERATIVE METHODS*

K. Anderson[†], Y. Hao, FRIB, Michigan State University, East Lansing, MI, USA
L.-H. Yu, Brookhaven National Laboratory, Upton, NY, USA

Abstract

The Hénon Map represents a linear lattice with a single sextupole kick. This map has been extensively studied due to its chaotic behavior. The case for the two-dimensional phase space has recently been revisited using ideas from KAM theory to create an iterative process that transforms nonlinear perturbed trajectories into rigid rotations. The convergence of this method relates to the resonance structure and can be used as an indicator of the dynamic aperture. The studies of this method have been extended to the four dimensional phase space case which introduces coupling between the transverse coordinates.

4-D HÉNON MAP

The following is the form of the 4-D area preserving Hénon map:

$$\begin{pmatrix} x \\ p_x \\ y \\ p_y \end{pmatrix}_{n+1} = \begin{pmatrix} \mathbf{R}(\mu_x) & 0 \\ 0 & \mathbf{R}(\mu_y) \end{pmatrix} \begin{pmatrix} x \\ p_x - x^2 + y^2 \\ y \\ p_y + 2xy \end{pmatrix}_n, \quad (1)$$

where $\mathbf{R}(\theta)$ is a clockwise two by two rotation matrix of angle θ , and μ is 2π times the linear tune and whose subscript denotes the dimension. The physical interpretation of this map is a linear one-turn map of a lattice followed by a single thin sextupole kick.

The linear matrix can be diagonalized by using the complex variables $z_x = x - ip_x$ and $z_y = y - ip_y$ which creates the following one turn map:

$$z'_x = \frac{e^{i\mu_x}}{4} \left(-i(z_x^*)^2 - 2iz_x^*z_y + i(z_y^*)^2 + 2iz_y^*z_x - iz_x^2 + 4z_x + iz_x^2 \right) \quad (2)$$

$$z'_y = \frac{e^{i\mu_y}}{2} \left(-iz_x^*z_y^* + iz_x^*z_y + iz_y^*z_x + iz_xz_y + 2z_y \right), \quad (3)$$

where the prime denotes the variable after one turn.

In this article, we are expanding a method that transforms the trajectory within the central island to a rigid rotation in a two-dimensional phase space to a four-dimensional phase space.

RIGID ROTATION

Finding a diffeomorphism to a rigid rotation in the 4-D phase space is very analogous to the 2-D derivation [1]. As

before we are looking at bounded pseudo-periodic orbits $(z_{x,y}^{(0)}, z_{x,y}^{(1)}, \dots, z_{x,y}^{(n)}, \dots)$. KAM theory [2] showed that the invariant tori survive under small nonlinear perturbations and this idea is still applicable to this system so we can expect this diffeomorphism to exist for this case. The significant change is the motion in x and y are coupled so the diffeomorphisms transforming the motion in each θ are not uncoupled and dependent on both rigid rotation angles as this section will show.

As before we express $z_{x,y}$ in terms of a complex phase: $z_{x,y} = e^{i\theta_{x,y}}$. The real part of each θ represents the arguments of z while the imaginary parts relate to the logarithm of the amplitudes of each z . We can then define $f_{x,y}$ as the function of the change in θ after one turn and is dependent on $\theta_x, \theta_x^*, \theta_y, \theta_y^*$ i.e.:

$$\frac{z'_{x,y}}{z_{x,y}} = \exp i(\theta'_{x,y} - \theta_{x,y}) = \exp i f_{x,y}(\theta_x, \theta_x^*, \theta_y, \theta_y^*). \quad (4)$$

In the case that z_x and z_y are pseudo-periodic we expect θ_x and θ_y to be as well. We can then find diffeomorphisms to a rigid rotation in both θ_x and θ_y :

$$\theta_x = \alpha + h(\alpha, \beta) \quad (5)$$

$$\theta_y = \beta + g(\alpha, \beta), \quad (6)$$

where h and g are smooth complex functions, which are periodic with respect to α and β and each have a period of 2π . Note that compared to the 2-D phase space, the motion in h and g are coupled and dependent on two angles instead of one. However β and α are still the angles of pure rigid rotations:

$$\alpha_{n+1} = \alpha_n + \rho_x \quad (7)$$

$$\beta_{n+1} = \beta_n + \rho_y, \quad (8)$$

where ρ_x and ρ_y are the rotation numbers:

$$\rho_{x,y} = \lim_{n \rightarrow \infty} \frac{\theta_{x,y}^{(n)} - \theta_{x,y}^{(0)}}{n}. \quad (9)$$

Since h and g are periodic it is useful to express them as their Fourier series.

$$h = \sum_{m,n=-\infty}^{\infty} \hat{h}_{n,m} e^{im\alpha + in\beta} \quad (10)$$

$$g = \sum_{m,n=-\infty}^{\infty} \hat{g}_{n,m} e^{im\alpha + in\beta}. \quad (11)$$

From Eq. 4 we use an iterative method to solve for the diffeomorphisms and the rotation numbers starting from

* Work supported by Accelerator Stewardship program under award number DE-SC0019403.

[†] anderske@frib.msu.edu

SPACE CHARGE DRIVEN THIRD ORDER RESONANCE AT AGS INJECTION*

M. A. Balcewicz[†], Y. Hao¹, FRIB, East Lansing, MI, USA
H. Huang, C. Liu, K. Zeno, BNL, Upton, NY, USA
¹also at BNL, Upton, NY, USA

Abstract

Resonance line crossings at significant space charge tune shifts can exhibit various phenomena due to periodic resonance crossing from synchrotron motion and manifests as halo generation and bunch shortening along with the more mundane emittance growth and beam loss. An injection experiment is conducted at the AGS using the fast wall current monitor and electron collecting Ionization Profile Monitor (eIPM) to probe third order resonances to better characterize the resonance crossing over a 4 ms time scale. This experiment shows some agreement with previous experiments, save for lack of bunch shortening, possibly due to relative resonance strength.

INTRODUCTION

Resonance crossings with significant space charge effects has been of particular scholastic interest in part due to the inherent non-linearity of space charge effects and the non-trivial interaction of these effects with the resonance terms. A bunched beam of inhomogeneous bunch density will have only specific longitudinal slices of the bunch in resonance at a time. Subsequent synchrotron motion drives particles in and out of resonance periodically. This is known as a periodic resonance.

Previous experimental observations of periodic resonances have been performed at the GSI's SIS [1] and at CERN's PS [2]. Both previous experiments had their periodic resonances saturate comparatively slowly (~ 1 s). Since this phenomena has only been studied in comparatively few machines, there is value in driving such resonances with another accelerator. The AGS at injection was chosen to perform one of these experiments.

Most of these resonances have been performed with respect to third order resonances. While third order resonances have been studied in the AGS in the past [3] there has been little interest in studying these resonances (specifically $n = 26$) post installation of warm and cold partial snakes [4]. The addition of these optics adjusted the operating tunes away from these resonances to preserve polarization. But even with partial snakes installed it is still possible to cross these resonances. It should also be noted that there are operational compensation sextupole families which can modify third order stopbands strength as necessary.

Periodic Resonances

In the presence of significant space charge the betatron oscillations will be defocused by these effects [5]. Space charge effects can be split into a coherent linear oscillator and an incoherent nonlinear oscillator. The magnitude of the oscillator detuning is a function of the particle distribution. This means that for smooth distribution particles with different longitudinal positions will oscillate at different frequencies compared to one another. This gives rise to tune variation due to space charge along the longitude. This in combination with chromaticity will splay out a bunch's operating tunes over a wide area of tune space.

If a resonance crosses a bunch's operating tunes, it will resonantly drive some longitudinal portion of the beam causing emittance growth and/or loss. Synchrotron motion will eventually move these particles out of resonance, but other particles will correspondingly move back into resonance. Depending on the exact parameters and speed of tune variation [6], there are two regimes a periodic resonance can enter.

First is the Adiabatic Regime. If changes to the tune as particles cross the resonance are smooth enough, some portion of the particles move to the islands of stability. This limits the particle loss and emittance growth. Particle loss is fairly evenly distributed across the longitudinal domain. If in the Non-Adiabatic regime the changes in tune are not smooth as particles cross the resonance. This causes particles that were in an island of stability in a previous synchrotron oscillation to no longer necessarily be in a stable island this turn. Over many synchrotron periods this can lead to the loss of particles that cross the resonance, and eventually all particles with a sufficiently large longitudinal position (bunch shortening). That continues until the loss of particles and emittance growth drives the tune shift above the resonance crossing.

EXPERIMENTAL SETUP

The experiment in question was performed at the AGS on April 12th 2022 with protons. Since the objective of the study was to cross the resonance line with the beam, optical parameters should not be adjusted nor energy ramped after injection as that could shift the portion of the bunch in resonance. Thus the study was performed at injection, and the single particle injection tune was adjusted down very close to the resonance line. The horizontal tune for these experiments is $Q_x = 8.73$. Each experiment is injected at a specific vertical tune within the range $8.666 < Q_y < 8.756$ to adjust the resonance crossing.

* Work supported by Brookhaven Science Associates, LLC under Contract No. DE-SC0012704 with the U.S. Department of Energy

[†] balcewic@frib.msu.edu

AUTOMATION OF SUPERCONDUCTING CAVITY AND SUPERCONDUCTING MAGNET OPERATION FOR FRIB*

W. Chang[#], S. Zhao, Y. Choi, X. Du, W. Hartung, S. Kim, T. Konomi, S. Kunjir, H. Nguyen, J. T. Popielarski, K. Saito, T. Xu

Facility for Rare Isotope Beams, Michigan State University, East Lansing, MI, USA

Abstract

The superconducting (SC) driver linac for the Facility for Rare Isotope Beams (FRIB) is a heavy ion accelerator that accelerates ions to 200 MeV per nucleon. The linac has 46 cryomodules that contain 324 SC cavities and 69 SC solenoid packages. For linac operation with high availability and high reliability, automation is essential for such tasks as fast device turn-on/off, fast recovery from trips, and real-time monitoring of operational performance. We have implemented several automation algorithms, including one-button turn-on/off of SC cavities and SC magnets; automated degaussing of SC solenoids; mitigation of field emission-induced multipacting during recovery from cavity trips; and real-time monitoring of the cavity field level calibration. The design, development, and operating experience with automation will be presented.

INTRODUCTION

The Facility for Rare Isotope Beams (FRIB) driver linac is designed to accelerate ion beams, from hydrogen to uranium, to 200 MeV/u. It has a folded layout as shown in Fig. 1, which consists of three linac segments (LS1, LS2 and LS3) connected with two folding segments (FS1 and FS2), and a beam delivery system to deliver the accelerated beam to target. Linac segments and folding segments have 46 cryomodules with 324 superconducting (SC) cavities for accelerating, 69 SC solenoid packages for transverse focusing and steering. Four SC dipoles has been installed in FS2 to steer and deliver beam from LS2 to LS3 [1]. To operate large scale SC devices with high availability, the implementation of automation tools is necessary and important.

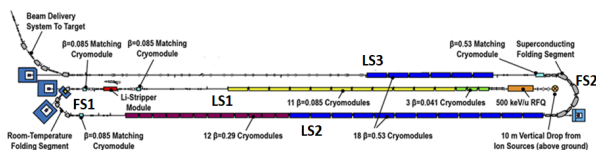


Figure 1: Schematic layout for FRIB driver linac.

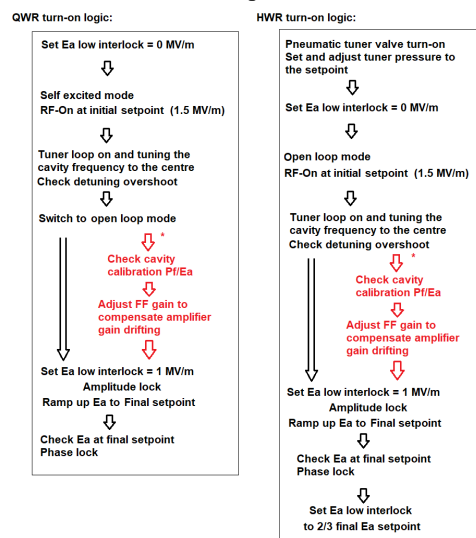
AUTOMATION FOR SC CAVITY

Cavity Auto Turn-on

The FRIB cryomodules contain 104 quarter-wave resonators (QWR) and 220 half-wave resonators (HWR)

*Work supported by the U.S. Department of Energy Office of Science under Cooperative Agreement DE-SC0000661.
[#] chang@frib.msu.edu

for beam accelerating. Manually turn-on each cavity is time consuming and not suitable for the user operation. Since all cavity had been commissioned, the automatic turn-on program has been developed based on experts' commissioning experience. Two auto turn-on programs for QWR and HWR single cavity are developed [2]. After commissioning test succeed, they are duplicated for all QWRs and HWRs and running at Experimental Physics and Industrial Control System (EPICS) Input/output controller (IOC) level. With cavity control parameters be optimized, the cavity can be turned on in 1 minute [2]. The auto turn-on program is also improved, in each cavity commissioning or maintenance time period, new logic update will be tested to enhance the performance and reliability. Figure 2 shows the QWR and HWR auto turn-on logic sequence. Currently there are two new steps for performance improvement, which will be tested during the next linac maintenance time period.



* Red part is the next updated version ready for test

Figure 2: FRIB QWR and HWR auto turn-on logic. Black part: current logic, red part: new logic for next update.

Reliable single cavity level auto turn-on program can be integrated to the group one button turn on. So far, for the LS1 and FS1 104 QWR cavities, a simple CS-Studio OPI control page has been made (Fig. 3, left) for operators to use. Operators are able to turn-on all QWRs within 2 minutes with "one button". For 220 HWRs, currently the auto turn-on is performed by SC cavity experts, all cavities can be group turn-on through a Python script (Fig. 3, right). Similar OPI will be developed in the future after HWR single cavity level auto turn-on program being improved further.

SUPERCONDUCTING CAVITY COMMISSIONING FOR THE FRIB LINAC*

W. Chang[#], S. Kim, W. Hartung, T. Konomi, S. Kunjir, J. T. Popielarski, K. Saito, T. Xu, S. Zhao
 Facility for Rare Isotope Beams, Michigan State University, East Lansing, MI, USA

Abstract

The superconducting driver Linac for the Facility for Rare Isotope Beams (FRIB) is a heavy ion accelerator which has 46 cryomodules with 324 superconducting (SC) cavities that accelerate ions to 200 MeV per nucleon. Linac commissioning was done in multiple phases, in parallel with technical installation. Ion beams have now been accelerated to the design energy through the full linac; rare isotopes were first produced in December 2021; and the first user experiment was completed in May 2022. All cryomodules were successfully commissioned. Cryomodule commissioning included establishing the desired cavity fields, measuring field emission X-rays, optimizing the tuner control loops, measuring the cavity dynamic heat load, and confirming the low-level RF control (amplitude and phase stability). Results on cryomodule commissioning and cryomodule performance will be presented.

INTRODUCTION

The Facility for Rare Isotope Beams (FRIB) driver linac is designed to accelerate ion beams, from hydrogen to uranium, to 200 MeV/u with 46 superconducting cryomodules (SCMs). Four accelerating SCM types SCM041 ($\beta = 0.041$), SCM085 ($\beta = 0.085$), SCM29 ($\beta = 0.29$), SCM53 ($\beta = 0.53$) and two matching SCM types SCM085-matching ($\beta = 0.085$), SCM53-matching ($\beta = 0.53$) has been built in three straight segments, Linac Segment 1 through 3 (LS1, LS2, LS3), and two folding segments (FS1 and FS2). LS1 contains 3 SCM041 and 11 SCM085, LS2 contains 12 SCM29 and 12 SCM53, LS3 contains 6 SCM53, 1 SCM085-matching and 1

SCM53-matching are located in FS1 and FS2, as shown in Fig. 1.

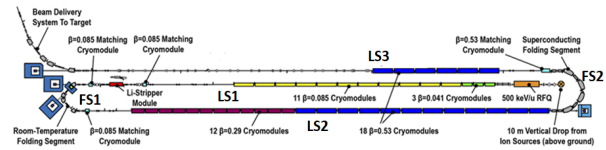


Figure 1: Layout of the FRIB driver linac.

Four types of cavity (Fig. 2): $\beta = 0.041$ quarter-wave resonator (QWR), $\beta = 0.085$ QWR, $\beta = 0.29$ half-wave resonator (HWR) and $\beta = 0.53$ HWR make up FRIB six different types of SCM [1]. Table 1 shows the configuration of FRIB SCMs. A total of 324 cavities has been installed in FRIB SCMs.

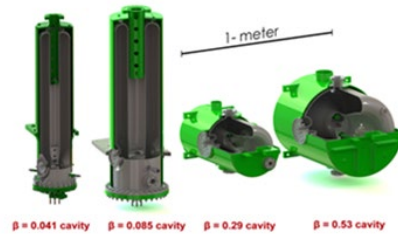


Figure 2: FRIB $\beta = 0.041$ QWR, $\beta = 0.085$ QWR and $\beta = 0.29$, $\beta = 0.53$ HWR cavities.

All cavities had been successfully commissioned in 3 phases. In the first phase all QWR cavities in LS1 and FS1 were commissioned [2]; in the second phase 168 HWRs in LS2 were commissioned; in the last phase the rest 52 HWRs in LS3 and FS2 were commissioned.

Table 1: Configuration of FRIB Cryomodules

Cryomodule type	CA	CB	CH	CC	CD	CG
Number of cryomodules	3	11	1	12	18	1
β	0.041	0.085	0.085	0.29	0.53	0.53
Operation frequency (MHz)	80.5	80.5	80.5	322.0	322.0	322.0
Cavity type	QWR	QWR	QWR	HWR	HWR	HWR
Cavities per cryomodule	4	8	4	6	8	4
Design accelerating gradient E_a (MV/m)	5.1	5.6	5.6	7.7	7.4	7.4

*Work supported by the U.S. Department of Energy Office of Science under Cooperative Agreement DE-SC0000661.

[#] chang@frib.msu.edu

DESIGN OF A 185.7 MHz SUPERCONDUCTING RF PHOTO-INJECTOR QUARTER-WAVE RESONATOR FOR THE LCLS-II-HE LOW EMITTANCE INJECTOR*

S. Kim^{†,1}, C. Adolphsen⁴, L. Ge⁴, W. Hartung¹, F. Ji⁴, M. Kelly², T. Konomi¹, J.W. Lewellen⁴, S. Miller¹, M. Patil¹, T. Petersen², P. Piot^{2,3}, J. Popielarski¹, K. Saito¹, L. Xiao⁴, T. Xu¹, T. Xu¹,

¹Facility for Rare Isotope Beams, Michigan State University, East Lansing, MI, USA

²Argonne National Laboratory, Argonne, IL, USA

³Northern Illinois University, DeKalb, IL, USA

⁴SLAC National Accelerator Laboratory, Menlo Park, CA, USA

Abstract

A 185.7 MHz superconducting quarter-wave resonator (QWR) was designed for the Low Emittance Injector of the Linac Coherent Light Source high energy upgrade (LCLS-II HE LEI). The cavity was designed to minimize the risk of cathode efficiency degradation due to multipacting or field emission and operate with a high RF electric field at the cathode for low electron-beam emittance. Cavity design features include (1) shaping of the cavity wall to reduce the strength of the low-field coaxial multipacting barrier; (2) four ports for electropolishing and high-pressure water rinsing; (3) a fundamental power coupler (FPC) port located away from the accelerating gap. The design is oriented toward minimizing the risk of particulate contamination and avoiding harmful dipole components in the RF field. The ANL 162 MHz FPC design for PIP-II is being adapted for the gun cavity. We will present the RF design of the cavity integrated with the FPC.

INTRODUCTION

SLAC plans to upgrade its LCLS-II to produce higher-energy X-rays for X-ray Free Electron Laser (XFEL) users. It is planned to add more accelerating cryomodules in linac to increase the electron beam energy and also to upgrade the injector to generate ultra-low emittance ($\sim 0.1 \mu\text{m}\cdot\text{rad}$ at 100 pC bunch charge) electron beam: LCLS-II High Energy upgrade (HE) Low-Emittance Injector (LEI) [1, 2]. The approach for the electron gun is use of a superconducting radiofrequency (SRF) gun in order to provide stable CW operation and a low-frequency option such as 185.7 MHz was chosen to minimize growth of the projected emittance due to time-dependent transverse RF field [3].

Michigan State University (MSU) – Argonne National Laboratory (ANL) – Helmholtz Zentrum Dresden Rossendorf (HZDR) collaboration team was selected to develop an SRF gun cryomodule integrating with a cathode load-lock system. We chose these technical options for the SRF cavity and FPC [1]: 185.7 MHz quarter-wave resonator (QWR), two-window fundamental power coupler (FPC) based on ANL's 162 MHz FPC as used in the PIP-II HWR cryomodule [4].

One of the design goals is the RF electric field at the cathode E_c (cathode gradient) higher than 30 MV/m, which has never been demonstrated in the other ‘production’ SRF guns that provided beams for user operations [5, 6]. The challenges of the past SRF guns in achieving such high cathode gradient were conditioning effects or excessive dark currents due to field emission and/or multipacting [5]. We designed our cavity integrated with an FPC improved from the past low-frequency SRF guns. In particular, these features are employed, as shown in Fig. 1:

- The anode-side cavity end wall is a “dome” shape, which helps to reduce the strength of low-field coaxial multipacting barrier,
- The cavity is equipped with four rinse ports that allows electropolishing and high-pressure rinsing,
- The FPC is installed on a rinse port instead of the beam port while not introducing harmful dipole mode. This was chosen to reduce possible field emission due to potential particulate cross-contamination during clean assembly.

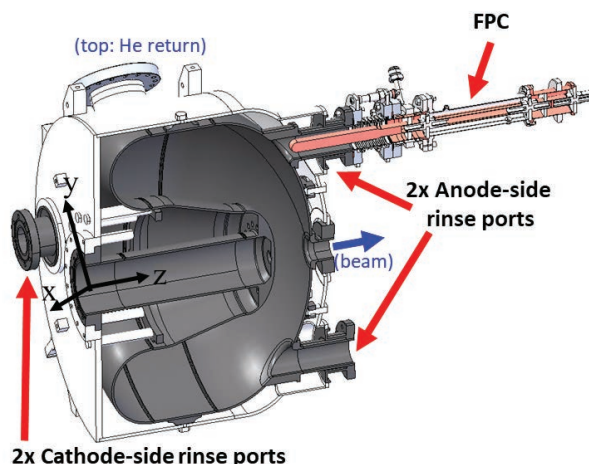


Figure 1: He-jacketed SRF Gun cavity integrated with the fundamental power coupler (FPC). This is a cross-sectional view on a ‘skew’ plan; x: horizontal, y: vertical, z: longitudinal axes. Another cathode-side rinse port exists on the other side of this view.

These are based on the experience with development and operation of low-frequency, low- β SRF cavities and cryomodules [7, 8]. We will present the details of cavity

* Work supported by the Department of Energy Contract DE-AC02-76SF00515.

[†]kims@frib.msu.edu

CONDITIONING OF LOW-FIELD MULTIPACTING BARRIERS IN SUPERCONDUCTING QUARTER-WAVE RESONATORS*

S. Kim[†], W. Chang, W. Hartung, J. Popielarski, T. Xu

Facility for Rare Isotope Beams, Michigan State University, East Lansing, MI, USA

Abstract

Multipacting (MP) barriers are typically observed at very low RF amplitude, at a field 2 to 3 orders of magnitude below the operating gradient, in low-frequency (<~100 MHz), quarter-wave resonators (QWRs). Such barriers may be troublesome, as RF conditioning with a fundamental power coupler (FPC) of typical coupling strength (external $Q = 10^6$ to 10^7) is generally difficult. For the FRIB $\beta = 0.085$ QWRs (80.5 MHz), the low barrier is observed at an accelerating gradient (E_{acc}) of ~10 kV/m; the operating E_{acc} is 5.6 MV/m. Theoretical and simulation studies suggested that the conditioning is difficult due to the relatively low RF power dissipated into multipacting rather than being a problem of the low barrier being stronger than other barriers. We developed a single-stub coaxial FPC matching element for external adjustment of the external Q by one order of magnitude. The matching element provided a significant reduction in the time to condition the low barrier. We will present theoretical and simulation studies of the low MP barrier and experimental results on MP conditioning with the single-stub FPC matching element.

INTRODUCTION

Coaxial multipacting appears at very low RF amplitudes (2-3 orders of magnitude lower than operating E_{acc}) in low-frequency (<~100 MHz) coaxial cavities [1]. This sometimes causes operational issues because it requires a relatively long conditioning time. It is claimed that a stronger coupling and/or a broad loaded-bandwidth helps faster conditioning. Accelerator facilities equipped with low-frequency QWRs such as ATLAS at ANL, ISAC-II at TRIUMF and ALPI-PIAVE at LNL use variable couplers to condition MP [2-4]. In the case of INFN – LNL linac, MP conditioning usually starts when the cavities are still warm [4].

In FRIB $\beta = 0.085$ 80.5 MHz QWRs, the low-field MP appears at E_{acc} of ~10 kV/m whereas the operating E_{acc} is 5.6 MV/m [5]. We found that this MP barrier requires a long conditioning time such as ~1 day or longer, which is not favorable from operation cost standpoints. We thus have been using an alternative method to conditioning: turning on RF with an initial amplitude higher than the MP band such that it passes through the MP band during the RF rising time before MP is built up. This technique has been working well and the downtime due to this MP issue has been negligible so far. However, operational complexities

*This is based upon work supported by the U.S. Department of Energy Office of Science under Cooperative Agreement DE-SC0000661, the State of Michigan and Michigan State University.

[†]kims@frib.msu.edu

still remain particularly because the low-field MP can be enhanced by field emission from neighboring cavities. We recently revisited low-field MP and performed R&D using the ReA6 cryomodule, one of the FRIB $\beta = 0.085$ 80.5 MHz QWR cryomodules, installed in the ReAccelerator linac of FRIB [6].

Figure 1 shows MP conditioning in one of the $\beta = 0.085$ 80.5 MHz QWRs in the ReA6 cryomodule. The forward RF power P_{fwd} was kept constant at 2 W. The accelerating gradient E_{acc} was initially stuck at ~6 kV/m but gradually increased and eventually jumped up at ~14 kV/m after 26 hours of CW conditioning. The vacuum activities were observed on the beamline cold-cathode gauge (green) during conditioning. The reflected RF power P_{rev} (magenta) gradually decreased as the MP was getting conditioned. Multipacting simulation using the CST PIC Solver confirmed that this is coaxial multipacting; for example, at 12 kV/m E_{acc} , the dominant multipacting is 1st order two-point multipacting between the cavity inner and outer conductors, as shown in Fig. 2.

Since the conditioning time of ~1 day per cavity is not favorable for operation, we investigated possibility of improvements of the conditioning time with higher P_{fwd} and/or stronger coupling. We will present theoretical prediction and experimental results.

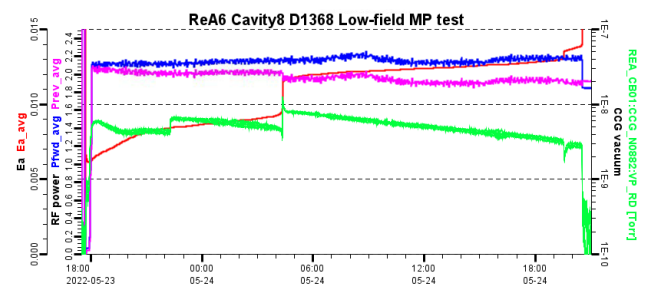


Figure 1: CW conditioning of the low-field MP barrier. This shows trends of P_{fwd} (blue), P_{rev} (magenta), E_{acc} (red), beamline cold-cathode gauge pressure (green) for ~26 hours.

THEORETICAL PREDICTION

When a coupler is coupled to a cavity, the time-dependent amplitude of the reflected wave can be represented by [7]

$$V_-(t) = V_+ \left[\left(1 - e^{-\frac{t}{\tau}} \right) \frac{2\beta}{1 + \beta} - 1 \right], \quad (1)$$

where τ is the RF filling time and β is the coupling coefficient, equal to Q_0/Q_{ext} . The first term in Eq. (1) can be interpreted as the wave radiated from the cavity whereas the

DESIGN OF THE CATHODE STALK FOR THE LCLS-II-HE LOW EMITTANCE INJECTOR*

T. Konomi[†], W. Hartung, S. Kim, S. Miller, D. Morris, J. Popielarski, K. Saito, A. Taylor, T. Xu
Facility for Rare Isotope Beams, Michigan State University, East Lansing, MI, USA

M. Kelly, T. Petersen, Argonne National Laboratory, Lemont, IL, USA

C. Adolphsen, J. Lewellen, SLAC National Accelerator Laboratory, Menlo Park, CA, USA

S. Gatzmanga, P. Murcek, R. Xiang, Helmholtz Zentrum Dresden Rossendorf, Dresden, Germany

Abstract

Superconducting radio-frequency (SRF) electron guns are attractive for delivery of beams at a high bunch repetition rate but moderate accelerating field. An SRF gun is the most suitable injector for the high-energy upgrade of the Linac Coherent Light Source (LCLS II-HE), which will produce high-energy X-rays at high repetition rate. An SRF gun is being developed for LCLS-II HE as a collaborative effort by FRIB, HZDR, ANL, and SLAC. The cavity operating frequency is 185.7 MHz and the target accelerating field at the photocathode is 30 MV/m. The photocathode is replaceable. The cathode is held by a fixture (“cathode stalk”) which is designed for thermal isolation and particle-free cathode exchange. The stalk must allow for precise alignment of the cathode position, cryogenic or room-temperature cathode operating temperature, and DC bias to inhibit multipacting. We are planning a test of the stalk to confirm that the design meets the requirements for RF power dissipation and biasing.

INTRODUCTION

XFELs are powerful tools for revealing structural dynamics at the atomic scale. The LCLS-II-HE will achieve a hard X-ray of 13 keV by doubling the beam energy to 8 GeV from that in LCLS-II. Furthermore, the photon energy of LCLS-II-HE can reach 20 keV by factor of two reduction in the electron source emittance [1].

The development of a low frequency quarter-wave resonator (QWR) SRF gun was proposed to achieve a low emittance beam. The advantage of such a gun is that it can provide a quasi-DC field in the accelerating gap and operate at 4K. As with other SRF guns, an ultra-low vacuum level can be achieved, which allows a wider range of photocathodes to be used.

One of the critical parameters for a high-brightness electron source is the cathode gradient. The goal of the gun cavity development is to demonstrate stable CW operation with a cathode gradient of at least 30 MV/m.

CATHODE STALK DESIGN

The cavity frequency was selected to be 185.7 MHz, which is one-seventh of the 1300 MHz LCLS-II linac frequency. The cavity shape was designed to mitigate multipacting and was evolved from the WIFEL design [2]. The cathode and the cathode stalk use components employed in the SRF gun at HZDR [3].

[†] konomi@frib.msu.edu

There are four main requirements for the cathode stalk. One is precise alignment control of the cathode position. If the cathode position is off-centre, the radial RF field on the cathode will be biased and emittance growth will occur. This growth is difficult to recover with the beam optics downstream of the SRF gun. Second requirement is that it can be biased up to 5kV DC to inhibit multipacting in the coaxial structure of the cathode and cathode stalk. The third requirement is that the temperature of the cathode can be changed if needed, which can improve photocathode performance. The fourth requirement is particle free cathode exchange to prevent field emission from contamination.

The cathode stalk assembly is shown in Fig. 1. The cathode port of the cavity is connected to the bellows flange of the cathode stalk. The tube of the cathode stalk is electrically isolated from the bellows by a ceramic ring. The head of the tube is made of copper and will be cooled by a pipe externally connected to a helium gas supply of either 300 K or 55 K. The tube body is made of stainless steel that is copper/gold plated on the outside to reduce RF loss and thermal emissivity. The cathode holder is conduction cooled through the contact surface with the tube head. The DC bias is connected to a cooling pipe that is electrically isolated using a ceramic break. Three manipulators will be used to adjust the cathode position. These extend to the outside of the cryomodule. The insertion arm for cathode exchange includes four segmented electrodes that are used to sense its transverse location. The cathode holder is inserted into a cone-shaped socket in the cathode head and held in place by a spring.

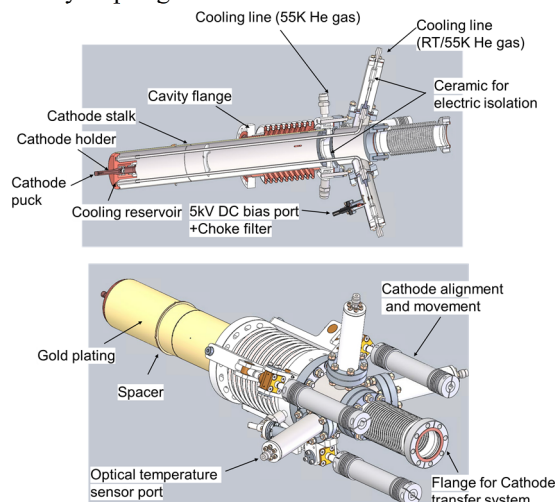


Figure 1: Cathode Stalk assembly.

FRIB AND UEM LLRF CONTROLLER UPGRADE*

S. Kunjir†, E. Bernal, D. Morris, S. Zhao, FRIB, Michigan State University, East Lansing, MI, USA
C-Y. Ruan, Dept. of Physics and Astronomy, Michigan State University, East Lansing, MI, USA

Abstract

The Facility for Rare Isotope Beams (FRIB) is developing a 644 MHz superconducting (SC) cavity for a future upgrade project. The current low level radio frequency (LLRF) controller at FRIB is not able to operate at 644 MHz. The Ultrafast Electron Microscope (UEM) laboratory within the Department of Physics at Michigan State University designed an LLRF controller based on analog RF components to operate a 1.013 GHz room temperature (RT) cavity. With requirements for improved stability, performance and user controls there was a need to upgrade the analog LLRF controller. The FRIB radio frequency (RF) group designed, developed and fabricated a new digital LLRF controller, with high-speed serial interface between system on chip field programmable gate array and fast data converters and capable of high frequency direct sampling, to meet the requirements of 644 MHz SC cavity and 1.013 GHz UEM RT cavity. This paper gives an overview of the upgraded digital LLRF controller, its features, improvements and preliminary test results.

INTRODUCTION

The Facility for Rare Isotope Beams (FRIB) conducted the first user scientific experiment in May 2022 [1]. It will make the majority (~80%) of the isotopes predicted to be bound available for experiments. These isotopes will allow researchers to understand atomic nuclei and their role in the Universe. “The tremendous discovery potential of FRIB can be further extended with an energy upgrade of the FRIB linear accelerator to 400 MeV/u and to higher energies for lighter ions (FRIB400)” [2]. Figure 1 shows footprint of the current (green and black) and upgraded (blue) FRIB linac.

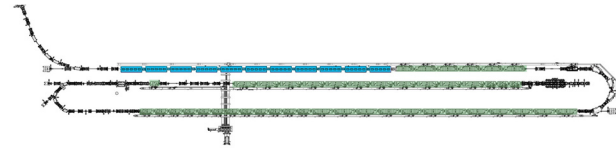


Figure 1: FRIB400 future upgrade.

The Ultrafast Electron Microscope [3] laboratory conducts research on nanoscale material processes at the fundamental length and time scales and studies the mechanisms of phase transitions (atomic and electronic) in low-dimensional systems, the photo-generated hot electron dynamics at interfaces, and the far-from-equilibrium phenomena that involve multiscale, inter-correlated channels of atomic and electronic relaxations following the creation of an excited state in complex and mostly nanostructured solids.

* Supported by the U.S. DOE Office of Science under Cooperative Agreement DE-SC0000661, the State of Michigan, Michigan State University and U.S. National Science Foundation grant DMR-1625181.

† kunjir@frib.msu.edu

MOTIVATION

The current LLRF controllers in operation at FRIB were fabricated in 2016 and support frequencies only between 40.25 MHz and 322 MHz. This is in part due to the limitation of multiple integrated chip (IC) specifications and design requirements. For example, on the current controller, the maximum sampling frequency of analog to digital converter (ADC) is 65 MSPS and digital to analog converter (DAC) is 400 MSPS. With the development of higher frequency cavity for the future upgrade and the requirement of migration from analog LLRF control to digital for UEM, the overarching motivation to upgrade the LLRF controller was the need to support higher frequency operation; 644 MHz for FRIB400 and 1.013 GHz for UEM.

LLRF DESIGN

One of the requirements for the development of a new LLRF controller was to leverage the latest technologies available for FPGAs and data converters with the goal of designing a controller that can be configured as a replacement of current RF systems as well as new higher frequency systems. Another significant requirement was modularity and backwards compatibility of the controller that simplifies hardware troubleshooting and facilitates targeted maintenance of individual components.

Figure 2 shows the new LLRF controller chassis and the hardware components. The new LLRF controller's hardware comprises of (1) FPGA board, (2) RF front-end board, (3) tuner board that can be either stepper, pneumatic or piezo, (4) switching power supply and (5) solid state drive (SSD). These hardware components reside in a 2U chassis designed to be stand-alone and rack mountable.

The FPGA board is a Xilinx ZCU102 [4] evaluation board that hosts a Zynq Ultrascale plus Multi-Processor System on Chip (MPSoC), gigabit ethernet interface for networking, serial advanced technology attachment interface for SSD, universal serial bus interface for serial console debugging, high pin count FPGA mezzanine card for interfacing with RF front-end board and high-speed serial transceivers for interfacing with ADC and DAC on the RF board via JESD204B protocol.

The RF front-end board hosts high-speed data converters, RF components such as digital attenuators, switches, filters, low noise amplifiers, non-volatile memory for configuration storage, low speed ADC and DAC for interfacing with external systems and phase locked loop (PLL) that generates clocks for data converters and FPGA. The tuner board can be either stepper motor driver, pneumatic driver or piezo actuator driver and depends on the cavity type the LLRF controller is used to operate. The switching power supply is 1U fan cooled and

RHIC ELECTRON BEAM COOLING ANALYSIS USING PRINCIPLE COMPONENT AND AUTOENCODER ANALYSIS*

A. D. Tran[†], Y. Hao

Facility for Rare Isotope Beam, Michigan State University, East Lansing, MI, USA

X. Gu, Brookhaven National Laboratory, Upton, NY, USA

Abstract

Principal component analysis and autoencoder analysis were used to analyze the experimental data of RHIC operation with low energy RHIC electron cooling (LEReC). This is unsupervised learning which includes electron beam settings and observable during operation. Both analyses were used to gauge the dimensional reducibility of the data and to understand which features are important to beam cooling.

INTRODUCTION

Beam cooling is an important technique that reduces the phase space area that is occupied by the particle's distribution. Strong hadron cooling, for the high energy and high-intensity hadron beam, will greatly benefit machines such as the future electron ion collider (EIC) to achieve a high luminosity result [1].

The optimization of the cooling performance involves tuning the parameters of the hadron accelerator, the cooler accelerator, and the alignment between them. Physics models are usually not precise enough to support physics-based optimization, therefore a data-driven approach may play an important role. With the presence of sufficient data, one can hopefully find hidden correlations and surrogate models for predicting and optimizing machine performance.

In this paper, we analyze the data-driven method using the averaged measured data of low-energy run of Relativistic Heavy Ion Collider (RHIC) with the Low Energy RHIC Electron Cooling (LEReC) [2]. The data were manually collected from each ramp of the RHIC run with cooling. These include the working points and collimating parameters of the RHIC ring, magnetic settings of the cooler magnets, alignments between the ion and electron beam, and the corresponding beam losses and luminosity.

The analysis being done is known as unsupervised learning, which is when we do not have a map between an input and the desired output. This helps us to find relationships between the variables as opposed to supervised learning which tries to predict the output given the input.

The following paper will first apply principle component analysis (PCA) and then an autoencoder analysis, to reduce the dimension and to understand which parameters are important when optimizing the beam cooling.

PCA ANALYSIS

PCA is a linear data analysis technique used to extract the most important information by compressing the size of the data [3]. The data was stored as a $L \times J$ matrix where L are observations and J are the features. Observations are the data from each run while features are the different inputs and outputs. After the dataset was cleaned, the resulted dataset had around 700 observations, each with 38 features. The data was standardized to a mean of 0 and a standard deviation of 1 with respect to the features. This resulted in the dataset X with matrix elements $\{x_{l,j} \in X | l \in L, j \in J\}$.

The inertia of a column is defined as

$$I_j = \sum_{l \in L} x_{l,j}^2, \quad (1)$$

while the inertia of the dataset is the total inertia, which is the sum of all the column inertia. The term inertia is used because values of a column J for all observation L can be thought of like a mass, and if each column has a zeroed mean, I_j would be the inertia. X is made of this inertia so if a column has a large inertia, it is said to explain more of the whole dataset.

PCA was used to project X into principle components and will be referred to simply as components. The first component has the largest inertia and subsequent ones have decreasing magnitudes while also being orthogonal to the previous components. The projection of X was calculated using standard value decomposition (SVD) as follows: Let the SVD of X be

$$X = U\Sigma Q, \quad (2)$$

then $F = U\Sigma$ is the projection of X on the principle components while Q is the projection matrix.

One of the goals of PCA is to project the matrix X into a matrix with fewer components (fewer variables) while maintaining the core information. This was used to create an approximate data matrix X_M with M principle components. The error between these two matrices is the residual sum of squares $RESS_M$,

$$RESS_M = \|X - X_M\|^2, \quad (3)$$

where $\| \cdot \|$ is the square root of the sum of all the squared elements of $X - X_M$. This is similar to mean square error (MSE). A lower number corresponds to a better recreation of the original data matrix. The analysis is shown in Fig. 1. With PCA, $RESS$ goes to zero as the number of components reaches the original number of components. The error

* Work supported by the US Department of Energy under contract No. DE-AC02-98CH10886.

[†] tranant2@msu.edu

RELATING INITIAL DISTRIBUTION TO BEAM LOSS ON THE FRONT END OF A HEAVY-ION LINAC USING MACHINE LEARNING*

A. D. Tran[†], Y. Hao, Michigan State University, East Lansing, MI, USA

J. L. Martinez Marin, B. Mustapha, Argonne National Laboratory, Argonne, IL, USA

Abstract

This work demonstrates using a Neural Network and a Gaussian Process to model the ATLAS front-end. Various neural network architectures were created and trained on the machine settings and outputs to model the phase space projections. The model was then trained on a dataset, with non-linear distortion, to gauge the transferability of the model from simulation to machine.

INTRODUCTION

A challenging problem in obtaining high beam power in hadron linacs, such as ATLAS, SNS, and FRIB, is understanding and minimizing uncontrolled beam loss, a major unexpected loss of the beam within the beamline. [1] In the low energy beam transport lines (LEBT), the beam must be carefully controlled to minimize the beam loss downstream. The beam is generally a collection of particles that can be described in six-dimensional space; three positions, and three momentum coordinates. For the DC beam in the LEBT, the longitudinal coordinates may contribute if the dipole is not controlled, but this effect will be ignored in this paper. Therefore, each charged particle is described by its location in the four-dimensional (4D) transverse phase space (x, x', y, y') , where primed coordinates are derivatives with respect to the longitudinal direction.

In the LEBT, multiple beam measurement devices such as Alison Scanners [2], Pepper-Pot emittance meters [3], wire scanners [4], and viewers are used to capture one-dimensional (1-D) or two-dimensional (2D) profile measurements, which are projections of the four-dimensional (4D) transverse phase space. Inferring the 4-D distribution from these projected 1-D and/or 2-D information is referred to as 4D tomography. Mathematical and physical methods, such as the maximum entropy principle [5, 6], has been successfully demonstrated to realize the 4-D tomography in accelerators.

In this paper, we tested a data-driven approach to predict the beam loss using 2D projections measurements. The data was generated from virtual diagnostic instruments simulated using the beam dynamics code TRACK. The simulation data was from a test lattice adopted from the LEBT of the ATLAS accelerator and were used to develop a convolutional autoencoder to encode the data into a meaningful lower-dimensional representation, which relates the phase-space information to the beam loss.

* This work was supported by a sub-reward from Argonne National Laboratory and by the U.S. Department of Energy, under Contract No. DE-AC02-06CH11357.

[†] tranant2@msu.edu

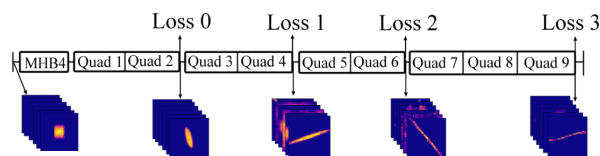


Figure 1: Cartoon of accelerator and beam measurements. The image shows where each beam measurement was collected from.

COLLECTING THE DATA

The presented study used data generated from the simulation of ATLAS's LEBT. The virtual diagnostic instruments capture the 4D phase space of the beam. The locations are shown in Fig. 1 where the phase-space projections of the 4D phase space and losses are measured and saved. This amount of information is currently hard to achieve in a real accelerator but it is used to study the feasibility of the method.

Generating Data Using TRACK

TRACK is a ray-tracing or particle-tracking code that can: (1) represent external fields accurately within the aperture. (2) calculate the particle coordinate at any point in the space. (3) determine beam loss in both the ideal case and in the presence of complex field errors and device misalignments [7].

TRACK simulations were used to gather data as machine data was unavailable. Over a million data point was generated on Michigan State University's high-performance computing cluster. This is needed since a significant amount of data will be required for training autoencoders to high fidelity. The parameters for these simulations were varied according to Table 1 and were chosen within and interperable range. The data was filtered so that the initial beam distributions were contained within the beam aperture, resulting in a final data set of around 430,000 simulation points.

2D phase-space projections were taken by depositing the particles onto an $n \times n$ grid using pairs of the coordinates axes, (x, x', y, y') . This resulted in 6 independent projections.

Non-linear Field

A separate data set was generated to test the generalizability of the model which will be explained later. This was done with a perturbation to the initial distribution by putting a non-linear magnetic field, such as a sextupole, at the beginning of the simulation.

PLASMA PROCESSING OF SUPERCONDUCTING QUARTER-WAVE RESONATORS USING A HIGHER-ORDER MODE*

W. Hartung, W. Chang, K. Elliott, S. Kim, T. Konomi, J. Popielarski, K. Saito, T. Xu
Facility for Rare Isotope Beams, Michigan State University, East Lansing, MI, USA

Abstract

Plasma processing is being developed as a method to mitigate possible future degradation of superconducting resonator performance. Plasma processing tests were done on quarter-wave resonators using the fundamental power coupler to drive the plasma. A higher-order mode was used to reduce the mismatch. Before-and-after cold tests on 3 cavities showed a significant reduction in field emission X-rays after plasma processing.

INTRODUCTION

The Facility for Rare Isotope Beams (FRIB) is a superconducting ion linac with acceleration provided by 104 quarter-wave resonators (QWRs) and 220 half-wave resonators (HWRs); user operations began in May 2022 [1].

Plasma processing is being developed to help reverse possible future degradation of QWR or HWR performance. In-situ plasma processing would be an alternative to removal and disassembly of cryomodules for refurbishment of each cavity via repeat chemical etching and rinsing, as the latter would be time-consuming and labour-intensive. In-situ plasma processing has been demonstrated at SNS [2]. Other plasma processing development efforts worldwide include work on HWRs [3] and spoke cavities [4].

Plasma processing is done at room temperature to avoid cryo-pumping of gases onto the cavity walls. The input coupling strength for FRIB cavities is such that there is a lot of mismatch at room temperature. Plasma processing tests on FRIB QWRs were done using a spare fundamental power coupler (FPC). As the FPC mismatch decreases with increasing frequency, a higher-order mode (HOM) at about 5 times the accelerating mode frequency was used for plasma processing with the FPC. Plasma processing with an HOM has been previously demonstrated for multi-cell $\beta = 1$ cavities using HOM couplers [5] and has been studied for spoke cavities using the FPC [4].

FRIB CAVITIES

Jacketed FRIB production cavities were procured from industrial suppliers. Bulk etching (buffered chemical polishing), hydrogen degassing, light etching, high-pressure water rinsing with ultra-pure water, cold testing [6], cryomodule assembly [7], and cryomodule testing [8] were done at FRIB. More information on FRIB cavity parameters and performance can be found elsewhere [6].

With FRIB production finished, present work is oriented toward producing spare cavities and cryomodules, along

with improvements in preparation procedures to reduce the incidence of field emission. Plasma processing tests are being done on FRIB QWRs in conjunction with these efforts.

PLASMA PROCESSING DEVELOPMENT

Development work was done on a FRIB $\beta = 0.54$ HWR (322 MHz) and a FRIB $\beta = 0.086$ QWR (80.5 MHz), driving the plasma with the fundamental mode. Input couplers with custom antenna lengths were used for an approximate match at room temperature. Some of the plasma parameters were inferred from the optical spectrum. More information can be found in a separate paper [9].

HWR with Matched Input Coupler

First plasma ignition and processing tests were done with an HWR. Plasma measurements were done with various gas mixtures and pressures; to determine the best gas parameters for efficient removal of surface hydrocarbons, reaction byproducts were monitored with a residual gas analyzer (RGA). After testing over a wide range of conditions, we inspected the inner surfaces and observed sputtered copper in the RF input port. We were able to remove the sputtered Cu with additional etching.

QWR with Matched Input Coupler

The first before-and-after cold tests of plasma processing were done using this configuration. The cavity (S85-986) had some field emission X-rays in the first cold test. Plasma cleaning was done with a mixture of neon and oxygen. A significant reduction in field emission X-rays was seen in the cold test after plasma processing [9]. Additional plasma processing and cold test iterations were done subsequently.

PLASMA PROCESSING: QWR WITH FPC

The FRIB QWR FPC includes a cold window [10]. Three FRIB $\beta = 0.086$ QWRs were plasma processed with the plasma driven through the FPC. A refurbished FRIB FPC was used, with the antenna position set near the maximum coupling strength ($Q_{ext,1} \approx 1 \cdot 10^{-6}$).

Higher-Order Modes

At room temperature, the FRIB FPCs are weakly coupled, with coupling factors ($\beta_1 = Q_0/Q_{ext,1}$) ranging from $2 \cdot 10^{-3}$ to 0.02 when set for maximum coupling strength. Accordingly, the RF electric field may be higher in the FPC than in the cavity. As seen in Fig. 1, HOM measurements show that the FPC mismatch decreases as the frequency increases. This indicates that, by driving the plasma with an HOM, we can reduce the coupler-field-to-cavity-field ratio. The TEM- $5\lambda/4$ HOM at about 404 MHz was selected

*Work supported by the US Department of Energy Office of Science under Cooperative Agreement DE-SC0000661.

PRODUCTION PATHWAYS FOR MEDICALLY INTERESTING ISOTOPES*

L. Rosado Del Rio, University of Puerto Rico, San Juan, Puerto Rico

A. Hutton, Jefferson Lab, Newport News, VA, USA

L. Dabill, Coe College, Cedar Rapids, IA, USA

Abstract

Radioisotopes are commonly used in nuclear medicine for treating cancer and new, more effective treatment options are always desired. As a result, there is a national need for new radioisotopes and ways to produce them. A computer program was created that evaluates the daughters for all known reactions of projectiles (gamma rays, protons or neutrons) with every stable target isotope by comparing the cross-sections for each reaction at a desired energy. It then outputs a list of the potential daughter isotopes that are most likely to be generated. The program then evaluates the decay chains of these daughters to provide a list of the possible decay chains that contain a radioisotope of interest. By knowing the daughter production and decay chain for each isotope, it is possible to go from the desired radioisotope to the stable isotope that can be used as a target for its production. This project facilitates the search for new pathways to creating useful theranostic isotopes.

INTRODUCTION

Radioisotopes are used in nuclear medicine for diagnostic, therapeutic, and preventive purposes. However, certain research radioisotopes still do not have a reliable production source, leading to a need for new isotope production pathways. Radioisotopes are produced by the irradiation of a target isotope with a projectile. The irradiated mother isotope may produce several daughters, some of which can decay further (granddaughters). There are many different decay chains for each daughter isotope; therefore, an efficient process is required to identify suitable target isotopes. Additionally, many other radioisotopes are co-produced during irradiation, some of which are potentially harmful. The initial focus was to examine new pathways for medically interesting radioisotopes identified by the Department of Energy Isotope Program (DOE IP) [1].

To carry out an overview of all known reactions of projectiles with stable isotopes, their decay chains, and the co-produced isotopes, the computer program SNIPP (Search for New Isotope Production Pathways) was developed. SNIPP evaluates possible target isotopes by analyzing direct and cascade reactions by irradiation production for all stable or long-lived isotopes with different projectiles and selecting reactions that produce medically useful radioisotopes to find new production pathways. Using the output

from the cascade reactions of the irradiation section, the program goes on to evaluate the isotope decay data and search for medically interesting radioisotopes that are produced. Lastly, it analyses the isotopes that are co-produced during the initial irradiation.

In evaluating the results, reactions that led to isotopes of the same element as the target were rejected. These would require isotopic purification of the radioactive target, a difficult, if not impossible task.

METHODS

The SNIPP program is divided into three sections: irradiation production, decay reactions, and post-processing.

Irradiation Production

The irradiation section analyzes reactions according to input parameters entered by the user. These include whether the target consists of the naturally occurring mix of isotopes (mixed) or has been isotopically purified (pure); the start and end isotope for the search list; the production method (direct or cascade); the projectile (gammas, fast or thermal neutrons, low or high energy protons); a minimum cross section and half-life window for the daughters; and the projectile energy. For purified isotopes, the isotopic purification percentage may be entered. The projectile parameters used for the data presented in this paper are those used for previous papers [2] and were selected considering the most likely production method. The cross-sections were obtained from the TENDL database [3] and the half-lives were obtained from National Nuclear Data Center Wallet Cards (NWC) [4]. Using these parameters, the program identifies reactions with cross sections and half-lives within the entered parameters.

Decay Reactions

The decay section tracks the decay paths of the radioisotopes produced by cascade reactions in the irradiation section. The data of the current existing isotopes, which includes the list of isotopes, their decay modes, and the branch percentages, was obtained from the Berkeley spreadsheet based on data from the NWC [4]. The program goes through the list of isotopes and follows each isotope's decay branch to find isotopes of interest according to the user entered list of isotopes.

Post-Processing

The post-processing section analyzes the results from the irradiation and decay sections. For both direct and cascade results from the irradiation section, it finds reactions that

* L. R. was supported by the U.S. National Science Foundation Research Experience for Undergraduates at Old Dominion University Grant No. 1950141. A. H. was supported by the U.S. Department of Energy, Office of Science, Office of Nuclear Physics under Contract No. DE-AC05-06OR23177

ANALYSIS METHODS FOR ELECTRON RADIOGRAPHY BASED ON LASER-PLASMA ACCELERATORS*

G. Bruhaug[†], G. W. Collins, H. G. Rinderknecht, J. R. Rygg, J. L. Shaw, M. S. Wei
 Laboratory for Laser Energetics, University of Rochester, Rochester, NY, USA
 M. S. Freeman, F. E. Merrill, L. P. Neukirch, C. H. Wilde
 Los Alamos National Laboratory, Los Alamos, NM, USA

Abstract

Analysis methods are presented for determining the resolution of both contact and projected electron radiography based on a laser-plasma accelerator. A means to determine the field strength of the electric/magnetic fields generated when a laser is incident on an object of interest is also outlined. Broad radiography results are reported and future plans for the diagnostic technique are outlined.

INTRODUCTION

Electron radiography (eRad) is a proven, highly penetrative radiography technique that has typically been performed with traditional linear accelerators (LINACs) [1, 2]. Recent work has extended electron radiography techniques into the laser-plasma acceleration (LPA) regime [3, 4] with an emphasis on the radiography of laser-driven dynamics systems.

To compare LPA eRad to traditional LINAC eRad and other radiography methods, the resolution and transmission of said source must be determined. In addition, LPA-based eRad can modify the properties of the object being radiographed via laser-generated plasma if the drive laser is not dumped [4]. Here we present analysis methods to determine the resolution for LPA eRad which include accounting for image distortion caused by the drive laser.

EXPERIMENTAL DETAILS

A polychromatic electron beam generated via LPA with an average energy of ~20 MeV and a bunch charge of up to 700 nC was used to radiograph test objects constructed with varying materials, thicknesses, and feature sizes to fully evaluate the potential of LPA eRad on this platform [4, 5]. Contact radiography was performed on Al, stainless

steel, Cu, Sn and W objects as shown in Figs. 1(a) and 1(b). Projection radiography was performed on solution cast polystyrene, Al, Cu and W objects as shown in Figs. 1(c) and 1(d). All radiographs were taken using MS image plates with 12.5 μm of aluminum in front to dump the laser. MeV-scale electrons have been found to have a relatively flat energy response in image plates and are detected at high efficiency [6]. On each shot, the image plates are saturated by the electron signal. Subsequently, they are scanned repeatedly until saturation no longer exists, and the final, unsaturated scans are used for analysis. Typical scan parameters are sensitivity of 1000 and resolution starting at 100 μm for speed and ending at 25 μm for the final scans in the series.

It should be noted that the majority of the LPA drive laser is transmitted through the LPA plasma source. In the projected configuration, Figs. 1(c) and 1(d), that laser impacts the front face of the projection radiography object with ~10¹⁵ W/cm² intensity and ~20 to 100 joules of laser energy depending on drive specifics. This excess laser energy will impact the target ~100 fs before the electron beam arrives and will generate plasma on the front surface of the object [4]. Consequently, even these supposedly “static” radiography objects were, in reality, laser-ablated dynamic radiography objects.

RADIOGRAPHY ANALYSIS METHOD

Images were then analysed via the software ImageJ [7] and the final scans were grayscale balanced to make the clearest images.

Contact Radiography Resolution

Contact radiography provides the ability to remove the transverse structure of the electron beam using the image plate placed in front of the radiography object as seen in Fig. 2 to record the beam transverse structure before the beam passes through the radiography object. Transverse structure from the beam adds additional blurring to the radiograph that can be eliminated via image division using the software ImageJ [7].

Using these adjusted images, image resolution was determined by creating a box lineout tens of pixels wide across the edges generated by the thickness steps in the radiography object, see Fig. 3(a), and across the edges of the holes in each thickness step. An error function of the form shown in Eq. (1) was then fitted to the lineout as shown in Fig. 3(b).

* This material is based upon work supported by the Department of Energy National Nuclear Security Administration under Award Number DE-NA0003856, the U.S. Department of Energy under Awards DE-SC00215057, the University of Rochester, and the New York State Energy Research and Development Authority.

This report was prepared as an account of work sponsored by an agency of the U.S. Government. Neither the U.S. Government nor any agency thereof, nor any of their employees, makes any warranty, express or implied, or assumes any legal liability or responsibility for the accuracy, completeness, or usefulness of any information, apparatus, product, or process disclosed, or represents that its use would not infringe privately owned rights. Reference herein to any specific commercial product, process, or service by trade name, trademark, manufacturer, or otherwise does not necessarily constitute or imply its endorsement, recommendation, or favoring by the U.S. Government or any agency thereof. The views and opinions of authors expressed herein do not necessarily state or reflect those of the U.S. Government or any agency thereof.

[†] gbru@lle.rochester.edu

DUAL RADIOFREQUENCY CAVITY BASED MONOCHROMATIZATION FOR HIGH RESOLUTION ELECTRON ENERGY LOSS SPECTROSCOPY*

A. Kulkarni[†], P. Denham[‡], A. Kogar, and P. Musumeci.

Department of Physics and Astronomy, University of California, Los Angeles, CA, USA

Abstract

Reducing the energy spread of electron beams can enable breakthrough advances in electron energy loss spectroscopy (EELS) investigations of solid state samples where characteristic excitations typically have energy scales on the order of meV. In conventional electron sources the energy spread is limited by the emission process and typically on the order of a fraction of an eV. State-of-the-art energy resolution can only be achieved after significant losses in the monochromatization process. Here we propose to take advantage of photoemission from ultrashort laser pulses (~ 40 fs) so that after a longitudinal phase space manipulation that trades pulse duration for energy spread, the energy spread can be reduced by more than one order of magnitude. The scheme uses two RF cavities to accomplish this goal and can be implemented on a relatively short (~ 1 m) beamline. Analytical predictions and results of 3D self consistent beam dynamics simulations are presented to support the findings.

INTRODUCTION

In conventional EELS instruments, fine energy resolution is obtained after a monochromator rids the initial beam of most of its electrons, as the initial energy spread from the cathode is typically on the order of 1 eV. After monochromatization, the beam can approach energy scales in the meV range, which are of most relevance to condensed matter systems [1]. For continuous beams, the main contribution to the spread in energies of the electrons is the initial spread in energies at the cathode coupled with the fluctuations in the high voltage power supply. If the initial beam is pulsed, the longitudinal phase space of the beam can be manipulated to trade off bunch length for energy spread as proposed in Duncan et al. [2]. As discussed in that paper, the limit in energy spread reduction is then set by the Liouville theorem-based requirement that the final longitudinal phase space area must be conserved. It follows then that if we could stretch the beam by 100 times in length, it would be possible to reduce the initial energy spread by a factor of 100 without any current loss. This approach is closely related to the work of Zeitler et al. [3] to reduce to eV levels the energy spread in relativistic RF photoinjectors beamlines.

In this paper we discuss a pulsed transmission electron energy loss spectroscopy (EELS) scheme which studies the implementation of this transformation for non-relativistic 40-100 keV table-top setups enabling the possibility to access

meV-scale energy resolution and outperform current EELS instruments by orders of magnitude in terms of beam brightness, a highly desirable result for time-resolved EELS [4]. The scheme is based on the use of a very short (40 fs full width half maximum -FWHM) laser pulse to emit a short burst of electrons from a flat photocathode in a high-tension DC gun. Two properly phased radiofrequency (RF) cavities are then used as a temporally magnifying telescope to stretch and collimate the electron bunch by nearly two orders of magnitude to 5-10 ps, while at the same time proportionally reduce its energy spread. Compared to the original approach presented in Duncan et al. [2] where there is a strong coupling between the transverse and longitudinal dynamics imprinted by the nanoscale dimensions of the electron emitter, here the flat photocathode allows to decouple the beam size evolution and to consider sizable electron charges in each bunch. The simplification also makes possible to analytically describe the longitudinal dynamics, uncovering the scaling laws and limits in energy spread reduction.

THEORY

A cartoon of the proposed beamline is depicted in Fig. 1. Therein, we suppose that a short (40 fs) electron bunch ($< 5000e$ potentially down to a single electron per pulse) is emitted by a DC 40 keV photo-injector. The beam is then accelerated down stream through two TM010-like cavities. The first cavity is set to act as a temporal defocusing lens which stretches the beam. According to Liouville theorem, a temporally stretching beam must simultaneously have its intrinsic energy spread compressed to conserve phase space area, as shown in the cartoon as the thickness of the longitudinal phase space ellipse decreases after the first cavity. As the beam exits the first cavity, the longitudinal phase space exhibits a positive correlation between position and energy. During the drift to the second cavity, the pulse stretches in time, meanwhile the uncorrelated energy spread (the thickness of the longitudinal phase space ellipse) decreases. The beam finally enters the second cavity at the correct phase to fully compensate the positive chirp with the end result of a significantly reduced energy spread.

We start by assuming that we can neglect transverse effects, focusing only on longitudinal single particle dynamics. In addition, we will ignore for now space charge effects (which will always be true in the limit of single-electron pulses). For an on-axis particle the effect of a cavity can be simply described by a sinusoidal change in its kinetic energy depending on the phase experienced by the particle. The energy gain imparted by the first cavity as a function of

* Work supported by National Science Foundation under Grant No. DMR-1548924.

[†] athkulkarni@gmail.com

[‡] pdenham@physics.ucla.edu

THE QUEST FOR THE PERFECT CATHODE*

J. W. Lewellen[†], J. Smedley, T. Vecchione

SLAC National Accelerator Laboratory, Menlo Park, CA, USA

S. Karkare, Arizona State University, Tempe, AZ, USA

J. M. Maxson, Cornell University (CLASSE), Ithaca, NY, USA

D. Filippetto, Lawrence Berkeley National Laboratory, Berkeley, CA, USA

P. Musumeci, University of California Los Angeles, Los Angeles, CA, USA

Abstract

The next generation of free electron lasers will be the first to see the performance of the laser strongly dependent on the material properties of the photocathode. A new injector proposed for the LCLS-II HE is an example of this revolution, with the goal of increasing the photon energy achievable by LCLS-II to over 20 keV. We must now ask, what is the optimal cathode, temperature, and laser combination to enable this injector? There are many competing requirements. The cathode must be robust enough to operate in a superconducting injector, and must not cause contamination of the injector. It must achieve sufficient charge at high repetition rate, while minimizing the emittance. The illumination wavelength chosen must minimize mean transverse energy while maintaining tolerable levels of multi-photon emission. The cathode must be capable of operating at high (~30 MV/m) gradient, which puts limits on both surface roughness and field emission. This presentation will discuss the trade space for such a cathode/laser combination, and detail a new collaborative program among a variety of institutions to investigate it.

NEEDS OF LCLS-II HE

The LCLS-II-HE project will build a new low-emittance injector (LEI) based on an SRF photoinjector to achieve a normalized transverse emittance of 0.1 μm with 100 pC in 3 ps at 100 MeV. This level of performance has never been demonstrated before and is a factor of 3-4 better than the state-of-the-art design of the LCLS-II photoinjector. It will enable the generation of 20 keV photons using an 8 GeV linac, and even harder x-rays when coupled to future superconducting undulators. To achieve this, simulations show that the SRF gun must operate at > 25 MV/m photocathode gradient and that the photocathode must have an intrinsic emittance of ≤ 0.3 $\mu\text{m}/\text{mm}$ [1], corresponding to a maximum allowable MTE of 184 meV.

The LEI performance goal has motivated a multi-institutional effort to address the main technical hurdles and explore the parameter spaces. The cathode MTE vs temperature and wavelength will be explored at moderate gradients for a selection of materials. The most promising will be tested in RF guns at LBL and UCLA. A DC HV test will also be explored. Each of these will be described in the following sections.

* Work supported by the Department of Energy Contract DE-AC02-76SF00515.

[†] lewellen@slac.stanford.edu

GENERAL APPROACH

Our collaboration is designed to both capitalize on leading-edge capabilities at our respective laboratories, while concurrently using multiple techniques to perform the desired characterizations. Our measurements will thus naturally be “cross-checked” as we progress through our experimental program. The approach not only provides additional confidence in our measurements, but will also provide insight as to the source of any discrepancies between measurements.

Broadly speaking, we expect the first year of the effort will be focused on low-field measurements, and on preparing for the start of high-field measurements (e.g. standardizing growth recipes, transfer chambers, etc.) Year 2 will see the start of high-field measurements. The third and final year will continue both low- and high-field measurements on the most promising materials.

LOW FIELD MEASUREMENTS

Our low-field measurements will begin with Cs_3Sb cathodes grown using various recipes on polycrystalline metal or single crystal Si substrates as well as on lattice matched (to Cs_3Sb) substrates like SiC and STO using different growth techniques (sequential deposition, co-deposition and layered growth followed by re-crystallization). Other alkali-antimonides such as K_2CsSb and Na_2KSb will also be investigated. The spectral response and MTE will be measured from these films. The MTE of photocathodes will be measured at low gradient in two locations, Cornell and ASU, to ensure reproducibility.

At ASU, MTE will be measured in the PhotoEmission Electron Microscope (PEEM) by measuring the transverse momentum distribution in the k-space imaging mode. MTE will also be measured at room and cryogenic temperatures in the 200kV DC cryogun at ASU [2]. The PEEM and the 200kV DC gun are connected to the growth chamber in UHV. The surface topography and work function variation of the films will be measured using an Atomic Force Microscope and a Kelvin Probe Force Microscope connected in UHV to the growth chamber [3]. The topography and work function variations will be correlated to the MTE measurements to investigate the effects of surface topography on MTE.

Cornell has a dedicated molecular beam epitaxy (MBE) growth chamber including real-time structural analysis of the photocathode during growth via reflection high energy electron diffraction (RHEED) (Figure 1) and has

TOWARDS HIGH BRIGHTNESS FROM PLASMON-ENHANCED PHOTOEMITTERS

Christopher M. Pierce^{1,2*}, Daniel B. Durham¹, Fabrizio Riminucci¹, Alimohammed Kachwala³,
Siddharth Karkare³, Ivan Bazarov², Jared Maxson², Andrew M. Minor¹, and Daniele Filippetto^{1†}

¹LBNL, 1 Cyclotron Road, Berkeley, CA, USA

²CLASSE, Cornell University, 161 Synchrotron Drive, Ithaca, NY, USA

³Department of Physics, Arizona State University, Tempe, AZ, USA

Abstract

Plasmonic cathodes, whose nanoscale features may locally enhance optical energy from the driving laser trapped at the vacuum interface, have emerged as a promising technology for improving the brightness of metal cathodes. A six orders of magnitude improvement [1] in the non-linear yield of metals has been experimentally demonstrated through this type of nanopatterning. Further, nanoscale lens structures may focus light below its free-space wavelength offering multiphoton photoemission from a region near 10 times smaller [2] than that achievable in typical photoinjectors. In this proceeding, we report on our efforts to characterize the brightness of two plasmonic cathode concepts: a spiral lens and a nanogroove array. We demonstrate an ability to engineer and fabricate nanoscale patterned cathodes by comparing their optical properties with those computed with a finite difference time domain (FDTD) code. The emittance and nonlinear yield of the cathodes are measured under ultrafast laser irradiation. Finally, prospects of this technology for the control and acceleration of charged particle beams are discussed.

SURFACE PLASMON POLARITONS

Surface plasmon polaritons (SPPs) are the evanescent electromagnetic waves that may exist at metal-dielectric interfaces. For a single planar interface, the wave's dispersion relation may be solved exactly starting from Maxwell's equations [3] with the result that,

$$k_x = \frac{\omega}{c} \left(\frac{\varepsilon_1(\omega)\varepsilon_2(\omega)}{\varepsilon_1(\omega) + \varepsilon_2(\omega)} \right)^{1/2}, \quad (1)$$

where $\varepsilon_1(\omega)$ and $\varepsilon_2(\omega)$ are the relative permittivity on either side of the interface. For a free-electron metal, $\varepsilon(\omega) = 1 - \omega_p^2/\omega^2$, where ω_p is the plasma frequency. If we consider a cathode application and take the dielectric to be the vacuum ($\varepsilon(\omega) = 1$) then the dispersion lies to the right of the light line with an asymptote at $\omega_{sp} = \omega_p/\sqrt{2}$ (Fig. 1).

The SPP dispersion relation has two consequences for photocathode physics. Firstly, plasmons may be confined to smaller spatial dimensions and achieve higher optical intensity than free-space light. This is due to the fact that SPPs may have a shorter wavelength than light in a vacuum for optical photon energies. Second, additional momentum may

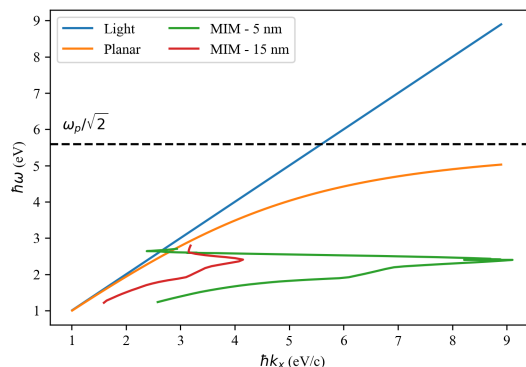


Figure 1: Dispersion relationship of an SPP at a gold-vacuum interface (Planar) for the free electron model (optical parameters from Ref. [4]). Dispersion relationship for two gap widths in a metal-insulator-metal system shown from Ref. [5] (MIM - 5 nm and MIM - 15 nm). Light line shown superimposed (Light).

be required to couple laser light in SPPs which in cathodes is commonly supplied with a grating structure.

ENGINEERED NANOGROOVE PHOTOCATHODES

Consider an otherwise flat gold photocathode patterned with a grating made of nanoscale trenches. Typical width and depth of the grooves are ~ 10 nm and ~ 50 nm. Typical grating pitch is ~ 700 nm. The two vertical walls of the grooves form a metal-insulator-metal system that supports coupled plasmons at the two interfaces. For small insulator width, the plasmon wavevector can become much longer than for free-space light at IR energies [6] (Fig. 1). Capping the insulator off at the bottom and leaving the cavity open at the top forces to the system to adopt Fabry-Perot like resonant modes [7]. These modes (an example of which is shown in Fig. 2) locally enhance the optical intensity at the groove edges. Prior research has shown that this may increase the nonlinear yield of the system by a factor of 10^6 over that of flat gold [1].

In our work, we fabricated nanogroove photocathodes in a variety of dimensions and studied the effect this had on their optical and photoelectric properties. Four pitches (670 - 700 nm) and groove widths (14 - 17 nm) were chosen with the depth fixed at ~ 50 nm. We measured reflectivity

* cmp285@cornell.edu

† dfilippetto@lbl.gov

EPITAXIAL ALKALI-ANTIMONIDE PHOTOCATHODES ON LATTICE-MATCHED SUBSTRATES

P. Saha*, S. S. Karkare, Arizona State University, Tempe, AZ 85287, USA
A. Galdi, Università degli Studi di Salerno, Fisciano, Italy
E. Echeverria, J. M. Maxson, C. A. Pennington, Cornell University, Ithaca, NY 14850, USA
E. J. Montgomery, S. Poddar, Euclid Beamlabs, LLC, Gaithersburg, MD 20879, USA

Abstract

Alkali-antimonides photocathodes, characterized by high quantum efficiency (QE) and low mean transverse energy (MTE) in the visible range of spectrum, are excellent candidates for electron sources to drive X-ray Free Electron Lasers (XFEL) and Ultrafast Electron Diffraction (UED). A key figure of merit for these applications is the electron beam brightness, which is inversely proportional to MTE. MTE can be limited by nanoscale surface roughness. Recently, we have demonstrated physically and chemically smooth Cs₃Sb cathodes on Strontium Titanate (STO) substrates grown via co-deposition technique. Such flat cathodes could result from a more ordered growth. In this paper, we present RHEED data of co-deposited Cs₃Sb cathodes on STO. Efforts to achieve epitaxial growth of Cs₃Sb on STO are then demonstrated via RHEED. We find that films grown via "deposition-recrystallization" method on substrates like STO and SiC (previously used to achieve single crystalline Cs₃Sb) exhibit QE higher than the polycrystalline Cs₃Sb cathodes, by an order of magnitude below photoemission threshold. Given the larger QE, lower laser fluence could be used to extract high charge densities, thereby leading to enhanced beam brightness.

INTRODUCTION

Alkali-antimonide photocathodes like Cs₃Sb, Na₂KSb, K₂CsSb have emerged as efficient electron sources, capable of driving a wide spectrum of linear accelerator based applications ranging from Energy Recovery Linacs (ERL), electron cooling of hadron beams to X-ray Free Electron Lasers (XFEL), Ultrafast Electron diffraction (UED) experiments. They satisfy to quite a good extent the various conflicting requirements for aforementioned applications, which include high Quantum Efficiency (QE) and low Mean Transverse Energy (MTE)/intrinsic emittance in the visible wavelengths, in addition to exhibiting relatively long lifetimes and sub-picosecond response times [1].

Electron beam brightness B which is a key figure of merit for such applications, scales inversely with the MTE as follows [1]:

$$B \propto \frac{1}{\text{MTE}}. \quad (1)$$

The MTE is not just a material intrinsic property, but is also characteristic of the surface geometry. It can get limited

by the nanoscale surface inhomogeneties, both topographical and chemical variations, arising due to the nature of the growth process of alkali-antimonide photocathodes.

Traditionally alkali-antimonides were grown as polycrystalline films with 100 nm tall features using sequential deposition. [2]. Co-deposition of alkali-antimonides has resulted in flatter cathodes, with reduction in roughness by almost an order of magnitude [3]. Efforts to grow atomically flat cathodes alkali antimonides have been pursued by growing on lattice-matched substrates such as silicon carbide 3C-SiC [4] and strontium titanate (STO) substrates [5] instead of the standard Si or polycrystalline metal substrates. It has been shown that high QE Cs₃Sb cathodes grown on STO were atomically flat with rms roughness ~ 0.3 nm and chemically homogeneous with ~ 2.5 mV rms roughness. These ultra smooth cathodes could result from a more ordered and possibly, epitaxial growth.

In this paper, we first report on the growth and Reflection High Energy Electron Diffraction (RHEED) data of co-deposited Cs₃Sb cathodes on STO. We then demonstrate our preliminary efforts to grow Cs₃Sb cathodes on STO via deposition-recrystallization technique, which has been used to achieve single crystalline Cs₃Sb cathode on SiC [6]. We compare the spectral response of QE data from Cs₃Sb cathodes grown via co-deposition and deposition-recrystallization technique, and attempt to explain the difference in QE profiles from such cathodes below photoemission threshold ~ 2.1 eV.

GROWTH

Several Cs₃Sb cathodes were grown on 10 mm by 10 mm Nb-doped STO substrates purchased from MTI Corp. The substrates were mounted on stainless steel omicron paddles compatible with the sample holder of the MBE chamber at Cornell University. A thin indium foil was used between the substrate and omicron paddle to provide better thermal and electrical contact. Prior to growth, the substrates were annealed at 600 °C for two hours. The pristine, single crystalline nature of the STO substrate was confirmed by observing the diffraction spots shown in Fig. 1, by RHEED.

Cs₃Sb cathodes were grown by standard co-deposition technique using pure metallic Sb pellets and Cs-In alloy as sources, placed in effusion cells equipped with pneumatic shutters. The sources were pre-calibrated in terms of flux rates with a quartz crystal microbalance at the growth position of the substrate.

* psaha6@asu.edu

DESIGN OF A 200 kV DC CRYOCOoled PHOTOEMISSION GUN FOR PHOTOCATHODE INVESTIGATIONS

G. S. Gevorkyan*, C. A. S. Cardenas, A. H. Kachwala, C. Knill, T. J. Hanks, S. Karkare
 Arizona State University, Tempe, AZ, USA

Abstract

We present the first results of the commissioning of the 200 kV DC electron gun with a cryogenically cooled cathode at Arizona State University. The gun is specifically designed for studying a wide variety of novel cathode materials including single crystalline and epitaxially grown materials at 30 K temperatures to obtain the lowest possible intrinsic emittance of UED and XFEL applications. We will present the measurements of the cryogenic performance of the gun and the first high voltage commissioning results.

INTRODUCTION

Advances in photoinjector technology has given rise to applications that are heavily dependent on the brightness of the initial photoemitted beam; these applications include X-ray Free Electron lasers (XFEL), ultrafast electron diffraction (UED) and microscopy, electron linear colliders for fundamental physics research, and more [1]. The electron source has recently become key to increased brightness in these devices. Brighter sources will bring next generation improvements to photon and pulse energies for XFELs and bring about the advent of compact XFELs built to fit inside a university laboratory. Similarly they offer improvements to UED to enable studies of crystals with larger lattice sizes. In most photoinjectors brightness follows the following proportionality relationship $B_{4D} \propto E_0^n / \text{MTE}$, where E_0 is the accelerating field gradient, MTE is the mean transverse energy and n is a number between 1 and 2 and depends on the photoinjector design. The MTE can be related to the intrinsic emittance of the cathode via the relationship $\epsilon_{n,x} = \sigma_x \sqrt{\frac{\text{MTE}}{m_0 c^2}}$, where σ_x is the rms spot size of the emitted electrons, m_0 is the rest mass of a free electron and c is the speed of light. Thus, along with maximizing the electric field, minimizing the MTE is critical to obtaining the maximum possible brightness.

There are a number of processes which increase the MTE of photocathodes. First is the excess energy (E_{excess}) or the difference between the photon energy and the cathode work function. At higher excess energies $\text{MTE} \approx E_{\text{excess}}/3$ [2]. If the photon energy can be tuned to the work function such that the excess energy is zero or slightly negative, electrons are emitted from the tail of the fermi distribution making $\text{MTE} = k_b T$, meaning that emitting from a colder source will further reduce the MTE [3]. MTE is also limited by the effects of surface non-uniformities (physical roughness and work function variations) [4], making it critical to use single crystalline atomically ordered cathode surfaces

for smallest possible MTE. Finally, other effects of band structure [5], many-body scattering with phonons [6], and non-linear photoemission [7] can contribute to increasing the MTE.

While RF photoinjectors have made huge strides in increasing the accelerating electric field to improve brightness, the photocathode technology they use is wanting. Typically they feature emission from materials with MTE in the few 100 meV range.

In recent years the advances in reducing MTE from photocathodes has been astounding. MTE as low as 5 meV was measured from near-threshold emission from Cu(100) surface cryocooled to 35 K [8]. By effectively using the electronic structure of the surface state of Ag(111), MTE as low as 20 meV with QE as high as 10^{-4} has been demonstrated. For extremely high QE and low MTE, Alkali-Antimonides have shown a lot of promise, but still have not demonstrated the thermal limit for MTE due to nanoscale physical roughness and work function variations or lattice defect states [9]. Methods for synthesizing these materials with atomically smooth flat [10] and ordered surfaces [11] have recently been developed. These methods require growing these films on single crystalline lattice matched substrates and show promise of obtaining the thermal limit along with QE in the 10^{-3} range or better. Future improvements are expected from novel single crystalline materials like topological insulators and Dirac semimetals used as cathodes [1].

Despite these success is measuring such low MTE from such novel single crystalline cathodes, none of the above technologies has ever been tested in an electron gun.

Even though there is interest to use advanced photocathodes in today's photoinjectors, the compatibility in most devices is simply not there. Most RF photoinjectors use the backside plate of the RF cavity, a piece of machined copper, as their photoemission source. New INFN style plugs as retractable cathodes in RF guns are becoming more popular, but they still don't allow for the use of single crystalline materials [12]. Several DC guns are designed to use single crystalline cathodes, especially for using GaAs based cathodes for spin-polarized applications. However, they are designed with a specific size and shape of the cathode that is not a standard easily available from vendors.

Use of single crystal cathodes also requires ultra-high-vacuum (UHV). Most DC guns are designed to achieve and operate in UHV, however, this is often a challenge for RF guns. Recently RF guns with upgraded pumping capabilities operating in the VHF [13] and S-band ranges have demonstrated UHV and can, in principle, use single crystalline cathodes.

* Ggevorky@asu.edu

COULOMB CRYSTALS IN STORAGE RINGS FOR QUANTUM INFORMATION SCIENCE*

K. A. Brown^{†1,2}, Brookhaven National Laboratory, Upton, NY, USA

B. Huang³, T. Robertazzi^{2,3}, Stony Brook University, Stony Brook, NY, USA

A. Aslam, S. G. Biedron, T. Bolin, S. Sosa Guitron
University of New Mexico, Albuquerque, NM, USA

C. Gonzalez-Zacarias², University of Southern California, Los Angeles, CA, USA

¹also at Stony Brook University, Stony Brook, NY, USA

²Department of Electrical and Computer Engineering

³Department of Applied Mathematics and Statistics

Abstract

Quantum computing is a burgeoning field which has seen significant advances in the last decade. However, we are still a long way from having a universal computer that can efficiently simulate quantum mechanical phenomena. Quantum computers, in principle, use a well-known quantum system (the computer) to predict the behavior of another quantum system (the system being simulated). In this paper we review recent work in developing systems for quantum information science (QIS) and the use of storage ring technologies to take QIS to large scales. We will discuss crystalline beams, the challenges faced in utilizing storage rings for QIS systems, the importance of quantum entanglement, and recent progress in tackling some of the challenges.

INTRODUCTION

Crystalline beams in storage rings have the potential to scale QIS systems well beyond current ion trap approaches [1,2]. Crystalline ion chains have been created in ion trap systems and have proven to be useful as the computational basis for QIS applications [3,4]. The same structures can be created in a storage ring, but the ions necessarily have a constant velocity and are rotating in a circular trap [5]. To be useful for QIS applications these crystals need to be cooled to ultra-low temperatures [6,7].

Quantum information science is a growing field that promises to take computing into a new age of higher performance and larger scale computing as well as being capable of simulating quantum phenomena using quantum systems [8,9]. Computer scientists have worked out many additional problems that could be solved efficiently using quantum computers rather than conventional computers. This is illustrated in Figure 1, which shows an Euler diagram of the different complexity classes. Beyond simulating physics problems, there are problems that are uniquely suited and more quickly solved on quantum computers.

The outstanding issue in practical quantum computing today is scaling up the system while maintaining interconnectivity of the qubits and low error rates in qubit op-

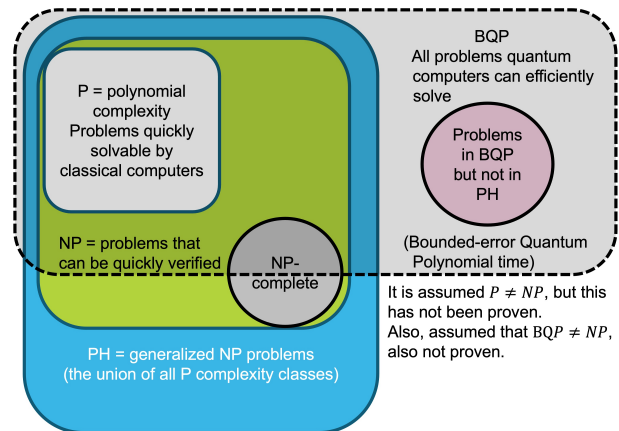


Figure 1: An Euler diagram illustrating the relationships of different complexity classes for classical and quantum computing. This is an active area of research, so this diagram is only meant to generally show how different classes of problems fit into either a classical or quantum computing universe [10].

erations to be able to implement error correction and fault-tolerant operations [11]. Trapped ion qubits offer long coherence times that allow error correction [12]. Error correction algorithms require large numbers of qubits. We can potentially create many thousands (or more) of qubits with long coherence states in a storage ring. A circular radio-frequency quadrupole (CRFQ), which is a large circular ion trap, acting as a Storage Ring Quantum Computer (SRQC), would be scalable and fault tolerant quantum information system. With computing demands potentially outpacing the supply of high-performance systems, quantum computing could bring innovation and scientific advances to nuclear and particle physics [13].

Trapped ions are isolated small quantum systems that have demonstrated low decoherence rates. Such systems can be controlled and measured using laser-induced manipulations of the ions. Stationary ions may be in the same inertial reference frame as the lasers and other systems used to control and measure eigenstates, but a single set of lasers can only operate on a small number of ions in the trap. Very long ion chains would not be easily addressable [14]. Moving ions,

* This work was performed under Contract No. DE-SC0012704 with the auspices of the U.S. Department of Energy.

[†] kbrown@bnl.gov

NEXT GENERATION COMPUTATIONAL TOOLS FOR THE MODELING AND DESIGN OF PARTICLE ACCELERATORS AT EXASCALE*

A. Huebl[†], R. Lehe, C. E. Mitchell, J. Qiang, R. D. Ryne, R. T. Sandberg, J.-L. Vay
Lawrence Berkeley National Laboratory, Berkeley, CA, USA

Abstract

Particle accelerators are among the largest, most complex devices. To meet the challenges of increasing energy, intensity, accuracy, compactness, complexity and efficiency, increasingly sophisticated computational tools are required for their design and optimization. It is key that contemporary software take advantage of the latest advances in computer hardware and scientific software engineering practices, delivering speed, reproducibility and feature composability for the aforementioned challenges. A new open source software stack is being developed at the heart of the Beam pLasma Accelerator Simulation Toolkit (BLAST) by LBNL and collaborators, providing new particle-in-cell modeling codes capable of exploiting the power of GPUs on Exascale supercomputers. Combined with advanced numerical techniques, such as mesh-refinement, and intrinsic support for machine learning, these codes are primed to provide ultrafast to ultraprecise modeling for future accelerator design and operations.

INTRODUCTION

Large-scale computer simulations of charged particle motion inside of particle accelerators play a crucial role in accelerator design and operation. In order to quickly simulate charged particle dynamics, including collective effects, advanced software must be developed to take advantage of state-of-the-art computer hardware.

With the onset of the Exascale supercomputing era, omnipresent GPU-accelerated machines require multi-level parallelism, multi-paradigm programming and dynamic load balancing. The U.S. Department of Energy Exascale Computing project addressed this need by co-developing applications and software for Exascale computing acquisitions. The laser-plasma modeling code WarpX [1], e.g., used in plasma-based particle acceleration, is a result of this project and recently provided the first full-scale runs at the first demonstrated Exascale machine, Frontier [2].

* Work supported by the Exascale Computing Project (17-SC-20-SC), a joint project of the U.S. Department of Energy's Office of Science and National Nuclear Security Administration, responsible for delivering a capable exascale ecosystem, including software, applications, and hardware technology, to support the nation's exascale computing imperative. This work was supported by the Laboratory Directed Research and Development Program of Lawrence Berkeley National Laboratory under U.S. Department of Energy Contract No. DE-AC02-05CH11231. This research used resources of the National Energy Research Scientific Computing Center (NERSC), a U.S. Department of Energy Office of Science User Facility located at Lawrence Berkeley National Laboratory, operated under Contract No. DE-AC02-05CH11231 using NERSC award HEP-ERCAP0020744.

[†] axelhuebl@lbl.gov

Beam, Plasma & Accelerator Simulation Toolkit

WarpX is a code in the Beam, Plasma & Accelerator Simulation Toolkit (BLAST, <https://blast.lbl.gov>), a suite of open source particle accelerator modeling codes. Originally developed under the name Berkeley Lab Accelerator Simulation Toolkit, included codes achieved compatibility through a common meta-data standard in I/O, openPMD [3], yet were implemented in disjoint code bases. BLAST has been renamed in 2021 to reflect international contributions from LIDYL (CEA, France), SLAC (USA), LLNL (USA), DESY (Germany), UHH (Germany), HZDR (Germany), Radosoft (USA), CERN (Switzerland) and more; BLAST development involves deep collaboration among physicists, applied mathematicians, and computer scientists.

With the emergence of the first Exascale Computing supercomputers, modeling codes that were originally designed for parallel CPU-powered machines need to undergo a fundamental modernization effort. This became necessary, as compute nodes are now equipped with accelerator hardware such as GPUs (and potentially FPGAs in the future). Selected as application for the Department of Energy Exascale Computing Project, the BLAST code WARP [4,5] underwent a complete rewrite from Fortran to modern C++ resulting in its successor WarpX [1]. Building on the momentum of this transition to form a more cohesive Accelerator Toolkit, the specialized plasma wakefield acceleration code HiPACE++ [6] and beam dynamics code ImpactX [7], presented herein, are developed.

Software Design

A central goal of the modernization of BLAST is modularity for efficient code reuse and tight integration for coupling, i.e., in hybrid particle accelerators with conventional and advanced (plasma) elements. Figure 1 shows the design of BLAST's software dependencies, with upper components depending and sharing lower blocks in the schema. Shared code, common application programming interfaces (APIs) and data standards ensure composability and connection to the AI/ML and data science ecosystems. Performance-critical routines are implemented and reused in modern C++, using a single-source approach to program both CPUs and GPUs via a performance-portability layer in AMReX [8]. The newly introduced ABLASTR library collects common particle-in-cell (PIC) routines.

Python high-level interfaces are used for user efficiency and to provide standardized APIs to data science and AI/ML frameworks, which are mostly driven from the same language. Documentation and examples are developed in lock-step with documentation and published on <https://>

AN OPEN-SOURCE BASED DATA MANAGEMENT AND PROCESSING FRAMEWORK ON A CENTRAL SERVER FOR SCIENTIFIC EXPERIMENTAL DATA*

A. Liu[†], W. Si, J. Callahan, S. Poddar, Euclid Techlabs, LLC, Bolingbrook, IL, USA
J. Gao, AJS Smartech, LLC, Naperville, IL, USA

Abstract

The ever-expanding size of accelerator operation and experimental data including those generated by electron microscopes and beamline facilities renders most proprietary software inefficient at managing data. The Findability, Accessibility, Interoperability, and Reuse (FAIR) principles of digital assets require a convenient platform for users to share and manage data on. An open-source data framework for storing raw data and metadata, hosting databases, and providing a platform for data processing and visualization is highly desirable. In this paper, we present an open-source, infrastructure-independent data management software framework, named by EuclidLIMS, to archive, register, record, visualize and process experimental data. The software was targeted initially for electron microscopes, but can be widely applied to all scientific experimental data.

INTRODUCTION

Particle beam accelerators and beamlines are used in a wide range of multidisciplinary research, including nuclear physics, advanced material physics, high energy physics, biophysics, and beyond. These facilities and instruments generate large amounts of valuable scientific experimental data, both for hardware diagnostics purposes and for scientific discoveries. The types of data generated in these experiments include images, text files, spreadsheets, proprietary file formats, and so forth. A lot of these data contain rich metadata information, such as the instrumentation name, model and settings, experimental conditions, purposes and configurations, and more.

With the rapid development of detectors and pre-analysis electronic systems, the volume and the speed of the data generation are both growing significantly. Keeping up with the explosive increase in scientific data creation has been practically impossible for many existing data management frameworks that are purely based on a local data and computing architecture, particularly for comparably smaller facilities where the infrastructure is still not fully developed yet. However, without a data management software, the scientific data collected can be easily unintentionally lost no matter whether it is stored on a portable storage disk, a personal or organizational computer, or on a local data server. Finding the data-of-interest from a sea of folders and files by filtering with the filename is rather cumbersome. Moreover, physical

properties like aforementioned are prone to being lost, either by being left behind or damages.

It is well accepted that a data management software can mitigate the above problems with the proper usage of a well-managed data server and a powerful software. Furthermore, in order to deploy the software on computers with old operating systems (OS), which are prohibited to be connected to a public network (WWW) and only support local network connectivity. Therefore, the software not only needs to provide all the necessary functionalities for the data management, but also is required to be “miniature” such that it can be adopted by most of the experimental computers.

Another desired capability of the software is providing an online data analysis platform for the raw data collected. With the fast advancement of cost-effective computing hardware, many experimental facilities are now equipped with computing servers that are able to handle not only the data storage, but also resource-demanding computing jobs. Therefore, it is beneficial to be able to launch computationally heavy jobs on the server so the managed data can be analyzed in the background.

EUCLID-NEXUSLIMS

Euclid has been collaborating with a group at NIST to develop a infrastructure, project and facility-independent software framework for data management and processing. The Euclid software framework is based on the NexusLIMS [1] open-source program developed by the NIST collaborators, and was initially named “Euclid-NexusLIMS”. LIMS stands for “laboratory information management system”. During the development of Euclid-NexusLIMS, we fully respected the open-source software and FAIR principles. One of our main goals was to accommodate a broader spectrum of scientific data management requirements by taking advantage of an already demonstrated framework instead of reinventing the wheel.

The framework is made of several main components. The ones that are present in both the original NexusLIMS and our Euclid-NexusLIMS are a data *logger* graphical user interface (GUI) that can be installed on control computers that are used to control the instrumentation to take data, a database record and metadata generator *backend*, and a *frontend* with Web interface for browser-based user interaction. A computing module in Euclid-NexusLIMS allows users to run data analysis jobs with workload managers like Slurm or Snakemake [2]. The infrastructure-specific portions have

* Work supported by the U.S. DOE Office of Science under contract number DE-SC0021512.

[†] a.liu@euclidtechlabs.com, ao@aoliu.tech

MACHINE LEARNING FOR ANOMALY DETECTION AND CLASSIFICATION IN PARTICLE ACCELERATORS*

I. Lobach[†], M. Borland, K. Harkay, N. Kuklev, A. Sannibale, Y. Sun
Argonne National Laboratory, Advanced Photon Source, Lemont, IL, USA

Abstract

We explore the possibility of using a Machine Learning (ML) algorithm to identify the source of occasional poor performance of the Particle Accumulator Ring (PAR) and the Linac-To-PAR (LTP) transport line, which are parts of the injector complex of the Advanced Photon Source (APS) at Argonne National Lab. The cause of reduced injection or extraction efficiencies may be as simple as one parameter being out of range. Still, it may take an expert considerable time to notice it, whereas a well-trained ML model can point at it instantly. In addition, a machine expert might not be immediately available when a problem occurs. Therefore, we began by focusing on such single-parameter anomalies. The training data were generated by creating controlled perturbations of several parameters of PAR and LTP one-by-one, while continuously logging all available process variables. Then, several ML classifiers were trained to recognize certain signatures in the logged data and link them to the sources of poor machine performance. Possible applications of autoencoders and variational autoencoders for unsupervised anomaly detection and for anomaly clustering were considered as well.

INTRODUCTION

This contribution investigates the possibility to use unsupervised and supervised Machine Learning (ML) methods for anomaly detection and classification in the Particle Accumulator Ring (PAR) and in the Linac-To-PAR (LTP) transport line in the injector complex of the Advanced Photon Source (APS) [1, 2] at Argonne National Lab. We create intentional perturbations in PAR and LTP, which result in poor injection and extraction efficiencies. Then, these data are used for training and testing of various ML models. We chose PAR and LTP for these studies, because a considerable dedicated study time is available in these parts of the APS complex without interruption of user operations.

DATA ACQUISITION

The data presented in this paper were collected during three studies in November, 2021 and during one study on January 30, 2022. Figure 1 illustrates the intentional perturbations of several Process Variables (PVs) on January 30, 2022 and their effect on the charge extracted from PAR. During our studies, the injection cycle rate was 2 Hz. Therefore, the machine state was also logged at 2 Hz as well. Overall, we logged about 9000 PVs related to PAR, LTP, and the

* The work is supported by the U.S. Department of Energy, Office of Science, Office of Basic Energy Sciences, under Contract No. DE-AC02-06CH11357.

[†] ilobach@anl.gov

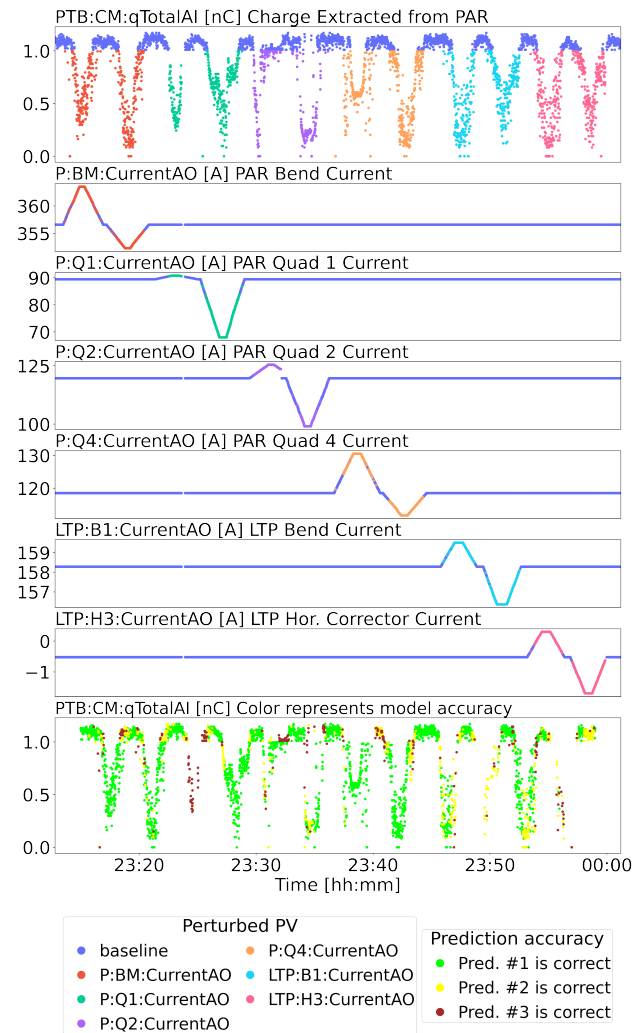


Figure 1: Intentional perturbations of some process variables in PAR and LTP and their effect on the extracted charge. Also, prediction performance of a neural network classifier (bottom panel).

linac. However, later we decided to only use up to 155 most relevant PVs as input for ML models. During the intentional perturbations, the beam charge was always kept above zero in order to use the signals from the Beam Position Monitors (BPMs) and to keep various control laws active. Although, most of the data for this paper were collected manually, the process, illustrated in Fig. 1, can be fully automated. We developed a script and tested it with several PVs.

SUPERVISED ML

The machine state snapshots collected at 2 Hz during the intentional perturbations, as in Fig. 1, constitute a labeled

THE ELECTRON-POSITRON FUTURE CIRCULAR COLLIDER (FCC-ee)*

M. Benedikt, F. Zimmermann[†], CERN, Meyrin, Switzerland

T. O. Raubenheimer, SLAC National Accelerator Laboratory, Menlo Park, CA 94025, USA

K. Oide¹, University of Geneva, Geneva, Switzerland

¹also at KEK, Tsukuba, Ibaraki, Japan

Abstract

The Future Circular electron-positron Collider (FCC-ee) is aimed at studying the Z_0 and W^\pm bosons, the Higgs, and top quark with extremely high luminosity and good energy efficiency. Responding to a request from the 2020 Update of the European Strategy for Particle Physics, in 2021 the CERN Council has launched the FCC Feasibility Study to examine the detailed implementation of such a collider. This FCC Feasibility Study will be completed by the end of 2025 and its results be presented to the next Update of the European Strategy for Particle Physics expected in 2026/27.

INTRODUCTION

The Future Circular electron-positron Collider, FCC-ee, is a proposed new storage ring of 91 km circumference, designed to carry out a precision study of Z , W , H , and $t\bar{t}$ with an extremely high luminosity, ranging from $2 \times 10^{36} \text{ cm}^{-2} \text{ s}^{-1}$ per interaction point (IP), on the Z pole (91 GeV c.m.), $7 \times 10^{34} \text{ cm}^{-2} \text{ s}^{-1}$ per IP at the ZH production peak and $1.3 \times 10^{34} \text{ cm}^{-2} \text{ s}^{-1}$ per IP at the $t\bar{t}$. In the case of four experiments, the total luminosity on the Z pole will be close to $10^{37} \text{ cm}^{-2} \text{ s}^{-1}$. FCC-ee will also offer unprecedented energy resolution, both on the Z pole and at the WW threshold.

The FCC-ee represents a low-risk technical solution for an electroweak and Higgs factory, which is based on 60 years of worldwide experience with e^+e^- circular colliders and particle detectors. R&D is being carried out on components for improved performance, but there is no need for “demonstration” facilities, as LEP2, VEPP-4M, PEP-II, KEKB, DAΦNE, or SuperKEKB already demonstrated many of the key ingredients in routine operation.

The FCC shall be located in the Lake Geneva basin and be linked to the existing CERN facilities. The FCC utility requirements are similar to those in actual use at CERN. The FCC “integrated programme” consists of the FCC-ee Higgs and electroweak factory as a first stage, succeeded by a 100 TeV hadron collider, FCC-hh, as the ultimate goal. This sequence of FCC-ee and FCC-hh is inspired by the successful past Large Electron Positron collider (LEP) and Large Hadron Collider (LHC) projects at CERN. A similar two-stage project is under study in China, under the name CEPC/SPPC [1].

The FCC technical schedule foresees the start of tunnel construction around the year 2030, the first e^+e^- collisions

at the FCC-ee in the mid or late 2040s, and the first FCC-hh hadron collisions by 2065–70.

DESIGN OUTLINE

The FCC-ee is conceived as a double ring e^+e^- collider. It shares a common footprint with the 100 TeV hadron collider, FCC-hh, that would be the second stage of the FCC integrated programme.

The FCC-ee design features a novel asymmetric interaction-region (IR) layout and optics to limit the synchrotron radiation emitted towards the detector (a lesson from LEP [2]), and to generate the large crossing angle 30 mrad, required for the crab-waist collision scheme [3].

The latest FCC layout features a superperiodicity of four, and can accommodate either two or four experiments, in four 1.4 km long straight sections, which are alternating with 2.14 km straight sections hosting technical systems, in particular radiofrequency (RF) cavities. Each of the 8 separating arc sections has a length of 9.6 km. Figure 1 sketches the layout and possible straight-section functions for the FCC-ee.

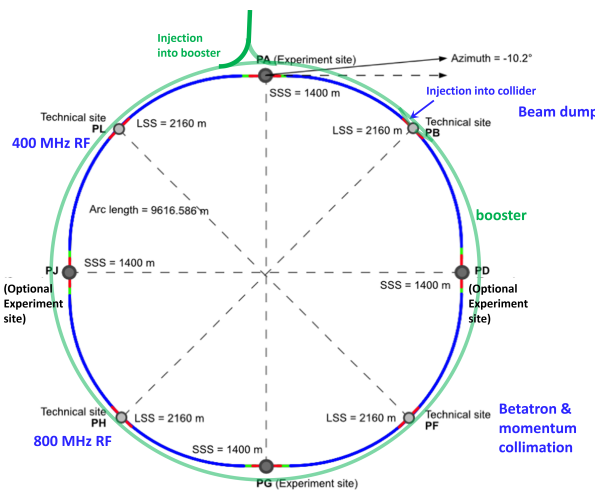


Figure 1: Schematic layout of the FCC-ee collider with a circumference of 91.1 km and four-fold superperiodicity. The full-energy booster and part of its injection transfer line are also indicated.

FCC-ee key parameters, evolved from those of the Conceptual Design Report (CDR) [4], are summarized in Table 1. Thanks to self-polarisation at the two lower energies (Z and W operation) [5], a precision energy calibration by resonant depolarisation is possible, down to 100 keV accuracy for m_Z and 300 keV for m_W [6, 7].

* Work supported by the European Union’s H2020 Framework Programme under grant agreement no. 951754 (FCCIS).

[†] frank.zimmermann@cern.ch

ULTIMATE LIMIT OF FUTURE COLLIDERS*

M. Bai[†], SLAC National Accelerator Laboratory, Menlo Park, CA, USA

V. Shiltsev, Fermilab, Batavia, IL, USA

F. Zimmermann, CERN, Meyrin, Switzerland

Abstract

With seven operational colliders in the world and two under construction, the international particle physics community not only actively explores options for the next facilities for detailed studies of the Higgs/electroweak physics and beyond-the-LHC energy frontier, but also seeks a clear picture of the limits of the colliding beams method. In this paper, we try to consolidate various recent efforts in identifying physics limits of colliders in conjunction with societal sustainability, and share our thoughts about the perspective of reaching the ultimate quantum limit.

THE LANDSCAPE OF COLLIDERS

The development of accelerators and beams in the past century has led to incredible discoveries in physics, chemistry, biology, etc. Up to date, about 25 Nobel Prizes in Physics and 7 in Chemistry were made possible thanks to significant contributions from particles accelerators and beams [1, 2]. Among the family of accelerators, the collider has been the most important engine of discovery for particle physicists to produce new particles and to understand the fundamental laws that govern the subatomic structure. Figure 1 shows how the energy of colliders has increased orders of magnitudes over the past half a century.

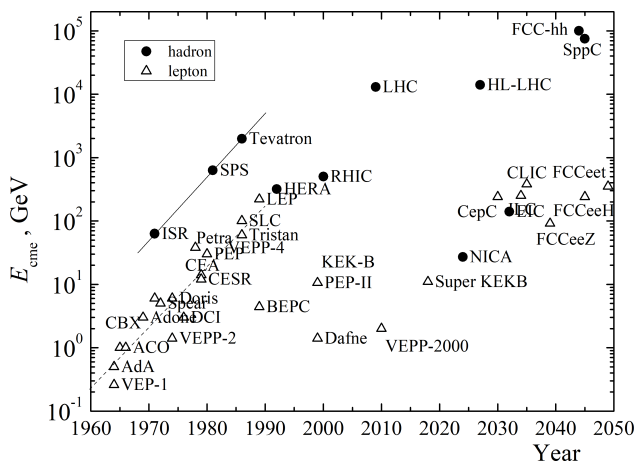


Figure 1: The so-called Livingston plot represents the evolution of the colliders from the past to the future [2].

Table 1 lists the colliders that are currently in operation and two which are under construction (NICA in Russia and the Electron Ion Collider at BNL in the USA).

Despite a noticeable slow-down in the increase of the energy frontier over the past couple of decades, the quest for further pushing the collider frontier has never abated. At the

* Work supported by DOE

[†] mbai@slac.stanford.edu

Table 1: Operational Particle Colliders

Collider	Location	Species	Energy beam [GeV]
LHC/HL-LHC	CERN, Europe	p, Pb, Xe	6800, 2560
RHIC	BNL, USA	p [†] , d, Au, etc	255, 100/n
SuperKEKB	KEK, Japan	e ⁺ e ⁻	7 e ⁻ , 4 e ⁺
BEPCII	IHEP, China	e ⁺ e ⁻	2.45
DAΦNE	LNF, Italy	e ⁺ e ⁻	0.51
VEPP-2000	BINP, Russia	e ⁺ e ⁻	1
VEPP-4M	BINP, Russia	e ⁺ e ⁻	6
NICA	JINR, Russia	Au, etc	4.5/n
EIC	BNL, USA	e [†] , p [†] , He3, Au. etc	18e ⁻ , 255p, 167/n, 100/n

latest US High Energy Physics long term strategy community process known as *Snowmass'21*, the high energy physics community has composed its long-term energy-frontier road map, which consists of three elements: to ensure the success of the ongoing LHC luminosity upgrade (HL-LHC), to realize Higgs factory e⁺e⁻ collider for studying the Higgs boson and electroweak physics with a high precision, and to develop multi-TeV colliders for probing the 10 TeV parton energy scale [3]. These requirements clearly push the future colliders, once again, into an hitherto unprecedented scale as shown in Fig. 2, where they may face many challenges both in terms of reaching the advertised performance as well as for maintaining societal support [4].

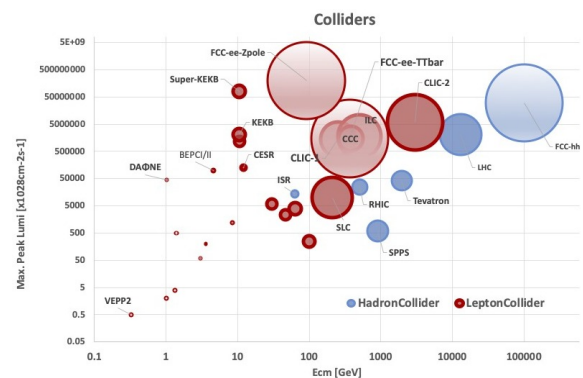


Figure 2: Collider peak luminosity and size as a function of centre-of-mass energy. The red bubbles represent the lepton colliders while the blue bubbles are the hadron colliders. For both cases, the semi transparent bubbles are the proposed colliders for future. The size (diameter or length) of the collider is represented by the size of the bubble.

EXPERIENCE AND CHALLENGES WITH ELECTRON COOLING OF COLLIDING ION BEAMS IN RHIC*

A. V. Fedotov[#], X. Gu, D. Kayran, J. Kewisch, S. Seletskiy
Brookhaven National Laboratory, Upton, NY, USA

Abstract

Electron cooling of ion beams employing rf-accelerated electron bunches was successfully used for the RHIC physics program in 2020 and 2021 and was essential in achieving the required luminosity goals. This presentation will summarize experience with electron cooling of colliding ion beams in RHIC, including various challenges. We also outline ongoing studies using rf-based electron cooler LEReC.

INTRODUCTION

Electron cooling is a well-established technique for obtaining low-emittance ion beams [1]. In this method, the phase-space density of an ion beam is increased by means of dissipative forces – the dynamic friction on individual ions undergoing Coulomb collisions with a lower temperature electron distribution.

Electron cooling of ion beams employing a high-energy approach with RF-accelerated electron bunches was recently successfully implemented at BNL [2-6]. During the 2019 RHIC run with Au ions, electron cooling was commissioned for 3.85 GeV/nucleon gold beams using electrons with a kinetic energy of 1.6 MeV and then for 4.6 GeV/nucleon gold beams using 2 MeV electrons. Electron cooling of colliding gold beams became fully operational during the 2020 RHIC physics run. It successfully operated in 2020 and 2021 for the RHIC Beam Energy Scan II physics program in search of the QCD critical point on the phase diagram and was essential in achieving the required luminosity goals [7, 8].

THE LEReC ACCELERATOR

LEReC is based on state-of-the-art accelerator physics and technology: reproducibly high quantum efficiency photocathodes with a sophisticated delivery systems which can hold up to 12 cathodes simultaneously (specifically designed to support long-term operation); a high-power laser beam with laser shaping and stabilization; a high-voltage high-current DC gun; RF gymnastics using several RF cavities; instrumentation, controls and a machine protection system (see, for example, Ref. [3] and references therein).

Electron bunches are generated by illuminating a multi-alkali CsK₂Sb photocathode, inserted into a DC gun with an operating voltage around 400 kV. A 704 MHz fiber laser is modulated to produce optical macro-bunches (~30 pulses per bunch) at 9 MHz frequency, which matches the repetition rate of ion bunches in RHIC. The resulting

macro-bunch of electrons consisting of 30 individual electron bunches is synchronized with each individual ion bunch, as illustrated in Fig. 1.

In the LEReC approach an individual electron bunch occupies only a small portion of the ion bunch and only selected ions experience the friction force during a passage through the cooling section. However, as a result of the synchrotron motion of ions, on successive passages all ions experience interactions with electrons and are cooled with characteristic times larger than the synchrotron period.

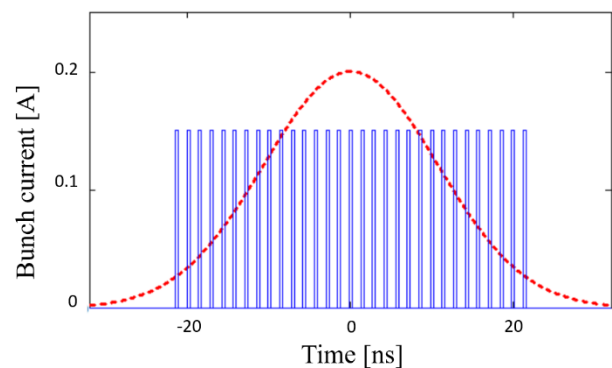


Figure 1: The LEReC beam structure. Thirty electron bunches (blue) spaced by 1.4 ns placed on a single ion bunch (red), with ion bunch repetition frequency of 9 MHz.

Once electron bunches of the desired quality are generated from the gun, they are further accelerated to the required energy by the 704 MHz SRF booster cavity, transported to the first cooling section in the Yellow RHIC ring, used to cool ions, turned around using a 180-degree dipole magnet, used to cool ions in the Blue RHIC ring and transported to the high-power beam dump. Figure 2 shows layout of the LEReC accelerator.

Unlike in any previous coolers, the LEReC cathode is not immersed in a magnetic field and no continuous magnetic field with precise solenoids is required in the cooling regions. This significantly simplifies the technical design. However, the requirements for the electron beam quality become more demanding since one needs to have tight control of the transverse electron velocities.

One more feature of LEReC is that the electron beam, after cooling ions in one RHIC ring, is used again to cool the ions in the other RHIC ring.

This is also the first implementation of electron cooling for colliding ion beams. The latter is of crucial importance in the context of using electron cooling in future high-energy colliders.

* Work supported by the US Department of Energy under contract No. DE-AC02-98CH10886.
[#] fedotov@bnl.gov

EXPERIMENTAL PHASE-SPACE TRACKING OF A SINGLE ELECTRON IN A STORAGE RING*

A. Romanov[†], J. Santucci, G. Stancari, A. Valishev
Fermi National Accelerator Laboratory, Batavia, IL, USA

Abstract

This paper presents the results of the first ever experimental tracking of the betatron and synchrotron phases for a single electron in Fermilab's IOTA ring. The reported technology makes it possible to fully track a single electron in a storage ring, which requires tracking of amplitudes and phases for both, slow synchrotron and fast betatron oscillations.

INTRODUCTION

Complete tracking of a charged particle in a circular accelerator will enable a new class of diagnostics capabilities. It will allow measurements of important single-particle dynamical properties, including dynamical invariants, amplitude-dependent oscillation frequencies, and chaotic behavior. The true single-particle measurements can be employed for benchmarking of long-term tracking simulations, for training of AI/ML algorithms, and ultimately for precise predictions of dynamics in present and future accelerators.

Observation of a single electron in storage rings has a long history that goes back to experiments at AdA, the first electron-positron collider [1, 2]. Several experiments using various instruments were done in the past to track single electron dynamics in storage rings, with the goal to track relatively slow synchrotron oscillations [3–5] and tracking of all 3 mode amplitudes [6].

If combined, state-of-the-art methods allow tracking of 4 dynamical variables out of 6 necessary to fully characterize particle motion in an accelerator. This study shows that it is possible to track betatron phases of a single particle in a storage ring with non-destructive measurements. There are two critical aspects that enable betatron phase tracking and that define its precision: the first is the quality of the measurements of the electron's coordinates; the second is the duration of the coherent betatron oscillations.

The described experiment, Betatron Oscillations Phase Tracking of a Single Electron (BOPTSE), helped define equipment parameters necessary for the full 6D tracking of a single electron in the IOTA ring by tracking a betatron phase in one plane [7].

EXPERIMENTAL METHOD

A straight-edge screen was placed in the focal plane of the synchrotron radiation imaging system at the M3L sta-

* This work was supported by the U.S. National Science Foundation under award PHY-1549132, the Center for Bright Beams. Fermi Research Alliance, LLC operates Fermilab under Contract DE-AC02-07CH11359 with the US Department of Energy.

[†] aromanov@fnal.gov

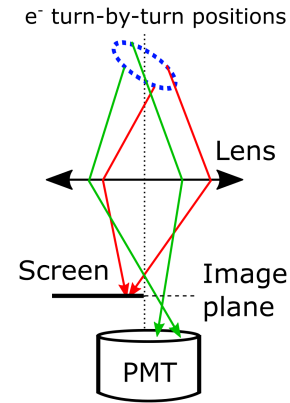


Figure 1: Optical scheme for betatron phase detection with shaded PMT.

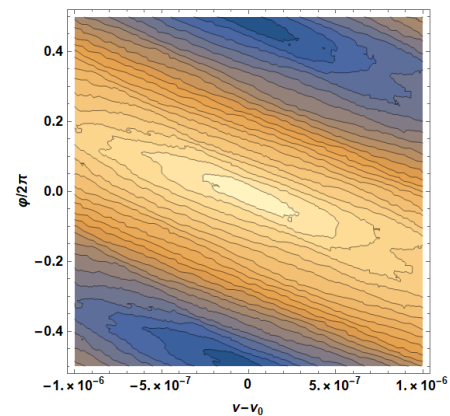


Figure 2: Contour plot of the correlation sum between simulated photons counts at PMT and model predictions for electron's position at corresponding turns depending on tune and phase of the betatron oscillations.

tion to block photons from one of the halves of the phase space (as shown in Fig. 1). The vertical orientation of the screen was used for tracking a phase of the horizontal betatron oscillations. The measured counting rate of the M3L photomultiplier (PMT) with no obstruction is 7.5 kHz. To place the screen in the middle of the beam image, its position was adjusted until the counting rate reached 50% of the base rate. Coherent betatron oscillations over 50 ms (about 4×10^5 turns), with about 200 detected photons from one half of the phase space will allow precise reconstruction of phase and tune of the betatron oscillations. Analysis of longer data streaks will provide information about statistical properties and coherence of the betatron phase of a single electron.

OPTIMIZING THE DISCOVERY OF UNDERLYING NONLINEAR BEAM DYNAMICS*

L. A. Pocher[†], L. Dovlatyan¹, I. Haber, T. M. Antonsen Jr., P. G. O'Shea
University of Maryland, College Park, MD, USA
¹also at Raytheon Tehcnologies, Tucson, AZ, USA

Abstract

One of the DOE-HEP Grand Challenges identified by Nagaitsev *et al.* relates to the use of virtual particle accelerators for beam prediction and optimization. Useful virtual accelerators rely on efficient and effective methodologies grounded in theory, simulation, and experiment. This paper uses an algorithm called Sparse Identification of Nonlinear Dynamical systems (SINDy), which has not previously been applied to beam physics. We believe the SINDy methodology promises to simplify the optimization of accelerator design and commissioning, particularly where space charge is important. We show how SINDy can be used to discover and identify the underlying differential equation system governing the beam moment evolution. We compare discovered differential equations to theoretical predictions and results from the PIC code WARP modeling. We then integrate the discovered differential system forward in time and compare the results to data analyzed in prior work using a Machine Learning paradigm called Reservoir Computing. Finally, we propose extending our methodology, SINDy for Virtual Accelerators (SINDyVA), to the broader community's computational and real experiments.

MOTIVATION

Nagaitsev *et al.* [1] have enumerated four Grand Challenges enabling future Department of Energy (DOE) High Energy Physics (HEP) programs. Grand Challenge #4 Beam Prediction poses the question: "How do we develop predictive 'virtual particle accelerators'?" We begin to address as aspect of this Grand Challenge in this paper. Our *aim* is to speed up commissioning and design studies of accelerators by uncovering underlying physics in virtual and real accelerators. Our *approach* is to apply an existing method from the data-driven, nonlinear dynamics community called Sparse Identification of Nonlinear Dynamics (SINDy) [2, 3] to uncover physics in problems that can't be solved analytically.

This method is both *Predictive* and *Productive*. The method is predictive in the context of providing an end result model that can be used to predict beam dynamics beyond the training dataset; the method is productive such that it produce actionable results. It is slightly different than the similar adjoint method as used by our collaborators at the University of Maryland (UMD) [4]. That method can be used to accelerate the design and optimization of lattices, whereas this method is more readily applicable to predicting

long-term behavior of underlying beam dynamics which can be used to intensify accelerator commissioning.

APPROACH

Our approach is to prescribe a mathematical model based upon the physics of an accelerator lattice. SINDy works by assuming one can model the evolution of some n -dimensional state vector $\mathbf{x} \in \mathbb{R}^n$ as a system of ordinary differential equations

$$\frac{d}{dt}\mathbf{x} = \mathbf{f}(\mathbf{x}). \quad (1)$$

The variable t is the independent variable, \mathbf{x} is the n -dimensional state vector of observe able either from a simulation or experiment, and $\mathbf{f}(\mathbf{x})$ is the n -dimensional equation governing how \mathbf{x} evolves.

After one obtains the number n of state variables, one can then take measurements of \mathbf{x} at m equidistant times $t_j \in \{t_1, t_2, \dots, t_m\}$ with j being and index into a matrix \mathbf{X} :

$$\mathbf{X} = \begin{bmatrix} \mathbf{x}^T(t_1) \\ \vdots \\ \mathbf{x}^T(t_m) \end{bmatrix} = \begin{bmatrix} x_1(t_1) & \dots & x_n(t_1) \\ \vdots & \ddots & \vdots \\ x_1(t_m) & \dots & x_n(t_m) \end{bmatrix}.$$

One then differentiates the matrix $d\mathbf{X}/dt = \dot{\mathbf{X}}$ which is then used in the discovery stage of SINDy. One proposes a candidate $\Theta(\mathbf{X})$ which consists of a number of intuited/desired basis functions for the underlying dynamics. The matrix $\dot{\mathbf{X}}$ is equated to $\Theta(\mathbf{X})$ times a *sparse* coefficient matrix $\Xi = [\xi_0 \ \xi_1 \ \dots \ \xi_{BF}]$ which is solved for the given appropriate optimization technique.

$$\dot{\mathbf{X}} = \begin{bmatrix} \dot{\mathbf{x}}^T(t_1) \\ \vdots \\ \dot{\mathbf{x}}^T(t_m) \end{bmatrix} = \begin{bmatrix} \dot{x}_1(t_1) & \dots & \dot{x}_n(t_1) \\ \vdots & \ddots & \vdots \\ \dot{x}_1(t_m) & \dots & \dot{x}_n(t_m) \end{bmatrix} = \Theta(\mathbf{X})\Xi$$

Our intuited dynamics consist of simple harmonic motion (SHM), Fig. 1(b), a Fourier series based on a Fourier transform of the lattice, Figs. 2(a) and 2(b), and a nonlinear interaction (NL) motivated by the power law observed in Fig. 2(b) and the oscillating amplitudes of the lowest order wavenumbers in the $x_c(z)$ spectrogram in Fig. 3:

$$\mathbf{f}(\mathbf{x}) \approx \underbrace{\xi_0 \mathbf{x}_0 + \xi_1 \mathbf{x}}_{\text{SHM}} + \sum_{i=1}^3 \underbrace{[\xi_c \cos(k_i z) + \xi_s \sin(k_i z)]}_{\text{Fourier}} + \underbrace{\xi_{nc} \mathbf{x} \cos(k_i z) + \xi_{ns} \mathbf{x} \sin(k_i z)}_{\text{NL}}. \quad (2)$$

* Work supported by US DOE-HEP grants: DE-SC0010301 and DE-SC0022009.

[†] lpocher@umd.edu

PARTICLE-IN-CELL SIMULATIONS OF HIGH CURRENT DENSITY ELECTRON BEAMS IN THE SCORPIUS LINEAR INDUCTION ACCELERATOR*

S. E. Clark[†], W. D. Stem, C. N. Melton, A. Fetterman, Y.-J. Chen, J. Ellsworth
 Lawrence Livermore National Laboratory, 7000 East Ave., Livermore, CA 94550, USA

Abstract

Particle-in-cell (PIC) simulations of a high current density ($I > 1$ kA), and highly relativistic electron beam ($E \sim 2$ -20 MeV) in the Scorpius Linear Induction Accelerator (LIA) are presented. The simulation set consists of a 3D electrostatic/magnetostatic simulation coupled to a 2D XY slice solver that propagates the beam through the proposed accelerator lattice for Scorpius, a next-generation flash X-ray radiography source. These simulations focus on the growth of azimuthal modes in the beam (e.g. Diocotron instability) that arise when physical ring distributions manifest in the beam either due to electron optics or solenoidal focusing and transport. The saturation mechanism appears to lead to the generation of halo particles and conversion down to lower mode numbers as the width of the ring distribution increases. The mode growth and saturation can contribute to the generation of hot spots on the target as well possible azimuthal asymmetries in the radiograph. Simulation results are compared to linear theory and tuning parameters are investigated to mitigate the growth of azimuthal modes in the Scorpius electron beam.

INTRODUCTION

Flash X-Ray Radiography has been used in the United States and around the world for many years as a diagnostic tool for imaging highly kinetic experiments. Hydrodynamic testing facilities such as the Lawrence Livermore National Laboratory (LLNL) Flash X-Ray (FXR) Linear Induction Accelerator (LIA) [1-4] and the Los Alamos National Laboratory (LANL) Dual-Axis Radiographic Hydrodynamic Test Facility (DARHT/DARHT-II) [5-6] have been developed and operated for many years. The Scorpius LIA has been conceived to improve the performance characteristics of the accelerator power systems by driving the accelerator with solid state pulsed power (SSPP). [7] This allows the pulses to be modulated to improve inter-pulse spacing, pulse rise times, energy variation, and current variation. These improvements in the pulse quality translate to superior multi-pulse radiographic performance by generating a sharper and flatter high voltage pulse. There is existing simulation work on DARHT-II in the injector [8] and the accelerator [9] which have focused on analysing component misalignment and instability growth. There also exists work for Scorpius to simulate the electron beam from cathode to target [10-11] using simulation tools like Trak, XTR, and LSP-slice.

This paper will focus assessing the impact of having non-monotonically decreasing beam density profile, which can lead to growth of the Diocotron instability. A 2D particle-in-cell (PIC) slice code will be used in conjunction with the 3D PIC code used in the diode (AK) gap region [12] of the injector to analyse the emittance growth of the beam throughout the accelerator. An updated Warp XY-slice solver was developed to model the accelerator gaps and the beam self-fields in the highly relativistic limit. This paper will discuss the analytical diocotron growth rate and how it compares to simulations of the Scorpius beamline. It will be shown that while there is diocotron instability growth, the observed emittance growth is tolerable in the Scorpius beamline.

ANALYTICAL GROWTH RATE FOR A NOMINAL HOLLOW BEAM

There has been much analysis of diocotron instability in one component plasmas, e.g. Penning-Malmberg traps [13-15] and in relativistic electron beams [16], which demonstrates that 2D particle-in-cell codes are well suited to modelling this phenomenon and that the growth rates match fairly well in the linear regime. The growth rate has been found to be $\gamma_D \propto \frac{\Omega_D}{2\gamma^2}$, where $\Omega_D = \omega_{pe}^2/\omega_{ce}$, γ_D is the characteristic growth rate for an e-fold, ω_{pe} is the electron plasma frequency, ω_{ce} is the electron cyclotron frequency, and γ is the relativistic gamma. The analytical growth rate for a hollow core beam with uniform density in an annulus is expressed as:

$$\gamma_D(l) = \frac{\Omega_D}{2\gamma^2} \left\{ 4 \left(\frac{b}{d} \right)^{2l} \left[1 - l \left(1 - \left(\frac{b}{d} \right)^2 \right) \left(\frac{d}{R} \right)^{2l} \right] - \left[2 - l \left(1 - \left(\frac{b}{d} \right)^2 \right) - \left(\frac{d}{R} \right)^{2l} \left(1 - \left(\frac{b}{d} \right)^2 \right) \right]^2 \right\}^{\frac{1}{2}}, \quad (1)$$

where R is the radius of the conducting wall, b is the inner radius of the beam annulus, and d is the outer radius of the beam annulus. It should be noted that in the highly relativistic case, the growth rate is divided by γ^2 to account for the self-generated beam magnetic fields.

Figure 1 shows the computed growth rates for one instance of beam radius. When examining different beam

*This work was performed under the auspices of the U.S. Department of Energy by Lawrence Livermore National Laboratory under Contract DE-AC52-07NA27344.

[†] clark245@llnl.gov

STUDIES OF ION BEAM HEATING BY ELECTRON BEAM*

S. Seletskiy[†], A.V. Fedotov, D. Kayran
Brookhaven National Laboratory, Upton, NY 11973, USA

Abstract

Presence of electron beam created by either electron coolers [1] or electron lenses in an ion storage ring is associated with an unwanted emittance growth (heating) of the ion bunches. In this paper we report experimental studies of the electron-ion heating at the Low Energy RHIC electron Cooler (LEReC).

INTRODUCTION

Low energy RHIC electron cooler (LEReC) [2-7] is the first electron cooler based on RF acceleration of electron bunches. LEReC utilizes a non-magnetized electron beam and provides the cooling of colliding ions with the same e-beam in both RHIC rings. LEReC was commissioned in 2019 and was successfully used in RHIC operations in 2020 (at $\gamma = 4.9$) and in 2021 (at $\gamma = 4.1$).

It was noticed that in the presence of the electron beam, and with the transverse cooling suppressed by an offset from the optimal e-beam energy, the transverse emittance of the ions starts growing at a rate, which is higher than the rate of intra-beam scattering (IBS). We call this extra growth of emittance – an electron-ion heating (e-i heating).

In this paper we discuss the status of dedicated measurements of the electron-ion heating.

EXPERIMENTAL SETUP

Electron bunches in LEReC are produced by a 375 keV photo-gun. In operations the CW electron beam consists of 9 MHz macrobunches, each containing 36 704 MHz electron bunches. Each ion bunch passing through the LEReC cooling section (CS) is overlapped with one electron macrobunch (Fig. 1).

The LEReC gun is followed by the SRF Booster, which accelerates the beam to 1.6-2 MeV. The transport beamline and the merger bring the beam to the cooling section in the Yellow RHIC ring, and then through the 180° bending magnet to the CS in the Blue RHIC ring. Finally, the extraction beamline sends electrons to the high-power beam dump. The LEReC layout is schematically shown in Fig. 2.

LEReC cooling section contains 8 short solenoids (not shown in Fig. 2) used for fine-tuning of the e-beam envelope. The distance between solenoid centers is 3 m. Since LEReC is a non-magnetized electron cooler, both the self space charge and the ions' space charge strongly affect transverse beam dynamics of e-bunches [7].

* Work supported by the US Department of Energy under contract No. DE-SC0012704

[†] seletskiy@bnl.gov

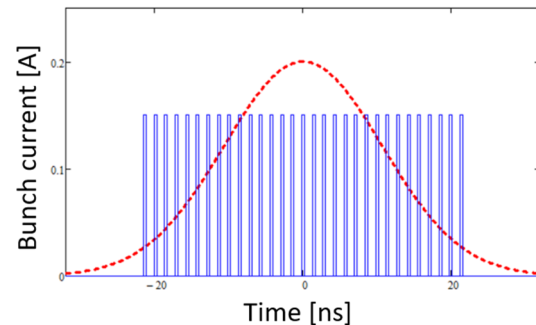


Figure 1: Ion bunch (red) overlapped with electron macrobunch (blue) in the cooling section

The bunches in the electron macrobunch sample slices of an ion bunch having different charges. Therefore, an electron bunch angular spread and size vary both along the cooling section and from one bunch to another. In this paper we characterize the angular spread and the transverse size of electron beam by values averaged over the CS length and over all the bunches of the macrobunch.

In our experiment we worked with ion bunches of reduced intensity, both to reduce the ion-electron focusing in the CS and to reduce the effect of the IBS-induced growth of the i-bunch emittance. We also used the ion bunches in the Yellow ring only to exclude the beam-beam effects.

All the measurements were performed with 1.6 MeV electrons.

MEASUREMENTS

Description of Measurement Procedure

We base calculation of the rate of i-beam emittance change on the measurements of the vertical size of the ion bunches performed with the H-jet [8].

To measure the electron-ion heating rate we first match γ -factors of electrons and ions [2] to pre-cool the ion bunches to a particular transverse emittance. Next, we offset electron beam energy by about 5 kV, which corresponds to $\approx 6\sigma_{\delta e}$ ($\sigma_{\delta e}$ is the rms relative momentum spread of electrons). Such an offset essentially zeroes the transverse cooling force (Fig. 3 demonstrates this effect). The growth of ions emittance observed under these conditions is driven by both the IBS and the e-i heating.

After that we pre-cool the ions to the same initial emittance and turn off the electron beam completely. For such a set-up the growth of ion emittance is determined only by the IBS.

The difference between the two measured growth rates gives us the rate of the electron-ion heating.

STUDIES OF ION INSTABILITY USING A GAS INJECTION SYSTEM*

J. Calvey, M. Borland, L. Emery, P.S. Kallakuri, ANL, Argonne, IL 60439, USA

Abstract

Residual gas ions can cause a variety of undesirable effects in electron storage rings, including coherent instability and incoherent emittance growth. This is a serious concern in next-generation light sources due to challenging emittance and stability requirements. A gas injection system was designed and installed in the present APS ring to study such effects using a controlled pressure bump. Measurements were taken under a wide variety of beam conditions, using a spectrum analyzer, pinhole camera, and bunch-by-bunch feedback system. The feedback system was also used to perform grow-damp measurements, allowing us to measure the growth rate of individual unstable modes. This paper presents some of the results of these experiments, along with simulations using the tracking code *elegant*.

INTRODUCTION

The APS-Upgrade is a 4th-generation light source currently under development at Argonne National Laboratory [1], with a design emittance of 42 pm at 6 GeV. In order to make use of this ultra-low emittance, potential instabilities must be anticipated and mitigated.

Ion instability is of particular concern. Trapped ions can produce a fast-growing transverse (usually vertical) instability, due to coupled motion of the beam and ions. Simulations predict a strong coherent ion instability for 324 bunch mode, which we plan to mitigate with a compensated gap scheme [2]. Additionally, incoherent effects such as emittance growth may still be an issue even if the coherent instability is damped.

To better understand the ion instability and anticipate issues in the APS-U storage ring, we installed a gas injection system in an empty insertion device (ID) straight section in Sector 25 (S25) of the present APS storage ring. This enabled us to create a controlled and localized pressure bump, and study the resulting instability. The system was later relocated to Sector 35 (S35). The lattice functions are quite different at the two locations, which allows for some interesting comparisons.

EXPERIMENTAL SETUP

The gas-injection system is described in detail in Ref. [3]. It allows creation of a controlled pressure bump of either 100 nTorr or 900 nTorr of N₂. The ion pump located next to the gas injection location is disabled for the study, while ion pumps upstream and downstream of the injection point are kept on to localize the bump. Measurements showed that

the bump was mostly localized to a ~6 m section in Sector 25, and a ~10 m section in Sector 35.

Figure 1 compares two relevant parameters at the two gas injection locations, over the approximate area of the pressure bumps. The first is the critical mass [4]; a lower critical mass will result in more ion trapping. The second parameter, $\tau_y \equiv 10^{10} \sigma_y (\sigma_x + \sigma_y) / \beta_y$ is proportional to the vertical instability growth time. A lower τ_y indicates a faster growing instability (at least initially).

At S25, A_{crit} and τ_y are highly correlated, meaning that locations with the most trapping have the highest growth rate. At S35, they are almost anti-correlated, so the locations with more trapping tend to have lower growth rates. Overall, both the critical mass and growth time are lower at S35, so the vertical instability should be stronger there.

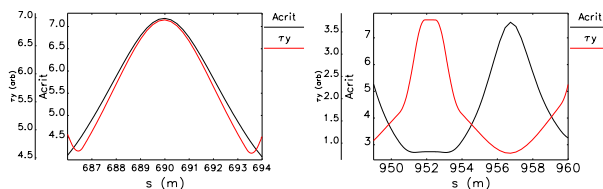


Figure 1: Critical mass and vertical instability growth times at S25 (left) and S35 (right). The gas injection point is at 690 m for S25, and 954.5 m for S35.

TRAIN GAP STUDIES

Several experiments were performed with this system, under a wide variety of beam conditions. Measurements were taken with a pinhole camera, spectrum analyzer, and Dimtel feedback system [5]. Where possible, measurements taken during the S25 experiment were repeated at S35. For one such study, we examined the effect of different train gaps on the instability. Four different bunch patterns were used: 1 train with no gaps, 4 trains with a 12 bunch gap in between them (“12bg”), 4 trains with 24 bunch gaps (“24bg”), and 4 trains with 12 bunch gaps and 6 double-charge guard bunches before and after the gap (“12bg 6gb”). A similar guard bunch scheme will be used at APS-U, to minimize rf transients and provide a stronger kick to the ions before the gap [2].

Basic ring and beam parameters for these experiments are given in Table 1. All measurements shown in this paper used the 900 nTorr pressure bump. With the 100 nTorr bump, only the no gap case had significant instability.

Table 2 lists emittances measured with the pinhole camera for both S25 and S35 experiments. For S25 with no gaps, there is a large blowup of both emittances. The horizontal blowup is mitigated by any type of gap (ϵ_x is slightly higher for all S25 cases, mostly likely due to a measurement error). For S35 without gaps, the vertical blowup is an order of

* Work supported by the U.S. Department of Energy, Office of Science, Office of Basic Energy Sciences, under Contract No. DE-AC02-06CH11357.

CHARACTERIZATION OF OCTUPOLE ELEMENTS FOR IOTA*

J. N. Wieland[†], Michigan State University, East Lansing, MI 48823, USA
J. D. Jarvis, A. L. Romanov, A. Valishev, Fermilab, Batavia, IL 60510, USA

Abstract

The Integrable Optics Test Accelerator (IOTA) is a research storage ring constructed and operated at Fermilab to demonstrate the advantages of nonlinear integrable lattices. One of the nonlinear lattice configurations with one integral of motion is based on a string of short octupoles. The results of the individual magnet's characterizations, which were necessary to determine their multipole composition and magnetic centers, are presented. This information was used to select and align the best subset of octupoles for the IOTA run 4.

INTRODUCTION

As part of the Integrable Optics Test Accelerator (IOTA) a string of octupoles (Fig. 1) is installed in a configuration to maintain the Hamiltonian as a constant of motion. During IOTA run 2 unexpected deviations in the closed orbit while the octupoles were energized suggested misalignment in the magnets or deviations in construction generating large low-order (quadrupole and dipole) transverse multipole components. The nominal values for the octupoles are in Table 1 [1].

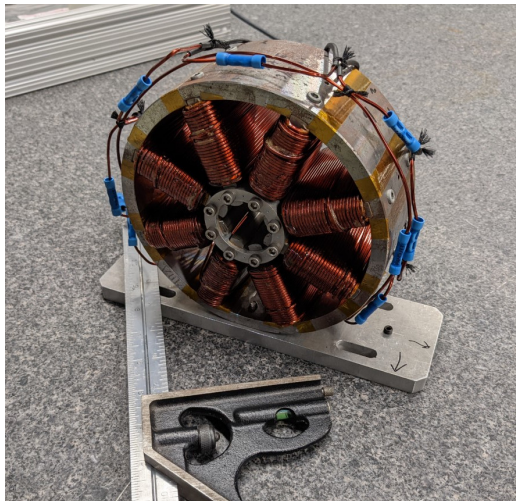


Figure 1: A single octupole from the string.

There are a number of conventions for presenting the multipole components, and the following format will be used in this paper, Eqs. (1) & (2).

$$B_y + iB_x = \sum_{n=1}^{\infty} C_n \left(\frac{x + iy}{R_{ref}} \right)^{n-1} \quad (1)$$

* Work partially supported by the US Department of Energy, Office of Science, High Energy Physics under Cooperative Agreement award number DE-SC0018362 and Michigan State University.

[†] wielan22@msu.edu

$$C_n = B_n + iA_n \quad (2)$$

Where B_n and A_n are the normal and skew terms respectively, R_{ref} is the reference radius for the measurements, and the multipole index "n" follows the European convention, i.e. $n = 1$ corresponds to the dipole term. The longitudinal component of the field was not considered in the characterization. The magnets were removed and characterized using a hall probe to determine potential outliers and align a set of nine magnets for installation in a new configuration before IOTA run 4. The figure of merit for selecting the magnets was the magnitude of low order multipoles.

Table 1: Nominal Octupole Parameters

Octupole Parameter	Design Value
Length	70 mm
Aperture	28 mm
Coil Turns per Pole	88
Maximum Excitation Current	2 A
Maximum Octupole Gradient	1.4 kG/cm ³
Effective Field Length	75 mm

TEST STAND MEASUREMENTS

Methods

The multipole components of the magnets were determined using a hall probe mounted on a three-axis test stand based on a procedure described in reference [2]. The test stand was composed of three, perpendicular rails actuated by linear stepper motors with a hall probe mounted along the nominal z-axis. The magnets were mounted to a support stand with alignment features for all degrees of freedom next to the test stand, see Fig. 2. Before any measurements were taken, the test stand was calibrated to the support stand using a precise flat and dial indicator to ensure that the axes of motion were perpendicular to each other.

All measurements were taken at an energizing current of 2 A, the maximum for these octupoles. The test stand measured the magnetic field at a preprogrammed set of points. In practice, this was an equidistant set of points on a circle in a number of planes along the magnet's axis. The field from the x and y hall sensors was combined into azimuthal data based on the relative angle of the points on the circle. A Fourier decomposition was then performed on the magnetic field data to find the multipole components. A coarse scan (smaller radius, fewer points) was performed first and the relevant offset was calculated using Eq. (3) assuming that the

SHEET ELECTRON PROBE FOR BEAM TOMOGRAPHY*

Vadim Dudnikov[†], M. A. C. Cummings, Muons, Inc. Batavia, IL, USA
Galina Dudnikova, UMD, Collège Park, MD, USA

Abstract

An electron beam probe has been successfully used for determination of accelerated particle density distributions. However, the apparatus used for this diagnostic had a large size and complex design which limit the broad use of this diagnostic for tomography of accelerated bunches. We propose a new approach to electron beam tomography: we will generate a pulsed sheet of electrons. As the ion beam bunches pass through the sheet, they cause distortions in the distribution of sheet electrons arriving at luminescent screen with CCD device on the other side of the beam that are interpreted to give a continuous measurement of the beam profile. The apparatus to generate the sheet beam is a strip cathode, which, compared to the scanning electron beam probe, is smaller, has simpler design and less expensive manufacturing, has better magnetic shielding, has higher sensitivity, higher resolution, has better accuracy of measurement and better time resolution. With this device it is possible to develop almost ideal tomography diagnostics of bunches in linear accelerators and in circular accelerators and storage rings.

INTRODUCTION

Advanced beam diagnostics are essential for high performance accelerator beam production and for reliable accelerators operation. It is important to have noninvasive diagnostics which can be used continuously with intense beams of accelerated particles. Non-invasive determination of accelerated particle distributions is the most difficult task of bunch diagnostics. Recently, a pencil electron beam probe was successfully used for determination of accelerated particle density distributions. However, the apparatus used for this is large and complex, which complicates the broad use of this technique for tomography of accelerated bunches.

In the novel device to be described in this report, a simple, strip cathode provides a sheet beam probe for tomography instead of a scanning pencil beam that was used in previous electron probe bunch profile monitors. The apparatus with the strip cathode is smaller, has simpler design and less expensive manufacturing, has better magnetic shielding, has higher sensitivity, higher resolution, has better accuracy of measurement and better time resolution. With this device it is possible to develop almost ideal tomography diagnostics of bunches in linear accelerators and in circular accelerators and storage rings.

Beam profile determination for high intensity accelerators implies the use of non-destructive methods. The basic physics and recent technical realizations of important non-

intercepting profile diagnostics are summarized in [1]. Ionization Profile Monitors (IPM) and Beam Induced Fluorescence Monitors (BIFM), developed and first used with intense proton beams by Dudnikov [2-8], are now routinely used in all proton and ion accelerators. Recent developments of IPM are presented in [1, 7, 8]. Transverse electron beam scanners (TEBS) were realized recently for use in the SNS storage ring by Aleksandrov et al. [9]. Laser beam scanners are used at H⁻ Linacs, Optical Transition Radiation screens, and Synchrotron Radiation Monitors for relativistic beams. Non-destructive transverse profile measurements are preferred not only for single-path diagnostics at different locations in a transfer line, but also to enable time resolved observations of a stored beam within a synchrotron. A more practical, however essential, reason for minimal invasive diagnostics is the large beam power available at modern hadron accelerators, which excludes the usage of intercepting methods like scintillation screens, SEM-grids or wire scanners due to the risk of melting when irradiated by the total beam intensity. Various methods are realized to determine the profile properties of typical widths $\sigma = 0.1$ to 10 mm of not necessarily Gaussian shapes. In most synchrotrons and storage rings the transverse profile of the circulating beam is monitored via detecting the ionization products from the collision of hadrons with residual gas by an Ionization Profile Monitor (IPM). These are relatively complex and expensive: the IPM system for the Tevatron cost ~\$0.3M.

ADVANCED SHEET ELECTRON PROBE BEAM PROFILE MONITOR

The advanced sheet electron probe beam profile monitor (SEPBPM) with the strip cathode is proposed as shown in Fig. 1.

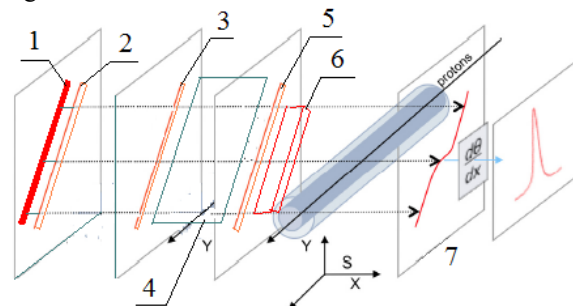


Figure 1: Sheet Electron probe beam profile monitor with a strip cathode: 1- strip cathode; 2- anode; 3- first slit of collimator; 4- deflecting plate; 5- second slit of collimator; 6- sheet slice of electron beam probe; 7- luminescent screen.

* Work supported by DOE Grant DE-SC0021581

[†] vadim@muonsinc.com

AN H^- INJECTOR FOR THE ESS STORAGE RING

V. Dudnikov†, M. Popovic, M. A. C. Cummings
 Muons, Inc., Batavia, IL, USA

Abstract

H^- charge exchange (stripping) injection into the European Spallation neutron Source (ESS) Storage Ring requires a 90 mA H^- ion source that delivers 2.9-ms pulses at 14-Hz repetition rate (duty factor $\sim 4\%$) that can be extended to 28-Hz (df 8%). This can be achieved with a magnetron surface plasma H^- source (SPS) with active cathode and anode cooling. The Brookhaven National Laboratory (BNL) magnetron SPS can produce an H^- beam current of 100 mA with about 2-kW discharge power and can operate up to 0.7 % duty factor (average power 14 W) without active cooling. We describe how active cathode and anode cooling can be applied to the BNL source to increase the average discharge power up to 140 W (df 8%) to satisfy the needs of the ESS. We also describe the use of a short electrostatic LEBT as is used at the Oak Ridge National Laboratory Spallation Neutron Source to improve the beam delivery to the RFQ.

INTRODUCTION

H^- charge exchange (stripping) injection [1] into the European Spallation neutron Source (ESS) Storage Ring requires 80 mA H^- ion source that delivers 2.9-ms pulses at 14-Hz repetition rate (duty factor $\sim 4\%$) [2, 3] that can be extended to 28 Hz (df 8%). This can be achieved with a magnetron surface plasma H^- source (SPS) with active cathode and anode cooling. The Brookhaven National Laboratory (BNL) magnetron SPS can produce an H^- beam current of 100 mA with about 2-kW discharge power and can operate up to 0.7 % duty factor (average power 14 W, energy efficiency up to 67 mA/kW) without active cooling [4]. An RF SPS in SNS have energy efficiency ~ 1 mA/kW [5]. We describe how active cathode and anode cooling can be applied to the BNL source to increase the average discharge power up to 140 W (df 8%) to satisfy the needs of the ESS. We also describe the use of a short electrostatic LEBT as is used at the Oak Ridge National Laboratory Spallation Neutron Source to improve the beam delivery to the RFQ.

ADVANCED DESIGN OF MAGNETRON SPS

An advanced design of magnetron SPS with the spherical focusing of emitted negative ions and forced cathode and anode cooling is shown in Fig. 1. This new magnetron SPS is capable for DC operation with high average negative ion current generation.

Cross sections of new magnetron are shown in Fig. 1 [6]. A disc shape cathode (1) has 18-mm diameter D and 12-mm thickness H . A surrounded anode (2) is separated from

the cathode by insulators (3). A vacuum gap between cathode and anode is $d \sim 1$ mm. Cathode is cooled by liquid or gas flux flowing through the cooling tube (5) with $OD \sim 4$ mm. The magnetron is compressed by ferromagnetic poles (4).

A working gas is injected to the discharge chamber through a channel (10). Cesium is added to discharge through second channel (11). Magnetic field, created by magnet (13) and formed by magnetic poles (4) has direction along axis of cooling tube (5).

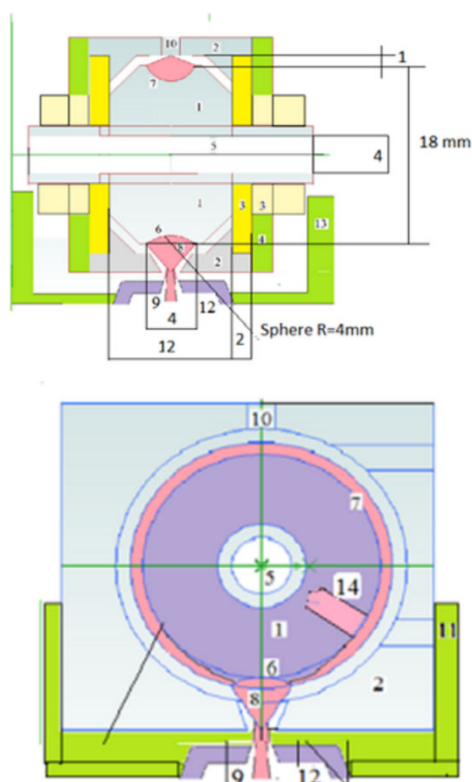


Figure 1: (Collar online) Cross sections of magnetron SPS with cathode cooling. (top- along the magnetic field; bottom- median transverse to the magnetic field section): 1-cathode disc; 2-anode; 3-insulators; 4-magnetic poles; 5-cooling tube; 6-spherical dimple (negative ion emitter, $R = 4$ mm); 7-cylindrical groove (discharge channel, $r = 3$ mm); 8-flux of focused negative ions; 9-negative ion beam extracted through emission aperture (2 mm diameter); 10-gas inlet; 11-cesium inlet; 12-extractor; 13-magnet; 14-hollow cathode.

The discharge in the crossed $E \times B$ fields is localized in the cylindrical groove (7) as in the semiplanotrons SPS. The cylindrical groove focus emitted negative ions to the anode surface and fast particles keep anode surface clean by sput-

† dvg43@yahoo.com

Content from this work may be used under the terms of the CC BY 4.0 licence (© 2022). Any distribution of this work must maintain attribution to the author(s), title of the work, publisher, and DOI

DESIGNING ACCELERATOR-DRIVEN EXPERIMENTS FOR ACCELERATOR-DRIVEN REACTORS

M. A. Cummings[†], R. P. Johnson, J. D. Lobo, R. Abrams, T. J. Roberts
Muons, Inc., Batavia, IL, USA

Abstract

Muons, Inc., with its collaborators, to the best of our knowledge is the only one of the several reactor concept companies in the US that is concentrating on an accelerator-driven subcritical high-power reactor design. The major objection to such systems has been that short interruptions of beam of even a few seconds would turn off fission power long enough to induce temperature-gradient shocks and subsequent fatigue of solid fuel elements. Mu*STAR solves this problem by using a molten-salt fuel. Mu*STAR is a reactor design that not only includes a particle accelerator as an integral part, but has several innovative features that make it a compelling solution to many problems. We note that the ADSR concepts being pursued by the Chinese Academy of Science (ADANES) and the Belgians (MYRRHA) are based on traditional solid fuel elements and require exceptional stability from their accelerator.

INTRODUCTION

The Mu*STAR Accelerator-Driven System includes a 500 MW subcritical, graphite-moderated, thermal-spectrum, molten-salt fueled, reactor design that was described in the Handbook of Nuclear Engineering in 2010 [1]. The reactor parameters are larger by a factor of 4 in linear dimension than the ORNL 8 MW Molten Salt Reactor Experiment (MSRE) [2] done in the late 1960s. The reactor operates subcritically, with additional neutrons generated by an internal spallation target that is driven by a superconducting RF (SRF) linear proton accelerator, similar to that in the ORNL Spallation Neutron Source (SNS). Unlike the SNS, the target is not subjected to shock from the beam, which in Mu*STAR is rastered over the face of a solid uranium target that is cooled by molten salt fuel. Muons, Inc. and its collaborators have simulated engineering solutions to combine the accelerator and reactor with an internal uranium spallation target that is cooled by the MS fuel.

In 2017, Muons, Inc. was awarded a GAIN voucher award [3] with ORNL, INL, and SRNL to design and cost a facility to convert LWR SNF into molten salt (MS) fluoride fuel suitable for use in Mu*STAR. Our expectations are that such a facility will be relatively small and inexpensive enough to consider building one at each of the existing reactor sites in the US and abroad wherever SNF is stored.

CONCEPTS AND INNOVATIONS

Our concept is to install Mu*STAR accelerator-driven subcritical systems at existing light-water reactor (LWR) sites, transform the LWR spent nuclear fuel (SNF) using

on-site technology developed under our GAIN award into molten salt fuel, and to burn it to produce electricity for at least 200 years. The concept is shown in Figure 1. The additional neutron flux provided by the accelerator permits a much deeper burn such that several times more energy can be produced from the SNF than was generated by the LWR. The limit is reached when the accelerator cannot economically overcome the neutron absorption by fission products. Schemes for reducing those products are described below. This innovative and disruptive concept eliminates the need for uranium mining, fuel enrichment, fuel rod manufacture, SNF off-site storage and transport, and encourages local communities to consider consent-based storage of SNF combined with continued operation of their power utility using Mu*STAR when their LWR is retired.

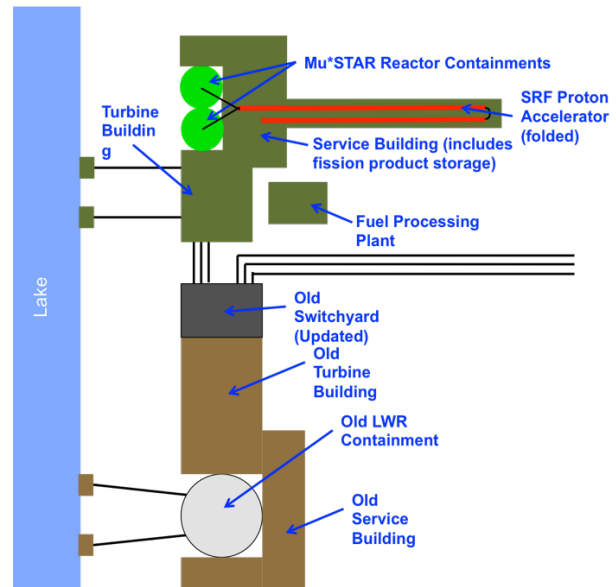


Figure 1: Mu*STAR installed at an old LWR site.

Leaving the SNF on the site where it was produced solves many problems that have long confounded the US government that is legally required to eventually take title to the SNF.

Two important consequences of the Mu*STAR are: 1) the conversion of the SNF to MS does not require fission products to be removed by chemical reprocessing and 2) the accelerator neutrons allow a deeper burn to extract as much as seven times as much energy from the SNF than was extracted by the LWR. Normalized to the energy produced, the amount and toxicity of the SNF will be reduced by more than a factor of 7 over the course of a few centuries of operation.

The reactor design since its inception has been concerned with development of self-cleaning technologies that simultaneously recover valuable nuclear materials along

[†] macc@muonsinc.com

MAGNET SYSTEM FOR A COMPACT MICROTRON SOURCE*

S. A. Kahn[†], R. J. Abrams, M. A. C. Cummings, R. P. Johnson, G. M. Kazakevich
 Muons, Inc., Batavia, IL, USA

Abstract

A microtron can be an effective intense electron source. It can use less RF power than a linac to produce a similar energy because the beam will pass through the RF cavity several times. To produce a high-quality low emittance beam with a microtron requires a magnetic system with a field uniformity $\Delta B/B < 0.001$. Field quality for a compact microtron with fewer turns is more difficult to achieve. In this study we describe the magnet for a compact S-band microtron that will achieve the necessary field requirements. The shaping of the magnet poles and shimming of the magnet iron at the outer extent of the poles will be employed to provide field uniformity. The extraction of the beam will be discussed.

INTRODUCTION

Microtrons provide a medium energy electron beam with low emittance and a repetition rate consistent with RF frequencies. A microtron is an accelerator based on a resonant kick given to the beam as it passes through an RF cavity multiple times. For a relativistic beam, the energy boost with each circulation through the RF cavity is the same and the trajectory length increases as a multiple of the initial turn. An illustration of the classic microtron is shown in Fig. 1. A description of microtron physics is described in Refs. [1-3].

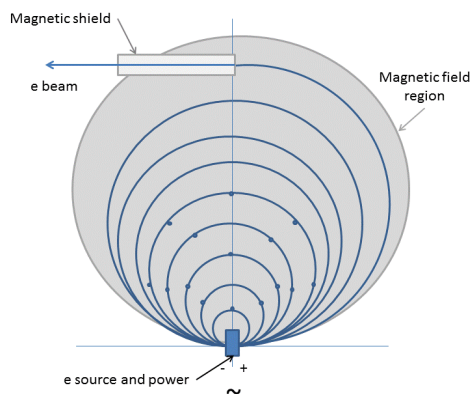


Figure 1: Illustration of microtron concept. Electrons are injected at a source inside the cavity. Electrons receive a boost at each passage through the cavity. Electrons are extracted by a magnetic shield after n turns.

A compact microtron can have industrial, security, and medical applications. To make a microtron more compact, one would reduce the number of turns and increase the magnetic field. This paper describes our approach to do

this and the adjustments to the magnet and extraction systems.

MAGNET SYSTEM

The uniformity of the magnetic field is an important consideration. The field must be uniform over the region where the beam traverses with a field non-uniformity error $\Delta B/B < 1/n^2$ where n is the number of orbital turns in the microtron. Generally with larger coil and pole radii the field is more uniform. However, we would like to reduce the microtron radius to make it more compact. Steel shims will be inserted to correct the field non uniformity associated with the smaller radius. Table 1 shows the parameters for an S-band II which is the subject of this study. Also shown are the parameters of an S-band I microtron previously studied [4] which is shown for comparison. Figure 2 shows a not-to-scale sketch of a concept for the microtron magnet. This will be described in a following section. By reducing the size of the microtron fewer turns with larger energy gain per turn will be needed to reach the final energy of the electrons.

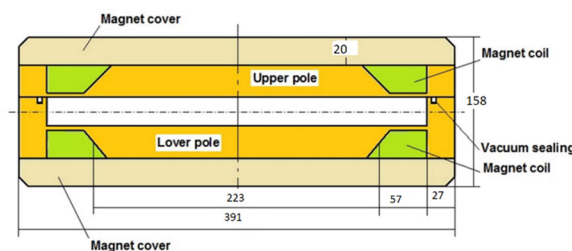


Figure 2: Sketch of microtron S-band II magnet.

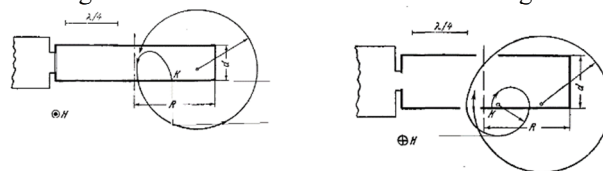


Figure 3: Type I (left) and type II (right) injection schemes as described in Ref.[1].

The parameter Ω shown in Table 1 is the ratio of the increase in energy per turn to its rest energy m_0c^2 . Also $\Omega = \frac{H}{H_0}$, in the fundamental mode, where H is the magnetic field and H_0 is the cyclotron field. Figure 3 shows two schemes for injection of electrons into the cavity from a source at the cavity wall. The Type I injection is most effective in the range $1.0 < \Omega < 1.25$ [1]. The Type II injection is most effective in the range $1.8 < \Omega < 2.2$.

* Work supported by U.S. D.O.E. SBIR grant DE-SC0013795.

[†] kahn@muonsinc.com

Content from this work may be used under the terms of the CC BY 4.0 licence (© 2022). Any distribution of this work must maintain attribution to the author(s), title of the work, publisher, and DOI

AFFORDABLE, EFFICIENT INJECTION INJECTION-LOCKED MAGNETRONS FOR SUPERCONDUCTING CAVITIES*

M. Popovic[†], M.A. Cummings, S.A. Kahn, R.P. Johnson, R. Lentz, M. Neubauer, T. Wynn
Muons, Inc., Batavia, IL, USA
T. Blassick, J. Wessel, Richardson Electronics Ltd., LaFox, IL, USA

Abstract

Existing magnetrons that are typically used to study methods of control or lifetime improvements for SRF accelerators are built for much different applications such kitchen microwave ovens (1kW, 2.45 GHz) or industrial heating (100 kW, 915 MHz). In this Phase I SBIR project, Muons, Inc. will work with Richardson Electronics LLC (RELL) to develop fast and flexible manufacturing techniques to allow many ideas to be tested for construction variations that enable new phase and amplitude injection locking control methods, longer lifetime, and inexpensive refurbishing resulting in the lowest possible life-cycle costs. In Phase II, magnetron sources will be tested on SRF cavities to accelerate an electron beam. A magnetron operating will be constructed and tested with our novel patented subcritical voltage operation methods to drive an SRF cavity. The critical areas of magnetron manufacturing and design affecting life-cycle costs that will be modelled for improvement include: Qext, filaments, magnetic field, vane design, and novel control of outgassing.

INTRODUCTION

Our plan is to use existing magnetron designs and try to modify them to create magnetron tubes that will satisfy the needs of particle accelerators. For example, we will consider a tube that will include a means to inject the locking signal directly into the tube.

To meet these goals, we are in process of studying two magnetron designs:

1. A strapped magnetron, where the RF power extraction method will be modified. For the purpose of injecting a phase locked signal, we are planning to introduce an additional port in one of the resonant cavities of magnetron.
2. A coaxial magnetron design will have a cooling structure that will allow CW operation and generate tens of kW of RF power. A phase lock signal will be introduced via an antenna attached to one of the vanes.

THE STRAPPED MAGNETRON OPTION

The tube below shown in Figure 1 is a 20kW CW, 1497 MHz tube designed and built by Muons Inc [1]. The tube has 10 strapped cavities and is water cooled. The power is extracted using a three-legged antenna that is enclosed in a ceramic dome.

* Work supported by DOE SBIR grant DE-SC0022586

[†] popovic@muonsinc.com

The cathode stalk has a 2 liter per second ion pump and connectors for high voltage and filament power input.



Figure 1: Photos show internal structure, ten cavities, straps and antenna attached to anode body. The new antenna design will have five legs.

In the new design under development, the antenna will have five legs and be attached to every other vane. The initial simulation shows that the corresponding (inner) strap can be removed without compromising mode separation. A five leg design will allow more power to be coupled out of

FAST FIRST-ORDER SPIN PROPAGATION FOR SPIN MATCHING AND POLARIZATION OPTIMIZATION WITH Bmad

J. M. Asimow, G. H. Hoffstaetter¹, D. Sagan, M. G. Signorelli, Cornell University, Ithaca, NY, USA
¹also at Brookhaven National Laboratory, Upton, NY, USA

Abstract

Accurate spin tracking is essential for the simulation and propagation of polarized beams, in which a majority of the particles' spin point in the same direction. Bmad, an open-sourced library for the simulation of charged particle dynamics, traditionally tracks spin via integrating through each element of a lattice. While exceptionally accurate, this method has the drawback of being slow; at best, the runtime is proportional to the length of the element. By solving the spin transport equation for simple magnet elements, Bmad can reduce this algorithm to constant runtime while maintaining high accuracy. This method, known as "Sprint," enables quicker spin matching and prototyping of lattice designs via Bmad.

INTRODUCTION

The Thomas-BMT equation describes the way that a particle's spin is perturbed via magnetic fields. At every point in phase space, a particle's spin \vec{S} precesses about the vector $\vec{\Omega}(z)$ according to the differential equation:

$$\frac{d\vec{S}}{ds} = \vec{\Omega}(z, s) \times \vec{S}. \quad (1)$$

Solutions to Eq. (1) are of the form $\vec{S}(s) = R(z, s)\vec{S}_0$, where R is a rotation matrix in $SO(3)$. One caveat is that the Bmad library uses quaternions to represent the net spin rotation, rather than matrices. Quaternions are a noncommutative associative extension of the imaginary numbers that follow the rule $\mathbf{i}^2 = \mathbf{j}^2 = \mathbf{k}^2 = \mathbf{ijk} = -1$. Quaternions need fewer computations than matrices to calculate a 3d rotation, and are thus preferable for computer applications. A quaternion rotation of angle θ about the unit vector $\vec{e} = e_x\hat{x} + e_y\hat{y} + e_z\hat{z}$ looks like:

$$q = \cos\left(\frac{\theta}{2}\right) + e_x \sin\left(\frac{\theta}{2}\right)\mathbf{i} + e_y \sin\left(\frac{\theta}{2}\right)\mathbf{j} + e_z \sin\left(\frac{\theta}{2}\right)\mathbf{k}. \quad (2)$$

The rotation resulting from two successive rotations q_0 and q_1 is described by the product q_1q_0 . Equation (1) describe an infinitesimal rotation around the vector $\vec{\Omega}$ by the angle $|\vec{\Omega}|ds$. The quaternion characterizing this rotation is therefore $dQ = 1 + ds\frac{1}{2}(\Omega_x\mathbf{i} + \Omega_y\mathbf{j} + \Omega_z\mathbf{k})$ [1]. The total rotation $q(s)$ then changes along s with the differential equation:

$$\frac{dq}{ds} = \frac{1}{2}\Omega q, \quad \Omega = \Omega_x\mathbf{i} + \Omega_y\mathbf{j} + \Omega_z\mathbf{k}. \quad (3)$$

Bmad can compute quaternions by numerically integrating Eq. (3) via interfacing with Etienne Forest's PTC code [2]. However, if Eq. (3) is linearized with respect to the phase space deviations from the accelerator's design orbit, one can compute the quaternions analytically for the typical magnet types. To do so, we split $\vec{\Omega}$ into a constant term $\vec{\Omega}_0$ and a first-order term $\vec{\omega}$ [3]. With g as the bend strength, k_1 as the quadrupole strength, and k_s as the solenoid strength, this Ω is

$$\Omega_{0x} = 0 \quad (4a)$$

$$\Omega_{0y} = -a\gamma \quad (4b)$$

$$\Omega_{0s} = -(1+a)k_s \quad (4c)$$

$$\omega_x = \left[(1+a\gamma) \left(-k_1y + \frac{1}{2}k'_sx \right) + (a\gamma - a)k_sx' \right] \quad (5a)$$

$$\omega_y = \left[(1+a\gamma) \left(-g^2x - k_1x + \frac{1}{2}k'_sy \right) + (a\gamma - a)k_sy' + \left(1 + \frac{a}{\gamma} \right) g\delta \right] \quad (5b)$$

$$\omega_s = \left[(1+a\gamma) (-g'y + k_s\delta) + (a\gamma - a)(gy' + g'y - k_s\delta) \right]. \quad (5c)$$

On the design orbit, the rotation resembles simple harmonic precession about $\vec{\Omega}_0$. Denoting this 0th order solution by the quaternion q_0 , we write the full solution as $q = (q_0 + \Delta q) = q_0(1 + \Delta b)$, with $\Delta b = \frac{\Delta q}{q_0}$. Equation (3),

$$\frac{d}{ds}(q_0(1 + \Delta b)) = \frac{1}{2}\Omega q \quad (6)$$

leads to the zeroth and first order expansions:

$$q'_0 = \frac{1}{2}\Omega_0q_0, \quad q'_0\Delta b + q_0\Delta b' = \frac{1}{2}\Omega_0\Delta b + \frac{1}{2}\omega q_0 \quad (7)$$

leading to:

$$\Delta b' = \frac{1}{2}q_0^{-1}\omega q_0. \quad (8)$$

For the linear phase space function ω in Eq. (5), Δb was integrated analytically.

Fringes were approximated using a hard-edge model, such that the fringe strength approaches a Dirac-Delta function. Misalignments were handled by shifting the center of the Taylor map, such that the constant term of the series includes the contributions from the misalignment.

DEVELOPMENT OF A CVD SYSTEM FOR NEXT-GENERATION SRF CAVITIES *

G. Gaitan[†], P. Bishop, A. Holic, G. Kulina, M. Liepe, J. Sears, Z. Sun
 Cornell University, Ithaca, NY, USA
 B. Wendland[‡], University of Minnesota, MN, USA

Abstract

Next-generation, thin-film surfaces employing Nb₃Sn, NbN, NbTiN, and other compound superconductors are destined to allow reaching superior RF performance levels in SRF cavities. Optimized, advanced deposition processes are required to enable high-quality films of such materials on large and complex-shaped cavities. For this purpose, Cornell University is developing a remote plasma-enhanced chemical vapor deposition (CVD) system that facilitates coating on complicated geometries with a high deposition rate. This system is based on a high-temperature tube furnace with a clean vacuum and furnace loading system. The use of plasma alongside reacting precursors will significantly reduce the required processing temperature and promote precursor decomposition. The system can also be used for annealing cavities after the CVD process to improve the surface layer. The chlorine precursors have the potential to be corrosive to the equipment and pose specific safety concerns. A MATLAB GUI has been developed to control and monitor the CVD system at Cornell.

INTRODUCTION

Niobium-3 tin (Nb₃Sn) is the most promising alternative material to niobium for SRF accelerator cavities. The material has the potential to double accelerating gradients and operating temperature of SRF cavities, decreasing costs and increasing efficiency of future accelerators, see Refs. [1–5]. A vapor diffusion-based growth process for Nb₃Sn has given the best RF performance to date, but maximum fields are still well below the ultimate predicted limit of this material (24 MV/m reached vs. 90+ MV/m ultimate limit). Defects (e.g., small tin-depleted regions) and surface roughness are limiting factors of these films.

Exploring alternative Nb₃Sn growth methods is therefore one direction for improving performance beyond current limits, and might offer more control over the growth process. Very thin (tens of nm) films of Nb₃Sn, NbN, NbTiN, and other compound superconductors might also promise superior RF performance levels in SRF cavities. Growing these will require advanced deposition processes to achieve high-quality, uniform films of such materials on large and complex shaped cavity surfaces.

* This work was supported by the U.S. National Science Foundation under Award PHY-1549132, the Center for Bright Beams

[†] gg465@cornell.edu

[‡] Summer REU student supported by the U.S. NSF under award PHY-2150125

Chemical Vapor Deposition (CVD)

CVD is a vacuum deposition method and it offers a potential path to grow high-quality films of Nb₃Sn, NbN, NbTiN on various substrates including niobium and copper. An example of the use of CVD is given in Ref. [6], and a paper detailing RF results for Nb CVD on a copper substrate is given in Ref. [7]. Cornell successfully tested first-ever fabricated CVD Nb₃Sn-on-copper SRF cavities [8]. These are comprised of copper substrates with thin-film interior surface coatings of niobium interlayer/CTE(coefficient thermal expansion)-bridge and Nb₃Sn formed via chemical vapor deposition (CVD). The coating was performed by industry partner Ultramet using unique CVD precursor materials developed by researchers at Florida State University. Ultramet observed a Sn concentration of 24-25 % on coupon samples. A critical temperature $T_c \approx 16.5$ K suggests that the uniformity of the Sn to Nb ratio needs to be improved on the cavity surface. The RF performance was limited by high residual resistance, likely due to contamination or defects on the surface. Further improvement in the coating process will be needed to improve RF performance.

Cornell University is therefore developing a dedicated cavity chemical vapor deposition growth system as described in the following sections.

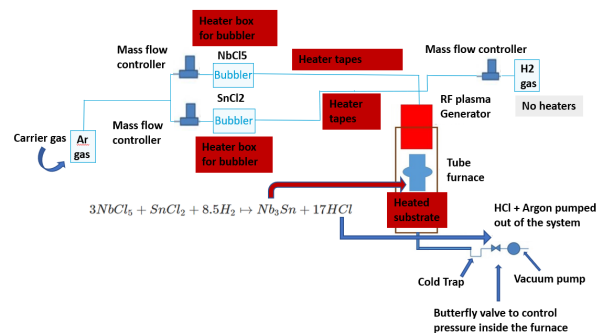


Figure 1: Schematic of the CVD setup at Cornell.

DESCRIPTION OF SYSTEM

The schematic of the system is shown in Fig. 1 and a picture of the system in Fig. 2. The basic layout and design has been described before in Ref. [9], so this paper will focus on recent progress and development.

The furnace has been used for annealing coupon samples and is now being developed to be ready for Nb₃Sn CVD. A branch of the vacuum system contains a roughing pump

SINGULARITY-FREE EXACT DIPOLE BEND TRANSPORT EQUATIONS

David Sagan*, Cornell University, Ithaca, NY, USA

Abstract

Exact transport equations for a pure dipole bend (a bend with a dipole field and nothing else) have been derived and formulated to avoid singularities when evaluated. The transport equations include finite edge angles and no assumption is made in terms of the bending field being matched to the curvature of the coordinate system.

INTRODUCTION

Pure dipole bend elements, that is bends with a pure dipole field and no higher order multipoles, are ubiquitous in lattices used to simulate many machines such as the LHC, SuperKEKB, RHIC, BEPC, etc., etc. Despite the fact that such a bend is conceptionally simple (the particle motion is circular), there is a wide range of algorithms used for particle tracking. For example, the MAD8 program uses a second order map [1], SixTrack uses splitting to approximately solve the exact Hamiltonian [2], PLACET [3] uses a linear matrix in the transverse coordinates with the bending strength scaled by the particle energy, the SAD program [4] implements an exact solution [4], and Elegant implements several tracking methods depending upon which type of bend is chosen [5].

An exact tracking solution [4, 6, 7] is to be preferred over an approximate one. However, up to now, the published algorithms for the exact solution suffer from singularities in the limit of zero reference bending angle or zero field. The singularities are removable, however, since the formulas involve multiple variables, this complicates implementation. To simplify matters, this paper formulates the exact solution in such a way as to avoid any singularities except for the standard $\text{sinc}(x) = \sin(x)/x$ function which is easily coded to be well behaved even in the vicinity of zero. The transport equations include finite edge angles and no assumption is made in terms of the bending field being matched to the curvature of the coordinate system.

Not covered here is tracking through fringe fields so the tracking algorithm assumes a hard edge to the dipole field. The algorithm is divided into three parts: entrance tracking for a finite entrance face angle e_1 , tracking the sector body, and finally tracking for a finite exit face angle e_2 .

SECTOR BODY TRACKING

This section covers tracking through the body of the dipole which is taken to be a sector bend as illustrated in Fig. 1. The particle phase space coordinate system used for the analysis is (x, p_x, y, p_y, z, p_z) where

$$p_{x,y} = \frac{P_{x,y}}{P_0}, \quad z = -\beta c(t - t_0), \quad p_z = \frac{P - P_0}{P_0} \quad (1)$$

with $P_{x,y}$ being the transverse momentum, P is the momentum, P_0 is the reference momentum, βc the particle velocity, t the time, and t_0 the reference time.

The particle's phase space coordinates are expressed with respect to a geometric (x, y, s) curvilinear coordinate system. The (x, y, s) coordinate system at the entrance to the dipole has origin at O_1 with y perpendicular to the plane of the dipole, and x and s in the plane of the dipole with x along the entrance edge, and s perpendicular to the entrance edge. The (x, y, s) coordinate system at the exit end has the origin at O_2 and has a similar orientation with respect to the exit edge as the entrance coordinates with respect the entrance edge.

As shown in Figure 1, at point 1 where the particle enters the bend, ϕ_1 is the angle of the particle trajectory in the plane of the bend with respect to the s axis. In terms of the entrance phase space coordinates, ϕ_1 is

$$\sin(\phi_1) = \frac{p_{x1}}{\sqrt{(1 + p_z)^2 - p_y^2}} \quad (2)$$

where the subscript "1" for p_z and p_y is dropped since these quantities are invariant.

The (u, v) coordinate system in the plane of the bend is defined with the u -axis along the exit edge of the bend and the v -axis is perpendicular to the u -axis. The origin is at the design center of the bend. The point (u_1, v_1) where the particle enters the bend is given by

$$u_1 = (\rho + x_1) \cos(\theta) \quad (3)$$

$$v_1 = (\rho + x_1) \sin(\theta) \quad (4)$$

where ρ is the design radius of curvature, x_1 is the offset of the particle from the design at the entrance point, and θ is the design bend angle

$$\theta = \frac{L}{\rho} = g L \quad (5)$$

with L being the design arc length and $g \equiv 1/\rho$.

The coordinates (u_0, v_0) of the center of curvature of the particle trajectory is

$$u_0 = u_1 - \rho_p \cos(\theta + \phi_1) \quad (6)$$

$$v_0 = v_1 - \rho_p \sin(\theta + \phi_1) \quad (7)$$

where ρ_p is the radius of curvature of the particle trajectory in the (u, v) plane

$$g_p = \frac{1}{\rho_p} = \frac{g_{\text{tot}}}{\sqrt{(1 + p_z)^2 - p_y^2}} \quad (8)$$

with g_{tot} being the bending strength of the actual field as opposed to g which is the bending strength defined by the geometry of the sector.

* Work supported in part by Department of Energy grant DE-SC0018370.

BEAM-BASED ALIGNMENT OF SEXTUPOLE FAMILIES IN THE EIC

J. C. Wang^{1*}, G. Hoffstaetter^{1,2}, D. Sagan¹, C. Montag²

¹Cornell University, Ithaca, NY, USA

²Brookhaven National Laboratory, Upton, NY, USA

Abstract

To steer the closed orbit in a storage ring through the center of its quadrupoles, it is important to accurately know the quadrupole centers relative to nearby beam position monitors. Usually this is achieved by beam-based alignment (BBA). Assuming the quadrupole strength can be changed individually, one finds the BPM reading where changing a quadrupole's strength does not alter the closed orbit. Since most quadrupoles are powered in series, they can only be varied independently if costly power supplies are added. For the EIC electron storage ring (ESR), we investigate whether sextupole BBA can be used instead. Individually powered sextupole BBA techniques already exist, but most sextupoles are powered in families and cannot be individually changed. We therefore developed a method where a localized bump changes the beam excursion in a single sextupole of a family, turning off all families that also have sextupoles in the bump. The bump amplitude at which the sextupole does not cause a closed orbit kick determines the sextupole's alignment. This study was made to investigate the precision to which this method can be utilized.

INTRODUCTION

The here presented Beam Based Alignment (BBA) procedure relies on the relationship between the kickers of a closed 3-bump when an active sextupole is within the bump. The strength of the kickers behind the sextupole will depend quadratically on the first kicker in order to close the bump. An example is shown in Fig. 1 where we model a very short sextupole to avoid length-effects in the analysis.

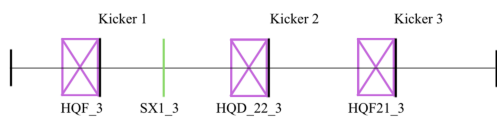


Figure 1: Diagram of a sextupole behind the first kicker of a 3-bump.

In an orbital bump with only linear elements and no sextupole magnets, the kick angles θ_2 and θ_3 provided by the second and third kicker required to close the bump are directly proportional to the bump amplitude from the first kicker θ_1 . The formulas for the bump settings using optical values [2] are provided as follows:

$$\theta_2 = -\sqrt{\frac{\beta_1 \sin(\psi_3 - \psi_1)}{\beta_2 \sin(\psi_3 - \psi_2)}} \theta_1$$

$$\theta_3 = \sqrt{\frac{\beta_1}{\beta_3}} \left(\frac{\sin(\psi_3 - \psi_1)}{\tan(\psi_3 - \psi_2)} - \cos(\psi_3 - \psi_1) \right) \theta_1 \quad (1)$$

Where β represents the β -function and ψ represents the phase functions. The equations from Eq. (1) must change from linearly proportional to θ_1 to quadratic when a sextupole is added to the bump as it gives a kick angle, θ_s equivalent to:

$$\theta_s = \frac{1}{2} K_2 L (x_s - x_0)^2 \quad (2)$$

where x_0 is the misalignment of the sextupole, $K_2 L$ is the integrated strength of the sextupole, and x_s is the position where the beam enters the sextupole which is linearly proportional to θ_1 ; θ_s then depends on θ_1^2 , forcing both θ_2 and θ_3 to have a 2nd order dependence on θ_1 in order to close the bump at any bump amplitude.

The only scenario where the bump can still close using the equations from Eq. (1) is where the beam enters the sextupole directly through its center, in which case k_s would be equal to 0. If the kick strengths of the second and third kicker needed to close the bump were graphed with respect to the bump amplitude k_1 , the intersection point between the quadratic curve and the linear curve for a bump with and without an active sextupole, respectively, would occur at the k_1 value needed to force the beam through the center of the sextupole as shown in Fig. 2. Because this method

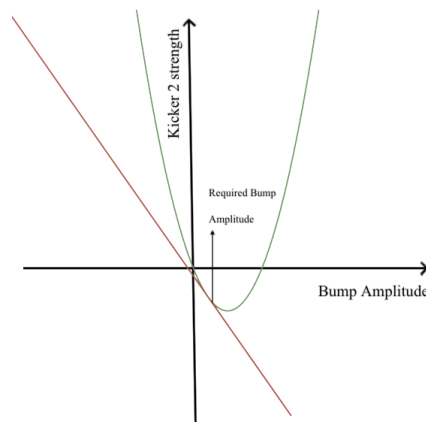


Figure 2: Graph of an example comparison between the bump settings and amplitude with and without a sextupole.

ensures that throughout the BBA procedure the bump is always closed, other nonlinear effects around the ring have

* jcw295@cornell.edu

PROMISE AND CHALLENGES OF A METHOD FOR 5X5 SIGMA MATRIX MEASUREMENT IN A TRANSPORT LINE*

M. Borland, V. Sajaev, K. P. Wootton, ANL, Argonne, IL, USA

Abstract

The Advanced Photon Source (APS) is upgrading the storage ring to a design that requires on-axis injection. Matching between the incoming beam and the ring is important in ensuring high injection efficiency. Toward this end, we have developed and tested a method for measuring all sigma matrix elements except those related to the time coordinate. We report on challenges encountered, based on simulation and real-world trials.

INTRODUCTION

Measuring beam size as a quadrupole is varied is a basic method of measuring beam emittance and beta functions. The method can be extended to scanning of multiple thickness quadrupoles [1] for two-plane measurements [2] and to allow measurement of the elements of the 4x4 sigma matrix [3]. This technique seems to be unworkable when there is dispersion in the transport line at the location of the quadrupoles being varied or of the screen used for beam size measurement, since the problem appears ill-defined [4].

Here we present a method of measuring the non-temporal sigma matrix elements in a transport line with dispersion. While the method works very well in simulation, real-world application has proven complex.

The transformation of sigma matrix Σ by a transport line follows [5]

$$\Sigma = R\hat{\Sigma}R^T, \quad (1)$$

where $\hat{\Sigma}$ is the starting sigma matrix, R is the transport matrix, and Σ is the final sigma matrix. If there is no vertical bending ($R_{36} = R_{46} = 0$), we can express the measurable elements of Σ as

$$\begin{aligned} \Sigma_{11} = & R_{11}^2 \hat{\Sigma}_{11} + 2R_{11}(R_{12}\hat{\Sigma}_{12} + R_{16}\hat{\Sigma}_{16}) + R_{12}^2 \hat{\Sigma}_{22} \\ & + 2R_{12}R_{16}\hat{\Sigma}_{26} + R_{16}^2 \hat{\Sigma}_{66} \end{aligned} \quad (2)$$

$$\Sigma_{33} = R_{33}^2 \hat{\Sigma}_{33} + 2R_{33}R_{34}\hat{\Sigma}_{34} + R_{34}^2 \hat{\Sigma}_{44} \quad (3)$$

$$\begin{aligned} \Sigma_{13} = & R_{11}R_{33}\hat{\Sigma}_{13} + R_{11}R_{34}\hat{\Sigma}_{14} + R_{12}R_{33}\hat{\Sigma}_{23} \\ & + R_{12}R_{34}\hat{\Sigma}_{24} + R_{16}R_{33}\hat{\Sigma}_{36} + R_{16}R_{34}\hat{\Sigma}_{46} \end{aligned} \quad (4)$$

In an extension of Ref. [1], these equations can be formed into a matrix equation for a series of measured values of ($\Sigma_{11}, \Sigma_{33}, \Sigma_{13}$) as a function of R_{ij} , with the latter being altered by the variation of several quadrupoles. This matrix equation can be solved for $\hat{\Sigma}$.

This method was implemented in the program `sdds5x5sigmaproc`, which is distributed with and uses data generated by `elegant` [6]. The program takes R

data from `elegant` as quadrupoles are varied, along with corresponding measured or simulated beam size data. It computes Σ_{ij} for $i = 1, 2, 3, 4, 6$, including error estimates. Multi-screen measurements from a common starting point are available by simply ensuring that the R data and corresponding beam moments measurements are organized into the same order in the input files.

CONSIDERATIONS FOR APS

The Advanced Photon Source (APS) booster-to-storage-ring (BTS) transport line features a dogleg that consists of an extraction kicker, several booster lattice elements, two extraction septa, five quadrupoles, and two bending magnets. Downstream of the latter are more quadrupoles and a YAG scintillator screen with digital camera. The R matrix computations start just upstream of the kicker, so we get $\hat{\Sigma}$ at this location.

Although the dogleg quadrupoles are nominally set to suppress the dispersion, the beam coming from the APS booster [7] may (depending on the booster lattice) originate in a location of non-zero $\hat{\Sigma}_{i6}$. From the equations above, we see that we can't hope to determine $\hat{\Sigma}_{i6}$ unless the transport line has non-zero R_{16} at the location of the measurements. Without this, we cannot correctly deduce the emittance of the beam, since the inferred transverse beam moments (e.g., $\hat{\Sigma}_{11}$) include unknown $\hat{\Sigma}_{i6}$ -related contributions. We can resolve this by varying quadrupoles before and after the final dipole of the dogleg. Varying quadrupoles before the final dipole will strongly vary the terms related to R_{16} . Varying quadrupoles downstream of the dogleg will ideally vary only the non-chromatic elements of R . In reality, we needn't strictly separate the variation of the quadrupoles, as long as quadrupoles in both regions are varied.

Any transport line that has a similar arrangement of quadrupoles before and after a bending magnet should be amenable to measurements using this method. One common configuration is a linac with a four-dipole bunch compressor containing dispersion-matching quadrupoles.

It is important to distinguish between two related quantities [4]: the dispersive matrix element R_{16} and the dispersion function η_x , which is directly related to the beam size. R_{16} can be measured by changing the beam energy at the entrance to the BTS by varying the extraction time from the linearly-ramping booster, while keeping the extraction magnets fixed in strength but timed to the bunch center. η_x depends on R_{16} , but also on the booster quadrupoles, the momentum offset (via the rf frequency), the slow bump, etc., none of which change the measured R_{16} . Hence, measuring "dispersion" in the BTS by varying the extraction energy from the booster does not allow determining the dispersive

* Work supported by the U.S. Department of Energy, Office of Science, Office of Basic Energy Sciences, under Contract No. DE-AC02-06CH11357.

AVOIDING COMBINATORIAL EXPLOSION IN SIMULATION OF MULTIPLE MAGNET ERRORS IN SWAP-OUT SAFETY TRACKING FOR THE ADVANCED PHOTON SOURCE UPGRADE*

M. Borland, R. Soliday, ANL, Argonne, IL 60439, USA

Abstract

The Advanced Photon Source (APS) is upgrading the storage ring to provide a natural emittance of 41 pm at 6 GeV. The small dynamic acceptance entails operation in on-axis swap-out mode. Careful consideration is required of the safety implications of injection with shutters open. Tracking studies require simulation of multiple simultaneous magnet errors, some combinations of which may introduce potentially dangerous conditions. A naive grid scan of possible errors would be prohibitively time-consuming. We describe a different approach using biased sampling of particle distributions from successive scans.

INTRODUCTION

A large bending-magnet error in a light source ring could allow injected-beam electrons to enter a photon beamline, perhaps resulting in beam exiting the tunnel. Similarly, such a failure could allow injected beam to hit structures near or within the front end, producing a potentially hazardous radiation shower down the beamline. One safeguard is to disallow injection with shutters open if there is no stored beam present [1], since stored beam is very unlikely if there is magnet error that is sufficiently large to allow hazardous endpoints for injected beam. Depending on the regulatory environment, this assertion may be considered sufficient or may need support from simulations [1–6]. In some cases [2, 4, 5, 7], the stored beam interlock was found insufficient, though this may be a result of conservative assumptions.

Simulation strategies include forward tracking of the potential injected beam phase space or backward tracking of the hypothetical phase space of hazardous particles. The latter is less beneficial when considering a radiation shower generated by beam striking components at the entrance of the photon beamline or in the front end. Since this a concern for APS-U [8, 9], which will operate in swap-out mode [10, 11], we have used forward tracking [12].

The present paper deals with the issue of multiple magnet errors in a multi-bend achromat lattice [13] with many independently-powered dipoles [8]. Our simulations use elegant [14, 15] to track through computed 3D field maps that extend over the photon channels, which reduces the need for approximations and assumptions in treating the character of the fields outside the good field region, including areas outside the magnet. Physical apertures and multiply-connected vacuum chambers are defined using midplane

boundaries around “no-go” regions, which allows very rapid determination of particle strikes using winding number computations [12].

SIMULATING MULTIPLE SIMULTANEOUS ERRORS

Previously [12], we simulated the effects of single magnet errors, which is manageable even with 10’s of millions of simulation particles and using relatively small (2%) steps in the error. The preliminary conclusion was that concerns exist, but typically for large magnet errors that are incompatible with stored beam.

However, nothing prevents faults in or adjustments to multiple magnets. For example, for a bending-magnet (BM) beamline, we consider eight magnets, designated A:Q7, A:M3, A:Q8, A:M4, B:Q8, B:M3, B:Q7, and B:M2. In single-magnet studies, only the A:M4, B:Q8, and B:M3 can steer particles to dangerous endpoints. To this list, we added consideration of three upstream magnets (A:Q7, A:M3, A:Q8) and two downstream magnets (B:Q7, B:M2). All except B:M2 have two power supplies: a main supply that varies the dipole and quadrupole field and a trim supply that varies only the dipole.

We plan to use software monitoring to prevent the current in any magnet from deviating by more than, say, 10% from its nominal setpoint. While we might naively imagine scanning each magnet over $\pm 10\%$ with a step size of 2%, this requires $11^{15} \approx 4 \times 10^{15}$ runs. In this naive concept, each run has specific errors in each magnet, but takes beam from the beginning to the end of the sector; we combine many runs to understand the landscape. An alternative approach involves tracking the beam through each magnet in turn, scanning as we go, with the beam building up the effect of the previous scans [6]. Except for the first run, each run includes only one magnet plus some downstream drift spaces. While the workload is reduced, the problem is still unmanageable since the number of particles increases dramatically after each element. To address this, we observe that many particles are close to other particles in (x, x', y, y', δ) phase space, and give redundant information. If we down-sample by a factor equal to the number of scan points in a single run, the workload is constant.

DOWN-SAMPLING

For a 31 x 31 grid scan of each magnet’s main and trim supplies, we should down-sample ~1000-fold. If tracking is limited to (x, x') , phase-space repopulation [6] can be used to create a new distribution, but this is problematic in five dimensions. Assuming constant phase-space density,

* Work supported by the U.S. Department of Energy, Office of Science, Office of Basic Energy Sciences, under Contract No. DE-AC02-06CH11357.

HYDRODYNAMIC AND BEAM DYNAMIC SIMULATIONS OF ULTRA-LOW EMITTANCE WHOLE BEAM DUMPS IN THE ADVANCED PHOTON SOURCE STORAGE RING*

J. Dooling[†], Y. Lee, M. Borland, A. Grannan, C. Graziani, R. Lindberg, G. Navrotski
Argonne National Laboratory, Lemont, IL 60439, USA
N. Cook, RadiaSoft, Boulder, CO 80301, USA
D. Lee, University of California, Santa Cruz, CA 95064, USA

Abstract

The Advanced Photon Source Upgrade will use a multi-bend achromatic lattice to reduce vertical and horizontal beam emittances by one- and two-orders of magnitude, respectively; the operating current will increase by a factor of two. The resulting electron beam will be capable of depositing more than 150 MGy on machine protection collimators creating high-energy-density conditions. Work is underway to couple the beam dynamics code *elegant* with the particle-matter interaction program MARS and the magnetohydrodynamics (MHD) code FLASH to model the effects of whole beam aborts on the collimators. Loss distributions from *elegant* are input to MARS, which provides dose maps to FLASH. We are examining MHD effects as well as the propagation of beam downstream after interacting with a collimator. Electron and positron components are tracked to determine locations of beam loss. In recent beam dump experiments, dose levels as high as 30 MGy were generated and resulted in severe damage to the collimator surfaces. The deformed collimator surface may lead to beam deposition in unexpected locations. A fan-out kicker will be used to mitigate the effects of whole beam dumps on the collimators.

INTRODUCTION

Particle-matter interaction simulations were conducted with MARS [1, 2], which takes beam-dynamics loss distributions generated by *elegant* [3, 4] as input. In this simulation study, it is indicated that the ultra-low emittance electron beams expected in the Advanced Photon Source Upgrade (APS-U) storage ring would damage most commonly used vacuum materials such as aluminum, titanium, copper, or tungsten.

Two irradiation experiments were carried out in the APS storage ring (SR) to assess the effects of high-intensity electron beams when the beam strikes the proposed collimator material for the APS-U [5]. These experiments indicated that high-energy-density (HED) conditions ($>10^{11} \text{J/m}^3$) [6] are generated in the struck material leading to significant

damage. This data has been used to benchmark our simulations thus far, with good results overall.

Electron loss distributions from *elegant* are used as input to MARS to calculate energy deposition (or dose) in the collimator material. Dose maps from MARS are, in turn, passed to FLASH [7–9] to solve magnetohydrodynamic evolution using the unsplit staggered mesh (USM) MHD solvers [10, 11]. The propagation of the beam after interaction with the collimator is a prime concern. Experimental data, as well as simulations, clearly indicate that rapid, unplanned whole-beam loss erodes the collimator surface. Therefore, we want to track the beam and shower components downstream of the collimator during a whole-beam loss event. The beam carries a significant magnetic field with it, but as such, the field is transitory.

MAGNETOHYDRODYNAMICS

After resolving issues with the hydrodynamic solver [12], attention has turned to the inclusion of magnetohydrodynamic (MHD) effects. In MHD mode, magnetic fields in FLASH are not self-starting; henceforth none would be present without an externally-applied field (i.e., from the bunch). The FLASH simulation approximates initial boundary conditions at the vacuum-collimator interface using image charges in a reasonably correct way. Unfortunately, this model is no longer accurate after the boundary begins to erode.

We can calculate the electromagnetic fields near an electron beam by directly summing the field contributions from all electrons. A single relativistic electron produces the transverse electric field

$$\mathbf{E}_{\perp}(x, y, z, t) = \frac{e}{2\pi\epsilon_0} \frac{x\hat{\mathbf{x}} + y\hat{\mathbf{y}}}{\gamma^2 \left[\frac{(x^2+y^2)}{\gamma^2} + (z - \beta ct)^2 \right]^{3/2}}, \quad (1)$$

and the transverse magnetic field is $\mathbf{B}_{\perp} = (\beta/c)\hat{\mathbf{z}} \times \mathbf{E}_{\perp}$. We consider the field from a collection of N_e relativistic electrons whose coordinates are described by the probability distribution function f . We further assume that the electron distribution function varies in the longitudinal direction over the characteristic length σ_z , and that we are interested in transverse distances such that $r^2 \ll \gamma^2 \sigma_z^2$. In this case, the field part of the integrand is a sharply peaked function which we can approximate by a delta function (see, e.g., Refs. [13, 14]).

* This research used resources of the Advanced Photon Source, a U.S. Department of Energy (DOE) Office of Science user facility and is based on work supported by Laboratory Directed Research and Development (LDRD) funding from Argonne National Laboratory, provided by the Director, Office of Science, of the U.S. DOE under Contract No. DE-AC02-06CH11357.

[†] dooling@anl.gov

MEASUREMENTS OF BUNCH LENGTH IN THE ADVANCED PHOTON SOURCE BOOSTER SYNCHROTRON*

J. Dooling[†], W. Berg, J. Calvey, K. Harkay, K. P. Wootton
 Argonne National Laboratory, Lemont, IL 60439, USA

Abstract

A bunch duration monitor (BDM) was installed at the end of a synchrotron light monitor (SLM) port in the Advanced Photon Source (APS) booster synchrotron. The BDM is based on a fast Hamamatsu metal-semiconductor-metal detector with nominal rise and fall times of 30 ps. Bunch length data is especially important as the bunch charge will be raised from 3 nC, used in the existing machine, to as much as 18 nC for APS-Upgrade operation. During preliminary high-charge studies, the SLM image is observed to move over a period of minutes, while the BDM signal intensity varies; the motion is likely due to thermal loading of the in-tunnel synchrotron light mirror. Work is underway to stabilize the position using a simple feedback system and motorized mirror mount, as well as a new synchrotron light mirror assembly with improved thermal load handling capability. The feedback system will maintain optical alignment on the BDM at an optimum position based on the SLM centroid location. The optical layout will be presented along with preliminary bunch length data.

INTRODUCTION

A second bunch length diagnostic, referred to as a bunch duration monitor (BDM), has been installed in the Advanced Photon Source (APS) booster synchrotron. The initial BDM diagnostic was installed in the APS particle accumulator ring (PAR) [1]. The new BDM detector and electronics are located outside of the booster radiation shield wall at the end of a synchrotron light monitor (SLM) optics line. Bunch length is important as we plan to raise the charge per bunch from 3 nC to 18 nC for the APS upgrade (APS-U) [2]. The BDM has been used to measure bunch length over the full cycle of the booster [3].

Recent measurements indicated growth in bunch length with charge were not in line with expectations. Further investigation showed the apparent growth in pulse duration was correlated with the input signal (light) levels rather than charge. In addition, during studies with high charge (>6 nC) and continuous injection (at 1 or 2 Hz) a loss of BDM signal with time was observed. This latter behavior is likely due to misalignment of the synchrotron light spot on the BDM caused by thermal effects from heating of the in-tunnel mirror.

* This research used resources of the Advanced Photon Source, a U.S. Department of Energy (DOE) Office of Science user facility at Argonne National Laboratory and is based on research supported by the U.S. DOE Office of Science-Basic Energy Sciences, under Contract No. DE-AC02-06CH11357.

[†] dooling@anl.gov

EXPERIMENTAL ARRANGEMENT

The detection system is based on a Hamamatsu metal-semiconductor-metal (MSM) G4176-03 photodetector with quoted rise and fall times of 30 ps. The device can be biased with either positive or negative DC voltage. Peak power must be kept under 50 mW, otherwise, the device output begins to saturate and the bunch duration will appear to increase. The schematic in Fig. 1 shows the arrangement of the BDM detector-amplifier and SLM camera. A motorized mirror mount is used to adjust position on both the SLM and BDM with a picomotor hand pad; this will be converted to EPICS control.

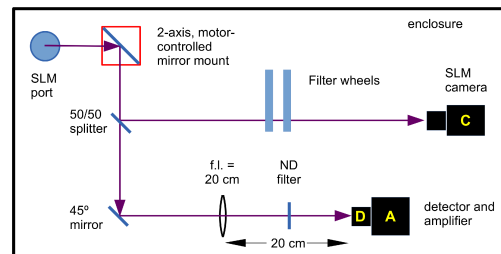


Figure 1: Schematic of the SLM and BDM optical paths.

BUNCH LENGTH MEASUREMENTS

Saturation Effects

BDM data were collected during high-charge studies in November 2021. Bunch charge was varied from approximately 7 to 12 nC. A plot of bunch duration versus charge is presented in Fig. 2. The data was collected 180 ms after injection corresponding to a beam energy of 5.6 GeV; the full acceleration interval in the booster is 225 ms. For normal APS operations, beam is extracted from the booster at an energy of 7 GeV. For APS-U the storage-ring energy is 6 GeV.

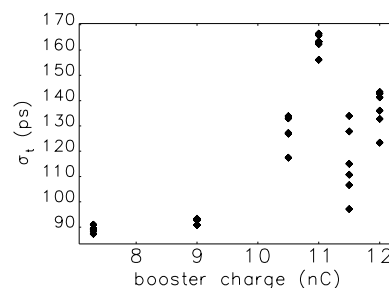


Figure 2: Booster bunch duration vs. charge.

FIRST BEAM RESULTS USING THE 10-kW HARMONIC RF SOLID-STATE AMPLIFIER FOR THE APS PARTICLE ACCUMULATOR RING*

K.C. Harkay[†], T. Berenc, J. Calvey, J.C. Dooling, H. Shang, T.L. Smith, Y-E Sun, U. Wienands
 Argonne National Laboratory, Lemont, IL 60439, USA

Abstract

The Advanced Photon Source (APS) particle accumulator ring (PAR) was designed to accumulate linac pulses into a single bunch using a fundamental radio frequency (rf) system, and longitudinally compress the beam using a harmonic rf system prior to injection into the booster. For APS Upgrade, the injectors will need to supply full-current bunch replacement with high single-bunch charge for swap-out injection in the new storage ring. Significant bunch lengthening is observed in PAR at high charge, which negatively affects beam capture in the booster. Predictions showed that the bunch length could be compressed to better match the booster acceptance using a combination of higher beam energy and higher harmonic gap voltage. A new 10-kW harmonic rf solid-state amplifier (SSA) was installed in 2021 to raise the gap voltage and improve bunch compression. The SSA has been operating reliably. Initial results show that the charge-dependent bunch lengthening in PAR with higher gap voltage agrees qualitatively with predictions. A tool was written to automate bunch length data acquisition. Future plans to increase the beam energy, which makes the SSA more effective, will also be summarized.

INTRODUCTION

The APS Upgrade (APS-U) is being designed for on-axis injection, where the injectors produce enough single-bunch charge to perform complete bunch replacement, also known as “swap-out” [1-3]. For the design APS-U bunch modes, the injected bunch charge goal is 5-17 nC. By comparison, the typical APS injected bunch charge is 2-4 nC.

The basic layout of the APS injectors for APS-U is shown in Fig. 1. The linac provides 1-nC pulses at a 30-Hz rate. Up to 20 pulses are accumulated and damped in the particle accumulator ring (PAR) [4] at the fundamental rf frequency. In the final 230 ms of the 1-s cycle, the single bunch is captured in a 12th harmonic rf system and the bunch length is further compressed. The bunch is injected into the booster where it is ramped to full energy and extracted into a transport line that was redesigned for matching into the APS-U storage ring (SR) [5].

One of the bottlenecks in achieving high charge in the injectors is significant bunch lengthening observed in PAR, which is due to both potential well distortion (PWD) and microwave instability [6]. The typical zero-charge PAR bunch length is 320 ps. Booster acceptance becomes an issue when the PAR bunch length becomes > 600 ps [7].

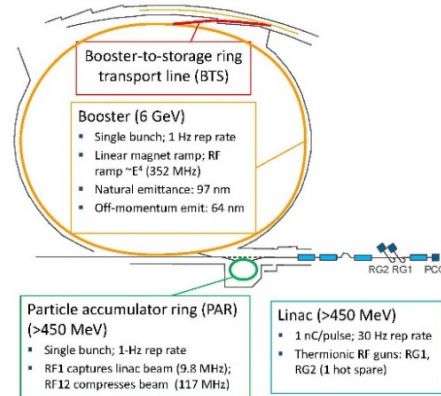


Figure 1: APS-U injector complex.

Mitigation of the PAR bunch lengthening follows two approaches [6]. The first is to increase bunch length compression in the harmonic rf system by raising the gap voltage. The second is to increase the beam energy to raise the instability threshold.

This paper discusses results for the first approach. A 10-kW 117-MHz SSA was installed to replace the 3-kW tube amplifier for the harmonic rf system. The higher rf power enabled raising the gap voltage from 21 kV to over 30 kV, which was the design goal. Increased bunch length compression was observed for bunch charge up to ~13 nC with 28 kV harmonic gap voltage, close to predictions.

HARMONIC RF AMPLIFIER

Tube Amplifier

The limitation of the present harmonic tube amplifier is illustrated in Fig. 2. The forward power saturates at < 3 kW at high charge. The result is that the gap voltage, nominally 21 kV, droops significantly above ~10 nC and bunch compression is compromised.

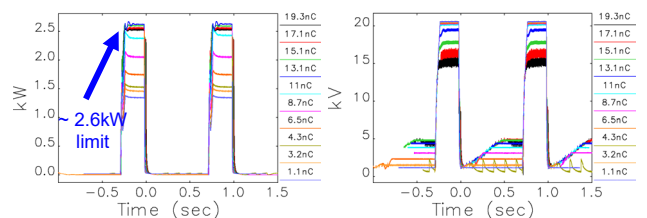


Figure 2: PAR harmonic tube amplifier forward power (left) and gap voltage (right) as a function of bunch charge (2.5 cycles are shown).

APS-U Requirements

Given harmonic rf cavity parameters $(R/Q)_a \approx 215.7 \Omega$ and Q (external) = 1900, it takes 3.6 kW of power to merely

* Work supported by U. S. Department of Energy, Office of Science, under Contract No. DE-AC02-06CH11357.

[†] harkay@anl.gov

FRINGE FIELD MAPS FOR CARTESIAN DIPOLES WITH LONGITUDINAL AND/OR TRANSVERSE GRADIENTS*

R. Lindberg, M. Borland, ANL, Argonne, IL, USA

Abstract

Fringe field effects in dipoles can give rise to important linear and nonlinear contributions. This paper describes how to extend the classic results of Brown (SLAC Tech. Rep. SLAC-R-75) and the more recent calculations of Hwang and Lee (doi:10.1103/PhysRefSTAB.18.122401) to Cartesian dipoles with transverse and/or longitudinal gradients. We do this by 1) introducing a more general definition of the fringe field that can be applied to longitudinal gradient dipoles, 2) allowing for quadrupole and/or sextupole content in the magnet body, and 3) showing how to employ the resulting fringe maps as a symplectic transformation of the coordinates. We compare our calculation results with tracking for longitudinal and transverse gradient dipoles planned for APS-U.

THEORY

This paper describes how to extend the classic results of Brown [1] and the more recent calculations of Hwang and Lee [2] to Cartesian dipoles with transverse and/or longitudinal gradients. Cartesian dipoles have straight magnetic poles parallel to the z -axis. In this case we can write the dimensionless magnetic vector potential $a = eA/p_0$ in a gauge with vertical component $A_y = 0$ as

$$A_z = \frac{x}{\rho} D(z) + \frac{x^3 - 3xy^2}{6\rho B_0} \frac{\partial^2 B_y}{\partial x^2} + \frac{x^2 - y^2}{2} KQ(z) - \frac{x^4 - 6x^2y^2 - y^4}{48} KQ''(z) \quad (1)$$

$$A_x = \frac{y^2}{2\rho} D'(z) - \frac{8y^4}{192\rho} D'''(z) + \frac{6x^2y^2 - y^4}{24\rho B_0} \frac{\partial^2 B_y'}{\partial x^2} + \frac{xy^2}{2} KQ'(z), \quad (2)$$

where the dimensionless, on-axis dipole and quadrupole field profiles are related to the generalized gradient representation [3] via

$$D(z) = \frac{q\rho}{p_0} C_1(z) \quad Q(z) = \frac{2q}{Kp_0} C_2(z), \quad (3)$$

while the field curvature term

$$\frac{1}{\rho B_0} \frac{\partial^2 B_y}{\partial x^2} = -\frac{q}{p_0} \left[\frac{1}{4} C_1''(z) - 6C_3(z) \right]. \quad (4)$$

The hard edge model approximates the full field dependence using piece-wise constant regions. We illustrate this in

* Work supported by the U.S. Department of Energy, Office of Science, Office of Basic Energy Sciences, under Contract No. DE-AC02-06CH11357.

Fig. 1, where we define the hard edge locations by matching the integrated bending field such that

$$\int_{z_-}^{z_+} dz B_y(0, 0, z) = \int_{z_-}^{z_+} dz C_1(z) \quad (5)$$

$$= (z_+ - z_{\text{edge}}) \Pi_1(z_+) + (z_{\text{edge}} - z_-) \Pi_1(z_-),$$

where the step function $\Pi_1(z)$ is defined in terms of the Heaviside function as

$$\Pi_1 = C_1(z_+) \Theta(z - z_{\text{edge}}) + C_1(z_-) \Theta(z_{\text{edge}} - z). \quad (6)$$

The edge models for quadrupole and sextupole components are defined by z_{edge} and their maxima/minima at z_{\pm} , while the difference between the actual fields from Eqs. (1) and (2) and the hard edge model defines the fringe fields. The full particle motion is governed by the expanded, dimensionless Hamiltonian

$$\mathcal{H}(x, p, \delta; z) \approx \frac{(p_x + a_x)^2 \sec^3 \theta}{2(1 + \delta)} + \frac{p_y^2 \sec \theta}{2(1 + \delta)} - \delta + \delta \cos \theta + (p_x + a_x) \tan \theta + a_z, \quad (7)$$

while the fringe field corrections are defined by the difference of \mathcal{H} and the hard edge Hamiltonian

$$\mathcal{H}_0 = \frac{\sec^3 \theta}{2(1 + \delta)} p_x^2 + \frac{\sec \theta}{2(1 + \delta)} p_y^2 - \delta + \delta \cos \theta + p_x \tan \theta + x \frac{q}{p_0} \Pi_1(z) + (x^2 - y^2) \frac{q}{p_0} \Pi_2(z) + (x^3 - 3xy^2) \frac{q}{p_0} \Pi_3(z). \quad (8)$$

Our perturbation theory proceeds by first defining $\mathcal{B}_0(z|z_-)$ to be the unperturbed map from $z_- \rightarrow z$ associated with \mathcal{H}_0 . Then, the full map \mathcal{M} for $\mathcal{H}_0 + \mathcal{H}_1$ can be written using the “reverse factorization” [4] as $\mathcal{M} = \mathcal{B}_1(z|z_-) \mathcal{B}_0(z|z_-)$, where \mathcal{B}_1 accounts for \mathcal{H}_1 such that

$$-\frac{d}{dz} \mathcal{B}_1 = \mathcal{B}_1 (\mathcal{B}_0 : \mathcal{H}_1 : \mathcal{B}_0^{-1}) = \mathcal{B}_1 : \mathcal{H}_1^{\text{int}} : . \quad (9)$$

We diagram these maps in Fig. 1. The fringe field map \mathcal{F} obtains by sandwiching the full dipole field map \mathcal{M} between unperturbed dipole maps \mathcal{B}_0 to and from the edge:

$$\mathcal{F} = \mathcal{B}_0(z_-|0) \mathcal{M} \mathcal{B}_0(0|z_+) = \mathcal{B}_0(z_-|0) \mathcal{B}_1(z_+|z_-) \mathcal{B}_0(0|z_-). \quad (10)$$

Finally, the fringe field map at the hard edge is written using the Magnus operator $\mathcal{F} = e^{:\Omega_M:}$ with Lie generator

$$\Omega_M = -\int_{z_-}^{z_+} dz \mathcal{H}_1^{\text{int}}(z|0) + \frac{1}{2} \int_{z_-}^{z_+} dz \int_{z_-}^z d\zeta : \mathcal{H}_1^{\text{int}}(\zeta|0) : \mathcal{H}_1^{\text{int}}(z|0) + \dots \quad (11)$$

LONGITUDINAL FEEDBACK DYNAMICS IN STORAGE RINGS WITH SMALL SYNCHROTRON TUNES *

R. Lindberg, ANL, Argonne, IL 60439, USA

Abstract

We analyze the dynamics of multibunch longitudinal instabilities including bunch-by-bunch feedback under the assumption that the synchrotron tune is small. We find that increasing the feedback response does not always guarantee stability, even in the ideal case with no noise. As an example, we show that if the growth rate of a cavity-driven mode is of the order of the synchrotron frequency, then there are parameter regions for which the instability cannot be controlled by feedback irrespective of its gain. We verify these calculations with tracking simulations relevant to the APS-U, and find that the dynamics do not depend upon whether the longitudinal feedback relies on phase-sensing or energy-sensing technology. Hence, this choice should be dictated by measurement accuracy and noise considerations.

THEORY

We will investigate multibunch stability in the presence of longitudinal feedback. For simplicity we assume that the ring is uniformly filled, and that all perturbing wakefields are approximately constant over each bunch. In this case the complex frequency Ω describing multibunch oscillations of mode μ satisfies the following dispersion relation:

$$1 = \left[\frac{4i\pi I_{\text{tot}} \sigma_t^2}{\alpha_c (\gamma mc^2/e) \sigma_\delta^2 T_0} \sum_{p=-\infty}^{\infty} \omega_{p,\mu} Z_{\parallel}(\omega_{p,\mu}) - \frac{24\pi G \sigma_t^2}{\alpha_c^2 \sigma_\delta^2 T_0^2} \sum_{p=0}^{\infty} \mathcal{E}_p e^{ip\Omega T_0} \right] \times \int d\mathcal{J} \bar{F}(\mathcal{J}) \sum_{m=1}^{\infty} \frac{m^2 |z_m(\mathcal{J})/\sigma_z|^2}{[\Omega/\omega(\mathcal{J})]^2 - m^2}. \quad (1)$$

Here, I_{tot} is the total current, α_c is the momentum compaction, $\sigma_z = c\sigma_t$ and σ_δ are rms bunch length and energy spread, respectively, $T_0 = 2\pi/\omega_0$ is the revolution period, $\bar{F}(\mathcal{J})$ and $z_m(\mathcal{J})$ are the equilibrium distribution function of action \mathcal{J} and the m^{th} Fourier component of the longitudinal coordinate z , while for M bunches $\omega_{p,\mu} = \omega_0(pM + \mu) + \Omega$. The first term in square brackets includes the long-range wakefields, while the second contains the feedback of gain G and \mathcal{E}_p that we describe shortly.

We will illustrate the basic stability properties contained in Eq. (1) by restricting ourselves to a specific form for the long-range wakefield. In particular, we consider longitudinal instabilities driven by a single higher-order mode (HOM) in the rf system, in which case the sum over the long-range impedance can be limited to the single term where the HOM

resonance line most closely overlaps a revolution harmonic. Then, we can reduce the dispersion relation to

$$\frac{\alpha_c \sigma_\delta}{\sigma_t} = \left[2\Lambda \frac{i + \varpi}{1 + \varpi^2} + \frac{6\sigma_t G}{\alpha_c \sigma_\delta T_0^2} \sum_{p=0}^{\infty} \mathcal{E}_p e^{ip\Omega T_0} \right] \times \int d\mathcal{J} 4\pi \bar{F}(\mathcal{J}) \sum_{m=1}^{\infty} \frac{m^2 |z_m(\mathcal{J})/\sigma_z|^2}{[\Omega/\omega(\mathcal{J})]^2 - m^2}, \quad (2)$$

where we define the nominal growth rate Λ and normalized detuning ϖ in terms of the HOM shunt impedance R_s , quality factor $Q \gg 1$, and frequency ω_{HOM} via

$$\Lambda = \frac{\sigma_t \omega_{\text{HOM}} I_{\text{tot}} R_s}{2\sigma_\delta (\gamma mc^2/e) T_0}, \quad \varpi = 2Q \frac{\omega_{\text{HOM}} - p\omega_0 - \Omega}{\omega_{\text{HOM}}}. \quad (3)$$

We assume that the effect of the feedback is given by a finite impulse response (FIR) filter whose coefficients are determined by a least-square fit of the phase's derivative [1]:

$$\sum_{p=0}^{\infty} \mathcal{E}_p e^{ip\Omega T_0} = \sum_{p=0}^{N-1} \frac{(N-1) - 2p}{N(N-1)} e^{ip\Omega T_0}. \quad (4)$$

We will furthermore assume that the feedback samples the longitudinal motion over a “short” number of turns, so that NT_0 is much smaller than both the synchrotron period and the growth time of the instability. Then, we expand the feedback sum to lowest order in ΩT_0 , in which case our results match those for both the usually employed sin-wave FIR filter [2] and for a simple energy-detection based system; this is because all these feedbacks contribute to the dispersion relation as the derivative of the bunch position $\propto -i\Omega T_0$.

Let's first assume that the longitudinal rf potential is quadratic in z . The resulting simple harmonic motion has $2\pi\sigma_\delta\sigma_z\bar{F}(\mathcal{J}) = e^{-\mathcal{J}/\sigma_z\sigma_\delta}$ and $z_{\pm 1} = \sigma_z\sqrt{\mathcal{J}/2\sigma_z\sigma_\delta}$, so that the dispersion relation reduces to

$$\Omega^2 - \omega_s^2 = 2\omega_s \Lambda \frac{i + \varpi}{1 + \varpi^2} + \frac{6G}{T_0^2} \sum_{p=0}^{\infty} \mathcal{E}_p e^{ip\Omega T_0}. \quad (5)$$

Solutions to Eq. (5) give the complex frequencies Ω for a storage ring in which longitudinal feedback works to stabilize multibunch oscillations driven by a single higher-order cavity mode. While it is straightforward to solve numerically, we will make a few additional simplifications.

First, we assume that the width of the HOM resonance is much broader than the complex mode frequency, $\omega_{\text{HOM}}/2Q \gg |\Omega|$. The APS-U cavities have HOMs whose widths are typically a few kHz, while $|\Omega|/2\pi \sim \omega_s/2\pi \lesssim 400$ Hz. This implies that we can neglect the contribution of Ω to the detuning ϖ . Next, we assume that the FIR feedback filter retains a small number of turns such that both

* Work supported by the U.S. Department of Energy, Office of Science, Office of Basic Energy Sciences, under Contract No. DE-AC02-06CH11357.

UPDATE ON THE DEVELOPMENT OF A LOW-COST BUTTON BPM SIGNAL DETECTOR AT AWA*

W. Liu[†], C. Whiteford, D. S. Doran, E. E. Wisniewski, G. Chen, J. G. Power, P. Piot, S. Kim, X. Lu
High Energy Physics Division, Argonne National Laboratory, Lemont, IL, USA

Abstract

Single-pulse high dynamic range BPM signal detector has been on the most wanted list of Argonne Wakefield Accelerator (AWA) Test Facility for many years. Unique capabilities of the AWA beamline require BPM instrumentation with an unprecedented dynamic range, thus cost-effective solution could be challenging to design and prototype. Our most recent design, and the results of our quest for a solution, are shared in this paper.

INTRODUCTION

Beam position monitor is a device widely used on accelerator beamlines worldwide. It can provide information on beam centroid nondestructively. One can also obtain charge information from the signals with careful calibrations. For some applications, BPM might even provide the temporal distribution information of charged bunch. Researchers around the world have studied the properties of many different BPM configuration in detail and published many review papers. For detail and quantitative expression on the BPM properties, one can find them in those review papers [1-6]. As presented in the references, a typical BPM system consists of a customized signal pick-up device and specialized processing electronics. The processing electronics are usually specialized to the BPM signals of the specific pickups chosen based on the specific beam parameters of the specific facilities and are usually expensive.

AWA is a small accelerator research facility which has limited budget and resources. But since BPM is such a wonderful device, we would like to install them as many as possible on our beamlines. In order to fulfill our need with our limited budget and resources, we decided to design our own BPM signal processing electronics.

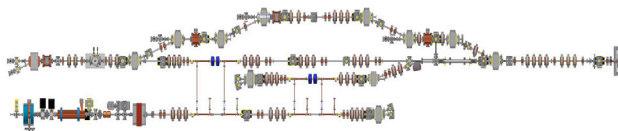


Figure 1: AWA beamline layout.

As shown in Fig. 1, there are many places on our beamline that can use the help of BPMs. With the help from BPMs, we will be able to monitor the beam positions on the beamline without using YAG screens, which gives us the opportunity to use feedback-control to stabilize and automatically tune the beam.

Currently at AWA, we have one stripline BPM pickup installed on our drive beam line right after the last linac.

This stripline BPM pickup was specially designed to maximize the signal response at 1.3 GHz, the L-band RF frequency of our RF system. The objective of this stripline BPM pickup is to enable us not only to obtain beam-position information but to obtain beam-phase information as well. We previously worked with Euclid TechLabs to develop such signal processing electronics, called Euclid BPPM funded by DoE 2009 SBIR Phase1 project under Contract # DE-SC0002513. The results were very promising but the project was cutoff due to lack of funding.

We also have few commercial in-flange button-type BPM pickups purchased from MDC Vacuum Products®. One is installed on our ACT (Argonne Cathode Test Stand) beamline, one on our EEX (Emittance Exchange) beamline and one on our Drive beamline. Some efforts were put into studying and characterizing the response of these button-type BPMs to our beam structure. Some preliminary efforts were also put into designing the signal processing circuitry [7].

Previous BPM signal-detector design efforts at AWA facility have been discussed in Refs. [8, 9]. In Ref. [8], three separate signal-detector design proposals were examined (RLC resonator-based circuit, half-wave rectifier with voltage-follower based circuit and modified peak-detector circuit). The final bench test and beam test results on those designs indicated that they were able to produce promising output results for beam charge-levels at or above 1 or 2 nC but were unsatisfactory in producing any meaningful results below those levels of charge. Based on some simulation studies, active filter using 2N2222 was proposed in that paper.

In Ref. [9], we presented the prototyping results of two active filter prototypes, one was using 2N2222 and another one was using 2SC4083. The 2N2222-based active-filter stretched out the BPM input-signal significantly to a FWHM width of approximately 3.5 ms. The peak-amplitude of the output-signal, as measured on the oscilloscope, was approximately 3 mV, a less-than-desired value for the incoming charge-beam of the experiment that had a charge-level of approximately 2 nC.

As reported in Ref. [9], the 2SC4083 based active filter prototype, comparing with the 2N2222 based prototype, can generate 20 times stronger output signal with only one third of the beam charge. For 0.5 nC beam, the output from the prototype was 60 mV. The performance was better than all other circuits we have tested, but it is still not good enough to declare the success. Search for the solution continues.

*Work supported by DOE Office of HEP and Office of BES.

[†] wmliu@anl.gov

MACHINE LEARNING FOR PREDICTING POWER SUPPLY TRIPS IN STORAGE RINGS*

I. Lobach[†], M. Borland, G. Fystro, A. Sannibale, Y. Sun
Argonne National Laboratory, Advanced Photon Source, Lemont, IL, USA
A. Diaw, J. Edelen, RadiaSoft, Boulder, CO, USA

Abstract

In the Advanced Photon Source (APS) storage ring at Argonne National Lab, trips in the magnet power supplies (PSs) lead to a complete electron beam loss a few times a year. This results in unexpected interruptions of the users' experiments. In this contribution, we investigate the historical data for the last two decades to find precursors for the PS trips that could provide an advance notice for future trips and allow some preventive action by the ring operator or by the PS maintenance team. Various unsupervised anomaly detection models can be trained on the vast amounts of available reference data from the beamtime periods that ended with an intentional beam dump. We find that such models can sometimes detect trip precursors in PS currents, voltages, and in the temperatures of magnets, capacitors and transistors (components of PSs).

INTRODUCTION

In the APS storage ring, trips in the magnet power supplies (PSs) lead to a complete electron beam loss about 7 times a year, on average. This results in unexpected interruptions of the users' experiments. This paper explores the possibility of using Machine Learning (ML) to give an advance warning about an impending PS trip, so that a preventive action can be taken by the operator or by the PS maintenance group. We analyzed two decades of historical data. Since the total number of recorded PS trips is relatively low (149), supervised ML methods cannot be used as they would be prone to overfitting. Instead, we focus on unsupervised anomaly detection methods, such as spectral residual saliency detection [1] and neural network autoencoders, which can be trained and tested on the vast amounts of available historical data.

HISTORICAL DATA

There is a spreadsheet with detailed records for each APS run dating back to 1997 [2]. The records include each beam fill time, each beam dump time, and the reason for the beam dump. We are interested in the records with an intentional beam dump (end of period) and in the records with a beam loss due to a magnet PS trip. More specifically, we focus on trips in the PSs for quadrupoles, sextupoles, horizontal and vertical correctors. The APS storage ring consists of 40 sectors. The total number of considered PSs is 1320 [3, 4]. Sev-

eral parameters of each PS and each magnet are constantly monitored and logged. We analyzed magnet temperatures, PS currents, voltages, capacitor temperatures, transistor temperatures. The capacitors are used to smoothen the input voltage. The transistors are used to regulate the currents in the magnets. Quadrupole and sextupole PSs have one transistor each. PSs for horizontal and vertical correctors have two transistors each, for positive and negative current. These parameters are logged at 1 point per 64 seconds, and the historical data go back to 2008. Another source of relevant data is the independent noise monitor [5] for the PS currents. Its raw-data acquisition rate is 100 Hz. However, only the processed data are logged. First, the mean and the mean absolute deviation (MAD) are calculated for every 500-sample window. Then, for the two obtained quantities, the minimum, the mean, and the maximum values are calculated in a 64-second long window. The 6 obtained process variables (MeanMin, MeanMean, MeanMax, MADMin, MADMean, MADMax) are logged at 1 point per 64 seconds for the most recent year. The older data are down-sampled to 1 point per 10 minutes and go back to 2001. PS data are labeled by the names of the corresponding magnets. Hence, the data may not always refer to the same physical PS, because of occasional PS replacements.

We analyzed the run history spreadsheets from 2001 to 2022 and found 629 beamtime periods that ended with an intentional dump and 149 beamtime periods that ended with a trip of one of the PSs (the records indicate which one). For further analysis, we pulled the data from the data archive for these beamtime periods and obtained 629 "reference" data files and 149 "trip" data files. These files can be as short as a half hour. However, most of them are several days long.

ANOMALIES IN TEMPERATURE DATA

The exact mechanism of most of the observed PS trips is not well understood. However, there are scenarios, in which a PS is programmed to trip, e.g., when the transistor temperature reading reaches 50 °C. Further, there are thermal switches on the magnets, which open and cause a trip at 71 ± 3 °C (water-cooled magnets) and at 95 ± 3 °C (air-cooled magnets). However, a thermal switch may open before the temperature reading reaches the manufacturer specified threshold, because the temperature is measured independently. Clearly, one could create an algorithm that warns the operator when the magnet temperature or the PS temperature crosses a certain threshold. However, we wanted to see whether there are more general anomaly detection methods that would not only be sensitive to higher-than-

* The work is supported by the U.S. Department of Energy, Office of Science, Office of Basic Energy Sciences, under Contract No. DE-AC02-06CH11357.

[†] ilobach@anl.gov

DEVELOPMENT OF A COMPACT 2D CARBON BEAM SCANNER FOR CANCER THERAPY*

B. Mustapha[†], J. Nolen, A. Barcikowski, Argonne National Laboratory, Lemont, IL, USA
 N. Tsoupas, Brookhaven National Laboratory, Upton, NY, USA
 V. Derenchuk, P. Osucha, ProNova Solutions, LLC, Maryville, TN, USA

Abstract

A novel trapezoidal coil 2D carbon beam scanner has been designed, and a prototype has been successfully developed and tested. The field performance of the magnet has been characterized and it is in excellent agreement with the simulations. A better than 1% field uniformity in both planes has been achieved within the useful aperture of the magnet. This represents a significant improvement over the prior art of the elephant-ear scanner design. A comparison of the two designs and the test results from the new trapezoidal-coil design will be presented and discussed. High power and online beam testing are planned in the future.

INTRODUCTION

In existing carbon ion and most proton beam gantries, the scanning magnets are placed prior to the last bend of the beam delivery system [1]. This requires the last gantry magnets to have a large aperture diameter of ~20 cm which greatly increases their mass and cost. Placing the scanning magnets in the final drift, as is presently implemented in the ProNova superconducting (SC) proton gantry [2], a next-generation carbon beam gantry can be much more cost effective. By demonstrating this technology with a working distance of ~3 m, it becomes feasible to implement SC carbon ion beam gantries with a footprint comparable to present day proton beam gantries [3]. For protons, this same scanner can double the field size or allow SC proton gantries and fixed beam delivery systems to be even more compact with a ~1 m working distance.

The scanners must have as short as possible working distance so that they can be placed after the last gantry bending magnet to enable the use of small aperture magnets. The concept of a 3D scan, in x-y, and energy is shown in Fig. 1 [4]. For compactness, the x-y scanners can be combined into a single combined function 2D scanner magnet. Combined with programmed intensity variation during the 3D scan, this method is known as Intensity Modulated Particle Therapy (IMPT).

SPECIFICATIONS AND DESIGN CHOICE

The general specifications for a carbon beam scanner magnet satisfying the requirements are shown schematically in Fig. 2 with more details listed in Table 1. While in most cases a 40 cm scanning field is not needed, some spine tumors require a wide field at least in one dimension.

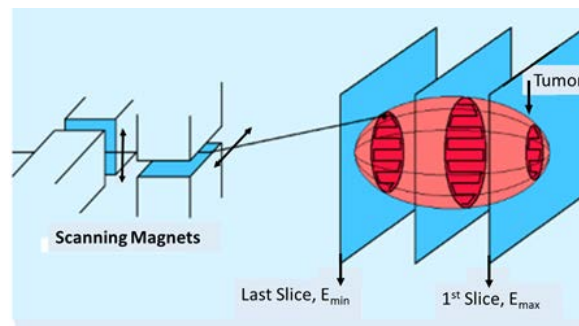


Figure 1: Concept of a 3D, x-y and depth scan of a tumor.

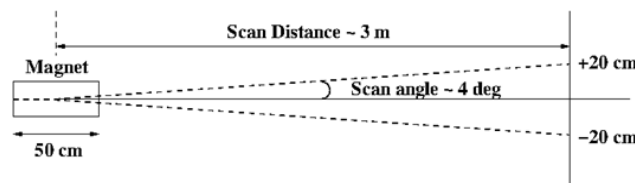


Figure 2: Schematic layout of 1D beam scanning using a 0.5 m long magnet with a working distance of ~3 m covering a +/- 20 cm field.

Table 1: Design specifications for a 2D carbon beam scanner magnet with ~3 m working distance and 40 cm scanning field.

Parameter	Value
Beam rigidity, T·m	6.6 (430 MeV/u C ⁶⁺)
x-y deflection angle, °	4.2 (40×40 cm at 3 m)
Bend radius, m	6.6
Peak field, T	1
Effective length, m	0.5
Good field area, cm	6
Scanning frequency, Hz	100

Based on these specifications, we have developed different design options for a compact 2D carbon beam scanner; the most promising were an elephant-ear design and a trapezoidal-coil design and selected the trapezoidal coil design for prototyping. The main criterion was the field uniformity in both planes, to avoid beam distortions due to non-linearity, which could affect the delivered dose conformity to the tumor during spot scanning. The trapezoidal coil design provides a better than 1% transverse field uniformity in both planes, while an equivalent elephant-ear design with rectangular coils [5] has asymmetric field uniformity of ~1% in one plane and ~9% in the other. We can clearly see this effect in Fig. 3, comparing both designs and

*This work was supported by the U.S. Department of Energy, under Contract No. DE-AC02-06CH11357. This research was supported through the DOE's Accelerator Stewardship program.

[†] brahim@anl.gov

SCU ENDS CONFIGURED AS PHASE SHIFTER*

M. Qian[†], Argonne National Laboratory, Lemont, IL, USA

Abstract

Phase shifters are usually needed in the interspace of a permanent magnet (PM)-based undulator array for purposes of phase matching when the field strength is changing. Unlike the PM-based undulators, the superconducting undulator (SCU) can change its end field with the help of varying currents in the end coils. By setting the end coil currents the phase-matching function could be realized, thus eliminating the need for standalone phase shifters, saving the interspace, as well as reducing the mechanical complexity of an undulator array. We developed a technique for determining the SCU end coil currents for phase shifting purposes and demonstrated it through numerical simulations. The procedure as well as the simulation results are described in this paper.

INTRODUCTION

In free electron laser (FEL) applications, undulators are installed in a line to form an undulator array. In the interspace between two undulator segments, there are elements such as phase shifter, quadrupole and steering magnets, and beam position monitor that take up longitudinal space. The packing fraction of an undulator array is defined as the ratio of the total length of the undulators to the total length of the whole array [1]. In most cases, a higher packing fraction is favored. To achieve a higher packing fraction without suppressing the interspace length, the hybrid permanent magnet undulators (HPMUs) for FELs can be up to 5 meters long. However, the lengths of the in-operating SCUs seldom exceed 1.5 m because of the engineering difficulties of fabricating a very long iron magnet core.

Given that the length of an individual SCU is limited, decreasing the interspace length should be considered. Unlike the HPMU cases, the end field of an SCU can be adjusted by independently powered coils. This opens the possibility of using the end field as a phase shifter. If the need for a standalone phase shifter can be eliminated, not only could the packing fraction be increased, but also the assembly of the SCU array would be significantly facilitated.

In this paper, we present our simulation experiments of configuring the adjustable SCU end coils as a phase shifter. We start with a technique to manipulate and optimize the trajectory in an SCU with the help of variable end coil currents, then we describe a feasible configuration using the end coils as phase shifters based on this technique.

*Work supported by LDRD funding from Argonne National Laboratory, provided by the Director, Office of Science, of the U.S. DOE under Contract No. DE-AC02-06CH11357.

[†] mqian@anl.gov

SIMULATION MODEL

Based on the symmetries of the magnetic field profile, an SCU can be categorized as an odd symmetrical configuration with even-numbered magnetic poles or an even symmetrical configuration with odd-numbered poles. In our study, a primary focus was given to the even symmetrical model.

The numerical experiments were carried out with the magneto-statics computer code OPERA3D [2], which is widely used in insertion device design and simulation. In the model environment the z -axis overlaps with the longitudinal direction of the SCU, x is the horizontal direction, and y is the main magnetic field direction.

The geometry of the SCU model is based on a previous device built at the APS [3]. The SCU has two soft iron cores; on each of them there are soft iron poles facing the gap. The coils are vertically wound on the cores. Figure 1 shows the 3D view of the OPERA model end part, while Table 1 presents the basic parameters of the model. Three end coils have adjustable currents; the ratios of these currents to the regular coil current are noted as c_1 , c_2 , and c_3 , respectively.

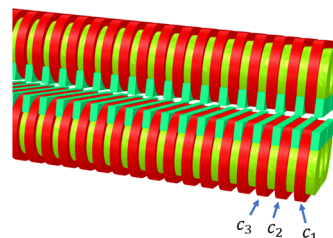


Figure 1: 3D view of the end part of the SCU OPERA model.

Table 1: Basic Parameters of the SCU Model

Parameter	Value	unit
Turns per coil	53	
Current	<588	A
Core and pole material	1008 soft iron	
Period length	21	mm
Gap	8	mm
Pole y^*z	4.9*4.4	mm
Core x^*y	100*32	mm

A global magnetic field in the SCUs was observed that caused a trajectory distortion [4]. This distortion is scaled to the square of the undulator length and is insignificant when the model is short. Thus, we set our simulation models to have 52 poles and a total length of 0.5 m, which is long enough to capture the main trajectory distortion.

MAGNETIC FIELD CALCULATION OF SUPERCONDUCTING UNDULATORS FOR A FEL USING MAXWELL 3D*

Y. Shiroyanagi[†], M. Kasa, Y. Ivanyushenkov
 Argonne National Laboratory, Lemont, IL 60439, USA

Abstract

An ANL-SLAC collaboration is working on design of a planar superconducting undulator (SCU) demonstrator for an FEL. As a part of this project, an SCU magnet prototype is planned to be built and tested. A planar SCU magnet consisting of a 1.0-m-long segment is being designed. Although OPERA is a standard tool for magnetic field calculation, ANSYS Maxwell 3D can also be used for a large and complex geometry. An ANSYS calculated magnetic field was benchmarked with the measured field profile of existing SCUs. This paper presents calculations of magnetic field and field integrals of 0.5-m-long and 1.0-m-long planar SCUs with a new end correction scheme. Then, an external phase shifter is also incorporated into the model. A crosstalk between a phase shifter and SCU magnetic structures is also presented.

INTRODUCTION

To meet FEL-SCU [1, 2] magnetic specifications, a straight trajectory is required. That means the angle (1st integral), total shift (2nd integral), and non-straightness (shape of the 2nd integral) of the trajectory must be minimized. Traditionally, correction was achieved by reducing the main turns and adjusting the current in the last two grooves at either end (two groove scheme) [3]. However, it tends to minimize either a shift or an angle, not both, and often takes higher correction current [4]. As the core becomes longer, its non-straightness increases and the optimal correction current for 2d and 3d models do not necessarily agree. Thus, a new end correction scheme is introduced [5]. By reducing the number of main turns in the last three grooves and using one or two correctors at the end grooves, optimal correction current is reduced, and the calculated trajectory becomes straight (three groove scheme).

MAGNETIC MODEL OF SCU WITH THREE GROOVE SCHEME

The three-groove scheme is applied to 21-mm-period SCU demonstrator model. The core material used is 1008 steel. Examples are shown for 2d and 3d models. Calculated 2nd integrals are compared for different lengths of SCUs.

Table 1 shows the undulator parameters for the demonstrator SCU. Figure 1 shows the end three grooves and three main grooves for the asymmetric case. The reduced main current is chosen to make the net ampere-turns close to zero.

Table 1: Undulator Parameters for the SCU

	Unit	Value
Period	mm	21
Periods	N	23.5 or 47.5
Groove dimension	mm	6.135*4.88
Magnetic gap	mm	8
Cond. diameter	mm	0.7
Full coil turns	N	53
main	A	588
1 st groove current	A	-6*main-15*corr1
2 nd groove current	A	+27*main-15*corr2
3 rd groove current	A	-47*main

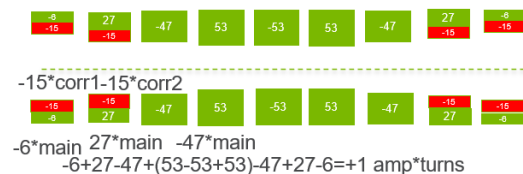


Figure 1: End correction scheme for all 2d and 3d models.

2d Model of a 21-mm-Period SCU

A static magnetic field is calculated using ANSYS Maxwell 2d. For all cases, symmetry boundary conditions are not used. Figure 2 (left) shows details of the end correctors of the SCU. Figure 2 (right) shows the 2d model geometry of 0.5-m-, 1.0-m-, and 1.9-m-long SCUs. Two end corrections are identical except in length.

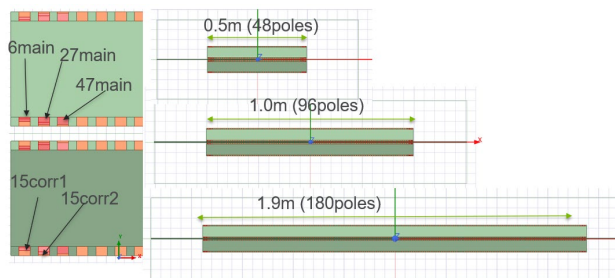


Figure 2: 2d models of 0.5-m-, 1.0-m-, and 1.9-m-long SCUs and details of the three end grooves.

Figure 3 (top) shows the calculated magnetic field of a 1-m-long SCU with optimal correction current (corr1=12.93A and corr2=12.58A). The peak field is 1.61 T (16100G). The 1st and 2nd integrals of this field are shown at the bottom.

* Work supported by the U.S. Department of Energy, Office of Science, under Contract No. DE-AC02-06CH11357.

[†] yshiroyanagi@anl.gov

MODEL-BASED CALIBRATION OF CONTROL PARAMETERS AT THE ARGONNE WAKEFIELD ACCELERATOR*

I. Sugrue^{†1}, P. Piot¹, N. Krislock, Northern Illinois University, DeKalb, IL 60115, USA
¹ also at Argonne National Laboratory, Lemont, IL 60439, USA
 B. Mustapha, J. Power, Argonne National Laboratory, Lemont, IL 60439, USA

Abstract

Particle accelerators utilize a large number of control parameters to generate and manipulate beams. Digital models and simulations are often used to find the best operating parameters to achieve a set of given beam parameters. Unfortunately, the optimized physics parameters cannot precisely be set in the control system due to, e.g., calibration uncertainties. We developed a data-driven physics-informed surrogate model using neural networks to replace digital models relying on beam-dynamics simulations. This surrogate model can then be used to perform quick diagnostics of the Argonne Wakefield accelerator in real time using nonlinear least-squares methods to find the most likely operating parameters given a measured beam distribution.

INTRODUCTION

Small-scale accelerator facilities supporting accelerator R&D have often limited diagnostics with operating parameters not precisely calibrated. The present research attempts to develop a digital twin model of the Argonne Wakefield Accelerator (AWA) where operating parameters dialed in the control system (with calibration errors) are calibrated against their physical values inferred from a Physics-informed surrogate model [1]. In this paper we discuss the development of a surrogate model using the Object-Oriented Parallel Accelerator Library (OPAL) which simulates the beam dynamics in the AWA beamline [2]. Our initial focus is to develop a digital twin of the beam-generation and acceleration section diagrammed in Figure 1. The section consists of an RF-gun followed by a linac (L1). The beamline incorporates 3 solenoid magnets (BF, M, and LS1). This required training a neural network to predict the outputs of 9 control parameters (the solenoid-magnet BF and M currents, the laser spot size on the photocathode, the phase and amplitudes of the RF gun and L1, and the transverse misalignment of L1) in the form of an image representing the transverse beam distribution captured at the scintillating screen YAG1. The goal was to gather data from OPAL, and train a network to predict the output that OPAL produced. After doing so, the same network was to be applied to the accelerator itself so that given an image one can infer the values of the 9 control parameters. Many mathematical techniques were used to aid in the creation and training of the neural network, which will be described in subsequent sections of this paper.

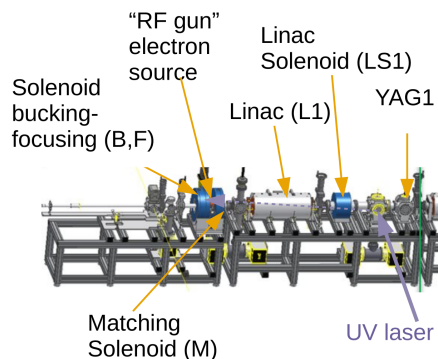


Figure 1: Overview of the AWA RF-gun and first linac considered for our surrogate model. The beam propagates from left to right.

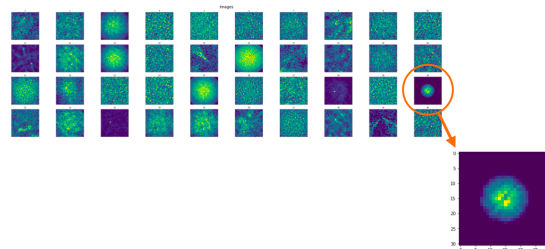


Figure 2: Unfiltered data set of YAG images. A good image was identified and isolated.

DATA FILTERING

Inputs of the Neural Network are 9 control parameters as vectors in \mathbb{R}^9 , and our outputs are YAG images, uploaded as 32×32 real-valued matrices. The data gathered from OPAL was initially randomly generated. However, this resulted in “unusable” data, and much of it had to be discarded. The useful data was identified based on whether the beam fit entirely within the dimensions of the generated image. To sort the data based on this criteria, we displayed a collection of images and searched for one that matched this description. Once this image was identified (see Figure 2), the first 400 images that were closest in norm were selected. We also rotated each image 90 degrees and copied it to make the dataset larger (size 1600) for training.

PRINCIPAL COMPONENT ANALYSIS

The application of Principal Component Analysis (PCA) to our images was inspired in part by [3]. To begin, we have a collection of 1600 matrices (images), each with dimension 32×32 . We subtract the mean image from each image to center the data, then flatten each image so that we have

* This work was supported by the U.S. Department of Energy, Office of Nuclear Physics, under contract DE-AC02-06CH11357 with ANL.

[†] isugrue@anl.gov

THE ADVANCED PHOTON SOURCE LINAC EXTENSION AREA BEAMLINE*

K. P. Wootton[†], W. J. Berg, J. M. Byrd, J. C. Dooling, G. Fystro, A. H. Lumpkin,
 Y. Sun, A. A. Zholents, Argonne National Laboratory, Lemont, IL, USA
 C. Hall, RadiaSoft LLC, Boulder, CO, USA

Abstract

The Linac Extension Area at the Advanced Photon Source is a flexible beamline area for testing accelerator components and techniques. Driven by the Advanced Photon Source electron linac equipped with a photocathode RF electron gun, the Linac Extension Area houses a 12 m long beamline. The beamline is furnished with YAG screens, BPMs and a magnetic spectrometer to assist with characterization of beam emittance and energy spread. A 1.4 m long insertion in the middle of the beamline is provided for the installation of a device under test. The beamline is expected to be available soon for testing accelerator components and techniques using round and flat electron beams over an energy range 150–450 MeV. In the present work, we describe this beamline and summarise the main beam parameters.

INTRODUCTION

The Linac Extension Area (LEA) at the Advanced Photon Source (APS) is an electron beamline for the demonstration of accelerator technologies, instrumentation and techniques. The beamline was designed to transport round and flat electron beams over an energy range 150–450 MeV.

In the present work, we outline the parameters of the three electron beam sources to LEA. We outline the beamline hardware and lattice. We conclude with an outlook on accelerator technologies and techniques that could be tested using the LEA beamline.

ELECTRON SOURCES

The APS linac provides electron beams to the injector complex, including LEA. Three electron sources can be configured to deliver electron beams to LEA, in different charge configurations. These include: a photocathode (PC) radiofrequency (rf) gun, two thermionic cathode (TC) rf guns, and the Particle Accumulator Ring (PAR). Parameters of beams from different electron sources are summarised in Table 1.

Photocathode RF Gun

The PC gun is the principal electron source for LEA [1–6]. An Nd:Glass laser oscillator and amplifier provides ps laser pulses at 1053 nm wavelength [7]. The laser wavelength is frequency-doubled twice to 263 nm using second harmonic

Table 1: Parameters Of Beams From The Electron Guns And PAR

Parameter	Units	PC	TC	PAR
Charge per cycle	nC	0.3	1.0	20
Bunch charge	nC	0.3	0.007	20
Bunch length	ps	1	1	1000
Bunches per cycle	...	1	29	1
Bunch spacing	ns	...	0.35	...
Repetition rate	s ⁻¹	6	30	1

generation in beta barium borate crystals. The electron bunch charge from the PC gun is typically up to ~0.3 nC.

Thermionic Cathode RF Gun

Two TC guns are the principal injectors for the APS injector complex [8–11]. The 2856 MHz rf frequency TC guns are typically operated providing a train of electron bunches of ~1 nC total train charge, over a bunch train duration of ~10 ns.

Particle Accumulator Ring

One interesting feature of the APS accelerator complex stems from its original design as a positron accelerator chain. Hence the injectors include the Particle Accumulator Ring (PAR), which is operated as an electron beam damping and accumulator ring [12].

Electron beam from the TC gun would be accumulated in the PAR, before transporting the extracted beam to LEA. This represents an electron source for experiments at LEA with high electron bunch charge (≤ 20 nC), for applications or experiments where ~1 ps electron bunch durations are not required.

Interleaving Beam Operations

The APS linac and injectors principally support injection into the APS storage ring, including top-up operation of the storage ring. Typical top-up intervals at the APS storage ring are 1–2 min. The injectors have been configured to support interleaving of the electron sources between directing beam to the storage ring for top-up (few seconds per minute), and to LEA [13–15].

LINAC EXTENSION AREA BEAMLINE

The longitudinal positions of the LEA beamline components are summarised in Table 2. The principal magnetic elements are quadrupole magnets, horizontal and vertical

* Work supported by the U.S. Department of Energy, Office of Science, Office of Basic Energy Sciences, under Contract No. DE-AC02-06CH11357.

[†] kwootton@anl.gov

A DISTRIBUTED BEAM LOSS MONITOR BASED UPON ACTIVATION OF OXYGEN IN DEIONISED COOLING WATER*

K. P. Wootton[†], Argonne National Laboratory, Lemont, IL, USA

Abstract

We propose a novel beam loss detection scheme whereby activation of deionised cooling water is used to observe elevated radiation around the APS storage ring. This is based on radioactivation of oxygen within deionised cooling water by gamma rays above 10 MeV and neutrons above 15 MeV. Losses would be detected using a gamma ray detector monitoring deionised water flow out of the accelerator enclosure. We anticipate that this could be used to provide a segmented, distributed loss monitor system covering the accelerator components closest to locations where radiation is generated.

INTRODUCTION

Particle accelerators are designed to produce beams of collimated ionising radiation. Consequently, when lost, these beams produce showers of particles, including ionising radiation. In order to diagnose accelerator faults, protect people and equipment, ionising radiation monitors ('loss monitors') have been used as diagnostics for accelerators all around the world [1].

Loss monitors can be classified a number of ways. They can be passive and integrate total dose over a long period of time (typically up to months), or have an active detector readout that provides close to real-time measurement of the radiation. They can also be classified as either a point detector (detecting the radiation at a single point), or distributed (detecting radiation over some larger area or distance) [2, 3]. A long ion chamber loss monitor was also designed for the Advanced Photon Source (APS) [4, 5].

The Advanced Photon Source (APS) has Cherenkov loss monitors [6]. Several fibre-based distributed loss monitors have also been tested in the Particle Accumulator Ring and at Storage Ring insertion devices [7]. Both of these systems are fast: able to detect losses within a single turn of the APS storage ring.

We propose a novel detection scheme whereby activation of deionised cooling water is used to observe elevated radiation around the APS storage ring. This is a technique proposed for detection of neutrons at the International Thermonuclear Experimental Reactor (ITER) [8]. In the present work, we summarise the relevant theory, we describe deionised water circuits for the APS storage ring, briefly discuss the time-resolution of the system, and outline a proposed experiment using the APS storage ring.

* Work supported by the U.S. Department of Energy, Office of Science, Office of Basic Energy Sciences, under Contract No. DE-AC02-06CH11357.

[†] kwootton@anl.gov

THEORY

Cooling water activation is routinely considered as part of the safety assessment of accelerators [9, 10]. Such analyses readily show that activation of deionised water at light source facilities does not present a significant hazard to human health.

Monitoring of cooling water for fission and fusion reactors is not new [11–15]. In particular, it appears that there are a few principal activation reactions of light nuclei in deionised cooling water that may be usable as a distributed loss monitor [16].

In particular, we consider the reactions $^{16}\text{O}(\gamma, n)^{15}\text{O}$ and $^{16}\text{O}(n, p)^{16}\text{N}$. The reaction $^{16}\text{O}(\gamma, n)^{15}\text{O}$ was assessed as the principal radioactivation nuclide present in the APS deionised water system during accelerator operation [17]. The reaction $^{16}\text{O}(n, p)^{16}\text{N}$ appears to be important for reactors, with principally a neutron flux. But this reaction may be relevant at high-energy electron storage rings such as APS [16]. Properties of both reactions are summarised in Table 1 below [8, 18].

We would plan to detect gamma rays as decay products of these reactions. ^{15}O decays via positron emission to ^{15}N . The positron annihilates with an electron to produce a pair of 511 keV gamma ray photons [19]. The disintegration of ^{16}N emits gamma ray photons of energy 6.13 MeV (68.8%) and 7.12 MeV (4.7%) [8]. In the absence of energy threshold discrimination, it appears that activity resulting from ^{15}O may dominate a measured count rate [13, 16].

DEIONISED WATER CIRCUITS AT THE ADVANCED PHOTON SOURCE STORAGE RING

Several water circuits are available to measure [20]. Essentially, deionised water for the storage ring is served by a centralised 'primary' system, which distributes water to multiple 'secondary' systems around APS. At APS, there is approximately one secondary system per sector. It appears that there are two circuits of interest: one is the deionised water that goes into the accelerator enclosure to cool accelerator components, and the other circuit is used to cool the magnet power supplies. Additionally, there is also an aluminum deionised water circuit which could be considered. We are principally interested in the 'secondary' circuit, supplying water to the accelerator magnets. The connection between the primary and secondary systems are illustrated schematically in Fig. 1 below.

In order to maintain pressure along the secondary circuit, the diameter of the deionised water piping within the accelerator tunnel gradually reduces from 4" to 1" diameter along the length of a sector. For a given loss event, this could

SUBLINEAR INTENSITY RESPONSE OF CERIUM-DOPED YTTRIUM ALUMINIUM GARNET SCREEN WITH CHARGE*

K. P. Wootton[†], A. H. Lumpkin, Argonne National Laboratory, Lemont, IL, USA

Abstract

Swap-out injection to the Advanced Photon Source Upgrade storage ring necessitates the injection of ~ 17 nC electron bunches at 6 GeV. To aid with machine tune-up and to measure the beam size, diagnostic imaging screens are envisaged at several locations in the beam transport line from the booster synchrotron to the storage ring. As such, it is important to determine whether the response of these screens to charge is linear. In the present work, we examine the effect of sublinear intensity quenching of a Cerium-doped Yttrium-Aluminium-Garnet scintillator screen. A 1.3 megapixel FLIR BlackFly monochrome digital camera was used to image the beam at the scintillator. At 7 GeV beam energy leaving the booster, over the charge densities investigated ($\rho \leq 10$ fC μm^{-2}), an approximately 10% reduction of the imaging intensity due to quenching of the scintillator was observed.

INTRODUCTION

Saturation of scintillator screens has represented a challenge for beam imaging at many facilities – in particular linacs – for example recently at Euro-XFEL [1]. At the Advanced Photon Source (APS), prior work on scintillator linearity included experiments on scintillators using the electron linac [2, 3]. Options of imaging techniques for beam profile monitors in the Booster-To-Storage Ring (BTS) transport line have also been considered [4, 5].

This prompts the question: with high-charge bunches through the BTS transport line for the Advanced Photon Source Upgrade (APS-U), will scintillator linearity with charge be a significant detrimental effect? In the present work, we evaluate the intensity response of a Cerium-doped Yttrium-Aluminium-Garnet (Ce:YAG) scintillator screen as a function of incident electron beam intensity. In particular, we evaluate whether charge linearity will inhibit accurate beam size measurements using the profile monitors.

SCINTILLATOR QUENCHING

Scintillator quenching occurs when the charge density of an incident beam depletes the vacancies in the crystal, and the crystal does not produce light output at a rate proportional to the input charge density [6–8]. We consider limits to quenching of the scintillator along the theory of Birks [9]. This results in approximate upper charge density limits of 16 fC μm^{-2} for LYSO scintillators [10], and 20 fC μm^{-2} for YAG:Ce scintillators [11]. Quenching is possible in

Chromox ($\text{Al}_2\text{O}_3:\text{Cr}$), however contemporary applications of Chromox scintillators for imaging are typically proton rather than electron beams. Optical Transition Radiation (OTR) has no quenching limit: the limit is probably the damage threshold of the material surface. In practice, if an electron bunch is short (\sim tens of fs duration), the practical limit for OTR is probably the presence of Coherent Optical Transition Radiation (COTR), which can potentially exceed the intensity of an OTR signal [12]. Even for bunches of \sim ps duration, COTR will occur when there is microbunching, or if there is a narrow current spike.

Quenching of the scintillator reduces the light output of the scintillator at locations on the screen with highest charge density. In effect, this results in fitting the ‘tails’ of the distribution, and essentially it appears that the image of the beam on a scintillator is larger than the rms electron beam size. A useful comparison of the relative performance of different scintillator materials is in Ref. [13].

METHOD

In the present work, we use a 7 GeV electron beam coming from the booster, imaged using the fluorescent screen BTS:FS3 [14].

Charge Density

We evaluate the electron beam size as a bivariate Gaussian distribution, in order to quantify the areal charge density.

The equation of a bivariate Gaussian distribution in coordinates x_i , with means μ_i , and standard deviations σ_i is given by [15]:

$$p = \frac{1}{2\pi\sigma_1\sigma_2} \left(-\frac{1}{2\sigma_1^2} (x_1 - \mu_1)^2 - \frac{1}{2\sigma_2^2} (x_2 - \mu_2)^2 \right). \quad (1)$$

Hence an electron beam with a profile that is Gaussian in two dimensions with root mean square beam sizes σ_1, σ_2 , we can describe the peak electron charge density ρ by:

$$\rho = \frac{q}{2\pi\sigma_1\sigma_2}. \quad (2)$$

RESULTS

Regular Beam

We acquired images of the electron beam using the normal Courant-Snyder lattice parameters using BTS:FS3 at charges up to 4.6 nC. Images of the beam on the BTS:FS3 scintillator as a function of charge are illustrated in Fig. 1.

The electron beam distribution was fitted using a bivariate Gaussian distribution. Beam sizes in both horizontal and vertical planes are plotted in Fig. 2. Peak values of the intensity at each charge level are plotted in Fig. 3.

* Work supported by the U.S. Department of Energy, Office of Science, Office of Basic Energy Sciences, under Contract No. DE-AC02-06CH11357.

[†] kwootton@anl.gov

APPLICATIONS OF MACHINE LEARNING IN PHOTO-CATHODE INJECTORS

A. Aslam¹, S. G. Biedron²

¹Department of Electrical and Computer Engineering, ²Department of Mechanical Engineering,

^{1,2}University of New Mexico, Albuquerque, NM, USA

M. Babzien, Brookhaven National Laboratory, Upton, NY, USA

Abstract

To configure a photoinjector to reproduce a given electron bunch with the desired characteristics, it is necessary to adjust the operating parameters with high precision. The fine tunability of the laser parameters are of extreme importance as we try to model further applications of the photoinjector. The laser pulse incident on the photocathode critically affects the electron bunch 3D phase space. Parameters such as the laser pulse transverse shape, total energy, and temporal profile must be controlled independently, any laser pulse variation over both short and long-time scales also requires correction. The ability to produce arbitrary laser intensity distributions enables better control of electron bunch transverse and longitudinal emittance by affecting the space-charge forces throughout the bunch. In an accelerator employing a photoinjector, electron optics in the beamline downstream are used to transport, manipulate, and characterize the electron bunch. The adjustment of the electron optics to achieve a desired electron bunch at the interaction point is a much better understood problem than laser adjustment, so this research emphasizes laser shaping.

INTRODUCTION

Delivering a laser pulse to the photocathode typically involves several optical elements to transport the pulse from the remote laser area to the electron gun. In addition, shaping optics are usually placed close to the photocathode, and diagnostic elements are also as close to the photo-emission gun as possible to provide accurate measurements of laser parameters on the photocathode. Copper photocathodes are very robust and long-lived in operation, and therefore are attractive for facilities requiring high availability. Work functions for most practical metals are 3-4 eV, and so UV laser pulses are used to generate photoemission, with typical wavelengths between 250-300 nm. This places stringent requirements on optical fabrication tolerances that are rarely achieved in practice. Moreover, at high current photoinjector beam photocathode and its uniformity is disturbed through ion bombardment [1] and increases vacuum pressure which thereby changes and alters the electron density from a given laser shape. More specifically, wavefront distortion at each optical surface of even 1/20th wave, corresponding to less than 15 nm, can lead to laser intensity modulation of 10% or more through diffraction, which then degrades electron bunch emittance. Partial mitigation of this and other detrimental effects is achieved using Fourier relay imaging throughout the laser system and transport

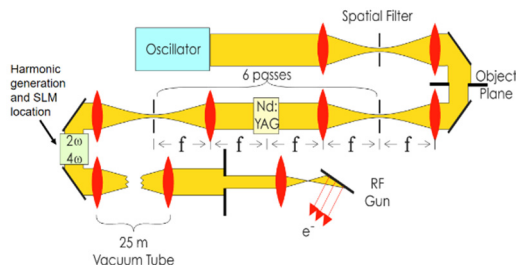


Figure 1: Facility configuration.

optics. This optical configuration as shown in Fig. 1, consists of a series of image planes transferred through the system by lens pairs in a 4f arrangement. An initial object plane is repeatedly imaged to critical elements such as amplifiers and harmonic generation crystals in the laser system, and finally to the photocathode. This will also enable the use of a spatial light modulator (SLM) between the two harmonic generation crystals for intensity control of the second harmonic of the ATF Nd:YAG laser at 532 nm. Subsequent fourth harmonic generation and image relaying will allow the profile at the photocathode to be controlled and optimized.

Li *et al.* demonstrated that ultraviolet laser transverse profile shaping could be utilized to improve X-ray free electron laser performance [1]. The authors employed a digital micromirror device to control the shape of a 253 nm drive laser at the linear coherent light source. However, due to the low damage threshold of the digital micromirror in the UV, the work is limited in its applications. On the other hand, Maxson *et al.* [2] used a SLM for shaping the drive laser of a dc photoemission gun. The authors created a simple shaping algorithm which results in a detailed transverse laser shaping with very high fidelity. An active feedback system was put in place which would take the unshaped electron beam image, and then create accurate detailed laser shaping further contributing to better efficiency. In this project we aim to use a liquid crystal based SLMs to control the transverse shape of the second harmonic of a Nd:YAG laser at 532 nm.

In order to enable optimization of laser profile for a specific photoinjector and electron beam parameters, a learning phase is required to train the neural network. Two methods may be used for the training process. First, an image of the photocurrent can be formed downstream with the magnetic optics that reproduces the emission profile at the photocathode. This profile can then be recorded by a phosphor screen and a camera. Image analysis will then permit the quality of fit between the ideal and measured

LANSCCE MODERNIZATION PROJECT AT LANL*

D. V. Gorelov[†], J. Barraza, D. A. Dimitrov, I. N. Draganic, E. Henestroza, S. S. Kurennoy
 Los Alamos National Laboratory, Los Alamos, NM, USA

Abstract

In the framework of LANSCCE Accelerator Modernization Project (LAMP) preliminary research and evaluation of critical technology elements it was found that the proposed RFQ design had not been yet demonstrated experimentally worldwide. Such an RFQ should combine the ability of traditional light ion RFQs, and flexibility of acceleration pre-bunched beams, like RFQs for heavy ions.

Proposed RFQ should be able to accelerate beams with 35mA beam current and at the same time preserve prescribed macro-bunch time structure required by experiments. New algorithms for RFQ geometry generation have been proposed and optimization algorithms are being developed at LANL.

LAMP technology demonstration plans also include development of new set of electrodes for our RFQ test stand that will allow us to demonstrate the critical technology in laboratory experimental setup with low duty factor and low energy.

LAMP PROJECT AT LANL

The LANSCCE Modernization Project (LAMP) is now at planning stage, and its CD-0 is expected this year. The LAMP goal is to replace the obsolete front end (FE) of the LANSCCE linac with a modern reliable front end [1, 2]. The existing FE evolved over the 40+ years and now provides five different beam flavors (beam species – protons and H⁻ ions, various beam currents, different beam pulse structures) for various end users. However, it is based on the obsolete Cockcroft-Walton (C-W) high-voltage injectors, and multiple components are in the near-failure state and cannot be readily replaced. The threshold requirements for the new injector are to provide reliably the presently available five beam flavors [1, 2]. The present conceptual design of the new front end is based on a single radio-frequency quadrupole linac (RFQ) that will accelerate all five beam flavors to 3 MeV [1, 2].

The RFQs are widely used, and their design and technology are well developed. However, for the beam currents comparable to the ones at LANSCCE, they are usually designed and optimized for a single beam flavor with continuous injection into RFQ, e.g., [3, 4]. Alternatively, there are multi-species RFQs that can preserve complicated pre-buncher beam structure, but only for very low beam currents typical for heavy ion beams, e.g., [5].

The proposed FE concept includes novel RFQ that combines the features of the two RFQ types mentioned above and can be considered critical technologies.

* This work is supported by experimental programs at LANSCCE
[†] gorelov@lanl.gov

Figure 1 shows the schematic view of the LANSCCE facility, and the Fig. 2 – LAMP upgrade close-up, which also includes DTL upgrade (not shown in the Fig. 2).

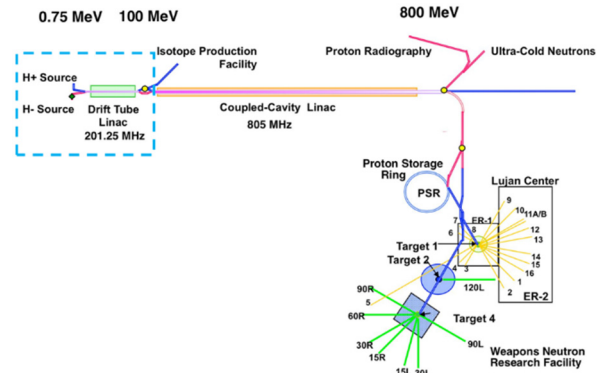


Figure 1: Schematic picture of the LANSCCE facility.

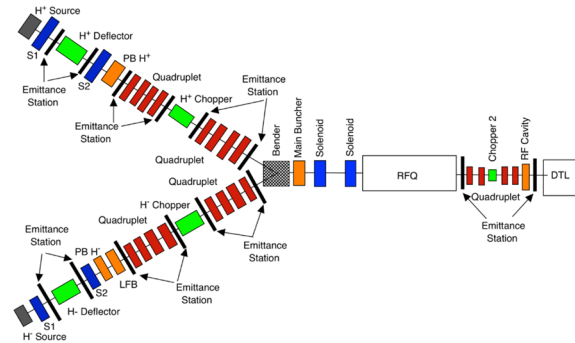


Figure 2: Schematic picture of the LAMP upgrade, including DTL.

RFQ BEAM DYNAMICS AND GEOMETRY GENERATION

The most prominent Critical Technology Element in LAMP project is the RFQ with the set of requirements unprecedented in any other RFQ accelerator design worldwide. New specific design procedure and algorithm were developed to meet the RFQ geometry requirements. In this contribution the proposed procedure and major parts of the developed algorithm are presented, and the preliminary longitudinal beam dynamics (BD) results are discussed.

The major difference of the proposed RFQ, compared to existing high current light ions RFQs [3, 4], is the requirement to start with the pre-bunched beam and preserve pre-existing time structure of the macro pulses or beam bunch trains in the RFQ and in the following DTL. At the same time, the beam loss and the beam halo formation requirements are usual for high beam current RFQs, and stricter compared to the heavy ion RFQs [5], that were designed to

NOVEL RF PHASE DETECTOR FOR ACCELERATOR APPLICATIONS

J. M. Potter[†], JP Accelerator Works, Inc., Los Alamos, NM, USA

Abstract

A novel phase detector has been developed that is suitable for use in an rf phase locked loop for locking an rf source to an rf accelerator structure or phase locking the accelerator structure to a fixed or adjustable frequency rf source. It is also useful for fast phase feedback to control the phase of an accelerator rf field. The principle is applicable to a wide range of frequencies and amplitudes. The phase is uniquely and unambiguously determined over 360°, eliminating the need for external phase shifters or phase references. The operation of this phase detector is described in detail. An application is described that uses a DDS-based LLRF source as the rf input to a high-power rf system.

THEORY OF OPERATION

Introduction

Phase locked loops are often used for frequency control of accelerators. What is required is to generate an error signal that passes linearly through zero at the desired frequency. This usually involves a phase detector with a reference phase that must be set to zero at the operating frequency, compensating for the phase shift in external components. There are systems that measure phase with timed phase detectors that use a reference frequency to obtain sine and cosine data.

We describe an analog/digital phase detector that measures the phase over a 360° range without an external phase reference and can be used to phase lock an rf source to a cavity or vice versa. This eliminates complicated setups since the circuit can be used to phase lock at any angle.

Phase Detector Circuit

Figure 1 is a schematic for a coupled line 3 dB hybrid coupler. The schematic shows how the outputs are related to the inputs for the lossless case. For a real hybrid coupler, the attenuations to each output don't necessarily match and there can be a few degrees phase error.

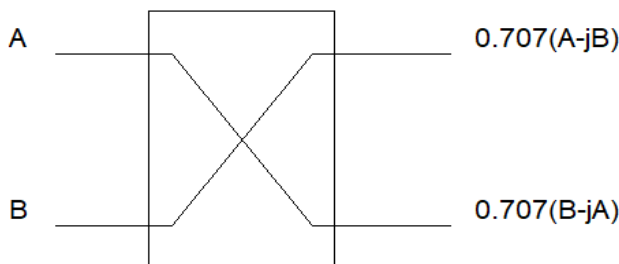


Figure 1: Hybrid coupler outputs relative to inputs.

Figure 2 shows the complete rf circuit of the JPAW phase detector.

[†]jpotter@jpaw.com

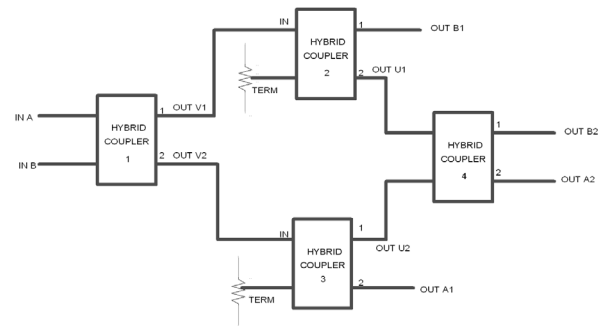


Figure 2: JPAW phase detector circuit.

The circuit has two inputs, A and B, and four outputs A1, B1, B2, and A2. Intermediate signals are labeled V1, V2, U1, and U2.

From the definition of a lossless, perfectly balanced 3dB hybrid coupler [1]

$$V1 = \frac{1}{\sqrt{2}}(A - jB) \quad \& \quad V2 = \frac{1}{\sqrt{2}}(B - jA).$$

The outputs B1 and A1 are

$$B1 = \frac{1}{2}(A - jB) \quad \& \quad A1 = -\frac{1}{2}(A + jB).$$

Outputs B2 and A2 are

$$B2 = -\frac{1+j}{2\sqrt{2}}(B + A) \quad \& \quad A2 = \frac{1+j}{2\sqrt{2}}(B - A).$$

We then define S and C as:

$$S = |A1|^2 - |B1|^2 = A1A1^* - B1B1^* = \frac{1}{2}jA(B - B^*),$$

$$C = |A2|^2 - |B2|^2 = A2A2^* - B2B2^* = \frac{1}{2}A(B + B^*).$$

With inputs A and B

$$A = A_0 \quad \& \quad B = B_0(\cos(\phi) + j \sin(\phi)),$$

we see that

$$S = A_0B_0 \sin(\phi) \quad \& \quad C = A_0B_0 \cos(\phi).$$

Since we can directly calculate $\sin(\phi)$ and $\cos(\phi)$ we can uniquely determine the phase angle over a full 360° range. These simple calculations can be performed by a microcontroller or FPGA.

PHASE DETECTOR APPLICATION

Low Level RF Source

One application of the phase detector is in a Low Level RF (LLRF) source for an rf linear accelerator. To create a phase-locked rf signal source we need to measure the initial phase angle and compare subsequent measurements to the initial measurement to generate an error signal. The error signal is then used to correct the frequency.

A PERSONAL HISTORY OF THE DEVELOPMENT OF THE LAMPF/LANSCE ACCELERATOR

J. M. Potter[†], JP Accelerator Works, Inc., Los Alamos, NM, USA

Abstract

The LAMPF/LANSCE accelerator has now been operational for 50 years. I arrived as a LASL employee in Group P11 in April 1964 at the beginning stages of its development. I participated in the development of the resonant coupling principle and went on to develop tuning procedures for the 805-MHz coupled cavity linac (CCL) structures and the post-stabilized drift tube linac (DTL). The resonant coupling principle is now well established as the basis for rf linear accelerators worldwide. I will discuss the development and building of the accelerator from my viewpoint as a member of a large, dedicated team of physicists, engineers, technicians, and support personnel.

DISCOVERY OF RESONANT COUPLING

Introduction

I came to Los Alamos in April 1964 with a brand-new BS in Physics from the University of Illinois to be the 19th member of Group P11 [1], which was in the beginning stages of designing a proton accelerator for meson physics research, Fig. 1.

NEW HIRES

James Martin Potter, Peoria, Illinois,
P-11.

Figure 1: Entry in the June 1964 edition of The Atom.

The Cloverleaf Structure

My initial job was measuring the mode spectrum of a sheet metal model of an 805 MHz Cloverleaf accelerator. Figure 2 shows the basic Cloverleaf geometry [2]. Note that the lobes are rotated 45° between cells to create a p-mode accelerating structure.

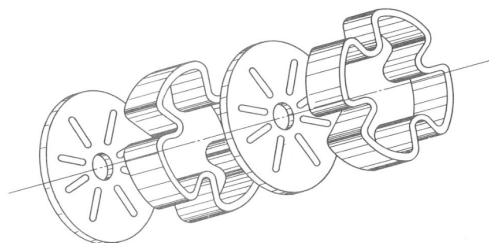


Figure 2: Basic 800 MHz Cloverleaf geometry.

Figure 3 is a photo of the 21-cell sheet metal Cloverleaf structure used for low power rf testing [2]. It was called a “cold” model because it was not intended for operation with high power rf.

[†] jpotter@jpaw.com

Figure 4 is a plot of the measured power flow phase shift along the 21-cell cold model when driven in cell 1 [2]. The solid curve is the theoretical phase shift based on a calculation of an effective coupling constant of 0.94 based on a fit to the mode spectrum at the p-mode.

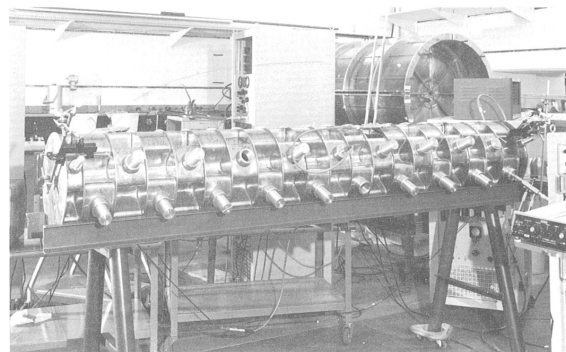


Figure 3: 21-cell Cloverleaf “cold” model.

The power phase shift is proportional to the square of the number of cells divide by the product of the coupling constant and the Q, based on the singly periodic coupled circuit theory.

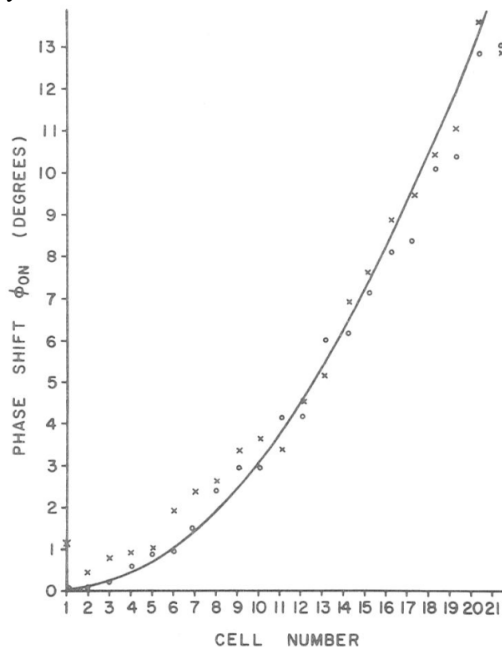


Figure 4: Measured and theoretical power flow phase shift in the 21-cell cold model.

The mode spectrum of the 21-cell cold model is plotted in Fig. 5 [2]. The stopband and upper passband are due to the resonant frequency of the slots. The slot frequency is close enough to the p-mode to affect the properties of the structure. Despite the large effective coupling constant, the passband is still quadratic near the p-mode resulting in high sensitivity to cell frequency errors. The tuning of the

UPGRADE FROM ADCs WITH CENTRALLY SCHEDULED TRIGGERS TO CONTINUALLY TRIGGERED WAVEFORM DIGITIZERS*

S. A. Baily[†], B. C. Atencio, A. J. Braidó, C. D. Hatch, J. O. Hill, M. S. Johnson, L. S. Kennel, M. Pieck, L. E. Walker, H. A. Watkins, E. E. Westbrook, K. Xu, D. D. Zimmermann
 Los Alamos National Laboratory, Los Alamos, NM 87545, USA

Abstract

The Los Alamos Neutron Science Center (LANSCE) control system includes many data channels that are timed and flavored, i.e., users can specify the species of beam and time within the beam pulse at which data are reported. The legacy LANSCE control system accomplished this task by queuing up application software-initiated requests and scheduling Analog to Digital Converter (ADC) readout with custom programmable time-delay gated and multiplexed Remote Information and Control Equipment (RICE). This year we upgraded this system to a new Experimental Physics and Industrial Control System (EPICS) system that includes signal dedicated waveform digitizer. An appropriate subset of the data is then returned as specified by each client. This is made possible by improvements to EPICS software, a Commercial Off-The-Shelf (COTS) Field Programmable Gate Array (FPGA) Mezzanine Card (FMC) based ADC and a COTS VPX FPGA card with EPICS embedded on a soft-core processor. This year we upgraded over 1200 waveform channels from RICE to the new TDAQ (Timed/flavored Data Acquisition) system.

BACKGROUND

The LANSCE Accelerator was designed and built with some unusual capabilities. LANSCE is a 120 Hz pulsed linear accelerator that can deliver beam to 6 different experimental areas. H⁺ and H⁻ ions can be accelerated simultaneously and delivered to two different areas on the same beam pulse. Within a 1 second “super-cycle” beam can be delivered to 5 different experimental areas. In addition, the beam energy can be controlled on a pulse-by pulse basis allowing for up to 3 different H⁻ beam energies within 1 second (delivered to different experimental areas). The original RICE control system at LANSCE was designed to support simultaneous data collection from multiple locations along the accelerator at a specified time within a beam pulse, and with a specified flavor [1, 2]. The RICE system allowed flavoring based on the presence or absence of any of 96 gates. The goal was to upgrade the existing RICE system to a new Timed/flavored Data Acquisition system (TDAQ) [3].

Flavor

Flavor refers to which beam areas will receive beam and whether RF is configured to accelerate beam. It is important to be able to measure beam delivered to a particular experimental area, because beam parameters can differ significantly on a pulse-to-pulse basis depending on the con-

figuration. Flavor must not only refer to the area of delivery, but also the combination of areas because on pulses where H⁺ and H⁻ beams coexist beam loading effects may be different than when one beam species is delivered alone.

At LANSCE, the flavor specification allows for each flavor element to be specified as required to be present, required to be absent, or not listed (do not care). The new system currently has only 11 active flavor elements resulting in 3¹¹ possible flavor specifications. Only a small subset of these flavor specifications will be useful, but an important consideration is that the set of useful combinations cannot be known a-priori and is instead determined based on the immediate daily demands of our operations staff as driven by the flexible reconfiguration of LANSCE experimental stations.

Timing

In the RICE system timing for data collection could be specified to be a time relative to the leading or trailing edge of any gate in the timing system and could encompass any time within the 8.33 ms cycle. Time could be specified in microseconds but was only accurate to +/- 1.5 μs. Recognizing that beam is only available for a small subset of the 8.33 ms cycle, we limited the new system to 4 ms of data collection per cycle.

RICE Implementation

In the RICE system, a central computer handled all data collection from remote instrumentation. Multi-signal vectored reads could be performed simultaneously across more than 50 different locations. However, a given input could only be measured at 120 Hz once per beam cycle, and only one vector read (of a single input at each location) could be performed each cycle. A sophisticated scheduling program kept track of which measurements were requested and would fill them with recently collected data or queue a new data take. Typically, data could be obtained with a delay of about 5 seconds. During tuning the data collection queue would sometime be as much as 60 deep, resulting in a delay of one minute to collect a single point from a flavor that is only scheduled to occur once per second. For example, it was therefore important to limit the number of simultaneous data consumers during emittance measurements.

TDAQ IMPLEMENTATION

The new system uses independent EPICS IOCs (Input/Output Controllers) with signal-dedicated waveform digitizers. Each TDAQ system operates independently and can simultaneously sample 16 inputs. At 120 Hz, a full 4 ms of data at ~1 μs intervals is available for each input. Client applications can then specify a subscription update

[†] sbaily@lanl.gov

EFFECT OF LATTICE MISALIGNMENTS ON BEAM DYNAMICS IN LANSCE LINEAR ACCELERATOR*

Y. K. Batygin[†], S. S. Kurennoy, Los Alamos National Laboratory, Los Alamos, NM 87545, USA

Abstract

Accelerator channel misalignments can significantly affect beam parameters in long linear accelerators. Measurements of misalignments of the LANSCE linac lattice elements were performed by the Mechanical Design Engineering Group of the Los Alamos Accelerator Operations and Technology Division. In order to determine effect of misalignment on beam parameters in the LANSCE linac, simulations of high-energy part of LANSCE linear accelerator were performed including measured displacements of quadrupoles and accelerating tanks. Effect of misalignments was compared with those due to beam space charge and distortion of RF field along the channel. Paper presents results of simulation and comparison with experimental data of beam emittance growth along the machine.

LANSCE ACCELERATOR FACILITY

Los Alamos Linear Accelerator consists of 201.25 MHz Drift Tube Linac (DTL) accelerating particles from 0.75 MeV to 100 MeV, and 805 MHz Side-Coupled Linac (CCL), accelerating particles from 100 MeV to 800 MeV (see Fig. 1). The accelerator facility is equipped with two independent injectors for H⁺ and H⁻ beams, merging at the entrance of a 201.25-MHz Drift Tube Linac. The DTL accelerates the two beams to 100 MeV. After the DTL, the Transition Region (TR) beamline directs the 100-MeV proton beam to the Isotope Production Facility (IPF), while the H⁻ beam is accelerated up to the final energy of 800 MeV in an 805-MHz Coupled Cavity Linac. The H⁻ beams, created with different time structures by a low-energy chopper, are distributed in the Switch Yard (SY) to four experimental areas: Lujan Neutron Scattering Center, Weapon Neutron Research Facility (WNR), Proton Radiography Facility (pRad), and Ultra-Cold Neutron Research Facility (UCN). The goal of this study is to evaluate effect of measured misalignments of the LANSCE linear accelerator on beam emittance growth, and to compare the effect of misalignments with other phenomena affecting beam degradation including beam space charge and RF field distortion in accelerating tanks.

BEAM EMITTANCE GROWTH AND MISALIGNMENT MEASUREMENTS

Beam emittance in LANSCE accelerator is controlled by multiple emittance measurement stations. Emittance of the beam with energy up to 100 MeV is measured using the slit-collector method. There are seven beam emittance measurement stations in the Low-Energy Beam Transport, and three stations after DTL. At the energy of 800 MeV,



Figure 1: Layout of Los Alamos accelerator facility.

Table 1: Normalized Transverse RMS Beam Emittance in Linac (π cm mrad)

Beam (Facility)	0.75 MeV	100 MeV	800 MeV
H ⁻ (Lujan/pRad/UCN)	0.022	0.045	0.07
H ⁻ (WNR)	0.028	0.058	0.124
H ⁺ (IPF), DTL only	0.005	0.026	

beam emittance is determined through measurement of beam sizes at various locations utilizing wire scanners, while emittance is recalculated using a matrix method.

Beam emittance in LANSCE accelerator facility experiences significant growth (see Table 1). The main sources of beam emittance growth and beam losses in the linac are mismatch of the beam with the accelerator structure, variation and instabilities of accelerating and focusing fields, transverse-longitudinal coupling in the RF field, misalignments and random errors of accelerator channel components, field nonlinearities of focusing and accelerating elements, beam energy tails from un-captured particles, particle scattering on residual gas and intra-beam stripping, non-linear space-charge forces of the beam, excitation of high-order RF modes. An extensive experience in beam dynamic simulations and understanding of LANSCE beam physics was achieved with previously developed models of beam dynamics in LANSCE accelerator. Results of simulations are summarized in Refs. [1, 2].

Among all phenomena affecting the beam, the impact of misalignment of LANSCE beam channel on beam dynamics has not been studied systematically. Laser tracker measurement of misalignment of the accelerating channel was performed within 2011-2015 by Claude Conner and co-workers of the LANSCE AOT Mechanical Design Group (see Fig. 2) [3]. Measured data were translated into

* Work supported by US DOE under contract 89233218CNA000001
[†] batygin@lanl.gov

INITIAL RESULTS OF THE 201.25 MHz COAXIAL WINDOW TEST STAND

T. W. Hall[†], J. Lyles, A. Poudel, A. Waghmare
 Los Alamos National Laboratory, Los Alamos, NM 87544, USA

Abstract

We have recently commissioned an RF window test stand for the Drift Tube Linear Accelerator (DTL) portion of the Los Alamos Neutron Science Center (LANSCC). The window test stand (WTS) consists of two RF windows that create a vacuum chamber which allows the windows to be tested to the peak power levels used in the DTL. Initial results clearly indicated multipactoring due to the increase of pressure at specific regions of peak forward power levels. Temperature measured at various azimuthal locations on both windows showed increased multipactor heating on the downstream window versus the upstream window. We present the effect of the titanium nitride coating that is presently applied to windows on both multipactor and window temperature. These results are discussed with respect to their impact on the LANSCC DTL performance.

INTRODUCTION

RF vacuum windows are a necessary component of the transmission lines that deliver RF power to accelerator tanks. These windows have multiple requirements including maintaining vacuum, withstanding mechanical and thermal stresses, and transmission of RF power. At LANSCC, the DTL coaxial windows have experienced periods of frequent failures [1].

The frequent window failures were attributed to electron charging effects. The windows were coated with TiN to mitigate electron charging of the windows, but this also introduced additional issues such as excessive heating. Multipactor is an electron phenomenon that is also of concern. This is when an electrons emitted from surfaces experience a resonant interaction with RF fields to generate an avalanche electron population, as described in numerous publications [1-4]. The titanium coating suppresses this effect and prevents chare accumulation [1, 5]. To test the performance of these coatings, the window test stand was built by Mega Industries in collaboration with electrical and mechanical engineers from LANSCC.

The window test stand has allowed us to investigate the unknowns of window performance. The vacuum level and window temperatures were of particular interest as they give key information about the window performance. The pressure can indicate the occurrence of multipactor, and the window temperatures are indicative of heating in the DTL.

EXPERIMENTAL SET-UP

RF power is delivered to the WTS by a Diacrod® amplifier, and the power is transmitted through the test stand into a load. Two windows are used to create a vacuum

chamber, and a data acquisition (DAQ) system captures important information about the window performance. Figure 1 shows the WTS installed and connected to the amplifier and the load.

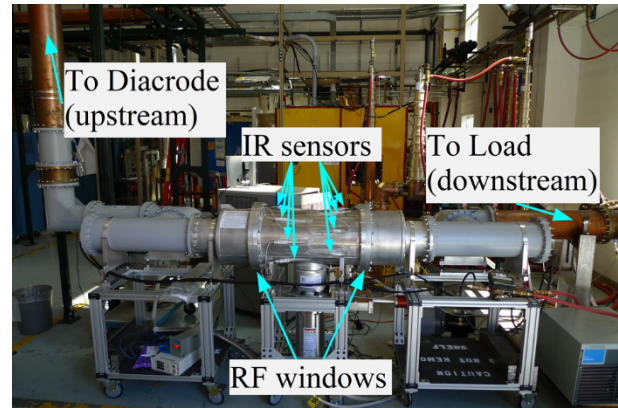


Figure 1: The window test stand in place for testing.

The WTS amplifier delivers similar power to what the windows experience in the DTL. The amplifier operates up to 2.5 MW peak power, and the RF is pulsed at a maximum of 120 Hz repetition rate and 1000 μ s pulse width. The load was only able to dissipate about 200 kW of average power. This gets the same peak voltage as in the DTL, but the average power is a less than the 310 kW in the DTL. This allows the same multipactor conditions that occur in the DTL to be tested in the WTS, but the windows being tested cannot experience the same RF heating as in the DTL. The windows are cooled via water that run into quarter wavelength stubs at the ends of the WTS, and the vacuum is pumped via a CTI-Cryogenics cryopump during testing.

There are several data that are collected via the DAQ system. The vacuum chamber has multiple ports for Micro-Epsilon IR temperature probes to measure the window temperature at various azimuthal locations of both windows. The pressure of the vacuum chamber is measured by a Granville-Philips gauge, and the RF power is measured by an in-house power detector that use the ADL 5511. The DAQ system is a National Instruments cDAQ chassis that communicates data via a LabView program, and this reads the data via voltage outputs from the measurement devices. This data is logged automatically at user-definable time intervals, and the power waveforms of a large number of pulses can also be recorded as requested.

RESULTS

The initial tests were done on three window configurations. Each test requires two windows, and for all three configurations, the upstream window was kept the same. The first configuration used two Rexolite® (crosslinked polystyrene) windows that did not have the TiN coating to establish a baseline measurement of multipactor. Next, a

* Work supported by U.S. Department of Energy.

[†] Corresponding author: twh@lanl.gov

MODELING OF NONLINEAR BEAM DYNAMICS VIA A NOVEL PARTICLE-MESH METHOD AND SURROGATE MODELS WITH SYMPLECTIC NEURAL NETWORKS*

C.-K. Huang[†], O. Beznosov, J. Burby, B. Carlsten, G. Dilts, J. Domine, R. Garimella, A. Kim, T. Kwan, H. N. Rakotoarivelo, R. Robey, B. Shen, Q. Tang
 Los Alamos National Laboratory, Los Alamos, NM, USA
 F.-Y. Li, New Mexico Consortium, Los Alamos, NM, USA

Abstract

The self-consistent nonlinear dynamics of a relativistic charged particle beam, particularly through the interaction with its complete self-fields, is a fundamental problem underpinning many accelerator design issues in high brightness beam applications, as well as the development of advanced accelerators. A novel self-consistent particle-mesh code, CoSyR, is developed based on a Lagrangian method for the calculation of the beam particles' radiation near-fields and associated beam dynamics. Our recent simulations reveal the slice emittance growth in a bend and complex interplay between the longitudinal and transverse dynamics that are not captured in the 1D longitudinal static-state Coherent Synchrotron Radiation (CSR) model. We further show that surrogate models with symplectic neural networks can be trained from simulation data with significant time-savings for the modeling of nonlinear beam dynamics effects. Possibility to extend such surrogate models for the study of spin-orbital coupling is also briefly discussed.

CSR MODELING WITH PARTICLE MESH METHOD

Nonlinear beam dynamics can arise from the nonlinearity of the lattice or the self-fields in an intense beam. These nonlinear dynamics are challenging to be modelled accurately and efficiently, especially over long term evolution. In Ref. [1], we have implemented a particle-mesh method for the self-consistent calculation of the self-fields of a high brightness beam, using wavefront/wavelet meshes following the characteristic of the Green's function of the Maxwell equations. Based on the time scale of field propagation, these self-fields are either calculated exactly from the particle trajectory or approximated due to the close proximity of the emission. The former leads to retarded interactions among the beam particles that are typically paraxial but sensitive to model/numerical errors, while the latter describes close-by interactions for which the usual static-state model is applicable. For an emitting particle, both retarded and close-by contributions to the beam self-fields are then interpolated from the particle's wavefront/wavelet meshes onto a moving mesh for dynamic update of the beam. This

method allows radiation co-propagation and self-consistent interaction with the beam in 2D/3D simulations at greatly reduced numerical errors. Multiple levels of parallelisms are inherent in this method and implemented in our code CoSyR to enable at-scale simulations of nonlinear beam dynamics on modern computing platforms using MPI, multi-threading, and GPUs.

Beam Dynamics in Chicane Compressor

For high brightness beam applications, such as free electron lasers, the transverse dynamics are of importance. Recently, there is interest to develop the understanding of the transverse effects of CSR beyond the 1D models, e.g., in Refs. [2, 3]. We have shown that the longitudinal and transverse beam dynamics in a bend happen in a complex manner [1], which is not captured in the 1D longitudinal CSR model. To further elucidate their role and interplay for a chirped beam in a chicane compressor, we simulated an initial beam of 50 MeV, 0.6 kA in a chicane with a compression ratio of about 3. CoSyR is used only for the first bend for 3 cases: without CSR, or with only longitudinal or full 2D steady-state CSR effect. The rest of the chicane is modeled with linear beam optics. The final beam slice emittance and current are compared in Fig. 1. The longitudinal CSR field introduces a large distortion of the current profile and slice emittance. However, much lower slice emittance growth is observed when the transverse field is also included in the simulation, and the beam profile is closed to the case without CSR.

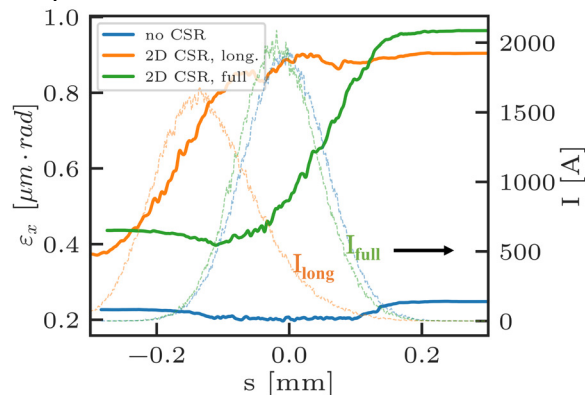


Figure 1: Beam slice remittances (left) and current profiles (right) without CSR, or with only longitudinal or full 2D steady-state CSR effect.

* Work supported by the LDRD program at Los Alamos National Laboratory and the ASCR SciML program of DOE.

[†] huangck@lanl.gov

PROGRESS TOWARD IMPROVING ACCELERATOR PERFORMANCE AND AUTOMATING OPERATIONS WITH ADVANCED ANALYSIS SOFTWARE*

J. E. Koglin[†], J. E. Coleman, M. McKerns, D. Ronquillo, A. Scheinker
 Los Alamos National Laboratory, Los Alamos, NM, USA

Abstract

The penetrating radiography provided by the Dual Axis Radiographic Hydrodynamic Test (DARHT) facility is a key capability in executing a core mission of the Los Alamos National Laboratory (LANL). A new suite of software is being developed in the Python programming language to support operations of the of two DARHT linear induction accelerators (LIAs). Historical data, built as hdf5 data structures for over a decade of operations, are being used to develop automated failure and anomaly detection software and train machine learning models to assist in beam tuning. Adaptive machine learning (AML) techniques that incorporate physics-based models are being designed to use non-invasive diagnostic measurements to address the challenge of time variation in accelerator performance and target density evolution. AML methods are also being developed for experiments that use invasive diagnostics to understand the accelerator behavior at key locations, the results of which will be fed back into the accelerator models. The status and future outlook for these developments will be reported, including how Jupyter notebooks are being used to rapidly deploy these advances as highly-interactive web applications.

DATA STRUCTURES AND ANALYSIS TOOLS

A new systematic data representation of calibrated DARHT accelerator diagnostics data has been developed that includes relevant information needed to describe the data as well as model the beam tune (i.e., metadata). Open-source Python libraries are used to load and calibrate DARHT data which include:

- Shot Based Data:
 - Scalar Data
 - Vector Data (e.g., waveforms and spectra)
 - 2D Arrays (e.g., camera images)
- Calibration Data:
 - Waveform attenuation
 - Integrator time constants
 - Time offsets
 - Scale factors
- Processing Information:
 - Waveform filter time scale
 - Waveform processing time windows
 - Configuration information for automated warnings and alerts

* Research presented in this conference paper was supported by the Laboratory Directed Research and Development program of Los Alamos National Laboratory under project numbers XXG2, XX8R and XXB6.

[†] koglin@lanl.gov

The DARHT data are structured as xarray Dataset objects [1], which map directly onto the HDF5 file format [2].

Highly-interactive applications for DARHT data analysis can be launched locally or hosted on a server and used by multiple users through web browsers. These applications are built using HoloViz [3], a set of high-level Python packages, in a way that allows for rapid deployment of new analysis tools. Figure 1 illustrates how increasingly higher-level packages are used to build interactive plots from named data arrays and high-level parameter objects. The apps are served directly from Jupyter notebooks either locally or from a server, providing a convenient programming platform for rapid development.

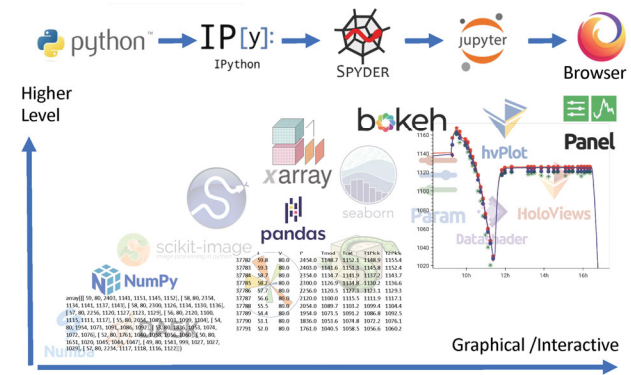


Figure 1: The graphic illustrates how increasingly higher-level packages are used to build interactive plots from named data arrays and high-level parameter objects. The apps are served directly from Jupyter notebooks either locally or from a server, providing a convenient programming platform for rapid development.

In order to promote code robustness and provide reusability, the data input/output and calibration/reduction modules are managed separately from interactive analysis and visualization tools. New analysis methods and data processing pipelines are typically developed using the IPython interactive interpreter [4] or a development environment like Spyder [5]. It is often more convenient to use Jupyter Notebook [6], a web-based application, for visualizing data and developing higher level analysis processes.

Jupyter Notebooks can also be used to create highly interactive analysis tools and dashboards from xarray Dataset objects and HoloViz libraries:

- hvplot [7]: provides high-level plotting directly from xarray data objects using Bokeh and HoloViews.

BEAM COUPLING IMPEDANCES OF ASYMMETRIC COMPONENTS OF THE SCORPIUS INDUCTION LINAC

S. S. Kurennoy, Los Alamos National Laboratory, Los Alamos, NM, USA

Abstract

The transverse beam coupling impedances of induction linacs must be minimized to avoid beam breakdown instability. The vacuum chamber of the Scorpius linac contains complicated asymmetric elements. We present calculations of the transverse impedances for three asymmetric discontinuities: (1) pumping section between accelerating cells, which contains vacuum plenum, pumping grid, and bellows; (2) fast flapper valve; and (3) debris blocker at the end of the linac. The dipole transverse impedances are calculated with CST Studio using both wake-field solver and eigensolver.

INTRODUCTION

Accelerator vacuum chambers contain multiple discontinuities such as insertions, connections between pieces of beam pipe, pumping holes, etc. The discontinuities contribute to the beam coupling impedances. It is important to make sure that these impedances are acceptable from the viewpoint of beam stability. For small discontinuities, a general analytical method for calculating the impedances was developed in [1]. The beam coupling impedances due to small discontinuities are inductive at low frequencies, i.e., well below the beam-pipe cutoff. Small discontinuities can create trapped modes near the cutoff; they also produce some high-frequency resonances well above the cutoff, at frequencies inversely proportional to discontinuity size.

In more general cases, the beam coupling impedances can be calculated numerically. For calculations of the transverse dipole impedance, which is the most important in induction linacs, asymmetric discontinuities present additional challenges. An approach for impedance calculations in asymmetric cases was first suggested in [2].

The transverse dipole impedance is defined as the ratio of the harmonic of synchronous transverse force induced in the structure to the harmonic of the beam dipole momentum that caused this force [3]. For calculations it is more convenient to use an expression that follows from Panofsky-Wenzel theorem: vertical transverse dipole impedance

$$Z_y(\omega) = cZ_L(\omega, d) / (\omega d^2), \quad (1)$$

where $\omega = 2\pi f$, $Z_L(d)$ is the longitudinal impedance calculated along the displaced path $(0, d)$, and d is the vertical displacement from the chamber axis. Similarly, for horizontal dipole impedance Z_x , the field integration path $(d, 0)$ is displaced in x . Equation (1) works for chamber elements with symmetry planes $x = 0$ and/or $y = 0$. For asymmetric elements, the vertical dipole impedance can be found as

$$Z_y(\omega) = [d_2 Z_y(d_2) - d_1 Z_y(d_1)] / (d_2 - d_1), \quad (2)$$

which is a weighted difference of two vertical impedances Eq. (1) calculated at different displacements d_1 and d_2 from the beam axis $(0, 0, z)$. The expression for Z_x is similar.

In general, finding impedances from computed wake potentials – time-domain approach [3] – works better for non-resonant or low-Q structures, such as cavities with damping ferrites [4]. For high-Q structures like resonators, it is usually easier to work in frequency domain [3], for example, by calculating eigenmodes.

INTER-CELL PUMPING SECTION

The inter-cell section of the Scorpius induction linac [5] is inserted between two accelerating modules (cells) to provide a connection for a vacuum pump. There are about one hundred such inserts along the linac. The section is a combination of small discontinuities (pumping slots, bellows) with a large asymmetric resonator (vacuum plenum) coupled to the beam pipe by slots. A simplified CST model of inter-cell section is shown in Fig. 1.

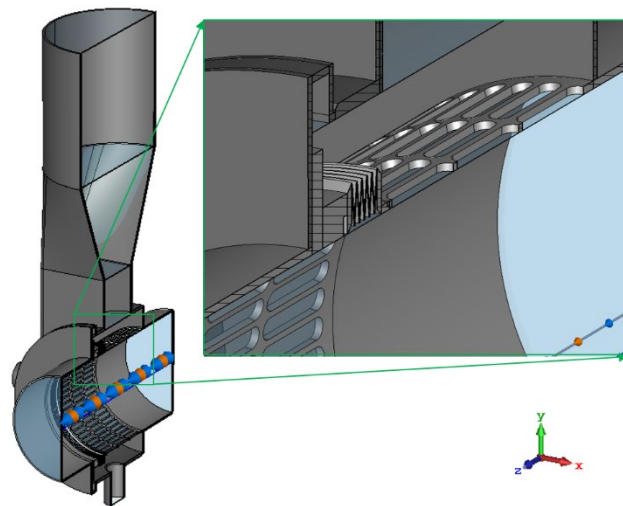


Figure 1: CST model of the inter-cell section: beam pipe, grid with pumping slots, bellows, and vacuum plenum (gray); vacuum volume is shown in transparent blue.

The beam pipe, grid, bellows, and plenum walls are made of stainless steel. The beam pipe and pumping grid both have ID 5.834" (inner radius 74.092 mm) and OD 6"; the grid thickness is 2.108 mm. The vacuum plenum starts as a cylindrical extension that surrounds the pumping grid. It is connected to a duct of rectangular cross section with dimensions 3" x 8", which transitions into a wide cylindrical pipe. There are other elements located nearby, but we will consider the inter-cell section as a single combined discontinuity on a uniform beam pipe.

We use CST wake-field solver to calculate wake potentials due to a Gaussian linear charge distribution with $\sigma_z = 25$ mm passing through the inter-cell section up to the distance of $s = 25$ m behind the bunch. The bunch path is taken on the beam axis ($x = y = 0$) for the longitudinal wake and

ELECTROMAGNETIC AND BEAM DYNAMICS MODELING OF THE LANSCE COUPLED-CAVITY LINAC

S. S. Kurennoy, Y. K. Batygin, D. V. Gorelov, LANL, Los Alamos, NM, USA

Abstract

The 800-MeV proton linac at LANSCE consists of a drift-tube linac, which brings the beam to 100 MeV, followed by a coupled-cavity linac (CCL) consisting of 44 modules. Each CCL module contains multiple tanks, and it is fed by a single 805-MHz klystron. CCL tanks are multi-cell blocks of identical re-entrant side-coupled cavities, which are followed by drifts with magnetic quadrupole doublets. Bridge couplers – special cavities displaced from the beam axis – electromagnetically couple CCL tanks over such drifts. We have developed 3D CST models of CCL tanks. Their electromagnetic analysis is performed using MicroWave Studio. Beam dynamics is modeled with Particle Studio for bunch trains with realistic beam distributions using the CST calculated RF fields and quadrupole magnetic fields to determine the output beam parameters. Beam dynamics results are crosschecked with other multi-particle codes.

INTRODUCTION

Realistic 3D models of accelerator structures proved to be useful for studying various EM effects, mechanical tolerances, and beam dynamics. One example is CST models of LANSCE drift-tube linac (DTL) tanks [1]. On various occasions, they were used to calculate details of DTL element heating, tuning sensitivities, fine features of beam dynamics and particle losses, etc. Another example is CST modeling of the FNAL 4-rod RFQ. We received a CAD model of this RFQ from its manufacturer, Kress GmbH, to help us evaluate a 4-rod RFQ option for LANL. The CAD model was imported into CST [2] and simplified for EM analysis. Our EM calculations revealed unexpected longitudinal fields in the end gaps, which are purely 3D effects and were not (and could not be) taken into account in the RFQ designed with standard codes. The beam dynamics study with CST Particle Studio showed that the end-gap field reduced the beam output energy. This incidental discovery helped our FNAL colleagues to understand the reason for the incorrect RFQ output energy, which puzzled them for over a year before that, and showed how to correct it [3]. Fortunately, the fix was easy: just removing an end-wall plug in the RFQ outer box.

Here we apply a similar approach to the LANSCE coupled cavity linac (CCL). As a first step, we build a simplified CST model of the first CCL tank (T1) in the module 5 (M5T1). The model is fully parametrized and applicable for all tanks in the CCL modules. More details and pictures can be found in report [4]. All geometrical and design electromagnetic parameters of CCL cavities are summarized in the original 1968 document [5].

CST MODELING OF CCL

EM Model of Module 5 Tank 1 (M5T1)

The first module of CCL, module 5 (M5; the count includes four preceding DTL modules), starts at beam energy of 100 MeV and consists of four tanks. Each tank in M5 contains 36 identical re-entrant accelerating cavities (cells, AC), which are side coupled by 35 coupling cavities (CC). The coupling cavities are located off axis (side-coupled structure) and alternate their transverse positions on both sides of the beam path. Drifts after each tank contain a doublet of two EM quadrupole magnets. For M5T1, the AC length is 8.0274 cm and inner radius 12.827 cm. The tank total length is 289 cm, and the drift after T1 is 72.3 cm.

The CST model of the AC cavity starts with creating a parametrized profile curve for a quarter of the cavity vacuum volume, making a figure of rotation, and its mirroring. The CC vacuum volume is then added to the AC, and the edges of the coupling slot formed by the AC-CC intersection are rounded. After that, the cavity frequency is tuned to the operating mode frequency, 805 MHz, by adjusting the AC gap. In practice, some additional metal was left on the drift-tube noses of manufactured half-cavities, and it was scraped by a special tool to adjust the frequency before cavity brazing. We follow a similar procedure in our CST model by adjusting the AC gap width, using an optimizer in the CST eigensolver. To find all the tank modes, we need to consider bridge couplers. The end cells are tuned such that the field amplitudes there for operating mode are the same as in inner cells, so it is sufficient to calculate fields in one structure period, shown in Fig. 1.

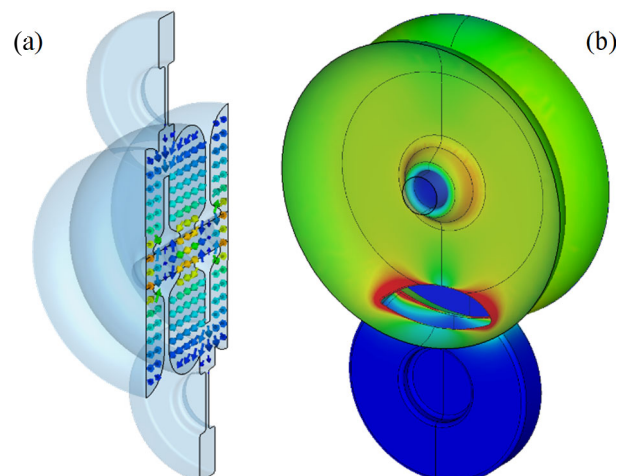


Figure 1: Electric field (a) and surface-current magnitude on the cavity inner surface (b) in one period of M5T1. Red color indicates higher values, blue – lower ones.

ITERATIVE TUNING OF THE BEAM FEEDFORWARD CONTROLLER FOR LANSCE LINAC DIGITAL LOW LEVEL RF CONTROL SYSTEM*

S. Kwon[†], A. Archuleta, L. Castellano, M. Prokop, P. Van Rooy, C. R. Rose, P. Torrez
Los Alamos National Laboratory, Los Alamos, NM, USA

Abstract

This paper addresses an iterative particle beam phase and amplitude feedforward controller tuning method based on the gradient search approach. The method does not need an a priori plant model as it only needs data collected in previous experimental runs. The controller is implemented on a field programmable gate array (FPGA) equipped with a real-time operating system and a network connection. Data from each RF pulse is collected and sent via the network to the FPGA for processing. The controller tuning is performed between the RF pulses. Once the tuning is performed, the controller parameters are downloaded to the controller in the FPGA and new controller parameters are applied at the upcoming RF pulse.

INTRODUCTION

The capabilities of the Los Alamos Neutron Science Center (LANSCE) experimental facilities include: 1) the Lujan Center, which requires short, high-intensity proton bunches in order to create short bursts of moderated neutrons with energies in the meV to keV range; 2) the Proton Radiography (pRad) Facility, which provides time-lapse images of dynamic phenomena in bulk material (for example, shock wave propagation) via 50-ns-wide proton bursts, repeated at time intervals as short as 358 ns with programmable burst repetition rates; 3) the Weapons Neutron Research (WNR) Facility, which provides unmoderated neutrons with energies in the keV to MeV range; 4) the Isotope Production Facility (IPF), which uses the 100-MeV H⁺ beam to make medical radioisotopes; and 5) the Ultra Cold Neutron (UCN) Facility, which creates neutrons with energies below the μeV energy range for basic physics research [1]. The ability of the digital low-level RF (DLLRF) control system to accommodate various beam loading conditions is crucial for successful LANSCE operations in which a wide variety of beam types of various levels of beam loading are present in the accelerator's RF cavities. To minimize the perturbation of the cavity field caused by beam loading, the LANSCE DLLRF control system implements both a proportional-integral (PI) feedback controller (FBC) and feedforward controller capabilities (Fig. 1). For a small peak current beam loading, the PI FBC is sufficient to compensate for the beam loading in the cavity field. However, for high peak current beam loading, the simple PI FBC is not sufficient and a feedforward controller is crucial to the beam loading compensation capability. In this paper, a network based self-tuning method of the beam feedforward con-

troller, an iterative feedforward controller tuning is proposed. The proposed iterative controller tuning uses collected data through the network and the controller gains are updated iteratively via gradient search of the cost function.

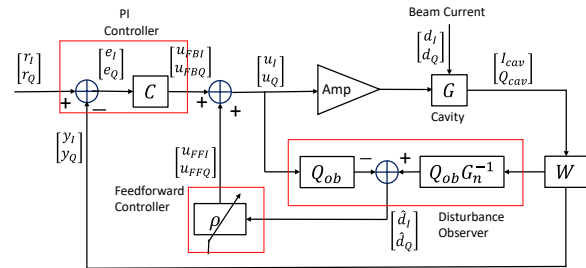


Figure 1: High-level functional diagram of the LANSCE digital low-level RF control system.

DECOUPLING CONTROLLER

The accelerator RF cavities are modelled as two-input-two-output (TITO) systems. When the detuning $\Delta\omega$ of the cavity is zero, the nominal plant function $G_n(s)$ is,

$$G_n(s) = \frac{h}{\tau_p s + 1} \begin{bmatrix} \cos(\theta) & -\sin(\theta) \\ \sin(\theta) & \cos(\theta) \end{bmatrix}. \quad (1)$$

where τ_p is the time constant of the cavity, h is the steady state loop gain, s is the Laplace operator, $j\omega$, and θ is the phase shift of the loop. A simple intuitive approach to control the TITO multivariate system is described as a two-step procedure where a multivariate decoupling controller is designed to minimize with the off-diagonal cross-talk in $G_n(s)$, and then two, single-input single-output (SISO) controllers are designed and applied to each channel of the TITO system. A decoupling controller of the TITO system is a post-compensator, $W(s)$ that produces a newly shaped plant function $G_p(s)$ in which the off-diagonal terms are zero and the gain is unity,

$$G_p(s) = W(s)G_n(s) = \frac{1}{T_p s + 1} \begin{bmatrix} 1 & 0 \\ 0 & 1 \end{bmatrix}. \quad (2)$$

The post-compensator $W(s)$ satisfying (2) is,

$$W(s) = \frac{1}{h} \begin{bmatrix} \cos(-\theta) & -\sin(-\theta) \\ \sin(-\theta) & \cos(-\theta) \end{bmatrix} \quad (3)$$

GRADIENT SEARCH METHOD APPLICATION FOR THE FEEDFORWARD CONTROLLER TUNING

From the view of the cavity field, the beam is an input disturbance. For small-current beam loading, a PI FBC is enough to compensate for the beam loading. For the high-current beam loading situation, in order to compensate for

* Work supported by U.S. Dept. of Energy.

[†] skwon@lanl.gov

RF SYSTEM UPGRADE FOR LOW ENERGY DTL CAVITY AT LANSCE*

J. T. M. Lyles[†], R. E. Bratton, T. W. Hall, M. Sanchez Barrueta
 Los Alamos National Laboratory, Los Alamos, NM 87545, USA

Abstract

The Los Alamos Neutron Science Center (LANSCE) 100 MeV Drift Tube Linac (DTL) uses four accelerating cavities. In May of 2021, a new RF amplifier system was commissioned to drive the first 4-MeV cavity. It had been powered for 30 years with a triode vacuum tube RF amplifier driven by a tetrode, along with four more vacuum tubes for anode high-voltage modulation. The new amplifier system uses one tetrode amplifier driven by a 20-kW solid state amplifier (SSA) to generate 400 kWp at 201.25 MHz. The tetrode amplifier is protected for reflected power from the DTL by a coaxial circulator. The new installation includes cRIO controls and a fast protection and monitoring system capable of reacting to faults within 10 μ s. A new digital low-level RF (LLRF) system has been installed that integrates I/Q signal processing, PI feedback, and feedforward controls for beam loading compensation. Issues with LLRF stability were initially encountered due to interaction from thermal-related RF phase changes. After these issues were solved, the final outcome has been a reliable new RF system to complete the overall upgrade of the LANSCE DTL RF power plant.

ORIGINAL RF POWER SYSTEM

Since LANSCE (LAMPF prior to 1995) was commissioned in 1972, the 201.25 MHz RF power amplifiers (PA) used a high-powered triode vacuum tube as the final stage. This RCA 7835 is the same power grid tube made by Photonis, used at proton injector linacs at Fermilab and Brookhaven National Laboratory. Amplitude modulation for pulse formation and for field (gradient) regulation was provided with a HV modulator for the triode, consisting of a chain of pulse amplifiers using four more power tubes. A Photonis 4616 tetrode was incorporated as driver stage for the triode. These six power grid tubes required to power a single cavity, with four DTL cavities, led to a sizable investment in different devices, some no longer made by trusted sources. The triode lifetime was unusually short, on the order of 15-20K hours before replacement was needed.

LLRF controls for field stabilization and beam loading compensation used a split function analog system, where the HV pulse modulator controlled the RF amplitude, with an electronic phase shifter inserted before the power amplifiers for phase modulation. This system had been designed decades earlier and lacked an ability to be improved with enhancements from a modern digital-based LLRF.

* Work supported by the United States Department of Energy, National Nuclear Security Agency, under contract 89233218CNA000001.

[†] jtml@lanl.gov

REPLACEMENT RF POWER SYSTEM

Installation of new RF amplifiers using high power tetrodes and Diacrodes[®] was completed for DTL cavities # 2-4 in 2016 [1]. The new PAs are linear and the LLRF uses I/Q topology common with modern systems. This simplified the design of the amplifier systems and reduced the number of power tubes used by 60%, with only two types remaining in the RF powerplant.

The first DTL cavity at LANSCE accelerates beam from 0.75 to 5 MeV and continued to operate using the old RF amplifier cascade (Fig. 1) operating with reduced voltages. An upgrade [2] had been delayed since the old RF system had ample headroom to continue operation, while necessary ancillary components were still in development. The delay was coincident through periods of staff shortages due to work restrictions from the COVID pandemic.

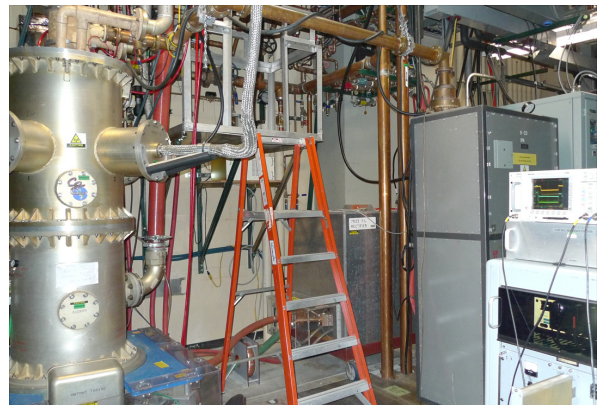


Figure 1: Old triode and tetrode RF amplifiers.

REPLACEMENT RF SYSTEM

The RF powerplant driving DTL cavity #1 was replaced during a normal maintenance shut-down in early 2021. Figure 2 represents the new amplifiers with a circulator before the DTL. Figure 3 shows the new RF installation with major components identified.

Amplifiers

The Thales TH781 tetrode operates in a cavity amplifier circuit provided by the same company. It is similar to the penultimate stage in the three previously upgraded DTL RF sources but with a larger 6-1/8 inch output and 1-5/8 inch input connections. This arrangement had been tested and approved for this application in 2004 [3]. Tube lifetime averages 47K hours for the TH781 at LANSCE, considered excellent for power grid tubes. In this application we expect shorter filament emission life with higher peak cathode current, but with acceptable operation having the matched load of a circulator.

LANSCE CONTROL SYSTEM's 50th ANNIVERSARY*

M. Pieck[†], C.D. Hatch, J.O. Hill, H.A. Watkins, E.E. Westbrook
 Los Alamos National Laboratory, Los Alamos, NM 87545, USA

Abstract

After almost exactly 50 years in service, the LANSCE (Los Alamos Neutron Science Center) control system has achieved a major milestone – replacing its original and reliable RICE (Remote Instrumentation and Control Equipment) with a modern customized control system. The task of replacing RICE was challenging because of its technology (late 1960's), number of channels (>10,000), unique characteristics (all-modules data takes, timed/flavored data takes) and that it was designed as an integral part of the whole accelerator. We discuss the history, RICE integral architecture, upgrade efforts, and the new system providing cutting-edge capabilities. The boundary condition was that upgrades only could be implemented during the annual four-month accelerator maintenance outage. This led to a multi-phased project which turned out to be about an 11-year effort.

INTRODUCTION

In early June 1972, the world's most intense proton beam was delivered through nearly a mile of vacuum tanks at the new Los Alamos Meson Physics Facility (LAMPF), now known as the Los Alamos Neutron Science Center, or LANSCE. As the facility has evolved over five decades, proton beam is now delivered to five state-of-the-art experimental areas, a capability that makes the accelerator unique among its peers. LANSCE has embarked on improvements to ensure that the facility remains a leader for the coming decades. Across the accelerator, teams are replacing older systems with newer, more capable, and safer ones [1]. The control systems also underwent a major upgrade to keep up with technology maturation and the increasing demand for more data at a higher quality.

CONTROL SYSTEM HISTORY

LAMPF, as LANSCE was called until the late 90's, was one of the first major accelerators to be designed in the 60's for computerized control [2]. All access to accelerator data was through a locally designed, centralized system with remote acquisition and control hardware called RICE. From the beginning the control system was in a continuous state of modifications. CAMAC devices were added to the system to complement RICE. By 1978 the control system provided access to approximately 4000 command-able devices and ~12,000 data points (~90% RICE & ~10% CAMAC). In the early 80's, the original System Engineering Laboratory SEL 840 control computer was not manufactured anymore, and a program started to replace it with

a dual VAX 11/780 cluster. The cluster computers were continuously updated throughout the 80's and 90's. In the late 90's the controls group finished installing the cluster of five VAX 4000-96 workstations. In the early 1990's the controls group began integrating Experimental Physics and Industrial Control System (EPICS) into the LANSCE control system. During a control room upgrade new Sun workstations were introduced. These six-headed machines displayed the operator interface screens connected to EPICS applications and interfaced to the VAX-based applications through X-windows technology. As the years have passed, some additional channels were moved to VME but ~10,000 channels remained in RICE by the year 2000.

RICE INTEGRAL ARCHITECTURE

The RICE architecture was designed as an integral part of the LAMPF accelerator facility, with capabilities custom crafted to support controls and monitoring hardware in the accelerator. The initial description of the RICE hardware was given at the very first Particle Accelerator Conference in Washington, D.C., in 1965 [3] and more in-depth discussion in the context of the history of the LAMPF/LANSCE control system, see [4]. One most notable characteristic of RICE is that it is a star configured data acquisition system which supports control and beam synchronized type of data acquisition. At its heart, the RICE Interface Unit (RIU) was able to issue a parallel RICE module read request that provided a transverse snapshot of the accelerator. This implementation resembles the functionality of a timing system triggering gates to distributed data acquisition equipment.

- Timed data – scheduled data read with a micro-sec. granularity relative to the 8 milli-sec. timing cycle.
- Flavored data – scheduled data read on a beam pulse with specific beam parameters. Up to 96 parameters could be specified, including the desired beam species, the beam energy, and the beam-chopping pattern.
- All-modules data – data from all 72 RICE modules could be acquired with each read. Thus, a single request can read correlated data along the entire length of the linac in a one-microsecond window; 72 individual reads would otherwise be spread over 600 milliseconds. Thus, for instance, one could get a snapshot of all linac spill monitors on the same beam pulse.

UPGRADE EFFORTS

In the early 1990s and after 20 years in operation, LANSCE controls engineers determined that RICE had become an operational risk to the facility and its scientific mission. A proposal was made to rebuild the system in standard electronics, providing a complete duplication of RICE capabilities. Declining budgets and high cost, along with the undesirability of an extended accelerator downtime, prevented funding of this effort [5]. In the early 2000s

* This work was supported by the U.S. Department of Energy (DOE) through the Los Alamos National Laboratory (LANL). LANL is operated by Triad National Security, LLC, for the National Nuclear Security Administration of U.S. DOE (Contract No. 89233218CNA000001).
[†] pieck@lanl.gov, LA-UR-2022-27901

ANALYSIS OF RESONANT CONVERTER TOPOLOGY FOR HIGH-VOLTAGE MODULATORS*

M. S. Barrueta[†], M. Morris, J. Lyles
 Los Alamos National Laboratory, Los Alamos, NM 87545, USA

Abstract

At the Los Alamos Neutron Science Center (LANSCE), we are considering various topologies to replace obsolete charging supplies and capacitor banks that provide high-voltage direct-current (DC) power to the 44, 805-MHz klystron modulators that drive the LANSCE Coupled Cavity Linac (CCL). Among the possible replacement topologies is the High Voltage Converter Modulator (HVCM), originally designed at LANSCE for use at the Spallation Neutron Source (SNS), to be used as a pulsed high-voltage power supply for klystron-based RF transmitters. The HVCM topology uses high frequency transformers with resonant LC networks for efficient energy conversion and a frequency dependent gain, which permits the use of frequency modulation as a control variable to afford pulse flattening and excellent regulation as demonstrated at SNS. A mathematical analysis is presented that links the converter resonant tank components to the frequency dependent output behaviour of the converter modulator.

INTRODUCTION AND PURPOSE

The LANSCE CCL is currently celebrating its 50-year anniversary since it first accelerated beam. Since its design, the system has largely remained unchanged with the exception of some life extension programs [1, 2]. In this aging system, component obsolescence is becoming an increasing problem, especially in the high voltage power supply. We are currently considering long pulse power converters such as the SNS High Voltage Converter Modulator (HVCM) [3, 4] or the ESS stacked multilevel (SML) modulator [5].

High power klystrons that can produce multiple MW of output peak power, typically require levels of around 100 kV of cathode voltage and several tens of Amperes of peak current to operate. Due to the current availability of solid-state switches, a pulsed voltage/current of this magnitude cannot be obtained in a single “boost” converter without parallel/series combination of the switches, therefore, designers use different techniques to produce the necessary output pulses. The SML modulator developed by ESS relies on series combination of output stages that combine to deliver the necessary voltage. The HVCM modulator currently used at SNS uses a quasi-resonant circuit to enhance the voltage gain already offered by the output transformer.

Multiple publications exist describing the behaviour of resonant converters, but none of these describes the

operation of the HVCM converter modulator, which has high oscillating currents in the transformer’s primary and cannot reliably add a series resonating capacitor due to its high peak power operation. This paper presents a mathematical analysis of an HVCM style pulsed power source.

TOPOLOGY AND ANALYSIS

The HVCM is composed of a full bridge Insulated Gate Bipolar Transistor (IGBT) input feeding a “boost” transformer (represented by its series and magnetizing inductance model) that in turn feeds a capacitor in parallel with a full bridge rectifier. The rectified output is connected to the load, in this case, one or several klystrons connected in parallel. This circuit is shown in Figure 1.

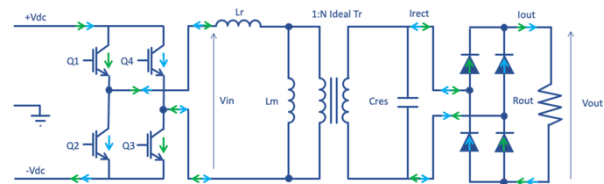


Figure 1: HVCM topology. Current directions in alternate cycles are shown in green or blue.

The First Harmonic Approximation (FHA), a method typically used in the analysis of resonant converters [6, 7] assumes that input to output power transfer is mainly due to the fundamental of the Fourier series components of voltages and currents. It provides a simplified method to examine resonant converters in the frequencies around resonance which is typically where these topologies are operated.

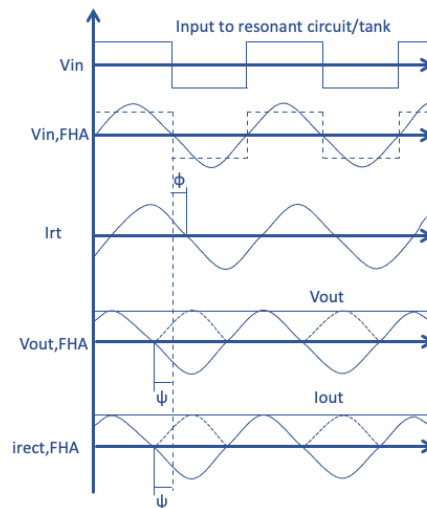


Figure 2: HVCM input and output waveforms and FHA simplification.

* Work supported by the United States Department of Energy, National Nuclear Agency, under contract No. 89233218CNA000001.

[†] maria.sanchez.barrueta@lanl.gov

MACHINE LEARNING FOR THE LANL ELECTROMAGNETIC ISOTOPE SEPARATOR

A. Scheinker*, K. Dudeck, C. Leibman
 Los Alamos National Laboratory, Los Alamos, NM 87544, USA.

Abstract

The Los Alamos National Laboratory electromagnetic isotope separator (EMIS) utilizes a Freeman ion source to generate beams of various elements which are accelerated to 40 keV and passed through a 75-degree bend using a large dipole magnet with a radius of 1.2 m. The isotope mass differences translate directly to a spread in momentum, Δp , relative to the design momentum p_0 . Momentum spread is converted to spread in the horizontal arrival location Δx at a target chamber by the dispersion of the dipole magnet $\Delta x = D(s)\Delta p/p_0$. By placing a thin slit leading to a collection chamber at a location x_c specific isotope mass is isolated by adjusting the dipole magnet strength or the beam energy. The arriving beam current at x_c is associated with average isotope atomic mass, giving an isotope mass spectrum $I(m)$ measured in mA. Although the EMIS is a compact system (5 m) setting up and automatically running at an optimal isotope separation profile $I(m)$ profile is challenging due to time-variation of the complex source as well as un-modeled disturbances. We present preliminary results of developing adaptive machine learning-based tools for the EMIS beam and for the accelerator components.

INTRODUCTION

The Los Alamos National Laboratory electromagnetic isotope separator (EMIS) utilizes a Freeman ion source to generate beams of various elements [1, 2], which are then accelerated to ~ 40 keV and passed through a 75-degree bend using a large dipole magnet with a radius of 1.2 m [3]. Because the isotopes are accelerated to a common kinetic energy their mass differences translate directly to a spread in momentum, Δp , relative to the design momentum p_0 . Momentum spread is then converted to a change in the horizontal arrival location Δx at a target chamber through the dispersion of the dipole magnet: $\Delta x = D(s)\Delta p/p_0$.

By placing a thin slit leading to a collection chamber at a location $x = x_c$ it is possible to isolate specific isotope mass by sweeping the dipole magnet strength or the beam energy. The arriving beam current at x_c can be associated with average isotope atomic mass, resulting in an isotope mass spectrum $I(m)$ measured in mA, as shown in Fig. 1 for a well-tuned EMIS with good isotope separation. Although the EMIS is a compact system (5 m) setting up and running at an optimal configuration at which the cleanest isotope separation is achieved with a desired $I(m)$ profile can be challenge due to time-variation of the complex source as well as un-modeled disturbances. In this work we present

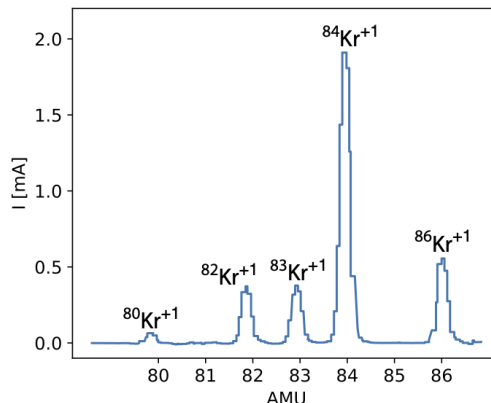


Figure 1: A typical Krypton spectrum is shown for a well tuned EMIS setup with sharp peaks between isotopes.

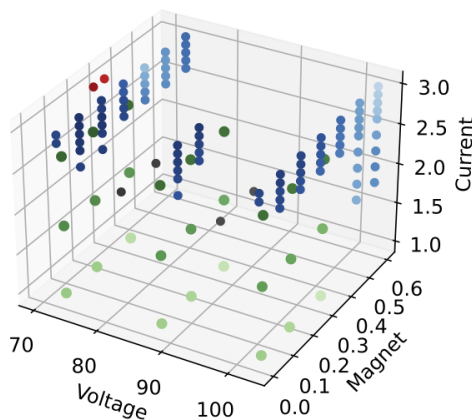


Figure 2: Data points collected for initial ML studies.

preliminary results of developing machine learning-based tools for the EMIS beam and for the accelerator components.

Initial data collection was carried out by adjusting the source voltage, the current of the source filament, and the current of a source magnet. For each setting the dipole magnet strength was swept over a wide range in order to record a full isotope spectrum $I(m)$. Figure 2 shows the data points which were collected during preliminary studies, with different colors corresponding to different collection days and different shades corresponding to the peak collector current at AMU 84.

ML MODELS

We first demonstrated a neural network (NN) design which acts as a surrogate model, $F(\mathbf{c})$, mapping the set of controlled or measured EMIS parameters $\mathbf{c} = (c_1, c_2, c_3)$, which

* ascheink@lanl.gov

IMPROVING CAVITY PHASE MEASUREMENTS AT LOS ALAMOS NEUTRON SCIENCE CENTER*

P. Van Rooy[†], M. Prokop, S. Kwon, P. Torrez, L. Castellano, A. Archuleta
 AOT-Division, Los Alamos National Laboratory, Los Alamos, NM, USA

Abstract

Control stability of the phase and amplitude in the RF accelerating cavity is a significant contributor to beam performance. The ability to measure phase and amplitude of pulsed RF systems at the accuracies of +/- 0.1 degrees and +/- 0.1 percent required for our systems is difficult and custom designed circuitry is required. The digital low level RF upgrade at the Los Alamos Neutron Science Center (LANSCE) is continuing to progress with improved cavity phase measurements. The previous generation of the cavity phase-amplitude measurement system has a phase ambiguity, which requires repeated calibrations to ascertain the correct phase direction. The new phase measurement system removes the ambiguity and the need for field calibration while improving the range and precision of the cavity phase measurements. In addition, the new digital low level RF systems is designed to upgrade the legacy system without significant mechanical, electrical or cabling changes. Performance data for the new phase measurement system is presented.

BACKGROUND

The low level radio frequency (LLRF) system at LANSCE is currently undergoing an upgrade from the original analog control systems to digital control systems. The upgrade began in 2014 and currently 30 of the 53 systems have been upgraded to digital control systems. As part of this upgrade, a new system for the measurement of the cavity phase and cavity amplitude signals is needed as the analog system is incompatible with the new digital systems. The requirements for the error of the LLRF system at LANSCE are 0.1 degrees for phase and 0.1% for amplitude. There have been multiple designs of the digital phase-amplitude measurement system.

CURRENT VERSION

The current version of the digital cavity phase-amplitude measurement system, as seen in Fig. 1, has an 180 degree phase ambiguity. The main integrated circuit (IC) used in the measurement of the phase is the Analog Devices AD8302 IC and the design of the phase measurement system is based on this IC. The AD8302 compares the phase of two input RF signals and determines the difference between the two input signals as voltage. The output is scaled to 10mV per one degree of phase difference. As seen in Fig. 2, a positive 90 degree and a negative 90 degree phase difference have the same voltage output, leading to the ambiguity in the current system. This ambiguity must be

accounted for at each module to determine if the phase slope is positive or negative. The calibration is completed by looking at sign of the predetermined conversion factor. For each calibration that is completed, the phase slope must be checked to ensure that the phase is located on the correct slope. If the phase is on the wrong slope, then the measured voltage is the correct value, but the phase is incorrect, causing issues with beam acceleration. The amplitude measurement system uses an Analog Devices ADL5511 IC which determines the amplitude of the input cavity amplitude signal as a voltage output.

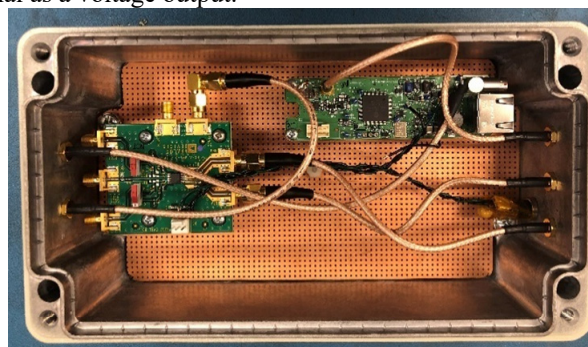


Figure 1: Current phase-amplitude measurement system.

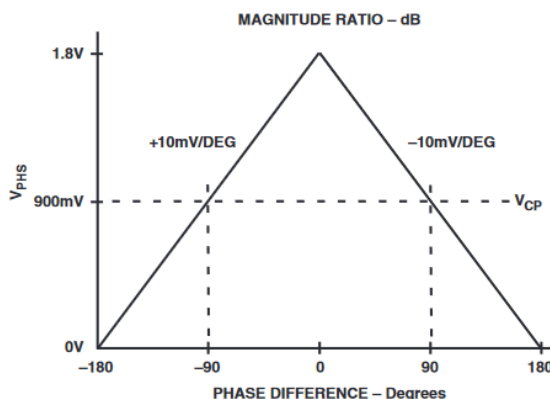


Figure 2: Output of AD8302.

NEW DESIGN

To remove the phase ambiguity of the current phase-amplitude measurement system, a new design was implemented and a prototype printed circuit board produced. The major difference between the current version and the new design is two AD8302 ICs are used, instead of only one. The cavity and reference lines are split into two and one of the cavity input signals is phase shifted by 90 degrees. To keep the phase shift consistent across various boards, the phase shift is completed by lengthening the RF trace on the printed circuit board. Any commercially available phase shifter has some variation in the exact phase shift

* Work supported by the United States Department of Energy, National Nuclear Security Agency, under contract 89233218CNA000001.

[†] pvanrooy@lanl.gov

COMPARISON STUDY ON FIRST BUNCH COMPRESSOR SCHEMES BY CONVENTIONAL AND DOUBLE C-CHICANE FOR MARIE XFEL*

H. Xu[†], L. D. Duffy, Q. R. Marksteiner, P. M. Anisimov
 Los Alamos National Laboratory, Los Alamos, USA

Abstract

We report our comparison study on the first stage electron bunch compression schemes at 750 MeV using a conventional and a double C-chicane for the X-ray free electron laser (XFEL) under development for the Matter-Radiation Interactions in Extremes (MaRIE) project at Los Alamos National Laboratory. Compared to the performance of the conventional C-chicane bunch compressor, the double C-chicane scheme exhibits the capability of utilizing the transverse momentum shift induced by the coherent synchrotron radiation (CSR) in the second C-chicane to compensate that generated in the first C-chicane, resulting in a compressed electron bunch with minimized transverse momentum along the beam. It is also found that the double C-chicane scheme can be designed to significantly better preserve the beam emittance in the course of the bunch compression. This is particularly beneficial for the MaRIE XFEL whose lasing performance critically depends on the preservation of the ultralow beam emittance.

INTRODUCTION

X-ray free electron laser (XFEL) is one of the candidate technologies to realize Matter-Radiation Interaction in Extremes (MaRIE) [1], in an effort to achieve the Dynamic Mesoscale Material Science Capability (DMMSC) at Los Alamos National Laboratory. A footprint design of the accelerator lattice using the laser assisted bunch compression method [2] has been established [3], with the first stage of the electron bunch compression at 750 MeV, enhancing the peak beam current from 20 A to 500 A.

A conventional bunch compressor consists of four dipole magnets, as illustrated in Fig. 1(a); a more complicated bunch compressor is implemented as a double C-chicane, as shown in Fig. 1(b), where the two C-chicanes symbolized by C-1 and C-2 are oriented in the opposite directions. In this paper, we discuss the designs and the performance of the first bunch compressor (BC1) for the MaRIE XFEL accelerator lattice, in the form of a conventional and a double C-chicane.

The motivation for the investigation of the double C-chicane scheme for BC1 is to explore the feasibility of using the horizontal momentum shift induced by the coherent synchrotron radiation (CSR) in the C-2 section to compensate that developed in the C-1 section, producing a bunched beam with minimized transverse momentum shift at BC1 exit. A

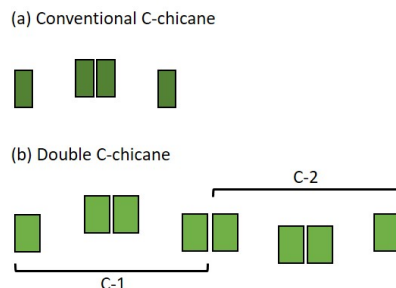


Figure 1: Schematic of (a) a conventional bunch compressor using a single C-chicane and of (b) a double C-chicane.

smaller magnitude of the beam transverse momentum shift is favorable to the ensuing beam acceleration in the linac sections, especially the initial acceleration stage.

To perform the optimization of the double C-chicane, an analytical and a numerical method using ELEGANT code [4] are introduced. In our study, the dipole length (0.60 m) and the field (0.24 T) of the bending magnets in C-1 are set as constants, and the three variables are the compression ratio of C-1 and the length as well as the magnetic field of the dipoles in C-2, forming a 3D parameter space.

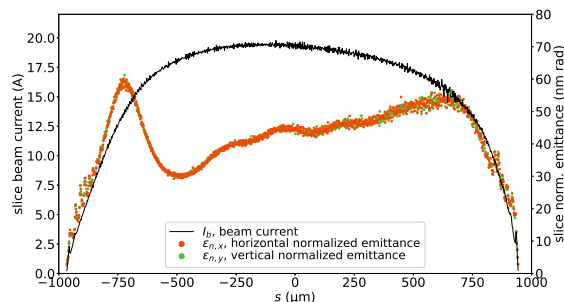


Figure 2: Distributions of the beam current and of the slice emittance of the electron beam upstream of BC1.

ANALYTICAL METHOD

The beam current as well as the slice emittance of the electron beam to be compressed by BC1 is given in Fig. 2. The analytical calculation of the CSR effects on the horizontal momentum shift of the beam as the beam traverses BC1 configured as a double C-chicane is based on the theoretical model developed by Saldin *et al.* [5], in Eq.(87). The perturbation on the energy profile of the beam due to CSR is then transferred to the horizontal momentum by the $R_{26} = \sin \phi_m$ element of the transfer matrix of the dipoles, as given in

* Work supported by the Laboratory Directed Research and Development program of Los Alamos National Laboratory under project number 20200287ER.

[†] haoranxu@lanl.gov

DESIGN AND LOW POWER TEST OF AN ELECTRON BUNCHING ENHANCER USING ELECTROSTATIC POTENTIAL DEPRESSION*

H. Xu[†], B. E. Carlsten, Q. R. Marksteiner, Los Alamos National Laboratory, Los Alamos, NM, USA
B. L. Beaudoin, A. C. Ting, T. W. Koeth, University of Maryland, College Park, MD, USA

Abstract

We present our experimental design and low power test results of a structure for the proof-of-principle demonstration of fast increase of the first harmonic current content in a bunched electron beam, using the technique of electrostatic potential depression (EPD). A primarily bunched electron beam from an inductive output tube (IOT) at 710 MHz first enters an idler cavity, where the longitudinal slope of the beam energy distribution is reversed. The beam then transits through an EPD section implemented by a short beam pipe with a negative high voltage bias, inside which the rate of increase of the first harmonic current is significantly enhanced. An output cavity measures the harmonic current developed inside the beam downstream of the EPD section. Low power test results of the idler and the output cavities agree with the theoretical design.

INTRODUCTION

Non-relativistic bunched electron beams find uses in a variety of applications including microwave sources, such as traveling wave tubes and klystrons, and initial sections of a particle accelerator. A well bunched electron beam is marked by a high value of the first harmonic current. This paper addresses the design of an experiment for demonstrating a beam processing architecture, the electrostatic potential depression (EPD) [1], for enhancing the first harmonic current content in a bunched beam over a very short longitudinal distance.

A modulated beam with the bunching enhanced by the technique of EPD exhibits a higher first harmonic current compared to that produced by only a conventional idler cavity, and the high first harmonic current of the beam is maintained for a much longer beam travel distance after the EPD section, adding to the flexibility of the configuration of the beamline elements downstream.

An EPD element in the beamline is a section of the beam pipe with a negatively biased voltage U_{EPD} ($U_{EPD} < 0$), as illustrated in Fig. 1. The beam pipe has an inner radius of r_w , and the solid electron beam has a radius of r_b . The Lorentz factors of the electron beam to be injected into the EPD section (γ_{inj}) and inside the EPD section (γ_0) have the relationship as given in Eq. (1),

$$\gamma_{inj} = \gamma_0 - \frac{eU_{EPD}}{m_e c^2} + \frac{I_0}{\beta_0 I_A} \left(1 + 2 \ln \frac{r_w}{r_b} - \frac{r^2}{r_b^2} \right) \quad (1)$$

* Work supported by the U.S. Department of Energy Office of Science through the Accelerator Stewardship Program.

[†] haoranxu@lanl.gov

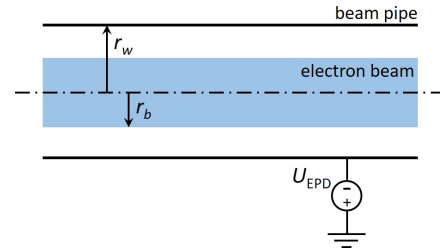


Figure 1: Configuration of an electrostatic potential depression (EPD) element.

where I_0 is the beam current, and $I_A = 4\pi\epsilon_0 m_e c^3 / e = 17.0$ kA.

When a modulated electron beam enters the EPD section, the beam energy is reduced according to Eq. (1), but the energy modulation amplitude is preserved. According to the linear space charge wave theory [2], the wavelength of the space charge waves become smaller when the beam energy is reduced. As a result, at the space charge limit, the distance that the beam covers for the bunching development is shorter. Meanwhile, the nonlinear space charge wave theory [3] indicates that the electron bunching can be further enhanced if the depth of the energy modulation becomes substantially large compared to the average beam energy, which is scenario we are investigating inside the EPD section.

In addition, Eq. (1) indicates that in the case of a solid electron beam, for more consistent processing of the electron beam bunching by the EPD section exploiting the linear as well as nonlinear space charge effects, a beam with a smaller perveance is preferred.

EXPERIMENTAL SETUP

The planned experiment uses an inductive output tube (IOT) developed at the Naval Research Laboratory [4] as the bunched electron beam source.

The schematic of the experimental setup is shown in Fig. 2. The IOT electron gun operates at 710 MHz and produces 24-keV 0.55-A average current bunched beams, the first harmonic current of which monotonically decreases as the beam travels downstream. The oxygen-free high thermal conductivity (OFHC) copper idler cavity adjusts the longitudinal phase space of the bunches with a gap voltage of 6 kV so that the first harmonic current of the beam will start to increase, which is the identical scenario as in a generic klystron idler cavity. The EPD section is biased at -12 kV for the fast enhancement of the electron beam bunching. A stainless steel output cavity is used to extract the information of the harmonic current content in the beam, after which the

NUMERICAL CALCULATIONS OF WAVE GENERATION FROM A BUNCHED ELECTRON BEAM IN SPACE*

H. Xu[†], L. D. Duffy, Q. R. Marksteiner, G. D. Reeves, G. L. Delzanno,
Los Alamos National Laboratory, Los Alamos, NM, USA

Abstract

We present our numerical approach and preliminary results of the calculations of whistler and X mode wave generation by a bunched electron beam in space. The artificial generation of whistler and X mode plasma waves in space is among the candidate techniques to accomplish the radiation belt remediation (RBR), in an effort to precipitate energetic electrons towards the atmosphere to reduce their threat to low-Earth orbit satellites. Free-space propagation of an electron pulse in a constant background magnetic field was simulated with the CST particle-in-cell (PIC) solver, with the temporal evolution of the beam recorded. The SpectralPlasmaSolver (SPS) was then modified to use the recorded electron pulse propagation to calculate the real-time plasma waves generated by the beam. SPS simulation results of the wave generation for the upcoming Beam-PIE experiment as well as an idealized bunched electron beam are shown.

INTRODUCTION

Energetic electrons at MeV level trapped inside the radiation-belt are known to cause damage to the electronics in low-Earth orbit satellites [1]. Theoretical calculations have shown that artificially generated plasma waves in space, e. g. the whistler and the X mode waves, are capable of precipitate these energetic electrons towards the atmosphere, accomplishing the Radiation-Belt Remediation (RBR). The plasma waves in space can be generated by antennas or by electron beams. This paper addresses the preliminary theoretical investigation of space plasma wave generation by an electron beam produced by a space-borne accelerator.

The simulations of plasma wave generation by a pulsed electron beam are performed using the SpectralPlasmaSolver (SPS) code [2], a high performance 3D fluid-kinetic numerical solver of Vlasov-Maxwell equations. The original version of SPS uses analytical expression of the current densities for the calculations of plasma wave generation, with which the initial simulations of the wave generation in the whistler and the X mode were carried out [3]. In order to study the plasma wave generation in a more realistic scenario, the SPS code was later modified to take the numerical description of the electron beam current density spatial distribution variation in time over the course of the beam propagation in a background magnetic field as the input, which was calculated by the CST [4] particle-in-cell (PIC) solver beforehand,

to perform simulations of the real-time generation of plasma waves during the travel of the beam.

Two types of the pulsed electron beams have been investigated in the wave generation simulations. The first type is an example electron beam from the theoretical calculations of the upcoming Beam-PIE experiment [5, 6], at 22.6 keV beam energy, with 13.9 nC total charge, and with an initial total beam pulse length of 2.45 μ s. The second type is an idealized bunched beam of 10.0 nC with a much shorter initial pulse total length of 0.10 μ s and with 15.0 keV beam energy.

The frequency range of the simulations of the plasma wave generation is from direct current (DC) to the upper hybrid resonance. In this frequency range, the generation of the whistler and the X mode waves is calculated. The power generation spectra are calculated using the surface integral of the Poynting vector over a transverse envelope surrounding the electron beam.

CST PIC SIMULATIONS

The input to the CST PIC solver is a prepared beam file of macroparticles, representing the electron beam as produced by the space-borne accelerator. In the CST PIC simulations, the free space drift of the electron beam along the background magnetic field is calculated. Meanwhile, the 3D position monitor is used to take the snap shots of the spatial charge distribution variation in time, saving the information of all the macroparticles at a constant time interval in the simulation.

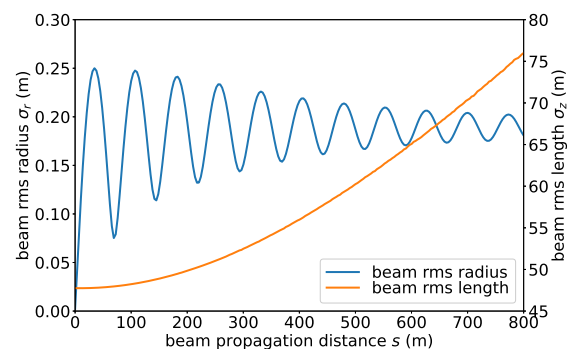


Figure 1: Evolution of the rms radius and the rms beam length of the simulated pulsed electron beam generated by the Beam-PIE experiment as it propagates parallel to the background magnetic field.

As an example, Fig. 1 shows the CST PIC results of the evolution of the simulated Beam-PIE experimental electron beam rms radius and rms beam length versus the distance of propagation of the electron beam parallel with the mag-

* Work supported by the Laboratory Directed Research and Development program of Los Alamos National Laboratory.

[†] haoranxu@lanl.gov

HIGH GRADIENT TESTING RESULTS OF THE BENCHMARK $a/\lambda=0.105$ CAVITY AT CERF-NM*

M. Zuboraj[†], D. Gorelov, W. Hall, M. Middendorf, D. Rai, E.I. Simakov, T. Tajima
Los Alamos National Laboratory, Los Alamos, NM, USA

Abstract

This paper will report initial status of high gradient testing of two C-band accelerating cavities fabricated at Los Alamos National Laboratory (LANL). At LANL, we commissioned a C-band Engineering Research Facility of New Mexico (CERF-NM) which has unique capability of conditioning and testing accelerating cavities for operation at surface electric fields at the excess of 300MV/m, powered by a 50 MW, 5.712 GHz Canon klystron. Recently, we fabricated and tested two benchmark copper cavities at CERF-NM. These cavities establish a benchmark for high gradient performance at C-band and the same geometry will be used to provide direct comparison between high gradient performance of cavities fabricated of different alloys and by different fabrication methods. The cavities consist of three cells with one high gradient central cell and two coupling cells on the sides. The ratio of the radius of the coupling iris to the wavelength is $a/\lambda=0.105$. This poster will report high gradient test results such as breakdown rates as function of peak surface electric and magnetic fields and pulse heating.

INTRODUCTION

In recent years, Los Alamos National Laboratory (LANL) has been conducting research on High gradient C-band (5.712 GHz) accelerator structure motivated by a number of LANL-specific mission needs. This includes potential high gradient C-band upgrade to Los Alamos Neutron Science Center (LANSCE) proton linac to increase the final energy of the proton beam to 3 GeV. In addition, material science research at LANL may benefit from a powerful directional high-repetition-rate X-ray source of 43 keV photons that may be produced by a 42 MeV electron beam through Inverse Compton Scattering (ICS). The goal of this research is to develop high gradient normal-conducting radio-frequency (NCRF) copper-based accelerator structures that withstand extreme electromagnetic field. In order to understand material's behavior under extreme fields, material science research along with experimental study of breakdown of copper alloys are very important to design, fabricate and test next-generation high gradient accelerator cavities. With a C-band high gradient test stand, LANL now has an appropriate tool to probe into material behavior and analyze them under extreme fields in C-band. [1].

We have recently commissioned the C-band Engineering Research Facility of New Mexico (CERF-NM) [2]. The

CERF-NM is powered by a 50 MW 5.712 GHz Canon klystron that produces 50 MW pulses with the pulse length between 300 ns and 1 microsecond, repetition rate up to 200 Hz, and is tunable within the frequency band of 5.707 GHz to 5.717 GHz. The RF power from the klystron fed through a WR187 rectangular waveguide which is attached to a magic tee that splits the power into two halves. The power-split is necessary to protect the Klystron from excess reflected power that may come from the device-under-test. The other half of power is then dumped into a water load. The waveguides were conditioned up to a maximum power of 30 MW, whereas the klystron was conditioned to full power 50 MW. During testing, the base pressure was 5×10^{-7} torr. Thermocouples were attached to the body of the cavity and RF windows to monitor temperature rise at the time of testing. There are two directional couplers and one Faraday cup for diagnostics purpose. The first directional coupler was placed immediately after the klystron and the other just before the cavity for measurements of incident and reflected powers. The Faraday cup was placed at the beam pipe after the structure to measure dark current which is indicative of vacuum breakdowns at the cavity being tested. All the data such as pulse count, breakdown pulse count, number of breakdowns, and real-time monitoring of signals are collected by a national instruments PXIE chassis that implemented in FPGA oscilloscope for real-time measurement. The control systems analysis code which is known as FEbreak was able to achieve a 95% pulse capture efficiency [3]. The details of the test stand, its capabilities are reported in Ref. [2].

Many cavities that we plan to test at CERF-NM are to be coupled on axis to reduce peak surface magnetic fields. Thus, the mode launchers were designed and fabricated for the test stand. The mode launchers convert the TE₁₀ mode of the rectangular WR187 waveguide into the TM₀₁ mode of the cylindrical waveguide for the on-axis coupling. Four mode launchers were fabricated and conditioned up to the maximum input power of 10 MW.

For more details on the mode-launcher design, fabrication, and testing, see Ref. [4].

We plan to test several cavities for high-gradient testing at CERF-NM. Right now, we are testing LANL-fabricated copper-based benchmark cavity which is intended to establish benchmark parameters for future high-gradient performance at C-band. This benchmark cavity is a three-cell test structure with the ratio of the iris radius, a , to the wavelength, λ , of $a/\lambda=0.105$. The structure was a direct scale of the similar test structures fabricated and tested by other institutions at the frequencies of X-band and S-band [5, 6]. This exact cavity shape is most commonly used to make comparison between high gradient performance of cavities

* This work was supported by Los Alamos National Laboratory's Laboratory Directed Research and Development (LDRD) Program.

[†] zuboraj@lanl.gov

X-BAND CAVITY BASED LONGITUDINAL PHASE SPACE LINEARIZATION AT THE UCLA PEGASUS PHOTOINJECTOR

P. Denham *, A. Ody, P. Musumeci

Department of Physics and Astronomy,
 University of California at Los Angeles, Los Angeles, CA 90095, USA

Abstract

Due to the finite bunch length, photoemitted electron beams sample RF-nonlinearities that lead to energy-time correlations along the bunch temporal profile. This is an important effect for all applications where the projected energy spread is important. In particular, for time-resolved single shot electron microscopy, it is critical to keep the beam energy spread below 1×10^{-4} to avoid chromatic aberrations in the lenses. Higher harmonic RF cavities can be used to compensate for the RF-induced longitudinal phase space nonlinearities. Start-to-end simulations suggest that this type of compensation can reduce energy spread to the 10^{-5} level. This work is an experimental study of x-band harmonic linearization of a beam longitudinal phase space at the PEGASUS facility, including developing high-resolution spectrometer diagnostics to verify the scheme.

INTRODUCTION

Controlling the details of the longitudinal phase space in high brightness beams is of paramount importance. Energy correlations along the bunch temporal coordinate affect the emittance compensation process, how lenses act on the transverse beam size and generally any application where monochromatic beams are required.

If a short (< 1 ps) electron bunch is generated at the injector (either by using a short laser pulse or by some form of beam compression), in an S-band RF acceleration cavity (2.856 GHz), the beam occupies less than 1 degree of RF phase and the variation of the beam energy along the beam can be neglected (especially when compared to the one induced by space charge effects). Conversely, if long beams are needed the spread in particle energies induced by the RF curvature can be significant and have a dominant effect on the beam evolution.

One scheme that has been put forward to compensate the RF-induced energy spread is the use of higher harmonic RF cavity to impart equal and opposite energy correlation and linearize the longitudinal phase space distribution [1, 2]. In this paper, we present our current status of experiments running at the UCLA Pegasus laboratory aiming to generate ultralow ($< 1e-4$) energy spread beams by compensating the higher order correlations in longitudinal phase space with an X-band RF cavity. In order to improve the energy resolution of the spectrometer currently installed on the beamline we added to the setup a pinhole to reduce the transverse emittance and a quadrupole to magnify the dispersion.

* pdenham@physics.ucla.edu

The data indicate that we can compensate up to 2nd order, the beam energy spread in agreement with start-to-end simulations of the injector column. These measurements suggest that chromatic aberrations in a single shot time-resolved TEM experiment, using the PEGASUS injector can be reduced to a small level similar to space charge aberrations, validating the feasibility of using the PEGASUS injector for single shot TEM with 10 nm-10 ps spatio-temporal resolution [3–5].

PEGASUS BEAMLINE AND X-BAND CAVITY DESCRIPTION

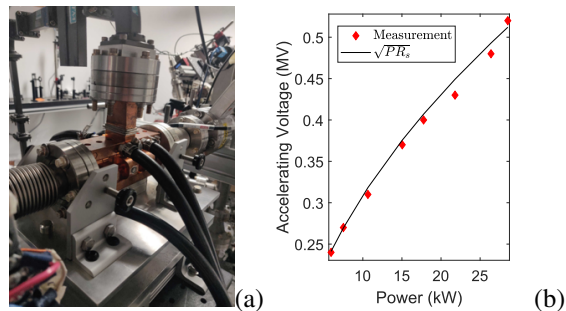


Figure 1: (a) X-band cavity installation at PEGASUS. (b) Shunt Impedance measurements of X-band cavity.

The injector layout is shown in Fig. 1. The photocathode is illuminated by a 266 nm drive Ti:Sa laser. The temporal profile of the laser is stretched from the initial 40 fs RMS temporal duration to a nearly uniform flat-top > 10 ps long pulse. To this end, we use 3 α -BBO crystals with respective lengths 8.75mm, 4.375mm, 2.1875mm, which splits the single 40fs beam into 8 beamlets spanning 13.3 ps [6]. The pulses are then sent through a MgF_2 crystal and a prism to further stretch each pulse and facilitate temporal overlap. After that, the laser is focused onto a NaKSb photocathode by a 175 mm focal length lens through a 72 degrees oblique incidence vacuum port. The oblique port allows the final lens to be brought closer to the cathode surface [7], but the illumination of the cathode is asymmetric. The alkali-antimonide photocathode is inserted in a BNL/SLAC/UCLA 1.6 cell clamped S-band RF gun [8] using a specially designed load-lock chamber. Note that operation of these cathodes using UV laser results in a relatively large MTE of 2 eV, which is not important for this particular experiment. A focusing solenoid immediately after the gun is followed by a 9.6 GHz x-band linearizing cavity and S-band Linac [9] centered 1.1 m and 1.7 m downstream of the cathode respectively.

Content from this work may be used under the terms of the CC BY 4.0 licence (© 2022). Any distribution of this work must maintain attribution to the author(s), title of the work, publisher, and DOI

CYBORG BEAMLINE DEVELOPMENT UPDATES

G. E. Lawler*, A. Fukasawa, N. Majernik, J. Parsons, Y. Sakai, J. B. Rosenzweig
 UCLA, Los Angeles, California, USA
 F. Bosco, Sapienza University of Rome, Rome, Italy
 B. Spataro, LNF-INFN, Frascati, Italy
 Z. Li, S. Tantawi, SLAC, Menlo Park, California

Abstract

X-ray free electron laser (XFEL) facilities in their current form are large, costly to maintain, and inaccessible due to their minimal supply and high demand. It is then advantageous to consider miniaturizing XFELs through a variety of means. We hope to increase beam brightness from the photoinjector via high gradient operation (>120 MV/m) and cryogenic temperature operation at the cathode (<77K). To this end we have designed and fabricated our new CrYogenic Brightness-Optimized Radiofrequency Gun (CYBORG). The photogun is 0.5 cell so much less complicated than our eventual 1.6-cell photoinjector. It will serve as a prototype and test bed for cathode studies in a new cryogenic and very high gradient regime. We present here the fabricated structure, progress towards commissioning, and beamline simulations.

INTRODUCTION

Beam brightness improvements at the cathode is one of the main goals of the next generation of linear accelerators. The methods by which we would like to achieve these improvements are typified by the scaling law shown in Eq. (1).

$$B_{1d} \approx \frac{2ec\epsilon_0}{k_B T_c} (E_0 \sin \varphi_0)^2 . \quad (1)$$

We note that this implies strong beam brightness increases with increasing launch field E_0 and decreasing cathode temperature T_c at or near the photoemission threshold [1]. The advantage of cryogenic operation of a photogun is further strengthened by fundamental physics research showing the increased accelerating gradient able to be sustained in a normal conducting cavity at low temperatures [2]. These effects should be able to be harnessed in variety of photogun designs. Of particular interest is the conceptual ultra-compact x-ray free electron laser (UCXFEL) photoinjector [3, 4]. The device in question is complicated and in many ways a new paradigm in photoinjector design. As a result, we are constructing a new beamline to study a new CrYogenic Brightness-Optimized Radiofrequency Gun (CYBORG) [5].

We then take this opportunity to highlight some of the significant engineering challenges associated with the construction and operation of the CYBORG beamline.

GUN DESIGN

As previously presented, the gun is a 1/2 cell C-band reentrant cavity with single RF feed through and symmetrized

* gelawler@physics.ucla.edu

dummy load port. It is a modified test geometry of the Tantawi-style distributed coupling optimization [6]. It was designed to operate at the frequency of 5.712 GHz at 77K when considering thermal contraction. The cavity was fabricated in 2 pieces and brazed in order to permit higher tolerance machining of the transverse coupling ports [5]. Furthermore, inspired by the FERMI photoinjector at Elettra, the back plane including the cathode is entirely demountable by hand [7]. This is especially useful in providing versatility to modify the gun where necessary.

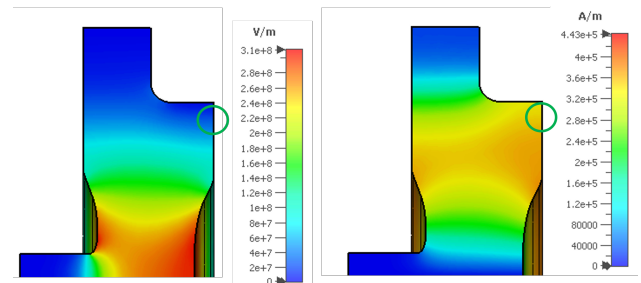


Figure 1: CYBORG RF simulations showing electric (left) and magnetic (fields). Circled is a low electric high magnetic field area ideal for tuning modifications.

Cavity Tuning

The first modification we have in mind is the introduction of a tuning groove. During fabrication excess braze material built up around the circumference of the cavity. As presented previously, low level RF tests have been performed showing a slightly higher frequency than design specifications by 5–6 MHz. We can use an LC circuit model of the cavity to understand this:

$$\omega = \sqrt{\frac{1}{LC}} . \quad (2)$$

The presence of braze material removes a small vacuum volume in high magnetic field region we decrease inductance increasing resonant frequency. To return to our design frequency of 5.695 GHz at room temperature we can add a small vacuum volume in high magnetic field region to increase inductance (i.e. adding smooth groove or dimples in surface by removing material in the back plane). The ideal location for this is shown in Fig. 1. We are especially careful not to place this groove in an area with high electric field since the added discontinuity in surface smoothness could increase the chance of electric breakdown by increasing the surface field beyond potentially manageable levels.

DESIGN OF A HIGH-POWER RF BREAKDOWN TEST FOR A CRYOCOOLED C-BAND COPPER STRUCTURE

G. E. Lawler*, A. Fukasawa, J. Parsons, J. B. Rosenzweig
UCLA, Los Angeles, CA, USA

E. I. Simakov, T. Tajima, LANL, Los Alamos, NM, USA

A. Mostacci, Sapienza University of Rome Departement SBAI, Italy

B. Spataro, INFN-LNF, Frascati, Italy

Z. Li, S. Tantawi, SLAC, Menlo Park, CA, USA

Abstract

High-gradient RF structures capable of maintaining gradients in excess of 250 MV/m are critical in several concepts for future electron accelerators. Concepts such as the ultra-compact free electron laser (UC-XFEL) and the Cool Copper Collider (C3) plan to obtain these gradients through the cryogenic operation (< 77 K) of normal conducting copper cavities. Breakdown rates, the most significant gradient limitation, are significantly reduced at these low temperatures, but the precise physics is complex and involves many interacting effects. High-power RF breakdown measurements at cryogenic temperatures are needed at the less explored C-band frequency (5.712 GHz), which is of great interest for the aforementioned concepts. On behalf of a large collaboration of UCLA, SLAC, LANL, and INFN, the first C-band cryogenic breakdown measurements will be made using a LANL RF test infrastructure. The 2-cell geometry designed for testing will be modifications of the distributed coupled reentrant design used to efficiently power the cells while staying below the limiting values of peak surface electric and magnetic fields.

INTRODUCTION

A major thrust of electron linear accelerator development is to increase the accelerating gradients accessible for different applications. Ultra high gradients have been heavily explored from a number of different perspectives [1]. Cryogenic operation of normal conducting cavities has been shown to significantly reduce breakdown rates (BDR) and in doing so increase the maximum accelerating gradient in cavities that we can consider from 120 MV/m to numbers in excess of 240 MV/m [2, 3]. Several concepts including the Cool Copper Collider (C3) and Ultra compact xray free electron laser (UCXFEL) intend to use high shunt impedance reentrant cavities with distributed coupling [4, 5]. Test of breakdown of these type of cavities then becomes a necessity at the relatively less explored Cband frequencies at which both machines intend to operate [6]. In addition, material additional material properties tests are required such as additional alloys, especially copper-silver of different concentrations [7].

* gelawler@physics.ucla.edu

CAVITY DESIGN

The cavities we intend to test are two cell reentrant cavities using the distributed coupling optimization used at SLAC [8]. It is a 2-cell cavity structure. Shown in Fig. 1 is an eigenmode solution showing electric field magnitude with arbitrary scaling used to illustrate certain relevant features. The resonant mode of 5.712 GHz is intended for 40 K operation. Multiple values for coupling β were considered with order μ s pulse length. The relevant numbers for this discussion are intended peak surface fields around 250 MV/m with and on access peak accelerating gradient of 200 MV/m. As part of our collaboration with LANL, these cavity measurements will be made at the newly commissioning high power Cband cryogenic test bed [9].

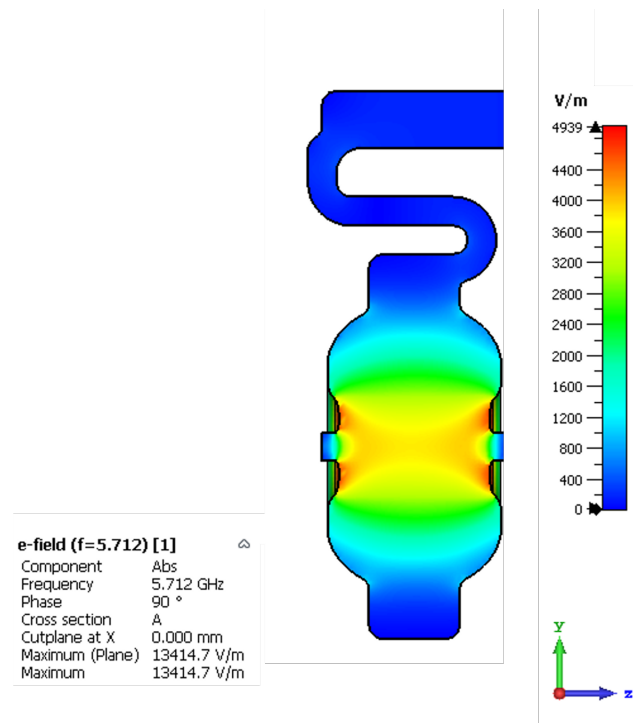


Figure 1: 1 cell of 2-cell cavity structure with electric field eigenmode solution of arbitrary scaling showing the distributed coupling waveguide structures.

TRANSVERSE STABILITY IN AN ALTERNATING SYMMETRY PLANAR DIELECTRIC WAKEFIELD STRUCTURE

W. Lynn*, G. Andonian, N. Majernik, S. O'Tool, J. Rosenzweig, UCLA, Los Angeles, CA, USA
S. Doran, SY. Kim, J. Power, E. Wisniewski, Argonne National Laboratory, Lemont, IL, USA
P. Piot, Northern Illinois University, DeKalb, IL, USA

Abstract

Dielectric Wakefield Acceleration (DWA) is a promising technique for realizing the next generation of linear colliders. It provides access to significantly higher accelerating gradients than traditional radio-frequency cavities. One impediment to realizing a DWA-powered accelerator is the issue of the transverse stability of the beams within the dielectric structure due to short-range wakefields. These short-range wakefields have a tendency to induce a phenomenon known as single-bunch beam breakup, which acts as its name implies and destroys the relevant beam. We attempt to solve this issue by leveraging the quadrupole mode excited in a planar dielectric structure and then alternating the orientation of said structure to turn an unstable system into a stable one. We examine this issue computationally to determine the limits of stability and based on those simulations describe a future experimental realization of this strategy.

INTRODUCTION

Since they were invented, accelerators have pushed the parameters of both energy and cost higher and higher over time. Dielectric Wakefield Acceleration (DWA) is proposed technique for decoupling these two parameters by introducing drastically higher accelerating gradients than traditional radio-frequency cavities and consequently significantly shortening the length of any planned accelerator. The general mechanism by which a DWA scheme operates, as seen in Fig. 1, is a "drive" beam is directed down a dielectric lined waveguide, historically cylindrical in shape, which excites wakefields which then accelerate a trailing "witness" beam [1, 2]. Experiments have demonstrated accelerating gradients in DWA structures in excess of 1 GeV/m [3, 4] which is extremely promising but these structures were relatively small when compared to the required multi-meter long accelerating regions required for a practical future accelerator [5].

A major limitation on the length of a DWA structure is the phenomenon known as single-bunch Beam Breakup (BBU) wherein the drive beam, in addition to generating a longitudinal accelerating wake, generates a short-range transverse deflecting wake that acts on itself [6]. In extreme conditions this wake can destabilize the drive beam significantly enough to strike the accelerator walls, completely defeating the purpose of the accelerator in the first place [7, 8]. Therefore, in order to make practical use of DWA based designs, BBU must be suppressed or at least mitigated.

* wlynn@physics.ucla.edu

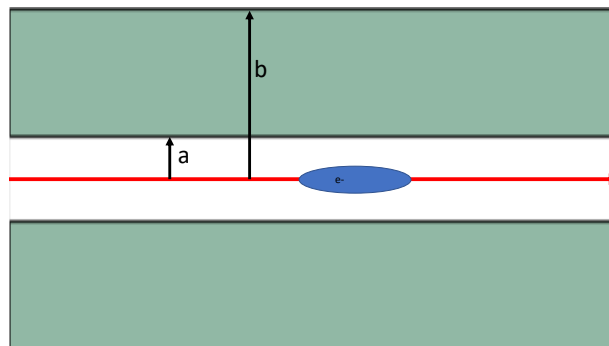


Figure 1: Schematic drawing of a basic DWA setup. Green is the dielectric material. Red is the beam axis and centerline. a is the distance from the centerline to the dielectric surface. b is the distance from the centerline to the exterior of the dielectric. Blue is the beam.

One proposed technique is to use an external magnetic Focusing and Defocusing (FODO) lattice to focus and correct the beam so that BBU effects do not destroy it. Unfortunately such a technique is inherently limited by the fact that in a cylindrical structure the longitudinal wakefields scale with a^{-2} but the transverse fields scale with a^{-3} ultimately capping the achievable accelerating gradient without inducing BBU [7].

Another approach is to abandon the cylindrical geometry and use a planar structure with a correspondingly planar beam. It has been shown that in the case of an infinitely wide beam in an infinitely wide planar structure the transverse wakefields vanish, unfortunately so do the longitudinal fields as well [8, 9]. Luckily, in the non-infinite case the transverse fields scale with σ_x^{-3} while the longitudinal fields scale with σ_x^{-1} implying that there exists a parameter region where the longitudinal fields are strong enough to be useful while the transverse fields are suppressed enough to not cause trouble [10]. Unfortunately while the primary deflecting fields are suppressed secondary quadrupole-like fields are not and are still strong enough to severely distort the tail of the beam leading to BBU [11].

Since the short-range transverse response of a planar dielectric structure to an on-axis particle is inherently quadrupole-like [10] it makes sense to attempt to leverage this effect instead of attempting to suppress it. The technique to leverage this quadrupole-like response is simply to abandon the flat beam concept and rotate the dielectric structure 90° periodically along the length of the interaction as seen in Fig. 2 [9, 12–14]. This alternates the direction of the focusing and defocusing elements of the transverse wakes re-

DERIVATIVE-FREE OPTIMIZATION OF MULTIPOLE FITS TO EXPERIMENTAL WAKEFIELD DATA

N. Majernik*, W. Lynn, G. Andonian, J. B. Rosenzweig, UCLA, Los Angeles, CA, USA
 T. Xu, P. Piot, Northern Illinois University, DeKalb, IL, USA

Abstract

A method to reconstruct the transverse self-wakefields acting on a beam, based only on screen images, is introduced. By employing derivative-free optimization, the relatively high-dimensional parameter space can be efficiently explored to determine the multipole components up to the desired order. This technique complements simulations, which are able to directly infer the wakefield composition. It is applied to representative simulation results as a benchmark and also applied to experimental data on skew wake observations from dielectric slab structures.

INTRODUCTION

Transverse self-wakefields are an important consideration in many facets of beam physics, arising in dielectric, metallic, and plasma structures. In some instances, they may be desirable and intentionally excited, e.g. streakers [1], but in others they may lead to beam breakup [2, 3]. Due to their small spatial and temporal scales and synchronization with a relativistic beam, it can be difficult to directly measure these wakefields. It can be possible to make certain inferences about the wakefields based on the frequency content of the outcoupled wakefields [3, 4] or by comparing experimental measurements to simulations to check for agreement, but a method to more directly determine the fields would be desirable. Other techniques have been proposed including tailored witness beams [5], but in this work we introduce a technique for estimating the self-wakefields without requiring any novel hardware.

It is possible to describe the transverse wakefields, \mathbf{W} , at each longitudinal position along the beam with the standard multipole convention [6]:

$$A + iV = \sum_{n=1}^{\infty} (a_n + ib_n)(x + iy)^n; \mathbf{W} = - \left\{ \frac{\partial V}{\partial x}, \frac{\partial A}{\partial x} \right\}, \quad (1)$$

where a_n and b_n are the n^{th} skew and normal multipole coefficients respectively. In this work, we make a thin lens approximation, *i.e.* that the beam's spatial distribution does not change over the length of the wakefield interaction and that the structure is longitudinally invariant. We will further assume that the wakefield at every longitudinal location is equal, up to a multiplicative constant, $\kappa(z)$. Provided that the beam's length is short compared to the wavelength of all modes which appreciably contribute to the overall wakefield, this is a reasonable approximation; it will be further justified below.

* NMajernik@g.ucla.edu

TRANSVERSE WAKEFIELD RECONSTRUCTION

The technique takes as input two scintillator screen images, taken by the same screen, downstream of the wakefield interaction point; one with the structure in place and one without. These images are used as probability distribution functions (PDF) which are sampled to create two populations of $n(x, y)$ points. A 2D grid of bins is defined that covers either beam, but with a bin spacing low enough to resolve the structure of the beams. The with-structure points are binned, yielding bin-wise counts $B_{i,j}$. The without-structure points are then transformed according to $(x, y) + (x_c, y_c) + \kappa \mathbf{W}$ where (x_c, y_c) are corrections for beam drift between the without-structure and with-structure shots (omitted for simulations where this effect is not present) and κ is the wakefield amplitude scale factor, sampled independently from the probability distribution function of the random variable \mathcal{K} . These transformed points are binned, yielding $\tilde{B}_{i,j}$. We then define the overall error as $\sum |\tilde{B}_{i,j} - B_{i,j}|/n$. A numerical optimizer is employed to minimize this error term by finding the best parameter vector $\{x_c, y_c, \mathcal{K}_1, \mathcal{K}_2, \dots, a_1, b_1, a_2, b_2, \dots\}$ where $\mathcal{K}_1, \mathcal{K}_2, \dots$ are free parameters that define the PDF of \mathcal{K} , with multipole coefficients a_i, b_i up to the selected order.

This random variable \mathcal{K} results from weighting the probability of the wakefield strength at a longitudinal position, $\kappa(z)$, by the current at that position, $I(z)$. Depending on the available information and the expected complexity, different definitions for the PDF may be used. For the simulated cases below, the values of $\kappa(z)$ and $I(z)$ can be found directly and used to construct the PDF. For experiments for which there are trusted simulations, this approach may be used. However, it is also possible to use less prior knowledge. For the experimental reconstructions below, a PDF with one optimizer parameter, \mathcal{K}_1 , was used. If this does not give satisfactory results, it is possible to define the distribution based on other assumptions or with a greater number of free parameters.

Several methods were attempted for optimization in this relatively high dimensional parameter space. Derivative-based optimizers struggled due to the discontinuous and noisy nature of the data, resulting from binning discrete particles. Bayesian optimization worked better, but the comparatively high overhead of this technique made it suboptimal. The best performance was found using derivative-free [7], global optimization, especially differential evolution. This approach is not guaranteed to arrive at the actual wakefields, but since wakefields are often dominated by a few, low degree multipole components, it will often arrive at a good approximation.

RECONSTRUCTING BEAM PARAMETERS FROM BETATRON RADIATION THROUGH MACHINE LEARNING AND MAXIMUM LIKELIHOOD ESTIMATION

S. Zhang^{*1}, M. Yadav^{†1,2}, N. Majernik¹, B. Naranjo¹, O. Apsimon², C. P. Welsch², J. Rosenzweig¹
¹Department of Physics and Astronomy, University of California Los Angeles, CA, USA
²Department of Physics, University of Liverpool, Liverpool L69 3BX, UK

Abstract

The dense drive beam used in plasma wakefield acceleration generates a linear focusing force that causes electrons inside the witness beam to undergo betatron oscillations, giving rise to betatron radiation. Because information about the properties of the beam is encoded in the betatron radiation, measurements of the radiation such as those recorded by the UCLA-built Compton spectrometer can be used to reconstruct beam parameters. Two possible methods of extracting information about beam parameters from measurements of radiation are machine learning (ML), which is increasingly being implemented for different fields of beam diagnostics, and a statistical technique known as maximum likelihood estimation (MLE). We assess the ability of both machine learning and MLE methods to accurately extract beam parameters from measurements of betatron radiation.

INTRODUCTION

In plasma wakefield acceleration, a dense drive beam generates a linear focusing force by repelling the plasma electrons away from its path while leaving the much heavier plasma ions uniformly distributed. Subject to this focusing force, electrons inside the witness beam then undergo harmonic transverse betatron oscillations that give rise to betatron radiation. Because information about the beam is encoded in betatron radiation, measurements of the radiation can be used to reconstruct beam parameters, allowing devices which record information about betatron radiation, such as the UCLA-built Compton spectrometer, to be used for beam diagnostics. Machine learning (ML) has the potential to be applied to betatron radiation diagnostics, as ML methods are already implemented for some fields of beam diagnostics [1]. For example, the application of convolutional neural networks at FAST is able to produce a prediction for various downstream beam parameters from simulated datasets [2]. Another method of extracting information about beam parameters from measurements of radiation is maximum likelihood estimation (MLE), a statistical technique used to determine unknown parameters from a given distribution of observed data. The goal of this work is to assess the ability of both maximum likelihood estimation and machine learning as methods for accurately extracting a beam parameters from measurements of betatron radiation [3–5].

* s.ziqianzhang@gmail.com

† monika.yadav@liverpool.ac.uk

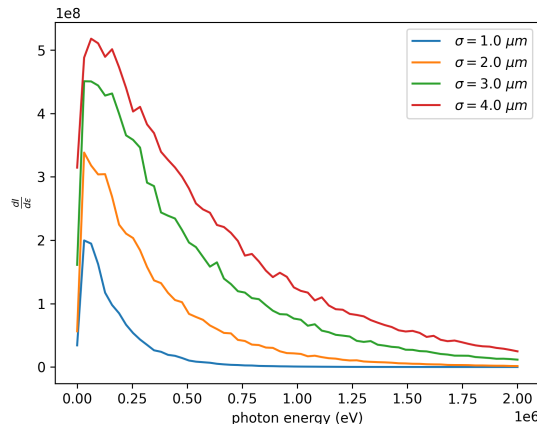


Figure 1: Examples of simulation-produced radiation spectra for spot sizes from 1–4 μm .

BEAM PARAMETER RECONSTRUCTION USING MLE

The method of maximum likelihood estimation involves a probability distribution function $f(x|\sigma)$, which specifies the probability of observing a data vector x given the parameter σ and is related to a likelihood function $L(\sigma|x)$ by $L(\sigma|x) = f(x|\sigma)$. Given a set of N observations of data vectors, the overall likelihood is the product of the likelihoods for each individual data vector [6], and the value of the parameter σ which is most likely to have produced the set of observed data is determined by maximizing the likelihood with respect to σ . To avoid possible problems with arithmetic underflow [7], log-likelihood was used instead of raw likelihood. The log-likelihood is given by

$$\ln L(\sigma|x_1, x_2, \dots, x_N) = \sum_{n=1}^N \ln L(\sigma|x_n), \quad (1)$$

where the product of likelihoods has been converted into a sum of log-likelihoods.

The first task tackled by this work was to correctly identify a beam's spot size from its radiation spectrum using MLE. Several simulations of betatron radiation from beam particles in a plasma wakefield accelerator were run for beams of different spot sizes, using a simulation in which particles are sampled from a beam and tracked through idealized fields and betatron radiation was computed using Liénard–Wiechert potentials [8, 9]. The betatron radiation

FIRST RESULTS FROM A MULTILEAF COLLIMATOR AND EMITTANCE EXCHANGE BEAMLINE

N. Majernik*, G. Andonian, C. Lorch, W. Lynn, J. B. Rosenzweig, UCLA, Los Angeles, CA, USA
S. Doran, S.-Y. Kim, P. Piot¹, J. Power, C. Whiteford, E. Wisniewski
Argonne National Laboratory, Lemont, IL, USA

¹ also at Northern Illinois University, DeKalb, IL, USA

Abstract

By shaping the transverse profile of a particle beam prior to an emittance exchange (EEX) beamline, drive and witness beams with variable current profiles and bunch spacing can be produced. Presently at AWA, this transverse shaping is accomplished with individually laser-cut tungsten masks, making the refinement of beam profiles a slow process. In contrast, a multileaf collimator (MLC) is a device that can selectively mask the profile of a beam using many independently actuated leaves. Since an MLC permits real-time adjustment of the beam shape, its use as a beam mask would permit much faster optimization in a manner highly synergistic with machine learning. Beam dynamics simulations have shown that such an approach is functionally equivalent to that offered by the laser cut masks. In this work, the construction and first results from a 40-leaf, UHV compatible MLC are discussed.

INTRODUCTION

In the context of beam-driven wakefield accelerators, the *transformer ratio*, $\mathcal{R} \equiv |W_+/W_-|$ [1], is the ratio of the maximum accelerating field experienced by the witness bunch to the maximum decelerating field experienced by the driver bunch. Increasing this ratio is a crucial consideration for the effective acceleration of a witness beam since this ratio sets a limit on how much energy can be coupled into the witness before the drive beam is depleted. For longitudinally symmetric bunches, the transformer ratio cannot exceed two [2]. But by using a drive bunch with an asymmetric longitudinal profile, it is possible to achieve transformer ratios greater than two [3], increasing the achievable energy gain by a witness bunch for a given driver energy. When coupled with the large, GV/m accelerating gradients demonstrated in wakefield accelerators [4, 5], a high transformer ratio, beam-driven accelerator is appealing.

Transformer ratios above two have been demonstrated for dielectric wakefield accelerators, *e.g.* $\mathcal{R} = 4.8$ [6], and plasma wakefield accelerators (PWFA). A record-setting transformer ratio of 7.8 was recently demonstrated in a PWFA experiment [7]. Both of these examples used asymmetric drive beam current profiles to more effectively couple energy into the witness beam from the drive beam.

There are a variety of options for creating shaped current profiles including combining wakefield chirping [8] or higher order multipole magnets [9] with a dispersive element,

laser pulse stacking [10], or transverse masking combined with emittance exchange (EEX) [6, 7]. EEX is one of the most versatile options for controlling the current profiles of high charge bunches. It works by exchanging the transverse phase space of a beam with its longitudinal phase space, often by placing a transverse deflecting cavity between two dog legs [1], although other beamline layouts are possible. By passing the beam through a mask prior to EEX, the beam's transverse profile is shaped, thus shaping the post-EEX current profile. This approach can generate high charge current profiles which would be difficult or impossible to achieve using other longitudinal shaping techniques. The EEX beamline at the Argonne Wakefield Accelerator Facility (AWA) [11] generated the beams used to demonstrate the record-setting transformer ratios of Refs. [6] and [7].

At AWA's EEX beamline, this transverse masking was previously done using laser-cut tungsten masks. Changing the mask shape required installing newly cut masks into the UHV beamline, a process which could take days. The latency of this process made it challenging to quickly iterate and refine the current profile. Our previous work in Refs. [12, 13] described a proposal to replace these laser cut masks with a multileaf collimator (MLC), a device with dozens of independently actuated leaves which mask the beam to create a custom aperture [14–16]. A common application for MLCs is their use in radiotherapy where they can be used to shape the radiation beam to precisely match the shape of the tumor from any angle, delivering an effective dose while reducing damage to healthy tissue nearby.

For an EEX beamline, our MLC enables real-time, nearly arbitrary control over the drive and witness spacing and current profiles. Due to the high number of free variables available for tuning and optimization, the MLC is expected to be highly synergistic with machine learning. In Ref. [12], start-to-end beam dynamics simulations were performed, comparing the beams produced by a practical MLC versus the existing laser cut masks, illustrating that the results were functionally equivalent. In Ref. [13] a revised design philosophy was introduced and benchtop tests were performed. Here, we discuss the final design and fabrication of a forty leaf, UHV compatible MLC and its first results from AWA's EEX beamline.

DESIGN AND FABRICATION

Based on our benchtop tests [12, 13], we settled on a 40 leaf MLC design. Each leaf is 2 mm wide with a tungsten tip which masks the beam. These tips are connected via

* NMajernik@g.ucla.edu

SIMULATIONS OF NANOBLADE CATHODE EMISSIONS WITH IMAGE CHARGE TRAPPING FOR YIELD AND BRIGHTNESS ANALYSES*

J. I. Mann[†], B. Wang, G. E. Lawler, J. B. Rosenzweig, UCLA, Los Angeles, CA 90024, USA
S. Karkare, Arizona State University, Tempe, AZ 85287, USA
J. K. Nangoi, T. Arias, Cornell University, Ithaca, NY 14850, USA

Abstract

Laser-induced field emission from nanostructures as a means to create high brightness electron beams has been a continually growing topic of study. Experiments using nanoblade emitters have achieved peak fields upwards of 40 GV/m according to semi-classical analyses, begging further theoretical investigation. A recent paper has provided analytical reductions of the common semi-infinite Jellium system for pulsed incident lasers. We utilize these results to further understand the physics underlying electron rescattering-type emissions. We numerically evaluate this analytical solution to efficiently produce spectra and yield curves. The effect of space-charge trapping at emission may be simply included by directly modifying these spectra. Additionally, we use a self-consistent 1-D time-dependent Schrödinger equation with an image charge potential to study the same system as a more exact, but computationally costly, approach. With these results we may finally investigate the mean transverse energy and beam brightness at the cathode in these extreme regimes.

INTRODUCTION

The ubiquitous field of nanostructured cathodes has seen applications in electron microscopes [1], ultra-fast (low energy) electron diffraction [2], and electron guns in general [3]. The most common structure, the nanotip, field emits on the scale of 10s of nm, yielding excellent emittances. However, the tip is limited in the peak enhanced surface field that may be achieved, with material breakdown occurring at fields on the order of 10 GV/m [4, 5]. The goal of increasing brightness may be progressed by a similar nanostructure. The nanoblade [6, 7], which is essentially an extruded nanotip, has superior thermomechanical properties to the nanotip while supplying sufficient field enhancement to be compatible with tabletop lasers. Surface fields likely exceed 40 GV/m where space-charge (image-charge) limited current dominates emission statistics [8]. Measured emission energies around 500 eV [9] imply the existence of enhanced surface fields up to 80 GV/m by semi-classical analyses [10].

In this paper we continue the investigations of Refs. [6, 7] to model strong laser field emission from gold coated nanoblades. We first provide an update on our progress of evaluating the results of Ref. [11] for finding spectra. We modify our analytical image-charge (IC) trapping model in Ref. [6] to allow us to find the IC-modified (IC-M) spec-

tra for exponential and arbitrary spectral profiles. In our full treatment of the system via the 1-D time-dependent Schrödinger equation (TDSE) with density-functional potentials, we transition from our planar-cylindrical Hartree model [6] to a solely cylindrical vacuum charge model to address computational issues noted in Ref. [7]. Unless otherwise stated we use Hartree atomic units (a.u.).

EVALUATION OF REF. [11]

Here we have progressed slightly from our previous results in Ref. [7]. We accelerated our implementation by improving parallelization and utilization of fast Fourier transforms. The yield at low incident fields agrees with the multi-photon emission order, $J \propto I^4$. However, at high fields where we would normally expect a tapering of yield due to channel closing, we instead observe a significant uptick in yield followed by noisy behavior. The energies supported in the calculation exceed $10U_p$ even within this problematic region, so mitigation of this problem is still in progress.

IMAGE-CHARGE TRAPPING MODEL

By treating the nanoblade as a long cylinder we may make great simplifications when analyzing the IC-M emissions. We note that laser-field emission tends to create broadband emissions, with a high-intensity direct emission process which decays exponentially with respect to emission energy on the scale of about $0.7U_p$, and with a low-intensity rescattering plateau which extends out to about $10U_p$. By making the assumption that electrons spatially resolve themselves quickly we may correlate their energy with their relative positions from the blade, with lower energies shielding higher energies.

The total image line charge λ_I within the cathode is equal and opposite to the total emitted line charge λ_0 . With the energy-position correlation there is an effective image charge observed for each energy shell,

$$\lambda_I(E) = - \int_E^\infty dE' \frac{d\lambda}{dE'} \quad (1)$$

with $\frac{d\lambda}{dE'}$ the emission spectrum without any IC in consideration. The electrostatic potential difference between the nanostructure surface and far-vacuum is then approximately

$$\phi_I(E) = -2 \ln \frac{a}{R} \int_E^\infty dE' \frac{d\lambda}{dE'} \quad (2)$$

for effective charge length a much larger than the apex radius of curvature R . If this is not true, then the original

* This research was funded by the Center for Bright Beams, National Science Foundation Grant No. PHY-1549132.

[†] jomann@physics.ucla.edu

SIMULATIONS FOR THE SPACE PLASMA EXPERIMENTS AT THE SAMURAI LAB

P. Manwani*, H. Ancelin, N. Majernik, O. Williams, Y. Sakai, A. Fukasawa, B. Naranjo,
 G. Andonian, G. Lawler, J. Rosenzweig, UCLA, Los Angeles, CA, USA

Abstract

Plasma wakefield acceleration using the electron linear accelerator test facility, SAMURAI, can be used to study the Jovian electron spectrum due to the high energy spread of the beam after the plasma interaction. The SAMURAI RF facility which is currently being constructed and commissioned at UCLA, will be capable of producing beams with 100s pC of charge with bunch lengths in the 100s of fs range with low transverse emittances in the 3–80 MeV range. Particle-in-cell (PIC) simulations are used to study the beam spectrum that would be generated from plasma interaction. Experimental methods and diagnostics are discussed in this paper.

INTRODUCTION

This study focuses on the generation of broadband electron energy spectra using a beam-driven plasma wakefield accelerator (PWFA) [1], that replicates specific characteristics of the Jovian electron spectrum [2]. The PWFA generated electron spectrum can be beneficial for space research and development as it can serve as a proxy for electron radiation exposure which can cause damage to high-end equipment and electronics used in satellites and flyby operations [3]. PWFA spectra characterization is one of the plasma experiments envisioned using the capabilities of the SAMURAI lab [4, 5], which is a linear accelerator facility currently being constructed on campus at UCLA headed by the Particle Beam Physics Laboratory group. Plasma wakefield accelerators can create high accelerating gradients in the GV/m range, but the magnitude of the accelerating field varies across the length of the blowout cavity that is created by the driving particle beam [6, 7]. A long electron bunch that extends across this blowout cavity interacts with this field, concomitantly imparting a large energy spread on the bunch and leads to the creation of a broadband electron energy spectrum which follows an exponential power law distribution [8]. The electron beam available at the SAMURAI facility is a suitable candidate for the driver of the PWFA and allows us to generate this electron spectrum using a 10 cm long plasma source. Particle-in-cell (PIC) simulations were used to investigate the beam and plasma parameters required to create this spectrum. The plasma and beam evolution are discussed in this paper along with experimental considerations. The simulations were performed using OSIRIS [9], a fully relativistic three dimensional PIC code.

* pkmanwani@gmail.com

Table 1: Parameters for the Space Plasma Simulations

Parameter	Value	Unit
Beam		
Charge, Q	2	nC
Energy, E_b	18	MeV
σ_z	300	μm
$\epsilon_{n,r}$	4	$\mu\text{m rad}$
Plasma		
Density, n_0	1.25×10^{15}	cm^{-3}
Simulation		
Simulation window (x,y,z)	(3, 3, 16)	k_p^{-1}
Grid	$(150)^2 \times 320$	-
Particles per cell	8	-
Timestep	0.012	ω_p^{-1}
Beam particles	4.07×10^7	-

SIMULATION RESULTS

The simulations were performed using the parameters specified in Table 1. An electron beam having an initial energy of 18 MeV is injected in a plasma having an initial ramp profile with a final density of $n_p = 1.25 \times 10^{15}$, while being externally focused to ensure proper matching conditions. The beam density of the 2 nC beam is sufficient to completely expel the plasma electrons from the beam channel, creating a blowout cavity. The transverse emittance of the beam increases in the initial ramp section as some of the particles of the beam are outside the blowout cavity and are not sufficiently focused by the linear focusing forces of the cavity. The beam evolution and plasma ramp profile are shown in Fig. 1. The beam and plasma electron densities along with the axial longitudinal electric field at $z = 1$ cm are shown in Fig. 2. The beam is long ($k_p \sigma_z = 2$) and extends well into the blowout cavity to ensure that it probes both the decelerating and accelerating fields. The non-uniform profile of the longitudinal electric field creates a large energy spread in the beam, and the spread increases with propagation distance. This is illustrated in Fig. 3, by binning the beam particles in 100 bins according to their energies. The energy of the head of the beam retains its energy as it is unaffected by the plasma wake, and this leads to a spike in the particle count at the initial energy point of the electron spectrum. Some of the particles outside this region are not focused and are lost, while some of them are trapped behind the primary wake and lose energy more rapidly than the rest of the beam. These particles form the outliers that can be seen on the left bottom of the figure, and can be neglected as they can be readily deselected in experimental setups.

STORAGE RING TRACKING USING GENERALIZED GRADIENT REPRESENTATIONS OF FULL MAGNETIC FIELD MAPS*

R. Lindberg, M. Borland, ANL, Argonne, IL, USA

Abstract

We have developed a set of tools to simulate particle dynamics in the full magnetic field using the generalized gradients representation. Generalized gradients provide accurate and analytic representations of the magnetic field that allow for symplectic tracking. We describe the tools that convert magnetic field data into generalized gradients representations suitable for tracking in `elegant`, and discuss recent results based upon tracking with the full field representations for all magnets in the APS-U storage ring.

PREPARING THE GENERALIZED GRADIENT EXPANSION FOR ELEGANT

It has long been known that symplectic integration is important for long-term tracking in storage rings. Symplectic dynamics requires the divergence of the field to vanish, $\nabla \cdot \mathbf{B} = 0$, or in other words means that the magnetic field must be derivable from a vector potential \mathbf{A} . While this may not be an issue theoretically, it does pose a problem when one wants to use magnetic field data obtained from either measurements or simulation programs such as OPERA. In this case the quality of the data is not only limited by measurement or numerical precision, but also by the finite grid on which the values of \mathbf{B} are known. At first glance it is not obvious how to interpolate the magnetic field to an arbitrary point in a way that satisfies Maxwell's equations, much less how to do this in a numerically optimal manner.

Fortunately, Dragt and collaborators have worked out most of these issues by introducing the generalized gradient representation of the magnetic field (see, e.g., [1–3]). The first important point is that the generalized gradient expansion gives a Taylor-series representation of the magnetic field anywhere in the transverse (x, y) plane at a sequence of longitudinal (z) coordinates. The resulting magnetic field is derivable from a vector potential, and therefore is divergence-free and suitable for symplectic tracking. Furthermore, the \mathbf{B} -field satisfies the source-free Ampère's law $\nabla \times \mathbf{B} = 0$ up to the order of the Taylor series.

The second important point is that the generalized gradient expansion is determined using only the field values on the boundary of a surface. Since both the “true” magnetic field and the numerically determined one satisfy $\nabla^2 \mathbf{B} = 0$, their difference achieves its maximum value on the boundary. In other words, in the interior the difference between the “true” and calculated field is everywhere smaller than its largest value on the boundary.

In more concrete terms, we note that in free space the magnetic field can be described by either the vector potential via $\mathbf{B} = \nabla \times \mathbf{A}$ or the scalar potential $\mathbf{B} = \nabla \psi$; the latter can be expanded in terms of the generalized gradients as the following power series [3]:

$$\psi = \sum_{\ell=0}^{\infty} \sum_{m=1}^{\infty} \frac{(-1)^\ell m!}{2^{2\ell} \ell! (\ell + m)!} (x^2 + y^2)^\ell \times \left\{ C_{m,s}^{[2\ell]}(z) \mathfrak{I}(x + iy)^m + C_{m,c}^{[2\ell]}(z) \mathfrak{R}(x + iy)^m \right\}. \quad (1)$$

Here, $C_{m,s}(z)$ is the “sine-like” generalized gradient that gives the usual multipole of order m , while $C_{m,s}^{[2\ell]}$ is its $2\ell^{\text{th}}$ derivative with respect to z . The $C_{m,c}^{[2\ell]}$ are the “cosine-like” generalized gradients that give rise to skew components in the field. As another example relevant to tracking, the longitudinal component of the vector potential is

$$A_z(x, y, z) = -xC_{1,s}(z) - (x^2 - y^2)C_{2,s}(z) - (x^3 - 3xy^2)C_{3,s}(z) + \dots, \quad (2)$$

where C_1 , C_2 , and C_3 are the on-axis dipole, quadrupole, and sextupole components, respectively, and the ‘...’ include higher order multipoles, skew components, and terms involving their z -derivatives.

Now, we “only” have to find the generalized gradients from the field data. To this end we have developed two companion programs, `computeCGGE` and `computeRGGE` [4] to compute the generalized gradient expansion (GGE) from the normal field data on a cylinder or rectangular prism, respectively. The former applies the algorithm of Ref. [2] while the latter follows that provided in [1]. The output is formatted for particle tracking with `elegant`'s [5] `BGGEXP` element. The `BGGEXP` element itself can compute the vector potential \mathbf{A} from the GGE to symplectically integrate the trajectories using the implicit midpoint algorithm; alternatively, an explicit integrator is also available that sacrifices symplecticity for speed.

We show examples of results obtained from simulated magnetic field data in Fig. 1. Panel (a) plots the on-axis quadrupole, dipole, and sextupole components obtained from APS-U's transverse gradient reverse bend Q4 dipole. The magnetic model was computed using OPERA and is described further in Ref. [6]. Figure 1(b) shows the on-axis dipole field for the A:M1 longitudinal gradient bend, along with the difference ΔB_y between the OPERA data and that predicted by the GGE. We see that the two agree to one part in $\sim 10^5$ for the body fields, and differ in the fringe regions between magnetic segments at the $\sim 10^{-3}$ level or better.

Similar GGE models were prepared using OEPRA data for the rest of the APS-U magnets, including an additional four

* Work supported by the U.S. Department of Energy, Office of Science, Office of Basic Energy Sciences, under Contract No. DE-AC02-06CH11357.

MAP TRACKING INCLUDING THE EFFECT OF STOCHASTIC RADIATION

D. Sagan*, G. Hoffstaetter†, Cornell University, Ithaca, NY, USA
 É Forest‡, KEK, Tsukuba, Japan

Abstract

Using transfer maps to simulate charged particle motion in accelerators is advantageous since it is much faster than tracking step-by-step. One challenge to using transfer maps is to properly include radiation effects. The effect of radiation can be divided into deterministic and stochastic parts. While computation of the deterministic effect has been previously reported, handling of the stochastic part has not.

In this paper, an algorithm for including the stochastic effect is presented including taking into account the finite opening angle of the emitted photons. A comparison demonstrates the utility of this approach. Generating maps which include radiation has been implemented in the PTC software library which is interfaced to the Bmad toolkit.

INTRODUCTION

Particle in accelerators tracking is an important and widely used simulation tool since it is the only reliable technique that can accurately and reliably probe the nonlinear effects, such as particle loss, that can develop in particle beams over many turns [1]. Routinely, particle tracking is done either by tracking step-by-step which is slow, or by using one or more transfer maps which is fast but potentially inaccurate.

Radiation effects, when relevant, complicate tracking. While one can include the radiation effects into step-by-step tracking, this is generally not done when using transfer maps or is done using a simple energy kick at the end of a map which in many cases is not accurate enough. In this paper we show how to incorporate the radiation effect with map tracking.

The reaction of a particle due to the emission of a photon can be modeled as the sum of two kicks: There is the "deterministic" kick which is the average radiation emitted at the emission point plus a "stochastic" kick which represents the fluctuations around the average. If the effect on a particle via emission of a photon is small, which is generally the case in any practical machine, the stochastic kick can be modeled as having Gaussian probability profile [2].

Inclusion of the deterministic part has been previously reported [3, 4], handling of the stochastic part has not and this is the subject of this paper. Comparisons of map tracking with element-by-element tracking demonstrate the utility of this approach.

RADIATION EMISSION

The phase space coordinate system used for the analysis is (x, p_x, y, p_y, z, p_z) where

$$p_{x,y} = \frac{P_{x,y}}{P_0}, \quad z = -\beta c(t - t_0), \quad p_z = \frac{P - P_0}{P_0} \quad (1)$$

with $P_{x,y}$ being the transverse momentum, P is the momentum, P_0 is the reference momentum, βc the particle velocity, t the time, and t_0 the reference time. It will be assumed that the particle energy is large enough so that p_z can be approximated by $(E - E_0)/E_0$ where E is the particle total energy and E_0 is the reference energy. If this approximation is not valid, it is fairly straightforward to extend the results here to lower energies.

The energy loss ΔE over some small path length L_p is modeled via [2]

$$\frac{\Delta E}{E_0} = -k_E \equiv - \left[k_d \langle g^2 \rangle L_p + \sqrt{k_f \langle g^3 \rangle L_p} \xi_E \right] p_r^2 \quad (2)$$

where $p_r \equiv 1 + p_z$, g is the bending strength ($1/g$ is the orbital bending radius), ξ_E is a Gaussian distributed random number with unit sigma and zero mean, and $\langle \dots \rangle$ is an average over the path length. In the above equation, the deterministic k_d and stochastic k_f coefficients are given by

$$k_d = \frac{2r_c}{3} \gamma_0^3, \quad k_f = \frac{55r_c \hbar}{24\sqrt{3} m c} \gamma_0^5 \quad (3)$$

where γ_0 is the energy factor of an on-energy particle and r_c is the particles "classical radius" given by $r_c = q^2/4\pi\epsilon_0 m c^2$ where q is the particle's charge and m is the particle's mass.

Ignoring the finite opening angle for now, radiation emitted in the forward direction preserves the angular orientation of the particle's motion which leads to the following equations for the changes in the momentum phase space coordinates

$$(\Delta p_x, \Delta p_y) = -\frac{k_E}{p_r} (p_x, p_y), \quad \Delta p_z \approx \frac{\Delta E}{E_0} = -k_E \cdot \quad (4)$$

The fact that an emitted photon is not exactly collinear with the particle direction (often called the "opening angle") can be modeled as a separate process from the energy loss. The change Δp_\perp in the momentum transverse to the bending plane is given by

$$\Delta p_\perp = \sqrt{k_v \langle g^3 \rangle L_p} \xi_v \quad (5)$$

* david.sagan@cornell.edu

† Work supported in part by Department of Energy grant DE-SC0018370.

‡ patrice.nishikawa@kek.jp

BENCHMARKING SIMULATION FOR AWA DRIVE LINAC AND EMITTANCE EXCHANGE BEAMLINE USING OPAL, GPT, AND IMPACT-T*

S.-Y. Kim[†], G. Ha, J. Power, G. Chen, S. Doran, W. Liu, E. Wisniewski
 Argonne National Laboratory, Lemont, IL, USA
 P. Piot, E. Frame, Northern Illinois University, DeKalb, IL, USA

Abstract

At the Argonne Wakefield Accelerator (AWA) facility, particle-tracking simulations have been critical to guiding beam-dynamic experiments, e.g., for various beam manipulations using an available emittance-exchange beamline (EEX). The unique beamline available at AWA provide a test case to perform in-depth comparison between different particle-tracking programs including collective effects such as space-charge force and coherent synchrotron radiation. In this study, using AWA electron injector and emittance exchange beamline, we compare the simulations results obtained by GPT, OPAL, and IMPACT-T beam-dynamics programs. We will specifically report on convergence test as a function of parameters that controls the underlying algorithms.

INTRODUCTION TO THE AWA BEAM TEST FACILITY

A research program to develop methods to control high-brightness and high-charge beam distributions is being carried out at the AWA beam test facility [1]. The AWA facility house three RF photocathode beamlines and, the present study uses the AWA drive-beam photoinjector. The drive-beam linac consists of an L-band RF gun followed by six standing-wave cavities [2]. The beamline can produce electron bunches with charges ≤ 400 nC and energies ≤ 63 MeV. The gun is nested within three solenoid magnets (referred to as bucking, focusing, and matching solenoids) to control the beam and its transverse emittance [3]. The linac section also incorporate three solenoid magnets mostly use to focus high-charge beams. The emittance-exchange (EEX) beamline, located downstream of the drive linac section, consists of an L-band transverse deflecting cavity (TDC) flanked between two dogleg sections.

AWA's bunch control program aim at developing methods to tailor the bunch's current profile [4, 5]. An example of method used for current shaping consists in inserting a mask to transversely shape the beam upstream of the EEX and use the EEX beamline to transfer this shape in the longitudinal phase space. So far current profiles produced have successfully supported the experimental demonstration of record transformer ratio in dielectric slab and plasma [6, 7]. AWA's program in beam-manipulation techniques relies on accurate models to achieve the required precise beam shapes.

Table 1: Global Parameters for Convergence Test

	Charge (nC)	Matching solenoid (A)	UV radius (mm)
Case 1	0.1	240	1.0
Case 2	1.0	240	2.0
Case 3	10.0	240	4.0
Case 4	50.0	230	7.0

Moreover, for the high-charge beam case, it is expected that collective effects, such as the space-charge force (SC) and coherent synchrotron radiation (CSR), will be the main sources of 6D phase space degradation. Therefore, in addition to the particle motion in a linear system, validation of the collective effects calculated by the simulation is critical. Some prior studies on benchmarking of the OPAL simulation [8] with GPT [9] and ASTRA [10] were performed but limited to the RF-gun section [11]. In this paper, we extend the benchmarking study to the full AWA beamline. We first present a convergence test of the OPAL simulation and then compare the results from OPAL, GPT, and IMPACT-T [12] for the AWA drive linac and EEX beamline.

OPAL CONVERGENCE TEST

The convergence studies consider the drive-linac beamline for bunch charges and configuration listed in Table 1.

First, we performed a parameter scan with the OPAL simulation code for the AWA drive linac section by varying global parameters *NBIN* and *EMISSIONSTEPS* [8] that impact the emission process. In all cases, the initial photocathode-laser ultraviolet (UV) pulse is considered to have a transverse uniform distribution and a Gaussian temporal profile with duration of 0.3 ps (FWHM). The bucking- and focusing-solenoid currents are both set to 550 A, and the drive-linac solenoids were not used. The phases of the gun and 6 linac accelerating cavities are tuned for maximum energy gain. The simulation time step was set to 1.0 ps in the cavities and 10.0 ps in drift spaces. It was confirmed that, in our parameter space, normalized emittance after drive linac section is converged regardless of the value of *NBIN* (setting *NBIN* = 1 is also valid for the simulations). In addition, we have checked that the emittance value was converged when *EMISSIONSTEPS* ≥ 500 ; in other words, the time step near the cathode should be less than 2.0 fs.

* The research at Argonne National Laboratory is funded by the U.S. DOE under contract No. DE-AC02-06CH11357.

[†] seongyeol.kim@anl.gov

ELECTRON CLOUD MEASUREMENTS IN FERMILAB BOOSTER*

S. A. K. Wijethunga[†], J. Eldred, C. Y. Tan, E. Pozdeyev
Fermi National Accelerator Laboratory, Batavia, IL, USA

Abstract

Fermilab Booster synchrotron requires an intensity upgrade from 4.5×10^{12} to 6.5×10^{12} protons per pulse as a part of Fermilab's Proton Improvement Plan-II (PIP-II). One of the factors which may limit the high-intensity performance is the fast transverse instabilities caused by electron cloud effects. According to the experience in the Recycler, the electron cloud gradually builds up over multiple turns in the combined function magnets and can reach final intensities orders of magnitude greater than in a pure dipole. Since the Booster synchrotron also incorporates combined function magnets, it is important to discover any existence of an electron cloud. And if it does, its effects on the PIP-II era Booster and whether mitigating techniques are required. As the first step, the presence or absence of the electron cloud was investigated using a gap technique. This paper presents experimental details and observations of the bunch-by-bunch tune shifts of beams with various bunch train structures at low and high intensities and simulation results conducted using PyELOUD software.

INTRODUCTION

In particle accelerators, free electrons are always present inside the vacuum chambers due to many reasons such as ionization of residual gas molecules, stray beam particles striking the chamber walls, etc. These electrons can be accelerated by the electromagnetic fields of the beam to the energies of several hundreds of eV to a few keV, depending on the beam intensity. When such electrons impact vacuum chamber walls, secondary electrons can be generated according to their impact energy and the Secondary Electron Yield (SEY) of the surface. Repeating this process, especially with a proton beam with closely spaced bunches can lead to an avalanche creating the so-called electron cloud (EC) [1-4].

These ECs can severely limit the performance of high-intensity proton accelerators due to transverse instabilities, transverse emittance growth, particle losses, vacuum degradation, heating of the chamber's surface, etc. The Super Proton Synchrotron (SPS), Proton Synchrotron (PS), and Large Hadron Collider (LHC) at CERN [5-6], Relativistic Heavy Ion Collider (RHIC) at Brookhaven national laboratory (BNL) [7], Proton Storage Ring (PSR) at the Los Alamos National Laboratory (LANL) [8] are few of the high-intensity accelerator facilities that encountered operational challenges due to EC effects.

In 2014, The Recycler at Fermilab also experienced fast transverse instabilities. Early studies by J. Eldred *et al.* [4]

hypothesized that the instabilities might be due to the EC build-up in the Recycler. Further investigations by S. A. Antipov *et al.* [3] confirmed EC build-up in the Recycler, concentrated in the combined function magnets. The field gradient of the combined function magnets can create a magnetic mirror effect which facilitates electron trapping. According to his simulations, EC accumulates over many revolutions inside a combined function magnet and can reach final intensities orders of magnitudes higher than inside a pure dipole.

The Fermilab Booster [9] is a 474.2 m circumference rapid-cycling (15 Hz) synchrotron containing 96 combined function magnets. It accelerates the beam from 0.4 GeV at injection to 8.0 GeV at extraction over 33.3 ms (the rising portion of the sinusoidal current waveform) in about 20000 turns, where each turn contains 84 buckets filled with 81 bunches during High Energy Physics (HEP) cycle. The proposed Fermilab's Proton Improvement Plan-II (PIP-II) requires the Fermilab Booster to deliver a high-intensity beam of 6.5×10^{12} protons per pulse which is a 44% increase in the current intensity [10]. Thus, it is important to discover any existence of an EC in the PIP-II era Booster, and if it does, whether it poses any limitations to the desired performance and whether any mitigating techniques are required.

As the first step, the presence or absence of the EC was investigated using a gap technique. Further, corresponding simulations were carried out with PyELOUD [11]. This paper presents the experimental details and observations of the bunch-by-bunch tune shifts of beams with various bunch train structures at low and high intensities and simulation results.

EXPERIMENTAL TECHNIQUE

According to past observations, a train of closely spaced bunches is required for the electrons to trap in the magnetic field. In the absence of a following bunch, the existing secondary electrons can go through a few elastic reflections and get absorbed by the vacuum chamber. Hence, if a trapped EC is present in the machine, a single bunch following the main batch can be used to clear the EC as it kicks the electrons into the vacuum chamber.

Since an EC act as a lens providing additional focusing or defocusing to the beam, this clearing of the EC can be observed in shifting the betatron tune. According to S. A. Antipov's analysis, a positive tune shift in the horizontal direction indicates the presence of an EC at the beam center, and a negative tune shift in the vertical direction indicates the maximum density of the EC near the walls of the vacuum chamber [3]. Adding a clearing bunch can reduce these tune shifts.

* This manuscript has been authored by Fermi Research Alliance, LLC under Contract No. DE-AC02-07CH11359 with the U.S. Department of Energy, Office of Science, Office of High Energy Physics.

[†] swijethu@fnal.gov

POSITRON ACCELERATION IN LINEAR, MODERATELY NON-LINEAR AND NON-LINEAR PLASMA WAKEFIELDS

G. J. Cao[†], E. Adli, University of Oslo, Oslo, Norway
 S. Corde, LOA, ENSTA Paris, CNRS, Ecole Polytechnique,
 Institut Polytechnique de Paris, Palaiseau, France
 S. Gessner, SLAC National Accelerator Laboratory, Menlo Park, CA, USA

Abstract

Accelerating particles to high energies with high efficiency and beam quality is crucial in developing accelerator technologies. The plasma acceleration technique, providing unprecedented high gradients, is considered as a promising future technology. While important progress has been made in plasma-based electron acceleration in recent years, identifying a reliable acceleration technique for the positron counterpart would pave the way to a linear e^+e^- collider for high-energy physics applications. In this work, we show further studies of positron beam quality in moderately non-linear (MNL) plasma wakefields. With a positron bunch of initial energy 1 GeV, emittance preservation can be achieved in optimized scenarios at 2.38 mm-mrad. In parallel, asymmetric beam collisions at the interaction point (IP) are studied to evaluate the current luminosity reach and provide insight to improvements required for positron acceleration in plasma. It is necessary to scale down the emittance of the positron bunch. In the MNL regime, a positron beam with 238 μm -mrad level emittance implies compromise in charge or necessity for ultra-short bunches.

INTRODUCTION

Several proposals have been made for future colliders as we enter a new era of discovery and precision measurements, including circular lepton and hadron colliders [1-3], linear $\gamma\gamma$ colliders [4, 5] and circular $\mu^+\mu^-$ colliders [6, 7]. A linear electron-positron collider is one of the leading options for its non-convoluted nature during the collision [8-13]. In order to make any linear collider economical in both funding and space, high-gradient acceleration is highly desired. Plasma accelerators have been shown to provide multi-GeV gradient in experiments for electron acceleration [14, 15]. Electrons can be accelerated with high efficiency and quality in a full blow-out regime, where focusing is provided by plasma ions and acceleration is achieved at a certain phase of the wakefields created by a particle or laser driver [16-19]. Positrons, on the other hand, cannot be accelerated in the same regime due to the defocusing nature of the positively charged ions, which is detrimental to the positron beam quality.

In a recent study [20], positron acceleration is optimized in the linear regime using a gaussian electron driver and in the non-linear regime using a donut-shaped electron driver, in the context of drive-to-main energy transfer efficiency and uncorrelated energy spread. The uncorrelated energy

spread is introduced as an important limit that cannot be compensated easily, unlike the correlated energy spread where several techniques have been proposed and tested to minimize or compensate for the chirp [21-23]. The result of the optimizations and comparison in different regimes, presented in Fig. 8 of Ref. [20], is that the MNL regime can achieve simultaneously high efficiency ($>30\%$) and low uncorrelated energy spread ($<1\%$). At the time of publication, other important beam qualities, such as emittance and emittance preservation, had not been studied in detail in this regime. In this proceeding, we first introduce the moderately non-linear (MNL) regime, followed by emittance studies in the regime towards collider requirements, and conclude with implications in working towards collider parameters for positron acceleration in plasma. In the study, we use an electron drive beam to be consistent with the previous publication.

THE MODERATELY NON-LINEAR REGIME

Traditionally, a linear plasma wakefield is created by a drive beam with $n_b/n_o \ll 1$. All fields are sinusoidal; weak loading and discrete positioning of the positron trailing bunch inside the linear part of the transverse fields ensure emittance preservation. However, only low-charge, low-gradient acceleration is obtainable in this regime. On the other hand, with a drive beam density $n_b/n_o \gg 1$, non-linear wakefields are created. Such a regime sustains much higher acceleration gradients but suffers from poor efficiency due to high drive-beam charge and poor beam quality due to plasma electron motion inside the positron bunch. The MNL regime takes the middle-ground between the two traditionally known regimes, where the drive beam has a density $n_b/n_o \cong 1$.

Using 3D quasistatic simulation code QuickPIC [24-26], an example of the fields and plasma response produced by such a driver is shown in Fig. 1. The bubble-like cavity is only a partial blow-out where the plasma electron density is greater than 0 inside. In this regime, an elongated positron focusing and acceleration region, provided by plasma electrons returning to axis in a similar way as in the non-linear blowout regime, can be found between two partial blow-outs. In this case, the drive electron beam has a tri-gaussian profile with parameters $\sigma_{x,y} = 8.6 \mu\text{m}$, $n_b = n_o = 5 \cdot 10^{16} \text{ cm}^{-3}$, $\sigma_z = 16.7 \mu\text{m}$. The tri-gaussian positron beam parameters are given in row 1 of Table 1. The average accelerating field sampled by the positron bunch is 4.2 GeV/m, the energy efficiency 15% and total

[†] jiawei.cao@fys.uio.no

DESIGN AND FABRICATION OF A METAMATERIAL WAKEFIELD ACCELERATING STRUCTURE

D. C. Merenich¹, X. Lu^{1,2}, J. G. Power², D. S. Doran²

¹Northern Illinois University, Dekalb, USA

²Argonne National Laboratory, Dekalb, USA

Abstract

Metamaterials (MTMs) are engineered materials that can show exotic electromagnetic properties such as simultaneously negative permittivity and permeability. MTMs are promising candidates for structure-based wakefield acceleration structures, which can mitigate the impact of radio frequency (RF) breakdown, thus achieving a high gradient. Previous experiments carried out at the Argonne Wakefield Accelerator (AWA) successfully demonstrated MTM structures as efficient power extraction and transfer structures (PETS) from a high-charge drive beam. Here we present the design, fabrication, and cold test of an X-band MTM accelerating structure for acceleration of the witness beam in the two-beam acceleration scheme. The MTM structure was simulated using the CST Studio Suite and optimized for high gradient when excited by a short RF pulse extracted from an X-band metallic PETS. Cold test of the fabricated structure shows good agreement with simulation results. Future work includes a beam test at AWA to study the short-pulse RF breakdown physics, as an important component towards a future compact linear collider based on two-beam acceleration.

INTRODUCTION

Structure-based wakefield acceleration (SWFA) is an advanced accelerator concept, where a witness bunch is accelerated by the high-gradient wakefield excited by a drive bunch. One scheme of SWFA is the two-beam acceleration (TBA), where the power extracted from the drive bunch in a power extraction and transfer structure (PETS) is delivered to a separate accelerating structure to accelerate the witness bunch [1, 2]. SWFA shows promise to mitigate breakdown risks in RF accelerators. Empirical studies have found that the breakdown rate is proportional to $E_{\text{grad}}^{30} \times t_{\text{pulse}}^5$, where E_{grad} is the gradient, and t_{pulse} is the RF pulse length. This means that operating the structure at short pulse lengths can help lower the breakdown probability at a given gradient. SWFA with the pulse length on the order of a few nanoseconds requires advanced, specially design structures. Metamaterial (MTM) structures [3, 4] are found to be promising candidates for wakefield acceleration, in a series of previous experiments at the Argonne Wakefield Accelerator (AWA), where a peak power of 565 MW was extracted by a MTM PETS [5] from a high-charge beam.

MTM structures are periodic structures engineered to possess novel electromagnetic properties such as simultaneously negative permittivity and permeability in the so-called double-negative MTMs. MTMs of this type have

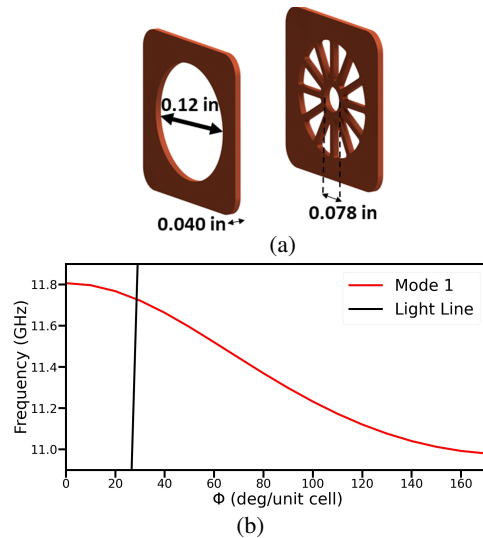


Figure 1: (a) Unit cell of the MTM accelerating structure. (b) Dispersion curve for the fundamental TM_{01} -like mode of the optimized unit cell.

negative group velocity and can overcome the limitation from the trade-off between the group velocity and the shunt impedance in conventional RF structures with positive group velocity. Therefore, MTMs can achieve higher gradients when used as wakefield structures.

This paper outlines the design, fabrication, and cold test of an MTM accelerating structure at 11.7 GHz for two-beam acceleration. A future high power test is planned at AWA, where short RF pulses with a peak power of 500 MW and a 3-nanosecond flattop will be extracted from an X-band metallic PETS [4] placed on the AWA 65 MeV drive beam and then fed into the MTM accelerating structure to generate a gradient of over 300 MV/m for RF breakdown studies.

DESIGN AND SIMULATIONS

Unit Cell Design

The MTM structure is designed as a periodic copper structure, with one period consisting of one wagon wheel plate and one spacer plate. The unit cell design is shown in Fig. 1a. The optimization of the structure is carried out using the CST Studio Suite. Figure 1b shows the dispersion curve of the fundamental TM_{01} -like mode, which has an interaction frequency with the 65 MeV electron beam at 11.7 GHz, aligned with the center frequency of the input RF pulse provided by the X-band metallic PETS.

DESIGN OF A PIP-II ERA Mu2e EXPERIMENT

M.A.C. Cummings[†], R. Abrams, R.P. Johnson, T.J. Roberts, Muons, Inc., Batavia, IL, USA
D.V. Neuffer, Fermilab, Batavia, IL, USA

Abstract

We present an alternative Mu2e-II production scheme for the Fermilab PIP-II era based on production schemes we devised for muon-collider and neutrino-factory front ends. Bright muon beams generated from sources designed for muon collider and neutrino factory facilities have been shown to generate two orders of magnitude more muons per proton than the current Mu2e production target and solenoid. In contrast to the current Mu2e, the muon collider design has forward-production of muons from the target. Forward production from 8 GeV protons would include high energy antiprotons, pions and muons, which would provide too much background for the Mu2e system. In contrast, the 800 MeV PIP-II beam does not have sufficient energy to produce antiprotons, and other secondaries will be at a low enough energy that they can be ranged out with an affordable shield of ~ 2 meters of concrete.

INTRODUCTION

The Mu2e experiment at Fermilab will search for evidence of charged lepton flavor violation by searching for the conversion of a negative muon into an electron in the Coulomb field of a nucleus, without emission of neutrinos. The current Mu2e experimental production setup will be capable of producing $\sim 2 \cdot 10^{17}$ negative muons per year. Regardless of the Mu2e outcome, a next generation experiment, Mu2e-II, with a sensitivity extended another factor of 10 or more, has a compelling physics case. This upgrade will require a complete re-design of the muon production and transport, which is the subject of this proposal.

The current Mu2e design is optimized for 8 kW of protons at 8 GeV. The proposed PIP-II upgrade project is a 250-meter-long CW linac capable of accelerating a 2 mA proton beam to a kinetic energy of 800 MeV (total power 1.6 MW). This would significantly improve the Fermilab proton source to enable next-generation intensity frontier experiments. Much of the beam will be utilized for the Fermilab Short Baseline Neutrino and Long Baseline Neutrino Facility neutrino programs, but more than 1 MW of 800 MeV protons will be available for additional experiments. It is expected that Mu2e-II will require about 100 kW.

PREVIOUS WORK ON MU2E

In 2015 Muons, Inc. had a subcontract from Fermilab's Mu2e Project to perform an initial study of how PIP-II would affect the Mu2e experiment, in particular the impact of using 800 MeV protons. This was specifically in the context of the current Mu2e design, with the intent of

evaluating minimal changes required to use 800 MeV protons at ~ 10 times the power, to obtain 10 times the rate of stopping muons. We have used the Muons, Inc. software package G4Beamline [1] in these studies. Figure 1 shows a G4Beamline simulation of the current Mu2e experiment.

Muons, Inc. did initial studies of Mu2e in the PIP-II era, looking at three scenarios. The first scenario attempted to put 800 MeV protons onto the Mu2e production target, using the same hole in the HRS as the 8 GeV beam. We found that while it is possible to hit the target, it is not possible for the beam to miss the HRS. The HRS (obviously) cannot handle the full 100 kW beam. The production solenoid field was varied from 3 T to 5 T (baseline, 4.5 T), but it is not possible to use 800 MeV protons with the current HRS, production solenoid, and target.

The second scenario considered drilling a new beam hole into the HRS and moving the beamline ahead of the HRS to match. By moving the incoming proton beam closer to the production solenoid axis, it is possible to hit the target and miss the HRS. But this was found unacceptable for three reasons: 1) One or more transport solenoid coils were always in the way. 2) The brass HRS was found to be inadequate to protect the production solenoid coils from 100 kW of beam. 3) It is unlikely that holes could be drilled, as the HRS will be highly radioactive after Mu2e operation.

The third scenario introduced a modest change, removing one TS coil, so two of the gaps between coils would be combined into one gap about 20 cm wide. By putting the proton beam right down the production solenoid axis, it is possible to hit the target and miss the HRS. This would require a re-design of the HRS and target, plus the change to the TS, and the beam absorber must be moved (Fig. 2).

So the "modest change" approach would require:

- Removing one TS coil and drilling a hole for the beam in its cryostat.
- Replace the HRS with one made of tungsten.
- Move the beamline ~ 100 mm closer to the TS, slight angle.
- Move the target, add active cooling.
- Move the beam dump.

FORWARD PRODUCTION MU2E PIP-II

The conclusion of this earlier work was that for Mu2e in the PIP-II era, using the 800 MeV beam requires a redesign of the beamline, target, shielding, production solenoid, and beam absorber at minimum. In this case a whole new configuration of the front end should be considered. We proposed that our **forward production** schemes for muon colliders and neutrino factories be considered as an alternative.

[†] macc@muonsinc.com

UPGRADE OF THE FRIB ReACCELERATOR*

A. C. C. Villari[†], B. Arend, G. Bollen, D. B. Crisp, K. D. Davidson, K. Fukushima, A. I. Henriques, K. Holland, S-H. Kim, A. Lapierre, Y. Liu, T. Maruta, D. G. Morris, D. J. Morrissey, S. Nash, P. N. Ostroumov, A. S. Plastun, J. Priller, S. Schwarz, B. M. Sherrill, M. Steiner, C. Sumithrarachchi, R. Walker, T. Zhang, Q. Zhao
 Facility for Rare Isotope Beams, Michigan State University, East Lansing, MI, USA

Abstract

The ReAccelerator facility at FRIB was upgraded to provide new science opportunities. The upgrade included a new ion source to produce stable and long lived rare isotopes in a batch mode, a new room-temperature rebuncher, a new $\beta = .085$ quarter-wave-resonator cryomodule to increase the beam energy from 3 MeV/u to 6 MeV/u for ions with a charge-to-mass ratio of 1/4, and a new experimental vault with beamlines.

INTRODUCTION

The ReAccelerator (ReA) at FRIB [1] is a worldwide unique facility accelerating rare isotope beams to energies of 3 MeV/u for ions with a charge-to-mass ratio of 1/4. The rare isotopes are initially produced in-flight by projectile fragmentation or fission, stopped in gas cells and re-injected in ReA for reacceleration. ReA has been operated since 2015.

In order to provide broader opportunities for nuclear experiments with higher beam energies, an upgrade of ReA was started in May 2019 with the goal to double the final beam energy and to add experimental stations. The ReA facility upgrade, which was completed in April 2021, included a new Batch Mode Ion Source (BMIS) to provide beams of longer-lived isotopes, a room-temperature rebuncher at 161 MHz, a new cryomodule with $\beta = 0.085$ quarter wave resonators to increase the beam energy from 3 MeV/u to 6 MeV/u for ions with a charge-to-mass ratio of 1/4, and two beamlines in a new experimental vault.

In this contribution we shall present the new Batch-Mode-Ion-Source (BMIS), the rebuncher as well as the new cryomodule and beam lines, the beam optics calculations, and commissioning results. Finally, we shall provide the list of beams used for experiments after the commissioning of the upgrade.

THE ReACCELERATOR

The ReA was originally built to reaccelerate beams of rare isotopes produced and separated in-flight by the Coupled Cyclotron Facility. With the completion of the FRIB facility, ReA will be able to reaccelerate beams produced with primary beams from a superconducting heavy-ion

linac and separated by the Advanced Rare Isotope Separator ARIS [2].

After separation, rare isotope beams are injected in one of two beam stopper systems [3], are mass separated and injected into a beam-cooler-buncher (BCB). The BCB is a buffer-gas filled linear radio-frequency quadrupole ion trap with axial and radial confinement of ions in a buffer gas, designed to improve the optical properties by cooling and to convert the incoming continuous beam into bunches for efficient injection and capture in the Electron Beam Ion Trap (EBIT) [4]. In the EBIT, trapped ions are charge-bred for achieving charge states compatible with the needs for acceleration and beam purity. After the EBIT, the beam is mass selected in an achromatic Q/A separator and injected into a multi-harmonic buncher at an energy of 12 keV/u. There it is bunched to match the operation frequency of the Radio Frequency Quadrupole (RFQ) of 80.5 MHz [5].

Following the RFQ, the beam is injected into a sequence of 3 cryomodules with quarter wave resonators (QWR) and superconducting solenoids (SS). A total of seven QWR with $\beta = 0.041$, eight QWRs with $\beta = 0.085$, and eight SS provide acceleration and focusing for the ensemble initially called ReA3. Following the accelerator, the beam can be energy-analyzed and sent to an experimental area with three beam lines: One is dedicated to the recoil spectrometer SECAR [6] for astrophysics studies, while two others are general purpose beam lines. With the accelerator upgrade the beam can now be rebunched and injected into the new cryomodule, which allows acceleration up to 6 MeV/u for a charge-to-mass ratio of 1/4 and sent to a new experimental area with two beam lines for experiments.

Stable beams and more recently long living rare isotopes can also be accelerated by ReA. Two 1+ ion sources can inject beams directly into the BCB. The BMIS, located in the N4 vault, is based on the ISOLDE/VADIS target/ion source [7] coupled to a front-end. Its initial purpose was to provide beams of stable and long-lived rare isotope beam for reacceleration during the time NSCL's coupled cyclotron facility was shut down in the transition phase of FRIB project completion and start of operation. Following its successful operation, BMIS will also be used for stand-alone operation of ReA in the FRIB era.

THE ReA PROJECT

The upgrades to the ReAccelerator are shown in Fig. 1. The ReA6 cryomodule and the new experimental areas are located in shielded vaults designed for the purpose of

*This material is based upon work supported by the US Department of Energy, Office of Science, Office of Nuclear Physics and user resources of the Facility for Rare Isotopes (FRIB), which is a DOE Office of Science User Facility under Award Number DE-SC0000661 and the NSF under grant PHY15-65546.

[†] villari@frib.msu.edu

IMPROVEMENTS TO THE RECYCLER/MAIN INJECTOR TO DELIVER 850 kW+

R. Ainsworth*, P. Adamson, D. Capista, N. Chelidze, K. Hazelwood, I. Kourbanis,
O. Mohsen, D. K. Morris, M. J. Murphy, M. Wren, M. Xiao
Fermi National Accelerator Laboratory[†], Batavia, IL, USA
C. Gonzalez-Ortiz, Michigan State University, East Lansing, MI, USA

Abstract

The Main Injector is used to deliver a 120 GeV high power proton beam for neutrino experiments. The design power of 700 kW was reached in early 2017 but further improvements have seen a new sustained peak power of 895 kW. Two of the main improvements include the shortening of the Main Injector ramp length as well optimising the slip-stacking procedure performed in the Recycler to reduce the amount of un-captured beam produce and eventually making its way into the Main Injector. These improvements will be discussed in this paper as well as future upgrades to reach higher beam powers.

INTRODUCTION

The Recycler (RR) and Main Injector (MI) are part of the Fermilab accelerator complex, as shown in Fig. 1, used to deliver high intensity beams for Neutrino experiments. The Recycler is a 8 GeV permanent magnet machine while the Main Injector can ramp from 8 GeV to 120 GeV. Both machines share the same enclosure. The Recycler also sends beam to the muon campus and the Main Injector also performs slow extraction for test beam experiments. These modes will not be discussed further in this paper.

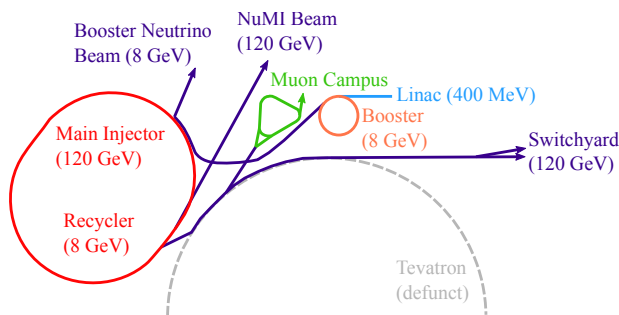


Figure 1: The Fermilab Accelerator complex.

For the high intensity neutrino beams the source produces H^- ions which are accelerated to 400 MeV in a normal conducting linac. Upon injection into the Booster, foil stripping is used to convert the H^- ions to protons. Here they are accelerated to 8 GeV and then sent to the Recycler ring. The slip-stacking procedure (which will be discussed in more detail in a later section) is used to double the bunch intensity.

* rainswor@fnal.gov

[†] Operated by Fermi Research Alliance, LLC under Contract No.De-AC02-07CH11359.

The protons are then extracted to the Main Injector which accelerates them to 120 GeV and are finally sent down the NuMI line to the experiments.

Figure 2 shows the beam power per hour since the Recycler was first used as a proton stacker in 2013. The steps to achieve the design power of 700 kW have already been described in [1]. Following further improvements, a record beam power of 895 kW was achieved at the end of the FY22 year run. It should be noted that the record beam powers are achieved when beam is only sent to the high energy neutrino experiments. If muon campus or test beam are requesting beam, the hourly power will drop by 5-15%. A large period of no beam is seen during 2020, this was caused partly due to the covid-19 pandemic as well as a longer shutdown planned for LBNF construction work. In the following sections, the improvements that led to the record beam power are described. While increasing beam intensity, losses around the rings are continually monitored to keep activation of the accelerator components to a minimum. Radiation surveys [2] are performed to compare with online beam loss monitoring.

FASTER RAMP

During long shutdown in 2013 the Main Injector ramp time was reduced to 1.33 s. For PIP-II, the ramp time needed to be reduced further to 1.2 s. Efforts to demonstrate this started in late 2018 and was implemented operationally in late 2019. Figure 3 shows a comparison of the two up ramps as well as the acceleration rate \dot{P} . While the maximum acceleration rate remained at 240 GeV/s for both ramps, the speedup came from by going much faster during the early parabola.

The reduction in MI cycle times leads to a 10% in beam power. However, it's important to note that in the case when muon campus is requesting beam, the Main Injector ramp must include an extra 0.2 s so the power increase cannot be taken advantage of.

RADIAL OFF-CENTER SLIP-STACKING

The Recycler has harmonic number h of 588 meaning it can accept 588 bunches. Each batch from the booster consists of 84 bunches so the Recycler can in principle accept 7 batches however this is limited to 6 batches to allow space for kicker rise times. In order to surpass the intensity limit that the booster can provide, slip-stacking is used allow the injection of 12 batches into the Recycler which are then combined into 6 double intensity batches.

ELECTRON CLOUD SIMULATIONS IN THE FERMILAB RECYCLER*

A.P. Schreckenberger[†], University of Illinois Urbana-Champaign, Urbana, IL, USA
 R. Ainsworth, Fermi National Accelerator Laboratory, Batavia, IL, USA

Abstract

We present a simulation study to characterize the stability region of the Fermilab (FNAL) Recycler in the context of secondary emission yield (SEY). Interactions between electrons and beam pipe material can produce electron clouds that jeopardize beam stability in certain focusing configurations. Such an instability was documented in the Recycler, and the work presented here reflects improvements to better understand that finding. We incorporated the Furman-Pivi Model into a PyECLOUD analysis, and we determined the instability threshold given various bunch lengths, intensities, SEY magnitudes, and model parameters.

SECONDARY EMISSION YIELD

The secondary emission phenomenon holds a prominent position in the history of high-energy particle physics. Interactions between sufficiently-energetic incident particles and materials have the capability to liberate secondaries, and applications exploiting this effect have filled niches in scientific study—with photomultiplier tubes standing out as a dominant example. These instruments formed essential components of numerous particle physics experiments.

Conversely, the emission of secondary particles can have detrimental impacts in some scenarios. We are interested in the potential impact secondary electrons pose to the stability of the FNAL Recycler, the interactions between in-vacuum electrons and beam pipe materials, the subsequent generation of electron clouds, and a mapping of the expected stability region as a function of the SEY amplitude. The following sections of this manuscript will address the historical context of SEY investigations at FNAL and present new findings that arise from the latest simulation study.

We typically quantify the SEY strength via the δ coefficient as a function of the incident electron energy. The shapes of these functions also depend on the angle of incidence as well as the specific material surface, and they fundamentally characterize the number of electrons liberated from the impacted material by an incident particle. Analyses with an accelerator physics focus gravitate towards beam characteristics, beam pipe materials, SEY-reducing coatings, conditioning time frames, and optics-amplified instabilities. A simulated SEY curve is shown in Fig. 1, which was generated using PyECLOUD software [1] and the Furman-Pivi (FP) Model [2]. In this example, we specified inputs that describe the Recycler optics, beam intensity, and bunch structure. FP parameters, which inject surface characteristics into the electron cloud simulation, were chosen to reflect the stainless steel wall of the beam pipe.

* Work supported by the Fermilab Accelerator Division and the University of Illinois Urbana-Champaign

[†] wingmc@fnal.gov, currently employed by Fermilab

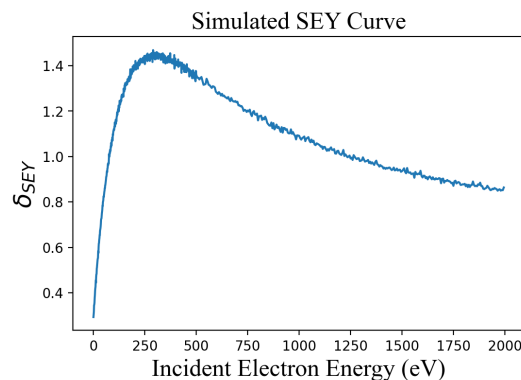


Figure 1: An SEY curve produced with PyECLOUD and the Furman-Pivi Model. Input parameters reflect conditions in the FNAL Recycler. The depicted example specifically reflects normal ($\theta = 0$) electron incidence.

The Furman-Pivi Model considers three categories of electrons in its construction of material interactions: 1) elastic electrons, which are reflected off the surface boundary, 2) rediffused electrons, which penetrate molecular layers of the material before re-emerging, and 3) true secondaries, which are ejected from the material and can add to the number of electrons in the final state. In practice, elastic and rediffused electrons do not undergo distinct mechanisms. Both are subject to atomic scatterings that lead to a reflection of the incident particle that conserves the number of electrons in the initial and final states. The distinction in the probabilistic model stems solely from the advantages the categorization provides the phenomenological fitting process [2]. In this method, $\delta(\theta, E)$ can now be represented as the sum of its categorical components, namely:

$$\delta(\theta, E) = \delta_{ts}(\theta, E) + \delta_r(\theta, E) + \delta_e(\theta, E), \quad (1)$$

where ts , r , and e refer to true secondary, rediffused, and elastic; θ is specified, and $\delta = \text{Max}(\delta(\theta, E)) = \delta_{\text{max}}(\theta, E)$.

With the SEY curves generated to reflect the conditions in the FNAL Recycler, PyECLOUD calculates the expected electron density in the beam region as a function of time. Three examples of the simulated outputs are illustrated in Fig. 2, which demonstrates how the density behavior can change when the δ coefficient is scaled. For the dotted line in the figure with $\delta = 1.3$, we observe that the electron density holds steady during the first $1.6 \mu\text{s}$ when proton bunches enter the accelerator and then decays over time to a final value $n_f \ll n_i$, where f and i designate the final and initial densities.

When δ is scaled to 1.7 and 2.0, the decay behavior after the peak persists, but the maximum density increases by orders of magnitude. Furthermore, we see a reversal in

MODEL/MEASUREMENT COMPARISON OF THE TRANSVERSE PHASE SPACE DISTRIBUTION OF AN RFQ-GENERATED BUNCH AT THE SNS BTF*

K. Ruisard[†], A. Aleksandrov, S. Cousineau, A. Hoover, A. Zhukov
 Oak Ridge National Laboratory, Oak Ridge, TN, USA

Abstract

The research program at the SNS Beam Test Facility is focused on resolving observed model/measurement discrepancies that preclude accurate loss prediction in high-power linacs. The current program of study is focused on deploying direct 6D measurements to reconstruct a realistic model of the initial beam distribution at the RFQ output. This detailed characterization also provides an opportunity for benchmark of RFQ simulations. Here we compare PARMTEQ predictions against 5D-resolved (x, x', y, y', w) phase space measurements of the BTF H- bunch, focusing on the transverse distribution. This work is an extension of previous research, which focused on the longitudinal phase space.

INTRODUCTION

The application of accelerator modeling to predict beam loss will require significant improvement in model accuracy. This includes a more complete description of the initial beam distribution. Typical reconstruction methods rely on fully projected phase space distributions and assume no interplane correlations. Beams with 3D space charge break this assumption, as shown in Ref. [1] for bunches in the Beam Test Facility (BTF) at the Spallation Neutron Source (SNS). Subsequent work has focused on advancing measurement capabilities in order to map the initial 6D beam distribution with enough accuracy to enable predictive modeling of beam halo.

A previous publication on BTF measurements compared data from high-dimensional phase space measurements to predictions from RFQ simulations. This work reported that measured emittances were 20 – 30% lower than predicted in the most realistic simulation case [2]. However, observed space-charge-driven longitudinal-transverse dependencies [1] are reproduced in simulation.

The comparison in Ref. [2] is limited to the longitudinal distribution. This paper extends this comparison from the perspective of the transverse bunch distribution using 5D distribution measurements. This comparison is facilitated by higher transverse resolution enabled by reducing the measurement dimension from 6D to 5D.

MEASUREMENT APPROACH

The BTF is a replica of the SNS front-end, consisting of H- ion source, 65 keV LEPT, 402.5 MHz radiofrequency

quadrupole (RFQ) and 2.5 MeV MEBT. The 6D diagnostic is located at the beginning of the MEBT, 1.3 meters downstream of the RFQ. The BTF beamline includes periodic FODO section followed by a second 5D-capable phase space diagnostic.

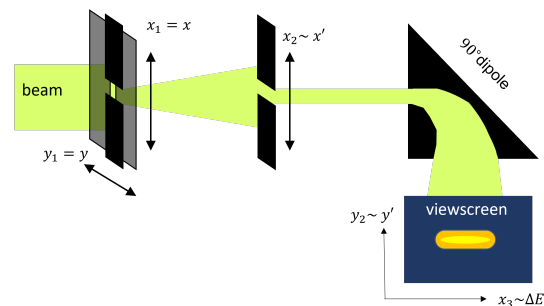


Figure 1: Geometry of 5D measurement apparatus.

This paper discusses a measurement of the 5D distribution, $\int d\phi f(x, x', y, y', \phi, w)$, 1.3 meters downstream of the RFQ exit. Here w is the spread in kinetic energy relative to the mean energy of the bunch. The measurement apparatus uses 3 slits and a phosphor-coated viewscreen, illustrated in Fig. 1. The resolution in the slit coordinates is nearly 4× higher than for the 6D measurement, which requires at least 23 hours. The dynamic range is also improved, from 2 to 3 orders of magnitude, as a result of reducing the number of slits inserted. The 5D data discussed here is a result of two measurements: (1) 4 hours on 12/3/2022 with 30.2 ± 0.3 mA RFQ output current and (2) 7.6 hours on 7/15/2022 at 26.73 ± 0.06 mA.

The position of the 3 slits and the 2 viewscreen axes of are converted to phase space coordinates using matrix operations. The pixel intensity values are linearly interpolated onto a regular grid in phase space coordinates using the griddata function in scipy [3]. The resolution along the viewscreen axes is reduced to avoid high memory load. After processing the 5D density is defined on a regular grid in (x, x', y, y', w) coordinates. The 30.2 mA data is interpolated to a $33 \times 41 \times 32 \times 101 \times 200$ grid. The 26.7 mA data is interpolated to a $45 \times 45 \times 45 \times 50 \times 80$ grid.

SIMULATION APPROACH

A PARMTEQ [4] model of the SNS RFQ design is used to predict the beam distribution at the MEBT entrance. This paper presents results from the "realistic case" using measured LEPT distributions. More details can be found in Ref. [2]. The input beam current is assumed to be 50 mA. The vane

* This material is based upon work supported by the U.S. Department of Energy, Office of Science, Office of High Energy Physics.

[†] ruisardkj@ornl.gov

THERMIONIC SOURCES FOR ELECTRON COOLING AT IOTA

M. K. Bossard*, N. Banerjee, J. Brandt, Y.-K. Kim, University of Chicago, Chicago, IL, USA
 M. Krieg, St. Olaf College, Northfield, MN, USA
 B. Cathey, S. Nagaitsev, G. Stancari, Fermilab, Batavia, IL, USA

Abstract

We are designing and fabricating two new thermionic sources of magnetized electrons for use in the electron lens project at the Integrable Optics Test Accelerator (IOTA) at Fermilab. These electron sources will be used for cooling of 2.5 MeV protons in the presence of intense space-charge. Furthermore, we are constructing an electron source test stand at the University of Chicago which will validate the electrical, thermal, and vacuum characteristics of thermionic sources. In this paper we present the progress made so far and the upcoming steps for the thermionic electron sources for electron cooling and the test stand.

INTRODUCTION

Electron sources have played an important role in many areas throughout their rich history, such as the development of vacuum-tube technology, microscopy, modern electronic circuits, and particle accelerators [1]. Electron emission is the process by which electrons are emitted off of a material as their energies overcome the material's work-function [2]. There are many different physical stimuli which can supply the energy for electron emission, such as thermal-energy, photons, ion or electron bombardment, and high magnetic fields [3]. Thermionic electron sources are often used in electron lenses, which are flexible instruments for beam physics research and particle accelerator operations [4].

Electron lenses operate on the principle of a magnetically confined, low-energy electron beam overlapping with a recirculating beam in a storage ring [4]. They are able to produce highly stable electron beams through the solenoidal magnetic field in the region of the beam. Electron lenses interact with the recirculating charged particles through electromagnetic fields allowing us to change the distribution of recirculating particles in phase-space. Example uses of electron lenses include space-charge compensation, beam-beam compensation [5, 6], halo reduction [7], and electron cooling.

The Integrable Optics Test Accelerator (IOTA) is a re-configurable 40 m storage ring at Fermilab [8, 9]. It acts as a test facility dedicated to research on intense beams, including the areas of Non-linear Integrable Optics (NIO) [10], space-charge [11], beam cooling [4], and single electron storage [12]. It can circulate both electrons and protons at kinetic energies up to 150 MeV and 2.5 MeV, respectively [11]. The layout of IOTA, along with the location of the electron cooler is shown in Fig. 1. In the ring, protons enter in section A. The beam circulates clockwise and co-propagates with the electrons in section DR.

* mbossard@uchicago.edu

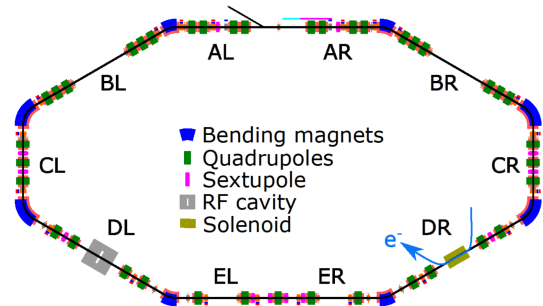


Figure 1: Schematic of the Integrable Optics Test Accelerator (IOTA). The ring is separated into sections, where the blue arrow in section DR represents the cool electron beam path.

Our goals in this project are to design, test, and commission two thermionic electron sources at IOTA. One source will be used as a tool for cooling proton beams with relatively small currents, to perform beam manipulations relevant for other experiments in IOTA. The other source will be used to investigate the dynamics and control of proton beams under intense space-charge [11].

In the upcoming sections, we will discuss electron cooling and its placement in IOTA, the cooler source designs, and the development of the test stand for the sources. We then will conclude and present the next steps.

ELECTRON COOLING

In a recirculating ion beam's center of mass frame, the ions have random transverse velocities, corresponding to large emittance and large thermal energy. The thermal energy of a beam is increased by non-linear forces and interactions in the beam-line, such as space-charge effects, intra-beam scattering, and external non-linear magnetic fields throughout the accelerator path. To decrease the thermal energy of the ion beam, a cooling method must be employed.

In electron cooling, a beam of ions exchanges thermal energy with a co-propagating beam of electrons. As the beam of ions re-circulates through the accelerator, its thermal energy increases. To reduce this, it is periodically mixed with a bath of cold, low-energy electrons. The electrons move at the same average longitudinal velocity as the ions and the beams undergo Coulomb scattering, thus approaching thermal equilibrium and reducing the beam's thermal energy [13, 14].

Figure 2 shows the location of the electron cooler, zoomed into the DR section of the IOTA ring. It depicts the electron

ARDAP's PERSPECTIVE ON ACCELERATOR TECHNOLOGY R&D IN THE U.S.

B. Carlsten[†], E. Colby, R. Marsh, M. White

Office of Accelerator R&D and Production, U.S. Department of Energy, Germantown, MD, USA

Abstract

DOE operates several particle accelerator facilities and is planning several new forward-leaning accelerator facilities over the next decade or two. These new facilities will focus on discovery science research and fulfilling other core DOE missions. Near and mid-term examples include PIP-II and FACET-II (for High Energy Physics); LCLS-II, SNS-PPU, APS-U, and ALS-U (for Basic Energy Sciences); FRIB (for Nuclear Physics); NSTX-U and MPEX (for Fusion Energy Sciences); and Scorpions (for NNSA). Longer-term examples may include future colliders, the SNS-STs, LCLS-II HE, and EIC. In addition to domestic facilities, DOE's Office of Science (SC) also contributes to several international efforts.

Together, these new facilities constitute a multibillion-dollar construction and operations investment. To be successful, they will require advances in state-of-the-art accelerator technologies. They will also require the National Laboratories to procure a variety of accelerator components.

This paper summarizes how DOE is working to address these upcoming R&D and accelerator component production needs through its new office of Accelerator R&D and Production (ARDAP).

ACCELERATOR R&D IN THE OFFICE OF SCIENCE

Facility-specific accelerator R&D is the purview of the specific SC Program Office (Fig. 1) planning the facility. For example, Basic Energy Sciences is responsible for the R&D needed for the high-average current, high-brightness electron injectors needed for LCLS-II and LCLS-II HE; Nuclear Physics will be responsible for the R&D needed for ion cooling for the upcoming EIC; and High Energy Physics will be responsible for the high-field magnet R&D needed for a 100-TeV hadron collider. The amount of accelerator R&D required for upcoming SC facilities is very significant, with several key enabling technologies still elusive (e.g., advanced accelerator schemes for future multi-TeV lepton colliders). Moreover, several emerging technologies may impact multiple facilities crossing different SC Program Offices, and the coordination of the required R&D between these offices needs to be considered.

While accelerator facility construction and operations costs have increased over the last decade, accelerator R&D in SC has decreased both in absolute terms (from about \$164M in FY2011 to about \$96M in FY2022) and in relative terms (from about 12% of the entire accelerator budget in 2011 to a minimum of 3.7% in FY2020, recovering somewhat to 5.2% in FY2023), as shown in Fig. 2.

Data calls and a Request for Information have helped quantify specific supply chain issues in accelerator technology and to outline the challenges faced by domestic industrial suppliers. In addition, over half of accelerator procurements for SC accelerator facility construction and operations are now coming from off-shore.

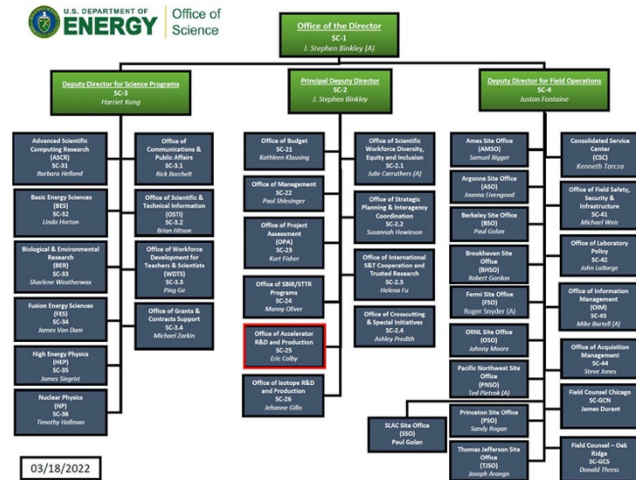


Figure 1: SC organization [1], including the Science Programs and the new Office of Accelerator R&D and Production (outlined in red).

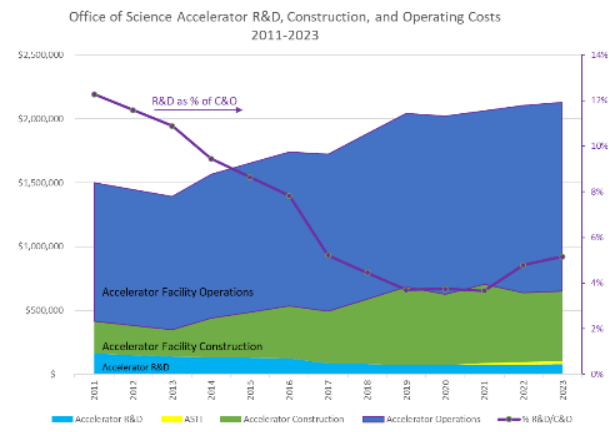


Figure 2: SC accelerator R&D, construction, and operating costs from FY2011 to FY2022 [actual] and FY2023 [request] (where "C&O" means construction and operations).

THE OFFICE OF ACCELERATOR R&D AND PRODUCTION

As part of a larger reorganization in SC, a new Office of Accelerator R&D and Production (ARDAP) was established to serve as a focal point for coordinating accelerator

[†] email address: bruce.carlsten@science.doe.gov

Content from this work may be used under the terms of the CC BY 4.0 licence (© 2022). Any distribution of this work must maintain attribution to the author(s), title of the work, publisher, and DOI

MAGNETRON R&D PROGRESS FOR HIGH EFFICIENCY CW RF SOURCES OF INDUSTRIAL ACCELERATORS*

H. Wang[#], K. Jordan, R. M. Nelson, R. A. Rimmer, S. A. Overstreet
 Jefferson Lab, Newport News, VA 23606, USA
 B. R. Coriton, C. P. Moeller, K. A. Thackston
 General Atomics, San Diego, CA 92121, USA

J. N. Blum, Virginia Commonwealth University, Richmond, VA 23284 USA

J. L. Vega, College of William and Mary, Williamsburg, VA 23185 USA

G. Ziemyte, University of Kentucky, Lexington, KY 40506 USA

Abstract

After the demonstration of using high efficiency magnetron power to combine and aim to drive a radio frequency accelerator at 2450 MHz in CW mode [1], we have used trim coils adding to a water-cooled magnetron and three amplitude modulation methods in an open-loop control to further suppress the 120 Hz sideband noise to -46.7 dBc level. We have also successfully demonstrated the phase-locking to an industrial grade cooking magnetron transmitter at 915 MHz with a 75 kW CW power delivered to a water load by using a -26.6 dBc injection signal. The sideband noise at 360 Hz from the 3-Phase SCRs DC power supply can be reduced to -6.2 dBc level. Their power combing scheme and higher power application to industrial accelerators are foreseeing.

INTRODUCTION

The industrial heating type magnetrons at 915 MHz operated in CW mode have more than 90% of DC to RF efficiency and making cost of effective ~1 \$/W market value [2]. Under the accelerator stewardship program, we have set up a test stand intending to drive radio frequency accelerators for 1–10 MeV electron beam energy and up to 1 MW of beam power applications [3]. Since May 2019, the first AMTek® 75 kW magnetron transmitter has been setup as a high powers test stand at Jefferson Lab (JLab) [4]. Due to the COVID-19 pandemic restrictions, the experimental progress was mostly made at 2450 MHz RF systems at JLab and General Atomics (GA) and with help of summer interns of Research Experience for Undergraduates (REU) students [1]. The utility connections and Programmable Logic Controller (PLC) modification had been made to the first unit. A second 75 kW transmitter unit has been delivered to JLab, we are going to combine these two units by a WR975 waveguide magic-tee to have 2×75 kW of power available with the injection phase-locked performance for both electron linac booster and the SRF accelerator.

INJECTION PHASE-LOCK DEMONSTRATION OF 915 MHz MAGNETRON

After first tuning on the 75 kW magnetron in manufacture control mode, we have measured the anode I–V and I–E curves with a careful high voltage reading check and a

TRL calibration for the RF power meters. The injection phase-lock scheme has been set up as in Fig. 1 by using double isolation of two WR975 circulators. A special care to the bench measurement to have the optimized circulator/water load performance in isolations, transmissions reflections (particularly on the primary circulator) is important to have a best S/N ratio for the injection signal.

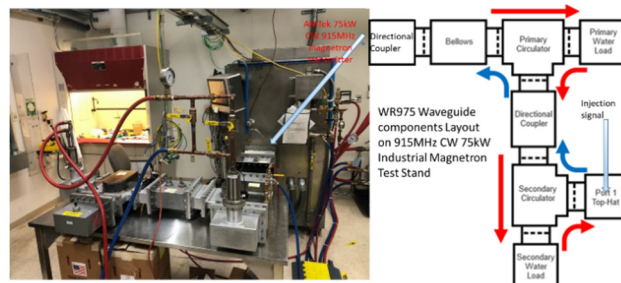


Figure 1: AMTek® 915 MHz, 75 kW CW magnetron test stand at JLab with back injection layout for phase-lock. Blue arrows indicate the injection path. Red arrows direct the RF power to primary and secondary water loads.

Table 1 lists the optimized bench measurement data of this waveguide circuit before and after the waveguide assembly. Removing excessive iron plates from the circulator magnet shunts and relocating them are critical technique in the magnetic field trimming [5].

Table 1: TRL S-parameters measurement at 915 MHz after trimming on circulator magnet shunts with the Port 2 at output power direction as indicated in Fig. 1. The last row data was for fine-tuned assembled system at 912.5 MHz.

Circulator water load pair	Isolation S12 (dB)	Reflection S11 (dB)	Reflection S22 (dB)	Transmission S21 (dB)
Primary	-43.15	-22.73	-22.80	-0.15
Secondary	-17.13	-15.63	-18.08	-1.40
Combined	-57.04	-14.71	-22.85	-1.90
Assembled	-53.22	-15.51	-23.46	-1.59
912.5 MHz	-51.05	-16.00	-23.82	-1.70

We have first observed locking state at 65 kW level as shown on a spectrum analyser (Fig. 2). Once locked at 75 kW level, a frequency counter could monitor the frequency variation being only within a sub-Hz range, indicating a strong lock performance. The injection power is at -26.6 dBc level. We have expected major 360 Hz noise peaks with 60 Hz intervals coming from the 3-phase SCR

* Authored by Jefferson Science Associates, LLC under U.S. DOE Contract No. DE-AC05-06OR23177, and DOE OS/HEP Accelerator Stewardship award 2019-2022.

haipeng@jlab.org

MANUFACTURING THE HARMONIC KICKER CAVITY PROTOTYPE FOR THE ELECTRON-ION COLLIDER*

S. Overstreet[†], M. Bruker, G. A. Grose, J. Guo, J. Henry,
 G. T. Park, R. A. Rimmer, H. Wang, S. R. Williams

Thomas Jefferson National Accelerator Facility, Newport News, VA, USA

Abstract

High-bunch-frequency beam-separation schemes, such as the injection scheme proposed for the Rapid Cycling Synchrotron at the Electron-Ion Collider, demand rise and fall times an order of magnitude below what can realistically be accomplished with a stripline kicker. Nanosecond-time-scale kick waveforms can instead be obtained by Fourier synthesis in a harmonically resonant quarter-wave radio-frequency cavity which is optimized for high shunt impedance. Originally developed for the Jefferson Lab Electron-Ion Collider (JLEIC) Circulator Cooler Ring, a hypothetical 11-pass ring driven by an energy-recovery linac at Jefferson Lab, our high-power prototype of such a harmonic kicker cavity, which operates at five modes at the same time, will demonstrate the viability of this concept with a beam test at Jefferson Lab. As the geometry of the cavity, tight mechanical tolerances, and number of ports complicate the design and manufacturing process, special care must be given to the order of the manufacturing steps. We present our experiences with the manufacturability of the present design, lessons learned, and first RF test results from the prototype.

BACKGROUND

In January of 2020, the U.S. Department of Energy (DOE) chose Brookhaven National Laboratory (BNL) as the site for building an Electron-Ion Collider (EIC) over the competing Jefferson Lab Electron-Ion Collider (JLEIC), creating a new partnership between the two labs [1]. The Harmonic Kicker cavity was originally intended for the JLEIC Circulator Cooler Ring (CCR), a hypothetical 11-pass ring driven by an energy-recovery linac at Jefferson Lab [2], but is now envisioned with BNL as a potential injection device for their Rapid Cycling Synchrotron (RCS) [3].

The JLEIC cavity is a harmonically resonant quarter-wave radio-frequency cavity driven with the Fourier synthesis of odd multiples (1, 3, 5, 7, and 9) of its designed fundamental resonant frequency, which is the frequency between the injected and extracted bunches in and out of the CCR. In principle, this Fourier synthesis produces a narrow pulse, as shown in Fig. 1, that will kick every eleventh electron bunch without disturbing intermediate bunches [4].

The first prototype cavity was a simplified half-scale version with a fundamental resonant frequency of 95.26 MHz

* This material is based upon work supported by the U.S. Department of Energy, Office of Science, Office of Nuclear Physics under contract DE-AC05-06OR23177.

[†] sarahann@jlab.org

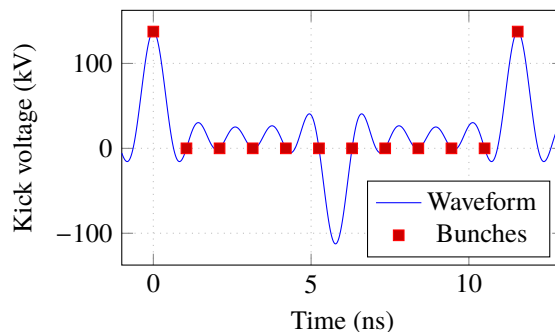


Figure 1: Kick action only on bunches at a bunch frequency equal to the fundamental of the kick waveform, $f_{HK} = 86.6$ MHz; in this example, all 11 buckets are filled at a bunch frequency of $11 f_{HK} = 952.6$ MHz.



Figure 2: The original model of the JLEIC high-power kicker cavity.

and was built and tested at Jefferson Lab in 2016 [5]. Presently, a high-power, water-cooled, vacuum-compatible JLEIC prototype with a fundamental resonant frequency of 86.6 MHz is nearly complete and will undergo a beam test at Jefferson Lab's Upgraded Injector Test Facility (UITF) by mid-October. The properties of this final JLEIC version of this cavity give rise to a multitude of challenges that have complicated the design and manufacturing processes as outlined in the following sections.

KICKER CAVITY DESIGN EVOLUTION

Even at first glance, the early model of the JLEIC high-power kicker cavity in Fig. 2 looks like the complicated machine that it is. Its field defined by the coaxial geometry of the body and the inner conductor combined, it relies on concentricity and imposes tight tolerances on the components and their respective joints. One can easily imagine how this deceptively simple model might rapidly evolve to the models shown in Fig. 3 after the start of fabrication. The

COMPACT, HIGH-POWER SUPERCONDUCTING ELECTRON LINEAR ACCELERATORS FOR MW INDUSTRIAL APPLICATIONS

J. C. T. Thangaraj[†] and R.C. Dhuley, Fermilab, Batavia, IL, USA

Abstract

Fermilab has developed a novel concept for an industrial electron linac using Nb₃Sn coating technology and conduction cooling. These conduction-cooled linacs can generate electron beam energies up to 10 MeV in continuous-wave operation and reach higher power (≥1 MW) by combing several modules. Compact and light enough to mount on mobile platforms, our machine is anticipated to enable new in-situ environmental remediation applications such as waste-water treatment for urban areas, X-ray medical device sterilization, and innovative pavement applications. We highlight a few aspects of a 1-MW design of such a machine in this paper.

BACKGROUND

Superconducting RF cavities made of Nb₃Sn, with cryogenic operation near the temperature of 4 K, exhibit minimal RF wall dissipation (about six orders of magnitude smaller than copper cavities of similar shape and size), allowing their operation at 100% RF duty cycle (continuous wave or CW operation). SRF accelerators can generate very high average power e-beams suitable for high-volume irradiation applications for altering materials' physical, chemical, molecular, and biological properties. These include polymerization, medical and food sterilization, environmental remediation, wastewater treatment, sludge, and biosolids treatment [1]. This paper briefly describes the design of an e-beam accelerator designed to treat high volume (several million gallons per day) of municipal wastewater. The accelerator uses a cryocooled elliptical 650-MHz Nb₃Sn SRF cavity, designed to produce a 10-MeV, 1-MW average power electron beam. A detailed plan is in [2].

ACCELERATOR DESIGN

The accelerator layout is divided into three sections (shown in Fig. 1): preaccelerator, accelerator (called cryomodule), and the beam delivery system. The preaccelerator comprises a thermionic electron source (gun), an RF injector cavity, and a focusing solenoid magnet. The electron beam exiting the preaccelerator is fed into the accelerator, which energizes the beam to the 10-MeV target energy. The accelerator uses an Nb₃Sn (SRF) cavity operating near 4 K, conduction cooled via cryocoolers. Two fundamental power couplers pierce the vacuum vessel through two ports at 180° to each other to feed RF power into the SRF cavity. The beam exits the accelerator with 10-MeV energy. It then enters the beam delivery system, where it is conditioned using a raster magnet and beam horn for irradiating a stream of wastewater.

[†]jtobin@fnal.gov

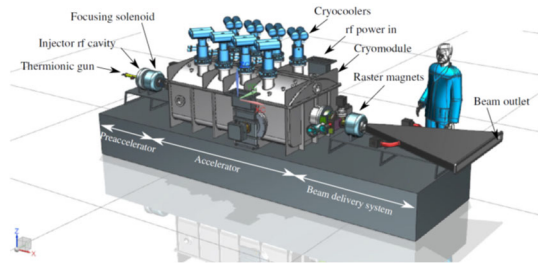


Figure 1: Graphic rendering of an industrial SRF e-beam accelerator components and layout. The overall size is ~4 m long (end-to-end), ~2 m wide, and ~2 m tall.

Electron Gun

The preaccelerator herein uses a triode RF gun with a gridded thermionic cathode. In this gun, the cathode emits low-energy electrons via thermal emission, which are then shaped into electron bunches using the RF voltage applied to the grid-cathode gap, superimposed on a constant dc voltage. The emitted electrons are then captured and accelerated by the electric field of the RFRF gun. The gun's operating RF amplitude and phase interval are determined for producing a 100-mA average current with a 154-pC electron-beam bunch charge. Figure 2 shows its parameters.

Parameters	Unit	Value
Frequency	MHz	650
Cathode diameter	inch	0.5
Beam current	mA	100
Current density	A/cm ²	2.35
DC bias voltage	kV	2.6
Output Energy	keV	3.5
Bunch rms size	Deg	<15
Energy rms size	%	<25

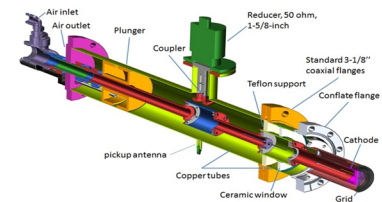


Figure 2: RF gun design parameters and components.

Injector Cavity

The injector cavity, located immediately downstream of the RF gun, captures the thermionically emitted electrons and accelerates them to ~300-keV energy. The 650-MHz cavity RF design aims to maximize the shunt impedance to get the required accelerating voltage with minimum heat dissipation. Taking copper as the injector cavity material, the voltage gain of ~300 kV would dissipate 11.6 kW of heat, which can be extracted using a forced flow of cooling water around the cavity.

RF Cavity Design

We based our design on five-cell, 650-MHz cavities designed to produce the 10-MeV electron beam. The cavity inlet port has a 35-mm diameter, equal to that of the inject-

FIRST HIGH-GRADIENT RESULTS OF UED/UEM SRF GUN AT CRYOGENIC TEMPERATURES*

R. Kostin[†], C. Jing, Euclid Beamlabs LLC, Bolingbrook, IL, USA
S. Posen, T. Khabiboulline, D. Bice, Fermilab, Batavia, IL, USA

Abstract

Benefiting from the rapid progress on RF photogun technologies in the past two decades, the development of MeV range Ultrafast Electron Diffraction/Microscopy (UED and UEM) has been identified as an enabling instrumentation. UEM or UED use low power electron beams with modest energies of a few MeV to study ultrafast phenomena in a variety of novel and exotic materials. SRF photoguns become a promising candidate to produce highly stable electrons for UEM/UED applications because of the ultrahigh shot-to-shot stability compared to room temperature RF photoguns. SRF technology was prohibitively expensive for industrial use until two recent advancements: Nb₃Sn and conduction cooling. The use of Nb₃Sn allows to operate SRF cavities at higher temperatures (4 K) with low power dissipation which is within the reach of commercially available closed-cycle cryocoolers. Euclid is developing a continuous wave (CW), 1.5-cell, MeV-scale SRF conduction cooled photogun operating at 1.3 GHz. In this paper, we present first high gradient results of the gun conducted in liquid helium.

INTRODUCTION

The use of SRF photogun brings certain benefits compared to normal conducting guns such as: unprecedented repetition rates (CW), reduced almost to zero RF losses, higher RF stability. As long as beam current is very low for UED/UEM applications, MW-level RF power source is not required and can be as low as several Watts. However, SRF was not user-friendly because it requires sophisticated cryomodules, experienced personnel and expensive cryogenics until recent proof of principle of conduction cooling at Fermilab [1], in which Euclid participated and Jlab [2].

Euclid is developing a CW, 1.5-cell L-band conduction-cooled SRF photogun operating at 1.3 GHz for UED/UEM applications [3,4]. The design of the gun was initially based on an existing cavity with an "on-axis" coaxial coupler developed by Euclid [5], however it was later changed to a standard Tesla end-cell with side couplers [6] to lower manufacturing costs. No beam quality degradation has been found in simulations. The half-cell geometry was optimized using CST, which was bench marked by ASTRA code. The beam parameters were optimized and are suitable for UED/UEM [7]. Beam energy out of the gun is 1.65 MeV which requires field on the cathode (on axis) of 20 MV/m. This field corresponds to accelerating gradient of 10 MV/m and can be found in Fig. 1.

* Work supported by US DOE SBIR grant DE-SC0018621.

[†] r.kostin@euclidtechlabs.com

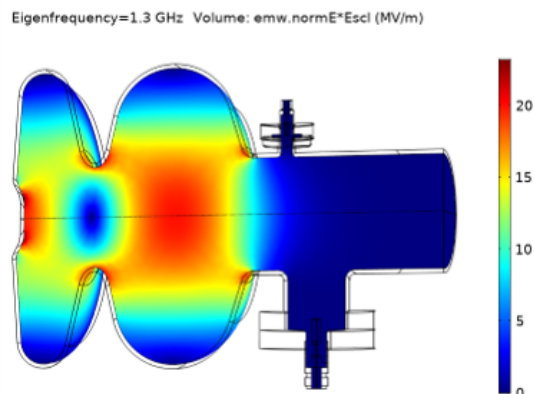


Figure 1: E-field distribution in the gun at $E_{acc}=10$ MV/m.

The RF dissipated power is below 1 W at quality factor of $Q_0=1.1 \times 10^{10}$ and accelerating gradient of 10 MV/m. This field level and quality factor is achievable nowadays even for 9-cell Tesla cavity [8]. The gun will be cooled using welded Nb equator rings - Fermilab's conduction cooling approach developed in collaboration with Euclid [9]. The "dry" cryomodule has been developed and is ready to host the cavity (see details in Ref. [4]) once the gun performance covered with Nb₃Sn is demonstrated in liquid helium at 4 K.

THE GUN TUNING

Tuning fixtures were designed to tune the gun field balance and frequency and can be found in Fig. 2.



Figure 2: 1.5 cell Nb SRF gun with cooling rings welded.

The fixtures consist of: turnbuckle-style connecting rods, side aluminium plates, split ring installed on the gun iris, longitudinal titanium rods. The fixtures without the split ring and turnbuckles is used for cavity support under vacuum

MAGNETIC FLUX EXPULSION IN SUPERCONDUCTING RADIO-FREQUENCY NIOBIUM CAVITIES MADE FROM COLD WORKED NIOBIUM*

B. D. Khanal¹, S. Balachandran², S. Chetri², P. J. Lee², P. Dhakal^{3†}

¹Department of Physics, Old Dominion University, Norfolk, VA, USA

²Applied Superconductivity Center, Tallahassee, FL, USA

³Thomas Jefferson National Accelerator Facility, Newport News, VA, USA

Abstract

Trapped residual magnetic field during the cooldown of superconducting radio frequency (SRF) cavities is one of the primary source of rf residual losses leading to lower quality factor. Historically, SRF cavities have been fabricated from high purity fine grain niobium with grain size 50 - 100 μm as well as large grain with grain size of the order of few centimeters. Non-uniform recrystallization of fine-grain Nb cavities after the post fabrication heat treatment leads to higher flux trapping during cooldown, hence the lower quality factor. We fabricated two 1.3 GHz single cell cavities from cold-worked niobium from different vendors and processed along with cavities made from SRF grade Nb. The flux expulsion and flux trapping sensitivity were measured after successive heat treatments in the range 800 – 1000 °C. The flux expulsion from cold-worked fine-grain Nb cavities improves after 800 °C/3 hours heat treatments and it becomes similar to that of standard fine-grain Nb cavities when the heat treatment temperature is higher than 900 °C.

INTRODUCTION

The performance of the SRF cavities is influenced by several intrinsic and extrinsic parameters. One of the significant contributing factor being the trapped magnetic flux due to the insufficient flux expulsion of ambient magnetic field from the SRF cavities when cavities cool-down through the superconducting transition temperature [1–4]. In theory, during the superconducting phase transition, all residual magnetic flux should be expelled from the bulk of the superconductor. However, material defects, dislocations, segregation of impurities provide favorable sites for magnetic flux pinning, which contribute to an additional rf loss when exposed to the rf field. It has been demonstrated that several different pinning mechanism plays a role to the rf losses due to vortices [4]. Studies showed that doped cavities are more vulnerable to the vortex dissipation loss due to the presence of the dopant on cavities rf surface [3, 5, 6].

Earlier studies on flux expulsion and rf losses due to pinned vortices showed that the better flux expulsion can be achieved when the cavity annealing temperature is in-

creased [7]. The increase in annealing temperature minimizes the pinning centers by removing the clusters of dislocations and impurities. In addition, the metallurgical state with larger grain size is expected as the annealing temperature is increased. Fine-grain recrystallized microstructure with an average grain size of 10 - 50 μm leads to flux trapping even with a lack of dislocation structures in grain interiors [8]. Here, we have conducted a systematic study on cold work SRF niobium in an attempt to correlate the metallurgical state with respect to the flux expulsion, flux pinning and flux trapping sensitivity. One of each 1.3 GHz TESLA shape single cell cavities were fabricated from cold work sheet from two different vendors as well as the standard cavity grade SRF niobium. The cavities were fabricated and processed together along with witness samples to analyze the metallurgical state as well as pinning strength with respect to the process applied to cavities.

CAVITY FABRICATION AND SURFACE PREPARATIONS

Fine grain Nb sheet of thickness ~ 3 mm SRF grade high purity with residual resistivity ratio greater than 350 were purchased from two different Nb vendors. In addition, a special order was made with vendors to provide the cold work with no post processing at vendor site. The vendors did not provide any material specifications for cold work sheets, however the sheets were made out of the same batch of SRF grade niobium and the final recrystallization step was omitted. The electron backscattered diffraction–orientation image (EBSD-OI) on two sets of Nb sheet along with the two single cell cavities fabricated at Jefferson Lab are shown in Fig. 1 from material provided by Tokyo Denkai. The second set of cavities were fabricated at cavity manufacturer from the material provided by Ningxia. The fabrication of cavities were followed the standard practice of deep drawing to half cells, trimming, machining of the iris and equator of the half-cells, electron beam welding of the beam tubes (made from low purity niobium).

After the cavity fabrication, the cavities were chemically polished by electropolishing (EP) in a horizontal, rotating setup, using a mixture of electronic grade $\text{HF}:\text{H}_2\text{SO}_4 = 1:9$ at a constant voltage of ~ 14 V, temperature of 15 - 20 °C and a speed of 1 rpm. The total bulk removal of ~ 150 μm at cavity equator was removed by EP. The first cycle of heat treatment of the cavity was done at 800 °C for 3 hours in UHV furnace.

* The work is partially supported by the U.S. Department of Energy, Office of Science, Office of High Energy Physics under Awards No. DE-SC 0009960. The manuscript has been authored by Jefferson Science Associates, LLC under U.S. DOE Contract No. DE-AC05-06OR23177.

† dhakal@jlab.org

BEAM DYNAMICS OPTIMIZATION OF A LOW EMITTANCE PHOTOINJECTOR WITHOUT BUNCHER CAVITIES*

J. Qiang[†], LBNL, Berkeley, CA, USA
 F. Ji, T. Raubenheimer, SLAC, Menlo Park, CA, USA

Abstract

The photoinjector plays an important role in generating high brightness low emittance electron beam for x-ray free electron laser applications. In this paper, we report on beam dynamics optimization study of a low emittance photoinjector based on a proposed superconducting gun without including any buncher cavities. Multi-objective optimization with self-consistent beam dynamics simulations was employed to attain the optimal Pareto front.

INTRODUCTION

The high brightness, coherent x-ray Free Electron Laser (FEL) provides an important tool for scientific discoveries in basic energy science. The LCLS-II-HE as a high energy upgrade of the high repetition rate X-ray FEL, LCLS-II [1, 2], will increase the final electron beam energy from 4 GeV to 8 GeV and photon spectral range to 12.8 keV with a potential to be extended through 20 keV [3]. In order to attain the 20 keV shorter wavelength x-ray radiation using the 8 GeV electron beam, a low emittance injector based on a 185 MHz superconducting RF (SRF) gun [4], one or two buncher cavities, and a superconducting RF cryomodule of boosting cavities has been actively pursued [5]. In this paper, we explored an alternative design of the low emittance injector without using any buncher cavities. Figure 1 shows the schematic layout of such an injector. The photo-electron beam out of the SRF gun is focused by a solenoid and accelerated by eight 1.3 GHz superconducting boosting cavities. Such an injector has a simpler structure and lower cost than the nominal design. The disadvantage of this injector is lack of flexibility.

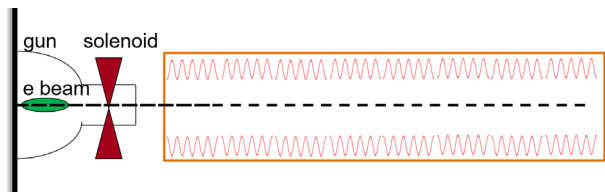


Figure 1: Schematic layout of the low emittance photoinjector.

MULTI-OBJECTIVE BEAM DYNAMICS OPTIMIZATION METHOD

A multi-objective optimization algorithm based on the differential evolution with varying population size and external storage was used in study [6]. In this method, the population size varies from one generation to next genera-

tion. Only nondominated solutions are kept in the population of each generation. Here, the nondominated solution is a solution that at least one component (i.e. one objective function) of this solution is better than the same component of all other solutions. An external storage is used to save all nondominated solutions from previous generations. The next generation parent solutions are selected from both the present generation offspring solutions and the external stored solutions. The advantage of using a variable population size with external storage is to reduce the number of objective function evaluations and to improve the speed of convergence. The new algorithm is summarized in the following steps: (i) Step 0: Define the minimum parent size, NP_{\min} and the maximum size, NP_{\max} of the parent population. Define the maximum size of the external storage, NP_{ext} . (ii) Step 1: An initial NP_{ini} population of parameter vectors are chosen quasi-randomly to cover the entire solution space. (iii) Step 2: Generate the offspring population using a unified differential evolution algorithm. (iv) Step 3: Check the new population against the constraints. (v) Step 4: Combine the new population with the existing parent population from the external storage. Nondominated solutions (NP_{ndom}) are found from this group of solutions and $\min(NP_{\text{ndom}}, \text{Next})$ of solutions are put back to the external storage. Pruning is used if $NP_{\text{ndom}} > NP_{\text{ext}}$. NP parent solutions are selected from this group of solutions for next generation production. If $NP_{\min} \leq NP_{\text{ndom}} \leq NP_{\max}$, $NP = NP_{\text{ndom}}$. Otherwise, $NP = NP_{\min}$ if $NP_{\text{ndom}} < NP_{\min}$ and $NP = NP_{\max}$ if $NP_{\text{ndom}} > NP_{\max}$. The elitism is emphasized through keeping the nondominated solutions while the diversity is maintained by penalizing the overcrowded solutions through pruning. (vi) Step 5: If the stopping condition is met, stop. Otherwise, return to Step 2. The differential evolution method is used to generate new trial solutions from the parent solutions. This method makes use of the difference between the current solution and best solution to emulate the gradient information and the difference of two randomly selected solutions and mutation to enhance the diversity of the solution [7, 8]. The differential evolution method as a simple but powerful method has been widely used in many applications. This multi-objective evolutionary optimizer is integrated with a parallel beam dynamics simulation code, IMPACT-T [9], to optimize the final electron beam quality at the exit of the injector. The IMPACT-T code is a three-dimensional macroparticle tracking code based on the particle-in-cell method. It simulates the electron beam emission from the photocathode and the electron beam transport and acceleration through the injector including the self-consistent space-charge effects. Here, the space-charge effects were computed by solving the three-dimensional Poisson equation in the beam frame using an integrated Green's function method. The fast Fourier transform

* Work supported by the Director of the Office of Science of the US Department of Energy under Contract no. DEAC02-05CH11231.
[†] jqiang@lbl.gov

BEAM DYNAMICS STUDIES ON A LOW EMITTANCE INJECTOR FOR LCLS-II-HE *

F. Ji[†], C. E. Adolphsen, C. Mayes, T. O. Raubenheimer, R. Coy, L. Xiao, L. Ge
SLAC National Accelerator Laboratory, Menlo Park, CA, USA
J. Qiang, Lawrence Berkeley National Laboratory, Berkeley, CA, USA

Abstract

The SLAC High Energy upgrade of LCLS-II will double the beam energy to 8 GeV, increasing the XFEL photon energy reach to about 13 keV. The energy reach can be extended to 20 keV if the beam emittance can be halved, which requires a higher gradient electron gun with a lower intrinsic emittance photocathode. To this end, the Low Emittance Injector (LEI) will be built that will run parallel to the existing LCLS-II Injector. The LEI design will be based on a state-of-the-art SRF gun with a 30 MV/m cathode gradient. The main goal is to produce transverse beam emittances of 0.1 mm-mrad for 100 pC bunch charges. This paper describes the beam dynamics studies on the design of the LEI including the simulations and multi-objective genetic algorithm optimizations. Performance with different injector layouts, cathode gradients and bunch charges are presented.

INTRODUCTION

X-ray Free Electron Lasers (XFELs) provide ultrafast coherent X-ray pulses for the study of structural dynamics on atomic spatial (Å) and time (fs) scales [1]. Such measurements provide critical insights into the fundamental processes in complex functional materials, gas phase molecules and biological systems [2]. The LCLS-II High Energy Upgrade (LCLS-II-HE) is a 4 GeV extension of the LCLS-II SRF linac that increases the high repetition rate XFEL photon energy reach from 5 keV to 13 keV [3]. The photon spectral range can be extended to 20 keV if the beam emittance can be halved. To this end, a Low Emittance Injector (LEI) will be built that will run parallel to the existing LCLS-II injector. The LEI design is based on a state-of-the-art 185.7 MHz, quarter-wave resonator (QWR) type Superconducting RF (SRF) gun [4] with a 30 MV/m cathode gradient. The goal is to produce 100 pC bunches with transverse emittances of 0.1 mm-mrad and lengths of $\sigma_z = 1$ mm (corresponding to 10 A peak current). In this paper, we describe the injector design optimization and performance with different injector layouts, cathode gradients and bunch charges.

INJECTOR OPTIMIZATION OVERVIEW

The strategy to achieve low emittance is to use both a higher cathode gradient and a lower Mean Transverse Energies (MTE) photocathode than those in LCLS-II [5, 6]. A MSU-ANL-HZDR collaboration is building a prototype

QWR type SRF gun based on a cavity design developed at SLAC for this application [4]. The initial goal is to achieve stable operation with a metal cathode plug for cathode gradients up to 30 MV/m. Based on experience with Alkali Antimonide photocathodes illuminated with green laser light, a MTE of 184 meV (i.e., intrinsic emittance = 0.6 $\mu\text{m}/\text{mm}$) was chosen as the working assumption for the LEI emittance optimization studies.

Once the beam is generated in the gun, space charge forces induce a bunch slice phase space mismatch that can cause transverse emittance degradation downstream. The standard approach for compensating such emittance degradation is to use a set of solenoids to rotate the slices differentially to re-align them downstream (i.e., emittance compensation [7]). To this end, a compact ferrite-based solenoid was simulated and the solenoid to cavity anode distance was optimized for emittance compensation. To better optimize the emittance over a range of cathode gradients and bunch charges, two sets of windings were included that could be independently powered so that both the solenoid strength and magnetic centroid could be varied.

Figure 1 illustrates two LEI configurations that were evaluated. The Compact configuration includes an SRF gun, gun solenoid, buncher cavity, second solenoid and an LCLS-II-HE type cryomodule (CM). The compact layout is similar to the LCLS-II injector except that a 9-cell SRF cavity is used for bunching, which allows a voltage gain of up to 16 MV. Although the resulting emittance was acceptable, the optimized layout left little space between the gun and the buncher, and as discussed below, the emittance grew rapidly at lower gradients. The Complex layout utilizes a two stage bunching strategy: an LCLS-II type normal conducting (NC) buncher and solenoid are included between the gun solenoid and the 9-cell buncher. The NC buncher is located 0.91 m from cathode, which allows the 9-cell buncher to be located 3.4 m from cathode, freeing up space for a full LCLS-II like diagnostic section. As an alternative, an LEI configuration without a buncher has been explored [8].

For both Compact and Complex configurations, the performance was evaluated with cathode gradients of 20 and 30 MV/m and bunch charges of 25, 100 and 200 pC. The cathode MTE was fixed at 184 meV and 10,000 macro particles were used when running the Multi-Object Genetic Algorithm(MOGA) NSGA-II code. The z locations of the beamline components were fixed for this study and were set to the optimized values for a 30 MV/m gradient and 100 pC charge. Table 1 lists the parameters that were varied and their ranges during MOGA optimizations.

* Work supported by U.S. Department of Energy Office of Science, Basic Energy Sciences under Contract No. DE-AC02-76SF00515.

[†] fuhaoji@slac.stanford.edu

STATUS OF THE SLAC/MSU SRF GUN DEVELOPMENT PROJECT*

J. W. Lewellen[†], C. Adolphsen, R. Coy, L. Ge, F. Ji, M. Murphy, L. Xiao
SLAC National Accelerator Laboratory, Menlo Park, CA, USA
M. Kelly, T. Peterson, Argonne National Laboratory, Lemont, IL, USA
Y. Choi, C. Compton, X. Du, D. Greene, W. Hartung, S-H. Kim, T. Konomi, S. J. Miller,
D. Morris, M. S. Patil, J. T. Popielarski, L. Popielarski, K. Saito, T. Xu
Facility for Rare Isotope Beams, East Lansing, MI, USA
A. Arnold, S. Gatzmaga, P. Murcek, R. Xiang
Helmholtz-Zentrum Dresden-Rossendorf, Dresden, Germany

Abstract

The LCLS-II-HE Project at SLAC seeks to increase the photon energy reach of the LCLS-II FEL to at least 20 keV. In addition to upgrading the undulator system, and increasing the electron beam energy to 8 GeV, the project will also construct a low-emittance injector (LEI) in a new tunnel. To achieve the LEI emittance goals, a low-MTE photocathode will be required, as will on-cathode electric fields up to 50% higher than those achievable in the current LCLS-II photoinjector.

The beam source for the LEI will be based around a superconducting quarter-wave cavity resonant at 185.7 MHz. A prototype gun is currently being designed and fabricated at the Facility for Rare Isotope Beams (FRIB) at Michigan State University (MSU). This paper presents performance goals for the new gun design, an overview of the prototype development effort, status, and future plans including fabrication of a “production” gun for the LEI.

AN SRF GUN FOR LCLS-II-HE

The beam source for the LCLS-II-HE Project’s Low-Emitance Injector will be a continuous-wave (CW) superconducting (SRF) quarterwave (QW) radiofrequency (RF) electron gun (hereafter referred to as the QW-SRF gun), resonant at 185.7 MHz.

Several alternatives to a superconducting QW RF gun were considered for the LEI, including normal-conducting RF guns evolved from the LCLS-II gun design [1]. However, compared to normal-conducting designs, the combination of an intrinsically outstanding vacuum environment (for cathode lifetime), and the potential for a larger ultimate performance envelope, led to the decision to pursue development of the QW-SRF gun.

DEVELOPMENT PROGRAM OVERVIEW

Overall Schedule

In late 2020, the HE Project issued a call for proposals for development of a quarterwave SRF gun. In April ’21, the proposal from FRIB was selected, and the project formally commenced in October ’21, with Argonne National Laboratory (ANL) and Helmholtz-Zentrum Dresden-

Rossendorf (HZDR) joining as subcontractors to MSU. The program is expected to run through early 2025, concluding with a RF test of a prototype SRF gun in a standalone cryomodule at FRIB.

Performance Requirements

The performance requirements for the QW-SRF gun itself are given in a Technical Specification and Statement of Work [2], and, as part of the Low-Emitance Injector, in the Conceptual Design Report for the LEI [1]. Some key performance requirements for the QW-SRF gun include:

- Resonant at 185.7 MHz (7th subharmonic of 1.3 GHz);
- On-cathode electric field gradients of > 20 MV/m (target: > 30 MV/m);
- Beam energy > 1.6 MeV (kinetic);
- Capable of supporting a high-QE “green” photocathode with a mean transverse energy < 184 meV;
- Cathode lifetime > 1 week (target: > 1 month);
- Field emission / dark current @ 30 MV/m < 10 nA.

The target on-cathode gradient is approximately 50% higher than that in the normal-conducting LCLS-II gun. Experimental SRF guns are pushing to much higher fields on cathode [3], but achieving routine operation at 30 MV/m in a user-facility setting is expected to be challenging.

Design Approach

The SLAC/MSU program incorporates design and testing approaches intended to explicitly address areas of difficulty encountered in past SRF gun development efforts. These include the cathode system (RF joints, multipacting and RF power dissipation); field emission / dark current; multipacting in the SRF cavity; and, generally, late-stage problem emergence.

Two broad strategies have been adopted: parallel development tracks for the cavity/cryomodule and cathode systems, and a design/test/verify approach that extends throughout the project and to the subsystem level. Combined, these strategies allow early verification of critical component performance, and provide a “separation-of-problems” approach intended to facilitate troubleshooting and remediation. Throughout the design phase, beam physics modeling is used to confirm that the evolving design continues to meet program requirements.

Figure 1 shows a cross-section view of the cavity and cathode system concept.

* Work supported by the Department of Energy Contract DE-AC02-76SF00515

[†] lewellen@slac.stanford.edu

SIMULATING TWO DIMENSIONAL TRANSIENT COHERENT SYNCHROTRON RADIATION IN JULIA

W. Lou*, C. Mayes, Y. Cai, SLAC National Accelerator Laboratory, Menlo Park, CA, USA

Abstract

Coherent Synchrotron Radiation (CSR) in bending magnets poses a potential limit for electron beams to reach high brightness in novel accelerators. While the longitudinal wakefield has been well studied in one-dimensional CSR theory and implemented in various simulation codes, transverse wakefields have received less attention. Following the recently developed two and three-dimensional CSR theory, we developed software packages in Python and Julia to simulate the 2D CSR effects. The Python packages, PyCSR2D and PyCSR3D, utilize parallel processing in CPU to compute the steady-state CSR wakes. The Julia package, JuliaCSR2D, additionally computes the 2D transient CSR wakes with GPU compatibility. We applied these codes to simulate the 2D CSR effects in the FACET-II particle accelerator at the SLAC National Accelerator Laboratory.

INTRODUCTION

When an electron traverses a curved trajectory, synchrotron radiation is emitted and can apply energy kicks to the other electrons in the same bunch. The low frequency components of the radiation spectrum, with wavelengths on the order of the bunch length, can add coherently, and is termed coherent synchrotron radiation (CSR). CSR can result in undesired effects including increase in energy spread and beam emittance, energy loss, and potential micro-bunching instability. For a beam with high bunch charge Q and short bunch length σ_z , the effects tend to be more severe. Because the current FACET-II chicane design at SLAC calls for great longitudinal beam compression ($Q \sim 2$ nC, $\sigma_z \sim 0.5 \mu\text{m}$ at the final bunch compressor, CSR effects can be significant [1].

For fast computation, many simulation codes apply only the one-dimensional CSR model while neglecting the 2D/3D CSR effects. The negligence is considered acceptable if the transverse beamsizes $\sigma_{x,y}$ satisfy $\sigma_{x,y} \ll \sigma_z^{2/3} \rho^{1/3}$, where ρ is the bending radius [2]. However in the middle of the FACET-II BC2 chicane compressor, this limit is not satisfied, and inclusion of the 2D/3D effects might be necessary. The 2D/3D CSR theory with a constant ρ has been recently developed in [3, 4]. In 2021 we developed Python codes, *PyCSR2D* and *PyCSR3D*, to efficiently compute the steady-state (s-s) wakes [5–7]. This paper shows how we developed codes in Julia to efficiently calculate the 2D *transient* wakes based on the theory, including the entrance and exit wakes within a bending magnet. The code is named *JuliaCSR2D*, and is open-source on Github [8]. The benchmarking results with 1D transient CSR theory and tracking results with the FACET-II chicane are also presented here.

* wlou@slac.stanford.edu

2D TRANSIENT WAKE COMPUTATION

The 2D transient longitudinal and horizontal CSR wakes solved in [3] are given in the form of:

$$W_s(z, x) = \int_{-\infty}^{\infty} dx' \int_{z-g(x-x')}^{z-f(x-x')} dz' E_s\left(\frac{z-z'}{2\rho}, \frac{x-x'}{\rho}\right) \lambda_b(z', x'),$$

$$W_x(z, x) = \int_{-\infty}^{\infty} dx' \int_{z-g(x-x')}^{z-f(x-x')} dz' E_x\left(\frac{z-z'}{2\rho}, \frac{x-x'}{\rho}\right) \lambda_b(z', x'),$$

in which λ_b is the bunch distribution, and E_s and E_x are the longitudinal and horizontal *fields* solved in terms of ρ and the relativistic γ . The fields and the functions in the integration limits (f and g) take different forms depending on the location of the observation point (z, x) and the source point (z', x') . When the observation point is located inside the bending magnet, the wakes are called the *entrance* wakes. For a Gaussian bunch, the longitudinal entrance wake becomes the s-s wake when the observation point traverses beyond the over-taking distance $L_0 = (24\sigma_z \rho^2)^{1/3}$. Thus for a short magnet, the s-s might not be reached. When the observation point is located downstream to the magnet, the wakes are called the *exit* wakes.

In the s-s case, these integrals can be efficiently computed numerically by using an FFT-based convolution [7]. However this trick is no longer valid due to the *finite* limits in the dz' integral. Moreover, the field functions (E_s and E_x) have severe numerical spikes or singularities around $z' \sim z$, especially for large γ . To numerically resolve the spikes, we apply the Tanh-Sinh Quadrature (QTS) method to evaluate the dz' integrals [9]. QTS allows the integrand to decay at the two boundaries with a double exponential rate. To ensure consistent convergence with various parameters, effort was spent in developing an algorithm to numerically

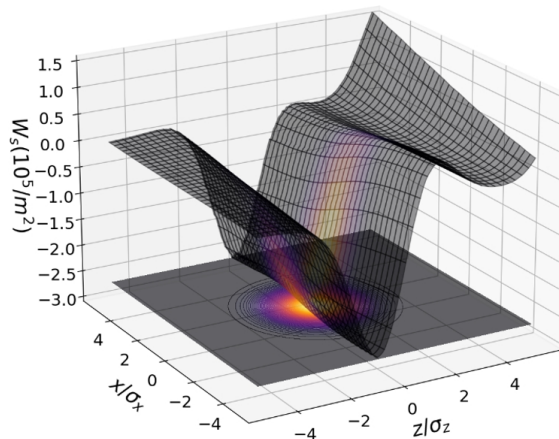


Figure 1: A contour plot of the longitudinal entrance wake $W_s(z, x)$ of a Gaussian bunch distribution. Parameters used: $\gamma = 10,000$, $\rho = 1.5$ m, $\sigma_z = \sigma_x = 0.5 \mu\text{m}$.

DESIGN AND OPERATION EXPERIENCE OF A MULTI-COLLIMATOR/YAG SCREEN DEVICE ON LCLS II LOW ENERGY BEAMLINE*

X. Liu†, C. Adolphsen, M. Santana-Leitner, L. Xiao, F. Zhou
SLAC National Accelerator Laboratory, Menlo Park, CA, USA

Abstract

A new device has been designed and installed on the Linac Coherent Light Source II (LCLS II) injector low energy beamline. It is made of a 15 mm copper plate, with four round apertures of 6, 8, 10, and 12 mm radius respectively. Two yttrium aluminum garnet (YAG) screens and their corresponding mirrors are added at the end of the collimator plate for beam/halo profile imaging. The collimator plate is electrically insulated from the chamber so that it can also be used for measuring the dark current. A motor-driven ultrahigh vacuum (UHV) compatible linear translator shifts the device between positions. Besides design details, beam dynamics and radiation analyses as well as operation experience are presented.

INTRODUCTION

In advance of the installation of LCLS II main linac, commissioning of its normal conducting Very High Frequency (VHF) radio frequency (RF) gun started a few years ago with the low energy beamline. It was observed that field emission (dark current) of roughly $2 \mu\text{A}$ level is present under normal operation of the gun. While the dark current of this level is deemed manageable with existing beamline configurations, it is desired in precaution to add a collimator on the low energy beamline to block the dark current, in case that the dark current situation worsens over time. It is desired to have multiple aperture sizes due to the unpredictability of possible new field emitters. YAG screens are also required on the same device for beam and halo profile monitoring. In addition, it is desired for the device to have the capability to measure dark current.

MECHANICAL DESIGN

Since the device has 7 different nominal operating positions, it utilizes a motorized UHV compatible linear translator to change position instead of an air cylinder, which is commonly used in a typical in-and-out actuation. See Figure 1 for the 3D model of the assembly. A translation degree of freedom in the other transverse (x) direction is also desired for precision positioning of the collimator, but it is impractical because of space constraints. The alignment error in x direction is controlled to within acceptable range by using special assembly features and machining sequences.

Figure 2 shows the collimator plate subassembly. Both the collimator plate and the shaft are made of oxygen-free

* Work supported by US DOE under contract AC02-76SF00515.

† liuxh@slac.stanford.edu

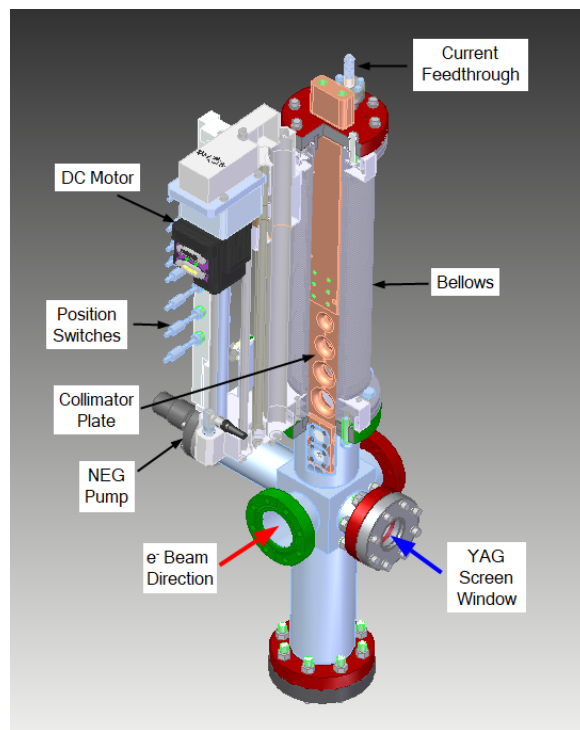


Figure 1: A cut-away view of the 3D model of the device. The absolute linear encoder and the radiation shielding enclosure are not shown in this view.

electronic (OFE) copper. The thickness of the collimator is chosen based on radiation simulation. The large cross section area ensures effective conduction of heat from the collimator plate to outside of the collimator flange. The radius of the four circular apertures are 6, 8, 10, and 12 mm respectively. The spacing between the collimator apertures is made large enough so that the aperture is the only direct pass through the device when the center of the aperture is aligned with the axis of the beam pipe.

The YAG screens have a diameter of 20 mm and a thickness of $50 \mu\text{m}$. They have a 20-nm-thick indium tin oxide (ITO) coating on one side to prevent accumulating charges. They are clamped securely in place with an annealed copper wire around the edge to ensure reliable electrical contact and mechanical support. The 45° mirrors are made of 304L stainless steel and polished to mirror finish. The thickness of the mirrors is 1 mm.

On the air side of the triaxial current feedthrough, a bleeding resistor connects the collimator plate to the chamber ground to prevent the collimator from becoming electrically floating when the current signal cable is disconnected.

A PARALLEL AUTOMATIC SIMULATION TOOL FOR CAVITY SHAPE OPTIMIZATION*

L. Ge[†], Z. Li, C.-K. Ng, L. Xiao
 SLAC National Accelerator Laboratory, Menlo Park, CA 94025, USA
 O. Klaas, B. Downie, M. W. Beall
 Simmetrix Inc., 10 Executive Park Drive, Clifton Park, NY 12065, USA

Abstract

We present a parallel automatic shape optimization workflow for designing accelerator cavities. The newly developed 3D parallel optimization tool Opt3P based on discrete adjoint methods is used to determine the optimal accelerator cavity shape with the desired spectral response. Initial and updated models, meshes and design velocities of design parameters for defining the cavity shape are generated with Simmetrix tools for mesh generation (MeshSim), geometry modification and query (GeomSim), and user interface tools (SimModeler). Two shape optimization examples using this automatic simulation workflow will be presented here. One is the TESLA cavity with higher-order-mode (HOM) couplers and the other is a superconducting rf (SRF) gun. The objective for the TESLA cavity is to minimize HOM damping factors and that for the SRF gun to minimize the surface electric and magnetic fields while maintaining its operating mode frequency at a prescribed value. The results demonstrate that the automatic simulation tool allows an efficient shape optimization procedure with minimal manual operations. All simulations were performed on NERSC supercomputer Cori system for solution speedup.

INTRODUCTION

Simulations play an important role in the design and optimization of accelerator cavities and components. The use of automated optimization techniques to improve cavity designs will result in significant cost savings and performance improvements for accelerator applications. However, usually optimizing cavity geometry subject to various design criteria is performed manually and the optimized design is achieved by the expertise of the designer. Optimization codes that exist are hard to use especially for complicated 3D geometries when one has to deal with changes of design parameters and the updates of the model and the subsequent mesh at each iteration of the optimization procedure.

At the time when computing power keeps on increasing through parallel computation, an automatic cavity optimization code, Opt3P, has been developed in ACE3P [1, 2] which is an advanced multiphysics parallel simulation suite, including integrated electromagnetic, thermal, and mechanical solvers, developed by researchers at the SLAC National Accelerator Laboratory. Opt3P, incorporating advanced geometry properties computation and mesh

adaptation with respect to changes in design parameters, will definitely relieve designers from spending the time on laborious manipulations and free them up for more creative thinking to come up with a better design.

CAVITY SHAPE OPTIMIZATION

PDE Constrained Optimization

A shape optimization based on the adjoint method has been implemented in ACE3P's frequency-domain eigensolver module Omega3P [3, 4], which calculates the electromagnetic properties of resonant modes in an accelerator cavity. One critical step in the optimization cycle (see Fig. 1) is to calculate the design velocity field ($\partial x_r / \partial d_j$) – the motion of each mesh surface node due to a change in each design variable. Analytic expressions for design velocities can be derived for simple geometric shapes. However, for complex 3D geometric entities, one used to have to resort to moving the mesh surfaces by hand to evaluate the design velocity, which requires code implementation whenever a new structure optimization is done. In this work we developed a general approach to calculating the design velocity, providing a fully automatic shape optimization procedure. In the following, we will describe the major components that have been implemented in Opt3P optimization workflow.

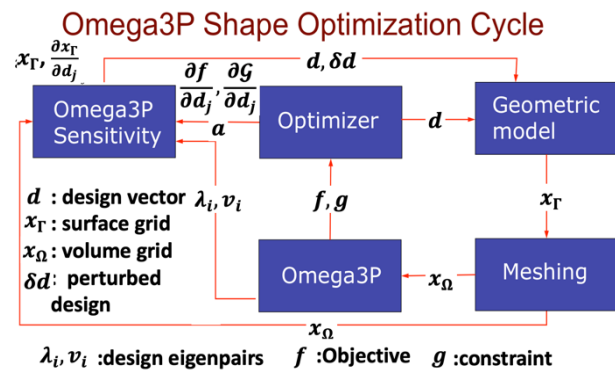


Figure 1: Flow chart for adjoint optimization method.

Objective Functions for Cavity Shape Optimization

The optimization objectives with constraints for accelerator cavity shape optimization can be categorized in the following: 1) Maximize the shunt impedance of the operating mode; 2) Minimize external quality factors of higher-order-modes (HOM); 3) Minimize surface electric or magnetic field on cavity wall; 4) Constrain the operating mode

*Work supported by US DOE under contract AC02-76SF00515 and contract DE-SC0018715.

[†]lge@slac.stanford.edu

DETERMINATION OF LCLS-II GUN-2 PROTOTYPE DIMENSIONS*

L. Xiao[†], C. Adolphsen, E. Jongewaard, X. Liu, F. Zhou
 SLAC National Accelerator Laboratory, Menlo Park, CA, USA

Abstract

The LCLS-II spare gun (Gun-2) design is largely based on the existing LCLS-II gun (Gun-1), in which there is significant captured dark current (DC) that originates on the high field copper surface near the cathode plug gap opening. To help suppress DC, the Gun-2 cathode and anode noses and the cathode plug opening are elliptically shaped to minimize the peak surface field for a given cathode gradient. In addition, stainless steel (SS) cathode and anode nose inserts are used in Gun-2 to further reduce dark current as SS has a lower potential for field emission. The cavity full 3D RF simulations were performed including vacuum slots, input couplers and probe and view ports. The thermal and structural analyses were done to investigate the effects of atmospheric pressure and RF heating. The multi-physics simulation results provided the information needed to determine the Gun-2 prototype dimensions. The Gun-2 cathode-to-anode gap distance will be made 1 mm longer than the nominal gap with the expectation that less than 1 mm will be machined off to meet the target frequency. In this paper, the Gun-2 frequency correction calculations are presented, and the cathode-to-anode gap determination is discussed.

2D CAVITY DESIGN

The LCLS-II spare gun (Gun-2) design is largely based on the existing LCLS-II gun (Gun-1), which was designed and built at LBNL. To help suppress dark current, the Gun-2 cathode and anode nose and the cathode plug opening are elliptically shaped to minimize the peak surface field for a given cathode gradient by LBNL and further optimized by SLAC [1]. The Gun-1 and Gun-2 RF parameters are listed in Table 1. The peak surface electric field in Gun-2 is lower by 10%.

Table 1: RF Parameters for a 750 keV Energy Gain

2D Cavity	Gun-1	Gun-2
Frequency (MHz)	186.850	186.018
Accelerating gap (mm)	40	40
Quality factor Q_0	$\sim 3.12 \times 10^4$	$\sim 3.12 \times 10^4$
Shunt impedance R/Q (Ω)	202	208
Cathode E_c (MV/m)	19.5	19.8
Peak surface E_{peak} (MV/m)	24.4	21.6
RF power loss (kW)	87	85

3D CAVITY RF SIMULATIONS

There are two sets of identical loop fundamental power couplers (FPC) in Gun-2, which are of the same design as used in Gun-1. The Gun-2 3D RF simulations were performed using the SLAC parallel finite-element

electromagnetics code suite ACE3P [2]. The 3D gun cavity is shown in Fig. 1 including vacuum slots, input couplers and probe and view ports. The angles of the FPC loop antennas can be adjusted to achieve critical external coupling Q_{ext} , that is $Q_{ext} = Q_0$ with fixed antenna intrusions of 4.47 mm. The resonant mode electric and magnetic fields for the critical coupling are shown in Fig. 2 for a loop angle of 70° . The frequency is 226 kHz lower due to the 3D features. Removing the antennas and blanking off the FPC ports, the cavity frequency reduces by 40 kHz. Taking off the cathode plug increases the cavity frequency by 6 kHz.

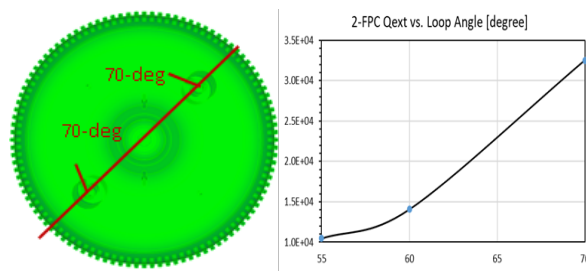


Figure 1: The Gun-2 3D geometry showing the couplers and their loop orientations at the critical coupling (left) and Q_{ext} versus the loop angle in degrees (right).

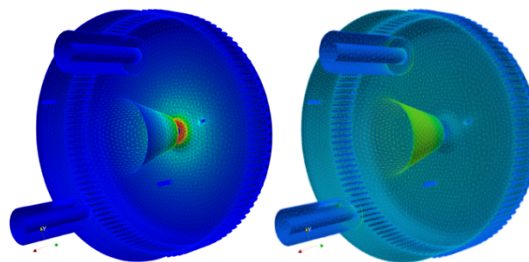


Figure 2: The complex electric (left) and magnetic (right) fields in the Gun-2 3D geometry when $Q_{ext} = Q_0$.

CAVITY THERMAL AND STRUCTURAL ANALYSIS

Atmospheric Pressure

The Gun-2 engineering design tries to maintain the overall dimensions of Gun-1 so it will be plug compatible with Gun-1. In particular, the dimensions DIM-A, DIM-B and DIM-C shown for Gun-1 in Fig. 3 are similar for Gun-2. However, there are some minor differences due to the improvements that were made for Gun-2.

A quarter of Gun-1 and Gun-2 solid models without the FPCs and small ports shown in Fig. 4 are simulated for thermal and structural analysis.

* Work supported by US DOE under contract AC02-76SF00515.

[†] liling@slac.stanford.edu

OPERATIONAL EXPERIENCE OF THE NEW BOOSTER CRYOMODULE AT THE UPGRADED INJECTOR TEST FACILITY*

M. Bruker[†], R. Bachimanchi, J. Grames, M. McCaughan, J. Musson, P. Owen,
 T. Plawski, M. Poelker, T. Powers, H. Wang, Y. Wang
 Thomas Jefferson National Accelerator Facility, Newport News, VA, USA

Abstract

Since the early 1990s, the injector of the CEBAF accelerator at Jefferson Lab has relied on a normal-conducting RF graded-beta capture section to boost the kinetic energy of the electron beam from 100 / 130 keV to 600 keV for subsequent acceleration using a cryomodule housing two superconducting 5-cell cavities similar to those used throughout the accelerator. To simplify the injector design and improve the beam quality, the normal-conducting RF capture section and the cryomodule will be replaced with a new single booster cryomodule employing a superconducting, $\beta = 0.6$, 2-cell-cavity capture section and a single, $\beta = 0.97$, 7-cell cavity.

The Upgraded Injector Test Facility at Jefferson Lab is currently hosting the new cryomodule to evaluate its performance with beam before installation at CEBAF. While demonstrating satisfactory performance of the booster and good agreement with simulations, our beam test results also speak to limitations of accelerator operations in a noisy, thermally unregulated environment.

INTRODUCTION

In the interest of reducing space-charge-related beam-optical limitations as well as helicity-correlated variations of beam properties, the control of which is important for demanding parity-violation experiments such as MOLLER [1], the CEBAF injector at Jefferson Lab is undergoing a series of upgrades aiming to raise the initial beam energy to 200 keV and make the beam relativistic with as few extra elements as possible [2]. We are planning to replace the arrangement of capture section and double-five-cell SRF structure with a single compact SRF unit consisting of a pair of cavities: a new 2-cell capture cavity that provides a well-defined longitudinal focus for ballistic bunch compression upstream, and a C100-style 7-cell cavity to boost the energy [3, 4]. Table 1 lists the parameters, while Fig. 1 shows a model of the cryomodule.

Originally designed for a test of the HDIce in-beam cryostat [5] with a low-current electron beam at a maximum energy of 10 MeV, the Upgraded Injector Test Facility (UITF) is hosting the new booster cryomodule as its central element, allowing us to evaluate the performance of the device with beam prior to installing it in the CEBAF injector. The UITF gun operates at 180 keV, very close to the projected CEBAF

Table 1: Nominal Parameters of the Booster Cryomodule

	2-cell	7-cell
Final kinetic beam energy (MeV)	0.533	5
Peak on-axis E field (MV m^{-1})		
nominal	4.6	13.2
maximum	8.0	26.0
Beam current (mA)		
nominal	0.38	
maximum	1.0	
Q_0 min.	4×10^9	8×10^9

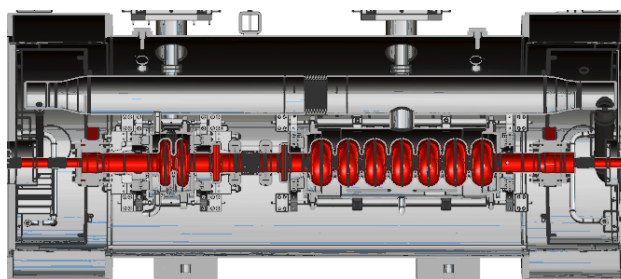


Figure 1: CAD model of the booster cryomodule excluding cryogenic attachments (cutplane view from the side; beam from left to right). The beam vacuum is highlighted in red, showing the 2-cell and the 7-cell cavity. Picture by J. Henry.

value of 200 keV [6]. Figure 2 shows a schematic model of the beam line components relevant to this study.

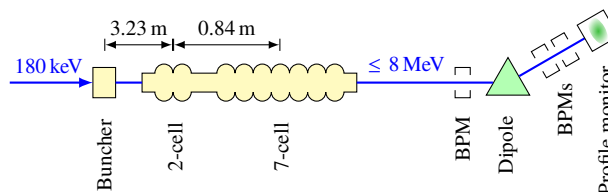


Figure 2: Relevant components of the beam line. A set of quadrupoles between booster and dipole (not shown) can be configured to provide a low β function at the diagnostic devices.

FIELD CALIBRATION

The dependency between energy gain and field amplitude of the booster has been the subject of many disagreements due to the non-relativistic velocity at the input, warranting a simulation study. While an empirical setup of the RF parameters based on the final beam momentum can be good enough

* This material is based upon work supported by the U.S. Department of Energy, Office of Science, Office of Nuclear Physics under contract DE-AC05-06OR23177.

[†] bruker@jlab.org

NEW RESULTS AT JLAB DESCRIBING OPERATING LIFETIME OF GaAs PHOTO-GUNS*

M. Bruker[†], J. Grames, C. Hernández-García, M. Poelker, S. Zhang
 Thomas Jefferson National Accelerator Facility, Newport News, VA, USA
 V. Lizárraga-Rubio, C. Valerio-Lizárraga, FCFM-UAS, Culiacan, Sinaloa, Mexico
 J. T. Yoskowitz, Old Dominion University, Norfolk, VA, USA

Abstract

Polarized electrons from GaAs photocathodes have been key to some of the highest-impact results of the Jefferson Lab science program over the past 30 years. During this time, various studies have given insight into improving the operational lifetime of these photocathodes in DC high-voltage photo-guns while using lasers with spatial Gaussian profiles of typically 0.5 mm to 1 mm FWHM, cathode voltages of 100 kV to 130 kV, and a wide range of beam currents up to multiple mA. In this contribution, we show recent experimental data from a 100 kV to 180 kV setup and describe our progress at predicting the lifetime based on the calculable dynamics of ionized gas molecules inside the gun. These new experimental studies at Jefferson Lab are specifically aimed at exploring the ion damage of higher-voltage guns being built for injectors.

INTRODUCTION

Polarized photoelectron guns employ a photocathode with a certain chemical composition and surface structure designed to absorb photons and photoemit free electrons. The constant of proportionality between the two, η , is called *quantum efficiency* (QE):

$$\eta = \frac{\text{number of electrons}}{\text{number of photons}} = \frac{I}{P} \frac{hc}{e\lambda} \quad (1)$$

with the electron current I , the laser power P , and the laser wavelength λ .

Photocathodes are subject to various damage mechanisms that reduce η as a function of time or extracted charge; GaAs, while important because of the high degree of spin polarization it provides [1], is a particularly sensitive cathode material. Despite technological advances that have had dramatic effects in reducing damage rates – e.g., improving gun vacuum, suppressing beam loss originating from stray light, or reducing laser heating – the prevailing limitation remains: ionized residual-gas molecules being accelerated backwards by the electric field in the gun acceleration gap and colliding with the cathode surface, which is referred to as *ion back-bombardment* [2–4].

Because these ions are generated by the electron beam, their total number scales with extracted charge. Although the physical mechanism by which they degrade the QE is

still subject to research [5], the decay rate is observed to be characteristically exponential, giving rise to the concept of a *charge lifetime* τ_C , i.e.,

$$\eta(Q) = \eta_0 \exp(Q/\tau_C) \quad (2)$$

for any integrated amount of charge Q .

In recent years, there has been considerable development to increase the maximum voltage of DC photo-guns, primarily to reduce space-charge effects in the beam [6], but also with the expectation that the rate of ion back-bombardment should fall. Figure 1(top) shows that the ionization cross section for H_2 , the predominant gas in a baked photogun, declines logarithmically with electron energy. Taking into account the field geometry of the cathode-anode gap, while the maximum ion production takes place just in front of the photocathode, there are still substantial contributions from high-energy ions, see Fig. 1(bottom). As ion energy factors into photocathode damage vis-a-vis the roles of ion sputtering and ion implantation [5], lifetime improving with higher voltage is not necessarily a given.

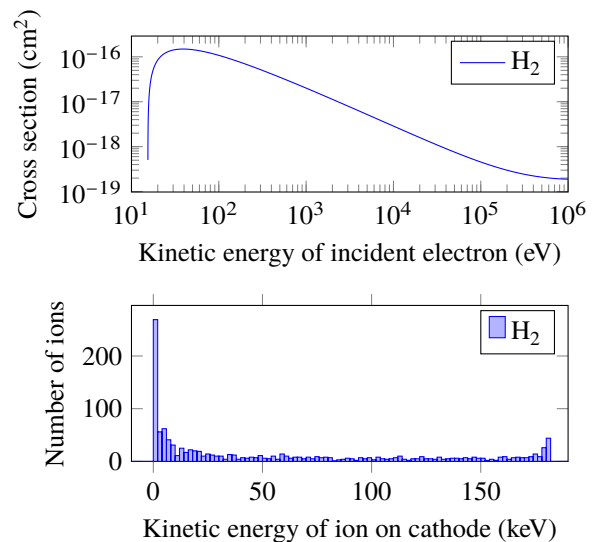


Figure 1: Ionization cross section of H_2 [7, 8] (top) and histogram of simulated kinetic energies of ions for a real gun geometry at 180 kV gun voltage (bottom). This simulation was performed with GPT as described below and assumes a homogeneous molecule density of $3 \times 10^{10} \text{ m}^{-3}$ and an extracted charge of 1 mC; the cathode-anode distance is 8 cm. The number of ions scales with gas density and charge.

* This material is based upon work supported by the U.S. Department of Energy, Office of Science, Office of Nuclear Physics under contract DE-AC05-06OR23177.

[†] bruker@jlab.org

HIGH-FIELD DESIGN CONCEPT FOR SECOND INTERACTION REGION OF THE ELECTRON-ION COLLIDER*

B.R. Gamage[†], R. Ent, R. Rajput-Ghoshal, T. Satogata, A. Seryi, W. Wittmer, Y. Zhang,
Jefferson Lab, Newport News, VA, USA

D. Arbelaez, P. Ferracin, G. -L. Sabbi, Lawrence Berkeley National Laboratory, Berkeley, CA, USA

E.-C. Aschenauer, J.S. Berg, H. Witte, Brookhaven National Lab, Upton, NY, USA

V.S. Morozov, Oak Ridge National Lab, Oak Ridge, TN, USA

F. Savary, CERN, Geneva, Switzerland

P. Vedin, CEA saclay, Gif-sur-Yvette Cedex, France

A. Zlobin, FNAL, Batavia, IL, USA

Abstract

Efficient realization of the scientific potential of the Electron Ion Collider (EIC) calls for addition of a future second Interaction Region (2nd IR) and a detector in the RHIC IR8 region after the EIC project completion. The second IR and detector are needed to independently cross-check the results of the first detector, and to provide measurements with complementary acceptance. The available space in the existing RHIC IR8 and maximum fields achievable with NbTi superconducting magnet technology impose constraints on the 2nd IR performance. Since commissioning of the 2nd IR is envisioned in a few years after the first IR, such a long time frame allows for more R&D on the Nb₃Sn magnet technology. Thus, it could provide a potential alternative technology choice for the 2nd IR magnets. Presently, we are exploring its potential benefits for the 2nd IR performance, such as improvement of the luminosity and acceptance, and are also assessing the technical risks associated with use of Nb₃Sn magnets. In this paper, we present the current progress of this work.

INTRODUCTION

The start of EIC operation is planned with the single main IR located at IP6. A secondary IR is being considered as a possible later upgrade of the EIC. If warranted, it is expected to be commissioned a few years after the primary IR. This additional time frame gives the second IR an opportunity to consider a new, more advanced magnet technology such as Nb₃Sn. It can provide significantly higher fields to control the beam. This paper explores potential performance improvements that can be gained using Nb₃Sn magnets in the forward section of the second IR. Its main elements are four final focusing quadrupoles and two spectrometer dipoles. Figure 1 shows the layout of the EIC collider rings and the placement of the two IRs. The IRs are denoted according to their locations in the RHIC tunnel with the primary IR named IR6 and the second IR named IR8.

* This material is based upon work supported by Jefferson Science Associates, LLC under Contract No. DE-AC05-06OR23177, Brookhaven Science Associates, LLC under Contract No. DE-SC0012704 and UT-Battelle, LLC, under contract No. DE-AC05-00OR22725 with the U.S. Department of Energy.

[†] randika@jlab.org

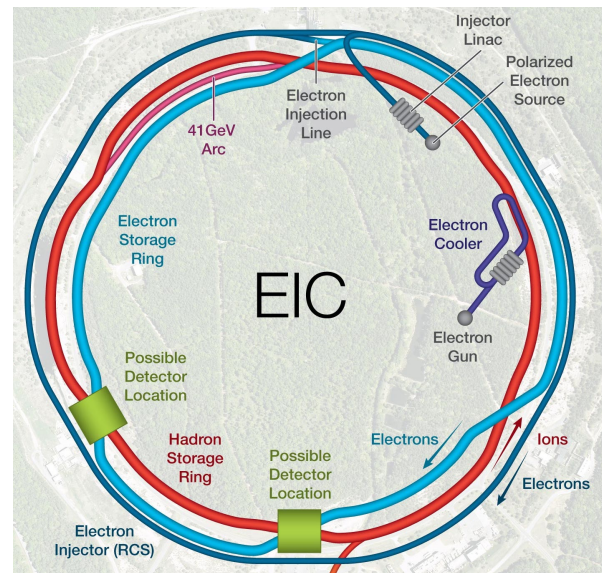


Figure 1: Layout of the EIC complex indicating the hadron storage ring (HSR), electron storage ring (ESR) and rapid cycling synchrotron (RCS). The primary IR is located at the 6 o'clock position while the second IR is located in the 8 o'clock position.

IR8 Design

The second IR is designed to provide complementary measurements to the primary IR by covering additional parameter space of the scattered particles. It has a secondary focal point in the forward ion beam line where space is reserved for placement of Roman pots. They can detect scattered charged particles with low transverse momentum ($p_T \rightarrow 0$) and longitudinal momentum close to that of the beam ($x_L \rightarrow 1$) [1, 2]. To achieve this, while maintaining the necessary clearance for detection of high p_T charged particles, the magnet apertures have to be sufficiently large but, at the same time, provide high field gradients required for beam focusing. Compared to conventional NbTi magnets, Nb₃Sn magnets can be operated at about 2.7 times higher field in their coils. This significant increase of the maximum available field can be used to design larger-aperture magnets giving a higher acceptance coverage, increase the magnet

A 500 kV INVERTED GEOMETRY FEEDTHROUGH FOR A HIGH VOLTAGE DC ELECTRON GUN*

C. Hernandez-Garcia[†], D. Bullard, J. Grames, G. Palacios-Serrano, M. Poelker
Thomas Jefferson National Accelerator Facility, Newport News, VA, USA

Abstract

The Continuous Electron Beam Accelerator Facility (CEBAF) injector at Jefferson Lab (JLab) utilizes an inverted-geometry ceramic insulator photogun operating at 130 kV direct current to generate spin-polarized electron beams for high-energy nuclear physics experiments. A second photogun delivers 180 keV beam for commissioning a SRF booster in a testbed accelerator, and a larger version delivers 300 keV magnetized beam in a test stand beam line. This contribution reports on the development of an unprecedented inverted-insulator with cable connector for reliably applying 500 kV dc to a future polarized beam photogun, to be designed for operating at 350 kV without field emission. Such a photogun design could then be used for generating a polarized electron beam to drive a spin-polarized positron source as a demonstrator for high energy nuclear physics at JLab. There are no commercial cable connectors that fit the large inverted insulators required for that voltage range. Our proposed concept is based on a modified epoxy receptacle with intervening SF₆ layer and a test electrode in a vacuum vessel.

INTRODUCTION

In 2010 JLab embarked on a R&D program to test and implement conical ceramic insulators (known as inverted geometry) in high voltage direct current (dc) photoemission electron guns (photoguns thereafter) [1], as an alternative to large cylindrical ceramic insulators for electrically isolating the cathode electrode [2-4]. With an inverted-insulator design, the cathode electrode in vacuum electrically connects to the high voltage power supply using a commercial high voltage cable, while the insulator serves as the electrode support structure. Compared to large bore cylindrical insulator photoguns, the inverted insulator design has less metal biased at high voltage contributing to field emission, smaller vacuum chamber resulting in better achievable vacuum, and no exposed high voltage components; thus, a sulphur hexafluoride (SF₆) tank is not required to suppress corona discharge.

The first inverted ceramic insulators photoguns built at JLab employed ceramic insulators that were compatible with commercial high voltage cables [1, 5, 6]. In these designs, the rubber cable termination conforms to the conical insulator shape. By applying a thin layer of silicone grease to the cable termination, and sufficient compression, a snug fit without trapped air bubbles is ensured for robust operation without electrical breakdown.

* Work supported by U.S. Department of Energy, Office of Science, Office of Nuclear Physics under contract DE-AC05-06OR23177.

[†] chgarcia@jlab.org.

These activities resulted in the construction of a 130 kV dc high voltage photogun at CEBAF [1], a 200 kV prototype photogun for the ILC [7], presently providing 180 keV polarized beams at a testbed accelerator, and a 300 kV photogun designed for generating magnetized beams in a testbed beam line [8, 9]. A new polarized-positron source initiative at JLab [10] would benefit from a photogun capable of reaching 500 kV. Other project might also benefit from such a photogun, such as the EIC and ILC [11, 12].

The purpose of this work is aimed at evaluating the performance of a very large doped inverted ceramic insulator that was developed for a proposed 500 kV dc photogun but never used [13]. There are no commercial high voltage cables compatible with this insulator design. This contribution describes the novel method by which high voltage is applied to the cathode electrode using a homemade high voltage cable interface. Figure 1 shows a picture of the insulators and electrodes used in these photoguns, compared to the proposed 500 kV insulator [14].



Figure 1: Inverted geometry insulators and electrodes utilized in JLab photoguns. From left to right: 200 kV R28, 300 kV R30, and the 500 kV assembly currently under testing.

A photogun capable of meeting the stringent requirements of such applications, must be designed to produce polarized electron beams without field emission at the operating voltage. Additionally, dynamic vacuum conditions must be $\sim 1 \times 10^{-12}$ Torr to provide photocathode lifetime comparable to that in the CEBAF photogun [15], but with nearly 3 orders of magnitude higher CW beam current. These initiatives provide the motivation for this work: to develop an inverted insulator compatible with a commercial cable for applying 500 kV dc to a future polarized beam photogun providing sufficient margin for high voltage conditioning. The resulting photogun must operate reliably and field-emission-free at 350 kV dc. Such an insulator/cable termination design does not exist.

IMPROVED ELECTROSTATIC DESIGN OF THE JEFFERSON LAB 300 kV DC PHOTOGUN AND THE MINIMIZATION OF BEAM DEFLECTION*

M. A. Mamun[†], R. Suleiman, C. Hernandez-Garcia, B. Bullard, J. Grames, M. Poelker
Thomas Jefferson National Accelerator Facility, Newport News, VA 23606, USA
S. A. K. Wijethunga, G. Palacios-Serrano, J. R. Delayen, G. A. Krafft¹
Old Dominion University, Norfolk, VA 23529, USA

¹also at Thomas Jefferson National Accelerator Facility, Newport News, VA 23606, USA

Abstract

Electron beam with high bunch charge and high repetition rate is required for electron cooling of ion beam to achieve the required high luminosity of proposed electron-ion colliders. Improved design of the -300 kV DC high voltage photogun at Jefferson Lab was incorporated toward overcoming the beam loss and space charge current limitation as experienced in the original design. To reach the bunch charge goal of \sim few nC within 75 ps bunches, the existing DC high voltage photogun electrodes and anode-cathode gap were modified to increase the longitudinal electric field (E_z) at the photocathode. The anode-cathode gap was reduced to increase the E_z at the photocathode and the anode aperture was spatially shifted with respect to the beamline longitudinal axis to minimize the beam deflection introduced by the geometric asymmetry of the inverted insulator photogun. The electrostatic design and the beam dynamics simulations were performed to determine the required modification. Beam based measurement from the modified gun confirmed the reduction of the beam deflection which is presented in this contribution.

INTRODUCTION

DC high voltage photo-guns have been employed by accelerator facilities to produce both polarized and non-polarized beam for different application. The Continuous Electron Beam Accelerator Facility (CEBAF) at Jefferson Lab uses a DC high voltage photogun to produce highly polarized electron beams at currents \sim 100 μ A and sub-pC bunch charge for nuclear physics research [1,2]. Other applications that employ DC high voltage photoguns and typically require very high average current (mA) and high bunch charge ($>$ 100 pC) include free electron lasers (FELs) [3-6], energy recovery linacs (ERLs) [7,8], and electron cooling [9-10].

The majority of these photo-guns have a Pierce geometry at the cathode front to focus the beam [11,12]. In addition, inverted insulator geometry photoguns like the Jefferson Lab design serve to connect the high voltage cable to the cathode electrode, and have a shield to minimize the electric field at the insulator metal-vacuum interface known as the triple point junction [12]. However, the

Pierce geometry reduces the E_z at the cathode, thus increasing space charge effects and reducing bunch charge extraction. Additionally, the inverted insulator and triple point junction shield, asymmetric NEG pumps altogether introduce asymmetric electric fields in the anode-cathode gap which then result in deflecting the beam vertically at the exit of the anode, causing difficulty in beam steering, and ultimately beam losses [11-14]. This work explored the beam based performance of the Jefferson Lab's redesigned -300 kV photogun to address the above design issues. The electrostatic design of the modified photo-gun was achieved using CST Studio Suite's electromagnetic field solver to obtain a higher E_z at the cathode while keeping the beam on-axis in comparison with the original photogun [15]. Beam simulations were conducted using GPT software [16] implementing the electrostatic field map obtained from the modified electrodes which are presented in detail by Wijethunga et al [17].

This contribution presents the beam based results from the redesigned photogun to confirm the beam deflection minimization in the offset anode design.

MODIFICATION OF THE PHOTOGUN

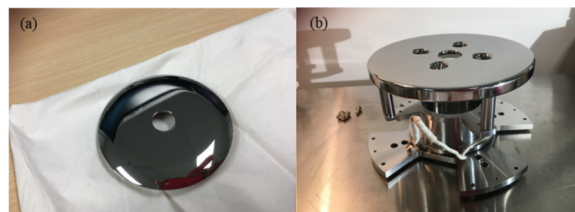


Figure 1: For the modified (flat) design: (a) front surface of the flat cathode that mates the spherical ball electrode and (b) the flat anode. The anode aperture (the hole at the center of the anode) is shifted by -1.6 mm.

The 300 kV DC high voltage photogun at Jefferson Lab was redesigned to deliver electron beams with much higher bunch charge and improved beam properties. The modifications include removing the 25° Pierce geometry of the cathode electrode and decreasing the anode-cathode gap from 9 to 5 cm to enhance the longitudinal electric field magnitude E_z from -2.5 to -7.8 MV/m. To correct the beam deflection with minimum changes, the anode offset with respect to the beamline longitudinal axis is incorporated.

* Authored by Jefferson Science Associates, LLC under U.S. DOE Contract No. DE-AC05-06OR23177. Additional support comes from JSA initiatives fund program and Laboratory Directed Research and Development program.

[†] mamun@jlab.org

He PRODUCTION UPDATE AT JLab – INTRODUCING AN ENHANCED NITROGEN PURGE FOR CLEAN STRING ASSEMBLY

P. Owen, Thomas Jefferson National Accelerator Facility, Newport News, VA, USA

Abstract

A major limitation to cryomodule performance is field emission caused by particulates within the superconducting cavities. To reduce contamination of the inner surfaces during assembly in a cleanroom, the whole string can be connected to a purge system which maintains a constant overpressure of dry, clean nitrogen gas.

Following the successes of similar systems at XFEL and Fermilab, Jefferson Lab followed this example for the production of LCLS-II-HE cryomodules. Implementing this system required new procedures, infrastructure, and hardware, as well as significant testing of the system before use in actual production. This poster summarizes the implemented controls and procedures, including lessons learned from Fermilab, as well as the results of mock-up tests.

Based on the latter, the system was used for the assembly of the first article string in April 2022, as well as during a rework required due to issues with cold Fundamental Power Coupler (FPC) ceramics two months later. The benefits of using a purge system with regards to procedure, time savings, and added flexibility for potential rework have already proven to provide a significant improvement for the production of LCLS-II-HE cryomodules at Jefferson Lab.

INTRODUCTION

LCLS-II-HE cryomodules share most of their same design with the LCLS-II modules. Likewise, production of these modules is split between Jefferson Lab and Fermilab. Once received from the vendor, each cavity is kept under vacuum and tested in a vertical dewar. Along with other qualifying criterion, if the test produces no field emission (detectable above background levels), the cavity is cleared for assembly. Because the interior of the cavity has therefore been proven to be clean, great care is taken to preserve the state. Cavities are taken into an ISO-4 cleanroom and undergo a thorough external cleaning.

For assembly, the interior space must be backfilled from vacuum to atmospheric pressure. The temporary input antenna for vertical testing is replaced, and eight cavities are joined together to form a string. These three steps pose the greatest risk in introducing particulate to the inner surface of the cavity, potentially causing field emission during cryomodule test and in later operation. This preservation of cleanliness was a key issue during LCLS-II production at both partner labs. Following an extensive audit, Fermilab implemented a nitrogen-purge system to be used during the stages of string assembly [1]. Combined with other improvements, the system was successful in reducing field emission in later cryomodules.

For LCLSII-HE production, Jefferson Lab was instructed to develop a similar system and procedures for string assembly. Due to fundamental differences in cleanroom infrastructure from Fermilab, a new design of gas supply, control, and tubing was needed.

SYSTEM DESIGN

Throughout the assembly process, there will be a flow of nitrogen available to keep the interior of the cavity clean. The supply is boil-off gas from a nitrogen dewar which is then passed through several filters before reaching the cavity. The final filter is placed as close as possible to the cavity to avoid the gathering of moving particulate from bellows flex hoses or valves into the cavity (Fig. 1).



Figure 1: Filtered nitrogen supply and vacuum hose connected to cavity in the cleanroom.

Control and Instrumentation

The nitrogen flow must be carefully controlled for three main reasons. A flow rate that is too small will be ineffective in keeping particulate out of the cavity. Too much flow could lift and redistribute particles in the cavity, potentially leaving particulate on a more critical surface. Finally, once the flange is sealed and the assembly is completed, the flow must be shutoff to prevent overpressure and harm to any component.

To meet these flow criteria, each line of nitrogen supply was designed with a mass flow controller (MFC), pressure gauge, and pneumatic shutoff valve. A cRio system from National Instruments was programmed to communicate with and control these three elements for each of the three nitrogen supply lines. A test fit of this control hardware is shown in Fig. 2.

HIGH-GRADIENT WIEN SPIN ROTATORS AT JEFFERSON LAB*

G. Palacios-Serrano[†], C. Hernandez-Garcia, P. Adderley, J. Grames, M. Poelker
Thomas Jefferson National Accelerator Facility, Newport News, VA, USA

Abstract

Nuclear physics experiments performed in the Continuous Electron Beam Accelerator Facility (CEBAF) at Jefferson Laboratory (JLab) require spin manipulation of electron beams. Two Wien spin rotators in the injector keV region are essential at CEBAF to establish longitudinal polarization at the end station target, and to flip the polarization direction by π rad to rule out false asymmetries. In a Wien filter, the homogeneous and independent electric and magnetic fields, along with the velocity vectors of the electrons that traverse it, form a mutually orthogonal system. The magnitude of the electrostatic field, established by biasing two highly-polished electrodes, defines the desired spin angle at the target yet deviates the beam trajectory due to the Lorentz force. The beam trajectory in the Wien is then re-established by adjusting the magnetic field, induced by an electromagnet encasing the device vacuum chamber. This contribution describes the evolution design and high voltage testing of Wien filters for spin manipulation at increased beam energies in the keV injector region, required by high precision parity violation experiments like MOLLER.

INTRODUCTION

The planned MOLLER [1] experiment at the Jefferson Lab (JLab) Continuous Electron Beam Accelerator Facility (CEBAF) requires 65 μ A current, 90% longitudinally-polarized, and highly stable 11 GeV electron beam. To fulfil these stringent requirements the CEBAF photogun was upgraded to be capable of producing 200 keV electron beam [2] in the low energy section. Wien filters have been used at JLab in a spin-rotator configuration at 130 keV to provide precise control of the beam spin orientation in the injector [3] and recently in a test-bed accelerator with 180 keV beam energy. The operation parameters of the Wien filters (based on the original design by SLAC [4]) are inextricably related to the beam energy, therefore it was necessary to upgrade the capabilities of the JLab Wien filters for the higher photogun beam energy. The upgrade modification process consisting of 3-dimensional modeling using Solidworks, electrostatic CST-EM studio simulations, and magnetostatic Opera simulations are described in a previous contribution [5] and briefly described in this document. Initial tests of the CEBAF Wien filters modified for higher electrode voltage, but retaining original brazed electrodes manufactured for 100 keV operation, showed ion pump current bursts while ramping up to twice the original bias electrode voltage (20 kV). This behaviour was hypothesised to be related to gas trapped during the bracing process of the electrode fabrication and released during the

HV tests. After installation in the upgrade CEBAF injector beamline, and following vacuum bake out, the Wien filters were high voltage conditioned and eventually the ion pump current bursts receded. The Wien filters are currently operational for 130 keV beam out of the photogun for CEBAF operations, and are deemed ready for 200 keV when the program moves to that energy next year.

A third Wien filter based on the CEBAF version upgraded for higher beam energy was constructed, but the brazed electrodes were replaced with electrodes machined from single-piece stainless steel pieces, aiming at eliminating the ion pump current bursts observed with the original brazed electrodes. Foreseeing the need of beam energies out of the photogun \sim 300 keV for the Electron Ion Collider (EIC) [6] and the International Linear Collider (ILC) [7], a smaller gap between electrodes (13 mm vs previous 15 mm) was implemented, which in combination with higher electrode voltage increases the electric field between electrodes by \sim 2.5 from the CEBAF Wien filter (at 130 keV) resulting in the highest-gradient Wien filter to date, reaching 3.9MV/m.

DEVICE DESCRIPTION

The Wien filters initially used at CEBAF based on the original SLAC [4] design were modified to operate with the 100 keV beam energy [8]. They consist of two stainless steel parallel plates biased inside a vacuum chamber, thus creating an electric field in the gap (15 mm). A magnetic field orthogonal to the electric field is produced by a current circulating through a pair of window frame coils outside the vacuum chamber, whereas a magnetic shell encasing shapes its profile. The Rogowski geometry of the electrodes was carefully designed for best possible match with the magnetic field profile. Later on, the CEBAF injector Wien filters were operated with 130 keV beam using a slightly bigger version of the original coil design. The electrode Rogowski geometry was also improved to increase the matching between field profiles, paramount to obtain proper beam transmission. To provide $\pm\pi/2$ rad spin rotation plus 10% margin, the electrode voltage had to be increased from 12 kV to 20 kV for 15 mm electrode gap. This required re-designing the high voltage feedthroughs as described in [5].

A third Wien filter was built for the Upgrade Injector Test Facility at JLab. Based on the higher voltage version of the CEBAF Wiens, this Wien filter features electrodes machined from a single piece of 304 stainless steel. The single-piece electrodes were improved over the original design with a spline profile (compared to the original ‘terrace’ profile) (Fig. 1) between their flat region and the Rogowski profile, aiming to more accurately match the electric and magnetic fields. The electrode gap was also reduced from 15 mm to 13 mm by modifying the mounting Inconel

* Work supported by U.S. Department of Energy, Office of Science, Office of Nuclear Physics under contract DE-AC05-06OR23177.

[†] gabrielp@jlab.org.

MEASURING THE ELECTRIC DIPOLE MOMENT OF THE ELECTRON IN A TWO-ENERGY SPIN-TRANSPARENT STORAGE RING*

R. Suleiman[†], Ya. S. Derbenev

Thomas Jefferson National Accelerator Facility, Newport News, VA, USA

V. S. Morozov, Oak Ridge National Laboratory, Oak Ridge, TN, USA

Abstract

This contribution presents a new design of a two-energy storage ring for low energy (0.2–2 MeV) polarized electron bunches. The new design is based on the transparent spin methodology that cancels the spin precession due to the magnetic dipole moment at any energy while allowing for spin precession induced by the fundamental physics of interest to accumulate. The buildup of the vertical component of beam polarization can be measured using standard Mott polarimetry that is optimal at low electron energy. These rings can be used to measure the permanent electric dipole moment of the electron, relevant to CP violation and matter-antimatter asymmetry in the universe, and to search for dark energy and ultra-light dark matter.

INTRODUCTION

The electric dipole moment (EDM) is very sensitive to physics beyond the Standard Model and new sources of Charge-conjugation and Parity (CP) violation [1, 2]. Such CP violation, beyond what is present in the weak interaction, could signal the presence of new physics and explain the puzzle of the matter-antimatter asymmetry in the universe. However, there are no direct measurements of the electron or proton EDMs. The EDM upper limit of the electron ($d_e < 1.1 \times 10^{-29} e \cdot \text{cm}$) has been extracted from a measurement using ThO molecule while the proton limit was obtained using ¹⁹⁹Hg atom. Direct measurements of the EDM upper limits only exist for the neutron and the muon where the muon limit was measured in conjunction with the anomalous magnetic dipole moment, $g - 2 (\equiv 2G)$.

Any measurement of EDM relies on measuring the spin precession rate in an electric field of a particle's rest frame, $d\vec{S}/d\tau = \vec{\mu} \times \vec{B}_{\text{rest}} + \vec{d} \times \vec{E}_{\text{rest}}$, where the magnetic (MDM) and electric dipole moments are defined as $\vec{\mu} = (G+1)(q/mc)\vec{S}$ and $\vec{d} = (\eta/2)(q/mc)\vec{S}$, q and m are the particle charge and mass, c is the speed of light, η is the electric dipole factor, and \vec{S} represents spin in the particle's rest frame. For a charged particle moving in electric and magnetic fields given in the lab frame, the generalized Thomas-BMT equation of spin precession is $d\vec{S}/d\tau = (\vec{\omega}_{\text{MDM}} + \vec{\omega}_{\text{EDM}}) \times \vec{S}$ with [3]:

$$\vec{\omega}_{\text{EDM}} = -\frac{\eta q}{2mc} \left(\frac{1}{\gamma} \vec{E}_{\parallel} + \vec{E}_{\perp} + \vec{\beta} \times \vec{B} \right), \quad (1)$$

* This work is supported by the U.S. Department of Energy, Office of Science, Office of Nuclear Physics under contract DE-AC05-06OR23177 and by UT-Battelle, LLC, under contract DE-AC05-00OR22725.

[†] suleiman@jlab.org

where $\vec{v} \equiv \vec{\beta}c$ and γ are the particle's velocity and Lorentz energy factor.

The basic principle of the EDM measurement in a ring relies on making MDM spin rotation effectively vanish. Observation of a spin rotation then indicates the presence of EDM. Strategies to cancel MDM spin precession can be formulated for particle motion along a closed reference design orbit, traditionally (but not necessarily) in a plane, that permit the effective stacking of the EDM precession turn by turn around the orbit. A flat reference orbit generally employs vertical magnetic (B_y) and horizontal transverse electric (E_x) fields. In the accelerator reference frame, spin then precesses due to MDM about vertical axis with angular frequency, ω_y :

$$\omega_{y,\text{MDM}} = -\frac{q}{mc} \left(GB_y - \frac{1 - \gamma^2 \beta^2 G}{\gamma^2 \beta} E_x \right). \quad (2)$$

Considering Eq. 2, two experimental approaches have been developed to compensate MDM spin rotation and thereby measure EDM in storage rings:

1. All-electric ring with $B_y = 0$ and $\gamma^2 = 1 + 1/G$, described as the Magic Energy (ME) approach. This works only for $G > 0$ (e.g., electron or proton) and at a very specific energy. Two experiments have been proposed to measure d_p with a sensitivity of $10^{-29} e \cdot \text{cm}$ at ME of 232.8 MeV in rings with ≥ 500 m circumference [4, 5]. To reduce systematic effects, clock-wise (CW) and counter clock-wise (CCW), beams will circulate concurrently.
2. Combined electric/magnetic ring with $GB_y = (1 - \gamma^2 \beta^2 G)/(\gamma^2 \beta) E_x$. An experiment is planned to measure the deuteron ($G = -0.143$) EDM (d_d) at 1.0 GeV/c with such a ring.

Notably, these experiments propose to measure d_p and d_d but not d_e . In fact, there is no d_e proposal at ME ($\gamma = 29.38$, 15.01 MeV) because there is no viable polarimetry at this energy.

This contribution presents a method to measure d_e in a small storage rings with beam energy below 1 MeV [6]. It is based on the Figure-8 spin-transparent (ST) configuration [7] where the MDM signal is naturally suppressed at any energy due to the ring topology and symmetry. Thus, there is no spin decoherence due to the beam energy spread. We consider an all-electric design with no magnetic fields to allow for counter-rotating (CR) electron beams.

SRF CAVITY INSTABILITY DETECTION WITH MACHINE LEARNING AT CEBAF*

D. Turner[†], R. Bachimanchi, A. Carpenter, J. Latshaw, C. Tennant, L. Vidyaratne
Thomas Jefferson National Accelerator Facility, Newport News, VA 23606, USA

Abstract

During the operation of the Continuous Electron Beam Accelerator Facility (CEBAF), one or more unstable superconducting radio-frequency (SRF) cavities often cause beam loss trips while the unstable cavities themselves do not necessarily trip off or present a fault. Identifying an unstable cavity out of the hundreds of cavities installed at CEBAF is difficult and time-consuming. The present RF controls for the legacy cavities report at only 1 Hz, which is too slow to detect fast transient instabilities. A fast data acquisition system for the legacy SRF cavities is being developed which samples and reports at 5kHz to allow for detection of transients. A prototype chassis has been installed and tested in CEBAF. An autoencoder based machine learning model is being developed to identify anomalous SRF cavity behavior. The model is presently being trained on the slow (1 Hz) data that is currently available, and a separate model will be developed and trained using the fast (5 kHz) DAQ data once it becomes available. This paper will discuss the present status of the new fast data acquisition system and results of testing the prototype chassis. This paper will also detail the initial performance metrics of the autoencoder model, which indicate good results on the available 1Hz data. This paper will also discuss high-level software applications developed to support the project.

INTRODUCTION

The Continuous Electron Beam Accelerator Facility (CEBAF) is a 5.5-pass, 12 GeV continuous wave (CW) electron accelerator. CEBAF is comprised of two anti-parallel superconducting RF linacs connected by two sets of recirculation arcs. Electron beams are then extracted into up to four experimental halls to support nuclear physics experiments (Fig. 1).

Each linac is comprised of 200 superconducting radio-frequency (SRF) cavities, plus 18 cavities in the injector, which provide electron beam acceleration. During the operation of CEBAF, any one unstable SRF cavity can cause beam loss trips while the unstable cavities themselves do not necessarily trip off or present a fault.

The existing tools and diagnostics for identifying unstable SRF cavities at CEBAF are presently rather limited. Out of the 418 SRF cavities at CEBAF, 306 are of the original legacy CEBAF design which lacks the fast data acquisition capabilities of the newer cavities. The legacy cavity diag-

nostics are limited to what is presented to the EPICS [1] control system which is limited to a data rate of 1 Hz, which is not fast enough to capture transient instabilities. Also, simply the number of cavities in the machine makes the search for instabilities time consuming. Work described in [2] addresses fault classification for the newer SRF cavities at CEBAF. This work addresses identifying unstable cavities of the legacy design.

To address these problems, a new fast data acquisition (DAQ) system has been designed and is being installed on the legacy SRF cavities at CEBAF. An autoencoder based machine learning anomaly detection model is being developed to identify cavity instabilities from the fast DAQ data along with archived EPICS data recorded by the MYA archiver [3].

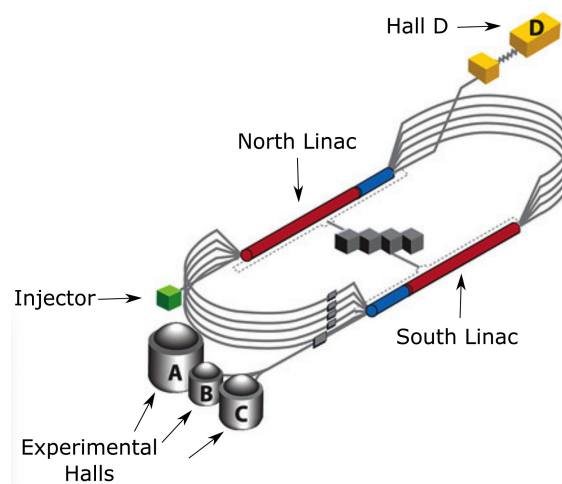


Figure 1: 12 GeV CEBAF overview. The legacy SRF cavities comprise most of the red regions of the linacs.

FAST DATA ACQUISITION SYSTEM

Each legacy SRF cavity has four analog outputs on its control module:

- GMES: Measured Gradient. Should mirror the GSET value in EPICS and should be stable to within 0.044% during normal operations. Has DC and AC components.
- PMES: Measured Phase. This is the phase in the cavity measured against the absolute 70 MHz reference. This also should mirror PSET in EPICS and should be varying less than $\pm 0.5^\circ$.
- GASK: Gradient Drive. The change in klystron incident power needed to maintain the GMES value within

* Notice: Authored by Jefferson Science Associates, LLC under U.S. DOE Contract No. DE-AC05-06OR23177. The U.S. Government retains a non-exclusive, paid-up, irrevocable, world-wide license to publish or reproduce this manuscript for U.S. Government purposes.

[†] dturner@jlab.org

pyJSPEC - A PYTHON MODULE FOR IBS AND ELECTRON COOLING SIMULATION*

H. Zhang[†], M.W. Bruker, Y. Zhang, S.V. Benson
 Thomas Jefferson National Accelerator Facility, Newport News, VA, USA

Abstract

The intrabeam scattering is an important collective effect that can deteriorate the property of a high-intensity beam and electron cooling is a method to mitigate the IBS effect. JSPEC (JLab Simulation Package on Electron Cooling) is an open-source C++ program developed at Jefferson Lab, which simulates the evolution of the ion beam under the IBS and/or the electron cooling effect. The Python wrapper of the C++ code, pyJSPEC, for Python 3.x environment has been recently developed and released. It allows the users to run JSPEC simulations in a Python environment. It also makes it possible for JSPEC to collaborate with other accelerator and beam modeling programs as well as plentiful python tools in data visualization, optimization, machine learning, etc. In this paper we will introduce the features of pyJSPEC and demonstrate how to use it with sample codes and numerical results.

INTRODUCTION

Intrabeam scattering (IBS) [1] is one important problem that hadron collider designers need to consider. Due to small-angle collisions between the ions, the emittance and the momentum spread of the ion beam gradually increase and therefore the luminosity of the collider decreases. Electron cooling [2] is an experimentally proven leading method to reduce the ion beam emittance by overlapping the ion beam with a low-temperature electron beam while both beams co-move inside the cooler in the same velocity to allow thermal energy to transfer from the ion beam to the electron beam. It can be used to mitigate the IBS effect. JLab simulation package for electron cooling (JSPEC) is a program to simulate the effects of both IBS and electron cooling. Although originally designed to support the then on-going electron-ion collider (EIC) project [3] at Jefferson Lab, JSPEC has been extended to include most frequently used formulas for the friction forces and variant models of the electron/ion beam [4] and is provided to the community as an open source tool for IBS and electron cooling simulations. The program is developed using C++ in consideration of efficiency and has been tested on both MS Windows 10 and Ubuntu 18.04 systems. Most computations are parallelized for shared-memory systems using OPENMP to take advantage of the multi-core processors widely available in desktop and laptop computers. The source codes, the documents, and the examples are all available in the *github* repository [5]. An online JSPEC based on an earlier version has been developed by Radiasoft and is accessible through their cloud service

SIREPO [6]. It allows one to run JSPEC and visualize the result inside a browser.

Although JSPEC runs independently, we see the need to simulate the IBS and electron cooling together with other collective effects, *e.g.* space charge effect and CSR effect, and the convenience of using optimization tools in accelerator design. This is the reason we developed pyJSPEC [7], which ports most functions in JSPEC to Python 3.x environment and brings the possibility to combine JSPEC with other Python tools for accelerator modeling and optimization.

FEATURES

The basic feature of JSPEC is to calculate the emittance growth rate of the ion beam under the IBS and/or the electron cooling effect. The rate at time t is defined as $r_i(t) = \frac{1}{\epsilon_i(t)} \frac{d\epsilon_i(t)}{dt}$, where $i = x, y, s$, representing the horizontal, vertical, and longitudinal direction, and ϵ_i is the emittance in the respective direction. For the IBS rate, JSPEC provides the Martini model [8], the original Bjorken-Mtingwa model [9] calculated by Nagaitsev's method [10], and the complete Bjorken-Mtingwa model with vertical dispersion and non-relativistic terms included [11]. The electron cooling rate is calculated statistically on a group of sample ions, each receiving a *kick* by the friction force. The rate is calculated as the relative change of the emittance per unit time before and after the kick. JSPEC provides several formulas [12-15] for both the non-magnetized and the magnetized friction force. Using different formulas in the transverse and the longitudinal direction is allowed.

JSPEC also simulates the evolution of the ion beam under the IBS effect and/or the electron cooling effect. The RMS dynamic model represents the ion beam by its macroscopic parameters, *i.e.* the emittances, the momentum spread, and the bunch length (for a bunched beam), calculates the instant expansion rate r at a time t and updates the parameters using $\epsilon_i(t + \Delta t) = \epsilon_i(t) \exp(r_i \Delta t)$ for the time step Δt . The particle model applies kicks due to IBS and electron cooling to sample ions and moves them by a random phase advance for the betatron and synchrotron oscillation in Δt . The turn-by-turn model is similar to the particle model but the betatron and synchrotron motion is modeled by a linear transfer matrix and the simulation is carried out in a turn-by-turn manner.

BENCHMARK

JSPEC has been benchmarked with BETACOOOL [12] for various scenarios. The two programs agree well. For the typical simulations we have done for the EIC project, a significant improvement of efficiency has been achieved

* Work supported by the U.S. Department of Energy, Office of Science, Office of Nuclear Physics under contract DE-AC05-06OR23177.

[†] hezhang@jlab.org

FIELD EMISSION MITIGATION IN CEBAF SRF CAVITIES USING DEEP LEARNING *

K. Ahammed[†], J. Li

Department of Electrical and Computer Engineering
 Old Dominion University, Norfolk, VA, USA

A. Carpenter, R. Suleiman, C. Tennant, L. Vidyaratne

Thomas Jefferson National Accelerator Facility, Newport News, VA, USA

Abstract

The Continuous Electron Beam Accelerator Facility (CEBAF) operates hundreds of superconducting radio frequency (SRF) cavities in its two main linear accelerators. Field emission can occur when the cavities are set to high operating RF gradients and is an ongoing operational challenge. This is especially true in higher gradient SRF cavities. Field emission results in damage to accelerator hardware, generates high levels of neutron and gamma radiation, and has deleterious effects on CEBAF operations. Therefore, field emission reduction is imperative for the reliable, high gradient operation of CEBAF that is required by experimenters. In this paper, we explore the use of deep learning architectures via multilayer perceptron and the use of tree-based models to simultaneously model radiation measurements at multiple detectors in response to arbitrary gradient distributions. These models are trained on collected data and could be used to minimize the radiation production through gradient redistribution. This work builds on previous efforts in developing machine learning (ML) models, and is able to produce similar model performance as our previous ML model without requiring knowledge of the field emission onset for each cavity.

INTRODUCTION

CEBAF is a high energy, recirculating continuous wave linear accelerator (linac) that delivers accelerated electron beams for experimental research in nuclear physics [1, 2]. Field emission is an ongoing operational challenge in CEBAF superconducting radio frequency (SRF) cavities. When SRF cavities are exposed to high operating RF gradient, electrons are emitted from the walls of the SRF cavities resulting in field emission [3, 4]. As the field emission has deleterious effect overall on CEBAF operation, it is mandatory to mitigate field emission for the reliable operation of CEBAF.

One of the primary negative effects of field emission is radiation production caused when field emitted electrons are accelerated and collide with another material. Each cavity has a unique gradient threshold over which field electrons are emitted, and these threshold values change over time. Measuring these thresholds requires an invasive procedure that disrupts beam delivery.

CEBAF is equipped with a purpose built neutron detection system, the NDX system. NDX detectors are capable of detecting both neutron and gamma radiation, and represent our best means of measuring the radiation produced by field emission throughout a linac during radio frequency (RF) system operation.

In this paper, we use a multilayer perceptron (MLP) based artificial neural network (ANN) architecture and the tree-based XGBoost (Extreme Gradient Boosting) model [5] to model the gamma and neutron radiation measured at six NDX detectors at the end of the North Linac based on nearby cavity RF gradients. The above mentioned models may support radiation minimization through gradient redistribution. The purpose of this work is to find a best model capable of modeling the radiation readings at NDX detectors given a set of nearby cavity gradients.

MATERIALS AND METHOD

Experimental Set Up and Data Collection

Jefferson Lab installed the new NDX detectors around the CEBAF in the summer of 2021. In August 2021, we measured the gamma and neutron radiation response of four C100 cryomodules (1L22-1L25) at the end of the CEBAF's north linac after NDX commissioning completed. We chose this small section of linac due to its high density of nearby NDX detectors and those cryomodules' history of field emission. We recorded the NDX measured dose rates as we stepped cavity gradients downward from their operation maximums in a process we refer to as a gradient scan. Gradient scans occurred in the absence of the electron beam, but with the RF system powered on. All cavities in the linac were set to their expected operational settings, but only the cavities in the four chosen C100s were changed during the study. We took multiple readings at each gradient configuration. Control system data from the collection process is shown in Fig. 1. More details on the data collection process are given in a previous publication [1].

Dataset and Data Preprocessing

We focus on the gradient scan data of zones 1L22 through 1L25 taken during August 2021. Radiation measurements were used from the six NDX detectors at 1L22-1L27. Zone 1L26 was unpopulated at this time. This data includes 32 cavity gradients to be used as model inputs, and 12 radiation measurements (one gamma and one neutron reading from

* This material is based upon work supported by the U.S. Department of Energy, Office of Science, Office of Nuclear Physics under contract DE-AC05-06OR23177.

[†] kaham001@odu.edu

197 MHz WAVEGUIDE LOADED CRABBING CAVITY DESIGN FOR THE ELECTRON-ION COLLIDER*

S. U. De Silva[†], J. R. Delayen, Old Dominion University, Norfolk, VA, USA
 J. Guo, R. Rimmer
 Thomas Jefferson National Accelerator Facility, Newport News, VA, USA
 B. Xiao, Brookhaven National Laboratory, Upton, NY, USA
 Z. Li, SLAC National Accelerator Facility, Menlo Park, CA, USA

Abstract

The Electron-Ion Collider will require crabbing systems at both hadron and electron storage rings in order to reach the desired luminosity goal. The 197 MHz crab cavity system is one of the critical rf systems of the collider. The crab cavity, based on the rf-dipole design, explores the option of waveguide load damping to suppress the higher order modes and meet the tight impedance specifications. The cavity is designed with compact dogbone waveguides with transitions to rectangular waveguides and waveguide loads. This paper presents the compact 197 MHz crab cavity design with waveguide damping and other ancillaries.

INTRODUCTION

The Electron-Ion Collider (EIC) is designed to collide electron and protons with center of mass energies varying from 20 to 100 GeV with possible upgrade to 140 GeV [1]. The goal for electron-proton luminosity is $\sim 10^{34} \text{ cm}^{-2} \text{ s}^{-1}$. EIC will be operating with a primary interaction region (IR) at IR6 and a second interaction region at IR8 planned in the upgrade of the machine as shown in Fig. 1.

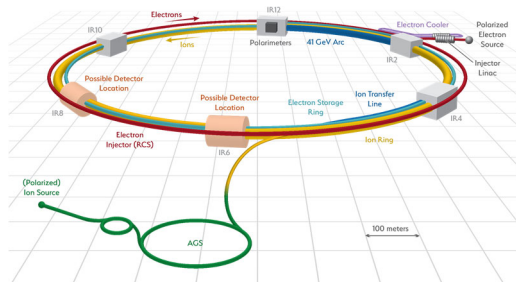


Figure 1: Layout of the Electron-Ion Collider.

Crabbing systems will be installed at both hadron storage ring (HSR) and electron storage ring (ESR) to achieve the required luminosity levelling.

- HSR \rightarrow 197 MHz and 394 MHz cavity systems
- ESR \rightarrow 394 MHz cavity system

The large crossing angle of 25 mrad requires higher transverse voltage in cancelling the effect due to Piwinski angle [2]. The transverse voltage requirements for the IR6 are listed in Table 1.

The 197 MHz crabbing cavity is one of the critical components identified among the EIC rf systems that will be prototyped first along with the 591 MHz single-cell cavity.

* Work supported by the U.S. Department of Energy, Office of Science, Office of Nuclear Physics under contract DE-AC05-06OR23177.

[†] sdesilva@jlab.org

Table 1: Total Transverse Voltage and Number of Cavities

System	HSR	ESR
197 MHz	33.83 MV	–
394 MHz	4.75 MV	2.90 MV
197 MHz	8	–
394 MHz	4	2

The system requirements for the 197 MHz crabbing cavity are listed below.

- Nominal transverse voltage per cavity = 8.5 MV
- Maximum transverse voltage per cavity = 11.5 MV
- Peak fields at 11.5 MV: $E_p < 45 \text{ MV/m}$ & $B_p < 80 \text{ mT}$
- Impedance thresholds per cavity (considering simultaneous operation of both interaction regions):
 - Longitudinal $< 10 \text{ k}\Omega$
 - Transverse-H $< 0.132 \text{ M}\Omega$
 - Transverse-V $< 0.66 \text{ M}\Omega$
- Dimensional constraints:
 - Beam pipe aperture = 100 mm
 - Cavity length (flange-to-flange) $< 1.5 \text{ m}$
 - Beam line space per side for HSR $< 12.5 \text{ m}$

197 MHz CRABBING CAVITY DESIGN

Both 197 MHz and 394 MHz crabbing cavities are based on the rf-dipole design [3]. The 197 MHz crabbing cavity design includes two HOM dampers, the fundamental power coupler (FPC) and pick up as shown in Fig. 2. The length of the bare cavity is 1.5 m and 0.6 m in diameter. The poles in the cavity were optimized to achieve a balance peak field of 1.78 mT/(MV/m). The optimized pole length is 524 mm with a pole height of 240 mm. The rf-properties of the 197 MHz crabbing cavity are listed in Table 2.

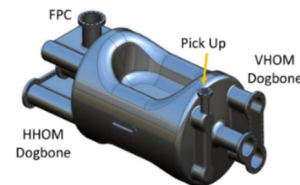


Figure 2: 197 MHz crabbing cavity.

The cavity is designed with four identical dogbone-shaped waveguides to maintain the field symmetry to a feasible extent. However, different dogbone waveguide lengths still contribute to the field asymmetry further enhanced by the FPC. The impact on the dynamic aperture

EFFECT OF DURATION OF 120 °C BAKING ON THE PERFORMANCE OF SUPERCONDUCTING RADIO FREQUENCY NIOBIUM CAVITIES*

B. D. Khanal¹, P. Dhakal^{†2}

¹Department of Physics, Old Dominion University, Norfolk, VA 23529, USA

²Thomas Jefferson National Accelerator Facility, Newport News, VA 23606, USA

Abstract

Over the last decade much attention was given in increasing the quality factor of superconducting radio frequency cavities by impurity doping. Prior to the era of doping, the final cavity processing technique to achieve the high accelerating gradient includes the “in-situ” low temperature baking of SRF cavities at temperature ~ 120 °C for several hours. Here, we present the results of a series of measurements on 1.3 GHz TESLA shape single-cell cavities with successive low temperature baking at 120 °C up to 96 hours. The experimental data were analyzed with available theory of superconductivity to elucidate the effect of the duration of low temperature baking on the superconducting properties of cavity materials as well as the rf performance. In addition, the rf loss related to the trapping of residual magnetic field referred as flux trapping sensitivity was measured with respect to the duration of 120 °C bake.

INTRODUCTION

The performance of superconducting radio frequency (SRF) cavities are measured in terms of quality factor as a function of accelerating gradient. Higher quality factor with high accelerating gradient are desirable for operation of high energy future particle accelerators. Over the last decades, high quality factor at medium accelerating gradient (20 - 25 MV/m) was achieved by impurity doping with Ti or N [1–3]. The effect of low temperature baking in the presence of nitrogen also resulted increase in quality factor at medium accelerating gradient and it was extended to higher accelerating gradient over the baseline measurement [4, 5]. Most recently, the medium temperature heat treatment also resulted in the increase in quality factor likely due to the decomposition of surface oxide phase and oxygen diffusion within the rf penetration depth [6, 7].

The role of the low temperature baking (120 - 150 °C) on the performance of SRF cavities was studied extensively, mainly eliminating the high field Q-slope and few models were proposed in the past [8–12]. The oxygen diffusion model proposed by G. Ciovati [13], qualitatively explains the diffusion of oxygen in to the rf surface of SRF cavities. The same model also describes well to the diffusion of oxygen during the mid-T heat treatment (300 - 400 °C) [7]. Here, we present a systematic study on the performance of

SRF cavities subjected to the low temperature baking to understand the effect of 120 °C baking duration. We extract the superconducting parameter from the temperature dependence of surface resistance and penetration depth.

CAVITY SURFACE PREPARATION AND RF MEASUREMENTS

Two TESLA-shaped 1.3 GHz single cell cavities ($G = 277.85$, $B_p/E_{acc} = 4.23$ mT/(MV/m)) were fabricated from high purity Nb. One of the single cells labeled TE1-05 was fabricated from fine-grain ASTM 5 Nb with RRR ~ 400 and second cavity labeled TE1-06 was fabricated from a cold work niobium sheet. The cavities were processed with several heat treatment cycles in the range of 800 - 1000 °C followed by ~ 25 μm electropolishing as the final surface preparation. The cavities were subjected to high pressure rinse, dried in clean room overnight and assembled with probes and pump-out port.

The cavities were loaded in the vertical Dewar to measure the flux expulsion when the cavity transitions to the superconducting state during cooldown. The details of flux expulsion technique are given in Refs. [14, 15]. Both cavities showed excellent flux expulsion when the temperature gradient across the irises is kept > 2.0 K. The baseline rf measurements were done with cavity cooldown in minimum residual magnetic field (< 1 mG) in Dewar with high temperature gradient ($\Delta T > 4$ K) across the cavity irises to ensure good flux expulsion of any residual magnetic field. The Q_0 vs. the helium bath temperature (T) measurement was done from 4.3 to 1.6 K at $B_p \sim 15$ mT. A representative plot for $R_s(T)$ is shown in Fig.1 for cavity TE1-06 after electropolishing followed by 120 °C bake for 3 hours. At 2.0 K, the Q_0 vs. E_{acc} measurement was carried out. The second set of measurements was done after warming the cavity above T_c and cooldown with ~ 20 mG residual magnetic field in Dewar. The cavity was cooled with temperature gradient across the cavity < 0.1 K ($B_{sc}/B_{nc} \sim 1$), ensuring that maximum ambient magnetic field was trapped during the cooldown. Again, the Q_0 vs. T measurement was repeated from 4.3 to 1.6 K and at 2.0 K, the Q_0 vs. E_{acc} measurement was done. This allows us to extract the flux trapping sensitivity, the increase in surface resistance due to the trapped residual magnetic field during cooldown.

The cavities were subjected to low temperature baking at 120 °C for several hours in the interval of (3, 6, 12, 24, and 48 hours) in a bake box. During the cavity baking process, the cavity was kept under vacuum ($< 10^{-7}$ torr). The rf measurements of Q_0 vs. T and Q_0 vs. E_{acc} were repeated

* The work is partially supported by the U.S. Department of Energy, Office of Science, Office of High Energy Physics under Awards No. DE-SC 0009960. The manuscript has been authored by Jefferson Science Associates, LLC under U.S. DOE Contract No. DE-AC05-06OR23177.

[†] dhakal@jlab.org

REAL-TIME CAVITY FAULT PREDICTION IN CEBAF USING DEEP LEARNING*

Md. M. Rahman[†], K. Iftekharuddin

Vision Lab, Department of Electrical and Computer Engineering,
Old Dominion University, Norfolk, VA 23529, USA

A. Carpenter, T. McGuckin, C. Tennant, L. Vidyaratne

Thomas Jefferson National Accelerator Facility, Newport News, VA 23606, USA

Abstract

Data-driven prediction of future faults is a major research area for many industrial applications. In this work, we present a new procedure of real-time fault prediction for superconducting radio-frequency (SRF) cavities at the Continuous Electron Beam Accelerator Facility (CEBAF) using deep learning. CEBAF has been afflicted by frequent downtime caused by SRF cavity faults. We perform fault prediction using pre-fault RF signals from C100-type cryomodules. Using the pre-fault signal information, the new algorithm predicts the type of cavity fault before the actual onset. The early prediction may enable potential mitigation strategies to prevent the fault. In our work, we apply a two-step fault prediction pipeline. In the first step, a model distinguishes between faulty and normal signals using a U-Net deep learning architecture. In the second step of the network, signals flagged as faulty by the first model are classified into one of seven fault types based on learned signatures in the data. Initial results show that our model can successfully predict most fault types 200 ms before onset. Our fault prediction model shows poor model performance on fast-developing fault types.

INTRODUCTION

The Continuous Electron Beam Accelerator Facility (CEBAF) at Jefferson Lab is a high power, continuous wave recirculating linear accelerator (linac) servicing four different experimental nuclear physics end stations [1]. CEBAF completed an energy upgrade from 6 GeV to 12 GeV in 2017 which required the installation of 11 additional cryomodules, called C100s for their capability to provide 100 MV of energy gain [2]. A schematic of CEBAF with locations of C100 cryomodules is shown in Fig 1. Each cryomodule is composed of 8 superconducting radio-frequency (SRF) cavities. In addition, a digital low-level radio frequency system (LLRF) is developed to regulate the new cryomodules.

CEBAF experiences frequent short machine downtime trips caused by numerous SRF system faults, especially when cavity gradients are being pushed to their limits. In 2019, CEBAF experienced an average of 4.1 RF downtime trips per hour, culminating in approximately 1 hr of beam time lost each day [3]. A data acquisition system is implemented in the C100 cryomodules to record data to

investigate the nature and the origin of the SRF faults. These recorded waveform data are analyzed by a subject matter expert (SME) to determine the cavity that caused the trip and the type of fault. This is a non-trivial, laborious task. Typically, a SME performs this task days or weeks after the events. Previous work successfully addressed this fault classification task with machine learning (ML) [4]. In this work, our goal is to develop deep learning-based artificial intelligence (AI) techniques to predict the fault before its onset.

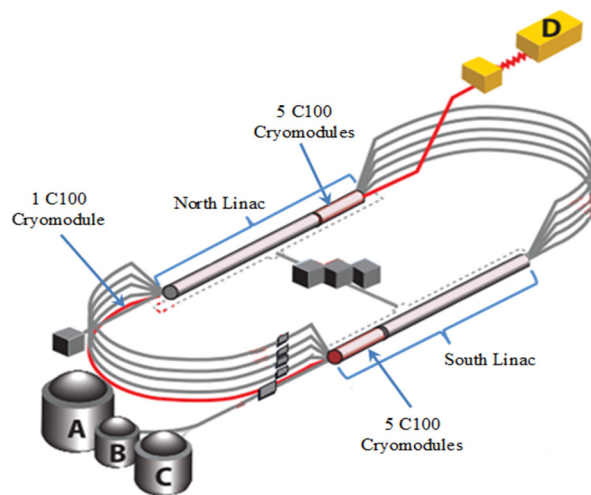


Figure 1: A schematic of CEBAF with the experimental halls (A, B, C, and D), and the locations of the C100 cryomodules labeled [3].

DATA

The data acquisition system in CEBAF synchronously acquires timestamps and saves waveform records of 17 different RF signals from the C100 cryomodule. The data acquisition system includes two primary components, the low-level RF (LLRF) controls and the experimental physics and industrial control system (EPICS), along with a collection of high-level applications. These two components work together to generate and save data for further analysis. Each of the recorded 17 signals is 8192-time steps long. The duration of the recorded signals is approximately 1637.4 ms at a sample interval of 0.2 ms.

There are two types of datasets used for this study. The first type is the normal running dataset which is representative of normal operating conditions (i.e. no faults). For this experiment, we use 60,000 normal running examples of a 100 ms time window. The second type of the

* This work is supported by the U.S. Department of Energy, Office of Science, Office of Nuclear Physics under Contract No. DE-AC05-06OR23177.

[†] mrahm006@odu.edu

Nb₃Sn COATING OF A 2.6 GHz SRF CAVITY BY SPUTTER DEPOSITION TECHNIQUE*

M. S. Shakel[†], W. Cao, H. E. Elsayed-Ali, Md. N. Sayeed, Old Dominion University, Norfolk, VA
G. Ereemeev, Fermi National Accelerator Laboratory, Batavia, IL, USA
U. Pudasaini, A. M. Valente-Feliciano
Thomas Jefferson National Accelerator Facility, Newport News, VA, USA

Abstract

Nb₃Sn is considered promising as a coating for superconducting radio frequency (SRF) cavities due to its high transition temperature $T_c \sim 18.3$ K and superheating field $H_{sh} \sim 400$ mT, almost twice that of Nb. A cylindrical DC magnetron sputtering system was built, commissioned, and used to deposit Nb₃Sn on the inner surface of a 2.6 GHz single-cell Nb SRF cavity. With two identical cylindrical magnetrons, this system can coat the cavity with high symmetry and uniform thickness. Using Nb-Sn multilayer sequential sputtering followed by annealing at 950 °C for 3 h, Nb₃Sn films are first deposited at the equivalent positions of the cavity's beam tubes and the equator. The films' compositions and crystal structures are characterized by energy dispersive spectroscopy (EDS) and X-ray diffraction (XRD), respectively. The T_c of the films are measured by the four-point probe method and are observed to be 17.61 to 17.76 K. Based on these studies, ~ 1.2 μm thick Nb₃Sn is deposited inside a 2.6 GHz SRF Nb cavity. We discuss the first results from samples and cavity coatings and the operation of the cylindrical sputtering system.

INTRODUCTION

Compared to Nb SRF cavities, Nb cavities coated with Nb₃Sn can achieve high-quality factors at 4 K and can replace the bulk Nb cavities operated at 2 K, hence reducing the operation cost significantly [1-4].

One of the methods used to deposit Nb₃Sn coating on Nb SRF cavities is Sn vapor diffusion [5-7]. Magnetron sputtering is another promising method for Nb₃Sn coating as it provides better control over stoichiometry than the Sn diffusion process [8]. Magnetron sputtering is applied in several methods to grow Nb₃Sn: Depositing multilayers of Nb-Sn followed by annealing, from a single stoichiometric Nb₃Sn target, or by co-sputtering of Nb and Sn [9-13].

We have commissioned a cylindrical DC magnetron sputtering system at Old Dominion University to coat the inside surface of a 2.6 GHz Nb SRF cavity with Nb₃Sn. By applying multilayer sequential sputtering to deposit Nb-Sn layers using the two identical magnetrons followed by annealing, Nb₃Sn thin film is grown on Nb at the equivalent positions of the 2.6 GHz SRF cavity beam tubes and the equator.

* Supported by DOE, Office of Accelerator R&D and Production, Contact No. DE-SC0022284, with partial support by DOE, Office of Nuclear Physics DE-AC05-06OR23177, Early Career Award to G. Ereemeev.

[†] mshak001@odu.edu

DESIGN OF CYLINDRICAL DC MAGNETRON SPUTTER COATER

The cylindrical magnetron sputtering system, schematically shown in Fig. 1, consists of the custom-designed high vacuum deposition chamber and two identical cylindrical magnetrons, designed and built by PLASMIONIQUE Inc. that can travel inside the cavity while depositing Nb or Sn.

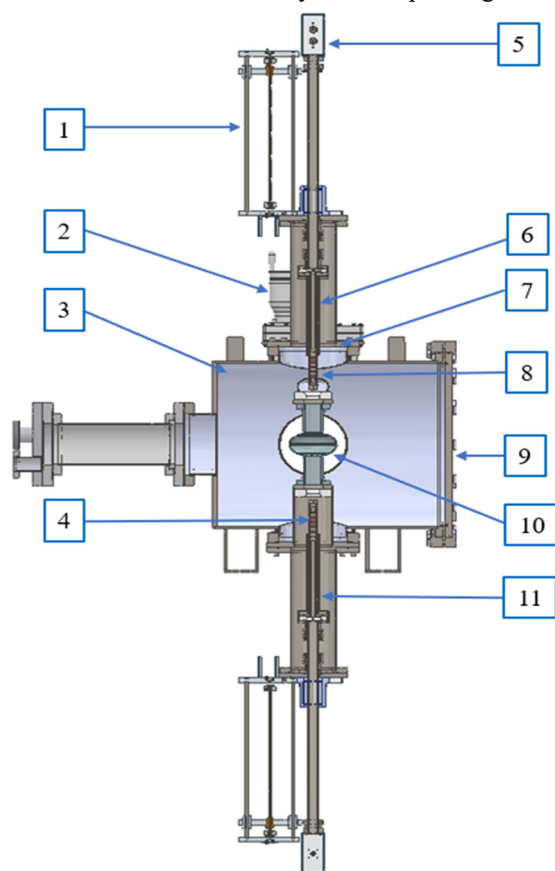


Figure 1: A sketch of the cylindrical DC magnetron sputtering system: (1) Magnetron movement controller shaft, (2) Gate valve, (3) Vacuum chamber, (4) Magnets, (5) Water flow controller, (6) Top magnetron, (7) 8" ConFlat (CF) port of top magnetron, (8) Tube target, (9) Chamber door, (10) 2.6 GHz Nb SRF cavity, (11) Bottom magnetron; The magnetrons are made by PLASMIONIQUE Inc to fit an ODU custom chamber.

LOWER TEMPERATURE ANNEALING OF VAPOR DIFFUSED Nb₃Sn FOR SRF CAVITIES*

J. K. Tiskumara[†], J. R. Delayen

Center for Accelerator Science, Old Dominion University, Norfolk, VA, USA

U. Pudasaini, Thomas Jefferson National Accelerator Facility, Newport News, VA, USA

G. Ereemeev, Fermi National Accelerator Laboratory, Batavia, IL, USA

Abstract

Nb₃Sn is a next-generation superconducting material for the accelerator cavities with higher critical temperature and superheating field, both twice compared to Nb. It promises superior performance and higher operating temperature than Nb, resulting in significant cost reduction. So far, the Sn vapor diffusion method is the most preferred and successful technique to coat niobium cavities with Nb₃Sn. Although several post-coating techniques (chemical, electrochemical, mechanical) have been explored to improve the surface quality of the coated surface, an effective process has yet to be found. Since there are only a few studies on the post-coating heat treatment at lower temperatures, we annealed Nb₃Sn-coated samples at 800 °C - 1000 °C to study the effect of heat treatments on surface properties, primarily aimed at removing surface Sn residues. This paper discusses the systematic surface analysis of coated samples after annealing at temperatures between 850 °C and 950 °C.

INTRODUCTION

Nb₃Sn is a potential alternative material to replace Nb in SRF cavities with a higher critical temperature T_c of 18.3 K, higher critical field, accordingly the lower surface resistance compared to Nb. Thus, Nb₃Sn could potentially give a lower dissipation than that of niobium at any given temperature. Nb₃Sn cavities can operate at 4 K delivering similar performance that of Nb cavities at 2 K promising significant reduction in the operational cost of SRF accelerators. Its superheating field of about 400 mT suggests a higher breakdown field for higher accelerating gradient, which can reduce initial cost to build SRF accelerators [1]. Because of brittleness and lower thermal conductivity, Nb₃Sn should be deposited as a thin film on RF structures. Among the available methods, the Sn vapor diffusion technique is successful technique pursued by several laboratories to coat Nb SRF cavities with different shapes and frequencies [2–6].

A Nb twin-axis cavity with complex geometrical shape was coated with vapor-diffused Nb₃Sn several times at JLab but resulting performance was not as good as expected for Nb₃Sn [1]. Further investigations pointed out

that the poor performance was caused by mechanical deformation of the cavity during the cool down to cryogenic temperatures. Other factors that could have contributed to the performance degradations were potential non-uniformity of the coating at hard-to-reach areas, and surface quality of the thin-film. Later coating experiments with samples positioned at strategic positions revealed uniform and complete coating inside the cavity, but Sn residue were present in most of the cavity witness samples. Note that the presence of Sn-residues on the coated surfaces had been reported before [7]. Most of the post-coating treatment explored in the past to improve surface quality resulted in surface degradation [8] or were inconclusive.

We updated the coating parameters to minimize the accumulation of Sn-residues. It included Sn-supply optimization by reducing the amount of Sn, the size of the crucible, and temperature profile modifications (discussed later). Although the updated coating parameters with multi-step coating temperatures and gradual cool down below 900 °C reduced residue sizes, complete elimination was challenging.

One potential post-coating treatment to remove Sn-residue could have been annealing the coated sample without Sn. Previous studies at JLab have shown that annealing the coating at >1000 °C resulted in residue eliminations along with Sn-loss from the Nb₃Sn layer, and unusual grain faceting that resulted in performance degradation [9]. Temperature below 1000 °C was not explored, which could have avoided the Sn loss from the coated layer and mitigated the effect of Sn residues, which may help to improve the RF performance of Nb₃Sn-coated cavities. In this contribution, we report surface studies of Nb₃Sn samples which received post-coating annealing at 850-950 °C.

EXPERIMENTAL

Sample Preparation and Nb₃Sn Coating

Samples used in this study were 10 mm × 10 mm coupons cut from high RRR, 3mm thick Nb sheet, similar to one used to fabricate SRF cavities. These samples received 100 μm of Buffered Chemical Polishing (BCP) to remove damaged layer from the surface. They were then heat treated at 800 °C for 3 hours for hydrogen degassing. Finally, these samples were subjected to 5 μm BCP removal before Nb₃Sn coating.

Typically, the samples for this study were coated using similar coating process used to coat single-cell cavities recently at JLab. The temperature profile included 1 hour of nucleation at 500 °C followed by about 3 h of coating (~40

* Research supported by DOE Office of Science Accelerator Stewardship Program Award DE-SC0019399 and DOE Award DE-SC0010081. Partially authored by Jefferson Science Associates under contract no. DEAC0506OR23177. This material is based upon work supported by the U.S. Department of Energy, Office of Science, Office of Nuclear Physics and Office of High Energy Physics.

[†] jtisk001@odu.edu

SPALLATION NEUTRON SOURCE CRYOGENIC MODERATOR SYSTEM HELIUM GAS ANALYSIS SYSTEM*

B. DeGraff†, R. Armstrong, J. Denison, M. Howell, S. H. Kim, D. Montierth, L. Pinion
Oak Ridge National Laboratory, Oak Ridge, TN, USA
M. Williamson, Lawrence Berkley National Laboratory, Berkeley, CA, USA

Abstract

The Spallation Neutron Source (SNS) at Oak Ridge National Laboratory (ORNL) operates the Cryogenic Moderator System (CMS). The CMS comprises a 20-K helium refrigerator and three helium to hydrogen heat exchangers in support of hydrogen cooled spallation moderation vessels. This system uses vessels filled with activated carbon as the final major component to remove oil vapor from the compressed helium in the cryogenic cold box. SNS uses a LINDE multi-component gas analyzer to detect the presence of contaminants in the warm helium flow upstream of the cold box including aerosolized oil vapor. The design challenges of installing and operating this analyzer on the CMS system due to normal system operating pressures will be discussed. The design, fabrication, installation, commissioning, and initial results of this system operation will be presented. Future upgrades to the analyzer system will also be discussed.

SYSTEM OVERVIEW

The Spallation Neutron Source (SNS) at Oak Ridge National Laboratory (ORNL) operates a linear accelerator (LINAC) comprised of both normal conducting and superconducting radio frequency (SCRF) cavities to produce a 1 GeV beam. This beam strikes a liquid mercury target at a power level of 1.4 MW. Spallation then creates high energy neutrons that are used in multiple beamlines to conduct research. Critical to producing the correct energy neutrons for research are four moderators that tailor the energy of the neutron to the research needs of the experiments. The Cryogenic Moderator System (CMS) is responsible for producing 20 K supercritical hydrogen for cooling three of the four moderators surrounding the SNS target.

Instead of using a hydrogen cryogenic cycle to produce the required cooling in the SNS target moderators, the CMS uses a cryogenic helium cycle to then cool the hydrogen to the required temperature. The CMS consists of a helium compressor, a 7.5 kW at 17 K helium refrigerator, helium to hydrogen heat exchangers and three separate supercritical 20 K cooling loops for SNS target moderators. The reliable operation of the CMS cryogenic cooling system is essential to the successful scientific objectives of the SNS beamlines. Maintaining and monitoring the purity of the helium at the inlet to the 17 K cold box is critical to long term reliable SNS operations. The combined helium and hydrogen cryogenic cycle is shown in Fig. 1.

* This work was supported by SNS through UT-Battelle, LLC, under contract DE-AC05-00OR22725 for the U.S. DOE.

† degraffbd@ornl.gov

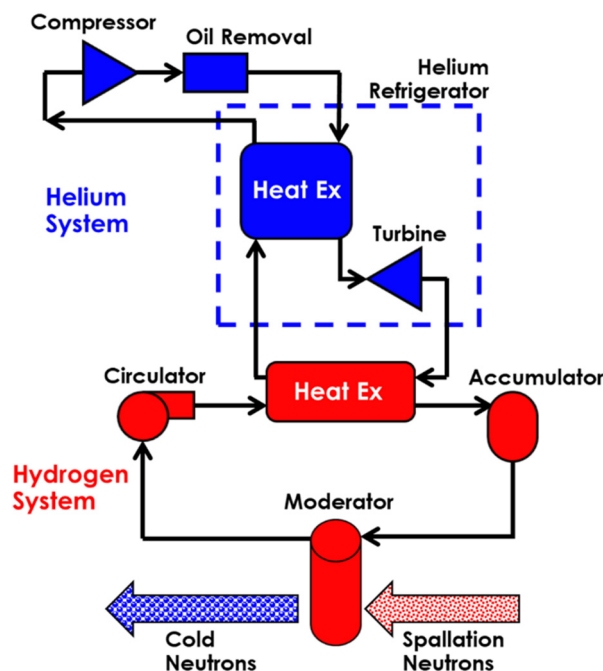


Figure 1: CMS cryogenic cycle.

HELIUM GAS ANALYSIS SYSTEM

System Layout

The CMS helium compressor is a single stage oil-flooded screw compressor which operates with a suction pressure ~40 psig and a discharge pressure ~260 psig. The system has suffered in the past from loss of capacity from suspected oil carryover into the helium cold box. A LINDE multi-component was purchased to analyze the helium both before and after the carbon bed on the oil removal system. However, this analyzer cannot provide accurate readings when discharging into suction of the main helium compressor. The only operating mode that was historically available to the CMS was occasionally turning the analyzer on to “spot-check” the system purity while venting the measured helium to atmosphere.

A project was started to install a small helium compressor and appropriate pressure control measures to maintain a pressure on the outlet of the LINDE analyzer. A diagram of the system layout is shown in Fig. 2. The hardware for the project contains the following pieces of equipment:

- Pressure regulator set to 200 psig on the supply high pressure supply

LASER STRIPPING FOR 1.3 GeV H⁻ BEAM AT THE SNS*

T. Gorlov, A. Aleksandrov, S. Cousineau, Y. Liu, A.R. Oguz,
 Oak Ridge National Laboratory, Oak Ridge, TN 37831, USA

M. Kay, Department of Physics and Astronomy, Univ. of Tennessee, Knoxville, TN 37966, USA

P. K. Saha, Japan Atomic Energy Agency, J-PARC Center, Tokai-mura, Ibaraki 319-1195, Japan

Abstract

A realistic full duty factor laser stripping charge exchange injection scheme for a future 1.3 GeV beam at the SNS is considered. Different schemes of laser stripping involving combinations of photoexcitation, photoionization and magnetic field stripping are calculated. The laser power and magnetic field strength needed for different approaches are estimated and compared. The most practical scheme of laser stripping is selected for development.

INTRODUCTION

Laser assisted charge-exchange injection of H⁻ beam has been studied theoretically and experimentally at the Spallation Neutron Source (SNS) in Oak Ridge. This novel method can replace foil assisted charge exchange injection. High beam power destroys stripping foils quickly due to beam heating [1].

A detailed review of laser stripping development can be found in a recent paper [2]. The first proof of principle experiment has been carried out at the SNS for a 900 MeV beam energy [3] using a three step laser stripping scheme [4]. A proof of practicality experiment has been performed for 1 GeV energy [5]. The main goal of laser stripping development is to optimize lasers, magnets and other tools so it would be practically reasonable to build the system. Lasers must have small average power and stripping magnets must be preferably non-superconducting. Recently we developed a sequential scheme of laser stripping that could reduce laser power by a factor of 10 and simplify the project [2]. J-PARC is considering using lasers only without stripping magnets for their low energy 400 MeV beam [6].

The choice of laser stripping scheme and its optimization depends mainly on the beam energy and other parameters of the beam. SNS is planning to upgrade the beam energy to 1.3 GeV within the PPU project [7]. In this paper we present all possible schemes and parameters for the 1.3 GeV beam using realistic expected parameters of the beam distribution. Based on these schemes we will select the most simple and practical method to consider for further development.

* This manuscript has been authored by UT-Battelle, LLC, under Contract No. DE-AC05-00OR22725 with the U.S. Department of Energy. The United States Government retains, and the publisher, by accepting the article for publication, acknowledges that the United States Government retains a non-exclusive, paid-up, irrevocable, world-wide license to publish or reproduce the published form of this manuscript, or allow others to do so, for United States Government purposes. The Department of Energy will provide public access to these results of federally sponsored research in accordance with the DOE Public Access Plan (<http://energy.gov/downloads/doe-public-access-plan>).

MAGNETIC STRIPPING

High energy H⁻ ion beam as well as H^{0*} excited state beam can be easily stripped/ionized in a strong magnetic field through Lorentz ionization. The first and the last step of the three step laser stripping have been performed by using non-superconducting electromagnets [3] or permanent magnets [5] of 1.5-2.0 Tesla. The beam energy was 0.9-1.0 GeV and H^{0*} was excited into the 3p state for easy magnetic field stripping. The first step H⁻ → H⁰ + e⁻ for 1.3 GeV ion beam can be performed by a simple permanent magnet with field of the order of 1 Tesla. The 3s, 3p and 3d excited states of the Hydrogen beam H^{0*} → p + e⁻ can be stripped by the same order of magnetic field.

In this section we will estimate stripping of the 2p excited state in a 1.3 GeV beam. The magnetic field profile B_x(z) along z-direction of a beam for a typical magnet can be characterized by a Gaussian shape:

$$B(z) = B_0 \exp\left(-\frac{z^2}{2\sigma^2}\right) \quad (1)$$

The ionization lifetime of the 2p excited state of the hydrogen atom in electro-magnetic field has been calculated from this work [8]. The stripping efficiency of single particle is calculated by integrating the stripping probability over B(z) Eq. (1). Figure 1 represents the stripping efficiency of the beam as a function of B₀ and σ.

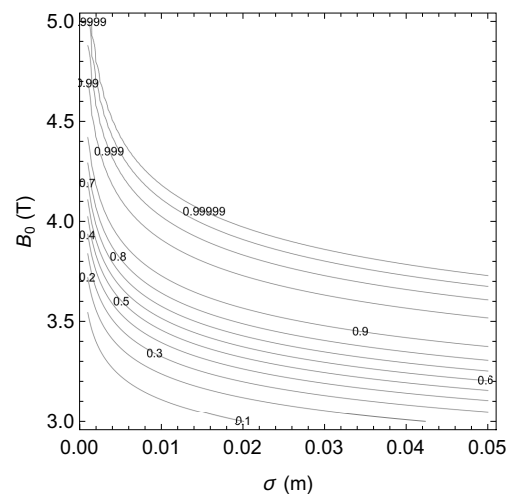


Figure 1: Stripping efficiency of 2p excited state in a 1.3 GeV hydrogen beam in a magnetic field (1).

From this picture it is seen that magnetic field of normal longitudinal size σ=1 cm requires 4.0-4.5 Tesla to strip more than 99% of the beam.

TRANSFER MAPS IN THE HARD-EDGE LIMIT OF QUADRUPOLE AND BEND MAGNETS FRINGE FIELDS*

T. V. Gorlov[†], Oak Ridge National Laboratory, Oak Ridge, TN, USA

Abstract

Beam dynamics of charged particles in the fringe field of a quadrupole and a dipole magnet is considered. An effective method for solving symplectic Lie map $\exp(: f :)$ in such cases has been developed. A precise analytic solution for nonlinear transverse beam dynamics in a quadrupole magnet with hard-edge fringe field has been obtained. The method of Lie map calculation considered here can be applied for other magnets and for soft edge type of fringe field.

INTRODUCTION

Nonlinear beam dynamics due to the fringe field effect of magnets can impact accelerator performance [1, 2]. In this paper we calculated an exact analytic nonlinear transfer map for beam dynamics in the fringe field of a quadrupole magnet using the Lie transformation $\exp(: f :)$ in hard-edge approximation. In accelerator physics, transverse beam optics of single particle is defined by 4D coordinates in a phase space $\{x, x_p, y, y_p\}$. Here $x_p = p_x/p_z$ and $y_p = p_y/p_z$ are angular coordinates. Solving the Hamiltonian flow with input coordinates $\{x, x_p, y, y_p\}_{in}$ gives a corresponding function \mathbf{M} called a transfer map with output coordinates $\{x, x_p, y, y_p\}_{out} = \mathbf{M}\{x, x_p, y, y_p\}_{in}$.

The beam dynamics for real quadrupole magnets is normally calculated numerically and the transfer maps is hard to solve precisely and analytically in the general case. For this reason, the magnetic field of the quadrupole as well as the beam dynamics is usually simplified by a so-called hard-edge model. The real 3D magnetic field of a quadrupole $\mathbf{B}(x, y, z)$ can be defined by its gradient components $G(z) = \partial B_y / \partial x = -\partial B_x / \partial y$ on the z-axis. The hard-edge model is represented by a rectangular profile with amplitude $G = G(z)_{max}$ and longitudinal size $L_{eff} = \int G(z) dz / G$ [3]. Single particle dynamics is well approximated by the hard-edge model consisting of a sequence of elements called lattice: drift space followed by nonlinear thin element of the entrance fringe field followed by thick linear element of the quadrupole magnet [3] then followed by thin nonlinear element of the exit fringe field. In this paper we consider the nonlinear beam dynamics of the entrance and exit fringe fields of the quadrupole and dipole. The nonlinear map in first order approximation over \mathbf{B} field gradient was originally derived by Lee-Whiting [4] in 1970. Some derivations for electrostatic and magnetic quadrupole lens can be found in [5]. Linear map due to fringe field can be found in [6].

The nonlinear transfer map can be obtained by calculating Lie transformation widely used in accelerator physics [7, 8]:

$$\exp(: f :) = \sum_{n=0}^{\infty} \frac{: f :^n}{n!} \quad (1)$$

Here $: f :^n$ is operator defined by recurrence equation:

$$: f :^n = \{f, : f :^{n-1}\} \quad (2)$$

with the initial condition $: f :^0 z_i = z_i$. Here z_i is one of the phase space coordinate to be transformed by Eq. (1) and

$$\{a, b\} = \frac{\partial a}{\partial x} \frac{\partial b}{\partial x_p} - \frac{\partial a}{\partial x_p} \frac{\partial b}{\partial x} + \frac{\partial a}{\partial y} \frac{\partial b}{\partial y_p} - \frac{\partial a}{\partial y_p} \frac{\partial b}{\partial y} \quad (3)$$

is the Poisson bracket operator expressed in terms of transverse phase space coordinates. f in expression Eq. (1) is called characteristic function [7, 9]. We will derive a precise nonlinear map for the entrance/exit fringe fields of quadrupole and dipole magnets by solving the Lie transformation Eq. (1) exactly.

QUADRUPOLE MAGNET

We will use magnetic field and its corresponding characteristic function f in the form of multipole approximation [7, 9]:

$$f = \mathbf{Re} \frac{C(x+iy)^n}{4(n+1)} \left(x p_x + y p_y + i \frac{n+2}{n} (x p_y - y p_x) \right) \quad (4)$$

This field is characterised by the lowest order harmonic n in the transverse direction while any real field contains an infinite number of harmonics according to Fourier theory.

In this section we solve precisely Lie transformation Eq. (1) with characteristic function Eq. (4) for the fringe field of quadrupole with $n = 2$:

$$\exp(: k [y_p (y^3 + 3x^2y) - x_p (x^3 + 3y^2x)] :) \quad (5)$$

Here we denote the strength coefficient

$$k = \frac{eG/p_0}{12(1 + \delta p_0/p_0)} \quad (6)$$

for simplicity, where G is the amplitude of the gradient of the magnetic field. Entrance and exit fringe fields are characterised by \pm sign in front of k coefficient while the sign of the coefficient k can be positive or negative independently. Before we solve the full transformation Eq. (1) with four phase-space terms of the characteristic function f we will first solve the Lie transform for only one term:

$$\exp(: -k x_p x^3 :) \quad (7)$$

* This manuscript has been authored by UT-Battelle, LLC, under Contract No. DE-AC05-00OR22725 with the U.S. Department of Energy.

[†] tg4@ornl.gov

EMITTANCE GROWTH DUE TO RF PHASE NOISE IN CRAB CAVITIES*

H. Huang[†], S. Zhao, Old Dominion University, Norfolk, VA, USA
V. Morozov, F. Lin, Oak Ridge National Lab, Oak Ridge, TN, USA
Y. Zhang, T. Satogata, Jefferson Lab, Newport News, VA, USA
Y. Luo, D. Xu, B. Xiao, Brookhaven National Lab, Upton, NY, USA

Abstract

The Electron-Ion Collider (EIC) incorporates beam crabbing to recover geometric luminosity loss from the nonzero crossing angle at the interaction point (IP). It is well-known that crab cavity imperfections can cause growth of colliding beam emittances, thus degrading collider performance. Here we report a particle tracking study to quantify these effects. Presently the study is focused on crab cavity RF phase noise. Simulations were carried out using Bmad. Dependence of emittance growth on phase noise level was obtained which could be used for developing crab cavity phase control specifications. We also benchmarked these simulations with theory.

INTRODUCTION

Crab crossing provides a head-on beam-beam collision for beams with a nonzero crossing angle. When a bunch passes through a crab cavity, as in an RF deflector, the phase is set so there is no kick on the longitudinal bunch centroid; only the head and tail of a bunch receive transverse kicks in opposite directions. Previous work [1] has shown that some imperfections of RF crab cavities could cause degradation of stored beams, leading to collider performance reduction.

One relevant imperfection is crab cavity RF phase noise, which can induce additional momentum kicks on passing particles and cause colliding beam emittance growth in the crabbing plane [2, 3]. Some key crabbing system parameters are the crab cavity synchronization and noise tolerances. Constraints on these tolerances come from the maximum acceptable emittance growth rate and maximum acceptable luminosity reduction. Previous studies found the transverse emittance growth is dominated by the crab cavity phase noise [2, 3], so it is critical to evaluate and quantify this growth to provide an important input to design specifications of the crab cavity controls.

In this paper, we focused our investigations and studies on the emittance growth due to the RF phase noise in crab cavities. In the first section, the simplified formulas are applied to estimate the value of emittance growth rate for a bunch passed through the crab cavities. The second section addresses what we observed in the numerical calculations and demonstrates the benchmarking work.

ANALYTIC THEORY AND PREDICTIONS

P. Baudrengnien and T. Mastoridis developed a theoretical model for the growth of beam transverse emittance induced by crab cavity noises [2, 3]. They argued the growth is dominated by phase noises, which can be written as,

$$\frac{d\varepsilon_x}{dt} = \beta_{cc} \left(\frac{eV_0 f_c}{2E_b} \right)^2 C_{\Delta\phi}(\sigma_\phi) \cdot \sum_{k=-\infty}^{\infty} \int_{-\infty}^{\infty} S_{\Delta\phi}[(k \pm \nu_b) f_c] \rho(v) dv \quad (1)$$

where β_{cc} is the horizontal β function at the crab cavity location, V_0 is the crab cavity voltage amplitude, f_c is the beam circulation frequency, E_b is the beam energy, $\rho(v)$ is the betatron tune distribution, $S_{\Delta\phi}$ is the phase noise power spectral density (PSD), and ν_b is the horizontal betatron tune. σ_ϕ is the rms longitudinal bunch line density (in radians at the crab cavity frequency) and $C_{\Delta\phi}(\sigma_\phi)$ is a function describing the growth rate dependence on the bunch length:

$$C_{\Delta\phi}(\sigma_\phi) = e^{-\sigma_\phi^2} [I_0(\sigma_\phi^2) + 2 \sum_{l=1}^{\infty} I_{2l}(\sigma_\phi^2)]. \quad (2)$$

$I_{2n}(x)$ is the modified Bessel function of the first kind. As the bunch length increases, the effect of phase noise on transverse emittance growth is reduced.

To simplify evaluation, we assumed that the betatron tune spread σ_{ν_b} is sufficiently narrow, since the power spectral density (PSD) is even symmetric, the effect of noise is independent of the actual tune distribution, then the following analytic formula was used for evaluating the emittance growth rate in our numerical predictions,

$$\frac{d\varepsilon_x}{dt} \approx 2\beta_{cc} \left(\frac{eV_0 f_c}{2E_b} \right)^2 S_{\Delta\phi} \left[\min_k |k \pm \nu_b| f_c \right]. \quad (3)$$

For general practice, the filtered noise centered around the betatron frequency is also used on PSD. In our calculation, suppose that Ergodic theory works here for the introduced phase noise, considering a stationary Gaussian random process with zero mean, a white Gaussian noise was included in crab cavities, and $S_{\Delta\phi}$ is simply as

$$S_{\Delta\phi} = \frac{\sigma_{\Delta\phi}^2}{f_c}, \quad (4)$$

* Work supported by Jefferson Science Associates, LLC under Contract No. DE-AC05-06OR23177, Brookhaven Science Associates, LLC under Contract No. DE-SC0012704 and UT-Battelle, LLC, under contract No. DE-AC05-00OR22725 with the U.S. Department of Energy.

[†] huang@jlab.org

BENCHMARKING AND EXPLORING PARAMETER SPACE OF THE 2-PHASE BUBBLE TRACKING MODEL FOR LIQUID MERCURY TARGET SIMULATION*

L. Lin[†], H. Tran, M. I. Radaideh, D. Winder
Oak Ridge National Laboratory, Oak Ridge, TN, USA

Abstract

High intensity proton pulses strike the Spallation Neutron Source (SNS)'s mercury target to provide bright neutron beams. These strikes also deposit extensive energy into the mercury and its steel vessel. Prediction of the resultant loading on the target is difficult when helium gas is intentionally injected into the mercury to reduce the loading and to mitigate the pitting damage on the vessel. A 2-phase material model that incorporates the Rayleigh-Plesset (R-P) model is expected to address this complex multi-physics dynamics problem by including the bubble dynamics in the liquid mercury. We present a benchmarking study comparing the measured target strains in the SNS target station with the simulation results of the solid mechanics simulation framework. We investigate a wide range of various physical model parameters, including the number of bubble families, bubble size distribution, viscosity, surface tension, etc. to understand their impact on simulation accuracy. Our initial findings reveal that using 8-10 bubble families in the model renders a simulation strain envelope that covers the experimental ones. Further optimization studies are planned to predict the strain response more accurately.

INTRODUCTION

The spallation reaction at the Spallation Neutron Source (SNS) at Oak Ridge National Laboratory involves an intense proton pulse hitting a mercury target to produce the most intense pulsed neutron beams in the world for scientific and materials discovery [1]. Unfortunately, the first target station at the SNS experienced frequent premature failures due to fatigue damage and pitting damage on the target's internal walls caused by the mercury cavitation [2,3]. Long-term diagnostics are very difficult because in-place devices will be damaged by the high radiation around the target in a very short time. Due to the absence of long-term diagnostics, high-fidelity modeling and simulation become important tools to facilitate the target's fatigue analysis and to improve the target's design [4]. The values of digital twins

of the mercury target have already been demonstrated by using ABAQUS [5]. However, a discrepancy between the simulated and measured strain has always been observed, especially when helium gas is intentionally injected into the mercury to reduce pitting damage [2, 6].

The injected helium bubbles in the mercury flow can significantly reduce the pitting damage on the vessel's internal wall and reduce the strain of the surrounding vessel [7–10]. The additional gas phase introduced by the helium bubbles also converts the mercury fluid into a fluid-bubble mixture. A 2-phase model that incorporates the Rayleigh-Plesset (R-P) model for the gas phase was developed [11] to incorporate the helium bubbles' dynamic behavior with liquid mercury. For convenience, the 2-phase model will be referred to hereafter as the R-P model. As for the R-P model itself, several physical parameters, such as bubble sizes and their group distribution, are still difficult to measure directly. More calibration methods are needed to inversely identify these physical parameters, or their ranges if possible. Therefore, improvement of this bubbly mercury model to predict the target vessel's dynamic stress/strain under pulsed loads within a reliable confidence range, becomes important for the design of current and future targets.

By leveraging the measured strain data for the target with helium bubbles injected, this research work investigates a wide range of various physical model parameters including the number of bubble families, bubble size distribution, viscosity, surface tension, and others to know their impact on simulation results. Our initial findings are reported in the following sections.

METHODS

The R-P model was developed to include bubble dynamics in liquid mercury contained in a flexible structure. However, the model itself relies on uncertain physics parameters that cannot be readily determined for the SNS target, and therefore must be calibrated with experimental measurement. Direct measurement or observation within the vessel turned out to be extremely difficult [3]. Instead, strain gauges attached on the vessel's external surface [2] have been successfully applied to monitor target's dynamic response. Figure 1 shows some of the sensor locations on the stainless steel vessel's external surface. The strong (23.3 kJ) but short (0.7 μ s) proton pulses result in stress/strain waves propagating to the stainless-steel vessel, which can be measured through the attached sensors. Measurements of the sensor strains for 2 milliseconds after the pulse delivery under the same pulse power level (1.4 MW) but different loading cycles have been

* This work was supported by the DOE Office of Science under grant DE-SC0009915 (Office of Basic Energy Sciences, Scientific User Facilities program). The authors like to thank Hao Jiang from ORNL for her suggestions to improve this paper. This research used resources of the Computer and Data Environment for Science (CADES) at the Oak Ridge National Laboratory, which is supported by the Office of Science of the U.S. Department of Energy under Contract No. DE-AC05-00OR22725. This manuscript has been authored by UT-Battelle, LLC, under contract DE-AC05-00OR22725 and DE-AC05-76RL0-1830 with the US Department of Energy (DOE).

[†] linl@ornl.gov

PROGRESS ON MACHINE LEARNING FOR THE SNS HIGH VOLTAGE CONVERTER MODULATORS

M. I. Radaideh*, C. Pappas, D. Lu, J. Walden, S. Cousineau
† Oak Ridge National Laboratory, Oak Ridge, TN, USA
T. Britton, K. Rajput, L. Vidyaratne, M. Schram
Jefferson Laboratory, Newport News, VA, USA

Abstract

The High Voltage Converter Modulators (HVCM) used to power the klystrons in the Spallation Neutron Source (SNS) linac were selected as one area to explore machine learning due to reliability issues in the past and the availability of large sets of archived waveforms. Progress in the past two years has resulted in generating a significant amount of simulated and measured data for training neural network models such as recurrent neural networks, convolutional neural networks, and variational autoencoders. Applications in anomaly detection, fault classification, and prognostics of capacitor degradation were pursued in collaboration with the Jefferson Laboratory, and early promising results were achieved. This paper will discuss the progress to date and present results from these efforts.

INTRODUCTION

The SNS uses a linac to accelerate protons to an energy of 1 GeV using high power RF delivered from klystrons. The klystrons are in turn powered by HVCMs which convert 13.8 kVAC to up to 130 kV, 1.3 ms long pulses at 60 Hz [1]. A simplified schematic of a HVCM is shown in Fig. 1. Figure 2 shows the layout of the SNS RF systems with 15 HVCMs, each driving multiple klystrons with the exception of the Coupled Cavity Linac (CCL) section where each HVCM drives a single klystron. The transformer T1, rectifier (Rec) and filter capacitors C1 and C2 convert the 13.8 kVAC to ± 1300 VDC. Insulated-gate bipolar transistor (IGBT) switches Qa1 to Qc4 switch at a nominal frequency of 20 kHz into pulse transformers which step the pulses up to high voltage. The high voltage pulses are then combined in parallel, rectified and filtered to produce the 1.3 ms, 60 Hz pulse train with an apparent switching frequency of 120 kHz. HVCMs have historically been a source of significant machine downtime at SNS, and still represent a significant percentage of lost user time. The HVCMs use a PXI based controller which digitizes up to 32 waveform channels at 50 MHz. Waveform and settings files are saved whenever there is a fault, and dec-

imated to 2.5 MS/s and saved approximately 30 minutes after turn on or after HVCM settings have changed. We recently opened-source the normal and fault data from the 15 HVCM powering the SNS, which are described in this paper [2] and can be downloaded from this Mendeley repository [3].

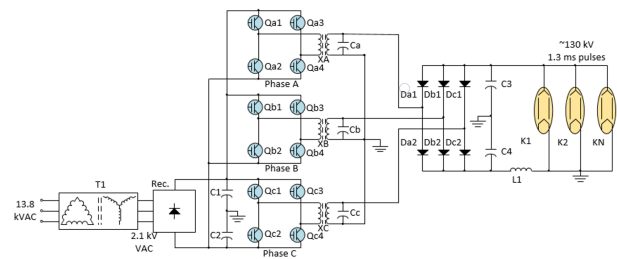


Figure 1: Simplified schematic of a HVCM.

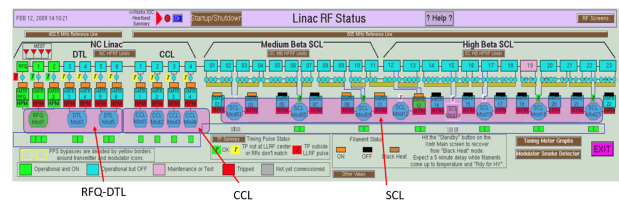


Figure 2: Layout of SNS RF system.

In addition to the HVCM real waveforms, a LTspice model (based on the SPICE circuit simulator) [4] of the HVCM circuit has been developed and validated, which we are using to generate a large amount of simulated data to model changes in values of circuit components and certain operating conditions such as IGBT switching frequency. To enable frequency modulation in the simulation, LTspice was coupled with MATLAB/SIMULINK. MATLAB is also being used for automation of LTspice execution to sweep ranges of component values. This helps generating LTspice simulations to model degradation of components such as plastic film capacitors. Thirteen of the waveforms related to the DC capacitor voltage, IGBT current, pulse transformer flux, and klystron voltage and current have been identified for the machine learning (ML) effort, since those have been the most useful in troubleshooting past failures. Figure 3 shows a comparison between the LTspice simulated waveform and a measured one for the magnetic flux in the A phase (A-flux).

* radaidehmi@ornl.gov

† This manuscript has been authored by UT-Battelle, LLC, under contract DE-AC05-00OR22725 and DE-AC05-76RL0-1830 with the US Department of Energy (DOE). The US government retains and the publisher, by accepting the article for publication, acknowledges that the US government retains a nonexclusive, paid-up, irrevocable, worldwide license to publish or reproduce the published form of this manuscript, or allow others to do so, for US government purposes. DOE will provide public access to these results of federally sponsored research in accordance with the DOE Public Access Plan.

THE L-CAPE PROJECT AT FNAL

M. Jain*, J. Strube¹, V. Amaty, G. Panapitiya
Pacific Northwest National Laboratory, Richland, WA, USA
B. Harrison, K. J. Hazelwood, W. Pellico, B. Schupbach, K. Seiya, J. St. John
Fermi National Accelerator Laboratory, Batavia, IL, USA
¹also at University of Oregon, Eugene, OR, USA

Abstract

The controls system at FNAL records data asynchronously from several thousand Linac devices at their respective cadences, ranging from 15 Hz down to once per minute. In case of downtimes, current operations are mostly reactive, investigating the cause of an outage and labeling it after the fact. However, as one of the most upstream systems at the FNAL accelerator complex, the Linac's foreknowledge of an impending downtime as well as its duration could prompt downstream systems to go into standby, potentially leading to energy savings. The goals of the Linac Condition Anomaly Prediction of Emergence (L-CAPE) project that started in late 2020 are (1) to apply data-analytic methods to improve the information that is available to operators in the control room, and (2) to use machine learning to automate the labeling of outage types as they occur and discover patterns in the data that could lead to the prediction of outages. We present an overview of the challenges in dealing with time-series data from 2000+ devices, our approach to developing an ML-based automated outage labeling system, and the status of augmenting operations by identifying the most likely devices predicting an outage.

INTRODUCTION

Machine Learning (ML) and Artificial Intelligence (AI) have become ubiquitous in recent years, with applications ranging from computer vision to speech recognition to increasing the autonomy of controlled systems. This development has in part been furnished by the proliferation of data sources: Cheap, easy to deploy sensors permit the instrumentation and monitoring of ever more systems. The controls system for the accelerator complex at the Fermi National Accelerator Laboratory (FNAL) monitors and issues commands to 4000+ control system parameters in the linear accelerator (Linac) at frequencies ranging from 15 Hz to once every few minutes. Upon the start of a beam interruption, this data is used by accelerator operators to investigate the source of the unplanned beam outage from the FNAL Main Control Room. The electric power consumed during these outages adds up to a considerable amount of energy used (see Table 1) and could be reduced significantly if the duration and type of outage were identified quickly and accurately. We present a pipeline to enable the use of ML/AI that augments the data flow to the control room with analytics of outages, reducing the time to label them meaningfully and minimizing the number of incorrect or inconsistent labels.

* milan.jain@pnnl.gov

Table 1: Energy Use During Beam Outages

Event Length	Event Count	Duration (hrs)	Energy (MWh)
< 5 s	1626	1.04	0.182
< 10 s	321	0.59	0.104
< 60 s	205	2.01	0.351
< 120 s	201	4.70	0.822
< 10 m	169	11.69	2.05
≥ 10 m	47	111.35	19.49

DESCRIPTION OF THE DATA SOURCES

The accelerator control system's Data Logger nodes record data streams into circular buffers. To store this data for a longer period than the lifetime of the circular buffers, this project requested a data acquisition pipeline to write the data to long-term storage using an industry standard format, HDF5 [1]. This pipeline was created by the Controls Department developers using modern tools to solve a common problem and is being used on other ML projects. This new pipeline allows projects to choose a data source without modifying requests allowing L-CAPE to switch from using historical data to live data seamlessly.

In the current configuration, L-CAPE makes 5567 requests over 4292 control system parameters and stores each request in an HDF5 group. The HDF5 output is collected by the hour with an average file size of 644 MB per period.

DATA PREPROCESSING PROCEDURES

Hourly raw data in HDF5 format is sampled from devices at their respective cadences and timestamped by independent front-end nodes' clocks. A reference clock is required to time align the data for analyzing and modeling the devices together. By using a reference clock capturing the highest frequency devices (which is 15 Hz in this case), loss of information can be avoided for all devices. Therefore, for time alignment, we use timestamps at 15 Hz starting at the first timestamp of each hourly data file. Because there is a new file every hour, the reference clock reset at the end of every hour, thus reducing shift in data over time because of 15 Hz sampling rate.

Using a reference clock and combining the data removes redundant timestamps, which, together with applying the lossless snappy compression algorithm [2], reduces the disk space taken by the data (~20x), accelerates data read/write operations, and allows practical analysis and visualization of multiple devices across many days simultaneously. Furthermore, for more speedup in read/write, this combined data is

MAXIMIZING OUTPUT OF 3 MeV S-BAND INDUSTRIAL ACCELERATOR

D. Fischer, M. Denney, R. LaFave, A. Mishin, S. Proskin, J. Roylance, L. Young
Varex Imaging Corporation, Salt Lake City, UT, USA

Abstract

Earlier, we have reported on a record-breaking 3 MeV Accelerator Beam Centerline (ABC) built in 2017-2018. An upgraded version of this 3 MeV S-band ABC has been developed at Varex Imaging as a key component for one of the most popular X-ray industrial linear accelerator systems, commonly used for security and non-destructive testing (NDT) applications. Being significantly strained by excessive backstreaming, increasing of the ABC output is a challenging task. We describe these challenges and highlight high power test results. The triode gun and structure design improvements allowed us to raise stable output up to 530 Rad/min/1m at 3 MeV and up to 220 Rad/min/1m at 4.5 MeV with a widely available 2.5 MW/2.7 kW magnetron, while maintaining the spot size at 2 mm.

CHALLENGES

In the last year we worked to improve upon the previous prototype of the S-band 3MeV ABC (ABC-3-S) [1, 2]. See Fig. 1 for a model of the upgrade. One of our main areas of focus was the spot size. Industry is used to seeing and using spot sizes of less than 2 mm. The spot size is a very important parameter for clarity of image and precision. While multiple aspects, like distance to the object being tested contribute to how clear the image is or geometric unsharpness, smaller spot sizes helps limit unsharpness, especially for thicker objects.

To enhance the image, we worked to reduce the spot size. We did this by redesigning aspects of the internal RF structure and simulating the results.

It is also highly beneficial to maximize dose rate output of an industrial accelerator. The feature improves throughput of objects being scanned. With such a short accelerator and utilization of a high power magnetron, fields in the accelerating structure are high enough for excessive backstreaming; which in turn becomes a large issue. When there is a lot of backstreaming, the electron gun (e-gun) cathode is overheated, and emission current becomes unstable. The latter leads to e-gun failure and decreases the longevity of the accelerating structure. In addition to unstable accelerator operation, at a certain average current value the e-gun high voltage is shut off due to e-gun driver safety electrical circuits. We were able to raise limits of average accelerator characteristics by simulating an improved e-gun anode shape and corresponding adjustments in the buncher of the accelerating structure. See Fig. 1 for a model of the upgraded accelerator.

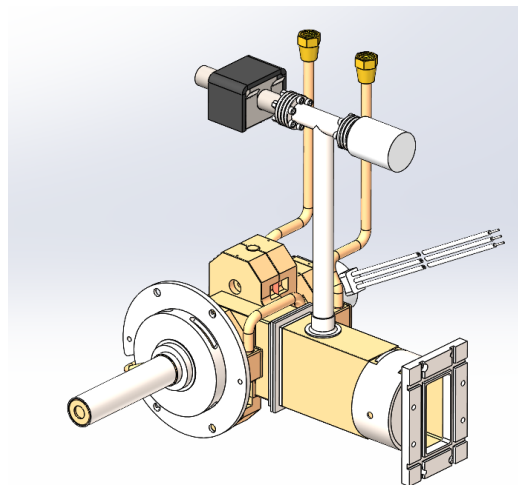


Figure 1: Model of the new accelerator, ABC-3-S-X-RS.

ACCOMPLISHMENTS

After adjusting the structure to reduce the spot size and building it, we used an exposed tape and measured the discoloration at FWHM for the e-beam distribution. Using Varex proprietary spot grid camera and radiographic film, we obtained images which we analyzed and found that our spot size reduced to 2.1 x 2.0 mm FWHM at 3 MeV. In addition to the grid camera and the radio graphic film method, the spot was also verified with two measurement techniques involving X-ray detector – a thin slit penumbra evaluation and duplex wire imaging.

When we redesigned the accelerating structure, we also increased dose rate output. In the design phase we concentrated on reducing the spot size and saw that our dose rate also increased in the simulations. We saw good agreement between simulations and testing. Where we saw a decrease in simulation spot size, we saw a similar decrease in testing. This held true for dose rate as well.

Another aspect that helped increase the dose rate was decreasing backstreaming. When we redesigned the first cavity, we also created optimum bunching which increased the dose rate. Overall, the dose rate increased to 530 Rad/min at 1 m from the target.

In researching the backstreaming effect we found a new feature to be useful in general linear accelerator system operation. The new configuration of the accelerating structure and anode design gave us an opportunity to lower e-gun high voltage required for stable accelerator performance. By keeping all parameters in specification at lower high voltage, one may possibly improve cathode lifespan, make it less demanding for e-gun control electrical circuit requirements, and achieve a safer operation.

A MODULAR X-RAY DETECTOR FOR BEAMLINE DIAGNOSTICS AT LANL*

P. Freeman[†], B. Odegard, R. Schmitz, D. Stuart, J. Yang
University of California Santa Barbara, Santa Barbara, CA, USA
L. Malavasi, Worcester Polytechnic Institute, Worcester, MA, USA

J. Bohon, M. Gulley, E. Huang, J. Smedley, Los Alamos National Lab, Los Alamos, NM, USA

Abstract

An X-ray detector is being developed for diagnostic measurement and monitoring of the Drift Tube LINAC (DTL) at the Los Alamos Neutron Science Center (LANSCÉ) at Los Alamos National Lab. The detector will consist of a row of X-ray spectrometers adjacent to the DTL which will measure the spectrum of X-rays resulting from bremsstrahlung of electrons created in vacuum by the RF. Two types of spectrometer modules are being developed. A large number (near 100) of inexpensive LYSO+SiPM-based modules will be deployed to measure the rate and energy of gammas along the beam and at different azimuthal angles. A smaller number of LaBr+PMT-based modules (one or two per DTL tank) will precisely measure the energy of X-rays at specific drift tube gaps in addition to reporting event rates.

Initial prototypes were tested during a beam development period at the LANSCÉ DTL just prior to this conference (July 30-Aug 3) and also during the RF conditioning in April 2022. An MFR proposal has been submitted for the funding of further development and deployment of this X-ray detector.

Bremsstrahlung X-rays

The detectors will monitor the bremsstrahlung spectrum of field emission electrons (FEE). FEE are generated in RF cavities and undergo bremsstrahlung in collision with the beam pipe and other structures, as illustrated in Fig. 1 [1].

Work in Ref. [2] demonstrated that a set of temporarily deployed LYSO+SiPM-based detectors adjacent to the beam line could be used to find the location of arcing in the DTL. The proposed X-ray detector would be a permanent installation to monitor the entire length of the DTL, which will be feasible due to small, lightweight, and inexpensive spectrometers which can be mounted directly onto the DTL.

LaBR+PMT-BASED PROTOTYPE

For the PMT-based prototype, shown in Figs. 2 and 3, LaBr crystal and a LYSO crystal are coupled to the two visible PMTs. Two PMTs beneath those also have NaI crystals, though our work has determined that LaBr is likely the preferable material due to its superior energy resolution and small form factor (10 mm long and 10 mm in

diameter). Spectra measured with known radioactive sources are shown in Fig. 4.

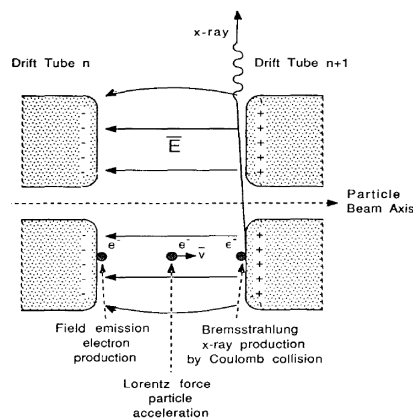


Figure 1: Diagram of FEE and resulting X-rays from Ref. [1].

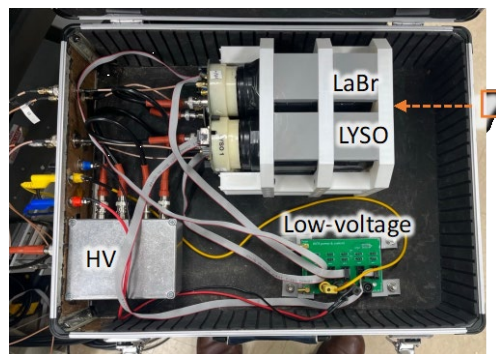


Figure 2: Interior of the LaBr+PMT-based prototype.



Figure 3: LaBr+PMT-based prototype at the LANSCÉ DTL with Pb blankets (yellow) to shield from background radiation arising from other DTL tanks.

*Funded by "Advanced Accelerator Diagnostics" grant from UC Lab Fees program.

[†] pmfreeman@ucsb.edu

SELF CONTAINED LINAC IRRADIATOR FOR THE STERILE INSECT TECHNIQUE (SIT)

A. Diego^{†*}, R. Agustsson, R. Berry, S. Boucher, O. Chimalpopoca, S. Coleman¹,
 S. V. Kutsaev, A. Yu. Smirnov, V. Yu, RadiaBeam Technologies, Santa Monica, USA
¹also at RadiaSoft, Boulder, USA

Abstract

A 3 MeV X-band linac has been developed employing a cost-effective split structure design in order to replace radioactive isotope irradiators currently used for the Sterile Insect Technique (SIT) and other applications. The penetration of a Co-60 irradiator can be matched with bremsstrahlung produced by a 3 MeV electron beam. The use of electron accelerators eliminates security risks and hazards inherent with radioactive sources. We present the current state of this X-band split structure linac and the rest of the irradiator system.

INTRODUCTION

Pest sterilization for insect population control has for decades used gamma irradiators with radioactive sources, however alternative sources have become available in part due to programs by the International Atomic Energy Agency. Sterile Insect Technique (SIT) is an important and environmentally conscious pest management technique developed and used for over 6 decades. SIT focuses on early incubation and sterilization of male insects at their pupa stage, thereby limiting a targeted insect's population when released into their natural habitat. To perform the sterilization, the pupae are placed in a canister in order to obtain a uniform dose ratio, with a target max/min dose ratio of approximately 1.3.

Currently, Co-60 isotope-based irradiators are commonly used for SIT. Although these Co-60 systems have been effective in pest control around the world, they are inherently costly to maintain and pose several safety concerns. In response to this problem, RadiaBeam is developing an inexpensive, compact 3 MeV split structure linac to act as the radiation source for a safe, self-contained irradiator for SIT and other applications. 3 MeV central energy was selected due to its similar output of the Bremsstrahlung spectrum produced by Co-60 isotope, 1.17 MeV and 1.33 MeV gamma particles [1]. Moreover, the X-band regime with a central frequency of 9300 MHz was chosen to reduce overall system dimensions, while exploiting the better RF consumption when compared to the more popular S-band systems [2].

Monte Carlo simulation show a dose uniformity ratio (DUR) less than 1.3 can be achieved for a 25 L water canister for a 3 MeV linac energy using an optimized tungsten and copper x-ray converter, and a 30-degree rms beam distribution. The overall system will take advantage of a

beamline with a defocusing quadrupole magnet and a horn design to allow beam spread before the X-ray converter.

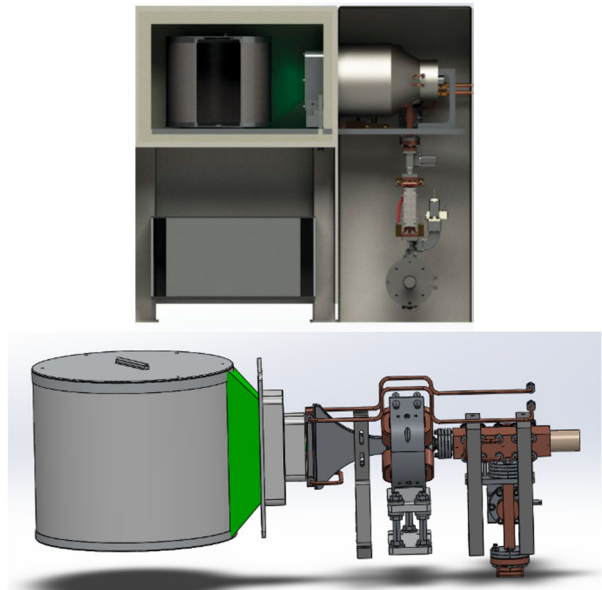


Figure 1: Conceptual design of SIT irradiation system (top), and designed accelerator section within SIT system (bottom).

Figure 1 illustrates the conceptual design layout for the SIT system (top), as well as a close up of the accelerating structure (bottom). We note the canister will be placed on a rotating plate (not shown) to allow uniform dose distribution on the target pupa. The quadrupole, horn, converter, and collimation are shown in the bottom of Fig. 1 to illustrate the defocusing design and beam trajectory to achieve a DUR < 1.3.

ACCELERATOR MANUFACTURING

To offset the cost of traditional high frequency accelerating structure manufacturing, RadiaBeam's SIT system design takes advantage of the split structure approach where two halves are brazed together rather than machining multiple single cells [3]. The full assembly consisted of three brazing steps, in which the planned brazing sequence ensures no piece of copper experiences more than three brazing cycles using a combination of gold (Au) and copper (Cu) alloys. This is to minimize the damage to the quality of the critical RF surfaces. In Fig. 2 we show the split structure halves post machining and fully assembled structure post final braze in Fig. 3.

* Work supported by US Department of Energy, SBIR grant no. DE-SC0020010.

† adiego@radiabeam.com

COMPACT INTER-UNDULATOR DIAGNOSTIC ASSEMBLY FOR TESSA-515*

T. J. Hodgetts[†], R. Agustsson, Y. C. Chen, A. Murokh, M. Ruelas
RadiaBeam, Santa Monica, CA, USA

P. E. Denham, A. C. Fisher, J. Jin, P. Musumeci, Y. Park, Department of Physics and Astronomy,
University of California Los Angeles, Los Angeles, CA, USA

Abstract

Beamline space is a very expensive and highly sought-after commodity, which makes the creation of compact integrated optics and diagnostics extremely valuable. The FAST-GREENS experimental program aims at demonstrating 10% extraction efficiency from a relativistic electron beam using four helical undulators operating in the high gain TESSA regime. The inter-undulator gap needs to be as short as possible (17 cm in the current plans) to maximize the output power. Within this short distance, we needed to fit two focusing quadrupoles, a variable strength phase shifter, a transverse profile monitor consisting of a YAG-OTR combination for co-aligning the electron beam and laser, and an ion pump. By making the quadrupoles tuneable with a variable gradient, in combination with vertical displacement, we can meet the optics requirements of matching the beam transversely to the natural focusing of the undulators. The two quadrupoles in conjunction with the electromagnetic dipole also serve as a phase shifter to realign the radiation and the bunching before each undulator section. This paper will discuss the mechanical design of this inter-undulator break section and its components.

INTRODUCTION

Available beamline space for adequate optics and diagnostics is a struggle for every accelerator layout that aims at efficiency and compactness; the FAST-GREENS experiment planned at the FAST beamline at FNAL is no exception. This experiment aims at demonstrating 10% extraction efficiency from a high brightness electron beam using Tapering Enhanced Stimulated Spontaneous Amplification (TESSA) [1]. It is based on using four tapered helical undulator section having 3.2 cm period and 1 m total length. The setup required the development of a compact multipurpose break section housing significant number of optical elements and e-beam and radiation diagnostic equipment between each undulator.

For a summary of design parameters for this experiment we refer to Ref. [2].

The TESSA undulator extraction efficiency was found in GENESIS simulations to be highly dependent on the drift length between the undulator sections (Fig. 1) [3]. Even with a phase shifter added to take care of the relative phase between the radiation and the electron bunching, increase in spot size and diffraction affect the output radiation power after each break section.

* Work supported by DOE grant DE-SC0009914, DE-SC0018559, and DE-SC0017102.

[†] tara@radiabeam.com

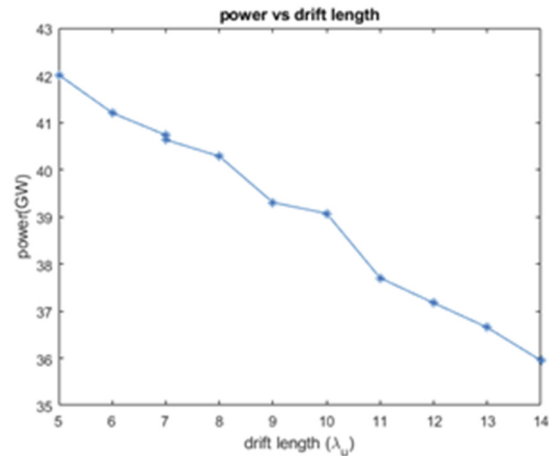


Figure 1: Power output from Genesis Informed Tapering optimized simulation vs. drift length. In this simulation we use four 29-periods-undulator sections, and we varied the drift length between undulators while optimizing the phase shifter. All other parameters, such as the seed laser Rayleigh length and tapering parameters, remain fixed.

Accordingly, special care was given to the design of the very dense inter-undulator break sections (Fig. 2). A strong focusing solution with a permanent magnet-based quadrupole doublet, with 106 mm center-to-center spacing, in between the undulator was adopted. This solution allows to focus the beam to a much smaller average beta function along the interaction than the more traditionally used single quadrupole channel. The implementation of this solution will be a first in high gain FELs and the experience gained from matching in this lattice could be relevant to future upgrades at larger facilities especially for cases where beam

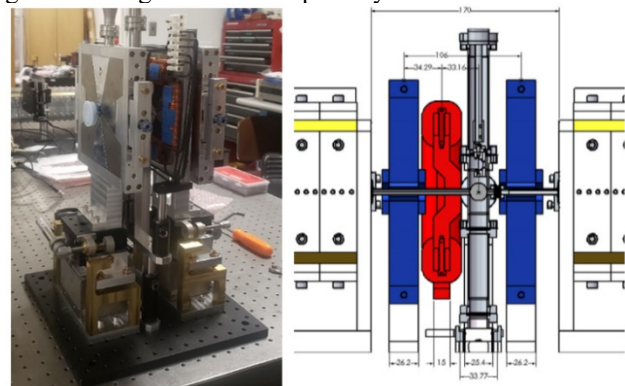


Figure 2: (left) Assembled break section. (right) Model of break section in-situ between undulators shown with size and spacing in mm.

PRACTICAL REVIEW ON BEAM LINE COMMISSIONING PROCEDURES AND TECHNIQUES FOR SCIENTIFIC AND INDUSTRIAL ELECTRON ACCELERATORS

M. Kravchenko[†], M. Ruelas, R. Berry, A. Diego, D. Gavryshkin
RadiaBeam Technologies LLC, Santa Monica, CA, USA

Abstract

Accelerator science constantly requires improvement in electron beam quality for both scientific and industrial applications. Examples of parameters on existing systems that affect overall beam quality include vacuum stability, component level alignment, RF phase matching, electron injection parameters, etc. A proper beam-commissioning process allows the characterization of initial parameters that tune system setup appropriately to improve net beam quality and becomes a valuable source of data to guide system operation. We discuss methods and possible obstacles during the commissioning process of accelerator systems experienced at RadiaBeam.

INTRODUCTION

While most scientific and research facilities have their procedures and guidelines for the accelerator beam line commissioning process it is important to update and validate these steps in terms of contemporary technologies and up-to-date scientific knowledge. The varying designs of RF linear accelerators requires validated instrumentation to characterize and commission these linacs. To aid in their commercial and contract production of different linacs, RadiaBeam has designed and constructed a multipurpose test beamline (Fig. 1) for commissioning different electron linear accelerators manufactured at RadiaBeam [1-3].

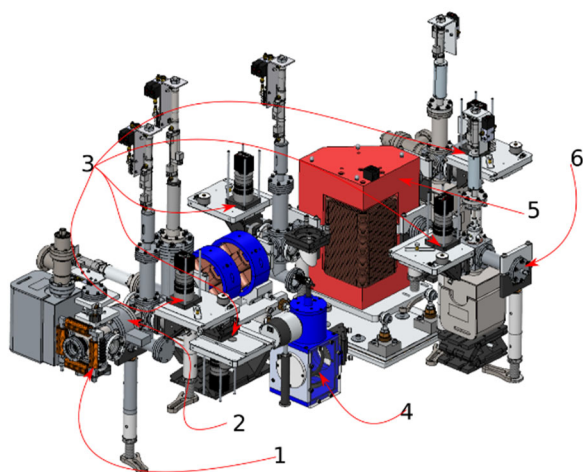


Figure 1: Test beam line for low energy (up to 10 MeV) accelerator commissioning. 1 – steering magnet, 2 – Turbo ICT, 3 – beam profile monitors, 4 – THz interferometer for bunch length [4], 5 – spectrometer dipole, 6 – Faraday cup.

[†]mkravchenko@radiabeam.com

This beamline is suited for six fundamental measurements important for any accelerator: beam charge, transverse position, shape, energy, bunch length, and emittance. Each parameter requires one or several different devices to be measured accurately and with a certain degree of reliability. Here we will discuss general procedures and techniques for commissioning test beamlines for scientific and industrial linear electron accelerators with modern measuring devices.

CHARGE MEASUREMENTS

Precise charge measurements are always a challenge in any case study. To accurately determine bunch charge three independent measuring systems are implemented: a Bergoz Turbo Integrating Current Transformer (ICT) [5], a traditional toroidal current transformer (CT) [6], and a commercial RadiaBeam impedance-matched Faraday cup [7]. The Faraday cup can be easily replaced to ensure full attenuation of higher energy electrons. Four important positions were monitored by these devices: drift section entrance with Turbo ICT, spectrometer bend section end with Faraday cup, straight beam line drift after spectrometer dipole with CT, and end of beamline with Faraday cup.

The Bergoz Turbo ICT is a toroid-based current sensor which performs integration with a secondary coil and therefore measures bunch charge in addition to average current measurements with low noise and high accuracy. The ability to measure ultra-short bunch charges down to a few pico-Coulombs upon external or internal triggering allows characterization of photocathode driven electron sources, such as RadiaBeam's commercially available 1.6-cell photoinjector guns.

Regular current transformers do not give direct bunch charge measurement but provide the average current reading over an RF pulse. A traditional current toroid is used to characterize dark current emissions of a linac while also being capable of measuring macro pulse current of thermionically-driven linacs, such as RadiaBeam's medical, industrial radiography, and sterilization linacs. The Turbo ICT can also be used to measure current by integrating the current values over a time constant. In addition to inductive charge measurements, a 50-Ohm impedance-matched Faraday cup is used to measure charge. The impedance matching gives a faster response time and the ability to measure the charge of short pulses. However, the small collector size of ~15-mm diameter (chosen for impedance matching to the 35-mm beam tube) requires careful beam alignment both for beam capture and to limit errors associated with

ELECTROMAGNETIC DESIGN OF A COMPACT RF CHOPPER FOR HEAVY-ION BEAM SEPARATION AT FRIB*

A. C. Araujo Martinez[†], R. Agustsson, Y. Chen, S. V. Kutsaev
RadiaBeam Technologies, LLC, Santa Monica, CA, USA

A. Plastun, X. Rao, Facility for Rare Isotope Beams, East Lansing, MI, USA

Abstract

Rare isotope beams are produced at FRIB via fragmentation of a primary heavy ion beam in a thin target. The isotope beam of interest is contaminated with other fragments, which must be filtered out to ensure the delivery of rare isotopes with desired rates and purities. One of the stages of fragment separation uses an RF deflecting cavity to provide time-of-flight separation. However, to avoid neighboring bunches overlapping with each other and with the contaminants, it is necessary to increase the inter-bunch distance by a factor of four, corresponding to a 20.125 MHz rate. To solve this problem, we have developed an RF chopper system for the 500 keV/u primary heavy-ion beams. The system consists of a deflecting quarter wave resonator (QWR) cavity operating at 60.375 MHz, two dipole steering magnets, and a beam dump. In this paper, we present and discuss the optimization of the electromagnetic design of the QWR cavity and magnets, as well as some aspects related to beam dynamics and conceptual engineering design.

INTRODUCTION

Radioactive beams play a key role in studies of nuclear structure, nuclear physics, and nuclear astrophysics [1, 2]. Among the different facilities around the world that perform experiments with rare-isotope beams, the Facility for Rare Isotope Beams (FRIB) will be a cutting-edge research facility to enable breakthrough discoveries in nuclear science [3-5].

At FRIB, isotope production is performed via projectile fragmentation. A high-power superconducting linear accelerator will be used to create rare isotopes by accelerating primary ion beams up to 200 MeV/u to strike a target [6, 7]. However, many isotope species including the desired rare isotopes are produced in this process. The secondary fragments must be removed to deliver rare isotopes with high rates and high purities [8].

An important component of FRIB is a next-generation three-stage magnetic projectile fragment separator, designed to handle the very intense primary and secondary beams [9]. For further beam purification on the proton-rich side, it is necessary to have an additional method for purifying the beam. This will be realized through time-of-flight separation [10] using an RF fragment separator (RFFS) [11], proposed at FRIB and designed by RadiaBeam and capable of producing a 4-MV transverse kick.

However, to avoid neighboring bunches mixing due to widening in the time difference before entering the separator cavity, it is necessary to increase the inter-bunch distance. For this purpose, an RF chopper (RFC) system is being designed for the FRIB facility at Michigan State University (MSU) in a collaboration between RadiaBeam and FRIB Accelerator Physics department.

The chopper system will be located in the Medium-Energy Beam Transport (MEBT) line of the FRIB superconducting RF (SRF) linac. It is designed to generate a clean 20.125-MHz bunch structure of the primary heavy ion beam accelerated in the FRIB linac to allow for the time-of-flight separation of the produced rare isotope beams [11]. The baseline 40.25-MHz bunch repetition rate at FRIB is generated by a multi-harmonic buncher (MHB) upstream of an 80.5-MHz radio frequency quadrupole (RFQ) section [12].

The RFQ produces accelerated high and low-intensity bunches alternating at the frequency of 80.5 MHz (see Fig. 1). The high-intensity bunches contain 97% of the beam intensity, and low-intensity ones, also called satellite bunches, contain another 3%. The high-intensity bunch rate is 40.25 MHz as they are formed by the 40.25 MHz MHB. The chopper system must kick every other high-intensity bunch to produce the 20.125 MHz separation between neighboring rare isotope bunches, as well as to clean the beam out of the satellite bunches. The kicked bunches will be sent to a beam dump.

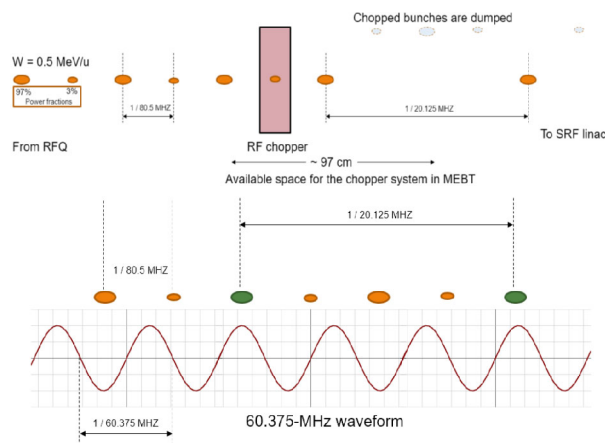


Figure 1: Bunch structure before and after the RFC system (top) and waveform of the 60.375-MHz deflecting field overlapped with the bunch structure of the incoming beam (bottom).

* This work was supported by the U.S. Department of Energy, Office of High Energy Physics, under SBIR grant DE- SC0020671.

[†] araujo@radiabeam.com

FERRITE-FREE CIRCULATOR FOR PRECISE MEASUREMENTS OF SRF CAVITIES WITH HIGH Q-FACTOR

A. I. Pronikov, A. Y. Smirnov, RadiaBeam Technologies, Santa Monica, CA, USA

A. Krasnok, Florida International University, Miami, FL, USA

V. P. Yakovlev, Fermi National Accelerator Laboratory, Batavia, IL, USA

S. N. Romanenko, Zaporizhzhya National Technical University, Zaporizhzhya, Ukraine

Abstract

In this work, we suggest and investigate new magnetless circulators based on three resonators connected in a loop and parametrically modulated in time with mutual phase lag. The first design consists of three Fano resonators with a spectrally asymmetric response, in contrast to schemes based on the Lorentz resonators explored thus far. The second design includes three Fano-Lorentz resonators, i.e., it also possesses spatial asymmetry. We demonstrate that the asymmetric approach provides strong and reversible isolation for the practically feasible modulation amplitude and rate. The results of our work are promising for precise measurements of superconducting radio frequency cavities with high Q-factor.

INTRODUCTION

Superconducting radio frequency (SRF) accelerators at modern scientific nuclear and high-energy physics facilities require continuous-wave operation with accelerating gradients of up to 20 MV/m. To operate in such a regime, SRF cavities must have low cryogenic losses and high intrinsic Q-factor. Recent breakthroughs in SRF technologies, such as nitrogen doping, fast cooling, and coating with novel materials, have improved the quality factor, which is now approaching levels of 10^{11} [1]. These cavities require affordable, reliable, and high-precision instruments to measure such a high Q-factor, especially *in situ*.

Precise Q-factor measurement can be done with an RF power balance technique by measuring the loss of power, which is the difference between input and reflected power. It is now recognized that significant errors can occur when performing these measurements with high intrinsic Q_0 values, especially when not critically coupled. These errors arise from variations in power measurements due to poor directivity, nonlinear losses, and phase/power-dependent effects [2].

A typical diagnostic system consists of four principal elements: RF probe, directional coupler, circulator, and RF load. All these components must have a low voltage standing wave ratio (VSWR) and high directivity in order to calculate the cavity power loss independently from the external Q-factor. Otherwise, systematic errors in cavity power measurement will be introduced [3]. Currently, the accuracy of ferrite-based circulators is limited by the power dependence of the ferrite's material properties, resulting in match and directivity parameter dependence [4]. Reducing the mismatch by eliminating ferrite can improve the accuracy of low-power Q-factor measurements of near-critically coupled cavities in the vertical test. Another

important reason for eliminating magnetic materials is the ability to put the circulator into a cryomodule for in-situ measurements of the Q-factor during the cavity operation.

MAGNETLESS CIRCULATOR

A circulator is a three-port nonreciprocal device. Reciprocity implies that the wave transmission between any two points in an arbitrary system is the same for opposite propagation directions as far as the time-reversal symmetry is preserved [5]. As mentioned above, conventional circulators utilize the approach to time-reversal symmetry breaking and nonreciprocity based on magnetic field biasing, which suffers from bulkiness and loss, motivating researchers and engineers to search for more practical approaches. Several approaches to magnetless isolation and circulation have been suggested, including new materials, parametric time modulation, active structures, nonlinearity, unidirectional gain and loss, etc. [6].

The concept of constructing an isolator using Lorentzian and Fano resonators, inside which there is such a nonlinear element as a varactor, is described in [7]. However, the practical realization of a 3-port circulator for cavity measurements based on this nonlinear approach is challenging because of the presence of reflected signals in all ports, which can destroy the asymmetry and hence nonreciprocity. To get around this obstacle, one can utilize an approach based on the time variation of resonant frequencies of three resonators connected to form a 3-port system. In contrast to the nonlinearity approach, the time variation approach to nonreciprocity does not suffer from the backscattered fields and hence allows the realization of a circulator.

Recently, Estep et al. [8] introduced the concept of what is currently known as STM-AM (spatiotemporal modulation – amplitude modulation) biasing to realize magnetless circulators. A conceptual diagram illustrating this concept is shown in Fig. 1. Here three resonators are coupled to form a resonant loop and their natural oscillation frequencies are modulated with signals having 0° , 120° , and 240° phases.

In our work, we used the advantages of both nonlinear and time modulation approaches to building a circulator. Two cases were considered: one using modulation time-modulated Lorentzian-Fano resonators similar to those described in work [7] and the simplified version comprising only Fano resonators. Both approaches demonstrate strong isolation ($>30\text{dB}$), but the latter one is simpler and less dependent on the input signal power.

INITIAL DEVELOPMENT OF A HIGH-VOLTAGE PULSE GENERATOR FOR A SHORT-PULSE KICKER*

J. R. Prager[†], K. E. Miller, K. Muggli, C. Schmidt, H. Yeager
 Eagle Harbor Technologies, Inc., Seattle, WA, USA

Abstract

Brookhaven National Laboratory (BNL) will be the site for the Electron Ion Collider (EIC), which will require new equipment and facilities, including a 150 MeV energy recovery LINAC (ERL). The ERL requires a new short-pulse stripline kicker. The kicker requires a power system that can deliver 50 kV pulses with a width less than 38 ns into a 50 Ω load with low jitter. Inductive adders are solid-state pulsed power systems that can robustly and reliably produce short, high-voltage pulses into a variety of loads. Eagle Harbor Technologies, Inc. (EHT) has modeled, designed, and built a single stage of an inductive adder. Through experimental testing, EHT demonstrated that a single stage can meet the pulse shape, jitter, and pulse repetition frequency requirements while switching 1 kA.

INTRODUCTION

The Electron Ion Collider will enable new research in nuclear physics and quantum chromodynamics and ensure US leadership in accelerator science and technology. This upgrade will make use of existing infrastructure at Brookhaven National Laboratory (BNL) that was constructed for the Relativistic Heavy Ion Collider. However, new equipment and facilities are required, including a 150 MeV energy recovery LINAC (ERL) that will provide continuous electron beams for strong hadron cooling [1].

The ERL requires new injection kicker power systems that can produce high-voltage pulses with faster rise times. The kicker design will be qualitatively similar to the Compact Linear Collider (CLIC) damping rings' stripline kicker that consists of two parallel electrodes housed inside a conducting cylinder. Each electrode is charged by an equal, but opposite polarity, high-voltage pulse [2-3].

The CLIC kicker power supply needed to produce ±12.5 kV pulses into 50 Ω loads (250 A). The 160 ns flat-top could deviate by no more than ±0.02% (±2.5 V) combined droop and ripple. The rise was less challenging (< 250 ns). The required pulse repetition frequency was 50 Hz [4].

The BNL kickers require higher voltage and shorter pulse widths. At that start of the Phase I program, the specifications for the ERL kickers were as follows:

- Output voltage: ±50 kV ±2% for flattop
- Output current: 1 kA
- Load impedance: 50 Ω

- Pulse shape: 6 ns rise, 20 ns flattop, 12 ns fall (with residual voltage below 1 kV after 38 ns)
- Pulse repetition frequency: 10 Hz (during operation) and 100 Hz (lifetime testing)
- Robust to faults (short/open/noise)
- High reliability: Operate 12–20 weeks out of the year (availability 99% or better)
- Jitter < 0.5 ns with respect to external clock

INDUCTIVE ADDERS

The CLIC kicker power system used an inductive adder topology. An inductive adder consists of N printed circuit boards (PCBs) that contain a solid-state switch, energy storage capacitor, and the primary winding of a transformer. The transformer primaries are connected in parallel, and their secondaries are connected in series. A four-stage inductive adder is shown in Fig. 1 with stray inductance on each primary stage. The gray toroids are the transformer cores. The transformer secondary consists of a central rod connected to ground on one end and the metal cylinder that goes around the outside of the transformer cores. The load is connected between the two or at the end of a transmission line.

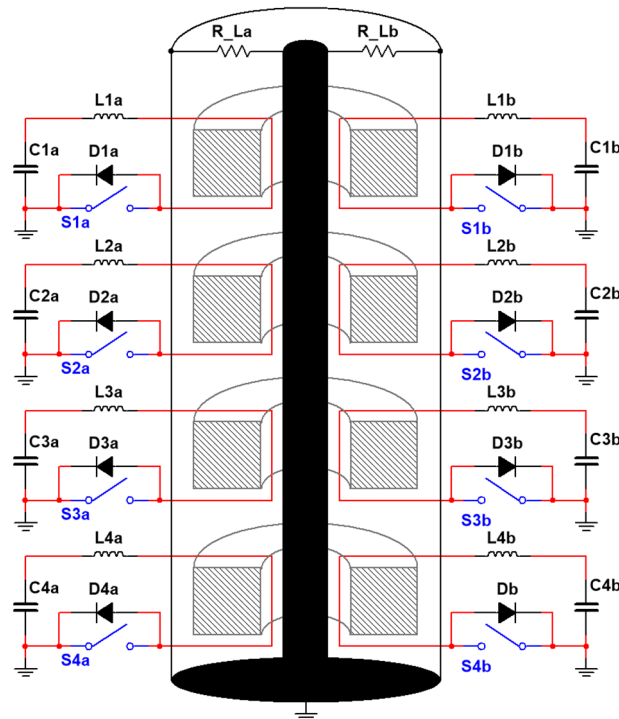


Figure 1: Four-stage inductive adder. The image is symmetric about the central stack.

* This material is based upon work supported by the U.S. Department of Energy, Office of Science, Office of Nuclear Physics, under Award Number DE-SC0021470.

[†] prager@eagleharbortech.com

DEMONSTRATION OF TWICE REDUCED LORENTZ FORCE DETUNING IN SRF CAVITY BY COPPER COLD SPRAYING*

R. Kostin[†], C. Jing, A. Kanareykin, Euclid Techlabs LLC, Bolingbrook, IL 60440, USA
G. Ciovati, Thomas Jefferson National Accelerator Facility, Newport News, VA 23606, USA
G. Brock, CTC, Inc., Johnstown, PA 15904, USA

Abstract

Superconducting RF (SRF) cavities usually are made of thin-wall high RRR Niobium that is susceptible to Lorentz Force Detuning (LFD) – cavity deformation phenomena caused by high magnitude RF fields. This type of deformation can be mitigated by using an additional copper layer deposited on the outer surface of the cavity. In this paper, we present both modeling results and experimental data of high gradient test of an SRF cavity at cryogenic temperatures. It was demonstrated that LFD can be significantly reduced (factor of two) by the copper cold spray reinforcement without sacrificing cavity flexibility for tuning. We also present a finite-element model that allows us to confirm our experimental results and optimize the cavity geometry for LFD reduction with incorporated coupled RF, structural and thermal modules.

INTRODUCTION

Cold-spray is a relatively new technique that allows spraying a metal powder on a substrate at very high speed in ambient conditions. As the metal particles hit the surface, they undergo a plastic deformation and bond to the surface. This approach was successfully used for conduction cooling of SRF cavity by a closed-cycle cryo-cooler. The cold-sprayed layer provided a robust bonding to the cavity and it was used as seed layer for electroplated copper [1].

Another application of this technology could be the stiffening of SRF cavities extending the barriers of current technological limitations. As of now, Lorentz Force Detuning (LFD) is minimized by Nb stiffening rings between cavity cells which are welded by electron beam. Cold-spray on the other hand provides a lot of flexibility. It is applied by a robotic arm manipulator with controlled thickness. The only limitation is that it is difficult to apply in the area close to the iris between the cells as the powder jet needs to be perpendicular to the surface for the deposited layer to have a good bonding to the substrate. The layer can be built-up about one inch higher from the iris. With this limitation in mind, Finite-Element-Analysis (FEA) was conducted using Comsol to investigate a possibility of LFD improvement. Copper was chosen as a material of deposition as the additional layer needs to have high thermal conductivity not to cause cavity overheating. The TESLA center-cell cavity shape was investigated [2]. The goal is to minimize LFD while keeping the cavity tunable. As long as the proposed approach will compete with standard stiffening technique

such as stiffening rings, the stiffness of the Tesla cavity with rings was taken as the limit.

MODEL STUDIES

Comsol Mechanical Studies

A 2D Comsol model of Tesla center-cell shape with no stiffening rings was created. The model was reduced down to a half-cell only with proper boundary conditions (BC) which resulted in stiffness of $k=41.4$ kN/mm. The results were compared with literature [3] and were in good agreement: for the 7-cell cavity stiffness will be around 3 kN/mm same as in [3]. Thus, the developed model provided reasonable results. At the next step, stiffness of the Tesla cell with stiffening rings at radius $R=55$ mm was found which equaled to 90 kN/mm for the half-cell geometry, thus this stiffness will be our limiting factor during cold-spray layer optimization. The results of the simulations can be found in Fig. 1, which demonstrates 11 μ m deformations under 1 kN of applied force to the cavity equator. The following mechanical properties were used: poisson ratio $\nu=0.38$, Young's modulus at 2 K $E=118$ GPa.

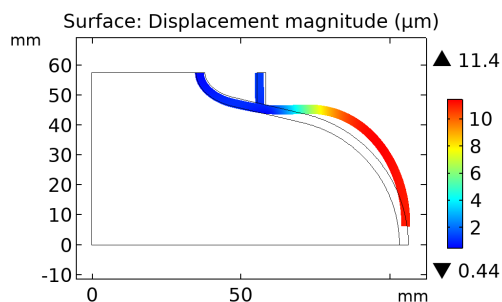


Figure 1: Tesla center half-cell deformation under 1 kN force.

The next step was to optimize the cold-sprayed Cu layer to reduce the Lorentz force detuning while keeping the cavity stiffness below 90 kN/mm for a half-cell model. A single center-cell Tesla Niobium cavity was available for cold-spray deposition and testing. The geometry of the cavity was built in Comsol for LFD optimization studies. The electric field in this model can be found in Fig. 2 below.

It is worth to mention, while the resonant frequency of the model with no beam pipes and with magnetic boundary condition at the iris was 1300 MHz (regular Tesla cell), single cell with beam pipes resonant frequency equaled to 1287.9 MHz. The field was scaled to 30 MV/m of accelerating gradient. The Cu layer was added at the equator region

* Work supported by US DOE SBIR grant DE-SC0019589

[†] r.kostin@euclidtechlabs.com

AN OPEN RADIOFREQUENCY ACCELERATING STRUCTURE

S. V. Kuzikov[†], Euclid TechLabs, Solon, OH, USA

Abstract

We report an open multi-cell accelerating structure. Being integrated with a set of open-end waveguides, this structure can suppress high-order modes (HOMs). All the accelerating cells are connected at the side to rectangular cross-section waveguides which strongly coupled with free space or absorbers. Due to the anti-phased contribution of the cell pairs, the operating mode does not leak out, and has as high-quality factor as for a closed accelerating structure. However, the compensation does not occur for spurious high-order modes. This operating principle also allows for strong coupling between the cells of the structure, which is why high homogeneity of the accelerating fields can be provided along the structure. We discuss the obtained simulation results and possible applications. Its include a normal conducting high-shunt impedance accelerator, a tunable photoinjector's RF gun, and a high-current, high-selective SRF accelerators.

INTRODUCTION

Progress of modern particle accelerators is associated with high intensity beams. An open accelerating structure that keeps all advantages of classical closed structures is a dream of all investigators dealing with high-current beams. We will show that the open structure can bring lots of other benefits.

In this paper we consider a π -mode standing wave accelerating structure only. The idea is to couple neighbour cells by means of a waveguide keeping symmetry. Because fields in the considered neighbour cells have opposite directions these cells cannot radiate power in the single mode waveguide, but near-field coupling is non-zero. Therefore, if the mentioned waveguide is long enough it can be open, this does not perturb any RF properties of the structure. Let us consider three examples.

HIGH SHUNT IMPEDANCE ACCELERATING STRUCTURE

Let us consider a 9.3 GHz normal conducting accelerating structure (Fig. 1). It consists of a chain of the cells so that each cell has two coupling holes. Each hole sees a single-mode waveguide that is to be open. For simulations we used absorbers shown in pink in Fig. 1 at far waveguide end ($\epsilon'=\mu'=1$ $\tan\delta_\epsilon=\tan\delta_\mu=1$). The E- and H- field structures of the operating mode for coupling hole size 8 mm in transverse to structure's axis direction are shown in Figs. 2 and 3, respectively. One can see that E-field distribution differs from the classical mode distribution in a closed cell only at coupling hole's area. There are no significant E or

H field enhancement. That is why, this structure made of copper at room temperature has high shunt impedance that exceeds 200 M Ω /m (Fig. 4). From this point of view, this open structure is similar to other side coupled structures, traveling wave [1] or standing wave [2]. In our case the side surface that is responsible for coupling and seen by RF power has the smallest area. This fact explains the mentioned high shunt impedance. Note that the larger coupling hole (stronger coupling) the less the shunt impedance.

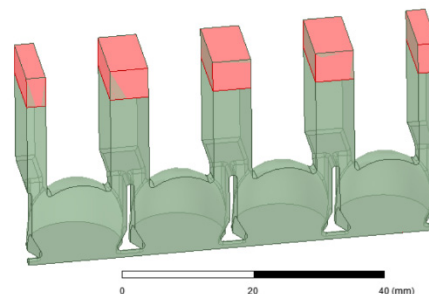


Figure 1: 9.3 GHz π -mode standing wave structure.

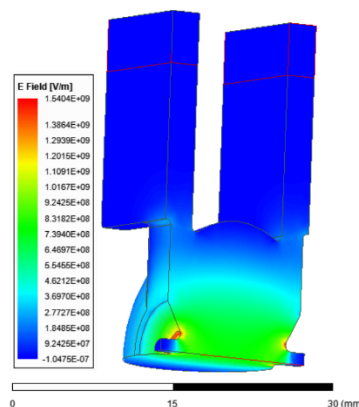


Figure 2: E-field distribution for the operating mode.

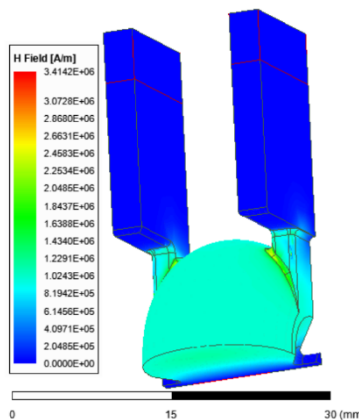


Figure 3: H-field distribution of the operating mode.

[†]s.kuzikov@euclidtechlabs.com

APPLICATIONS OF MACHINE AUTOMATION WITH ROBOTICS AND COMPUTER VISION IN CLEANROOM ASSEMBLIES*

A. Liu[†], W. Si, S. Miller, J. Callahan, E. Gomez, B. Wyderski
Euclid Techlabs, LLC, Bolingbrook, USA

Abstract

Modern linear particle accelerators use superconducting radio frequency (SRF) cavities for achieving extremely high-quality factors (Q) and higher beam stability. The assembly process of the system, although with a much more stringent cleanliness requirement, is very similar to the ultrahigh vacuum (UHV) system operation procedure. Humans, who are conventionally the operators in this procedure, can only avoid contaminating the system by wearing proper sterile personal protection equipment to avoid direct skin contact with the systems, or dropping particulates. However, humans unavoidably make unintentional mistakes that can contaminate the environment: cross contamination of the coverall suits during wearing, slippage of masks or goggles, damaged gloves, and so forth. Besides, humans are limited when operating heavy weights, which may lead to incorrect procedures, or even worse, injury. In this paper, we present our recent work on a viable and cost-effective machine automation system composed of a robotic arm and a computer vision system for the assembly process in a cleanroom environment, for example for SRF string assemblies, and more.

INTRODUCTION

Background

Modern particle accelerators use superconducting radiofrequency (SRF) cavities to achieve extremely high quality factors (Q) and higher beam stabilities [1–3]. Most of the SRF cavities and their associated systems need to be assembled in a dedicated cleanroom space and at a custom SRF test stand. The assembly process of the system, although with a much more stringent cleanliness requirement, is very similar to the ultrahigh vacuum (UHV) system operation procedure.

Humans, who are conventionally the operators in this procedure, can only avoid contaminating the system by wearing proper sterile personal protection equipment, such as coveralls, gloves, facial masks, goggles, etc., in order to avoid any direct skin contact with the system. The operators also need to pay special attention to avoid dropping lint or dander in the system [4]. The reasons why humans are needed in the assembly process are unquestionably clear: the ability to identify and solve problems *in operando*, and to evaluate the assembly quality and make adjustments based on rich experience. However, the disadvantages of having humans in the process are often ignored: humans make unintentional

mistakes that can contaminate the system - cross contamination of the coverall suits during wearing, slippage of masks or goggles, damaged gloves, and so forth.

High energy physics, nuclear physics and basic energy sciences experimental researchers have recently been investigating solutions in which the assembly can be done or at least dominated by robotic arms instead. Robotic arm manufacturers, such as Yaskawa, FANUC and KUKA have been actively developing robot systems that are suitable for cleanroom operations. The industrial arms can have their repeatability as high as $\pm 30 \mu\text{m}$ and maximum payloads of tens of kg. Although the convenience and benefits of using robotic arms in assembly processes have been widely recognized, the acceptance of robotic automation systems is still relatively low in R&D environments, compared to other industries like automotive manufacturing, welding, chemical processing, etc.

Our Methods

Under a grant from the DOE SBIR program, we were awarded for the development of a viable and fully automated robotics system equipped with computer vision hardware and AI/ML algorithms for the assembly process in a cleanroom environment, for SRF systems and other cleanroom assembly processes. Our computer vision system is powered by 3D cameras and image processing to identify arbitrary structures for robotic arms to mate parts together. Our solution provides the versatile integration of object recognition and repeatable specialized control of industrial grade robotic arms. It is capable of reducing or eliminating human interventions in the assembly procedure. Our system runs on high-level programming languages, which allows for both user customization and hassle-free operations without the need for controlling the arms using teaching pendants.

In our finalized product, for which the workflow is shown in Fig. 1, our system will first automatically detect a target object (object-of-interest) using a 3D camera mounted on the arm (“eye-in-hand”) and advanced vision algorithms. The computer vision system then registers the “pose”, which contains both the position and orientation, of the target object and passes that information to a robotic arm, on which the camera is mounted. Then, the arm will grab another object (object-in-hand) that needs to be assembled onto the object-of-interest, and mate the two objects together, based on a calculated path and instructions for the arm. In cases where fasteners are needed to tighten flanges or similar interfaces together, another robotic arm that is also equipped with an eye locates the mated objects, places the fasteners through the holes, and tightens them.

* Work supported by the U.S. DOE Office of Science under contract number DE-SC0021736.

[†] a.liu@euclidtechlabs.com

ENCAPSULATION OF PHOTOCATHODES USING HIGH POWER PULSED RF SPUTTERING OF hBN*

A. Liu[†], S. Poddar, J. Callahan, Euclid Techlabs, LLC, Bolingbrook, IL 60440, USA
M. Gaowei, J. Biswas, Brookhaven National Laboratory, Upton, NY 11973, USA

Abstract

Photocathodes of various materials are used in photoinjectors for generating high quality photoelectron beams. Of particular interest are the alkali antimonides because of their ultra-high quantum efficiency (QE), and metallic materials such as Cu and Mg which have lower QE but have considerably longer lifetime. The biggest challenge of using the alkali antimonide photocathodes is that it has a stringent requirement on vacuum because they are destroyed rapidly in air. Exposure of Mg and Cu in air also impacts their performance because of the oxidation. These photocathodes can be protected by encapsulating them with thin layers of 2D materials such as hexagonal boron nitride (hBN). In this paper, we will discuss the numerical modeling of the encapsulation, the QE measurements of encapsulated Cu as examples, and the feasibility of coating a photocathode with hBN by using high power pulsed reactive RF sputtering.

INTRODUCTION

Background

Alkali antimonide photocathodes are commonly used in high-brightness photoinjectors because of their ultra-high quantum efficiency (QE) at green light wavelength, small thermal emittance and relatively-low requirements for growth. One of the challenges of using the photocathode is that it has an extremely stringent requirement on the vacuum and can be destroyed by even small amounts of reactant gas, including O₂, H₂O, and so forth [1–3]. Meanwhile, the QE of metallic photocathodes like Cu and Mg that are more resilient to air also degrade over time in operations due to oxidation. However, the material and labor costs of building UHV photocathode transferring and storage systems to extend the lifetime of these photocathodes are very high.

Researchers have been exploring the feasibility of encapsulating photocathodes with thin-film materials to increase their lifetime and robustness against air. Previous research have studied thin-films of dielectric materials such as NaI, CsI, etc. [4]. However, the implementation was discontinued due to limited protection and spectral response [5]. Further research was done with thin-films of 2D materials, such as graphene (Gr) and hexagonal boron nitride (hBN). Theoretical modeling and simulations indicate that a monolayer of Gr or hBN can inhibit the photocathode material's reaction with the residual gas, while maintaining its high QE [6].

Our Methods

There are mainly two ways of generating a thin-film of 2D materials directly on a substrate. One is to make a “wet transfer” of the thin-film already grown on a base substrate like a copper foil onto the destination substrate. This method is not applicable for alkali antimonides, as the photocathode needs to stay in a UHV environment after being made, while the transfer requires the substrate to be operated in air and submerged in water. The other method is to directly grow the 2D thin-film on the substrate, which could be achieved via either a chemical vapor deposition (CVD) or physical vapor deposition (PVD). CVD growth of Gr and hBN requires a complex setup and substrate heating (to 750° or higher [7]) and therefore are logistically and physically infeasible.

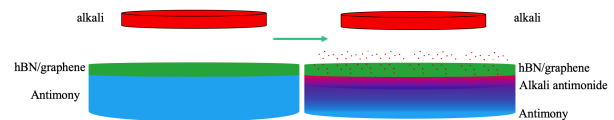


Figure 1: An illustration of the alkali intercalation process.

Recently, authors of this paper have been investigating a novel method to indirectly generate a 2D thin-film on alkali antimonides. In our approach, a process called intercalation is utilized where the alkali atoms penetrate a 2D thin-film of Gr or hBN on an antimony (Sb) coated silicon (Si) substrate to generate alkali antimonides. A conceptual illustration is shown in Fig. 1. We prepared the experimental samples by doing wet transfers of Gr monolayer thin-films on Sb coated Si wafers, denoted as Gr/Sb/Si, and heat treating the Gr/Sb/Si. Characterizations of the samples before, during and after the intercalations done at the NSLS-II beamlines of BNL indicated that Cs₃Sb structures were formed underneath the Gr monolayer. The results of the work are being submitted as a journal publication.

In this paper, we discuss the feasibility of using high power pulsed (HPP) reactive sputtering, which is a PVD method, to generate an hBN thin-film on a photocathode. We first show the density functional theory (DFT) simulations of an encapsulated Cu (111) substrate, and demonstrate the encapsulation protection effect by comparing the QE of naked and encapsulated Cu substrates. The instrumental setup of the HPP sputtering system is then presented and characterizations of the sputtered boron nitride thin-films are shown.

DFT SIMULATIONS

Density functional theory (DFT) was developed in the 1960's to calculate the electronic structures of materials and provide fundamental insights for properties such as adhesion,

* Work supported by the U.S. DOE Office of Science under contract number DE-SC0021511

[†] a.liu@euclidtechlabs.com

DESIGN AND COMMISSIONING OF THE ASU CXLS RF SYSTEM *

B. J. Cook[†], S. P. Jachim, G. I. Babic, J. R. S. Falconer, R. E. Larsen, M. R. Holl, W. S. Graves
Arizona State University, Tempe, AZ, USA

Abstract

The Compact X-ray Light Source (CXLS) uses inverse Compton scattering of a high intensity laser off a bright, relativistic electron beam to produce hard x-rays. The accelerator consists of a photoinjector and three standing wave linac sections, which are powered by two 6 MW klystrons operating at 9.3 GHz with a repetition rate of 1 kHz. This paper presents the design and commissioning of the CXLS RF systems consisting of both high-power RF structures and low power diagnostics. The high-power RF system is comprised of two solid state amplifier and klystron modulator sets, various directional couplers and three phase shifter power dividers. The low-level system consists of a master oscillator and laser phase lock, I/Q modulators, I/Q demodulators, and downconverters. We present measurements of the low-level and high-power RF phase and amplitude stability showing RMS timing jitter in the tens of femtoseconds and amplitude jitter below 0.1% at high power.

INTRODUCTION

Currently as tested the CXLS produces an electron beam capable of exceeding 30 MeV on a beam line that is approximately 10 meters in length. This would not have been possible without significant engineering effort and forethought for the RF system, both in high power delivery and in low power diagnostics. The high power RF energy provided by the two 6 MW klystron modulators, MOD1 and MOD2, are split such that MOD1 is dedicated to the photoinjector and a single linac, whereas MOD2 provides power to the other two linac structures.

DESIGN REQUIREMENTS

Design goals for the RF system were to have less than 1° phase jitter relative to the master oscillator at 9.3 GHz for the laser oscillator and in any accelerator structure. Additionally, both laser pulse arrival timing jitter at the cathode and electron beam timing jitter at the interaction point should be less than 500 fs.

SYSTEM DESCRIPTION

As seen in Fig. 1, the main RF signal for the entire system is 9.3 GHz provided from a master oscillator (MO). The MO is synchronized to a timing signal provided by a GPS module which also drives the timing of the laser and both klystron modulators. The MO also provides various other harmonics, namely 6975 MHz and 2325 MHz signals, used in the low level RF system. Each of these signals were based on their interactions to adjacent frequencies when

attempting to resolve intermodulation products [1]. The 6975 MHz signal acts as a local oscillator (LO) input into the down conversion (DNC) chassis, mixing with an RF input of 9.3 GHz creating a directly proportional 2325 MHz signal. The 2325 MHz is then fed into our In Phase and Quadrature Demodulation (IQD) chassis which provides an I and Q output in both polarities. Amplitude and phase changes are accomplished by adjusting the I and Q inputs to the In Phase and Quadrature Modulation (IQM) chassis or using the 4 port Phase Shifter Power Dividers (PSPD).

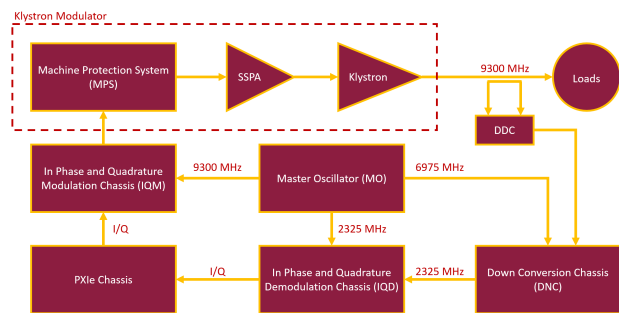


Figure 1: RF system block diagram.

MEASUREMENTS

The 9300 MHz signal output from the klystron modulators is directly measured using a Dual Directional Coupler (DDC) and attenuated to not exceed the input RF limits of the DNC chassis. Whereas the IF output signal is amplified to ensure readability when the signal reaches the PXIe chassis. The driving reason for this is based on measured conversion losses and LO leakage as shown in Figs. 2 and 3. There are notable outliers from this data, specifically with regards to LO Leakage. Those specific devices were placed in spare channels to minimize their impact.

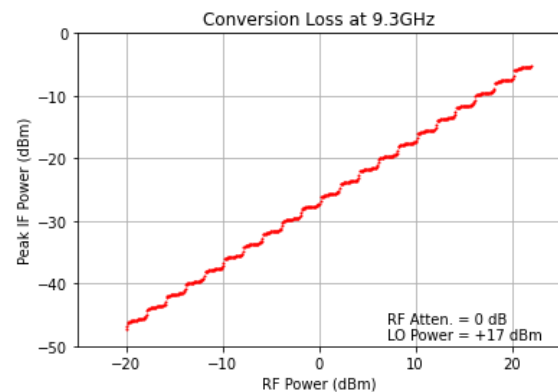


Figure 2: Down converter conversion loss.

* This work is supported in part by NSF award #1935994.

[†] bjcook8@asu.edu

EXTENSIONS OF THE COMPLEX (IQ) BASEBAND RF CAVITY MODEL INCLUDING RF SOURCE AND BEAM INTERACTIONS*

S. P. Jachim†, B. J. Cook, J. R. S. Falconer
Arizona State University, Tempe, AZ 85287, USA

Abstract

This paper extends prior work describing a complex envelope (i.e., baseband) dynamic model of excited accelerator RF cavities, including the effects of frequency detuning, beam loading, reflections, multiple drive ports and parasitic modes. This model is presented here in closed-form transfer function and state-variable realizations, which may be more appropriate for analytic purposes. Several example simulations illustrate the detailed insight into RF system behavior afforded by this model.

TRANSFER FUNCTION MODEL

Stated below are the baseband Laplace in-rail (cosine) and cross-rail (sine) impulse transimpedance responses of an intrinsic cavity, as developed in [1]. Here, the polynomial coefficients have been recast to conform to standard control theory nomenclature.

$$Z_c(s) = \frac{b_{1c}s + b_{2c}}{s^2 + a_1s + a_2};$$

$$Z_s(s) = \frac{b_{1s}s + b_{2s}}{s^2 + a_1s + a_2};$$

where:

$$a_1 = \frac{2}{\tau};$$

$$a_2 = \left(\frac{1}{\tau^2} + \Delta\omega^2\right);$$

$$b_{1c} = \frac{R_c}{\tau};$$

$$b_{2c} = \left(\frac{R_c}{\tau}\right) * \left(\frac{1}{\tau} - \frac{\Delta\omega}{2Q}\right);$$

$$b_{1s} = \frac{R_c}{2Q\tau};$$

$$b_{2s} = \left(\frac{R_c}{2Q\tau}\right) * \left(\frac{1}{\tau} + 2Q\Delta\omega\right);$$

τ = cavity damping time constant (s);
 $\Delta\omega = \omega_0 - \omega_d$ = detuning frequency (rad/s);
 ω_0 = cavity resonant frequency (rad/s);
 ω_d = drive frequency (rad/s);
 R_c = cavity shunt resistance (ohms);
 Q = intrinsic cavity quality factor.

In general, these functions are of second order, with a complex pair of poles and a real zero. However, with no detuning ($\Delta\omega=0$), pole-zero cancellation occurs, and the functions revert to first order, with a single real pole.

* This work was supported in part by NSF award #1935994.
 † Stephen.jachim@asu.edu

The complete response of the cavity is then:

$$\begin{bmatrix} V_{ci}(s) \\ V_{cq}(s) \end{bmatrix} = [Z(s)] \begin{bmatrix} I_{ci}(s) \\ I_{cq}(s) \end{bmatrix};$$

where:

$$[Z(s)] = \begin{bmatrix} Z_c(s) & -Z_s(s) \\ Z_s(s) & Z_c(s) \end{bmatrix};$$

$V_{ci,q}(s)$ = in/quadrature phase cavity voltage;
 $I_{ci,q}(s)$ = in/quadrature phase cavity current.

LOADED CAVITY RESPONSE

As described in Ref. [1], the terminal conditions that govern the interface between the drive line, intrinsic cavity and beam current are given by:

$V_c = V_f + V_r$;
 $I_c = (V_f - V_r)Y_0 + nI_b$;
 $V_{f,r}$ = forward/reverse drive line voltage;
 V_c = cavity voltage;
 Y_0 = drive line characteristic admittance;
 n = beam coupling transformer ratio;
 I_c = cavity current;
 I_b = beam current.

These relations are represented in block diagram form in Fig. 1. Note that all signals are complex-valued.

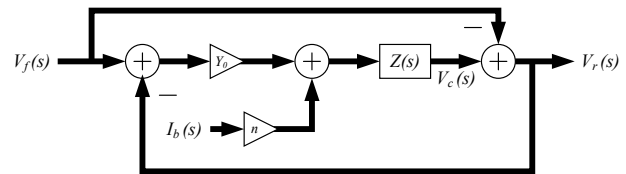


Figure 1: Operational block diagram of line/beam/cavity interactions.

While this operational model works well for simulation, algebraic equations may be more appropriate for analytical purposes. Thus, it can be shown that the following equations are equivalent to the loaded cavity model:

$$V_c = [I + Y_0Z(s)]^{-1}[Z(s)][2Y_0 \quad n] \begin{bmatrix} V_f \\ I_b \end{bmatrix};$$

$$V_r = V_c - V_f.$$

DESIGN AND COMMISSIONING OF THE ASU CXLS MACHINE PROTECTION SYSTEM*

S. P. Jachim[†], B. J. Cook, J. R. S. Falconer, A. J. Gardeck, M. R. Holl, R. S. Rednour,
D. Smith, J. Vela, W. S. Graves, Arizona State University, Tempe, AZ, USA

Abstract

To protect against fault conditions in the high-power RF transport and accelerating structures of the ASU Compact X-Ray Light Source (CXLS), the Machine Protection System (MPS) extinguishes the 6.5 MW RF energy sources within approximately 50 ns of the fault event. In addition, each fault is localized and reported remotely via USB for operational and maintenance purposes. This paper outlines the requirements, design and performance of the MPS applied on CXLS.

OVERVIEW

The purpose of the Machine Protection System (MPS) is to prevent damage to the high-power radio-frequency (HPRF) source and/or its various transmission and load components when a fault or arc occurs in the system. Fig. 1 shows a notional block diagram of the Compact X-Ray Light Source (CXLS) RF system, including the MPS.

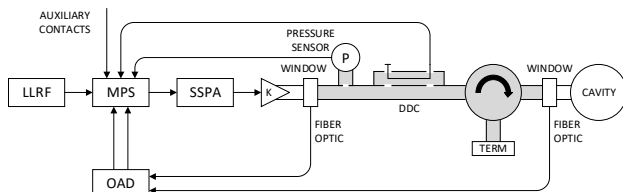


Figure 1: CXLS RF system block diagram.

Modulated 9.3 GHz RF pulses are generated by the Low-Level RF (LLRF) subsystem and are applied to the MPS. Under operating conditions the pulse is first amplified by a solid-state power amplifier (SSPA) and then by a Klystron (K). RF windows are employed to segregate the klystron and cavity vacuum regions from the RF waveguide, which is pressurized with SF₆.

The MPS senses fault conditions through a variety of sensors. A pressure sensor sends an alarm to the MPS when WG pressure falls below a prescribed level. Reverse RF power is sampled with a dual-directional coupler (DDC) and sent to the MPS. Light generated by arc flash at the WG windows is detected in the Optical Arc Detector (OAD) and then applied to the MPS. A number of auxiliary contact channels are provided for integration with other protection subsystems. When any of these faults are detected, the MPS interrupts the RF signal applied to the SSPA, extinguishing the klystron HPRF output.

* This work was supported in part by NSF award #1935994.

[†] Stephen.jachim@asu.edu

SIGNAL CONDITIONING

The front-end signal conditioning of the MPS analog signals is depicted in Fig. 2. The reverse RF power envelope is extracted in a fast diode detector, then passed to a threshold comparator channel. The OAD provides analog channels proportional to optical power. Four fast Schmitt trigger channels, with individually programmable thresholds, convert these four signals to binaries for event detection. Each channel has input overvoltage diode protection. The threshold circuits have nonvolatile memory to hold system thresholds over power interruptions.

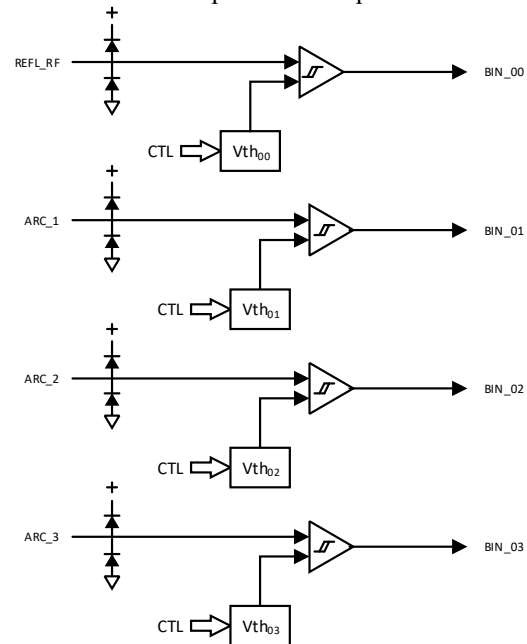


Figure 2: Analog signal processing.

EVENT CAPTURE

Figure 3 shows a collapsed schematic of the event capture and control section of the MPS. Along with the previous four binary signals, an additional twelve auxiliary inputs are serviced, each with a Schmitt trigger gate to minimize chatter and signal uncertainty. These inputs are pulled up in the MPS, so that a contact closure to ground indicates an alarm condition. One auxiliary channel services the waveguide pressure switch; others can be used as tie-ins to external systems, such as personnel interlocks. All sixteen channels then pass through invert/noninvert gates, selectable as needed. The state of these channels is reported as the “INPUT STATE” of each.

ON-CHIP PHOTONICS INTEGRATED CATHODES

A. Kachwala*, O. Chubenko, S. Karkare, Arizona State University, Tempe, AZ, USA
R. Ahsan, H.U. Chae, R. Kapadia, University of Southern California, Los Angeles, CA, USA

Abstract

Photonics integrated photocathodes can result in advanced electron sources for various accelerator applications. In such photocathodes, light can be directed using waveguides and other photonic components on the substrate underneath a photoemissive film to generate electron emission from specific locations at sub-micron scales and at specific times at 100 femtosecond scales along with triggering novel photoemission mechanisms resulting in brighter electron beams and enabling unprecedented spatio-temporal shaping of the emitted electrons. In this work we have demonstrated photoemission confined in the transverse direction using a nanofabricated Si_3N_4 waveguide underneath a 40 nm thick cesiated GaAs photoemissive film, thus demonstrating a proof of principle feasibility of such photonics integrated photocathodes. This work paves the way to integrate the advances in the field of photonics and nanofabrication with photocathodes to develop better electron sources.

INTRODUCTION

Photonic components nano-fabricated underneath a photoemissive film can result in advanced photocathode electron sources for several particle accelerator applications. For examples photonics waveguides under a thin film of a high quantum efficiency semiconductor cathode can cause the photons to be efficiently absorbed very close to the surface resulting in high quantum efficiency (QE), low emittance and quick response time simultaneously, thus providing higher brightness electron beams [1]. Photonics components underneath a photoemissive surface can also be used to spatio-temporally shape the emitted electron beam by guiding light pulses to specific locations at the surface with sub- μm spatial and near 100 fs temporal resolution. This can potentially result in a new method for spatio-temporal shaping of electron beams with unprecedented resolution and enable having correlations in the spatial and temporal profiles.

Practically developing such structures has significant technological challenges related to coupling light in the waveguide structures, obtaining a thin photoemissive film on the nano-fabricated photonics substrate and practically using such cathodes in electron guns. In this paper we present designs that can be used for coupling light, demonstrate the transfer of thin epitaxial GaAs films on to the photonics integrated substrates, demonstrate activation of these films using Cs and finally using a Photoemission Electron Microscope (PEEM) to show that electron emission can be confined using photonic components like waveguides. The results presented below are a proof-of-principle demonstration of photonics based cathode technology and significantly

alleviate the technological barrier towards integrating such sources in electron guns.

LIGHT COUPLING TECHNIQUES

Efficient coupling of light into the waveguides fabricated on the cathode substrates is essential to make effective photonics integrated cathodes. In most photonic applications, this is done by connecting an optical fiber to the waveguide and then coupling light into the fiber [2]. However, as these photocathodes are used under Ultra High Vacuum (UHV) conditions, this mechanism of coupling light into the waveguide is infeasible as the sample cannot be transferred into the UHV chamber of an electron gun with an optical fiber connected to it. Connecting the fiber to the sample while it is in the electron gun under UHV is also non-trivial. Owing to these constraints, we designed and developed two coupling mechanisms which were tested in PEEM under UHV. Both these mechanisms are also compatible with the geometry of many standard DC and RF electron guns.

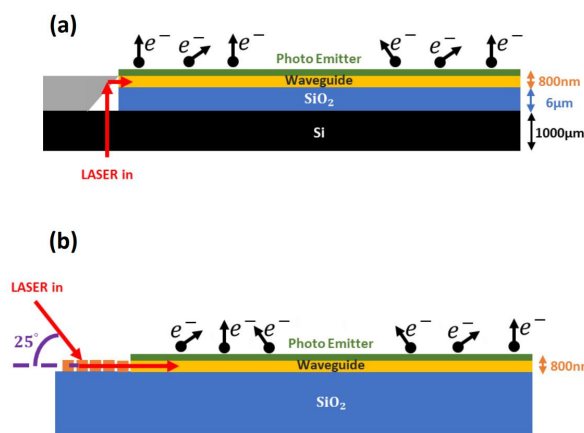


Figure 1: (a) Light Coupling into waveguide using Si etched mirror; (b) Light coupling into waveguide using grating coupler.

In the first mechanism, a gold coated Silicon (Si) mirror is etched onto the substrate. As shown in Figure 1(a) incoming laser beam is incident on this mirror at near normal incidence and after reflection gets coupled into the waveguide. The second mechanism uses grating coupler on the surface of the cathode with the laser incident at large angles with respect to the normal as shown in Figure 1(b). Although both these mechanisms resulted in photoemission confined to the waveguide region of the substrate as shown in section 4, the first mechanism was difficult to reproduce and fabricate as it requires precise alignment of

* akachwal@asu.edu

NEAR THRESHOLD PHOTOEMISSION FROM GRAPHENE COATED Cu SINGLE CRYSTALS

C. J. Knill*, S.S. Karkare, Arizona State University, Tempe, AZ, USA

E. Batista, N. Moody, G. Wang, H. Yamaguchi, P. Yang

Los Alamos National Laboratory, Los Alamos, NM, USA

H. Ago, K. Kawahara, Global Innovation Center, Kyushu University, Fukuoka, Japan

Abstract

The brightness of electron beams emitted from photocathodes plays a key role in the performance of accelerator applications like X-ray free electron lasers (XFELs) and ultrafast electron diffraction (UED) experiments. In order to achieve a maximum beam brightness, the electrons need to be emitted from photocathodes with the smallest possible mean transverse energy (MTE). Recent studies have looked at the effect that a graphene coating has on the quantum efficiency (QE) of the cathode [1]. However, there have not yet been any investigations into the effect that a graphene coating has on the MTE. Here we report on MTE and QE measurements of a graphene coated Cu(110) single crystal cathode at room temperature and cryogenic temperatures. At room temperature, a minimum MTE of 25 meV was measured at a 4.20 eV photon energy (295 nm). This MTE remained stable at 25 meV over several days. At 77 K, a minimum MTE of 9 meV was measured at a 4.28 eV photon energy (290 nm). We perform density functional theory (DFT) calculations to look at the effects of a graphene coating on a Cu(111) surface state. These calculations show that the graphene coating reduces the radius of the surface state, allowing for emission from a lower transverse energy state in comparison to bare Cu(111).

INTRODUCTION

The performance of accelerator applications like x-ray free electron lasers (XFELs) and ultrafast electron diffraction (UED) and microscopy (UEM) experiments is dependant upon the brightness of the electron beam emitted from photoinjectors. For XFELs a brighter electron beam will lead to an increase of x-ray lasing and pulse energies [2], as well as the development of smaller and more accessible university scale facilities [3]. For single shot UED, an increase in brightness will open new doors by enabling the study of larger crystal lattices like proteins [4]. And for stroboscopic UED/UEM experiments, a brighter beam will reduce the signal to noise ratio and the data acquisition time [5]. The key figure of merit in determining the brightness of the electron beam generated from a photoinjector is the mean transverse energy (MTE) of the photocathode [6]. Hence, understanding and reducing the MTE is necessary to achieving brighter electron beams from future, and existing, photoinjectors.

For metallic cathodes, the MTE is approximately equal to $MTE = E_{excess}/3$, where the excess energy (E_{excess}) is de-

finied as the difference between the photon energy ($\hbar\omega$) and the work function (ϕ) of the photocathode [7]. For excess energies that are low and negative, the electron emission occurs from tail of Fermi distribution and the minimum MTE is $k_b T$ where k_b is the Boltzmann constant and T is the temperature of the electrons in the lattice [8]. At low laser fluences the lattice and electrons are in equilibrium and thus their temperatures are equivalent. At room temperature, the minimum MTE is 25 meV, a result that has been experimentally verified with Sb photocathodes [9]. By reducing the temperature of the cathode to cryogenic temperatures, MTEs below 25 meV have been demonstrated experimentally [10]. However, as the cathode reaches cryogenic temperatures it becomes challenging to reach this minimum MTE. This is because near threshold the transmission probability is very small for low energy electrons [10, 11]. In addition, the surface nonuniformities of physical roughness and work function variation can lead to an increase in MTE [9, 12]. In order to minimize the effects that these nonuniformities have on the MTE, it is necessary to use atomically ordered single crystalline cathodes rather than polycrystalline cathodes [13].

For single crystals, the transverse momentum is conserved during photoemission. Therefore to minimize the MTE, it is crucial that cathodes are chosen that allow only electron emission from electronic states with a low transverse momentum [14]. By utilizing the low transverse energy states of a Cu(100) single crystal, a 5 meV MTE has been demonstrated when operating near the photoemission threshold and at 30 K [10].

A recent investigation looked into the effect that a graphene coating has on the QE of a Cu(110) single crystal [1]. They found that the graphene coating does not negatively impact the QE, and instead increases the stability by preserving the QE even up to atmospheric conditions. While this result is promising, further studies are needed to investigate the impact that a graphene coating has on the MTE.

In this paper we measure the MTE of a graphene coated Cu(110) single at room temperature and cryogenic temperatures. Our measurements show that we reach the thermal limit of 25 meV at room temperature, and that the MTE remains stable over several days. When the cathode is cooled down to 100 K and 77 K, we measured an MTE of 13 meV and 9 meV respectively. We show that these low, sub-25 meV, MTEs can be attained with a single anneal at 345°C for 3 hours rather than the intense in-situ surface prepara-

* cknill2@asu.edu

EFFECTS OF TRANSVERSE DEPENDENCE OF KICKS IN SIMULATIONS OF MICROBUNCHED ELECTRON COOLING*

W. F. Bergan[†], Brookhaven National Laboratory, Upton, NY, USA
 G. Stupakov, SLAC, Menlo Park, CA, USA

Abstract

Microbunched electron cooling (MBEC) is a cooling scheme in which a beam of hadrons to be cooled induces energy perturbations in a beam of electrons. These electron energy perturbations are amplified and turned into density modulations, which in turn provide energy kicks to the hadrons, tending to cool them. For simplification, previous work has modelled the electron-hadron interactions using a disc-disc model, assuming that the inter-particle kicks depend only on the longitudinal distances between individual hadrons and electrons. In reality, these kicks will also have a transverse dependence, which will impact the cooling process. We incorporate this transverse kick dependence into our simulations of the cooling process, allowing us to better understand the physics and provide improved design goals for the MBEC cooler for the Electron-Ion Collider.

INTRODUCTION

Microbunched electron cooling (MBEC) is a promising technique for cooling dense hadron beams in future colliders, and, in particular, is planned to be used in the Electron-Ion Collider (EIC) in order to counteract the effects of intrabeam scattering (IBS) [1]. This technique was first described in [2] and expanded upon in [3–6]. In short, the hadrons to be cooled co-propagate with a beam of electrons through a straight modulator section. This imprints an energy modulation on the electron beam which is correlated with the density of the hadron beam. One then separates the electrons and hadrons. The electrons are sent through a series of chicanes and straight sections which amplify their initial energy perturbations through the microbunching instability and turn them into density perturbations. Meanwhile, the hadrons pass through their own chicane, with their path length dependent on their energy and transverse offsets and angles in the modulator. The electrons and hadrons meet up again in a “kicker” straight. Through a proper choice of hadron optics, we can arrange for each hadron to receive an energy kick from the electron perturbation which it had induced which tends to reduce its initial energy offset and transverse actions.

Previous simulations [7–9] have focused on the simple 1D model of [3]. The electron/electron and electron/hadron interactions in the modulator and kicker are treated as those of 2D discs, with the force between the particles averaged over the transverse sizes of the beams and independent of

their real transverse coordinates. In order to incorporate the effect of the transverse position of each hadron in the modulator and kicker on its received wake, we model the hadrons as point charges, but treat the electrons as discs. We first consider a simplified theory where the transverse kick to the hadron falls off as a Gaussian in its transverse coordinates in the kicker. We then extend the theory in [5] to compute the real energy kick between a point-like hadron and disc-like electron and incorporate this new wake into our multi-turn simulations of MBEC at the EIC.

SIMPLIFIED THEORY

As a first attempt to understand the effect of transverse offsets of the hadrons on the cooling dynamics, we consider the simplified model where the kick which an electron disc imparts to a hadron in the kicker is given by

$$\Delta\eta(x, z) = \sqrt{1 + \frac{\Sigma_{h,x}^2}{\Sigma_{e,x}^2}} e^{-x^2/2\Sigma_{e,x}^2} A\Delta z \quad (1)$$

where x and z are respectively the horizontal and longitudinal offsets of the hadron relative to the electron disc, $A\Delta z$ is the linearized wake function between two discs, and the Σ s are the hadron and electron horizontal beam sizes. A similar prefactor can be included to account for vertical position, but we ignore it here for simplicity.

The longitudinal cooling rate (defined so a negative sign implies cooling) is given by

$$\lambda_z = \frac{\langle \Delta(\eta^2) \rangle}{2T_{rev}\sigma_\eta^2} \approx \frac{\langle 2\eta\Delta\eta \rangle}{2T_{rev}\sigma_\eta^2} \quad (2)$$

where the factor of 2 in the denominator represents the fact that the longitudinal action is split evenly between the energy offset and longitudinal position offset, but we only change the former. We have also made the approximation that the energy kick is small relative to the original energy offset, so that we only keep the linear term.

For a Gaussian beam with horizontal emittance ϵ and fractional energy spread σ_η , we can do the relevant integrals analytically, arriving at

$$\lambda_z = \frac{A}{T_{rev}(\Sigma_{x,h}^2 + \Sigma_{x,e}^2)} [R_{56}(\Sigma_{x,e}^2 + \epsilon\beta) + R_{16}(D'\Sigma_{x,e}^2 + D'\epsilon\beta + D\epsilon\alpha) - R_{26}D\Sigma_{x,e}^2] \quad (3)$$

where all the coordinates and optics parameters are evaluated at the *kicker* and we have made use of the expression for $\Delta\eta$ in Eq. (1) and the expression for longitudinal delay in terms of the kicker coordinates [5]

$$\Delta z = R_{16}x' - R_{26}x + R_{56}\eta \quad (4)$$

* This work was supported by Brookhaven Science Associates, LLC under contract No. DE-SC0012704 with the U.S. Department of Energy, and by the Department of Energy, contract DE-AC03-76SF00515.

[†] wbergan@bnl.gov

RECORD QUANTUM EFFICIENCY FROM SUPERLATTICE PHOTOCATHODE FOR SPIN POLARIZED ELECTRON BEAM PRODUCTION *

J.P. Biswas, L. Cultrera, W. Liu, E. Wang, J. Skaritka, K. Kisslinger
Brookhaven National Laboratory, Upton, NY, USA

S.D. Hawkins, S.R. Lee, J.F. Klem, Sandia National Lab., Albuquerque, NM, USA

Abstract

Electron sources producing highly spin-polarized electron beams are currently possible only with photocathodes based on GaAs and other III-V semiconductors. GaAs/GaAsP superlattice (SL) photocathodes with a distributed Bragg reflector (DBR) represent the state of the art for the production of spin polarized electrons. We present results on a SL-DBR GaAs/GaAsP structure designed to leverage strain compensation to achieve simultaneously high QE and spin polarization. These photocathode structures were grown using molecular beam epitaxy and achieved quantum efficiencies exceeding 15% and electron spin polarization of about 75% when illuminated with near bandgap photon energies.

INTRODUCTION

Polarized electron sources are used in fundamental research in many fields including condensed matter physics and elementary particle physics. Polarized electron sources are employed in polarized electron microscope [1] to study domain walls in ferromagnetic materials. Polarized positron beams can be generated by impinging polarized electron beams in high Z-target elements. The planned International Linear Collider is designed to collide spin-polarized electrons and positrons at large energies in the TeV range. The Electron Ion Collider [2] that will be operated in the USA also requires a spin-polarized electron source for nuclear physics study. Most facilities require a few hundred micro amperes of current that can be easily produced by the current state-of-the-art electron sources [3]. Other facilities such as the Large Hadron electron Collider plans to operate at a high average current of 20 mA, which is beyond the current state of the art.

Spin-polarized electron sources are generated from GaAs based photocathodes. Bulk GaAs with traditional Cs-O activation provides a high QE of around 10%, however, the maximum polarization is limited to 50% due to the degeneracy of the heavy-hole and light-hole at the $2p_{3/2}$ band state. Growing the photocathode strained eliminates the degeneracy thus maximizing the spin polarization. In the 1990s strained GaAs grown on GaAsP showed improved electron spin polarization (ESP) of 75-80%, whereas QE was limited to only about 0.3% [4]. Through the use of strained superlattices (SL) based on GaAs/GaAsP, it was possible to leverage quantum well structures to increase the separation between heavy and light hole bands and achieve even higher spin polarization (up to 85%) and QE (just above 1%) [5]. Ad-

vanced SL-based GaAs photocathodes consist of alternating layers with tensile and compressive strain thus effectively reducing the defect density due to the strain on the SL layer. By reducing defect density, spin polarization could be further increased up to 92% with a QE of just 1.6% [5]. Simultaneously achieving high QE and spin polarization is difficult. As the QE increase due to the larger thickness of the SL layer, spin polarization decreases due to the depolarization mechanism of the electron with the thick layer.

CATHODE WITH DISTRIBUTED BRAGG REFLECTOR

A distributed Bragg reflector (DBR) grown underneath the SL with a buffer medium layer creates a Fabry Perot resonator that effectively traps the light and enhances the QE [6, 7]. Instead of laser light passing through the cathode, it reflects repeatedly within the cavity, increasing photon absorption, which in turn, improves the QE. Such a structure demonstrated record performance achieving ESP of 84% and QE of 6.4% at 776 nm laser wavelength [6]. As the number of layers increases the growth of such structure with high QE and ESP becomes increasingly challenging.

The structural element of the photocathode used in this work is illustrated in Fig. 1. The DBR consists of alternating layer of high (n_H) and low (n_L) index of refraction material. The high refractive index layer is GaAs_{0.81}P_{0.19} and low refractive index layer is AlAs_{0.78}P_{0.22}. For a high reflectivity at a certain wavelength λ , the thickness of the DBR layers are, $\lambda_B/4n_H$, and $\lambda_B/4n_L$ respectively [8]. The bandwidth over which the DBR has high reflectivity can be according to [8] expressed as

$$\Delta\lambda_B = \frac{4\lambda_B}{\pi} \sin^{-1} \left(\frac{n_H - n_L}{n_H + n_L} \right) \quad (1)$$

GaAs	5 nm	$\rho = 5 \times 10^{19} \text{ cm}^{-3}$	} 30 pairs
GaAs _{0.62} P _{0.38}	4 nm	$\rho = 5 \times 10^{17} \text{ cm}^{-3}$	
GaAs	4 nm	$\rho = 5 \times 10^{17} \text{ cm}^{-3}$	
GaAs _{0.81} P _{0.19}	300 nm	$\rho = 5 \times 10^{18} \text{ cm}^{-3}$	} 10 pairs
AlAs _{0.78} P _{0.22}	65 nm	$\rho = 5 \times 10^{18} \text{ cm}^{-3}$	
GaAs _{0.81} P _{0.19}	55 nm	$\rho = 5 \times 10^{18} \text{ cm}^{-3}$	
GaAs _{0.81} P _{0.19}	2000 nm	$\rho = 5 \times 10^{18} \text{ cm}^{-3}$	
GaAs->GaAs _{0.81} P _{0.19}	2750 nm	$\rho = 5 \times 10^{18} \text{ cm}^{-3}$	
GaAs buffer	200 nm	$\rho = 5 \times 10^{18} \text{ cm}^{-3}$	
GaAs substrate		$\rho > 1 \times 10^{18} \text{ cm}^{-3}$	

Figure 1: Schematic of the superlattice GaAs photocathode with DBR structure. The GaAs surface layer was capped with amorphous As after the epitaxial growth.

* The work is supported by Brookhaven Science Associates, LLC under Contract DESC0012704 with the U.S. DOE. SNL is managed and operated by NTESS under DOE NNSA contract DE-NA0003525.

THE IMPACT ON THE VERTICAL BEAM DYNAMICS DUE TO THE NOISE IN A HORIZONTAL CRAB CROSSING SCHEME*

Yue Hao[†], Michigan State University, East Lansing, MI, USA
 Yun Luo, Brookhaven National Laboratory, Upton, NY, USA

Abstract

Several recent and future colliders have adopted the crab crossing scheme to boost performance. The lower RF control noise of the crab cavities has been identified as one of the significant sources that impact the transverse beam quality in the crabbing plane. However, through beam-beam interaction and other coupling sources, the effect may also affect the non-crabbing plane. In this paper, we report the simulation observations of the beam dynamics in the non-crabbing plane in the presence of phase noise in the crab cavity.

INTRODUCTIONS

The RF crab cavity noise has been identified as the source of the transverse emittance growth of the crabbing plane in the hadron ring of a collider. A linear theory has been reported to calculate the emittance growth rates in the presence of the voltage and phase error of the crab cavity respectively [1]. A feedback system can be helpful to reduce the emittance growth [2]. Recently, the noise effect is tested in SPS crab cavity test and the discrepancy of noise-induced emittance growth between the experimental observation and the theory are found to be explained by the coherent tune shift due to the transverse coupling impedance [3].

The crab cavity noise-induced emittance growth is limited in the crabbing plane if no coupling effect presents. The linear coupling is an obvious source to affect the non-crabbing plane, while at least theoretically, the linear coupling can be corrected and the feedback system will be effective for the coupled emittance growth in the non-crabbing plane. There are also inevitable nonlinear coupling effects due to the multi-pole magnets between the crab cavity pairs or the beam-beam interaction. The nonlinear coupled emittance growth in the non-crabbing plane usually is small and can be ignored. However, the statement needs to be carefully checked in the future electron-ion collider (EIC). In EIC, the electron beam naturally has a very flat beam profile and the proton beam is designed to match at IP to achieve high luminosity. The transverse flatness r , defined as $r = \sigma_y/\sigma_x$ at the interaction point(IP), is designed to be about 0.09. Due to the strong radiation damping of the electron beam, only the hadron beam can be affected by the crab noises.

In this article, we will use a simplified beam-beam model to verify the vertical emittance growth in a horizontal crabbing scheme. The parameter in simulation is adopted from the parameter table of future EIC, as shown in Table 1. Both

Table 1: Crab Crossing Parameters of EIC

	Electron	Proton
Energy (GeV)	10	275
H.beam size (IP) (μm)	95	95
V.beam size (IP) (μm)	8.5	8.5
β_x (IP) (cm)	55	80
β_y (IP) (cm)	5.6	7.2
Bunch length (cm)	6	0.7
crossing angle (mrad)	25	

the crab noise in the hadron ring and electron ring will create z dependent transverse offset in the interaction region. We will only focus on the noise effect of the crab cavity in the hadron beam due to the page limit.

SIMPLIFIED TRACKING MODEL

In the simplified model, we use a linear one-turn matrix at IP to represent the entire hadron ring. The crab cavities in the hadron ring are located in the ideal location which has $\pi/2$ horizontal phase advance away from IP.

Since the electron beam is much shorter than the hadron beam, in this simplified beam-beam model, a short electron beam is assumed. To avoid the computationally expensive Faddeeva function in the Bassetti-Erskine formula, we use the flat beam approximation form as below:

$$\Delta p_y = \frac{N_e r_0 \sqrt{2\pi}}{\gamma \sigma_x} \left(e^{-\tilde{x}^2} \text{erf}(\tilde{y}) - \frac{2r\tilde{y}}{\sqrt{\pi}} + \frac{4r\tilde{x}\tilde{y}}{\sqrt{\pi}} F(\tilde{x}) \right) \quad (1)$$

$$\Delta p_x = \frac{N_e r_0 \sqrt{2\pi}}{\gamma \sigma_x} \left(\frac{2F(\tilde{x})}{\sqrt{\pi}} - 2r\tilde{x}e^{-\tilde{x}^2} \left(\tilde{y} \text{erf}(\tilde{y}) + \frac{e^{-\tilde{y}^2}}{\sqrt{\pi}} \right) + r^2 \tilde{x} (1 + 2\tilde{y}^2) + r^2 (2\tilde{y}^2 - \tilde{x}^2 - 4\tilde{x}^2 \tilde{y}^2) F(\tilde{x}) \right) \quad (2)$$

where \tilde{x} and \tilde{y} are the transverse locations normalized by $\sqrt{2}\sigma_{x/y}$ respectively. $\sigma_{x/y}$ are the two transverse rms beam sizes at IP. In this limit, the two evaluations of the Faddeeva function are replaced by the calculation of the error function $\text{erf}(x)$ and Dawson's integral $F(x)$. This simplification not only speeds up the model to allow a broader scan of the emittance growth with various noise levels and other parameters, but also explores clearer mathematical dependence in the limit of flat beam. For simplicity, the energy kick due to the symplectic condition is not included, which is not essential in understanding the effect of the crab cavity noise in a short time range.

* Work Supported BY Brookhaven Science Associates, LLC under contract NO. DE-SC0012704 with the U.S. Department of Energy.

[†] yhao@bnl.gov, also joint appointed by Brookhaven National Laboratory

TENSOR DECOMPOSITION FOR THE COMPRESSION AND ANALYSIS OF 10 kHz BPM DATA *

J. Choi[†], Y. Hidaka, Y. Hu, G. Wang, BNL, Upton, NY 11973, USA

Abstract

In NSLS-II storage ring, during the user operation, fast-acquisition (FA) 10 kHz Beam Position Monitor (BPM) data are collected and their spectral properties are analyzed. Various periodograms and spectral peaks are being provided every minute, and they are very useful in identifying any changes in the orbit. Unfortunately, because of the big size of the data, only several numbers are being continually archived for the later study and the full raw data are saved only by hand when needed. We are developing methods utilizing tensor decomposition techniques to save and analyze the FA data and the paper is reporting the current status.

INTRODUCTION

As the user facility providing high-performance synchrotron light to the user, NSLS-II invests efforts constantly to maintain and improve the electron beam stability. As one of the efforts, we keep monitoring the 10 kHz BPM FA data properties. That is, every minute, we measure FA data for all BPMs for 10 seconds and their spectrum properties are displayed in the control system studio (CSS) pages. Because of the number of BPMs are more than 400 when we take account of the planes for each BPM, on top of the individual properties, representative spectrum properties are also displayed. The representative plots include averaged spectrum properties for dispersive region, non-dispersive region and ID BPMs.

Even though the plots are quite helpful and convenient tools to monitor the beam stability, all the FA data cannot be kept for the later use because of the big file size, and only some typical numbers are archived. Even though the archived numbers such as peak frequencies, power spectra are very useful, the contained information cannot be compared to the full FA data. Furthermore, the plots and the representative numbers are just being refreshed every minute, and picking up the moment when some variation is involved in beam stability is not easy.

In short, we searched the solution which compress the FA data to the reasonable size to keep all the files generated every minute and, at the same time, can provide several representative numbers showing the orbit status in real time. As a strong candidate, we tried the tensor decomposition analysis (TCA) which is well established in biology and medical society.

In the following sections, we introduce the TCA and shows how it is applied to NSLS-II storage ring FA data, together with the current status.

* Work supported by DOE under contract No. DE-SC0012704.

[†] jchoi@bnl.gov

TENSOR DECOMPOSITION

For the analysis of the matrices, principal component analysis (PCA) methods like singular value decomposition (SVD) or independent analysis (ICA) are well established and are playing critical roles in various fields of expertise. Similar techniques for high-dimensional array (tensor) are also well developed and being actively used in biology and medical society [1].

The main purpose of such analysis is identifying the limited number of factors which can explain the major part of the data. That means we can find low-rank representation of the tensor which can be used in compressing the data. The low-rank representation can reveal the factors behind the data. Also, we can have physical meanings for the identified factors.

There are several popular decomposition techniques [1], but here we choose CANDECOMP/PARAFAC (CP) decomposition. The CP decomposition is simple and small number of parameters can represent the tensor. Therefore, the method can compress the data efficiently when the system has clear low-rank behaviors.

Different from the biological or medical system, the physical system such as storage ring has a few clear physical parameters which dominate the beam behaviors. If we assume that the three-dimensional tensor X has R ranks, with the CP decomposition, it can be expressed as

$$X \approx \sum_{r=1}^R u_r^{(1)} \circ u_r^{(2)} \circ u_r^{(3)} \quad (1)$$

where u_r 's are vectors for each dimension and \circ is outer product. The schematic diagram of CP decomposition is shown in Fig. 1.

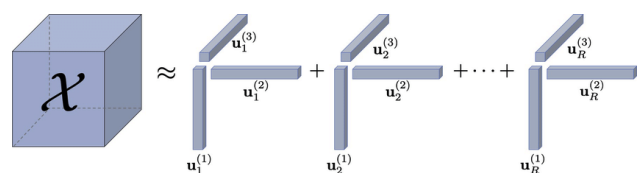


Figure 1: Diagram of CP decomposition (courtesy of Jean Kossaifi).

As in the case of matrix SVD, the magnitudes of u_r vectors are arbitrary as far as the products gives the correct tensor. Therefore, usually they are normalized and additional scale factors are introduced. Then, Eq. (1) can be represented as

$$X \approx \sum_{r=1}^R \lambda_r \times u_r^{(1)} \circ u_r^{(2)} \circ u_r^{(3)}. \quad (2)$$

UNIFIED ORBIT FEEDBACK AT NSLS-II*

Y. Hidaka[†], G. M. Wang, Y. Tian, R. Smith, Y. Li, X. Yang
Brookhaven National Laboratory, Upton, NY, USA

Abstract

We have developed an orbit correction / feedback program to unify the existing orbit-related feedback systems for stable beam operation at NSLS-II. Until recently only a handful of beamlines have been benefiting from long-term orbit stability provided by a local bump agent program. To expand this to all the beamlines as well as correct more frequently, a new slow orbit feedback program called unified orbit feedback (UOFB) was written from scratch that works with the fast orbit feedback transparently, while accumulated fast corrector strength is continuously shifted to the slow correctors and RF frequency is adjusted for circumference change. UOFB can lock 3 different types of local bumps to the target offsets/angles for days: those for insertion device (ID) sources with only ID RF beam position monitors (BPM) or mixtures of ID RF BPMs and X-ray BPMs, and those for bending magnet sources with arc BPMs between which orbit correctors, dipoles and quadrupoles exist. Furthermore, this feedback can accommodate beamline user requests to enable/disable the feedback loop for their beamline and to change bump target setpoints without turning off the loop.

INTRODUCTION

The most critical stability requirement for beamline users at a third-generation light source like National Synchrotron Light Source II (NSLS-II) [1] is beam orbit stability at the source points. Some beamlines require the long-term beam angle stability to be 100-10 nrad at samples [2]. An active beamline components feedback [3] can substantially help, but it requires raw electron beam (e-beam) orbit stability to be at least on the order of a few hundred nrad.

To satisfy the requirements for the most sensitive beamlines, the first local bump agent (LBA) was successfully commissioned and put into operation in 06/2018 [4]. The program has been expanded to 5 beamlines since then. However, further expansion to all was difficult due to 1) conflicts with adjacent agents, 2) accumulating fast corrector strengths, and 3) incompatibility of bending magnet bump agents and the RF frequency feedback (RFFB).

To solve all these issues, we have recently implemented UOFB whose goal is to unify the slow orbit feedback (SOFB), fast orbit feedback (FOFB) and RFFB with the ability to offload accumulated fast corrector strengths to slow correctors and the flexibility to adjust all types of local bumps at any time.

UNIFYING ORBIT FEEDBACKS

The main algorithm implemented in the Python script for UOFB to suppress the long-term orbit drift is the SOFB

* Work supported by U.S. DOE under Contract No. DE-SC0012704.

[†] yhidaka@bnl.gov

component of UOFB and is based on the following equations [5]:

$$\Delta\vec{I}_{\text{SOFB}} = \Delta\vec{I}_{1,\text{SOFB}} + \Delta\vec{I}_{2,\text{SOFB}}, \quad (1)$$

$$\Delta\vec{I}_{1,\text{SOFB}} = R_{\text{SOFB}}^{-1} \cdot \Delta\vec{U}, \quad (2)$$

$$\Delta\vec{I}_{2,\text{SOFB}} = R_{\text{SOFB}}^{-1} \cdot (R_{\text{FOFB}} \cdot \Delta\vec{I}_{\text{FOFB}}), \quad (3)$$

where $\Delta\vec{U}$ is the measured orbit error and $\Delta\vec{I}_{\text{SOFB}}$ is the final slow corrector setpoint change vector, which is the sum of $\Delta\vec{I}_{1,\text{SOFB}}$ (changes that would be applied to correct $\Delta\vec{U}$ when FOFB is not running) and $\Delta\vec{I}_{2,\text{SOFB}}$ (changes that will shift the DC part of fast corrector currents $\Delta\vec{I}_{\text{FOFB}}$ to slow corrector currents). The inverted (usually via singular value decomposition) orbit response matrix (ORM) for the slow correctors is denoted by R_{SOFB}^{-1} , while R_{FOFB} is the ORM for the fast correctors. Finally, to make the application of $\Delta\vec{I}_{\text{SOFB}}$ transparent to FOFB, we must modify the reference orbit of FOFB by $\Delta\vec{W}$ to match the predicted orbit movement [5]:

$$\Delta\vec{W} = R_{\text{SOFB}} \cdot \Delta\vec{I}_{1,\text{SOFB}}. \quad (4)$$

UOFB also includes the functionality of RFFB to compensate the long-term circumference change ΔC with an RF frequency adjustment. Since some of the slow correctors are in the dispersive sections at NSLS-II, the energy change δ induced by ΔC would be absorbed into $\Delta\vec{I}_{\text{SOFB}}$ if we simply use R_{SOFB} as is. To avoid this, we replace Eqs. (2) and (3) with the following:

$$\Delta\vec{I}_{1,\text{SOFB}} = \mathcal{N} \cdot \Delta\vec{\phi}_{1,\text{SOFB}}, \quad (5)$$

$$\Delta\vec{I}_{2,\text{SOFB}} = \mathcal{N} \cdot \Delta\vec{\phi}_{2,\text{SOFB}}, \quad (6)$$

where \mathcal{N} is the null space of the energy response matrix D for $\Delta\vec{I}_{\text{SOFB}}$ such that $D \cdot (\mathcal{N} \cdot \Delta\vec{\phi}) = 0$, i.e., preserving beam energy. The $\Delta\vec{\phi}$ vectors and energy changes can be obtained by solving

$$\begin{bmatrix} \Delta\vec{\phi}_{1,\text{SOFB}} \\ \delta_1/w \end{bmatrix} = Q^{-1} \cdot \Delta U, \quad (7)$$

$$\begin{bmatrix} \Delta\vec{\phi}_{2,\text{SOFB}} \\ \delta_2/w \end{bmatrix} = Q^{-1} \cdot (R_{\text{FOFB}} \cdot \Delta\vec{I}_{\text{FOFB}}), \quad (8)$$

where the total energy compensation needed by the frequency change is given by $\delta = \delta_1 + \delta_2$. The matrix Q is defined as

$$Q = [R_{\text{SOFB}} \cdot \mathcal{N} \quad w\vec{\eta}], \quad (9)$$

with $\vec{\eta}$ and w being the dispersion function and a scaling factor (10 for the NSLS-II storage ring), respectively.

LOCAL BUMPS

UOFB allows correction of local bump offsets and angles. There are 3 types of local bumps at NSLS-II. The first and most prevalent and simplest type is the ID RF-BPM bump. A user has a choice to specify an offset and an angle for a straight populated with IDs. This pair of setpoint values can be readily converted to the target position values

ANALYSIS OF BEAM-INDUCED HEATING OF THE NSLS-II CERAMIC VACUUM CHAMBERS

G. Bassi*, A. Khan, B. Kosciuk, V. Smaluk, R. Todd, C. Hetzel, M. Seegitz, A. Blednykh
Brookhaven National Laboratory, Upton, NY, USA

Abstract

We discuss the impedance and related beam-induced heating issues of the titanium coated ceramic vacuum chambers of the NSLS-II storage ring. The impedance of the two-layer electromagnetic system is calculated assuming a parallel plate model using the well known Field Matching Theory (FMT) and compared with the IW2D code. It is demonstrated that for the chamber coating thickness of interest, all power is dissipated on the titanium coating, with the longitudinal averaged two-dimensional power density independent on the vertical direction and Gaussian-distributed along the horizontal direction with a standard deviation equal to the thickness of the ceramic layer. These properties allow for a simplified model of the power density as input of ANSYS simulations for thermal analysis and comparison with measurements.

INTRODUCTION

To estimate the effects of shielding and impedances on power loss, it is important to find a reasonable thickness of Ti coating on a ceramic chamber [1]. Several accelerators including BESSY-II [2], ESRF [3], HLS [4], MAX-IV [5] and NSLS-II [6] stated overheating of their Ti coated ceramic chambers, which has been reported due to lack of coating uniformity with appropriate thickness or/and poor coating adhesion. Therefore, to avoid failure of ceramic chambers due to thermal stress cracking for a given ceramic shape and loss tangent, a sequence of simulations are usually performed to calculate the EM fields, impedance, heat source distribution, temperature map, and stress field.

At NSLS-II, one of the crucial milestone to achieve the 500 mA design current was the ceramic chambers, because of their overheating. The effect was mitigated by installing additional cooling fans [6, 7].

In this work, we discuss the field matching theory to compute the impedance of multi-layered chambers and compared it with the IW2D code. Further, we discuss the power density distribution for such chambers which is used for thermal analysis in ANSYS.

FIELD MATCHING THEORY

We assume the model shown in Fig. 1. Following the analytical approach adopted in [8], we extended the theory to consider the most general electromagnetic properties of the two-layer (metal-ceramics) system [9]. Assuming the two layers characterized by the complex relative permittivity $\hat{\epsilon}_{1r}$, $\hat{\epsilon}_{2r}$, and complex relative permeability $\hat{\mu}_{r1}$, $\hat{\mu}_{r2}$, where

* gbassi@bnl.gov

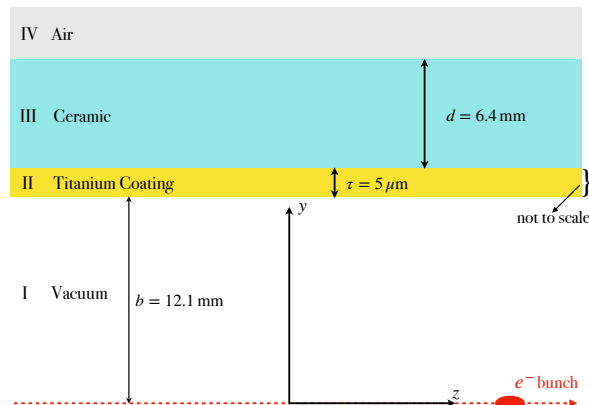


Figure 1: Geometry of the vacuum chamber in planar approximation. All the parameters correspond to the NSLS-II ceramic chamber with the Ti coating thickness value shown for illustration purpose.

the index 1 and 2 refers to the metal and ceramic layer respectively, it can be shown that the longitudinal impedance per unit length can be calculated using the following formula

$$\frac{Z_0^{\parallel}(k)}{L} = -i \frac{Z_0}{4\pi} k \int_{-\infty}^{+\infty} \frac{F(k, q)}{G(k, q)} dq, \quad (1)$$

where F is independent on b and G can be written in the form

$$G(k, q) = w_0 + w_1 \cosh 2bq + w_2 \sinh 2bq, \quad (2)$$

where w_0 , w_1 and w_2 are also independent on b . The functions F , w_0 , w_1 and w_2 are not shown here and are given in [9].

Table 1: Material properties of Ti coated ceramic chambers. The value of the Ti coating thickness is shown for just of the ceramic chambers.

Layers	ρ [Ωm]	$\tan(\delta)$	ϵ'	τ [mm]
Ti	4.3×10^{-7}	0	1	1.21×10^{-3}
Ce	0	1×10^{-3}	10	6.4
Air	2×10^{16}	0	1	Infinity

Benchmarking Field Matching Theory against IW2D simulations

We compare the FM theory with IW2D, a code developed at CERN to compute longitudinal and transverse impedance

NUMERICAL STUDIES OF GEOMETRIC IMPEDANCE AT NSLS-II WITH GdfidL AND ECHO3D

A. Khan*, V. Smaluk, M. Seegitz, R. Todd, A. Blednykh, BNL, NSLS-II, Upton, NY 11973, USA

Abstract

The beam intensity in low-emittance light sources with small gap wigglers and undulators is limited by the effects of short-range wakefields or impedance, especially by the beam-induced heating of the vacuum chamber components. We have cross-checked two electromagnetic solvers, GdfidL and ECHO3D, by simulation of the geometric impedance in the NSLS-II flange absorber and in the bellows to test the consistency and precision of the models.

INTRODUCTION

In modern and future low-emittance light sources, cross-sections of the vacuum chambers of strong focusing magnets and light-generating wigglers and undulators are quite small. Interaction of the electron beam with self-induced electromagnetic fields excited in the vacuum chamber components can have a significant impact on beam quality. The beam coupling impedance quantifies this interaction and allows for the prediction of the dynamics of high-intensity beams. Computation of wake functions and impedances for a given accelerator component is typically a complex task that requires the numerical solution of Maxwell's equations for certain particle distribution.

Even with the most powerful computers, the computation of wake fields of very short bunches in long structures is quite challenging. The choice of simulation code is determined by a variety of factors such as geometry, application, problem type, and computational effort, specifically computational time and memory size. Another key factor is the mesh size of the finite-difference equation solver. Furthermore, the length of wake fields required is an important factor in determining the code and algorithm.

The computed wakefield and its Fourier Transform, the impedance, are used to simulate the collective effects of beam dynamics. To estimate the beam-induced heating, the longitudinal loss factor is used [1]:

$$k_{\text{loss}} = \frac{1}{\pi} \int_0^{\infty} d\omega \operatorname{Re} Z_{\parallel}(\omega) e^{-\omega^2 \sigma_s^2 / c^2} \quad (1)$$

where Z_{\parallel} is the longitudinal impedance and σ_s is the bunch length.

SIMULATION TOOLS

At NSLS-II, we use GdfidL [2] to compute the impedance budget and started to use relatively new fast code ECHO3D [3]. Both codes use an STL input file created by external software as input to describe the geometry of the structure. Then the code creates the mesh, solves the 3D electromagnetic field, and calculates the wake potential using different

numerical techniques. Here is a brief summary of both codes.

GdfidL

GdfidL computes the electromagnetic fields using Yee's finite-difference time-domain method (FDTD). As any numerical mesh approach, this method is affected by an anisotropic numerical dispersion. This means the numerical wave phase speed is slower than the physical one. Hence, the high-energy particles can travel in vacuum faster than their own radiation. The resulting numerical error is comparatively large, especially, in calculations involving short bunches. As it is well known, the FDTD method at the Courant limit is dispersion-free along the grid diagonals and this property can be used effectively in numerical simulations [4]. However, the only reasonable choice, in this case, is to take equal mesh steps in all three directions. This is doable as GdfidL code has the ability to perform parallel computing.

ECHO3D

ECHO3D is based on a low-dispersive numerical technique for calculations of electromagnetic fields in accelerators. This technique allows for the calculation of wakefields of ultra-short bunches in very long structures by eliminating the numerical dispersion in the beam direction [5]. In accelerator applications, the domain of interest is very long in the longitudinal direction and relatively narrow in the transverse plane. The ECHO3D technique allows for giving high-quality results even on a coarse mesh in transverse directions with a large time step. The only limitation of ECHO3D is that it is only thread-parallelized.

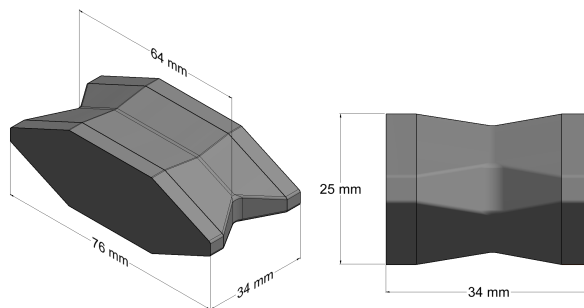


Figure 1: Schematics of the NSLS-II flange absorber.

CONVERGENCE STUDIES

We performed the convergence studies for the NSLS-II flange absorber and bellows using GdfidL and ECHO3D for various bunch distributions. Such cross-checking helps us

* akhan1@bnl.gov

CHARACTERIZATION OF FULLY COUPLED LINEAR OPTICS WITH TURN-BY-TURN DATA *

Y. Li[†], V. Smaluk, R. Rainer, Brookhaven National Laboratory, Upton, NY 11973, USA

Abstract

In future diffraction-limited light source rings, generation of round beam through fully coupled linear optics may be preferable. When the machine tunes approach linear difference resonances, small random errors, such as quadrupole rolls, can result in the desired fully coupled optics. Consequently, some uncertainty exists in such a configuration due to random error distributions. With turn-by-turn data from beam position monitors, the harmonic analysis method is demonstrated for the coupled Ripken Twiss parameters characterization.

INTRODUCTION

For some beamline applications in light source communities, round beam is preferred in place of traditional flat beam. The increased vertical beam size also has the added benefit of increasing the lifetime which is particularly desirable for low emittance storage rings. Considering such benefits, future diffraction-limited light source facilities such as ALS-U [1] and APS-U [2], have plans to operate with a round beam mode. Most light source rings have only horizontal bending magnets, which leads to an intrinsically flat beam. The beam motion can be coupled transversely through either dedicated devices such as skew quadrupoles, or through intrinsic magnet imperfections such as quadrupole roll errors. Conventionally in electron machines, geometrically round beam is obtained by: (1) equally distributing the natural horizontal emittance into the horizontal and vertical planes $\epsilon_x = \epsilon_y$ by shifting the machine's tune close to a linear difference resonance $\nu_x - \nu_y - n = 0$, with n as an integer, (2) adjusting the envelope Twiss functions so that $\beta_x = \beta_y$ at the location of radiators. As achromat lattices are often used for light source rings, it is assumed that the radiators are located at non-dispersive sections.

In the presence of linear coupling, the uncoupled 2-dimensional Courant-Snyder parameterization [3] can be generalized to the 4-dimensional coupled case. One such parameterization was proposed by Ripken et. al [4, 5] and further developed by Lebedev and Bogacz [6]. For our application, we used the harmonic analysis method [7] to characterize the coupled Twiss parameters with turn by turn (TbT) data from Beam Position Monitors (BPM). Some other exact parameterizations were also available such as [8–11], which are equivalent to Ripken's parameters, but not used in our application.

* Work supported by US DOE Office of Science operated by BNL under Contract No. DE-SC0012704.

[†] yli@bnl.gov

RIPKEN PARAMETERIZATION AND HARMONIC ANALYSIS

For a linearly coupled optics, after being kicked, beam performs a free betatron oscillation. The turn-by-turn data observed at the location a Beam Position Monitor (BPM) reads as,

$$\begin{bmatrix} x_i \\ y_i \end{bmatrix} = \begin{bmatrix} \sqrt{2J_1\beta_{1,x}} \cos(i \cdot 2\pi\nu_1 + \phi_{1,x}) + \sqrt{2J_2\beta_{2,x}} \cos(i \cdot 2\pi\nu_2 + \phi_{2,x}) \\ \sqrt{2J_1\beta_{1,y}} \cos(i \cdot 2\pi\nu_1 + \phi_{1,y}) + \sqrt{2J_2\beta_{2,y}} \cos(i \cdot 2\pi\nu_2 + \phi_{2,y}) \end{bmatrix} + \begin{bmatrix} x_{co,i} \\ y_{co,i} \end{bmatrix}, \quad (1)$$

here $J_{1,2}$ are the action variables associated with the initial amplitude, $\beta_{(1,2),(x,y)}$ are the envelope functions for the mode 1 or 2 at the horizontal x or vertical y planes respectively, i is the index of turns, $\phi_{(1,2),(x,y)}$ are the initial phases at the location of the BPM, $x_{co,i}$ and $y_{co,i}$ are the static closed orbit, and $\nu_{1,2}$ are the mode tunes. Depending on the stop-band width (SBW), they are separate with $|\nu_1 - \nu_2| \geq \Delta\nu_{SBW}$.

The analysis of two harmonics of $\nu_{1,2}$ can be implemented by computing their cosine and sine parts,

$$\begin{aligned} C_{(1,2),x} &= \sum_{i=1}^N x_i \cdot \cos(2\pi\nu_{1,2}i) \\ S_{(1,2),x} &= \sum_{i=1}^N x_i \cdot \sin(2\pi\nu_{1,2}i) \\ C_{(1,2),y} &= \sum_{i=1}^N y_i \cdot \cos(2\pi\nu_{1,2}i) \\ S_{(1,2),y} &= \sum_{i=1}^N y_i \cdot \sin(2\pi\nu_{1,2}i) \end{aligned} \quad (2)$$

Substituting Eq. (1) into Eq. (2), and considering a sufficient number of samples N and the orthogonality of trigonometric functions, Eq. (2) can be approximated as,

$$\begin{aligned} C_{(1,2),x} &\approx \frac{N}{2} \sqrt{2J_{1,2}\beta_{(1,2),x}} \cos \phi_{1,2} \\ S_{(1,2),x} &\approx -\frac{N}{2} \sqrt{2J_{1,2}\beta_{(1,2),x}} \sin \phi_{1,2} \\ C_{(1,2),y} &\approx \frac{N}{2} \sqrt{2J_{1,2}\beta_{(1,2),y}} \cos \phi_{1,2} \\ S_{(1,2),y} &\approx -\frac{N}{2} \sqrt{2J_{1,2}\beta_{(1,2),y}} \sin \phi_{1,2} \end{aligned} \quad (3)$$

The amplitudes $A_{(1,2),(x,y)}$ of the betatron oscillation observed at each BPM can be obtained as,

$$\begin{aligned} A_x &= \sqrt{2J_{1,2}\beta_{(1,2),x}} = \frac{2}{N} \sqrt{C_{(1,2),x}^2 + S_{(1,2),x}^2} \\ A_y &= \sqrt{2J_{1,2}\beta_{(1,2),y}} = \frac{2}{N} \sqrt{C_{(1,2),y}^2 + S_{(1,2),y}^2} \end{aligned} \quad (4)$$

and the phases as well,

$$\phi_{(1,2),x} = -\tan^{-1} \frac{S_{(1,2),x}}{C_{(1,2),x}}, \quad \phi_{(1,2),y} = -\tan^{-1} \frac{S_{(1,2),y}}{C_{(1,2),y}}, \quad (5)$$

here the quadrant of the phase ϕ depends on the signs of C and S .

The amplitudes in Eq. (4) are mixed with the global actions $J_{1,2}$, and s -dependent $\beta_{(1,2),(x,y)}$. In order to extract

6-D ELEMENT-BY-ELEMENT PARTICLE TRACKING WITH CRAB CAVITY PHASE NOISE AND WEAK-STRONG BEAM-BEAM INTERACTION FOR THE HADRON STORAGE RING OF THE ELECTRON-ION COLLIDER*

Y. Luo[†], J. S. Berg, M. Blaskiewicz, C. Montag, V. Ptitsyn, F. J. Willeke, D. Xu
Brookhaven National Laboratory, Upton, NY, USA

Y. Hao, Facility for Rare Isotope Beams, Michigan State University, East Lansing, MI, USA

J. Qiang, Lawrence Berkeley National Laboratory, Berkeley, CA, USA

V. S. Morozov, Oak Ridge National Laboratory, Oak Ridge, TN, USA

H. Huang, T. Satogata, Thomas Jefferson National Accelerator Facility, Newport News, VI, USA

Abstract

The Electron Ion Collider (EIC) presently under construction at Brookhaven National Laboratory will collide polarized high energy electron beams with hadron beams with luminosities up to $1 \times 10^{34} \text{cm}^{-2} \text{s}^{-1}$ in center mass energy range of 20-140 GeV. Crab cavities are used to compensate the geometric luminosity due to a large crossing angle 25 mrad in the EIC. It was found that the phase noise in crab cavities will generate a significant emittance growth for the hadron beams. The phase noise tolerance from the analytical calculation is very small for the Hadron Storage Ring (HSR) of the EIC. In this article, we present our preliminary numerical simulation results with a 6-d symplectic particle tracking to determine the proton emittance growth rate with crab cavity phase noise and beam-beam interaction for the HSR.

INTRODUCTION

The Electron Ion Collider (EIC) presently under construction at Brookhaven National Laboratory will collide polarized high energy electron beams with hadron beams with luminosities up to $1 \times 10^{34} \text{cm}^{-2} \text{s}^{-1}$ in the center mass energy range of 20-140 GeV. To achieve such a high luminosity, we adopt high bunch intensities for both beams, small transverse beam sizes at the interaction point (IP), a large crossing angle 25 mrad, and a novel strong hadron cooling in the Hadron Storage Ring (HSR) of the EIC [1]. Crab cavities are installed on both sides of IP in each ring to create a local closed horizontal crab dispersion bump to restore head-on collision condition.

For the HSR, the frequency of the main crab cavities is 197 MHz. The maximum crab cavity voltage on either side of IP is about 35 MV, which is provided by 4 cells of 197 MHz crab cavities in two cryomodules. To further straighten the bunch shape, second harmonic crab cavities with a frequency 394 MHz are installed on both sides of IP too. There are 2 cells of 394 MHz crab cavities in one cryomodule on each side, which provide a total voltage about 5 MV.

* Work supported by Brookhaven Science Associates, LLC under Contract No. DE-SC0012704 with the U.S. Department of Energy.

[†] yluo@bnl.gov

It has been found that phase noise in crab cavities will generate a significant emittance growth for hadron beams [2]. Experiments were also performed in CERN SPS and confirmed this growth [3]. Analytically, the emittance growth can be calculated with

$$\frac{d\epsilon_x}{dt} = \frac{\beta_x^{cc}}{N_{cav}} \left(\frac{eV_{cav} f_{rev}}{2E_b} \right)^2 C_{\Delta\phi}(\sigma_\phi) \frac{2\sigma_{\Delta\phi}^2}{f_{rev}} \quad (1)$$

where N_{cav} is the number of crab cavities, β_x^{cc} the β function at crab cavities, V_{cav} the voltage per cavity, E_b the beam energy, f_{rev} the revolution frequency, $\sigma_{\Delta\phi}^2$ the total beam sampled phase noise power, $C_{\Delta\phi}$ the crab cavity's phase power density spectrum, $\Delta\phi$ the bunch length measured in RF phase.

For the HSR, to keep a physics store for around 10 hours, we need to have the proton emittance growth less than a few %/hour. Based on Eq. (1), for example, to have a 10%/hour horizontal emittance growth rate, the crab cavity phase noise level $\sigma_{\Delta\phi}$ should be less than 2×10^{-6} rad, which is more than one to two orders in magnitude smaller than that current technology can deliver.

In the following, we will carry out numerical simulation to determine the proton emittance growth with crab cavity phase noise with code SimTrack [4]. The beam and machine parameters for the collision mode involving 275 GeV protons and 10 GeV electrons are used [5]. Instead of using a simplified ring model, we adopt the latest HSR design lattice. The purpose of this study is to verify the analytical estimate of phase noise tolerance and to include the effects of beam-beam interaction, nonlinear magnetic field errors in the interaction region (IR), magnet alignment roll errors, and so on.

SIMULATION SETUP

For the present HSR design lattice, the horizontal betatron phase advance between the crab cavities on both sides of IP is 175 degrees and therefore the horizontal crab dispersion bump is not locally closed. In simulation, we adjust the voltages of both side crab cavities to obtain the design horizontal crab dispersion $dx/dz = 12.5 \times 10^{-3}$ and $dx'/dz = 0$ at the IP. For this temporary setting, there will be horizontal crab dispersion leakage in the rest of ring.

RADIO FREQUENCY SYSTEM OF NSLS-II INJECTOR LINAC FOR MULTI-BUNCH-MODE BEAMS*

H. Ma[†], J. Rose, C. Sorrentino, Brookhaven National Laboratory, Upton, NY, USA

Abstract

The Multi-Bunch Mode (MBM) beam injection operation of NSLS-II LINAC requires a beam-loading compensation for its RF field. That requirement has a significant impact on its radio frequency system (RF), in both the low-level RF control and the high-power klystron transmitters. Specifically, for the RF control, it requires the output vector modulation have enough bandwidth to be able to respond the transients by the MBM beams of 40 to 300 ns long. For the high-power RF transmitters, it requires the klystrons operate in a near-linear region to be able to respond the linear RF control for the beam-loading compensation, which means a need of ~30% extra RF power overhead, compared to the single-bunch mode operations. The digital signal processing and the network configuration for the RF controllers are also the important areas in the implementation. The original system design was driven by the MBM beam operation requirements, and our system upgrade today continues to be guided by the same principles.

SYSTEM OVERVIEW AND DESIGN CONSIDERATIONS

LINAC Design Parameters

The NSLS-II LINAC is a 2.998 MHz, 200 MeV Pre-Injector to the following 3 GeV Booster Synchrotron which in turn serves as the injector to the final Storage Ring. It delivers minimum 0.5 nC of charge in Single-Bunch Mode, and up to 15 nC in Multi-Bunch Mode (MBM). The length of an MBM varies from 20 to 150 beam bunches, or 40 to 300 ns in time. The basic parameters are listed in Table 1 below, and more details can be found in Refs. [1, 2].

Table 1: NSLS-II LINAC Basic Parameters

Nominal Energy	200 MeV
Minimum Energy	170 MeV
Repetition rate	Single-shot to 10 Hz
Long Pulse Mode	
Pulse train length	40 – 300 ns
Bunch numbers at 500 MHz rep. rate	20 – 150
Maximum charge per pulse train	15 ns
Relative charge variation between bunches	< 10%

* This manuscript has been authored by Brookhaven Science Associates, LLC under Contract No. DE-SC0012704 with the U.S. Department of Energy.

[†] hengjie@bnl.gov

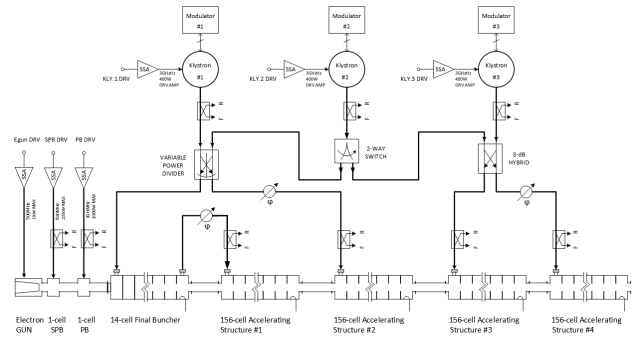


Figure 1: NSLS-II LINAC High-Power RF Configuration.

High-Power Klystron Transmitter System Design for High Operation Availability

The LINAC RF chain starts with the RF modulating grid PA for a YU-171 Electron Gun, followed by a 500 MHz Sub-Harmonic Buncher, a 3 GHz Pre-Buncher and a Final Buncher as the LINAC front-end. The following four traveling-wave structures LINAC powered by two 45 MW klystrons bring the beam energy to the required 200 MeV [1]. The configuration of the LINAC high-power RF system is shown in Figure 1. There are three 3 GHz, 45 MW klystrons in this system, two of which are needed for running the 200 MeV routine operation. The klystron station #2 in the middle functions as a standby hot spare, which can be readily switched in the system to substitute Klystron #1 or #3 should either one fail.

The 45 MW klystrons (Canon E37302A) are powered by three COTS high-performance, solid-state switching modulators (SSM) by ScandiNova [3]. These SSM's produce the klystron beam HV pulses that have a very smooth flat-top, which helps the LINAC beam energy jitter and dispersion stay within the specifications.

Digital RF Transmitter Front-end

The architecture of the digital RF controller as shown in Figure 2 is similar to that of standard base-station SDR (Software-defined-Radio), comprised of a digital receiver front-end Rx for the measurement and monitoring the RF field vectors in the cavities, and a digitally-controlled RF vector modulator front-end Tx at the transmitter input

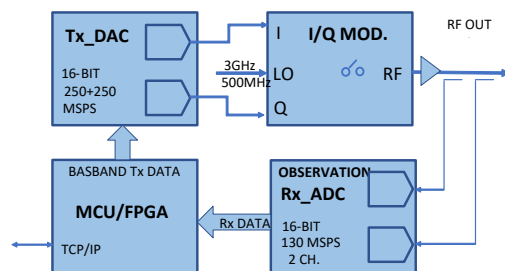


Figure 2: LINAC RF control front-end architecture.

A NEW PCB ROTATING COIL AT NSLS-II*

M. Musardo[†], J. Avronsart, F. DePaola, L. Doom, R. Faussete, F. Lincoln, S. Sharma, T. Tanabe
 Brookhaven National Laboratory, Upton, NY, USA
 A. Banerjee, Stony Brook University, NY, USA
 C. L. Doose, A. K. Jain, Argonne National Laboratory, Lemont, IL, USA
 D. Assell, J. DiMarco, Fermilab, Batavia, IL, USA

Abstract

Several R&D projects are underway at NSLS-II towards an upgrade of its storage ring with a new lattice that will use high field magnets with small bores of 16-22 mm. A large fraction of the high field magnets is expected to be of permanent magnet technology that will require precise magnetic measurements and field harmonics corrections. A new magnetic measurement bench has been built based on a printed circuit board (PCB) coil of 12 mm diameter and 270 mm active length. This PCB coil has the capability of measuring field quality to a level of 10 ppm of the main field up to the 15th harmonic with a sensitivity between 0.01 m² and 0.02 m² at the reference radius of 5 mm. This paper will describe the main features of the rotating coil bench and discuss the measurement results of a permanent-magnet Halbach quadrupole of 12.7 mm bore diameter.

INTRODUCTION

The National Synchrotron Light Source II (NSLS-II) is a 3 GeV, 500 mA, high-brightness synchrotron light source facility at the Brookhaven National Laboratory. A double-bend achromat (DBA) lattice was used for the storage ring.

A new lattice design based on a Complex Bend concept has been proposed for the future NSLS-II upgrade [1-2]. This new novel lattice consists of combined-function high-gradient quadrupoles to provide bending and focusing in the same physical space. This approach promises a reduction of the horizontal electron beam emittance and, consequently, a significant increase of the spectral brightness [3]. In order to demonstrate the Complex Bend approach, a prototype will be built by using high-gradient permanent magnet quadrupoles (PMQs) [4-6]. The PCB rotating coil system has been built to verify the field quality of these PMQs.

PCB ROTATING COIL

A 12-mm diameter PCB-based rotating coil was designed at Fermilab with specifications of measuring 10 ppm of the main field (0.1 “unit”) up to the 15th harmonic at the reference radius of 5 mm. It is the smallest PCB coil built to date with an active coil length of 270 mm and an overall probe length of 390 mm, capable to measure both quadrupole and sextupole magnets. The main parameters are shown in Table 1. The PCB rotating coil measurement bench, shown in the Fig. 1, uses essentially the same

hardware and software for the motion control as the rotating wire system [7].

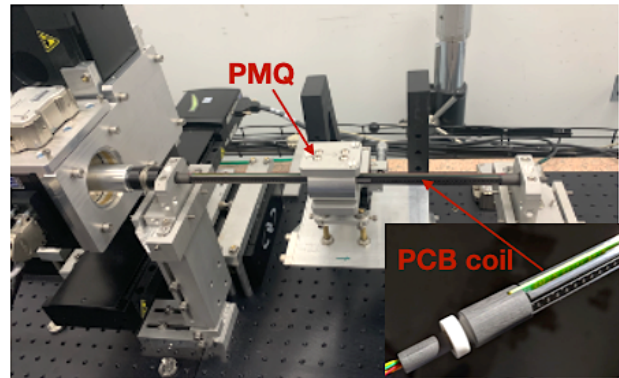


Figure 1: PCB rotating coil measurement bench.

This new bench has interchangeable supports to perform both rotating coil measurements, for field harmonics characterization, and rotating wire to determine the magnetic field center of the magnet with an RMS error less than 5 μm. This measurement system is based on the hardware design and LabView software developed for APS-U [8]. As shown in Fig. 1 the rotary stage is mounted on XYZ linear stages which permits the probe to be positioned within the aperture of the magnet under test. Three PCB coils were built. Each coil is encased in carbon-fiber supports to ensure sufficient stiffness against vibration and sag. The outer diameter of the PCB coil-structure is 12 mm. The ends have 6-mm outer/ 3-mm inner diameters to accommodate the 1.8 mm thick printed circuit board, wiring and ABEC 5 all-ceramic bearings.

Table 1: PCB Coil Parameters

Probe Diameter	12 mm
Reference Radius	5 mm
Probe Active Length	270 mm
Length of each end stem	25 mm
Total Probe Length	350 mm
Bucking	DB, DQB, DQSB

These PCB coils provide 4 signals: un-bucked (UB), dipole bucked (DB), dipole-quadrupole bucked (DQB) and dipole-quadrupole-sextupole bucked (DQSB) in order to ensure minimal spurious harmonics in measurements of both quadrupole and sextupole magnets. The quadrupole gradient measured with DB winding has an accuracy at the level of 0.1%-0.2%.

* Work supported by DOE under contract DE-SC0012704.

[†] Email address musardo@bnl.gov

PROTON-ELECTRON FOCUSING IN EIC RING ELECTRON COOLER*

S. Seletskiy[†], A.V. Fedotov, D. Kayran, J. Kewisch
Brookhaven National Laboratory, Upton, NY, USA

Abstract

The Electron Ion Collider (EIC) requires a cooling of protons at the top energy. The Ring Electron Cooler (REC) is a suitable option for such a cooling. In this paper we consider an effect of a proton-electron space charge (SC) focusing on the quality of the electron beam in the REC. We show that, with properly adjusted parameters of the Ring Electron Cooler, the SC focusing in the REC cooling section does not significantly affect the cooler performance.

INTRODUCTION

A recent success of Low energy RHIC electron cooler (LEReC) [1-6], the first RF-based non-magnetized electron cooler, demonstrated that operational electron cooling [7] does not require e-beam magnetization and can be achieved with a bunched electron beam. While LEReC operated at $\gamma = 4.1$ and $\gamma = 4.9$, LEReC approach becomes especially attractive for high energy electron coolers because it significantly simplifies the engineering aspects of a cooler design. For example, to cool protons in the Electron Ion Collider [8] at $\gamma = 293$ one can use an electron storage ring with non-magnetized electron bunches [9].

In electron coolers electrons co-propagate with a hadron beam with the same average velocity in a straight section of the storage ring, called a cooling section (CS). A hadron interacts with electrons in a CS via Coulomb force, which introduces dynamical friction [10] acting on each hadron. Over many revolutions in the accelerator the average friction reduces both the transverse and the longitudinal velocity spread of hadrons, thus increasing the 6-D phase space density of the bunch.

In a non-magnetized cooler, the cooling rate scales as $1/\sigma_\theta^2$, where $\sigma_\theta = \sigma_{\theta x} = \sigma_{\theta y}$ is the electron beam angular spread [11]. Therefore, it is important to carefully evaluate all effects which can influence the e-beam emittance.

High intensity proton bunches in the cooling section produce an additional space charge focusing on the electron beam. This proton-electron (p-e) focusing can significantly affect beam dynamics in the REC [12].

In this paper we show that for the most recent parameters of the REC the effect of p-e focusing on the electron beam emittance is tolerable. The current REC parameters relevant for this study are given in Table 1.

BEAM DYNAMICS WITH p-e FOCUSING

General Considerations

Consider a Gaussian, circularly symmetric transverse density distributions for both bunches in the cooling

section. The equation of motion of an individual electron in this case is [13]:

$$r'' = \frac{K_e}{r} \left[\left(1 - e^{-\frac{r^2}{2\sigma_e^2}} \right) - \frac{I_p}{I_e} \left(1 - e^{-\frac{r^2}{2\sigma_p^2}} \right) \right] - \kappa r \quad (1)$$

where generalized perveance $K_e = 2I_e/(I_A\gamma^3)$, Alfven current $I_A \approx 17$ kA, indexes “e” and “p” signify that respective parameter is given for an electron or a proton beam, I is a bunch’s peak current, $\sigma = \sigma_x = \sigma_y$ is the rms transverse size of the bunch, and the term κr represents a magnetic focusing.

Table 1: Optimized REC Parameters

Parameter	Value
γ -factor	293
Number of protons per bunch	6.88e10
rms p-bunch length [cm]	6
rms p-bunch momentum spread	6.6e-4
p-bunch geometric emittance (x/y) [nm]	9.6/1.5
p-bunch CS β -functions (x/y) [m]	200/1200
Number of electrons per bunch	1.4e11
rms e-bunch length [cm]	6
rms e-bunch momentum spread	8.9e-4
e-bunch geometric emittance (x/y) [nm]	15/15
e-bunch CS β -functions (x/y) [m]	100/100
CS length [m]	170
REC circumference [m]	426
REC tunes (x/y)	59.92/59.85

Defocusing caused by the self SC of the e-bunches alleviates the p-e focusing in the cooling section. We are dropping the self SC part in (1), thus intentionally overestimating the effect of the p-e focusing on beam dynamics. Then, we can rewrite (1) as:

$$\begin{aligned} x'' &= \frac{K_p}{x^2+y^2} \left(1 - e^{-\frac{x^2+y^2}{2\sigma_p^2}} \right) x - \kappa x \\ y'' &= \frac{K_p}{x^2+y^2} \left(1 - e^{-\frac{x^2+y^2}{2\sigma_p^2}} \right) y - \kappa y \end{aligned} \quad (2)$$

where $K_p = K_e I_p / I_e$.

We introduce Courant-Snyder variables ($\xi_{h,v}$, $\zeta_{h,v}$) for horizontal and vertical motion of an electron. For example, for horizontal direction:

$$\xi_h = \frac{x}{\sqrt{\beta}}; \quad \zeta_h = \frac{x\alpha}{\sqrt{\beta}} + x'\sqrt{\beta} \quad (3)$$

* Work supported by the US Department of Energy under contract No. DE-SC0012704.

[†] seletskiy@bnl.gov

PROGRESS ON CONVERGENCE MAP BASED ON SQUARE MATRIX FOR NONLINEAR LATTICE OPTIMIZATION*

L. H. Yu†, Y. Hidaka, F. Plassard, V. Smaluk, Brookhaven National Laboratory, Upton, NY, USA
Y. Hao, Michigan State University, East Lansing, MI, USA

Abstract

We report progress on applying the square matrix method to obtain in high speed a "convergence map", which is similar but different from a frequency map. We give an example of applying the method to optimize nonlinear lattice for NSLS-II. The convergence map is obtained from solving nonlinear dynamic equations by iteration of the perturbation method and studying the convergence. The map provides information about the stability border of the dynamic aperture. We compare the map with the frequency map from tracking. The result in our example of nonlinear optimization of NSLS-II lattice shows the new method may be applied in nonlinear lattice optimization, taking the advantage of the high speed (about 30 to 300 times faster) to explore horizontal, vertical, and the off-momentum phase space.

INTRODUCTION

A study of the long-term behavior of charged particles in storage rings is one of the topical applications of nonlinear dynamics. The analysis of the particle behavior is based on many iterations of the particle phase space transformation by the one-turn map representing the storage ring. The most accurate and reliable numerical approach is particle tracking in a magnet lattice model with appropriate integration methods. This approach is implemented in many computer codes. However, particle tracking is very demanding to computing resources, so parallel codes and long computation time are often required.

For fast analysis, however, one would like a more compact representation of the one-turn map out of which to extract relevant information. Among many approaches to this issue, we may mention canonical perturbation theory, Lie operators, power series, normal form, etc. [1–3]. The results are often expressed as polynomials. However, for increased perturbation, near resonance or for large oscillation amplitudes, these perturbative approaches often have insufficient precision. The stability analysis of the beam trajectory and calculation of the dynamic aperture requires an accurate solution of the nonlinear dynamic equation. Hence there is a need to extract information about long-term particle behavior from the one-turn map based on these polynomials with high precision and high speed.

The square matrix analysis [4] has a good potential to explore this area. On a basis of the square matrix method, we developed a novel technique of "convergence map", which is a much faster alternative to the tracking-based frequency map [5]. The convergence map provides

information about the dynamic aperture and can be applied to nonlinear lattice optimization, taking the advantage of the high speed (30 to 300 times faster than particle tracking). The computation speed ratio is larger for complex lattices with low periodicity, such as particle colliders.

SQUARE MATRIX METHOD FOR ANALYSIS OF NONLINEAR DYNAMICS

A novel method to analyze nonlinear dynamic systems using the square matrix has been developed at NSLS-II few years ago [4]. We showed that for a nonlinear dynamic system representing particle motion in a storage ring, we can construct a square matrix. Using linear algebra, the Jordan decomposition of the square matrix provides a tool for studying the fluctuation of particle oscillation frequency, the stability of the particle trajectories, and dynamic aperture. Thus, the analysis of a nonlinear dynamic system can be greatly simplified using linear algebra. The square matrix method is general and may be applied to other areas, for example, nonlinear dynamics in physics and astronomy.

The main feature of the new method is that we can achieve high order in one step. This is a significant advantage when compared with canonical perturbation theory and normal form, where the calculation is carried out order-to-order by a complicated iteration process. We also showed that the stability and precision of the Jordan decomposition are ensured by scaling the variables, and by removing the high-power invariant monomial terms.

We demonstrated that the action variable remains nearly constant up to near the boundary of the dynamic aperture and resonance lines. They successfully reproduce both the correct phase space structure and the betatron tune shift with amplitude. In addition, we tested several measures of the stability of particle trajectories and their betatron tunes.

The developed theory shows good potential in theoretical understanding of a complex dynamic system to guide the optimization of dynamic aperture in circular accelerators. Using analysis of the one-turn map to narrow down the searching range of the parameter space before the final confirmation by tracking, the new method can significantly speed up the optimization.

CONVERGENCE MAP VS PARTICLE TRACKING

We introduce a convergence map calculated using action-angle variables in the form of polynomials provided by a square matrix, which is derived from the one-turn map for an accelerator lattice. Since the iterations leading to the solution of the nonlinear dynamic equations expressed by these action-angle variables can be carried out by Fourier transform, the computation speed is very high. Using the

* Work supported by the U.S. Department of Energy, Contract No. DE-SC0012704.

† email address: lhyu@bnl.gov

TIME-RESOLVED EXPERIMENTS AT NSLS II: MOTIVATION AND MACHINE CAPABILITIES*

G. Wang[†], G. Bassi, B. Bacha, G.L. Carr, X. Chen, Y. Hidaka, W. Hu, Y. Hu, G. Kwon,
D. Leshchev, Y. Li, C. Mazzoli, D. Padrazo, R. Rainer, J. Rose, J. Sadowski,
V. Smalyuk, Y. Tian, L. Wiegart, G. Williams, X. Xiao, X. Yang
Brookhaven National Laboratory, Upton, NY 11973, USA

Abstract

NSLS-II is a 3-GeV third-generation synchrotron light source at Brookhaven National Lab. The storage ring has been in routine operations for over six years and hosts 28 operating beamlines. The storage ring performance has continuously improved, including 500-mA with limited insertion devices closed, and routine 400-mA top off operation with 90% uniform filling pattern. Recently, we are exploring different operation modes, uniform multi single-bunch mode, and camshaft mode with a high single-bunch charge, to support timing-resolved user experiments. In this paper, we explore the potential for scientific experiments using the pulsed nature of the NSLS, summarize the user requirements on the beam parameters and the progress of accelerator studies.

NATIONAL SYNCHROTRON LIGHT SOURCE II STATUS

The National Synchrotron Light Source II (NSLS-II) is a 3 GeV, ultra-small emittance (H: 1 nm-rad and V: 8 pm-rad), high brightness third generation light source at Brookhaven National Laboratory. It is to deliver a broad range of light, from IR to hard X-ray, with the brightness of 10^{22} photons/s/mm²/mrad²/0.1%BW to 60-70 beam lines at full built-out.

The storage ring was commissioned in 2014 and began its routine operations in the December of the same year [1, 2]. Figure 1 shows the trend of beam current increment for operation and machine study, operation reliability and ID beamline sources commissioning. Over the past years, beam current and operation IDs sources have been steadily increased, while reach and maintain beam in high reliability, >95% [3-6]. After three RF cavities in operation, we have machine runs at 400 mA (project goal 500 mA) with 2.5 minutes periodic top off injection to maintain SR current stability within $\pm 0.5\%$. Meanwhile we have demonstrated 500 mA in 2019 and performed several radiation survey insertion device and front end to prepare for high current operation since then. Now, there are 28 beamlines under construction. We support ~5000 hrs operation time per years and keep the reliability above 95%.

With more and more operation beamlines running in mature state, a discussion on possibilities for timing-resolved experiments at the NSLS-II rings has been initiated among

accelerator and beamline scientists. A taskforce team were formed since Mar. 2020 to identify science applications that will require the use of SR pulse structures at NSLS-II, define a set of operation modes at NSLS-II to server both high-intensity and timing experiments and specify the instrumentation needs in order to enable these special experiments for accelerator to deliver such timing mode, availability of timing signals at beamlines, tuneable delay lines etc.

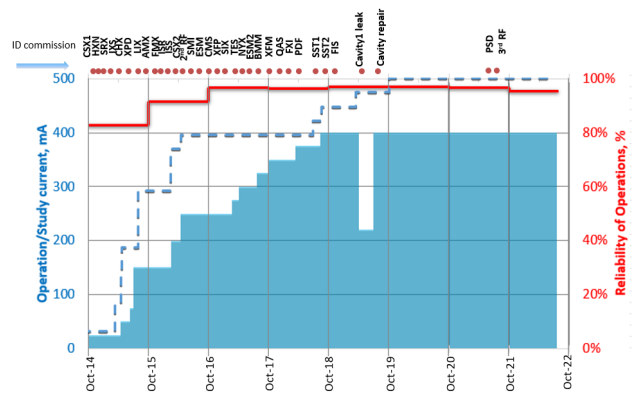


Figure 1: NSLS-II operation trend.

So far, seven beamlines have explored the potential timing-based experiments, including 1) full field imaging of structure in CDI beamline, 2) timing resolved Infra-Red science of materials in FISMET beamline, 3) timing resolved magnetization dynamics imaging in ESM beamline, 4) timing resolved pump-probe STXM to study the linear and nonlinear, magnetic excitations in magnetic micro- and nano-structures in SXN beamline, 5) timing resolved x-ray spectroscopy in ISS beamline, 6) timing resolved experiment for collective dynamics in CSX beamline and 7) high energy x-ray scattering in PDF beamline.

SCIENTIFIC CASES FOR TIMING MODES AT NNSLS-II

Time-resolved studies probe the dynamical properties of systems after being excited away from equilibrium. Exposure to light is among the most common methods for driving a system out of equilibrium—with the photon energy (wavelength) determining the nature of the initial excitation—and serves as an illustrative example of the more general “pump-probe” methodology.

Using a pulsed source for both the excitation—the “pump”—and interrogation—the “probe”—allows the study of fast processes. The light from a synchrotron storage ring is intrinsically pulsed due to the bunching of the stored electrons. We explore the potential for scientific

*This manuscript has been authored by Brookhaven Science Associates, LLC under Contract No. No. DE-SC0012704 with the U.S. Department of Energy.

[†] gwang@bnl.gov

EXTENDED SOFT-GAUSSIAN CODE FOR BEAM-BEAM SIMULATIONS*

D. Xu[†], Y. Luo, C. Montag, Brookhaven National Laboratory, Upton, NY, USA
Y. Hao, Michigan State University, East Lansing, MI, USA
J. Qiang, Lawrence Berkeley National Laboratory, Berkeley, CA, USA

Abstract

Large ion beam emittance growth is observed in strong-strong beam-beam simulations for the Electron-Ion Collider (EIC). As we know, the Particle-In-Cell solver is subject to numerical noises. As an alternative approach, an extended soft-Gaussian code is developed with help of Hermite polynomials in this paper. The correlation between the horizontal and the vertical coordinates of macro-particles is considered. The 3rd order center moments are also included in the beam-beam force. This code could be used as a cross check tool of PIC based strong-strong simulation.

INTRODUCTION

The beam-beam interaction is one of the most important phenomena to limit the luminosity in colliders. Beam-beam simulation is an essential tool to study beam-beam effects. Two models are often used in simulations: weak-strong and strong-strong. The weak-strong model is used to study the single particle dynamics, while the strong-strong model is used to study the coherent motion.

The particle-in-cell (PIC) approach is widely used in strong-strong simulation. This kind of method is self-consistent because the electromagnetic field is obtained by solving the Poisson equation with the updated charge distribution during beam collisions [1]. However, the PIC based strong-strong simulation is subject to numerical noise. The discrepancy between the weak-strong and strong-strong simulation for Electron-Ion Collider (EIC) has been found. It is important to understand the difference in case there is some coherent mechanism shadowed by the large numerical noise.

The soft-Gaussian model is a possible way to cross-check the PIC results. In the soft-Gaussian model, both beams are assumed to be an ideal Gaussian distribution during the collision. The second-order moments σ_x and σ_y are calculated from macro particles. Although the soft-Gaussian model is not self-consistent, the coherent motion is considered during the collision.

However, there is a possibility to over-simplify the problem in the soft-Gaussian model. In this paper, we develop a code to extend the soft-Gaussian model. In the extended soft-Gaussian model (ESG), the 3rd order moments are also taken into account in the calculation of electromagnetic field. The ESG would be a better benchmark tool for strong-strong simulation.

INCLUDING BEAM TILT

The beam-beam potential generated by an upright bi-Gaussian distribution is

$$U_g = \frac{Q_1 Q_2 N r_0}{\gamma_0} \int_0^\infty du \frac{\exp\left(-\frac{x^2}{2\sigma_x^2+u} - \frac{y^2}{2\sigma_y^2+u}\right)}{\sqrt{2\sigma_x^2+u}\sqrt{2\sigma_y^2+u}}, \quad (1)$$

where N is the total particle number, $r_0 = e^2/(4\pi\epsilon_0 mc^2)$ the classical radius, γ_0 the relativistic factor of the test particle, $Q_{1,2}$ the charge numbers of particles from two colliding bunches, and $\sigma_{x,y}$ are the RMS beam sizes at the collision point.

The deflection angle from the above bi-Gaussian beam can be obtained from the well-known Bassetti-Erskine formula [2],

$$U_y + iU_x = -\frac{Q_1 Q_2 N r_0}{\gamma_0} \sqrt{\frac{2\pi}{\sigma_x^2 - \sigma_y^2}} \left[w\left(\frac{x + iy}{\sqrt{2(\sigma_x^2 - \sigma_y^2)}}\right) - w\left(\frac{\frac{\sigma_y}{\sigma_x}x + i\frac{\sigma_x}{\sigma_y}y}{\sqrt{2(\sigma_x^2 - \sigma_y^2)}}\right) \exp\left(-\frac{x^2}{2\sigma_x^2} - \frac{y^2}{2\sigma_y^2}\right) \right] \quad (2)$$

where $U_{x,y}$ is the abbreviation of the derivative $\partial U_g / \partial y$ or $\partial U_g / \partial x$, x, y the coordinates of the test particle, and $w(z)$ is the Faddeeva function,

$$w(z) \equiv \exp(-z^2) \left(1 + \frac{2i}{\sqrt{\pi}} \int_0^z dt e^{t^2}\right) \quad (3)$$

In the long term tracking, both beams may tilt slowly in the $x-y$ planes because of the nonlinear coupling of beam-beam force. As a result, the non-zero σ_{xy} should be considered for more accurate calculation.

A general 2D Gaussian distribution can be described by its Σ matrix,

$$\Sigma = \begin{bmatrix} \sigma_{xx} & \sigma_{xy} \\ \sigma_{xy} & \sigma_{yy} \end{bmatrix} \quad (4)$$

$$\phi_g(x, y) = \frac{1}{2\pi\sqrt{\det \Sigma}} \exp\left[-\frac{1}{2}(x, y) \Sigma^{-1} \begin{pmatrix} x \\ y \end{pmatrix}\right], \quad (5)$$

where $\phi_g(x, y)$ is the 2D distribution in (x, y) plane. To use the Bassetti-Erskine formula Eq. (2), we can apply a rotation on the coordinates (x, y) ,

$$A = \begin{bmatrix} \cos \theta & \sin \theta \\ -\sin \theta & \cos \theta \end{bmatrix}, \quad \begin{bmatrix} \bar{x} \\ \bar{y} \end{bmatrix} = A \begin{bmatrix} x \\ y \end{bmatrix}, \quad (6)$$

* Work supported by Brookhaven Science Associates, LLC under Contract No. DE-SC0012704 with the U.S. Department of Energy.

[†] dxu@bnl.gov

LOCALIZED BEAM INDUCED HEATING ANALYSIS OF THE EIC VACUUM CHAMBER COMPONENTS*

M. Sangroula[†], J. Bellon, A. Blednykh, D. Gassner, C. Hetzel,
 C. Liaw, C. Liu, P. Thieberger, S. Verdu-Andres
 Brookhaven National Laboratory, Upton, NY 11973, USA

Abstract

The Electron-Ion Collider (EIC), to be built at Brookhaven National Laboratory (BNL), is designed to provide a high electron-proton luminosity of $10^{34} \text{ cm}^{-2} \text{ sec}^{-1}$. One of the challenging tasks for the Electron Storage Ring (ESR) is to operate at an average beam current of 2.5 A within 1160 bunches with a ~ 7 mm rms bunch length. The Hadron Storage Ring (HSR) will accumulate an average current of 0.69 A within 290 bunches with a 60 mm rms bunch length for the worst-case scenario in terms of thermal heating, although it will have 1 A with 1160 bunches for the high luminosity. Both rings require impedance budget simulations. The intense e-beam in the ESR can lead to the overheating of vacuum chamber components due to localized metallic losses and synchrotron radiation. This paper focuses on the beam-induced heating analysis of the ESR vacuum components including BPM, standard RF shielded bellows, and gate valve. To perform thermal analysis, the resistive loss on individual components is calculated with CST and then fed to ANSYS to determine the temperature distribution on the vacuum components. Preliminary results suggest that active water cooling will be required for most of the ESR vacuum components. Similar approach is applied for the HSR vacuum components. The thermal analysis of the HSR stripline injection kicker is presented.

INTRODUCTION

The intense beams of the ESR and HSR produce a large amount of beam-induced resistive losses that can lead to the overheating of EIC [1–3] vacuum chamber components. The impedance analysis of both the ESR and HSR vacuum chamber components can be found in [4–6]. In this paper, we present the thermal analysis of those components. To perform thermal analysis, the resistive loss on individual components is calculated using the 3D electromagnetic code CST [7], whose result is fed into the another code ANSYS [8] to determine the temperature distribution.

ESR COMPONENTS

Most of the ESR vacuum chamber components have elliptical profile having 80 mm horizontal, and 36 mm vertical dimension. These components experience maximum local heating with an average beam current of 2.5 A (27.6 nC per bunch) from 1160 bunches that are only 7 mm long. Therefore, we used these beam parameters to calculate the local

metallic losses for all the ESR components. We present our thermal analysis due to a central beam (no lateral offset) for the BPM, standard RF shielded bellows, and gate valve, which we discuss in the following subsections. In some regions of the ESR, beam experiences slight lateral offset for which the corresponding thermal analysis need to be done.

Beam Position Monitor (BPM)

The ESR BPM button design is shown in Fig. 1, that consists of total four molybdenum buttons (two on top and two on bottom). It has an elliptical shaped copper beam chamber having water cooling channels on the both sides of the horizontal plane. We chopped the beam chamber longitudinally into six small sections to calculate corresponding metallic losses to perform more accurate thermal analysis.

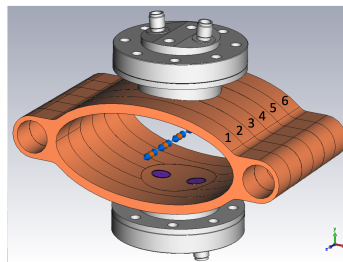


Figure 1: ESR BPM button design.

Figure 2(a) depicts a cut view of the BPM showing the internal design of the feedthroughs, and BPM buttons. The BPM buttons have a diameter of 7 mm, and the gap between the BPM housing and the button is $250 \mu\text{m}$. We used CST Wakefield Solver with the ESR beam parameters ($I_{avg} = 2.5$ A, $M = 1160$, $\sigma = 7$ mm) to calculate the resistive wall loss for this BPM which are listed in Table 1.

Table 1: Metallic Loss on the ESR BPM

Components	Material	Loss (Watts)
4-buttons	Mo	0.288
4-stems	Mo	0.017
4-pins	Cu	0.003
4-connectors	St. St. 316L	0.015
4-cavity liners	St. St. 316L	0.998
2-flanges	St. St. 316L	0.348
2-gaskets	Cu	0.198
2-surface sheets	Cu	1.033
Housing	St. St. 316L	2.231
Beam chamber	Cu	3.983
Total	NA	9.114

* Work supported by Brookhaven Science Associates, LLC under Contract No. DE-SC0012704 with the U.S. Department of Energy.

[†] msangroul@bnl.gov

6D PHASE SPACE DIAGNOSTICS BASED ON ADAPTIVE TUNING OF THE LATENT SPACE OF ENCODER-DECODER CONVOLUTIONAL NEURAL NETWORKS

A. Scheinker*, Los Alamos National Laboratory, Los Alamos, NM, USA

Abstract

We present a general approach to 6D phase space diagnostics for charged particle beams based on adaptively tuning the low-dimensional latent space of generative encoder-decoder Convolutional Neural Networks (CNN). Our approach first trains the CNN based on supervised learning to learn the correlations and physics constraints within a given accelerator system. The input of the CNN is a high dimensional collection of 2D phase space projections of the beam at the accelerator entrance together with a vector of accelerator parameters such as magnet and RF settings. The inputs are squeezed down to a low-dimensional latent space from which we generate the output in the form of projections of the beam's 6D phase space at various accelerator locations. After training the CNN is applied in an unsupervised adaptive manner by comparing a subset of the output predictions to available measurements with the error guiding feedback directly in the low-dimensional latent space. We show that our approach is robust to unseen time-variation of the input beam and accelerator parameters and a study of the robustness of the method to go beyond the span of the training data.

INTRODUCTION

Particle accelerators are large complex systems whose beams evolve according to dynamics governed by nonlinear collective effects such as space charge forces and coherent synchrotron radiation. Because of their complexity, the control of charged particle beams in accelerators and diagnostics of these beams can greatly benefit from the application of machine learning (ML) [1] methods and advanced control theory techniques [2].

The development of ML-based tools for particle accelerator applications is an active area of research. At CERN, supervised learning techniques are being applied for the reconstruction of magnet errors in the incredibly large (thousands of magnets) LHC lattice [3]. At the LCLS, Bayesian methods have been developed for online accelerator tuning [4], Bayesian methods with safety constraints are being developed at the SwissFEL and the High-Intensity Proton Accelerator at PSI [5], and at SLAC Bayesian methods are being developed for the challenging problem of hysteresis [6] and surrogate models are being developed for the beam at the injector [7].

Convolutional Neural Networks (CNN) have been used to generate incredibly high resolution virtual diagnostics of the longitudinal phase space (LPS) of the electron beam in the EuXFEL [8]. A laser plasma wakefield accelerator has

also been optimized by utilizing Gaussian processes at the Central Laser Facility [9].

Although ML tools such as deep neural networks can learn complex relationships in large systems directly from data, a major challenge faced by standard ML methods is that of time-varying systems or systems with distribution shift, which require extensive re-training whenever a system significantly changes. Accelerators continuously change and detailed beam measurements either interrupt operations or are only available for a few limited projections of the beam's 6D phase space. Therefore repetitive re-training is not a feasible solution except for very simple problems.

Recently, powerful model-independent feedback control methods, known as Extremum Seeking (ES), have been developed which can handle unknown and quickly time-varying nonlinear systems in which the direction of the controller's input is unknown and quickly time-varying [2, 10, 11]. For example, it is possible to use ES for RF cavity resonance control based only on ambiguous reflected power measurements [12]. While model-independent feedback such as ES is incredibly robust to un-modeled disturbances, noisy measurements, and can automatically track time-varying systems, a major limitation of local model-independent feedback is the possibility of getting stuck in a local minimum when operating in a complex high-dimensional parameter space.

Adaptive ML (AML) attempts to combine the complementary strengths of ML and model-independent feedback, to provide the best of both worlds: an ability to learn directly from large complex data, while maintaining robustness to time variation and distribution shift. The first demonstration of the AML approach was the use of neural networks together with ES for automatic femtosecond-level control of the time-varying longitudinal phase space distribution of the electron beam in the LCLS [13].

AML methods have also combined CNN and ES to track time-varying input beam distributions at the HiRES UED [14], and preliminary results have shown an ability to adaptively tune the low-dimensional latent space of encoder-decoder CNN to track all 15 unique 2D projections of beam's 6D phase space despite unknown and time-varying input beam distributions and accelerator and beam parameters [15]. Such AML methods are general tools applicable to a wide range of complex time-varying systems and have also been demonstrated for 3D reconstructions of the electron density of crystals for coherent diffraction imaging [16].

* ascheink@lanl.gov

ONLINE ACCELERATOR TUNING WITH ADAPTIVE BAYESIAN OPTIMIZATION*

N. Kuklev[†], M. Borland, G. Fystro, H. Shang, Y. Sun

Advanced Photon Source, Argonne National Laboratory, Lemont, IL, USA

Abstract

Particle accelerators require continuous adjustment to maintain beam quality. At the Advanced Photon Source (APS) this is accomplished using a mix of operator-controlled and automated tools. To improve the latter, we explored the use of machine learning (ML) at the APS injector complex. The core approach we chose was Bayesian optimization (BO), which is well suited for sparse data tasks. To enable long-term online use, we modified BO into adaptive Bayesian optimization (ABO) through auxiliary models of device drift, physics-informed quality and constraint weights, time-biased data subsampling, digital twin retraining, and other approaches. ABO allowed for compensation of changes in inputs and objectives without discarding previous data. Benchmarks showed better ABO performance in several simulated and experimental cases. To integrate ABO into the operational workflow, we developed a Python command line utility, `pysddsoptimize`, that is compatible with existing Tcl/Tk tools and the SDDS data format. This allowed for fast implementation, debugging, and benchmarking. Our results are an encouraging step for the wider adoption of ML at APS.

INTRODUCTION

Modern particle accelerators face increasing performance demands, resulting in tighter tolerances on accuracy and stability [1]. Due to cost, physical limits, and external factors, some amount of continuous parameter adjustment is constantly required. Historically, this tuning required expert guidance and intuition, with software tools only allowing for a partial automation. With the explosion of machine learning methods in the last decade, there is immense interest in making use of the newly available algorithms to improve reliability, reduce expert workload, and provide higher performance to the users.

A key application of ML for accelerators is in parameter optimization, whereby one or multiple objectives are tuned through an intelligent search of the parameter space. A number of conventional optimization methods are already in use, including simplex [2, 3], RCDS [4], genetic algorithms [5], extremum seeking [6], and several others. New ML methods include Bayesian optimization (BO) [7], reinforcement learning [8], and others. BO is of special interest since it allows efficient black-box function optimization with few samples, taking advantage of any prior physics model knowl-

edge provided to the algorithm. This paper first reviews the basic BO process, and then discusses our contributions - a set of improvements that permits for continuous, robust, and adaptive BO use for optimizing time-varying systems.

ADAPTIVE BAYESIAN OPTIMIZATION

In standard BO process, system output is described by

$$\mathbf{y} = f(\mathbf{x}) + \varepsilon \quad (1)$$

where $f(\mathbf{x})$ is the black-box function of interest and $\varepsilon \sim \mathcal{N}(0, \sigma_\varepsilon^2)$ the added noise. Vector \mathbf{x} has dimension of $n \times d$ where d is the parameter space size and n the number of measurements. Using Gaussian Process (GP) a surrogate model for f can be parameterized as a multivariate normal distribution with a mean $m(\mathbf{x})$ and covariance kernel $k(\mathbf{x}, \mathbf{x}')$ as

$$f(\mathbf{x}) \sim \mathcal{GP}(m(\mathbf{x}), k(\mathbf{x}, \mathbf{x}')) \quad (2)$$

The kernel is used to evaluate the similarity between values of f at \mathbf{x} and \mathbf{x}' , and its' appropriate choice is critical for good GP convergence. Existing knowledge about the system can be encoded through prior distributions on kernel and mean, with the distribution parameters called *hyper-parameters*. During model fitting hyper-parameters are updated using Bayes' rule (conditioned on observed data) and posterior probability distribution $p(\mathbf{f} | \mathbf{y}, \mathbf{x})$ can then be sampled to get model predictions [9]. BO evaluates a special 'acquisition' function over a fitted GP model so as to predict the best next location(s) to sample. A variety of analytic and Monte-Carlo acquisition functions exist, with one of simplest being the upper confidence bound (UCB)

$$\text{UCB}(\mathbf{x}) = \mu(\mathbf{x}) + \sqrt{\beta} * \sigma(\mathbf{x}) \quad (3)$$

where mean μ and variance σ are provided by the GP model. The parameter β allows for trade-off between exploration (risk for high reward) and exploitation (use known good configuration).

Time-varying GP Models

The above discussion grouped all input parameters into vector \mathbf{x} , representing for example several magnet currents. A simple BO process would proceed by using standard isotropic kernels, such as Matérn and radial basis function [9], and only fit freshly collected data. To improve convergence speed, previous work has successfully used historic data to train covariance distributions [10]. Such pre-training works well when conditions are reproducible. However, some accelerators also have undesired and poorly modelled time-dependent drifts. ML methods dealing with

* The work is supported by the U.S. Department of Energy, Office of Science, Office of Basic Energy Sciences, under Contract No. DE-AC02-06CH11357.

[†] nkuklev@anl.gov

A QUASI-OPTICAL BEAM POSITION MONITOR

S. V. Kuzikov[†], Euclid TechLabs, Solon, USA

Abstract

There is a strong demand for non-destructive electron Beam Position Monitors (BPMs) for non-perturbative diagnostics of the electron beam position. Challenges are related to the shortness of the electron beam and the noisy chamber environment that are typical for modern RF-driven and plasma-driven accelerators. We propose using a pair of identical high-quality quasi-optical resonators attached to opposite sides of the beam pipe. The resonators can introduce Photonic Band Gap (BPM) structures. These open resonators sustain very low numbers of high-quality modes. We intend to operate at the lowest mode among the others that are capable of being excited by the bunches. The mentioned mode has a coupling coefficient with the beam that depends on the distance between the bunch and the coupling hole. The lower this distance, the higher the coupling. Therefore, comparing the pick-up signals of both resonators with an oscilloscope, we can determine the beam position.

INTRODUCTION

For a classical Bunch Position Monitor (BPM) based on a proximity effect ultrashort bunches become inevitably shorter than the length of the capacitor antenna. In this case the capacitor must be considered as a broadband RF antenna. Such antenna sees lots of noise including the noise generated far from the BPM. These challenges can be approached by the excitation of resonator modes within a so-called cavity BPM shown in Fig. 1 [1-2]. Our idea is to develop the cavity BPM concept and to design a quasi-optical BPM (QBPM).

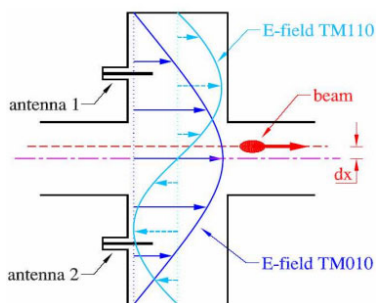


Figure 1: Pillbox cavity BPM.

We suggest using a pair of identical high-quality quasi-optical resonators attached to opposite sides of the beam pipe. The resonators, for example, can introduce Photonic-Band Gap (PBG) structures [3-4]. These open PBG resonators sustain a very low number of high quality factor

modes or even only one mode. We intend to operate in the lowest order mode among those that are capable of being excited by the electron bunches. The mode that we plan to use has a coupling coefficient with the beam that depends on the distance between the bunch and the coupling hole. The lower this distance, the higher the coupling coefficient will be. Therefore, by comparing the pick-up signals of the two resonators with an oscilloscope, we can determine the position of the beam. Unlike the mentioned cavity BPM in Fig. 1 our QBPM uses highly selective resonators that allow to suppress the noise. The frequency of our open resonator is below cutoff for the beamline where the QBPM installed. Therefore, the noise at the operating frequency generated far from the QBPM cannot spoil the received signal.

DESIGN OF QBPM

We suggest using a pair of identical high-quality open resonators attached to opposite sides of the beam pipe. These pairs of resonators operate as a quasi-optical bunch position monitor (QBPM) that can retrieve the beam position along one of the transverse coordinates. Figure 2 illustrates one such resonator. It consists of a periodically perforated rectangular cross-section waveguide. Such waveguides can work as a Bragg reflector for radiation that is below the cut off for the perforation holes.

The Q-factor of the operating mode depends on size of the coupling hole, and should be high enough to allow for receiving a sufficient number of oscillations of the 10-100 ns pick-up signals. Of course, the measurement procedure requires some calibration.



Figure 2: Open BPG resonator for QBPM based on Bragg reflector.

First, we simulated a 10-GHz rectangular cross-section Bragg reflector. Figure 3 represents the E-field distribution in the Bragg reflector that consisted of 6 periods. The S-parameters of this Bragg reflector are shown in Fig. 4.

[†] s.kuzikov@euclidtechlabs.com

XFEL AS A LOW-EMITTANCE INJECTOR FOR A 4TH-GENERATION SYNCHROTRON RADIATION SOURCE

Toru Hara[†], RIKEN SPring-8 Center, Sayo, Japan
on behalf of RIKEN-JASRI Joint Project Team

Abstract

Low-emittance beam injection is required for the future SPring-8-II due to its small injection beam aperture. To meet this requirement, the SACLA linear accelerator has started to be used as a low-emittance injector of the present SPring-8 storage ring. In order to perform beam injection in parallel with XFEL operation, three accelerators are virtually constructed in a control system for two XFEL beamlines and beam injection, and thus the parameters of accelerator can be independently tuned. Although the reference clock frequencies of SACLA and SPring-8 are not related by an integer multiple, the developed timing system achieves 3.8 ps (rms) synchronization between the two accelerators. To maintain bunch purity of $10^{-8}\sim 10^{-10}$, which is routinely requested at SPring-8, an electron sweeper and an RF knock-out system are introduced for the SACLA injector section and the SPring-8 storage ring. Although 0.1 nm-rad emittance of SACLA is increased by an order of magnitude at a transport line mainly due to quantum excitation of synchrotron radiation, it is still small enough for SPring-8-II. By shutting down an old dedicated injector accelerators, energy consumption has been significantly reduced and it contributes to create a low-carbon society.

INTRODUCTION

SPring-8-II is an upgrade project of the SPring-8 storage ring [1]. As a part of SPring-8-II, the linear accelerator of SACLA has been used as a low-emittance full-energy injector since 2020 [2]. To pursue low emittance, SPring-8-II

employs a multi-bend optics design, which increases non-linearity due to strong focusing magnets [3]. As a result, a small dynamic aperture for an injected beam becomes an issue, which is common to all recent low-emittance storage rings [4-6]. In SPring-8-II, traditional off-axis beam injection is planned using an in-vacuum septum magnet in combination with a low-emittance injection beam [7].

Figure 1 is a schematic layout of SACLA [8]. There are three FEL beamlines (BL1, BL2 and BL3), in which BL2 and BL3 are XFELs and BL1 is a soft x-ray FEL. BL1 is equipped with a dedicated 800 MeV linear accelerator, which was originally constructed as a proto-type accelerator called SCSS, and BL1 operates independently from the SACLA main linear accelerator [9, 10]. For the beam injection, the electron beam accelerated up to 8 GeV is delivered through a transport line named XSBT (XFEL to Storage ring Beam Transport). A beam repetition rate of SACLA is 60 Hz and the electron bunches are distributed pulse by pulse between BL2, BL3 and XSBT at a switchyard installed at the end of the linear accelerator [11, 12].

The beam injection from SACLA not only improves the emittance of the injection beam, but also saves electricity consumption and facility related costs. Dedicated injector accelerators of SPring-8 consisting of a 1 GeV linear accelerator and an 8 GeV synchrotron are more than twenty-year old and major renewal of their high-voltage power station was needed. By using a small portion of the SACLA electron beam, these renewal and operation costs of the old injector accelerators are no more necessary.

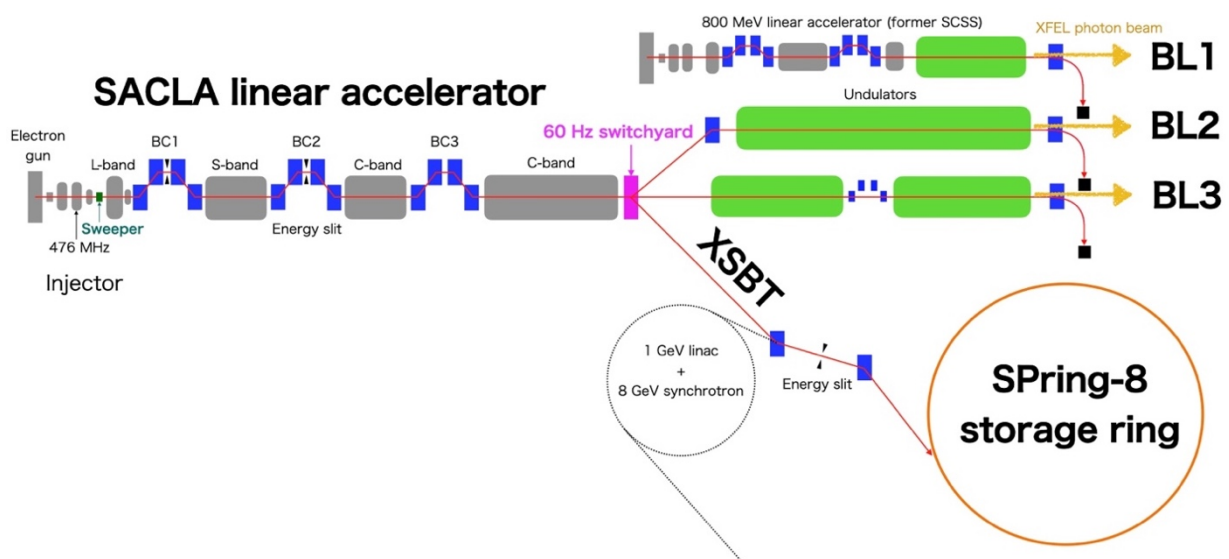


Figure 1: Schematic layout of the SACLA facility.

[†] toru@spring8.or.jp

UPDATE ON THE STATUS OF C-BAND RESEARCH AND FACILITIES AT LANL*

E. I. Simakov[†], A. M. Alexander, D. V. Gorelov, T. W. Hall,
M. E. Middendorf, D. Rai, T. Tajima, M. R. A. Zuboraj
Los Alamos National Laboratory, Los Alamos, NM, USA

Abstract

This paper reports on the status of two C-band test facilities at Los Alamos National Laboratory (LANL): C-band Engineering Research Facility in New Mexico (CERF-NM), and Cathodes and Rf Interactions in Extremes (CARIE). Modern applications such as X-ray sources require accelerators with optimized cost of construction and operation, naturally calling for high-gradient acceleration. At LANL we commissioned a high gradient test stand powered by a 50 MW, 5.712 GHz Canon klystron. The test stand is capable of conditioning accelerating cavities for operation at surface electric fields in excess of 300 MV/m. CERF-NM is the first high gradient C-band test facility in the United States. CERF-NM was fully commissioned in 2021. In the last year, multiple C-band high gradient cavities and components were tested at CERF-NM. Currently we work to implement several updates to the test stand including the ability to autonomously operate at high gradient for the round-the-clock high gradient conditioning. Adding capability to operate at cryogenic temperatures is considered. The construction of CARIE will begin in October of 2022. CARIE will house a cryo-cooled copper RF photoinjector with a high quantum-efficiency cathode and a high gradient accelerator section.

INTRODUCTION

High gradient C-band (5.712 GHz) accelerator research, development, and facility construction is ongoing at Los Alamos National Laboratory (LANL) motivated by a number of LANL-specific mission needs. LANL has proposed a high gradient C-band upgrade to Los Alamos Neutron Science Center (LANSCE) proton linac to increase the final energy of the proton beam to 3 GeV. Material science research at LANL may benefit from a powerful directional high-repetition-rate X-ray source of high energy (~ 100 keV) photons that may be produced by a multi-MeV energy electron beam through Inverse Compton Scattering (ICS). These needs must be met with an accelerator of a limited length and footprint due to the space limitations of the 50-year-old LANSCE facility, which naturally calls for acceleration at a high gradient. The number of photons generated by an ICS source is also highly dependent on the quality (low emittance and high brightness) of the accelerated electron beam, which may be achieved through a ground-up redesign of the core technology underpinning

*This work was supported by Los Alamos National Laboratory's Laboratory Directed Research and Development (LDRD) Program.

[†] smirnova@lanl.gov

modern accelerators, the radio-frequency (RF) photoinjector to allow operation of the photoinjector and the photocathode at high gradients. Achieving high gradient in normal-conducting radio-frequency (NCRF) copper-based accelerator structures and in RF photoinjectors with high quantum efficiency (QE) photocathodes requires understanding of material behavior under extreme electromagnetic fields and at its core is the material science problem. Understanding and designing new materials specifically suited for high gradient operation is the problem that LANL is perfectly positioned to address leveraging its extensive expertise in material science and specifically its specialization in materials-in-extremes.

C-BAND ENGINEERING RESEARCH FACILITY IN NEW MEXICO (CERF-NM)

At LANL, we constructed and commissioned the C-band Engineering Research Facility in New Mexico (CERF-NM) (Fig. 1) [1, 2], the very first high gradient C-band test facility in the United States. The high performance accelerator structure test stand CERF-NM is built around a 5.712 GHz Canon klystron made to supply up to 50 MW of power into an RF cavity. The klystron produces 50 MW RF pulses with the pulse length that can be varied between 300 ns and 1 microsecond, repetition rate up to 200 Hz, and is tunable within the frequency band of 5.707 GHz to 5.717 GHz. The RF power from the klystron is coupled into a WR187 rectangular waveguide. The power is split into two halves by a magic tee that is installed at the klystron's output and protects the klystron from excess reflected power that may come from the device-under-test. The WR187 waveguide brings power into a 3 foot by 4 foot lead box built to provide radiation protection to equipment and operators during high gradient testing. The lead box is radiologically certified for dark currents with electron energy up to 5 MeV and average current up to 10 μ A.

Various cavities and components have been tested at high gradients at CERF-NM in the last two years (Fig. 2). The first two cavities were 5.712 GHz single-cell proton accelerating cavities fabricated by SLAC National Accelerator Laboratory. The first cavity was made of copper and the second cavity was made of copper-silver with 0.085% of silver. The surface electric fields measured in the copper cavity at the end of high gradient conditioning were higher than 300 MV/m with breakdown probabilities below 10^{-4} 1/pulse/m. The surface electric fields measured in the copper-silver cavity at the end of high gradient conditioning were higher than 400 MV/m with breakdown probabilities below 10^{-4} 1/pulse/m [3].

PROGRESS ON THE APS-U INJECTOR UPGRADE*

J. Calvey, T. Fors, K. Harkay, U. Wienands, ANL, Argonne, IL, USA

Abstract

For the APS-Upgrade, it was decided to leave the present APS injector chain in place and make individual improvements where needed. The main challenges faced by the injectors are delivering a high charge bunch (up to 16 nC in a single shot) to the storage ring, operating the booster synchrotron and storage ring at different rf frequencies, and maintaining good charge stability during APS-U operations. This paper will summarize recent progress on the injector upgrade. Topics include bucket targeting with the new injection/extraction timing system, modeling of high charge longitudinal instability in the PAR, and measurements of charge stability for different modes of operation.

INTRODUCTION

The APS injector complex consists of a linac, particle accumulator ring (PAR), and booster synchrotron. These machines will remain for the APS-Upgrade [1], with several significant changes. The most important of these are a decoupling of the booster and storage ring rf frequencies, the capability of running with much higher charge per bunch, and a stricter standard for efficiency and charge stability. Key parameters for the PAR and booster are given in Table 1.

Table 1: PAR and Booster Parameters for the APS / APS-U

parameter	APS	APS-U	units
PAR			
Revolution time	102	102	ns
Energy	425	up to 475	MeV
Charge	0.5-3	2-20	nC
Booster			
Revolution time	1.22	1.22	μ s
Energy	0.4-7	0.4-6	GeV
Charge	0.5-3	2-17	nC
Momentum offset	-0.6	variable	%

This paper discusses recent progress on the injection/extraction timing system, understanding PAR longitudinal instability, and quantifying charge stability. Other important updates include a higher power 12th harmonic amplifier in the PAR [2], and an upgrade of the booster photon diagnostics [3].

INJECTION/EXTRACTION

* Work supported by the U.S. Department of Energy, Office of Science, Office of Basic Energy Sciences, under Contract No. DE-AC02-06CH11357.

TIMING SYSTEM

The APS-Upgrade storage ring will run at a slightly higher frequency than the present ring. In order to avoid a costly re-alignment of the booster, it was decided to decouple the booster and storage ring RF frequencies. Bucket targeting will be accomplished by adding a frequency “bump” in the middle of the booster ramp. This will change the amount of time the beam spends in the booster, so that it lines up with the correct storage ring bucket at extraction. We also have the option of adding an overall frequency ramp in the booster, so that both injection efficiency and extracted emittance can be optimized [4].

Figure 1 illustrates the difference between a targeting bump and frequency ramp. Both show the turn-by-turn horizontal beam position at a dispersive BPM. The measured position with no frequency bump or ramp is subtracted off. The left plot shows this measurement for two different targeting bumps. The starting and ending positions are the same, since there is no net change of frequency. Bucket 340 requires a small positive frequency bump, while bucket 320 requires a large negative bump. The latter bump is large enough to cross the cavity resonance, leading to Robinson instability. Of course, this situation should be avoided in regular operation.

For Fig. 1 (right), there is a net frequency ramp between injection and extraction, between -18 and $+12$ kHz. This is reflected in a horizontal position change at the dispersive location. Some cases seem to show an instability around turn 80,000; this is not presently understood.

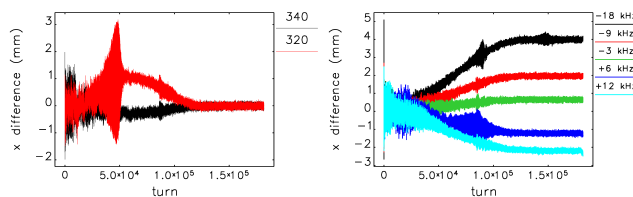


Figure 1: Horizontal position at a dispersive BPM (B1C4P1) in the booster. Left: effect of different targeting bumps. Right: effect of different frequency ramps.

Machine studies of increasing complexity have been done with the prototype system in the present APS ring. As of this writing we have:

- Verified we can control the three rf sources separately.
- Demonstrated bucket targeting in the Booster (bump).
- Tested transfer from the Booster to Storage Ring (SR) at different rf frequencies of both rings at extraction (ramp).
- Verified that we can inject into Booster and transfer to SR, with different rf frequencies at injection.

DEVELOPMENT OF NANOPATTERNED STRONG FIELD EMISSION CATHODES

G. E. Lawler*, J. Mann, N. Majernik, N. Montanez, J. B. Rosenzweig
UCLA, Los Angeles, CA, USA

Abstract

Increasing brightness at the cathode is highly desirable for a diverse suite of applications in the electron accelerator community. These applications range from free electron lasers to ultrafast electron diffraction. Many options for higher brightness cathodes are under investigation notably semiconductor cathodes. We consider here the possibility for an alternative paradigm whereby the cathode surface is controlled to reduce the effective area of illumination and emission. We fabricated nanoblade metallic coated cathodes using common nanofabrication techniques. We have demonstrated that a beam can be successfully extracted with a low emittance and we have reconstructed a portion of the energy spectrum. As a result of our particular geometry, our beam possesses a notably high aspect ratio in its transverse plane. We can now begin to consider modifications for the production of intentionally patterned beams such as higher aspect ratios and hollow beams.

INTRODUCTION

One of the main goals of the National Science Foundation Center for Bright Beams is to increase electron beam brightness for many applications including free electron lasers, ultrafast electron diffraction, etc. Many concepts are currently being considered to increase beam brightness at the cathode. High brightness semiconductor cathodes are very promising due to the low MTE of produced beams but are challenging to work with for several reasons including their sensitivity to vacuum conditions [1]. As an alternative, we consider here custom nanofabricated surfaces. By creating nanostructured surfaces we can produce high field enhancement in smaller areas thus reducing the effective spot size illuminated by the emission producing laser. One of the simplest geometries we use as our proof of principle study is inspired by nanotips used for electron microscopy where incident laser fields along with geometry-based field enhancement lead to electron emission via tunneling [2–4].

The physics responsible for the emission is complex and under continued theoretical investigation. It is, for example, dependent on re-scattering effects in the intense laser field which multiply the energy of the emitted electrons significantly. This work is more thoroughly covered in related publications [5, 6]. Instead we limit our discussion here to the implications to future cathode development given our previous observations of transverse structure, emittance, and emission energies [7, 8].

* gelawler@physics.ucla.edu

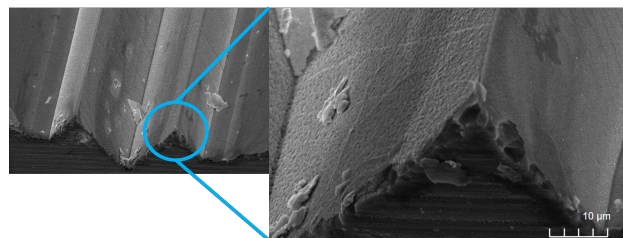


Figure 1: SEM image of nanoblades at the 10- μ m scale.

NANOBLADE FABRICATION

It is useful to first go through the nanofabrication process used successfully thus far and explain some of its advantages and limitations. The blades are made through two chemical wet-etches into a silicon wafer. The challenge of the process is precisely controlling the position and dimensions of each etch. The first etch creates the two grooves, the second etch cuts in between them to create the two blades. The multi step process uses well-established methods and at this point is fairly repeatable.

A 2-D design is made using L-edit software to make the photolithography masks. The primary pattern that we have used are multiple long thin rectangles used to etch the grooves as well as shapes (crosshairs etc) that are used to align with the second mask later on. Another 2-D design is made in L-edit to make the second mask. The long thin patterns (later, etches) to be made are between the ones in the first mask pattern. There are the same crosshairs to align to the pattern of the first mask.

We then use plasma enhanced chemical vapor deposition (PECVD), to deposit a layer of nitride on the silicon wafer followed immediately after by a thin layer of photoresist (PR) which is spun onto the silicon wafer. A machine designed for precision alignment is then used to place the mask on top of the wafer such that photolithography can be used to form the mask pattern on the photoresist. The nitride layer that is not covered by photoresist is then etched away using oxide etching. The photoresist can then be removed and the structures in silicon can be anisotropically etched away with a KOH solution. After this the remaining nitride is removed and the process is repeated to form additional features including, for the case of the cathodes like those in Fig. 1, the double blade geometry. A 10-20-nm metallic coating is then sputtered into the blades. One wafer is then diced into 40 usable cathode samples.

It is then necessary to address the nature of the nanoblade cathode reproducibility. In previous iterations of our man-

ARRIVAL TIME AND ENERGY JITTER EFFECTS ON THE PERFORMANCE OF X-RAY FREE ELECTRON LASER OSCILLATOR *

G. Tiwari [†], K.-J. Kim ¹, and R. R. Lindberg [‡], Argonne National Laboratory, Lemont, IL USA
¹also at the University of Chicago, Chicago, IL USA

Abstract

We report on the effects of electron beam arrival time and energy jitter on the power level and the fluctuations of the output of an X-ray FEL oscillator (XFEL). For this study, we apply the FEL driven paraxial resonator model of XFEL along with an analytical reflectivity profile to mimic the phase shift and spectral filtering effects of Bragg-crystals. The thresholds for acceptable timing and energy jitters are determined in terms of the fluctuations of the steady-state power output. We explore potential ways to mitigate the XFEL power fluctuations in the presence of unavoidable jitters.

INTRODUCTION

XFELs offer intense, stable, and coherent pulses with unprecedented spectral resolution [1–3], which would benefit measurements of various systems with increased accuracy (extending to the micro eV range) and open the possibility of adopting advanced optical techniques such as Q-switching [4], mode-locking [5], and parametric amplification, thereby bringing atomic laser properties to the X-ray regime [6].

Since XFELs are low-gain FEL devices, their stability and performance depend on the quality and precise alignments of both electron beams and optical cavity. In a separate report [7], we applied the FEL driven paraxial resonator model of XFEL to study the effects of transverse spatial misalignments on XFEL stability. Here we prioritize longitudinal misalignment induced by fluctuations in electron beam arrival time and energy and their subsequent effects on XFEL operation and stability.

SPECTRAL FILTERING BY CRYSTALS

An optical cavity for XFEL requires at least two-Bragg crystals to form a non-tunable cavity and four crystals for a tunable one [8]. Assuming the lenses provide minimal change in the wavefront of the propagating radiation beam, the filtering effects are primarily induced by the reflecting crystals through their reflectance/reflectivity. The reflected component of the incident field $\tilde{E}^{in}(\phi, \omega; z)$ upon interacting with a Bragg crystal is given by

$$\tilde{E}^{out}(\phi, \omega; z) = \mathcal{R}(\phi, \omega)\tilde{E}^{in}(\phi, \omega; z). \quad (1)$$

Here \mathcal{R} represents the reflectivity of the crystal. The tilde denotes the Fourier transformed field in the frequency-angular

* Work supported by U.S. Department of Energy Office of Sciences under Contract No. DE-AC02-06CH11357.

[†] gtiwari@bnl.gov, now at Brookhaven National Laboratory, Upton, NY.

[‡] lindberg@anl.gov

space. For typical XFELs with defined radiation beam waists $\sigma_{rx,ry} \sim 10 \mu\text{m}$ and Rayleigh range $z_R \geq 10 \text{m}$, the rms divergence of the mode matched radiation beam is $\sigma_{\phi_x, \phi_y} \leq 1 \mu\text{rad}$. Since diamond crystals considered for XFELs usually have Darwin widths greater than $4 \mu\text{m}$ (see [8] for example), we ignore the angular filtering imposed on the radiation by the crystals for the studies reported here.

We take a step further and approximate the overall crystals' spectral effects in the cavity using a gaussian filter given by

$$\mathcal{R}(\omega) = \sqrt{R} \exp \left[\frac{-(\omega - \omega_c)^2}{4\sigma_{\text{refl}}^2} + i \text{atan} \left(\frac{\omega - \omega_c}{2\sigma_{\text{refl}}} \right) \right], \quad (2)$$

where R is the power reflectivity, ω_c is the central frequency and rms bandwidth in frequency space σ_{refl} is equal to 1/4 of the Darwin width. The first gaussian amplitude invokes the filter within the Darwin width and the second phase part imitates the delay effect. This expression allows us to study the crystal effects in the evolution of linear supermodes in the oscillator analytically [3, 6, 9].

For simulation studies, we consider a 200-m optical cavity formed by a two crystals and two focusing mirrors configuration (see, for example [7]). For practical considerations, we consider the net rms bandwidth of these two crystals (and hence the cavity) to be 6.87 meV. The electron beam is a relatively long bunch with low peak current achievable in an energy recovery linac and is optimized for radiation emission at fundamental wavelength $\lambda_r = 1.0298 \text{ \AA}$ (12.4 keV). Other relevant parameters are listed in Table 1.

Table 1: XFEL Parameters for Simulations

Parameter	Symbol	Value
Electron beam		
Energy	$\gamma_0 m c^2$ (GeV)	7
Energy spread	σ_γ (MeV)	1.4
Energy shift	δE (MeV)	2.3
Normalized emittance	ϵ_n (mm- μrad)	0.2
Peak current	I (A)	10
Pulse length	σ_t (fs)	200.0
RMS width	σ_x (μm)	12.67
Undulator/Radiation		
Undulator periods	N_u	3000
Undulator length	L_u (m)	52.8
Radiation wavelength	λ_r (\AA)	1.0298
Rayleigh range	Z_R (m)	10

SUPERCONDUCTING UNDULATORS AND CRYOMODULES FOR X-RAY FREE-ELECTRON LASERS*

D. C. Nguyen[†], G. J. Bouchard, B. M. Dunham, G. L. Gassner, Z. Huang, E. M. Kraft,
 P. Krejcik, M. A. Montironi, H.-D. Nuhn, T. O. Raubenheimer, Z. R. Wolf, Z. Zhang
 SLAC National Accelerator Laboratory, Menlo Park, CA, USA
 J. M. Byrd, J. D. Fuerst, E. Gluskin, Y. Ivanyushenkov,
 M. Kasa, E. R. Moog, M. F. Qian, Y. Shiroyanagi
 Argonne National Laboratory, Lemont, IL, USA

Abstract

We present FEL-suitable superconducting undulator (SCU) and cryomodule (CM) designs based on previous SCU designs at Argonne National Lab. The new SCU and CM designs will allow us to connect one CM to the next to form a contiguous line of SCUs with no breaks in between the cryomodules. The SCU design will have correctors and phase shifters integrated into the main SCU magnet core, as well as external corrector magnets for trajectory corrections. There will also be a cryogenic magnetic quadrupole and a cold RF beam position monitor (BPM) inside each SCU CM. In addition to providing the usual FODO transverse focusing, the quadrupole and BPM will be used in the beam-based alignment technique that is necessary for X-ray FEL operation. In this paper, we present the conceptual design of the compact SCU CM as well as FEL simulations using three SCUs as the afterburners for the Linac Coherent Light Source (LCLS) hard X-ray undulators.

INTRODUCTION

Permanent magnet undulators (PMUs) have long been the critical components of synchrotron radiation facilities and X-ray free-electron lasers (XFELs) for generating intense monochromatic X-rays. In recent years, superconducting undulators (SCUs) have been developed and tested at the Advanced Photon Source [1] and the Angströmquelle Karlsruhe [2] synchrotron facilities. A previous R&D effort [3] was executed in 2014-2016 to develop and compare two competing planar SCU technologies for XFEL: NbTi at ANL and Nb₃Sn at LBNL. SLAC and ANL are presently collaborating in a project to design, build and test NbTi SCUs on the LCLS hard X-ray (HXR) undulator beamline. The goal is to demonstrate key features such as FEL suitable magnetic fields, thermo-mechanical properties, beam-based alignment, and FEL gains of SCUs in a working XFEL.

Worldwide Development of SCUs for XFELs

As of 2022, four FEL facilities in the world are developing SCUs for XFELs (Table 1). Besides the LCLS SCU project, the SHINE facility in Shanghai [4] and the European XFEL [5] in Hamburg are building SCUs to be driven by SRF linac. Fermilab is constructing an SCU prototype

* Work supported by the US DOE, Office of Science, Basic Energy Sciences, Accelerator and Detector Research, PM: Dr. Eliane Lessner.

[†] dinhnguy@slac.stanford.edu

Table 1: Parameters of SCUs for XFELs

	LCLS	SHINE	EXFEL	FNAL
SC material	NbTi	NbTi	NbTi	NbTi
Period (mm)	21	16	18	16
Vacuum gap (mm)	5	4	5	5
Magnet length (m)	2	2	2	<1.6
# magnets/CM	1	2	2	1
# CMs	3	40	5	TBD

that will be considered for use in the AQUA undulator line of the SPARC_Lab laser plasma accelerator (LPA) [6].

SCU BENEFITS FOR XFEL

SCUs deliver high magnetic field, a convenient way to vary the undulator field, improved resistance to radiation induced damage, and smooth electron beam chambers with high electrical conductivity surfaces to minimize resistive wall heating [7]. The SCU resistance to radiation allows them to be driven by the large-energy-spread and divergent electron beams from an LPA [8]. The large-bore high vacuum beam chambers facilitate operation with the high repetition rate electron bunches from a superconducting

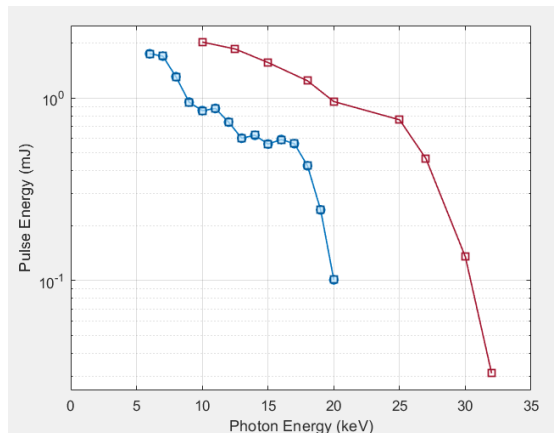


Figure 1: Expected performance of the LCLS-II-HE with 8-GeV electron beams driving the 26-mm-period HXR (blue) and 16.5-mm-period SCUs (red).

DEVELOPMENT OF AN ULTRA-LOW VIBRATION CRYOSTAT BASED ON A CLOSED-CYCLE CRYOCOOLER

R. Kostin*, E. Knight, Y. Zhao, Euclid Techlabs LLC, Bolingbrook, USA
 R. W. Roca, Illinois Institute of Technology, Chicago, USA

Abstract

Low temperature and low vibration cryostats are useful in a variety of applications such as X-ray diffraction, quantum computing, X-ray monochromators and cryo-TEMs. In this project, we explore an ultra-low vibration cryostat with the cooling provided by a closed cycle cryocooler. Closed-cycle cryocoolers inevitably introduce vibrations into the system, and in this project, flexible copper braiding was used to decouple vibrations and provide cooling at the same time. In order to develop the cryostat, capacity map of a two stage Sumitomo cryocooler was measured as well as vibration transmission through different copper braids using an IR interferometer. This paper covers the capacity map and vibration measurements in the first prototype.

INTRODUCTION

Low temperature sample environment is required for the next generation X-ray sources with a sub-micron beam size. The success of the full potential employment of small coherent X-ray beams will highly depend on the position control of the sample relative to the beam and the ability of sample stabilization. The cryostats currently in use are based on gas-gap barrier principle [1] and are heavy, cumbersome and can only be used at facilities where diffractometers with a through-hole on a phi stage or with an offset chi circle are installed. Many X-ray diffraction facilities utilizing high brightness synchrotron beamlines employ modern diffractometers for specifically designed sample stages which cannot fit cryostats currently available on the market [2, 3].

The project was devoted to the cryostat engineering design development and vibration measurements of a mock-up first generation cryostat. It is necessary to mechanically decouple the cryostat from different sources such as vacuum pumping system, cryocooler, the cryostat mounting table and sometimes from acoustic vibrations. The first generation of the cryostat was manufactured to make vibration measurement with Michelson interferometer. The cryostat was cooled by a closed cycle Gifford-McMahon (GM) cryocooler [4]. Vibration mitigation studies were conducted. The experimental results were used for the development of a full-featured cryostat in Phase I of the project.

SETUP

The capacity map of the cryocooler used for the vibration studies was measured in order to calibrate our system and to precisely predict the heat going to the stages by knowing their temperatures. Two cryogenic resistors were used as heaters.

* r.kostin@euclidtechlabs.com



Figure 1: Vacuum envelope with the cryocooler and pumping port on the left and the (blue) instrumentation volume with feed-throughs on the right.

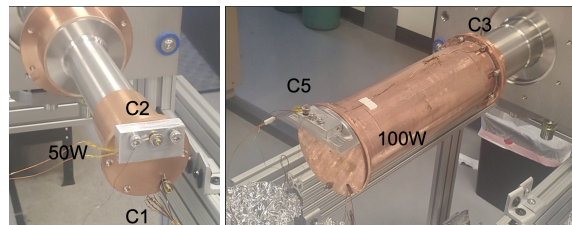


Figure 2: Temperature sensors: left – on the second stage cold head (C1) and heater block (C2); right – on the first stage (C3), at the end of the Cu radiation screen (C4, not seen) and the first stage radiation screen heater block (C5).

One can find out the dissipated heat by knowing their resistance and the current flowing through them. A Sumitomo RDE-418D4 Gifford-McMahon (GM) cryocooler [4] was coupled through a ISO-160 nipple and bellows to a small rectangular vacuum chamber ("vacuum box") with instrumentation feed-throughs as shown in Fig. 1.

The cryocooler consists of 2 stages, the first stage which brings the temperature down to about 30 K, and the second stage which can reach < 4 K. A copper radiation screen was installed around the second stage of the cryocooler and connected to the first stage of the cryocooler to intercept thermal radiation from the room temperature vacuum chamber.

The cooler was instrumented with the following for thermal measurements:

- two heaters built using resistors embedded inside 6061-aluminum blocks – 100/50 W units attached to the radiation screen and the second stage cold head;
- temperature sensors (Cernox) at five locations – on the first and second stage cold heads and the three heater blocks.

These are shown in Fig. 2.

ANALYSIS OF LOW RRR SRF CAVITIES*

K. Howard[†], Y.-K. Kim, University of Chicago, Chicago, IL, USA
 D. Bafia, A. Grassellino, Fermi National Accelerator Laboratory, Batavia, IL, USA

Abstract

Recent findings in the superconducting radio-frequency (SRF) community have shown that introducing certain impurities into high-purity niobium can improve quality factors and accelerating gradients. Success has been found in nitrogen-doping, diffusion of the native oxide into the niobium surface, and thin films of alternate superconductors atop a niobium bulk cavity. We question why some impurities improve RF performance while others hinder it. The purpose of this study is to characterize the impurity profile of niobium with a low residual resistance ratio (RRR) and correlate these impurities with the RF performance of low RRR cavities so that the mechanism of recent impurity-based improvements can be better understood and improved upon. Additionally, we performed surface treatments, low temperature baking and nitrogen-doping, on low RRR cavities to evaluate how the intentional addition of more impurities to the RF layer affects performance. We have found that low RRR cavities experience low temperature-dependent BCS resistance behavior more prominently than their high RRR counterparts. The results of this study have the potential to unlock a new understanding on SRF materials.

INTRODUCTION

As we approach the theoretical limit of niobium for superconducting radio-frequency (SRF) cavities, the last decade has brought immense improvements in quality factor (Q_0) and accelerating gradients though intentionally added impurities into the niobium surface [1, 2]. Many SRF studies follow a “clean bulk dirty surface” technique to optimize the BCS resistance by adding extrinsic impurities to the surface layer of high purity niobium [3–5]. Advancements have been made with nitrogen through N-doping, where cavities experience an anti- Q_0 slope and record breaking Q_0 's at mid fields [6–8]. Oxygen added through a low temperature bake (LTB) has also provided high Q_0 's and mitigation of the high field Q_0 slope typically seen in electropolished (EP) niobium cavities [9, 10]. The performance of these surface treatments is shown in Fig. 1.

The success of intentionally added impurities to the niobium surface has drawn deeper questions about how these impurities affect cavity behavior, and has prompted an investigation of cavities with a low residual resistance ratio (RRR). Low purity niobium has been studied in the past for the purpose of cost reduction and possible high Q_0 [11]. In this study, we look to use the intrinsic impurities as a resource

* This manuscript has been authored by Fermi Research Alliance, LLC under Contract No. DE-AC02-07CH11359 with the U.S. Department of Energy, Office of Science, Office of High Energy Physics. This work was supported by the University of Chicago.

[†] khoward99@uchicago.edu

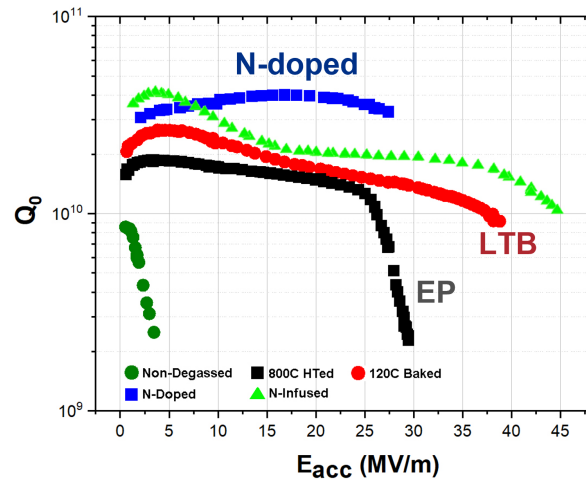


Figure 1: Comparison of quality factor versus gradient for surface treatments, adapted from [6].

to optimize the BCS resistance and understand the mechanism of impurity-based improvements. RRR and mean free path (mfp) have a direct relationship, so we might expect experience low BCS resistance behavior at low RRR, as seen in Fig. 2. We ask if the intrinsic impurities can improve performance, as we observe in extrinsic impurities.

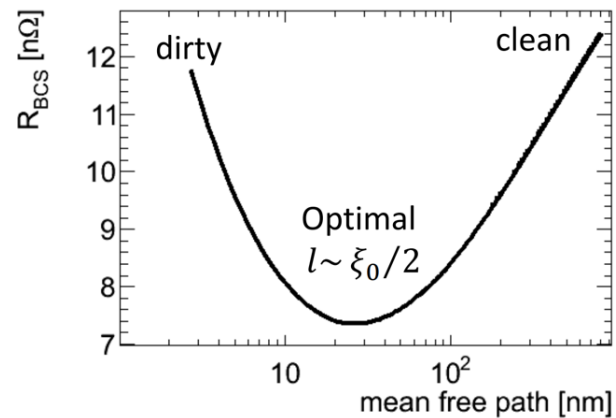


Figure 2: BCS resistance versus mean free path shows an optimization in BCS resistance for moderately dirty surface, adapted from [12].

In this study, we investigate a single-cell TESLA-shaped 1.3-GHz cavity with RRR 61. First, the cavity receives EP treatment to make the surface layer and bulk uniform [13]. The measurements in the vertical test stand include Q_0 versus accelerating gradient at 2 K and low temperature (< 1.5 K) [2]. We define the surface resistance as the geome-

FIRST DEMONSTRATION OF A ZrNb ALLOYED SURFACE FOR SUPERCONDUCTING RADIO-FREQUENCY CAVITIES *

Z. Sun[†], M. U. Liepe, T. Oseroff[‡]

Cornell Laboratory of Accelerator-Based Sciences and Education, Ithaca, NY 14853, USA

Abstract

RF surface design is a promising path to next-generation SRF cavities. Here, we report a new strategy based on ZrNb surface alloying. Material development via an electrochemical process is detailed. RF performance evaluated in the Cornell sample test cavity is discussed. Cornell demonstrates that ZrNb alloying is a viable new technology to improve the performance of SRF cavities.

INTRODUCTION

To boost the performance of superconducting radio-frequency (SRF) cavities, we are motivated to search for next-generation materials and surfaces, together with advanced methods to produce such surfaces. Recently, our theory collaborators at the Center for Bright Beams predict that ZrNb alloys allow large enhancement of the critical temperature and superheating field as compared to conventional niobium [1]. The work we present here aims to provide the experimental demonstration of a ZrNb alloyed SRF cavity.

ZrNb random alloys have been investigated decades ago [2], but the highest T_c reported (11 K) is lower than the theoretical prediction of 18 K T_c for either ordered cubic ZrNb [1, 3] or bcc Zr [4]. Also, thin film ZrNb samples made by sputtering showed T_c of 7.4 K [5]. One of the most critical factors to ensure a high T_c in the ZrNb system is maintaining the desirable cubic structure. Thus, the material design that induces cubic, ordered ZrNb alloys along with a maximized T_c is one goal of this work.

Moreover, ZrNb alloys have not been studied on the cavity scale yet. Calculations showed the addition of Zr in Nb could enable a 1.8 times improvement in the superheating field, a parameter that determines the maximum accelerating gradient for SRF applications [1, 6]. Developing the fabrication process of ZrNb cavities and evaluating their RF superconducting properties are necessary and novel.

We, at Cornell, are establishing the electrochemical deposition technique for surface-alloyed cavities [7–9]. The benefits include an inner-surface facilitated process that is compatible with a complicated 3-D cavity structure, in addition to some unique material products owing to the electrochemical reactions.

Here, we report the fabrication and characterization of electrochemically made ZrNb samples. We observed cubic Zr-Nb surfaces that show T_c values exceeding literature values of ZrNb random alloys. Also, we report the RF per-

formance of ZrNb-alloyed surface in a test cavity. We show the improved BCS resistance of the alloyed sample owing to the high T_c phase as compared to the baseline Nb. Note that a thorough analysis can be found in Ref. [10].

METHODS

A three-electrode electrochemical deposition system was used to deposit Zr films on the Nb surface in an inert gas glovebox. Fig. 1a shows the setup used for process optimization on the sample scale. Pt counter, Nb working, and pseudo reference electrodes were employed together with a hotplate with temperature feedback control. We optimized precursor concentration, deposition temperature, electrochemical potential, and deposition time.

Before Zr deposition, Nb substrates were electropolished with a nominal 100 μm removal. These substrates were HF soaked to remove surface oxides and impurities before any deposition in the glovebox. ZrNb samples were made through the electrochemical reaction under 2 – 10 hours duration. These samples were subsequently annealed in the furnace under 10^{-7} – 10^{-6} Torr vacuum.

Material characterization was performed. X-ray photoelectron spectroscopy (XPS) was used to determine the Zr depth profiles, while energy dispersive X-ray spectroscopy (EDS) imaging was performed to preliminarily confirm the elemental information. High resolution X-ray diffraction (Rigaku XRD) was used to identify the crystal phase. Scanning electron microscopy (Zeiss Gemini 500 SEM) was used to probe the surface morphology.

After the electrochemical and annealing conditions were optimized, we scaled up the process to sample sizes used with the Cornell TE-mode sample test cavity [11] for measuring surface resistances and quench fields at 4 GHz and 5.2 GHz. We measured the critical temperature using two

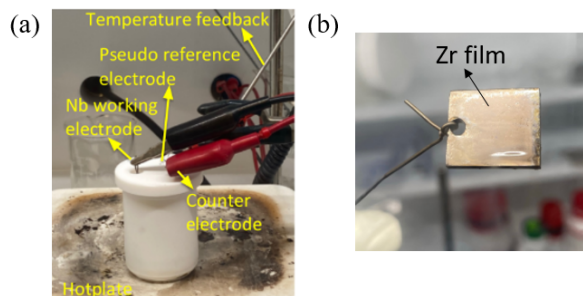


Figure 1: (a) Three-electrode setup for Zr electrochemical deposition at Cornell. (b) Picture of the electrochemically fabricated Zr film on a Nb surface.

* This work was supported by the U.S. National Science Foundation under Award PHY-1549132, the Center for Bright Beams.

[†] zs253@cornell.edu

[‡] teo26@cornell.edu

INSTANT PHASE SETTING IN A LARGE SUPERCONDUCTING LINAC *

A. S. Plastun, P. N. Ostroumov

Facility for Rare Isotope Beams (FRIB), Michigan State University, East Lansing, MI, USA

Abstract

The instant phase setting reduces the time needed to setup 328 radiofrequency cavities of the Facility for Rare Isotope Beams (FRIB) linac from 20 hours to 10 minutes. This technique uses a 1-D computer model of the linac to predict the cavities' phases. The model has been accurately calibrated using the data of the 360-degree phase scans — a common procedure for phasing of linear accelerators. The model was validated by comparison with a conventional phase scan results. The predictions applied to the linac are then verified by multiple time-of-flight energy measurements and the response of the beam position/phase monitors (BPMs) to an intentional energy and phase mismatch.

The presented approach not just reduces the time and the effort required to tune the FRIB accelerator for new experiments every couple of weeks, but it also provides an easy recovery from cavity failures. It is beneficial for user facilities requiring high beam availability, as well as for radioactive ion beam accelerators, where quick time-of-flight energy measurement via the BPMs is not possible due to the low intensities of these beams.

INTRODUCTION

The Facility for Rare Isotope Beams (FRIB) is a new U.S. Department of Energy (DOE) Office of Science user facility [1]. Maintaining high beam variability and availability are our goals. The variability is important because the user experiments last only about a week or two, and the facility needs to be quickly retuned for a new user. The beam availability is essential for good user experience and scheduling of the experiments.

The FRIB driver linac is a folded superconducting RF (SRF) accelerator, as shown in Fig. 1. The number of independently phased RF cavities in the linac is 328 [2–4] (see Table 1), which makes it very flexible for acceleration of various ion species to different energies. Changing the beam velocity profile requires the rephasing of many cavities. The variance of the energy loss of different ion species in the charge stripper makes scaling from one beam to another challenging. When the tune is established and the experiment is running, statistically the chance of a cavity (or its RF circuit) failure is not negligible [5]. The fault scenarios may require the retuning of several cryomodules or even linac segments. If it is done by conventional phase scans, it takes many hours. In this paper, we describe a model-based phasing approach that allows us to change velocity profiles in just several minutes.

* This work is supported by the U.S. Department of Energy Office of Science under Cooperative Agreement No. DE-SC0000661, the State of Michigan, and Michigan State University.

PHASING OF A LINEAR ACCELERATOR

Tuning of field amplitudes and phases of cavities is intended to match the design velocity profile and to provide sufficient stability of longitudinal motion of the beam particles [6]. Usually, it is performed by a phase scan procedure when the cavity phase is scanned in a range of up to 360° and the beam energy is measured. The measurement can be done in different ways, for example, using a sole calibrated dipole magnet [7] or in a combination with a beam position detector [11], using silicon detectors [8, 9], or various time-of-flight techniques by means of gamma-ray detectors [7], fast current transformers [10], beam position/phase monitors (BPPMs or BPMs) [12, 13] and even cavities as the beam phase detectors [14, 15]. The measurements are usually fitted into a model, which sets cavities to a given accelerating (also known as synchronous or reference) phase.

A first-order model, coupling the input W_{in} and output W_{out} beam energies, follows from the Panofsky equation [6, 16] (which was originally derived for an accelerating gap of a drift-tube linac) and can be written as:

$$W_{out} = W_{in} + \Delta W_{max} \cos(\varphi_{cav} + \Delta\varphi), \quad (1)$$

here ΔW_{max} is the maximum energy gain of a charged particle, which can be achieved in the cavity at a given field level, φ_{cav} is the cavity phase control variable, and $\Delta\varphi$ is the phase offset of the cosine-like waveform which depends on delays in the cavity's RF circuits and the beam arrival time to the cavity. The cavity is tuned to a given synchronous phase φ_s when $\varphi_{cav} + \Delta\varphi = \varphi_s$. Assuming the input energy is known from the phasing of an upstream cavity, Eq. (1) has two unknowns, namely the ΔW_{max} and the $\Delta\varphi$, which can be found from at least two sets of (φ_{cav}, W_{out}) .

In SRF linacs phase scans may look significantly different from a cosine curve due to high accelerating field amplitudes and low beam energies. Figure 2 presents several examples obtained by particle tracking, as well as their first and second-order approximations [17]. In such cases, the cavity phase φ_{cav} corresponding to the desired φ_s should be set in the same way as the particle tracking (beam dynamics) codes do that.

Table 1: FRIB Linac Cavities

Type	#	Segments	β_{opt}	V_a (MV)
Buncher	2	MEBT	0.038	0.10
QWR041	12	LS1	0.043	0.81
QWR085	92	LS1, FS1	0.086	1.78
IH-Buncher	2	FS1	0.185	1.00
HWR029	72	LS2	0.290	2.09
HWR053	148	LS2, FS2, LS3	0.543	3.70

DESIGN OF 3-GeV HIGH-GRADIENT BOOSTER FOR UPGRADED PROTON RADIOGRAPHY AT LANSCE*

Y. K. Batygin[†], S. S. Kurennoy, Los Alamos National Laboratory, Los Alamos, NM 87545, USA

Abstract

Increasing the proton beam energy from the present 800 MeV to 3 GeV will improve the resolution of the Proton Radiography Facility at the Los Alamos Neutron Science Center (LANSCE) by a factor of 10. It will bridge the gap between the existing facilities, which covers large length scales for thick objects, and future high-brightness light sources, which can provide the finest resolution. Proton radiography requires a sequence of short beam pulses (~20 x 80 ns) separated by intervals of variable duration, from about 300 ns to 1-2 μs. To achieve the required parameters, the high-gradient 3-GeV booster is proposed. Utilization of buncher-accelerator-debuncher scheme allows us to combine high-gradient acceleration with a significant reduction of beam momentum spread. Paper discusses details of linac design and expected beam parameters.

INTRODUCTION

Proton Radiography (pRad) was developed in the Los Alamos National Laboratory in the mid-1990s as a multi-pulse flash technique for deep-penetrated hydro test objects study [1]. It utilizes an 800-MeV proton beam from Los Alamos linear accelerator with a beamline for beam imaging (see Fig. 1). Increasing the proton energy from the present 800 MeV to 3 GeV will significantly improve the resolution of radiography. Such an improvement can bridge the gap between the existing LANL DARHT facility and future high-brightness light sources like MaRIE and DMMSC [2]. One important requirement to the 3-GeV booster is a significant reduction of beam momentum spread from the existing value of $dp/p = 1 \cdot 10^{-3}$ to the new value of $dp/p = 3.3 \cdot 10^{-4}$. The proposed booster is based on high gradient (HG) cavities. Stepwise increase of the RF operating frequency in the booster from S-band to C-band allows us to combine high accelerating gradient with high beam capture and low emittance growth. This paper discusses a layout of the proposed accelerator for 3 GeV pRad enhancement.

TIME STRUCTURE OF PROTON BEAM

The time structure of the LANL proton radiography beam is presented in Fig. 2, and parameters of existing and future pRad beams are presented in Table 1. Proton radiography pulse contains 60 ns triggering beam pulse followed by 100 μs time interval and by a sequence of beam imaging pulses. These pulses are of the length of 60 - 80 ns containing up to 16 linac bunches with bunched beam current

* Work supported by US DOE under contract 89233218CNA000001.
[†] batygin@lanl.gov

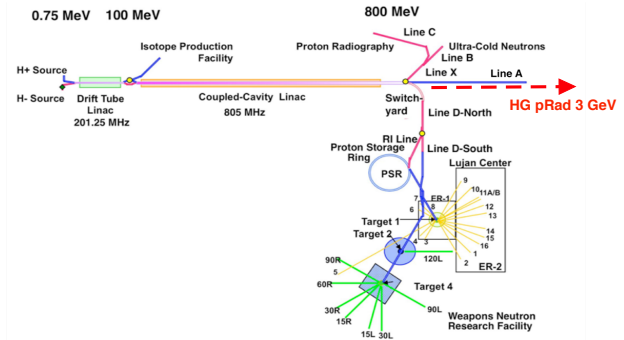


Figure 1: LANSCE accelerator facility and potential location of 3 GeV High-Gradient pRad booster.

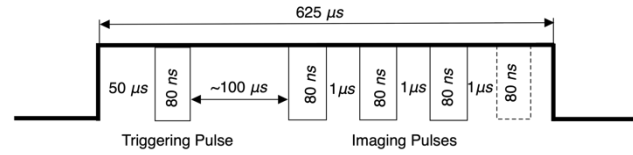


Figure 2: Time structure of LANSCE pRad beam.

Table 1: Parameters of Proton Beam

Parameter	Existing	Upgraded
Energy (GeV)	0.8	3
Momentum spread, dp/p	1×10^{-3}	3.3×10^{-4}
Beam current / bunch (mA)	10	19
Protons per pulse	5×10^9	9.5×10^9

$I = 10$ mA. Bunches follow with the RF period of 5 ns defined by the linac RF frequency $f = 201.25$ MHz.

Each bunch contains a charge of $Q = I/f = 4.9 \cdot 10^{-11}$ C which corresponds to $3 \cdot 10^8$ protons per bunch. The 16 bunches work cumulatively to produce one image with the total number of protons $\sim 5 \cdot 10^9$. For multiple images (movie of a dynamic event), pRad uses a few such pulses separated by a time interval of about 1 μs. Peak beam current per bunch in LANL accelerator is limited by the value of ~20 mA which, in turn, is limited by the power of 805 MHz klystrons. The number of protons per imaging session can be doubled in the existing LANL accelerating facility.

DESIGN OF HIGH-GRADIENT PRAD BOOSTER

High-gradient booster for pRad expansion at LANL was proposed in Ref. [3], and a preliminary design was performed in Ref. [4]. One of the main issues in the design is the minimization of the size of the accelerator with high beam capture and low emittance growth. Beam

Content from this work may be used under the terms of the CC BY 4.0 licence (© 2022). Any distribution of this work must maintain attribution to the author(s), title of the work, publisher, and DOI

ACCELERATING STRUCTURES FOR HIGH-GRADIENT PROTON RADIOGRAPHY BOOSTER AT LANSCE

S. S. Kurennoy, Y. K. Batygin, E. R. Olivas, LANL, Los Alamos, NM, USA

Abstract

Increasing the energy of proton beam at LANSCE from 800 MeV to 3 GeV improves radiography resolution ~10 times. We proposed accomplishing such an energy boost with a compact cost-effective linac based on normal conducting high-gradient (HG) RF accelerating structures. Such an unusual proton linac is feasible for proton radiography (pRad), which operates with short RF pulses. For a compact pRad booster at LANSCE, we have developed a multi-stage design: a short L-band section to capture and compress the 800-MeV proton beam followed by the main HG linac based on S- and C-band cavities, and finally, by an L-band de-buncher. Here we present details of development, including EM and thermal-stress analysis, of proton HG structures with distributed RF coupling for the pRad booster. A simple two-cell structure with distributed coupling is being fabricated and will be tested at the LANL C-band RF Test Stand.

INTRODUCTION

Proton radiography employs high-energy proton beams to image material behavior under extreme conditions. It was invented and developed at LANL. The pRad program at the Los Alamos Neutron Science Center (LANSCE) has performed hundreds of successful experiments, both static and dynamic. While the LANSCE 800-MeV linac accelerates both protons and H^- ions, the pRad uses H^- beam, which is presently the only beam species that can be chopped in the front end and directed to the pRad facility. For dynamic experiments, pRad uses multiple pulses from the linac, which produce movies up to a few tens of frames. Each short pRad beam pulse consists of several successive bunches from the linac, which follow at the linac DTL repetition rate of 201.25 MHz, to multiply the pulse total intensity. This is because the H^- bunch current at 800 MeV is limited to ~10 mA, mainly by the ion source, but also by losses in the linac. On the other hand, the pRad pulses are restricted to 80 ns in length, i.e., contain no more than 16 linac bunches, to prevent image blur.

Increasing the beam energy for pRad at LANSCE from present 800 MeV to 3 GeV would provide significant improvements: for thin objects, the radiography resolution would increase about 10 times, and much thicker objects could be also imaged [1]. A superconducting (SC) option for a pRad booster to 3 GeV was considered in [1]. Assuming a typical real-estate gradient of 15 MV/m, it leads to a rather long booster, at least 150-m long. This option is also expensive, in part because it requires a new cryogenic plant. We proposed a much shorter and cheaper booster based on high-gradient (~100s MV/m) normal-conducting RF accelerating structures operating at low duty factors [2].

HIGH-GRADIENT PRAD BOOSTER

Requirements for pRad Booster Cavities

HG structures with phase velocity $\beta = 1$ were developed for acceleration of electrons [3]. Accelerating gradients up to 150 MV/m have been demonstrated in X-band copper cavities at room temperature. When such cavities are operated at cryogenic temperatures (cryo-cooled), gradients up to 250 MV/m were achieved. HG C-band cavities at room temperature provide gradients 50-60 MV/m, but at liquid-nitrogen (LN_2) temperature one can expect gradients two times higher. 800-MeV protons at the exit of the LANSCE linac have velocity $\beta = v/c = 0.84$, and at 3 GeV $\beta = 0.97$. Therefore, HG cavities must be modified for protons to cover this velocity range.

Operating the HG pRad booster at liquid-nitrogen temperatures makes structures more efficient and reduces the required RF power. Such operation of pRad booster seems practical: the pRad needs only 1-20 beam pulses per event spread by about 1 μ s; no more than a few events per day. Even if some nitrogen evaporates due to heating caused by RF losses in cavity walls during one event, it can be easily refilled before the next one.

There are additional requirements for HG structures for pRad booster. First, they must accept the large proton bunches out of the existing linac both longitudinally – this limits RF frequency from above – and transversely, which limits the cavity aperture from below. Second, high accelerating gradients lead to beam defocusing by RF fields, so a strong focusing is required. There are also important requirements to the output beam: energy stability pulse-to-pulse, pulse timing, and low energy spread. For better quality of radiographs, it is desirable to reduce the relative momentum spread, $dp/p = 10^{-3}$ at the exit of our 800-MeV linac, as $1/p$, i.e., to $3.3 \cdot 10^{-4}$ at 3 GeV.

Further considerations are related to the LANSCE layout and operations. The facility delivers five different beam types [4] to multiple users, and it is important to preserve this capability. The closest point where a new booster can start is about 38 m away from the 800-MeV linac exit, after the existing switchyard. The exiting beam spreads in this drift, so we need to lower RF frequency in the first cavities to capture it longitudinally. All the above requirements led to a multi-stage compact booster design [5].

pRad Booster Design

The booster starts with an L-band buncher operating at 1408.75 MHz, the 7th harmonic of the linac bunch frequency 201.25 MHz, to capture 800-MeV linac bunches. The booster includes S-band structures at 2817.5 MHz to the energy of 1.6 GeV and continues with C-band struc-

AN 8 GEV LINAC AS THE BOOSTER REPLACEMENT IN THE FERMILAB POWER UPGRADE*

D. Neuffer[†], S. Belomestnykh, M. Checchin, D. Johnson, S. Posen,
 E. Pozdeyev, V. Pronskikh, A. Saini, N. Solyak, V. Yakovlev
 Fermilab, Batavia, IL 60510, USA

Abstract

Increasing the Fermilab Main Injector (MI) beam power above ~ 1.2 MW requires replacement of the 8 GeV Booster by a higher intensity alternative. Earlier, rapid-cycling synchrotron and linac solutions were considered for this purpose. In this paper, we consider the linac version that produces 8 GeV H^- beam for injection into the Recycler Ring (RR) or MI. The new linac takes ~ 1 GeV beam from the PIP-II linac and accelerates it to ~ 2 GeV in a 650 MHz SRF linac, and then accelerates to ~ 8 GeV in an SRF pulsed linac using 1300 MHz cryomodules. The linac components incorporate recent improvements in SRF technology. This Booster Replacement linac (BRL) will increase MI beam power to DUNE to more than 2.5 MW and enable next-generation intensity frontier experiments.

INTRODUCTION

The PIP-II project will provide an 800 MeV proton beam with CW capability, with beam power up to the MW level available for user experiments [1]. However, the amount of beam that can be transmitted to the Main Injector (MI) is limited by the 0.8–8.0 GeV Booster capacity. The next Fermilab upgrade should include a replacement for the Booster [2]. The upgrade could be based on a continuation of the 800 MeV linac to ~ 2 GeV followed by either a Rapid Cycling Synchrotron (RCS) [3] or continuing the linac to 8 GeV. The 8 GeV linac would use PIP-II 650 MHz cryomodules followed by relatively inexpensive LCLS-II [4] or ILC-style cryomodules that use 1300 MHz SRF cavities, which have already been designed and mass-produced. This approach has been documented in a Snowmass 2021 white paper [5]. In this paper, we discuss the 8 GeV linac option. We begin with some discussion of the beam requirements and potential layouts for the linac. Constraints and features of the scenarios are then discussed.

LINAC SCENARIO REQUIREMENTS

The Fermilab Proton Improvement Plan II (PIP-II) provides a new 800 MeV superconducting RF (SRF) linac that replaces the previous 400 MeV linac, enabling higher intensity injection into the Fermilab Booster and providing 800 MeV proton beam to other experiments. The primary purpose of PIP-II is to provide enhanced beam power delivery from the Main Injector to DUNE (Deep Underground Neutrino Experiment) [3]. This is enabled by increasing the beam energy and intensity delivered by the

linac to the Fermilab Booster and increasing the Booster cycle rate. Table 1 shows high-level parameters of the Fermilab beam to DUNE before and after PIP-II, as presented in the Fermilab PIP-II Design Report. PIP-II increases the Booster cycle rate to 20 Hz and the beam intensity to 6.6×10^{12} protons/pulse, enabling beam power of ~ 1 to 1.2 MW at beam energies of 60 to 120 GeV.

Further improvements will require replacement of the Booster with a higher-capacity injector. The initial design specification for the upgrade is that it should enable at least ~ 2.4 MW to DUNE from the MI [6]. High-level performance goals are presented in Table I.

Table 1: High-Level Parameters for PIP, PIP-II and the Booster Replacement Linac

Parameter	PIP-I	PIP-II	BRL	Unit
Linac Energy	400	800	8000	MeV
Beam Current	25	2	2	mA
Pulse length	0.03	0.54	2.1	ms
Pulse Rep. Rate	15	20	20	Hz
Protons/pulse	4.2	6.5	26.0	10^{12}
8 GeV power	80	166	700	kW
Power to MI	50	83-142	176-300	kW
MI protons/pulse	4.9	7.5	15.6	10^{13}
MI cycle time (120 GeV)	1.5	1.2	1.2	s
MI Power to DUNE	0.7	1.2	2.5	MW
8 GeV other users	30	83	500	kW

LAYOUT

The BRL must take beam from the PIP-II linac into the MI/RR. The configuration is constrained by the fixed location of PIP-II and its proximity to the MI. Figure 1 shows a possible scenario. The PIP-II linac is extended to ~ 1 GeV by adding 2 cryomodules within the lattice at the end of the PIP-II tunnel, using drift spaces reserved for future extensions. The beam exiting that linac is bent at $\sim 45^\circ$ into a $1 \rightarrow 2.4$ GeV linac, which uses ~ 10 – 12 PIP-II 650 MHz cryomodules, requiring ~ 120 – 150 m. The total length available is ~ 290 m; the additional length will be used for optics matching and collimation. The transition energy depends on future design optimizations and applications; we consider 2.4 GeV as an initial choice.

The beam then goes through an achromatic bend of approximately 105° to be pointed toward injection into the Recycler Ring (RR) at MI-10. The following ~ 500 m

*Work supported by Fermi Research Alliance, LLC under Contract No. DE-AC02-07CH11359 with the U.S. Department of Energy, Office of High Energy Physics.

[†] neuffer@fnal.gov

DEVELOPING CONTROL SYSTEM SPECIFICATIONS AND REQUIREMENTS FOR THE ELECTRON ION COLLIDER*

A. Blednykh[†], E. Aschenauer, P. Baxevanis, M. Blaskiewicz, A. Drees, D. Gassner, T. Hayes, J. Jamilkowski, G. Marr, S. Nemesure, V. Schoefer, T. Shrey, K. Smith, F. Willeke
 Brookhaven National Laboratory, Upton, NY, USA
 B. Dalesio, Osprey DCS, Ocean City, MD, USA

Abstract

An Accelerator Research facility is a unique science and engineering challenge in that the requirements for developing a robust, optimized science facility are limited by engineering and cost limitations. Each facility is planned to achieve some science goal within a given schedule and budget and is then expected to operate for three decades. In three decades, the mechanical systems and the industrial IO to control them is not likely to change. In that same time, electronics will go through some 4 generations of change. The software that integrates the systems and provides tools for operations, automation, data analysis and machine studies will have many new standards. To help understand the process of designing and planning such a facility, we explain the specifications and requirements for the Electron Ion Collider (EIC) from both a physics and engineering perspective.

INTRODUCTION

The Electron-Ion Collider (EIC) is being built to research the high energy spin-polarized particle beams in order to quantify contribution of the intrinsic spins, orbital momenta of quarks, anti-quarks and gluons to the characteristic spins of observe particles [1]. High collision luminosity 10^{33} - 10^{34} $\text{cm}^{-2} \text{s}^{-1}$ over a broad range in center-of-mass energies (ECM) from 20 GeV to 140 GeV will enable precise determination of the confined momentum and spatial distributions of the sea of quarks and gluons in nucleons and nuclei. One of the most challenging tasks is to obtain high luminosity. The EIC consists of electron and hadron accelerators with an interaction region to produce collisions of electron and proton beams with high intensity (shown in Fig. 1). The electron injection scheme includes: a 400 MeV LINAC, a Rapid Cycling Synchrotron (RCS) with energy ramp from 400 MeV to 18 GeV, and an Electron Storage Ring (ESR) with operation at 5 GeV, 10 GeV and 18 GeV energies. The average current of the electron beam at 5 GeV and 10 GeV is $I_{av} = 2.5$ A within $M = 1160$ bunches with a $\sigma_s = 7$ mm bunch length. The average current at 18 GeV is much smaller, $I_{av} = 0.23$ A. The standard vacuum chamber for ESR has an elliptical profile with 80 mm x 36 mm (copper). The Ion Injection Scheme is based on the existing RHIC accelerator complex, where the proton beam will be accelerated to 41 GeV, 100 GeV and 275 GeV energies. The entire complex includes a

200 MeV LINAC, Booster, Alternating Gradient Synchrotron (AGS) and a Hadron Storage Ring (HSR) with more aggressive beam parameters as $I_{av} = 0.69$ A within $M = 290$ bunches with a $\sigma_s = 60$ -mm bunch length. The present RHIC vacuum system will be fully updated, and it includes amorphous carbon (aC) and copper (Cu) coated stainless steel beam screen chambers, which are actively cooled [2]. To achieve 10^{34} $\text{cm}^{-2} \text{s}^{-1}$ luminosity, the strong hadron cooling concept (SHC) is being developed.

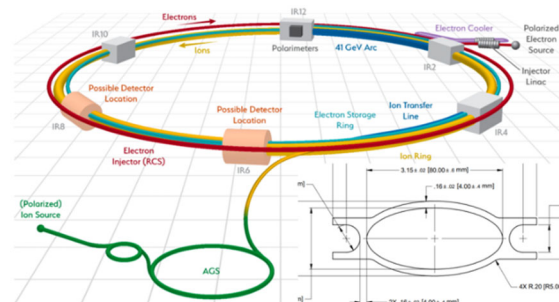


Figure 1: EIC layout with profile of the vacuum chamber for the electron storage ring.

This paper focuses on e activity to capture the control system specifications. These specifications include the integration of all instrumentation to meet the needs of the facility for construction, implementation, integration, subsystem commissioning, beam commissioning and operations. Developing these specifications for a new accelerator facility requires a broad range of skills to determine both the necessary capabilities and the potential capabilities to improve efficiency throughout the life cycle of the project.

CONTROL SYSTEM COMPONENTS

The control system includes a broad range of functionality. The lowest level the control system provides electrical and computer interfaces to all instrumentation for control and monitoring. It also includes the standard network and the commercial computer hardware for all hardware integration. It includes the middle layer services to collect, manage and provide aggregated data such as time series archives and configuration data such as the lattice. The controls group provides the operator stations and storage to provide Supervisory Control and Data Acquisition (SCADA) functionality. For accelerators, there are a special set of requirements for control and monitoring Infrastructure that support the synchronization of control and data acquisition of beam-related instrumentation.

* Work supported by Brookhaven Science Associates, LLC under Contract No. DE-SC0012704 with the U.S. Department of Energy.

[†] blednykh@bnl.gov

AN ELECTRODLESS DIAMOND BEAM MONITOR*

P. Avrakhov, S. Kuzikov[†], C. Jing^{1,2}, E. Knight, Euclid TechLabs, Solon, IL, USA
 J. Power, D. S. Doran, E. Wisniewski, ANL, Lemont, IL, USA

Abstract

Being a wide-band semiconductor, diamond can be used to measure the flux of passing particles based on a particle-induced conductivity effect. We recently demonstrated a diamond electrodeless electron beam halo monitor. That monitor was based on a thin piece of diamond (blade) placed in an open high-quality microwave resonator. The blade partially intercepted the beam. By measuring the change in RF properties of the resonator, one could infer the beam parameters. At Argonne Wakefield Accelerator we have tested 1D and 2D monitors. To enhance the sensitivity of our diamond sensor, we proposed applying a bias voltage to the diamond which can sustain the avalanche of free carriers. In experiment carried out with 120 kV, ~1 μA beam we showed that the response signal for the avalanche monitor biased with up to 5 kV voltage can be up to 100 times larger in comparison with the signal of the same non-biased device.

INTRODUCTION

Beam halo has a relatively low charge density. However, for high intensity beams, the actual number of particles in the halo is typically quite large. For this reason, the halo is associated with an uncontrolled beam loss, and must be monitored and mitigated [1]. In our proposal, we consider the use of diamond for a sensing material, because of its extraordinary mechanical, electrical, and thermal properties. Large bandgap, radiation hardness, high saturated carrier velocities, and low atomic number make diamond an attractive candidate for the detection of ionizing radiation and charged particles. Previously we proposed an electrodeless measurement of the charged particle-induced conductivity of the diamond by means of a microwave resonator reflection measurement [2-3]. A diamond blade is used to intercept electrons. The blade is inserted inside a critically coupled resonator, i.e., when fed microwaves at the resonant frequency, there will be no reflection from the resonator. Due to electron interactions with the diamond, the diamond becomes weakly conductive. Because of that, the microwave properties of the resonator change, and it starts to reflect power at the resonant frequency, a signal whose amplitude is correlated to the intercepted charge from the halo.

2D BEAM HALO MONITOR

The Figure 1 shows the overall view of the 2D scanning beam halo monitor (BHM) that photograph is shown in Fig. 1. The device utilizes the 4.5" bellow to allow 1D

scanning range ±15 mm. The bellow is controllable by a precise motor with a controller. The motor allows to move the resonator with diamond blade across beam +/- 1 inch in each X- or Y- direction. The resonator itself has the same design which was used for the 1D monitor version [3]. The resonator (f=6.7 GHz, Q~400) relates to the copper WR112 waveguide which is located inside the motorized bellow. A ceramic RF window separates ultra-high vacuum part of the monitor from air.

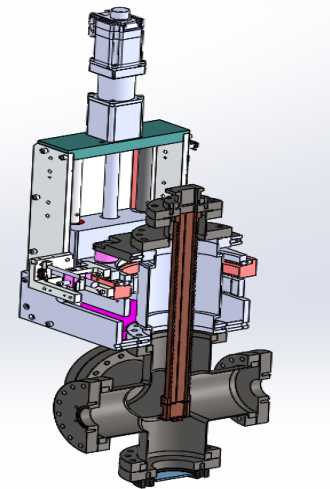


Figure 1: Engineering design of the 2D scanning beam halo monitor.

The 2D BHM monitor was tested at AWA with MeV level electron beam (Fig. 2). The preliminary results from the recent experiment with the 2D BHM at AWA demonstrate good coincidence of the beam maps plotted with the YAG screen and with our monitor (compare Fig. 3 and Fig. 4 respectively). Remarkably, the halo monitor was capable to show so small signals that were not visible for the conventional YAG screen. More accurate data processing is coming to eliminate BHM nonlinear response and to mitigate diamond blade size influence.



Figure 2: 2D scanning beam halo monitor at AWA beam-line.

* Work supported by DoE SBIR grant #DE-SC0019642.

[†] s.kuzikov@euclidtechlabs.com

¹also at Euclid Beamlabs LLC, Bolingbrook, IL, USA

²also at ANL, Lemont, IL, USA

EXPERIMENTAL CHARACTERIZATION OF GAS SHEET TRANSVERSE PROFILE DIAGNOSTIC

N. Burger^{*}, G. Andonian¹, T. Hodgetts, D. Gavryushkin, A.L. Lamure, M. Ruelas,
RadiBeam Technologies, Santa Monica, CA, USA
N. Norvell, University of Santa Cruz, Santa Cruz, CA, USA
N. Cook, A. Diou, Radiasoft LLC, Boulder, CO, USA
C. Welsch, M. Yadav¹, University of Liverpool, Liverpool, UK
P. Denham, P. Musumeci, A. Ody,
University of California Los Angeles, Los Angeles, CA USA
¹also at University of California Los Angeles, Los Angeles, CA USA

Abstract

The non-invasive characterization of high intensity charged particle beams is necessary in modern accelerators. Here, we present an update on a diagnostic that operates on the principle of beam-induced ionization across a spatially localized gas distribution. As the beam traverses through the gas sheet, the ionization cloud is transported and imaged on a detector to reveal beam transverse distributions. A modular gas jet transport allows for tunability of gas sheet parameters, while a tunable array of electrostatic lenses allows for the imaging of a variety of ion species. The benchtop results of gas sheet characterization using an insertable periscope probe are presented. In addition, preliminary results on the ion imaging system, including focusing with electrostatic lenses and detection on a micro-channel plate are shown for a low energy test case.

BACKGROUND

Non-invasive and non-destructive beam diagnostics are necessary for applications where beam quality is important and where high intensity beams preclude operation of standard techniques. In this paper, we present the development of a transverse beam profile monitor that operates on the principle of gas ionization. A supersonic gas jet is tailored, using an array of precision skimmers, into a thin curtain-shaped sheet (approximately 150 μm thick) oriented at 45° with respect to the beam axis. The localized gas density is introduced in the center of a diagnostic chamber orthogonal to the main beam. The charged particle beam passes through the gas sheet, and ionizes the neutral gas particles in its path; depending on the beam intensity, different ionization regimes may be considered. The ionization cloud is then imaged on a spatial detector, revealing information encoded by the passing particle beam. Reconstruction algorithms trained on simulation data provide further details in a rapid feedback system. A rendering of the complete gas sheet monitor is shown in Fig. 1.

^{*} nburger@radiabeam.com

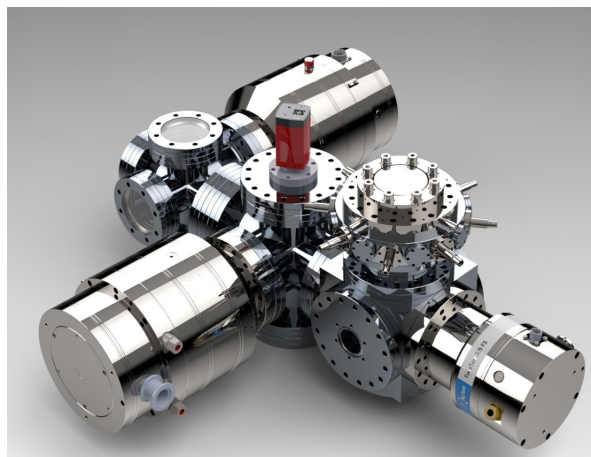


Figure 1: Rendering of gas sheet ionization monitor. The overall footprint of the monitor is < 1 m in the transverse direction, and < 200 mm in the longitudinal direction (i.e. beam axis).

GAS SHEET MONITOR

The gas sheet ionization monitor is based on a successful design used prior for low energy beams [1]. The monitor incorporates a number of distinct engineering developments for complete operation. First, the gas delivery system includes multiple nozzles and skimmers and a fast-piezo valve. The shaped nozzles serve to first collimate the supersonic gas jet, and the second skimmer is used to shape the gas jet profile at the interaction region. The fast valve is used to decrease the gas load on the turbo-molecular pumps of the main chamber. Using a scheme that incorporates differential pumping, UHV levels of 1×10^{-9} mbar are maintained outside the localized density region of the interaction point. Using the gas delivery system, a local gas sheet of density $\sim 10^{12}$ – 10^{16} cm^{-3} is able to be achieved, with a pulse duration variable from 40 μs - 400 μs [2], up to 1 kHz repetition rate.

In order to characterize the gas density, a diagnostic method was developed for bench top tests to compare against simulation results using the code MolFlow [3]. Figure 2 shows a sample measurement of the gas sheet density at the interaction region. In place of the ion microscope at the inter-

MEASUREMENTS OF THE FIVE-DIMENSIONAL PHASE SPACE DISTRIBUTION OF AN INTENSE ION BEAM*

A. Hoover[†], K. Ruisard, A. Alexandrov, A. Zhukov, S. Cousineau, ORNL, Oak Ridge, TN, USA

Abstract

No simulation of intense beam transport has accurately reproduced measurements at the level of beam halo. One potential explanation of this discrepancy is a lack of knowledge of the initial distribution of particles in six-dimensional (6D) phase space. A direct 6D measurement of an ion beam was recently performed at the Spallation Neutron Source (SNS) Beam Test Facility (BTF), revealing nonlinear transverse-longitudinal correlations in the beam core that affect downstream evolution. Unfortunately, direct 6D measurements are limited in resolution and dynamic range; here, we discuss the use of three slits and one screen to measure a 5D projection of the 6D phase space distribution, overcoming these limitations at the cost of one dimension. We examine the measured 5D distribution before and after transport through the BTF and compare to particle-in-cell simulations. We also discuss the possibility of reconstructing the 6D distribution from 5D and 4D projections.

INTRODUCTION

The phase space distributions of intense beams tend to develop halo during low-energy transport [1]. The existence of beam halo at higher energies leads to uncontrolled losses that limit the performance of high-power accelerators [2]. Attempts to reproduce measurements at the halo level in computer simulation have been unsuccessful [3–5], likely due to an inaccurate initial distribution of particles in 6D phase space.

The Spallation Neutron Source (SNS) Beam Test Facility (BTF) is poised to resolve these discrepancies. The BTF is a replica of the front-end of the SNS — the H^- ion source, 65 keV low-energy beam transport (LEBT), 402.5 MHz radio-frequency quadrupole (RFQ), and 2.5 MeV medium energy beam transport (MEBT) — followed by a 9.5-cell FODO transport line [6]. There are two emittance measurement stations: one 1.3 meters downstream of the RFQ and one after the FODO line. The two-dimensional (2D) horizontal and vertical phase space distributions can be measured at either station with a dynamic range above 10^6 [7], large enough to image the beam halo [8]. The 6D phase space distribution can be measured at the first station [9].

One goal of the research program at the BTF is to reproduce the measured halo at the second emittance station in simulation. Unfortunately, it is not currently possible to generate a realistic initial bunch due to the limited resolution (10 points per dimension) and dynamic range (10^1) of 6D

measurements.¹ Improvements to the scan efficiency are under development; in this paper, we consider the use of three slits and one screen to measure a 5D projection of the 6D phase space distribution, overcoming these limitations at the cost of one dimension. We examine the measured 5D distribution at both emittance stations and discuss how the measurements might contribute to the goal of halo prediction at the BTF.

MEASUREMENTS OF THE INITIAL DISTRIBUTION IN THE BTF

The measurement apparatus is described in [10]; it consists of two vertical slits to select the horizontal position x and momentum x' , a vertical slit to select the vertical position y , and a scintillating screen after a dipole bend. The vertical momentum y' is linearly related to the vertical position on the screen; the energy deviation w is a function of the horizontal position on the screen and the x and x' selected by the upstream slits. The scan consists of a series of "sweeps" where the vertical slits are held fixed while the horizontal slit moves at a fixed speed, collecting the image on the screen on every beam pulse at a 5 Hz repetition rate. A rectilinear scan pattern is employed with a linear correlation between x and x' to align the grid with the x - x' distribution. The data is linearly interpolated onto a regular grid after transforming to phase space coordinates.

Revisiting Hidden Features in the Beam Core

We first examine a measured 5D distribution at the first emittance station. 57,766 images were collected over 4.9 hours as the slits traversed a $32 \times 32 \times 32$ grid. The beam current during the measurement was stable at 30.6 mA. The full projections of this data set are shown in [10]; the density profiles vary smoothly in all projections and there are no visible inter-plane correlations.

Yet previous high-dimensional measurements of the beam exiting the RFQ have revealed nonlinear transverse-longitudinal correlations in the beam core: the energy and phase distribution of particles at the center of transverse phase space ($x \approx x' \approx y \approx y' \approx 0$) is hollow and bimodal while the full projection is unimodal [9]. This is a space-charge-driven effect [11] and has a clear dependence on the beam intensity. The relationship between the energy and transverse coordinates has been examined by slicing the distribution in the transverse plane before projecting the distribution onto the energy axis; i.e., by inserting slits upstream of the longitudinal emittance measurement diagnostic. The

* This manuscript has been authored by UT-Battelle, LLC under Contract No. DE-AC05-00OR22725 with the U.S. Department of Energy. This research used resources at the Spallation Neutron Source, a DOE Office of Science User Facility operated by the Oak Ridge National Laboratory.

[†] hooveram@ornl.gov

¹ A 6D measurement with these parameters took over thirty-two hours in Ref. [9] but has been reduced to twenty-four hours with improved data acquisition software.

SUPPRESSING THE MICROBUNCHING INSTABILITY AT ATF USING LASER ASSISTED BUNCH COMPRESSION*

Q. R. Marksteiner[†], P. M. Anisimov, B. E. Carlsten, G. A. Latour, E. I. Simakov, H. Xu
 Los Alamos National Laboratory, Los Alamos, NM, USA

Abstract

The microbunching instability in linear accelerators can significantly increase the energy spread of an electron beam. The instability can be suppressed by artificially increasing the random energy spread of an electron beam, but this leads to unacceptably high energy spreads for future XFEL systems. One possibility of suppressing this instability is to use laser assisted bunch compression (LABC) instead of the second chicane in an XFEL system, thereby eliminating the cascaded chicane effect that magnifies the microbunching instability. An experiment is proposed at ATF to test this concept, and numerical simulations of the experiment are shown.

INTRODUCTION

There are several reasons why the eSASE [1] and LABC [2] schemes are promising and are being considered for future, more affordable X-ray free electron lasers, including the fact that they can reduce the effects of CSR, ISR, and undulator wakes [3]. One of the most important differences of an eSASE or LABC accelerator compared with a conventional accelerator is that these accelerators reduce the effects of the microbunching instability (MBI) [4]. Here we propose an experiment where an electron beam is compressed to similar amounts with 2 bulk chicanes and with the LABC scheme, in order to verify that this technique can suppress the MBI.

The Accelerator Test Facility (ATF) at Brookhaven National Laboratory (BNL) is an ideal location for experimentally verifying if the proposed compression architecture can suppress the MBI [5].

One of the most complicated aspects of our planned experiment is the existence of the dogleg at ATF. If we are not careful, the dogleg can modify the longitudinal current profile of the electron bunch, and can alter the results of our experiment. By carefully tuning the quads in the dogleg, the dispersive properties can be eliminated. We will show with simulation that the proposed compression architecture can meet its MBI suppression goal. The ATF beamline as well as the laser modulator and small chicane needed for the MBI suppression experiment are modeled in the numerical ELEctron Generation ANd Tracking (ELEGANT) code [6].

In Fig. 1, we show the predicted microbunching gain of our experiment, for both the bulk compression and the LABC case. The idea is that we need to eliminate dispersion from the dogleg at wavelengths that are relevant to the microbunching gain, so that MBI will be preserved. In the

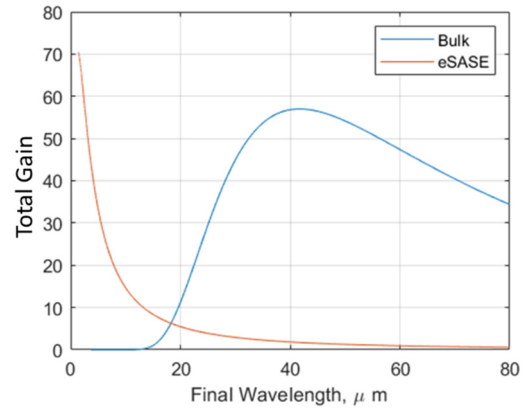


Figure 1: Predicted microbunching gain for the proposed eSASE and bulk compression schemes at ATF.

following, we will discuss three issues that arose when trying to set up the beamline simulation to transport an electron bunch while also preserving the longitudinal structure we wish to analyze. Further, we provide matching optics parameters for bunches with two different energy spreads.

MINIMIZING DISPERSION

A schematic of the relevant optics that will be modeled is shown in Fig. 2. The dogleg must be tuned such that the amount of dispersion introduced to the bunch is minimized. Particles with varying momenta will be deflected differently by the two bending magnets that constitute the dogleg, i.e. higher momentum particles will be bent through a smaller angle and lower momentum particles through a larger angle. In addition, some particles will have a different path length through the dogleg than the ideal particle. This path length difference will result in particles arriving at the end of the dogleg at different times relative to their neighbors and the mismatch in arrival times will smear the longitudinal structure of the beam.

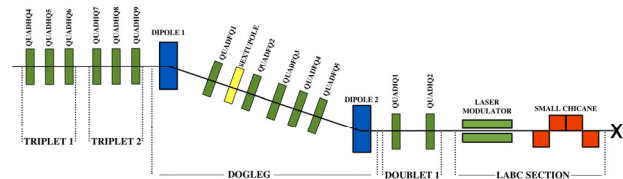


Figure 2: Drawing of the ATF beamline section that we model in ELEGANT. The beam propagates towards the right through the beamline.

In order to preserve the longitudinal structure of the beam, the matching optics in the dogleg need to be tuned such that the difference in path length, l , between particles of differing momenta is zero, i.e. $\Delta l \equiv 0$ between the

* We gratefully acknowledge the support of the US Department of Energy through the LANL LDRD program.

[†] qrm@lanl.gov

BUNCH LENGTH MEASUREMENTS AT THE CEBAF INJECTOR AT 130 kV *

S. Pokharel^{†1}, G. A. Krafft¹

Center for Accelerator Science, Old Dominion University, Norfolk, VA 23529, USA

A. S. Hofler, R. Kazimi, M. Bruker, J. Grames, S. Zhang

Thomas Jefferson National Accelerator Facility, Newport News, VA 23606, USA

¹also at Thomas Jefferson National Accelerator Facility, Newport News, VA 23606, USA

Abstract

In this work, we investigated the evolution in bunch length of beams through the CEBAF injector for 8–770 fC charge per bunch. Using the software General Particle Tracer (GPT), we have simulated beams through the beamline of the CEBAF injector to predict bunch lengths at the location of a beam chopper for comparison with measurements and to validate the model. We performed these simulations with the existing injector using a 130 kV gun voltage. The measurements have been done using chopper phase scanning technique for two injector laser drive frequencies 499 MHz and 249.5 MHz.

INTRODUCTION

The Continuous Electron Beam Accelerator Facility (CEBAF) injector at Jefferson Lab provides beams to the main accelerator, two recirculating linacs operating at 1497 MHz, connected by beam transport arcs. The beams are delivered to the experimental halls at either 499 MHz or 249.5 MHz. The CEBAF polarized electron source creates a spin-polarized electrons beams using a DC high-voltage photo-gun. The electron beam itself is composed of four interleaved electron beams created using four lasers, allowing four experimental halls to simultaneously receive electron beams [1]. This paper describes the main elements of the injector relevant to the longitudinal beam dynamics, and bunch length measurement methods and gives the results of such measurements.

BASIC DESCRIPTION

General Layout

Figure 1 is a schematic representation of the general layout of the CEBAF injector, showing the elements related to bunching and timing of the beam. The elements are the 130 kV photo-cathode gun where the beams are created, a 1497 MHz pre-buncher cavity where some bunching is provided when the current is high, a 499 MHz chopper system, a 1497 MHz buncher cavity where the main bunching starts, a 1497 MHz capture cavity, which accelerates the beam to 500 keV, and two 1497 MHz superconducting cavities (SRF) where some bunching is performed and the beams are accelerated to 5 MeV. Finally two 1497 MHz cryomodules

accelerate the beams to a final energy of 123 MeV before injection to the first linac.

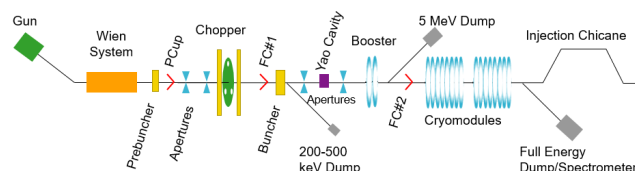


Figure 1: A schematic representation of the CEBAF injector at Jefferson Lab.

CEBAF RF Chopper and Faraday Cup

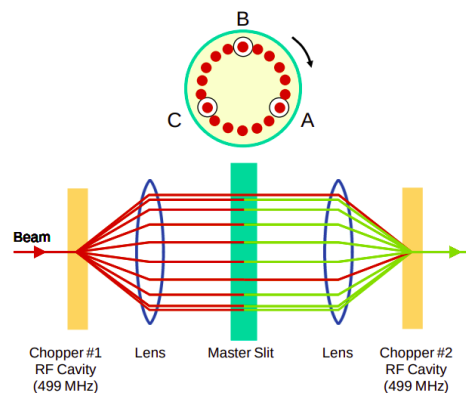


Figure 2: Schematic of the CEBAF three beam chopping systems containing two 499 MHz RF chopper cavities, two solenoid lenses, and a master slit [2].

The four beams are produced at the same spot on the cathode using four independent laser beams. The time structure of the beams originating from the gun is the same as the time structure of the laser light. Each laser micro-pulse frequency is either 499 MHz or 249.5 MHz, ~ 50 ps full width at half maximum (FWHM), however the lower rep rate of the gain-switched laser is somewhat longer. Figure 2 shows a schematic of the three beam chopping system showing possible trajectories of an electron beam. The beams from the 130 kV photo-cathode pass through two 499 MHz RF Chopper cavities with two solenoid lenses and a master slit in between is shown in Fig. 2 [2]. The distance between the gun and the chopping system is about 7.6 meters. The beam enters the first RF chopper cavity and is deflected by transverse magnetic fields along a cone whose apex is at

* Work supported by U.S. DOE, Office of Science, Office of Nuclear Physics under contract DE-AC05-06OR23177

[†] spokh003@odu.edu

BAYESIAN ALGORITHMS FOR PRACTICAL ACCELERATOR CONTROL AND ADAPTIVE MACHINE LEARNING FOR TIME-VARYING SYSTEMS

A. Scheinker*, Los Alamos National Laboratory, Los Alamos, NM 87544, USA
R. Roussel†, SLAC National Accelerator Laboratory, Menlo Park, CA 94025, USA

Abstract

Particle accelerators are complicated machines with thousands of coupled time varying components. The electromagnetic fields of accelerator devices such as magnets and RF cavities drift and are uncertain due to external disturbances, vibrations, temperature changes, and hysteresis. Accelerated charged particle beams are complex objects with 6D phase space dynamics governed by collective effects such as space charge forces, coherent synchrotron radiation, and whose initial phase space distributions change in unexpected and difficult to measure ways. This two-part tutorial presents recent developments in Bayesian methods and adaptive machine learning (ML) techniques for accelerators. Part 1: We introduce Bayesian control algorithms, and we describe how these algorithms can be customized to solve practical accelerator specific problems, including online characterization and optimization. Part 2: We give an overview of adaptive ML (AML) combining adaptive model-independent feedback within physics-informed ML architectures to make ML tools robust to time-variation (distribution shift) and to enable their use further beyond the span of the training data without relying on re-training.

INTRODUCTION

Particle accelerators are large complex systems whose beams evolve according to dynamics governed by nonlinear collective effects such as space charge forces and coherent synchrotron radiation. Because of their complexity, the control of charged particle beams in accelerators and diagnostics of these beams can greatly benefit from the application of machine learning (ML) [1, 2] methods and advanced control theory techniques [3].

The development of ML-based tools for particle accelerator applications is an active area of research. At CERN, supervised learning techniques are being applied for the reconstruction of magnet errors in the incredibly large (thousands of magnets) LHC lattice [4]. At the LCLS, Bayesian methods have been developed for online accelerator tuning [5], Bayesian methods with safety constraints are being developed at the SwissFEL and the High-Intensity Proton Accelerator at PSI [6], at SLAC Bayesian methods are being developed for the challenging problem of hysteresis [7] and surrogate models are being developed for the beam at the injector [8], and at LANL researchers have been developing methods to combine neural networks with model-independent adaptive feedback for automatic control of the

(z, E) longitudinal phase space (LPS) of intense short electron beams [9]. Convolutional neural networks (CNN) have been used to generate incredibly high resolution virtual diagnostics of the LPS of the electron beam in the EuXFEL [10]. A laser plasma wakefield accelerator has also been optimized by utilizing Gaussian processes at the Central Laser Facility [11].

In this tutorial we give a brief introduction to some machine learning methods including neural networks, Bayesian algorithms, and adaptive feedback.

BAYESIAN METHODS

Bayesian optimization (BO) [12] is a model based optimization method that is well suited for online accelerator control problems [13–15]. BO consists of three components, shown in Fig. 1, a Bayesian statistical model of the objective function known as a Gaussian process (GP) [16], an acquisition function which characterizes the value of making potential observations and a numerical optimizer that optimizes the acquisition function to pick the highest valued point. This method excels at optimizing functions that are expensive to evaluate (such as quadrupole scan emittance measurements) because GP models provide uncertainty information when making predictions, allowing BO to balance exploration and exploitation when searching for global optima. Furthermore, GP models used in BO explicitly model noisy systems such as accelerators, making optimization less sensitive to jitter relative to other black box optimization algorithms.

Bayesian inference is the process of systematically updating prior statistical beliefs in the presence of experimental measurements. Imagine a parametric model $y = f(\mathbf{x}; \theta)$, where we have collected training data pairs $D = \{X, \mathbf{y}\}$ and θ parameterized the model. Bayes rule applied to determining model parameters is given by

$$p(\theta|X, \mathbf{y}) = \frac{p(\mathbf{y}|X, \theta)p(\theta)}{p(X, \mathbf{y})} \quad (1)$$

where $p(\theta)$ represents the *prior*, $p(\mathbf{y}|X, \theta)$ is the *likelihood* or *evidence*, $p(\theta|X, \mathbf{y})$ is the *posterior* and $p(X, \mathbf{y})$ is the *marginal likelihood* and $p(\cdot|\cdot)$ denotes a conditional probability. Bayes rule is useful in fitting model parameters due to the weighting of a prior distribution which regularizes predictive values of model versus the strength of experimental evidence. In the case of a uniform prior (no prior information is known) and a Gaussian likelihood (Gaussian statistical noise) Bayes rule reduces to non-linear least squares regression. Gaussian processes use Bayes' rule to predict objective function values based on approximate prior knowledge of

* ascheink@lanl.gov

† rroussel@slac.stanford.edu